Multi-mode atomic force microscope as a versatile tool for bionanotechnology

Philipps University of Marburg

Fang Yang

2016

Marburg an der Lahn

Multi-mode atomic force microscope as a versatile tool for bionanotechnology

Dissertation

zur Erlangung des Doktorgrades

der Naturwissenschaften

(Dr. rer. nat.)

dem

Fachbereich Chemie

der Philipps-Marburg Universität

vorgelegt von
Fang Yang

Marburg, 2016

Vom Fachbereich Chemie der Philipps-Marburg Universität als Dissertation angenommen am:

Erstgutachter: Prof. Dr. Norbert Hampp

Zweitgutachter: Prof. Dr. Wolfgang Parak

Prüfer: Prof. Dr. Norbert Hampp

Prüfer: Prof. Dr. Wolfgang Parak

Prüfer: Prof. Dr. Lars-Oliver Essen

Tag der mündlichen Prüfung: 09. November. 2016

Fang Yang

Universitätsstraße, 47

35037 Marburg

Deutschland

Email: yangfa@staff.uni-marburg.de; dongbeihu_wh@hotmail.com

Phone: (0)49-015772702227

Table of Contents

Zusammenfassung

Der Kern dieser Arbeit ist die Multi-Mode-Rasterkraftmikroskopie, die ein nützliches und leistungsfähiges Werkzeug zur Charakterisierung von Proben im Mikro- und Nanogrößenbereich darstellt. Verschiedene Modi können spezifizierte Anforderungen verschiedener Proben erfüllen, wie u.a. Messung der Topographie, des elektrostatischen Potentials der Oberfläche, magnetische Domänen, einzelne molekulare Kraftanalyse und Echtzeit-Monitoring-System. Dabei kann in Luft, Flüssigkeit und im Vakuum gemessen werden. Das macht das Rasterkraftmikroskop (AFM) zu einem flexiblen, universellen Werkzeug für die biologische Nanowelt. Die Themen bestehen aus unterschiedlichen Arbeitsweisen in Richtung biologische Anwendungen mit Multi-Mode-Rasterkraftmikroskopie.

Zuerst wurde anhand quantitativer, topographischer Messungen die Zellmorphologie und Oberflächenveränderungen nach Aufnahme verschiedener Nanopartikel beobachtet. Bei konzentrationsabhängigen Experimenten konnte das Volumen und die Anzahl von Filopodien anhand der topologischen AFM-Aufnahmen berechnet werden. Dadurch wurde bestätigt, dass die zelluläre Morphologie eine wichtige Rolle für die quantitative Angabe schädlicher Auswirkungen durch Nanopartikel auf Zellen spielt. Zusätzlich wurden die Nanopartikel enthaltenen Zellen einem rotierenden Magnetfeld ausgesetzt und anschließend ihre Oberfläche erneut vermessen. Die Rauigkeit der Zelloberflächen, die aus Störungen der Zellmembranintegrität resultierte, wurde für die Untersuchung von magneto-Zell-Porenbildung und magneto-Zell-Analyse herangezogen.

Als weiterer Teil dieser Arbeit wurden durch Einzelmolekülkraftspektroskopie an Goldnanopartikeln (AuNP) mit verschiedenen Durchmessern, die mit Polyethylenglykol (PEG) unterschiedlicher Dicke beschichtet waren, Elastizitätsmessungen durchgeführt. Hierzu wurde mit einer konischen Spitze auf die Nanopartikel gedrückt und die Auslenkung der Spitze in Funktion ihrer vertikalen Position gemessen. Zur Berechnung der Elastizität wurde die Sneddon-Gleichung genutzt. Die Elastizität dient als eine der grundlegenden physikalisch-chemischen Parameter der Beschreibung struktureller und funktioneller Zellparameter.

Im dritten Teil dieser Arbeit wurden superparamagnetische Eisendioxid (Fe_3O_4)–Nanopartikel mit Tetradine beschichtet (co-geladene NP) und in Zellen internalisiert. Anschließend wurden die magnetischen Eigenschaften dieser Zellen mit AFM gemessen. Die beobachteten magnetischen Domänen waren den Fe_3O_4-Nanopartikeln zuzuordnen. Diese Nanopartikel können durch ihre magnetische Eigenschaft zur Ablation von Tumorzellen verwendet werden, sodass verbesserte Anti-Krebs-NP realisiert werden können.

Im nächsten Teil dieser Arbeit wurde das elektrostatische Potential der Oberfläche einer mutierten Purpurmembran (PM), die durch funktionelle Nanopartikel modifiziert war, anhand elektrostatischer Kraftmikroskopie (EFM) mit der AFM gemessen. Dazu wurde eine Spannung zwischen einer leitenden, oszillierenden Spitze und der modifizierten PM angelegt. Die Spitze wurde in einem vertikalen Offset zur Probe so angehoben, dass sie eine langfristige elektrostatische Kraft ohne Wirkung der molekularen Abstoßungskraft ausüben konnte. Aus der Phasenverschiebung der Oszillation der Spitze bei einer bestimmten Frequenz wurde das EFM-

Signal extrahiert und zur Charakterisierung der elektrostatischen Eigenschaften dieser neuartigen Biomembran herangezogen.

Im letzten Teil dieser Arbeit wurde ein System zur Beobachtung der Lebendigkeit von Zellen in Echtzeit entwickelt. Dieses System basiert auf Zelladhäsionseigenschaften in Zusammenspiel mit dem Schwingungssystem des AFM. Die Amplitude eines bei einer definierten Frequenz schwingenden Cantilevers ist stark abhängig von dessen Masse. Durch Aufbringen von Zellen auf den Cantilever konnte die Gesamtmasse des Cantilevers erhöht werden, somit stieg auch die Amplitude der Schwingung. Nach Apoptose ließ die Zellhaftung stark nach und die Amplitude sank wieder. So konnte die toxische Wirkung verschiedener Substanzen auf die Vitalität der Zellen in Echtzeit aufgenommen und quantitativ beschrieben werden.

Abstract

The kernel of this dissertation is multi-mode atomic force microscopy (AFM) which is a useful and powerful tool for characterizing and analyzing samples of nano- or micro size. Various modes can satisfy specified requirements according to different samples, i.e., topography, surface electrostatic potential, magnetic domain visual observation, single molecular force analysis and a novel real-time monitoring cell viability system based on modification of AFM. No matter whether samples are in air or in liquid, topological image can be realized. Hence, the flexibility makes AFM a universal tool for exploring the biological nano-world. The subjects consist of different working modes towards biological applications.

Firstly, topography is aimed at quantitative analysis of cellular morphology and surface changes, which are effected by uptake of nanoparticles. In the case of concentration-dependent experiments, the volume and number of filopodia is calculated by analyzing topological images of AFM. It is verified that cellular morphology plays an important role for quantitative indicating of harmful effects of NPs to cells. In addition, the roughness of the cellular surface which derives from disruption of cell membrane integrity, when the cells internalized magnetic NPs subjected to a rotating magnetic field, is evaluated for exploring magneto-cell-poration and magneto-cell-analysis.

Secondly, single molecule force microscopy is aimed at quantitative analysis of elasticity of gold nanoparticles (Au NPs), which are coated with polyethylene glycol (PEG), whereby the diameter of the gold cores as well as the thickness of the shell of PEG was varied. A conical tip indent into single NP and then Sneddon's equation is employed for calculating the elasticity, which serves

as one of the basic physicochemical parameters having effect on structural and functional cell parameters.

Thirdly, magnetic force microscopy is aimed at qualitative visual observation of magnetic domains of the sample, which is a multifunctional co-loading NP with anti-drug tetradine and superparamagnetic iron dioxide (Fe_3O_4) NPs. The magnetic domains of co-loading NPs, which is reflected in phase section, can present magnetic profile which is attributed to the Fe_3O_4 NPs. Thus such multifunctional co-loading NPs are further used for magnetic ablation to tumor cells, so that a dual enhanced anti-cancer NP can be successfully realized.

Fourthly, electrostatic force microscopy (EFM) is aimed at qualitative visual observation of electrostatic potential on surface of the sample, which is a mutant purple membrane (PM) modified by functional NPs. A bias voltage between a conductive tip and the modified PM is applied in an oscillating mode. The tip is lifted such that it can induce a long term electrostatic force without effect of molecular repulsive force. Thus electric gradient dependent on surface of the PM makes phase shift in a given frequency and then the EFM signal is extracted. Therefore, the electric property of such a novel biomembrane is characterized.

Fifthly, a generally applicable quantitative real-time cell viability monitoring system which uses cell adhesion property is successfully setup based on the oscillation system of AFM. The amplitude of an oscillating cantilever at a given frequency is highly dependent on the mass of the cantilever, in this situation, the mass of attached cells on the cantilever. In our method, the dynamic toxic process can be observed and recorded, and can be analyzed even at an early stage of intoxication. Therefore, this will be a greatly promising method for real-time exploring and quantitatively analyzing of cellular toxicity.

Introduction

Multi-mode atomic force microscope

Since its revolutionary invention by Gerd Binnig of IBM research center in 1986[1], atomic force microscopy has become one powerful tool in nanotechnology. As precursor of AFM, the STM was wildly used for surface imaging of conductive samples. However the invention of AFM breaks through the limitation and brings nano-scale observation into a non-conductive area. According to interaction between sample surface and a tip doped on the end of a cantilever, AFM can topologically characterize specimen surfaces which are even not conductive.

While a cantilever is approaching a sample surface, the force between atoms of the sample and the tip leads to a deflection of the cantilever according to Hooke's law. Because of AFM employing a laser beam deflection for force deflection, the vertical deflection of the cantilever from the equilibrium position on the surface can be recorded by laser irradiation. This laser is directly radiated on the top of the cantilever and reflected to a photodiode which transfers the optical signal to a digital signal. The position of the laser signal on the photodiode is determined by a voltage difference and measured in volts. It is useful to indicate the deflection of the cantilever in nanometers. The deflection is directly proportional to the change in measured signal on the photodiode. The proportionality factor is called deflection sensitivity ("Deflection Sensitivity", DS, [nm / V]). It is dependent on the position of the cantilever and thus of the laser, as well as of the orientation of the mirror and the refraction of the medium surrounding the cantilever. The DS has to be determined after each change in the alignment of the laser, the mirror or the cantilever. Hence, after further digital analysis a topological image of the sample surface can be characterized. After laser detector accepted the feedback signal, a piezo-element gives a feedback to the scanner in order to regulate the cantilever for keeping equilibrium (see scheme I). The piezo-element consists of a special

mechanical sensitive crystal and some electrodes for reflecting electric feedback by mechanical activation. When a dielectric is subjected to an external force in a certain direction, the inner dipole moment will be changed and it will induce internal polarization. Therefore an electric tension will be in occurrence. In addition this phenomenon can be reversed as electric tension change caused piezo-element deformation. In AFM scanner the piezo-element regulates the x-, y- and y- position of the probe for keeping equilibrium on the sample.

Atomic force microscopy utilizes Van der Waals force between atoms or atomic groups for characterization of the sample surface. Therefore the resolution is much higher than with light microscopes: it is up to 5~10 Å vertically and ~300 Å laterally. Hence, an object of nano-meter size can be clearly observed. Another advantage is the ability to measure samples in liquids and any atmospheres. It is very important for the measurements of biochemical samples like polymers, lipids, proteins, DNA and cell which need harsh environment. Minko et.al probed conformation of adsorbed flexible polyelectrolyte chains based on AFM 3D images[2]. Unsay et.al utilized AFM for imaging and supporting lipid layers[3]. In addition Hamon et.al used high-resolution AFM for imaging DNA complexes[4] and Lyubchenko et.al described protein-DNA by topography[5]. AFM can measure any samples of different physical properties, no matter whether they are conductive or non-conductive, stiff or soft, and flat or rough. Thus, due to such flexibility AFM serves as not only a universal tool for exterior characterization but also a useful tool for biological applications.

With rapid development of nanotechnology more and more novel materials can be further modified and characterized by different physical analysis. A multi mode AFM is such a versatile tool that among all applications it allows researchers to reveal mechanical, magnetic and electrical properties as well as the structuring of surfaces through to positioning and operating an individual atom

etc. Some scientists demonstrated single molecule operation, unfolding protein based on single molecule force spectroscopy (SMFS), whereby the adhesion property of a DNA string[6] and the binding force of a polymer to a substrate[7] were investigated. In addition multi functional sub nano-substrates were observed for magnetic domains based on magnetic force microscopy (MFM)[8, 9] and the electrostatic potential distribution of the sample surface was presented via electrostatic force microscopy (EFM)[10]. Thus the multi mode AFM reveals a promising method for characterizing and exploring nano-sized subjects.

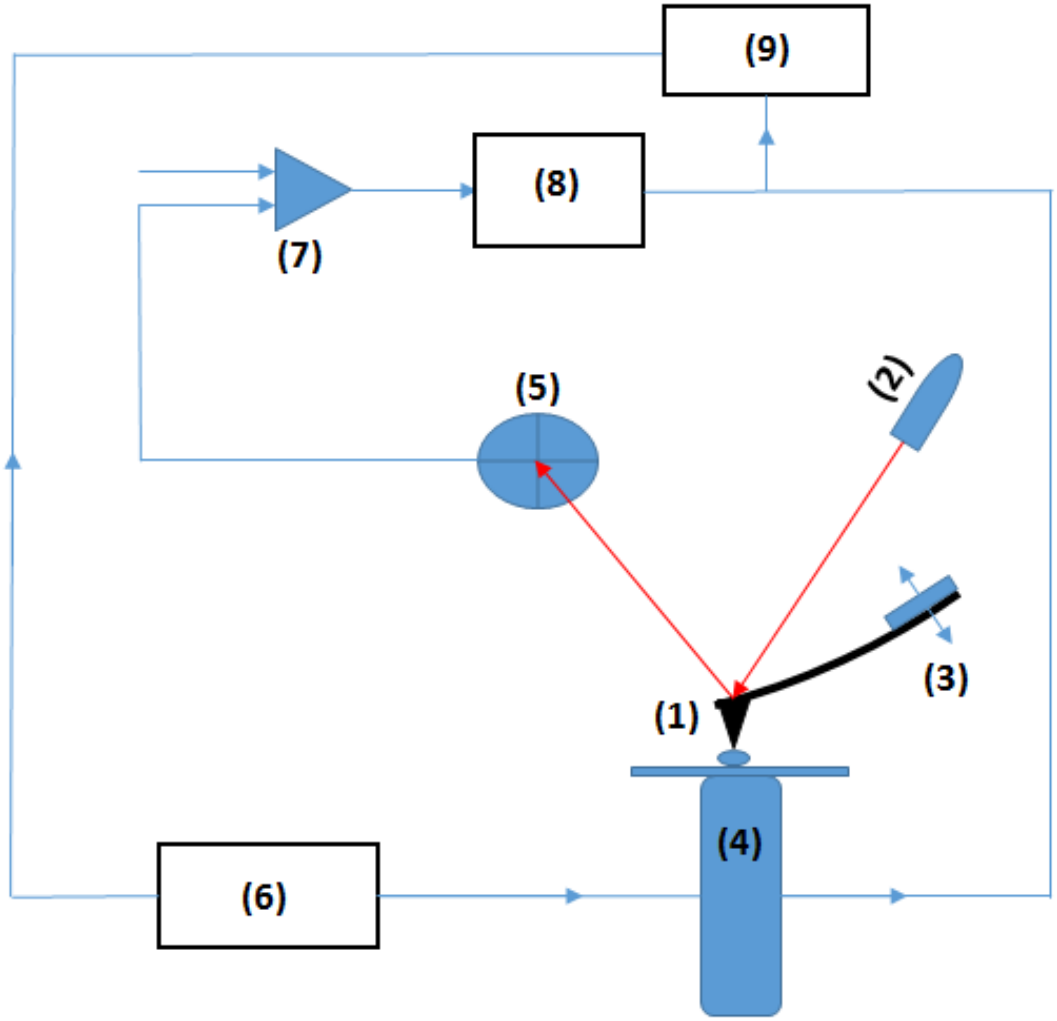

Scheme I: Typical configuration of an atomic force microscope. (1) Cantilever (2) The modulated laser light from a laser beam (3) Piezo-element for oscillating cantilever at a given frequency (4) Piezo-

element for driving the cantilever and sample in x-, y- and z- direction. (5) Photodiode as a detector for reflecting laser light from the top of cantilever (6) Scanning signal analyzer for treating and calculating electric signal (7) Signal multiplier for extending electric signal from photodiode and position –sensitive detector (8) Feedback controller for analysis of electric signal and adjusting x-, y- z-piezo-element (9) computer for imaging

Functional nanoparticles

With the progress of science and technology developing rapidly, a lot of new materials appear for further applications involving nanotechnology and nanomedicine. The materials of nanometer size draw the attention of many people, because of their special physico-chemical properties and great promise in development of new nano-devices. Some of them inspired many areas which may involve our daily life as well as biomedical applications[11, 12]. In this introduction a focus will be set on functional nanoparticles (NPs) which have physico-chemical properties and great potential use for further biomedical applications. In fact, given the thriving investigative and industrial interest calls, the functional NPs emergence serves as a key for unsolved scientific and technical problems. Hence, some efforts in trying to synthesize and functionalize NPs have been made to keep up with the pace to rapid development. Nowadays, a lot of NPs with different materials, sizes, shapes, organic ligands and functional binding molecules have been obtained by means of chemical and physical approaches. In addition, more characterization methods exist to measure and analyze their properties, so that we can study the NPs. Compared to bulk materials[13] the NPs have quite special and different physico- chemical properties, which are mainly reflected in such aspects: optical-, electrostatic- , magnetic-, and mechanical properties.

As one of the most commonly used metallic NPs, Au NP are wildly used in the field of nanotechnology. The importance can be attributed to its stability and physico-chemical properties as well as the unique optical properties. For instance, a bulk gold (Au) appears golden but a bottle of spherical Au NPs solution appears red in figure I. That is because the Au NPs (<50 nm) strongly absorb light of a certain wavelength (~ca. 520nm), while the excitation light is shooting at the core of Au NP. Due to energy activation the electron clouds of its surface are oscillating to be a plasmon that interacts strongly with light resulting in a polariton. In this case, the oscillation of the Plasmon is resonated with light frequency and then causes a loss of energy known as surface plasmon resonance. The resonance is even enhanced and localized known as localized surface plasmon resonance (LSPR). This phenomenon occurs in the order of magnitude of the mean free path of electrons to downscaling of the NPs. Therefore, if the Au NPs have the diameters between 3 nm-100 nm, this coupling occurs in 390 nm-1400 nm and the LSPR effect shift to the red region with increasing diameter. In addition, local dielectric environment plays an important role as well, thus by adsorption of molecules onto the surface of NPs, the surface enhanced raman scattering occurs as well. According to figure 1, the suspension with Au NPs of smaller size is red and the suspension of Au NPs of biggest size is purple. If the size of Au NPs is even smaller than 3 nm, due to quantum confinement effect the free path of electrons are restricted and then the LSPR effect disappear. The suspension of the Au NPs will be yellow or brown. Moreover different sizes and shapes, and even binding molecules can lead to a coupling of the electronic wave functions and to more red-shifting of the LSPR. Usually, based on such optical property LSPR spectroscopy, UV/Vis spectroscopy and dynamic light scattering (DLS) are universal methods to characterize the NPs.

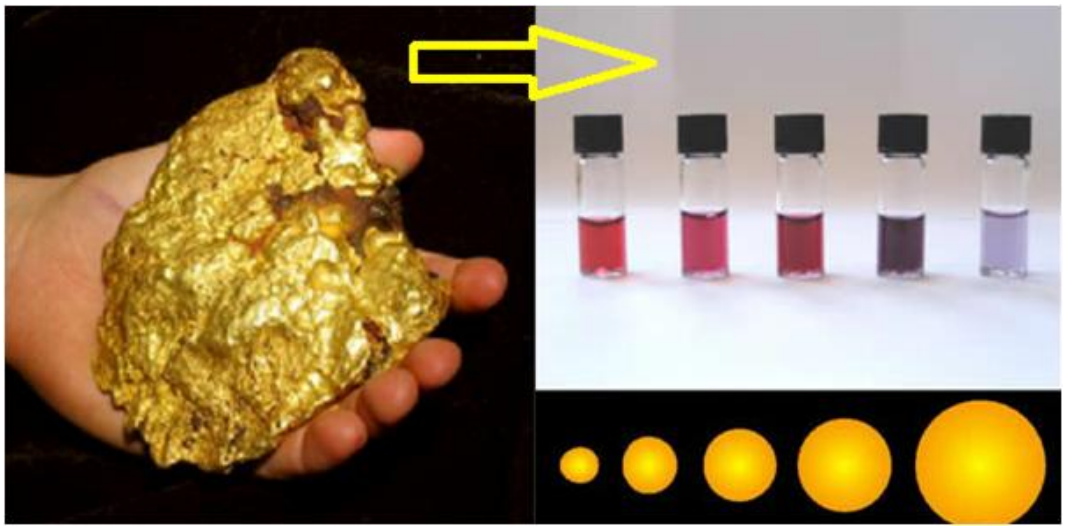

Figure I: Difference between bulk gold (left in a hand) and gold-nanoparticle suspensions with different sizes (right in the bottles) ("size does matter: nano vs microscopic world" news from manuscript Edit homepage).

Au NPs are the most extensively studied NPs and the center of fascination among scientific community not only because of their unique optical property but also their excellent electronic properties. On their surface free electrons under a voltage will easily make an orientated flowing and according to the sensing electric current, the electric properties, such as surface charge density and distribution can be correctly detected utilizing Zeta-potential spectroscopy or electrostatic force microscopy. In addition, a dielectric polarization occurs due to the energetic electron on the surface of the Au NP. Thus conductivity is one of the essential properties for Au NPs. Owing to their excellent conductivity, Au NPs are great promising materials for amplifying biorecognition signals in the area of electrochemical biosensors and they have been used for bioelectronics due to their electron transfer property. Besides the essential electronic properties, the Au NPs have also high potential of surface modification. Many efforts have been devoted to tailor the specific electronic property based on the modified Au NPs conjugated by different

functional molecules or ligands, so that they can provide great potential to design some nano-devices in the field of energy and nanomedicine[14][15].

In order to better understand Au NPs, it is necessary to study their mechanical properties. In particular properties of special interest include stiffness and adhesion. With respect to nanoscale entities, stiffness is called rigidity which is defined as a resistance of a material to deformation in response to an applied force, while adhesion is defined as a tendency to keep substances contacting close together. Quantitative understanding of the stiffness and adhesion is important for improving the design of functional Au NPs and studying modeling of cellular uptake. There are some publications about quantitative stiffness[16] and adhesion[17] of different Au NPs. The results presented that the stiffness and adhesion are dependent on material, size, shape, and chemical conjugations of the Au NPs. With the cellular investigations, the fact is that the mechanical properties are related to interaction between NPs and cells. Therefore, understanding how to quantitatively measure mechanical properties will be helpful for characterizing specific NPs in further biological applications.

Magnetic materials are classified into diamagnetic, paramagnetic including superparamagnetic and ferromagnetic materials according to their susceptibility to magnetic fields. Diamagnetic materials have an opposite magnetic field to an externally applied magnetic field and disappear immediately when the external magnetic field is removed. This non-persist magnetic property occurs in paramagnetic materials as well. On the contrary, in ferromagnetic material the magnetic properties continue even after removing the external magnetic field. The relation of magnetic moment and magnetic field can be clearly shown in their hysteresis loops (figure II). In a certain extent, their magnetic properties promise huge benefits due to size dependence. Therefore, besides Au NPs there is a class of metallic NPs which are commonly used for

magnetic researches and applications. Such NPs are made of highly ordered orientation of magnetic atoms like iron, nickel and cobalt or their chemical compounds. Normally, magnetic material often presents multi-domain structure in order to reduce the energy level of demagnetizing field in the system known as magnetic domain wall. When the size of magnetic material is getting small till to the range of the magnetic single-domain structure, the original crystal periodic boundary condition will be destroyed and some novel effects, such as disordered magnetic orientation and magnetic coercivity decrease as well as the Curie temperature. In this case, the ferromagnetic NPs turn to paramagnetic NPs. However, if the magnetic material is small enough (with nano size), the magnetic NPs are superparamagnetic in room temperature because coercivity disappears. Due to such advanced property, nanometer-sized magnetic NPs have been investigated for characteristic study and used for further biological and nanomedical applications.

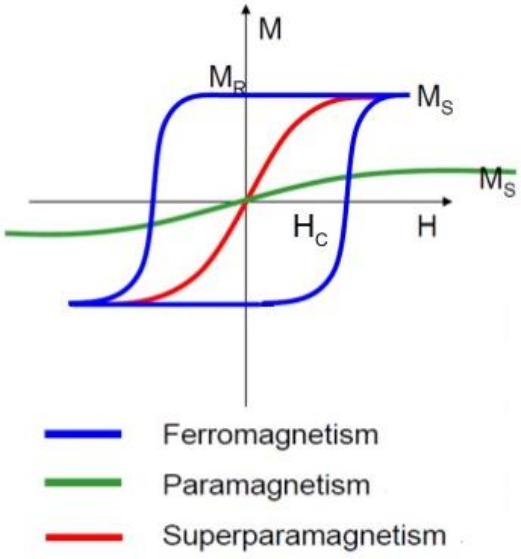

Figure II: Different hysteresis loops. Ferromagnetic state has an open loop with large saturated magnetization Ms, paramagnetic state has no open loop with small saturated magnetization Ms, and superparamagnetic state has no open loop with saturated magnetization Ms.

Biological applications

Nanoparticles are at the leading edge of the rapidly developing field of nanotechnology. Studying and investigating NPs properties is a key to apply them for further biological uses. Their highly favorable properties, i.e., the unique optical and electronic properties and available surface modification of the Au NPs, as well as superparamagnetic property of the magnetic NPs, have led to a series of applications in the biotechnical area which are many including biomarker and biosensor and in biomedical area which are many including therapy and toxicity. As mentioned above, the excellent range of possibilities for tuning optical properties of Au NPs offers a versatile platform to create a biosensor based on a colorimetric assay. Yin et.al pointed out that the colorimetric change is dependent on the pressure loaded on the polymerized Au NPs[[18]]. Concerning sensing mechanical strength, such functional polymerized Au NPs are of particular interest. Another biosensor based on the functional Au NPs for sensing heavy metal ions which are hazardous for human health as well as a big trouble for environment now has been presented by Wu et.al. The functional Au NPs as target were used to detect Hg^{2+}, Pb^{2+} and Cu^{2+} etc which are considered as contaminants for water in China[[19, 20]]. Thus, this easy and effective determination will be wildly used in China with promising sensing capabilities. A biomarker based on Au NPs linked to functional polymers or molecules are successfully synthesized for labeling cells and investigation of the cellular environment. To obtain a water-soluble NP coated by a functional amphiphilic polymer with hydrophilic side (carboxyl group) on the outermost surface is a feasible method[21] till now. This kind of NP offers a great opportunity to conjugate the other functional molecules in order to be an ideal biomarker[[22]]. In addition, as the Au NPs can conjugate the pH sensing molecules, a pH nano-indicator can be used for sensing the cellular environment. For this purpose Parak et.al succeeded in getting a pH

sensitive Au NP and visually detecting the pH inside the cells[23]. Apart from the contributions of Au NPs mentioned above, recently, there has been a great deal of interest in the applications for photothermal cancer therapy. Hyperthermia is known to induce apoptosis of cell death in tissues and has been demonstrated to increase survival in radiotherapy and chemotherapy in clinical trials due to the low thermotolerance of tumor. In order to improve efficiency of the cancer therapy, Au NP serves as an important tool for thermal destruction due to photothermal heating ability. However, the spherical particles with absorption from 510 nm-580 nm for the size from 10 nm-100 nm diameter were not effective for the therapy, because these wavelengths can't penetrate the skin or tissue. Thus, different shapes of the Au NPs have been successfully synthesized for the heating-source under a near-infrared light[24]. Despite these great promising applications, the advantages and innovations of any NPs must be thoroughly compared with their disadvantages and harmful effect, in current situation, toxicity. Before each new NP toward clinical trial, risk assessment to human healthy should be anticipated. Thus, many kinds of biological assay in vitro even in vivo are used for performing the interaction of living cells with NPs and effect of NPs in tissue, in order to determine the toxicity of the NPs[25]. Au NP serves as one of the commonly used nanomaterials. Therefore, a lot of publications presented that the toxicity of Au NPs are correlated to many properties, including stabilities, shapes, sizes, surface charges, concentrations and stiffness. In this thesis, some works about the interaction of cells with the Au NPs and determination of toxicity will be demonstrated in further chapters.

Besides Au NPs, the specific magnetic NPs, due to their excellent superparamagnetic property, were wildly used in biological applications, including drug delivery, biomedical diagnostics and hyperthermal therapy, and biomedical physical-treatment. Normally the delivery of NPs has two different methods: 1. A passive way to tumor tissue: The uptake of NPs by reticuloendothelial

system (RES) 2. An active way to tumor tissue: The uptake of NPs by external factors. However, magnetic NPs are polymerized with anti-cancer drugs and then the co-loaded magnetic polymers gather at the tumor tissue by an external factor, current situation, a magnetic field in order to improve efficiency of drug delivery and drug release[26]. Additionally, the superparamagnetic NPs are usually utilized in biomedical diagnostic[27] like magnetic resonance imaging (MRI) whereby the NPs serve as contrast agent that is bound to the therapeutics[28] and in magnetic hyperthermal therapy whereby the localized NPs are heated in an alternative magnetic field[29]. Moreover, comparing with high magnetic field, the cancerous-cell ablation based on shear force is a reliable promising mechanical therapy in a weak rotating magnetic field[30]. This method offered the opportunities of exploring mechanical effect for cancer therapy. In order to satisfy the needs for development of biological applications, some novel synthetic routes allowing control of the morphology of magnetic NPs, has triggered the interest in hybrid magnetic structures such as bi-magnetic core/shell NPs and ferrite NPs. Among them, An antiferromagnetic core/ ferromagnetic shell NP has been investigated by Nogués et.al[31] and its enhanced magnetic properties have been demonstrated as well. Additionally, Del Pino and Pralle et.al[32] have provided a guide to maximize the hysteretic loss by matching the design and synthesis of the superparamagnetic ferrite NPs for further hyperthermal applications as well as how to model the expected heat loss. These core-shell systems not only combine the properties of the different constituents, but also improve their properties for opening new avenues for innovative biological applications. In this thesis, some specific core/shell magnetic NPs were used for the investigation about the enhancing effect of anti-cancer drugs. More details will be presented in the following chapter.

As the NPs are so frequently used for biological applications and play so important role in development of nanotechnology, finding a normal and universal tool to characterize and assess the risk of NPs is a major subject till now. Multi mode AFM comprising topological mode, electrostatic force observation mode, magnetic force observation mode and single molecule operating mode can be an optimal solution. Besides the high resolution images, non-contact mode can avoid damaging the samples during measurements and the flexibility makes AFM a useful tool for exploring the hydro-world. Till now about 40% of current AFM research is performed in liquids, of which study on biological materials constitutes a high proportion. With importance of NPs applied in biological application multi mode AFM as a rapidly growing and universal tool serves as a key to open the door to bio-nanotechnology. The number of the articles about this topic utilizing multi mode AFM has grown exponentially in the last years. Additionally, the ability of the AFM to achieve high resolution in liquids and to probe the electric property, magnetic property, and mechanical property make this instrument increasingly interesting for the study of nanomaterials and investigation of interaction effect between NPs and cells, tissue even human body. In this case, along with a potential risk for human healthy and the environment, AFM serves as a great tool for describing and analyzing the relation between the physico-chemical properties of the NPs and cells. Moreover, with the strong foundation to build on, a generally applicable quantitative real-time cell viability monitoring system will be successfully set up, based on the oscillation system. This thesis will present some recent investigations to illustrate results in the next part.

Multi-mode atomic force microscope towards characterizations of NPs and biological cells

This chapter is to give an overview of the works in my doctoral study about characterization of NPs and biological cells based on multi mode AFM. Different working modes were used for different projects regarding functional NPs, biological cells and biomembranes. Topological mode towards sample surface and morphology will be discussed in Chapter 3.1. Then chapter 3.2 will be related to single molecule force spectroscopy for calculating force curves and analyzing stiffness. Magnetic force microscopy and electrostatic force microscopy for observation of magnetic domain and surface electrostatic potential distribution will be presented in chapter 3.3 and in chapter 3.4 respectively. At the end a new real-time monitoring system for toxicity assay based on AFM oscillation system will be demonstrated in chapter 3.5.

Topological mode towards biological cells and biomembranes

Topological imaging function is a basic and main working mode in AFM. A sharp tip fixed on the end of a cantilever scans above a surface of sample. The surface can be imaged nondestructively due to Hooke law depending on the spring constant of the cantilever which makes the force and distance linearly. Particularly in contact mode the reflecting force of the cantilever exerting on the sample can be evaluated by deflection with interaction between the tip and sample. Hence, a topological image of the sample is reconstructed via monitoring the records about the deflection. Based on the topological image morphological information can be further analyzed, i.e., roughness, height and surface area. In order to avoid losing any digital data, contact mode with high resolution is used as an effective way for completely observing and investigating a surface.

Nowadays given that colloidal NPs are wildly used for biological and biomedical applications, their harmful effects were presented by biochemical assays or probes from molecular biology like cellular viability, gene expression profiles, etc. However, the harmful effect can be reflected from the morphology of cells as well[33]. As one of essential parameters to decide the morphology of cells, filopodia which is a plasma-membrane mostly containing actin-binding protein plays an important role in cell migration[34]. Just like an antennae, the filopodia can feel and probe the extracellular environment whereby the cells promote the coupling of membrane-bound proteins to the backward flow of actin, in order to produce the pulling force needed for cell migration. The harmful effect of NPs to cells will influence the number and volume of protruding filopodia. Hence, in order to satisfy that the morphology of cells should be monitored in liquid and recorded without lack of any deflection signal, contact mode of AFM is the best option. In this study concentration of NPs was referred to indicate quantitative harmful effects of NPs to cells. Two cell lines (HeLa, Huvecs) were incubated with NPs, respectively. As cell migration plays a crucial role in tumor growth and metastasis, this study is of great interest in preclinical research.

The cells internalized by NPs were imaged with AFM (Nanoscope IV, Vecco, Santa Barbara, CA). A silicon-tip on nitride cantilever (SNL, spring constant k = 0.08 N/m, resonance frequency f = 12-24 kHz, Bruker, Karlsruhe, Germany) was used under contact mode. The scanning process was performed in phosphate buffered saline (PBS) and the deflection set point was adjusted to 0.8 V. Because the cantilever had a low spring constant, meaning that the loading force can be well below the force which would disturb the atoms of cells sites as well as the scanning area was chosen to be 40*40 μm^2 for imaging and scanning angle was set to 90^o, the tip would not scratch the cellular surface but determinate the filopodia correctly.

Resulting images are presented below in figure III. From these images number of filopodia were counted by nAnostic TM method from proprietary algorithms (Serend-ip GmbH, Münster, Germany) as well as total area and height of filopodia, so that the local deviational volume of filopodia V_{filo} can be calculated. Based on figure IV below mean number, total area, average height and total volume of filopodia can be clearly demonstrated.

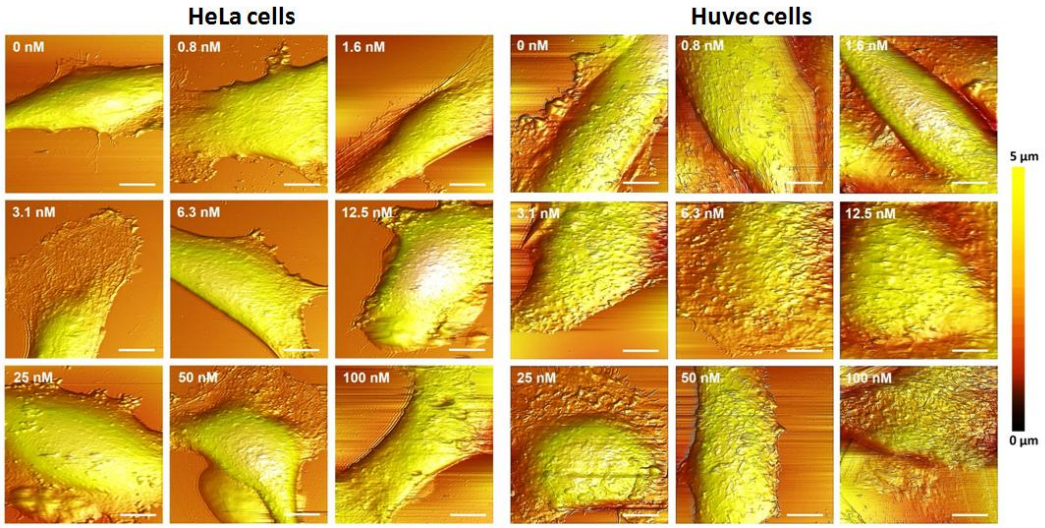

Figure III: Topological images of HeLa cells (left) and Huvec cells (right) in dependence of different concentrations of internalized AuNPs. The scale bar corresponds to 10 µm.

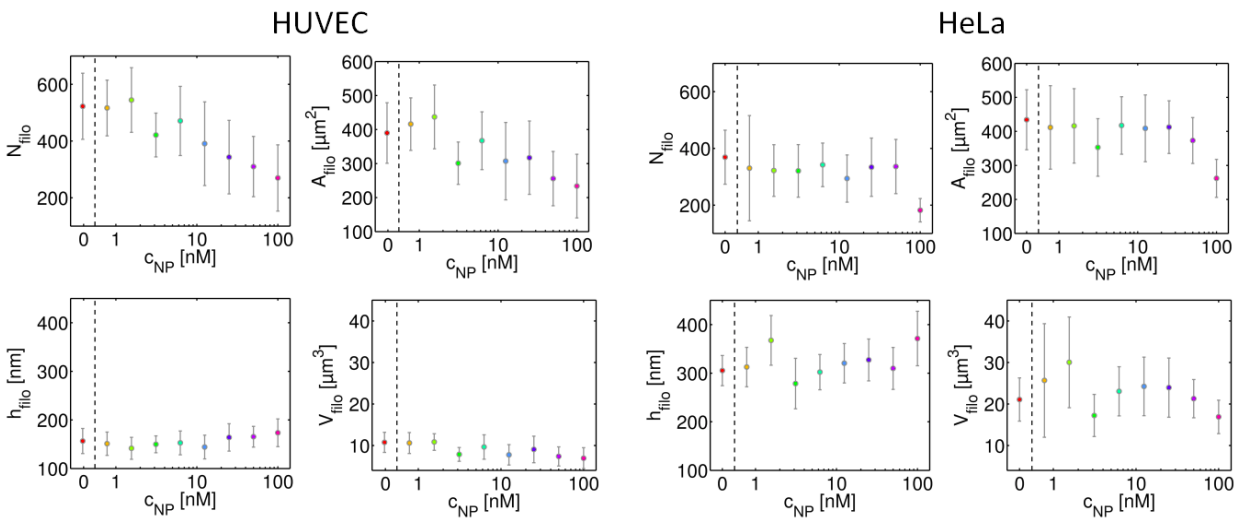

Figure IV: diagrams toward numbers, area, height and volume of filopodia from Huvec cells (left four grids) and HeLa cells (right four grids).

Besides contact mode for topological image, tapping mode based on the cantilever oscillating above the sample is also used to characterize biological material. The principal advantage of this method is the reduction of lateral forces which may adsorb and damage the sample. Virtually this mode without any "touching" and adhesion force is now becoming the most useful method for biological samples in air and liquid.

Purple membrane is a natural membrane with the functional and only protein bacteriorhodopsin (BR) which converts light energy into chemical energy via light-driven proton pump across the membrane. PM as a promising material comprises lipids (25%) and BR (75%) an integral functional membrane protein which contains a trimer forming a hexagonal two dimensional crystalline lattice. The retinal, embedded in the BR, can change conformation when absorbing light (ca.570 nm), which converts light energy into chemical energy via light-driven proton pump across the membrane. Owing to the special photonic characteristic, the BR has photochromism, photoelectrism, photoreaction and photosynthesis properties. Therefore, PMs

have been widely used for assembly and modification of biological systems and optical storage and security systems. In addition, BR features 7-alpha helix domains consists of amino acids chain impenetrate into lipid bilayer embedded in freely spanning PM. The unfolding of secondary structure offers great opportunity for functional and formal modification, whereas the specific amino acids in terminal can conjugate the chemical molecules. Thus, genetic modification of wild-type PM is applied to induce mutation of amino acids, in order to obtain the mutant PM which has enough specific amino acids on terminal of the chain. In particular, functional NPs were covered on the top side of the genetic mutant of wild-type PM which has specific amino acids on the surface, so that a biomineral protein membrane can be imaged by tapping mode[35]. Herein, silica NPs were growing on the top of Arginine7-mutant PM, bearing a hepta-Arg sequence in the C-terminus depending on the concentration. The topological pictures of AFM with height analysis are presented in figure V.

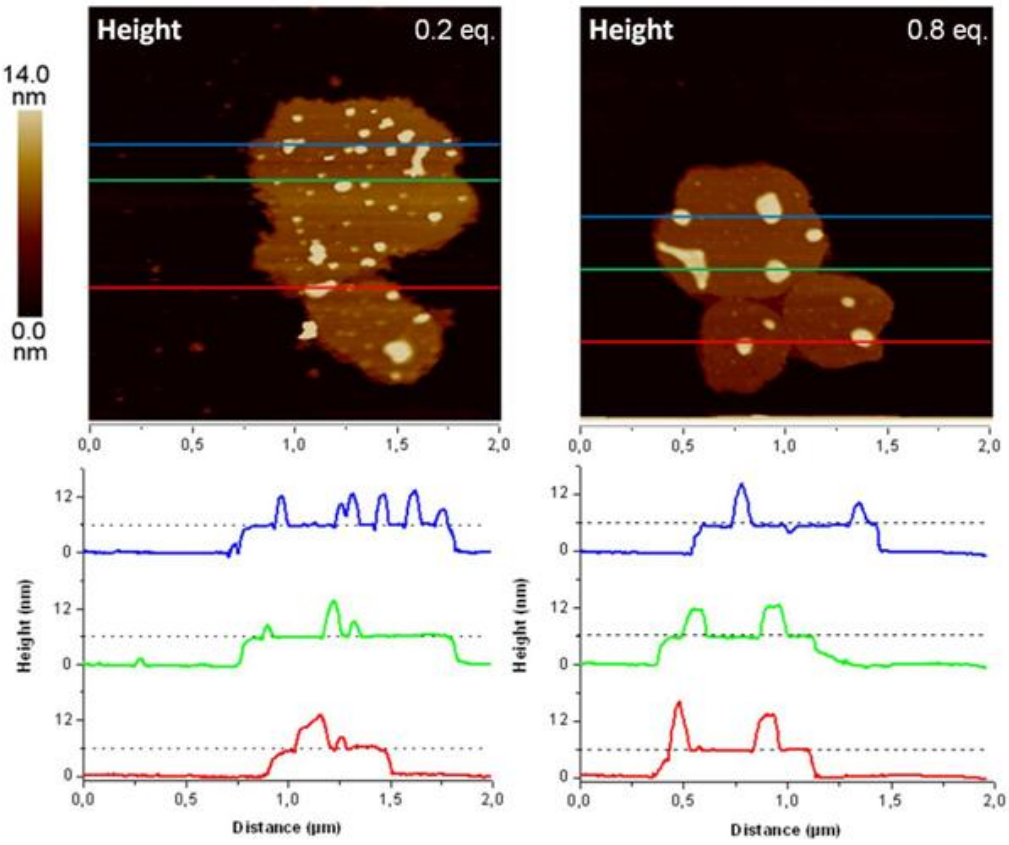

Figure V: Topography of Arginine7-mutant PM with attached silica nanoparticles and nanoisland as well as height diagrams for describing thickness of the PM and the nano objects.

Single molecule force spectroscopy to determine the stiffness of gold nanoparticles for biological effect

Nanoparticles, which serve as one of the most important ingredients in nanotechnology, offer great opportunities to construct novel compounds for many different applications, i.e., electrical devices, solar cells, biomedical therapy and so on. In biomedical areas in which, firstly, the functional NPs should bear a potential risk for human healthy. Therefore, each new class of NPs must be compared against the risk by some biological assay, so that the use of the functional NPs holds enormous promise. In line with the evaluations of the assay, the basic physico-chemical

properties of NPs including hydro stability[36], catalytic activity[37], zeta-potential[38], elasticity are intrinsic parameters for influencing toxicity and biological effects[16, 39]. The outmost chemical molecules of the NPs provide colloidal stability due to hydrophobic and hydrophilic non compatibility and electrostatic repulsion whereby particles agglomeration occurs only if the primary minimum is located at lower distance and indicates a state where two NPs are irreversibly fused[40]. Moreover, it is easy to estimate the diameter in vacuum by statistical calculation under transmission electron microscope (TEM) and also detect the hydrodynamic diameter by dynamic light scattering spectroscopy (DLS). In addition, the shape can be observed by TEM, and AFM and surface charge can be determined by Laser Doppler Anemometry (LDA). But as a primary important parameter, stiffness always serves as a key for completely understanding NP's physical property that influences cells uptake and toxicity. In the course of this, it is necessary to find a useful and accurate tool for detecting stiffness. Recently, a novel qualitative method was demonstrated for distinction of stiff NPs and soft NPs, in which the soft zwitterionic nanogels can pass through physiological barriers, in this situation, the splenic filtration, easier than the stiffer one, in order to avoid splenic accumulations and extend circulation half-life[41]. However, we still need a tool or method for quantitative calculation and analysis of stiffness. Hence, SMFS is to satisfy this problem.

In order to quantitatively explain the correlation between the basic physico-chemical properties and biological influences, a homogenous library of PEGylated Au NPs was synthesized. The Au NPs were successfully prepared and characterized for TEM-size (in figure VI), hydrophilicity, absorption, zeta-potential and catalytic activity. Additionally, the Au NPs with different core size and different PEG coating have the same hydrodynamic size (see scheme II), in order to demonstrate physicochemical properties highly dependent on polymer thick.

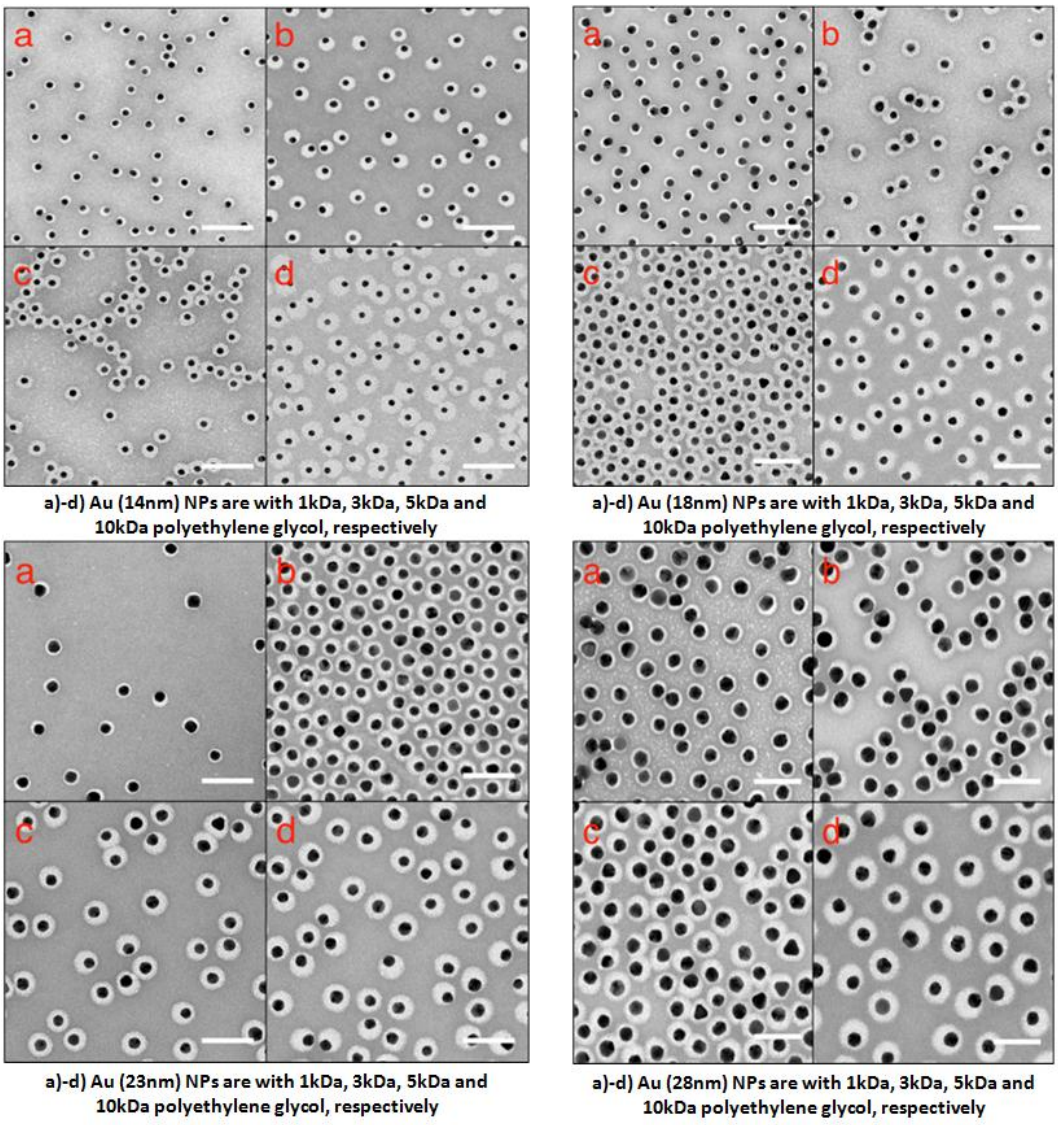

Figure VII: selected negative staining TEM images of the PEGylated Au NPs. Scale bar corresponds to 100 nm.

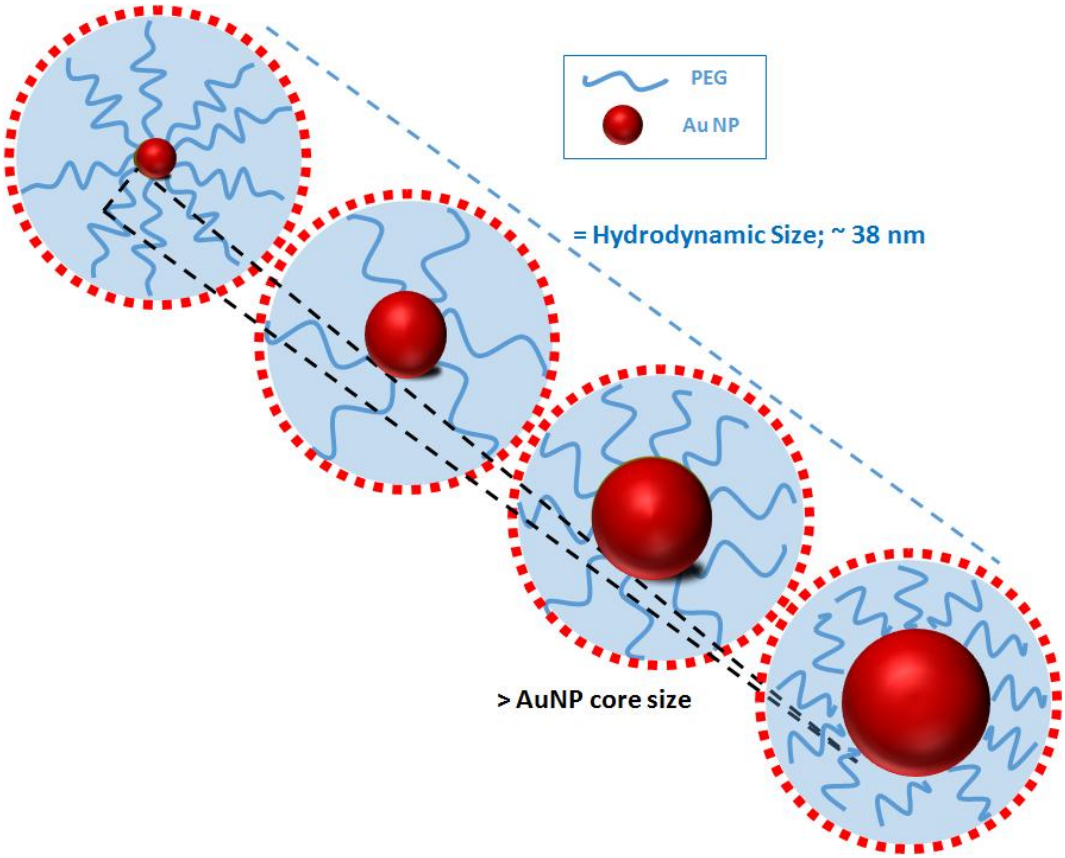

Scheme II: Different Au NPs have the same hydrodynamic size via coating with the different PEG. The hydrodynamic size is ca.38 nm .

For the measurements of stiffness, experimental process and results will be presented below: All the solutions were diluted 10 times to avoid aggregation and then were dropped on 1*1 cm piece of stainless steel which has a smooth surface (roughness ca.1nm). All stainless steel patches were cleaned with aceton and chloroform and then kept drying at 18 ^{o}C in vacuum. After dropping it is necessary to wait 20-30 minutes till the NPs submerged onto the bottom of the substrate. For imaging and location of NPs on the substrate the measurements (see figure VII) were performed using a JEOL JSM-7500F high resolution SEM which is equipped with a backscattered electron detector (Y1Si2O7: Ce^{3+}; Yttrium Aluminum Garnet activated by Ce^{3+}, Autrata, Czech Republic).

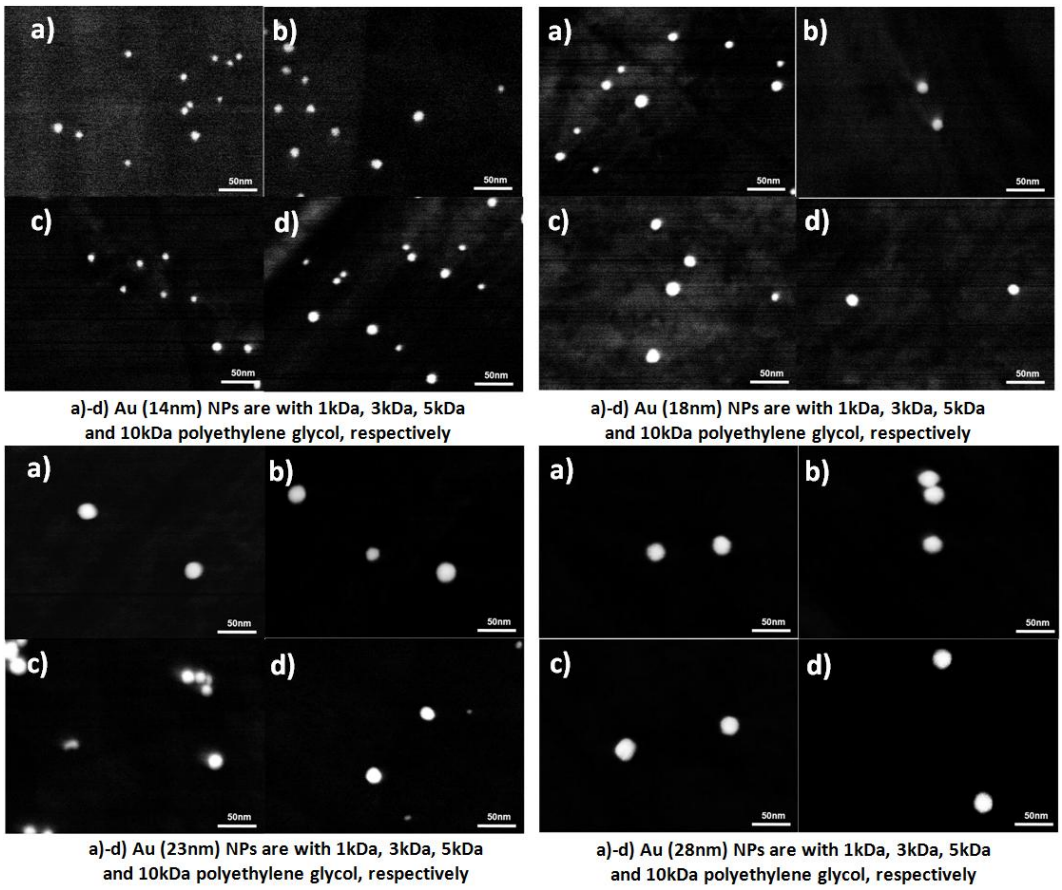

Figure VII: Selected AFM topological images of the PEGylated Au NPs. Scale bar corresponds to 50 nm.

Considering that interaction of water content in PEG can influence the results of stiffness all the samples were measured in water and in vacuum (water content lower than 2%). After submerging process all the samples can be calculated directly under AFM with water. For measurements in vacuum, all the samples were dried naturally for 8 hours till the water disappeared in order to make NPs dispersed on the substrate. After treating in vacuum for 1 hour the sample measured with AFM immediately. This process was followed one by one due to water interference. Multi-mode IV (Veeco, Santa Barbara, CA) atomic force microscopy was chosen for measurements. The topological images (see figure VIII) were performed using Tapping Mode (TM) with constant amplitude attenuation. The cantilever approach (Silicon-tip

on nitride lever, k = 0.32 N/m, f = 40-75 kHz) was utilized with an initial drive amplitude of 0.499 V (tip oscillation amplitude 1.5 V).

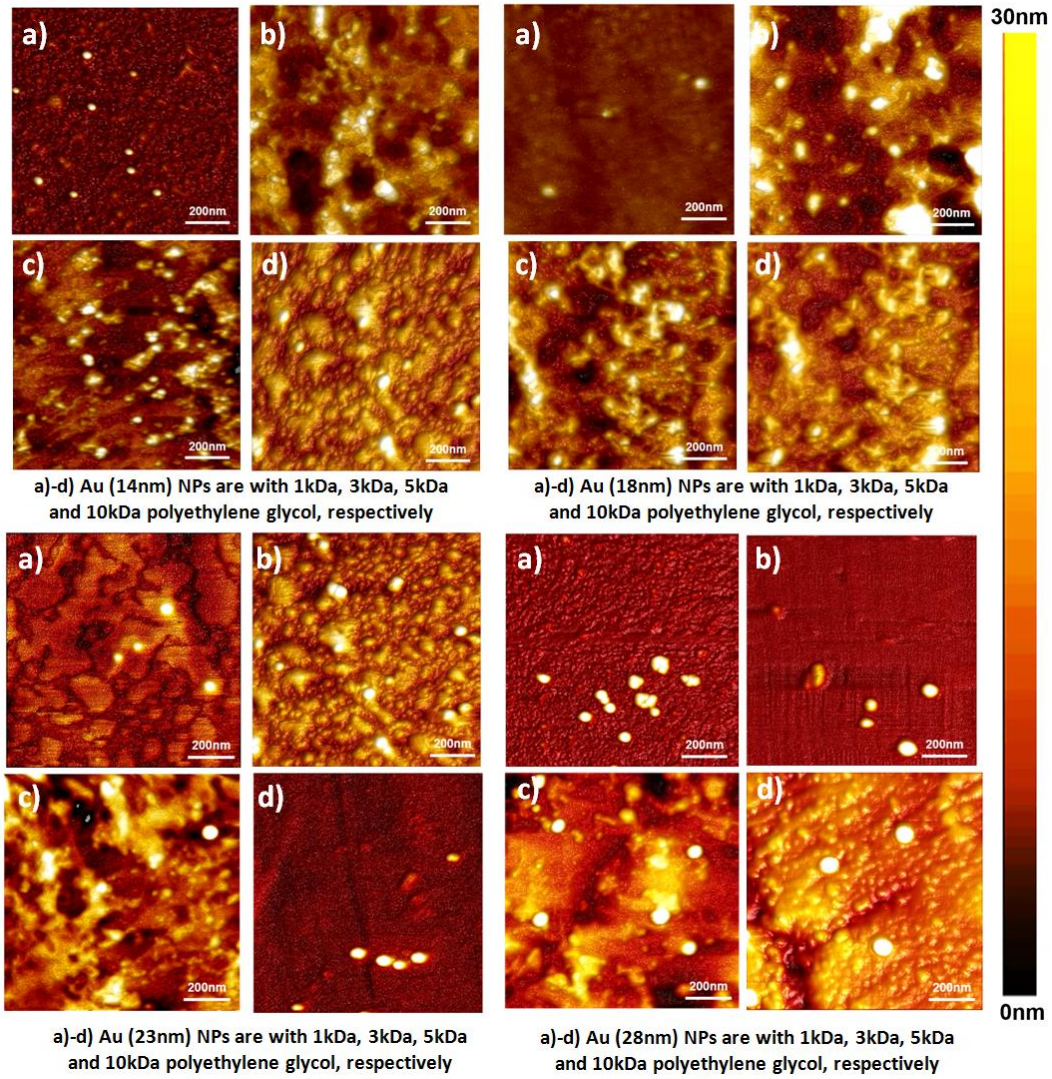

Figure VIII: Selected AFM topological images of the PEGylated Au NPs. Scale bar corresponds to 100 nm.

The indentation behavior of the surface terminated with Au NPs-PMA-PEG was reflected, and single force curves against distance of the cantilever was recorded at the same time, so that the Young's Modulus can be calculated by analysis of the approaching process (see figure IX). A

calibration procedure was performed in order to analyze the exact area of the conical tip which was used for all measurements. Each NP has been approached about 60 times and more than 15 NPs which were from different areas on the substrate were measured. By mean of that there are more than 1000 curves for each set of samples that have been calibrated with NanoScope Analysis 1.5 (Brucker Corporation 2013).

All trace curves are quantitatively calculated for indentation, which is related to the equation of Young's modulus. The Young's modulus represents elasticity known as stiffness depending on tip radius, deflection sensitivity, spring constant, tip half angle and Poisson ration. Due to conical sharp of tip the Sneddon's equation was selected for analyzing the stiffness of the Au NPs (details in scheme III). The results including diagrams and 3D heat maps of the young's modulus and size are demonstrated in figures from X to XV which are related to experiments in vacuum and in water, respectively. In addition, due to huge statistic calculations in figure XI and figure XIV the Gauss distribution for each measurement is shown, as well as the average values calibrated from all experimental data, respectively. As you see from the diagrams, the Young's modulus is related to the size of NP and the molecular weight of PEG. It was investigated that the Young's modulus increased with increasing core size of NPs modified by the same molecular weight of PEG and the ones increased with increasing molecular weight of PEG for same size of NPs. In addition, the Young's modulus in water is much more than in vacuum. By mean of that it reveals that water content in PEG plays an important role for hardness of the NPs, due to crosslinking of PEG ligands that interacted with water molecules, so that NPs in water will be harder than in vacuum. From a statistical point of view, NPs in water have a bigger hydrodynamic size than in vacuum, thus the tip will touch a more effective area of NP (see scheme III).

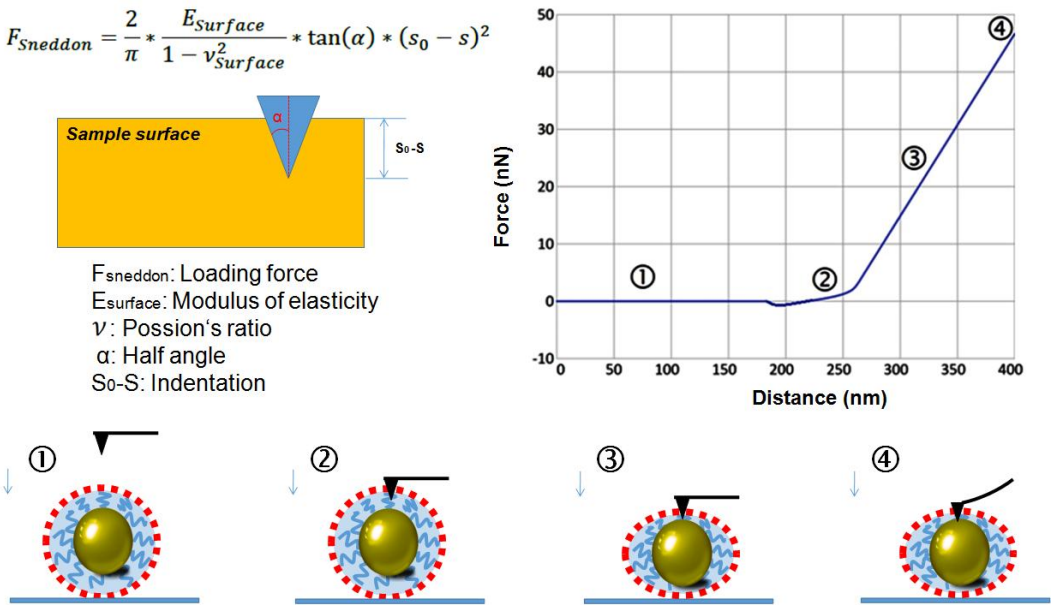

Figure IX: Conical cantilever indent into single AuNP. Force curve of indentation from single molecule force spectroscopy is depending on the indentation. 1) Cantilever is approaching to the NP and force remains zero. 2) The tip indents the polymer firstly and force increases slowly. 3) The tip indents continuously till touch the core and force increases faster which means the slope is more than process 2). 4) The whole NP is pressed down and force increases as same as process 3). The stiffness calculation will be successes according to Sneddon equation.

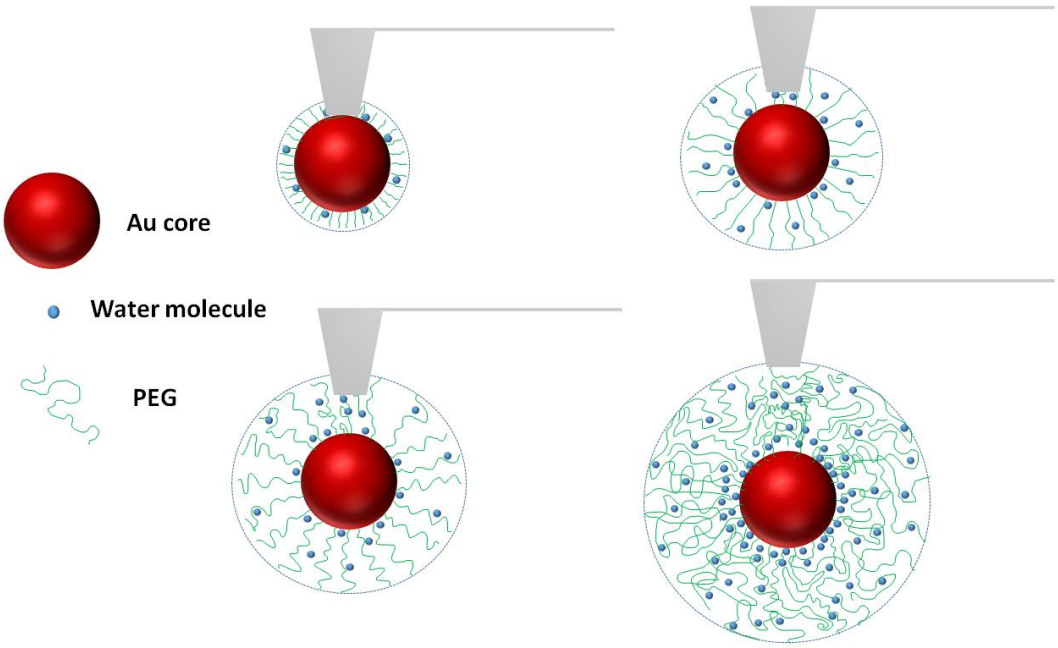

Scheme III: Description of conical tip intending into single NP in water. Water molecules are trapped by PEG ligands

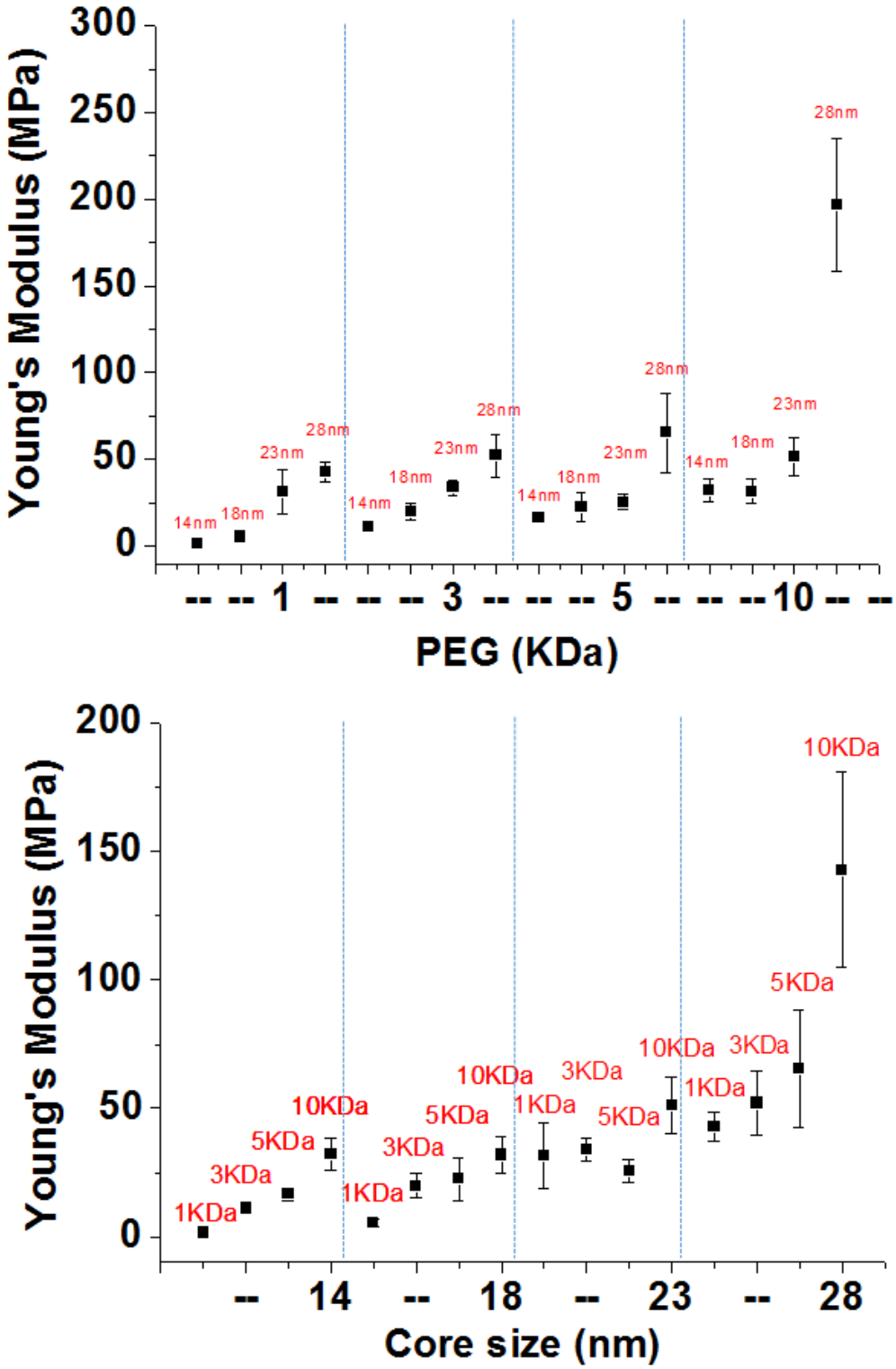

Figure X: Diagrams about Young's modulus of all the Au NPs. The measurements are all finished in air.

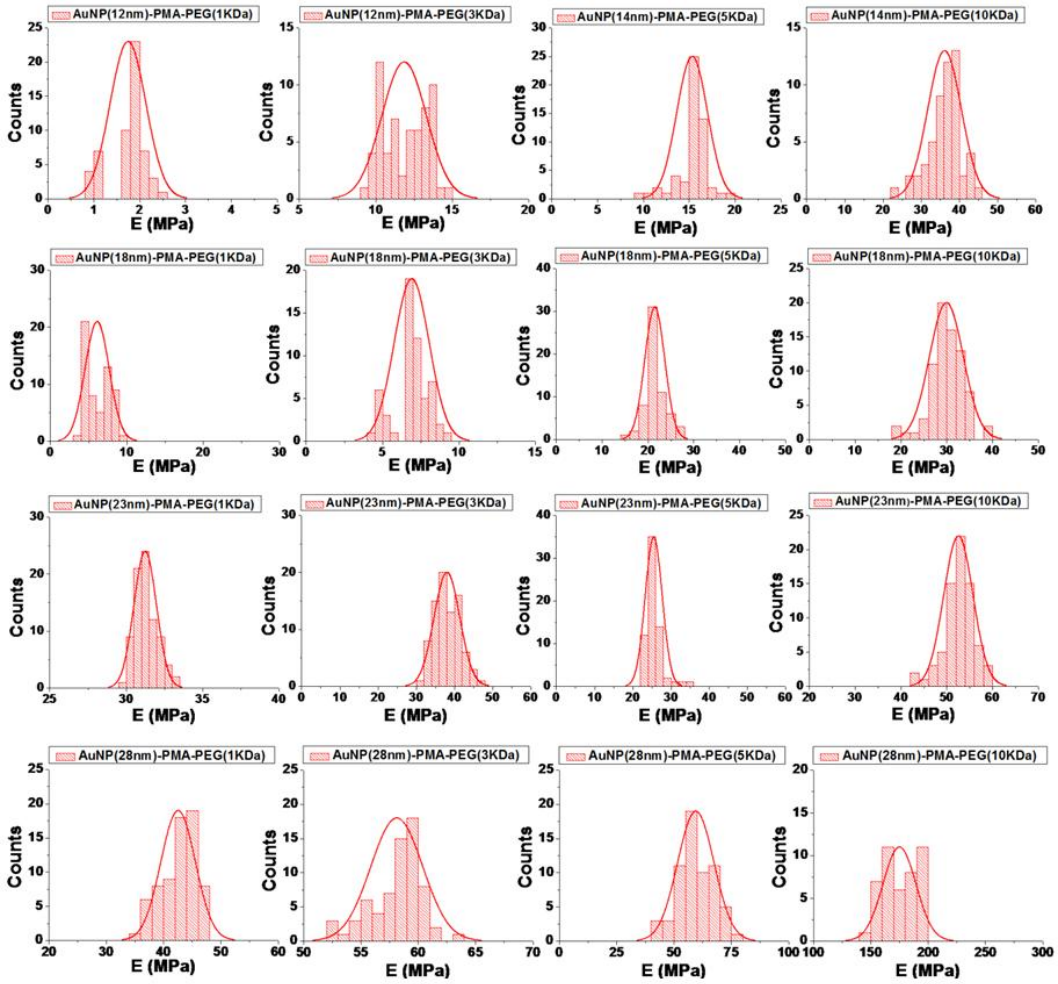

Figure XI: Stiffness measurements in air. The Gauß's distribution of the Young's modulus in air is plotted.

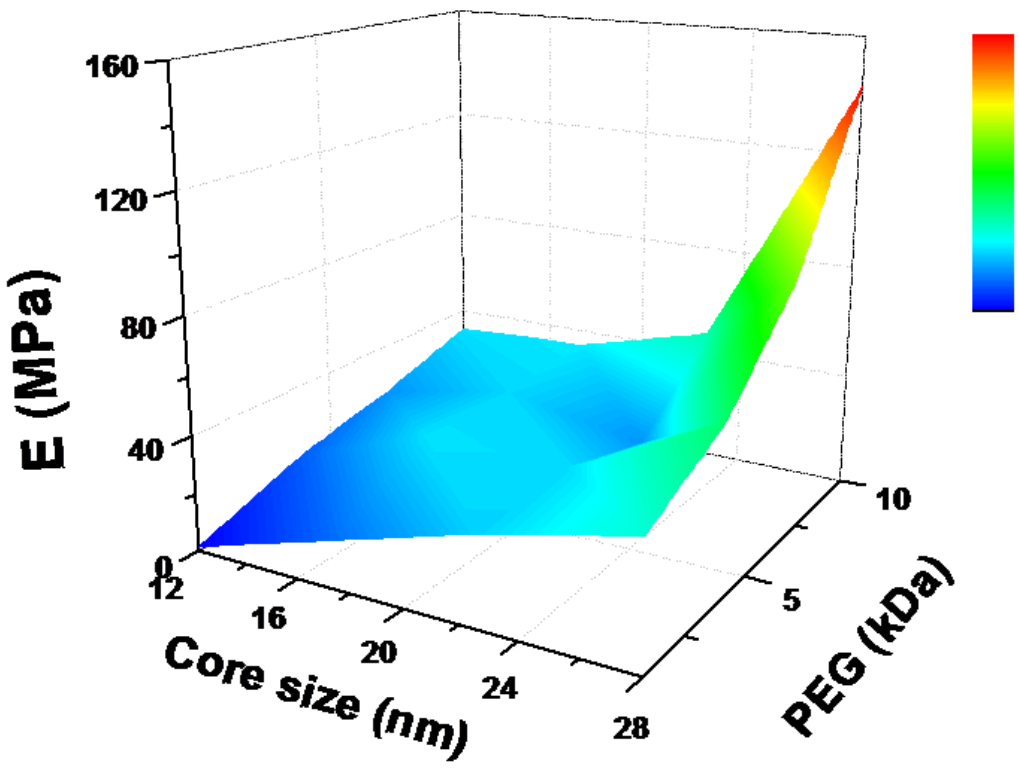

Figure XII: 3D heat map of the Young's modulus. The 3D heat-map of the Young's modulus in air (modulus of the elasticity E) vesus core sizes and molecules weight of PEG is plotted.

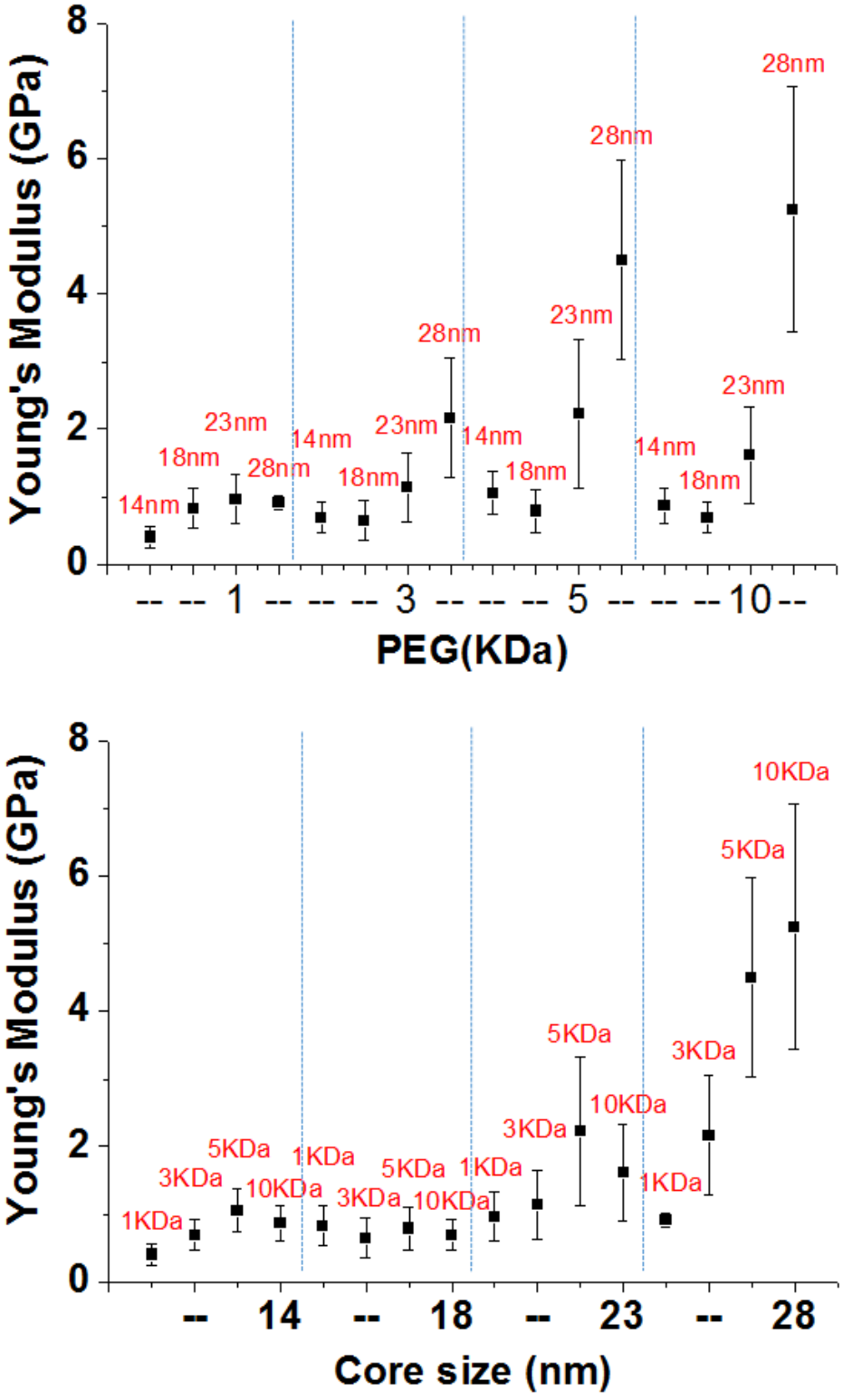

Figure XIII: Diagrams about Young's modulus of all the Au NPs. The measurements are all finished in water.

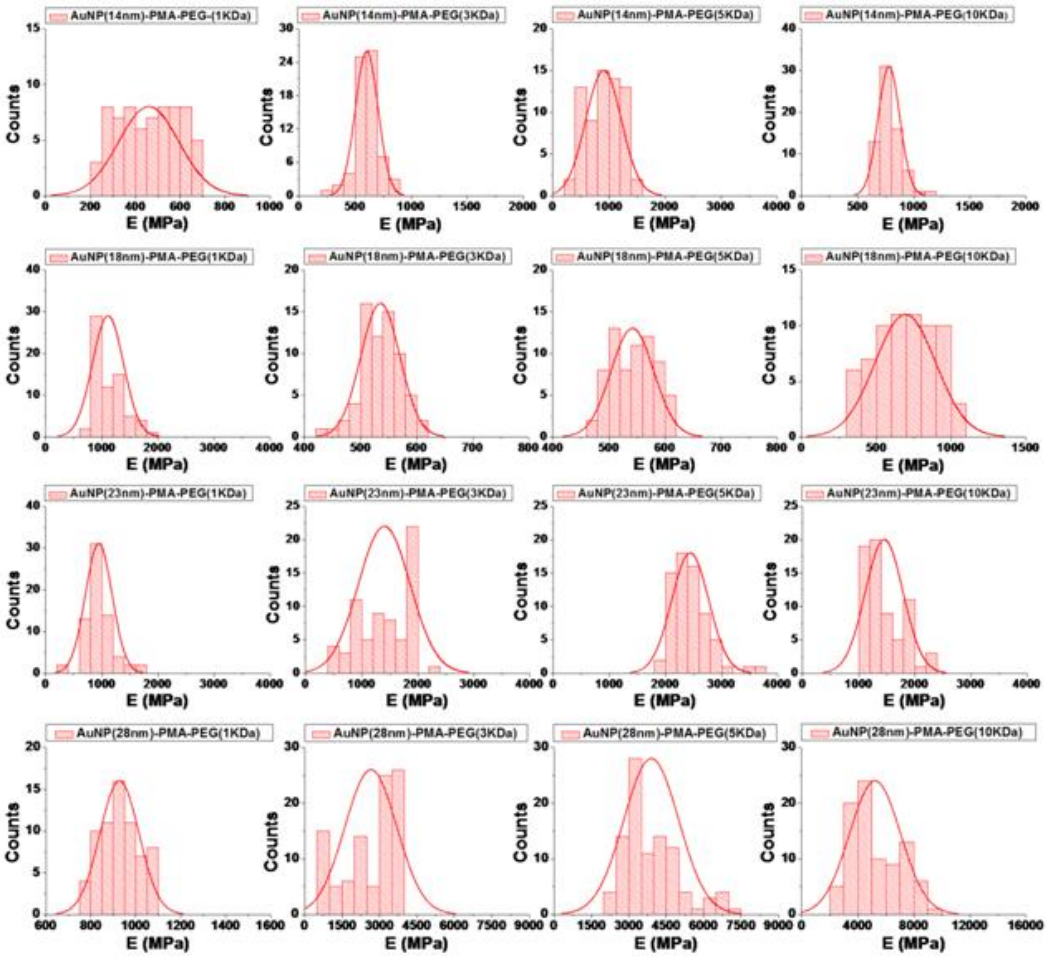

Figure XIV: Stiffness measurements in water. The Gauß's distribution of the Young's modulus in water is plotted.

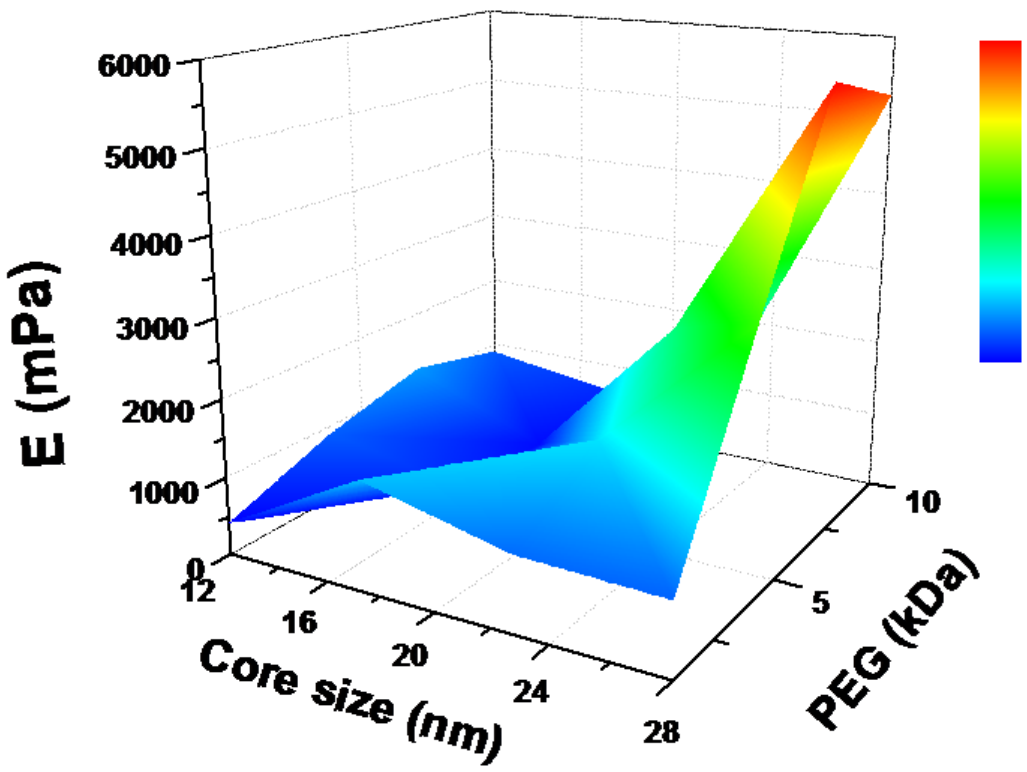

Figure XV: 3D heat map of the Young's modulus. The 3D heat-map of the Young's modulus in water (modulus of the elasticity E) vesus core sizes and molecules weight of PEG is plotted.

Magnetic force microscopy towards magnetic nanoparticles

As one of the most watched topics in the past decade, magnetic properties associated with NPs and biological applications were always a highlight in the scientific focus. From magnetic NPs to magnetic protein biocompass[42], by now it has been starting a frenzy of magnetism. Magnetic NPs in biological and biomedical application are getting attractive for scientists and even pharmacologists, because the superparamagnetic NPs were proved that they can be used to kill tumor cells and even tumor tissue in hyperthermal therapy[43] and can be used to ablate tumor cells and even tumor tissue by an external weak rotating magnetic field[30]. Hence, a multi functional magnetic NP loaded with anti-cancer drugs may be an excellent idea to open up a

pathway for clinical research against cancer. Herein, a polymeric NP based on poly (lactic-co-glycolic acid) (PLGA) loaded with a natural anticancer drug tetrandrine[44] and superparamagnetic iron oxide. Such multifunctional magnetic NPs can not only be exerted for determination of the toxic effect by cellular morphology but also can be used for multi-therapeutic effects against the tumor cells in biomedical and clinical applications via controllable magnetic rotation. By now the key point will be how to characterize such multi-functional magnetic NPs. MFM is a secondary imaging mode derived from tapping mode. It is utilized to determine magnetic domains via interaction between a magnetized tip and the sample. The measurements based on magnetic behavior of the samples can be realized by using a magnetized Cobalt-Chromium tip from given voltage. The scan procedure will be: firstly, topographic profile of each line will be scanned and then due to the approaching lift height (the grounded tip first acquires surface topography in the tapping mode, then the tip is lifted up, and retraces the surface profile maintaining a constant tip-surface separation) the tip can induce magnetic domains above the sample on second pass, so that the magnetic signal can be extracted (scheme IV) by phase contrast, because the accepted deflection will lead to phase shifting.

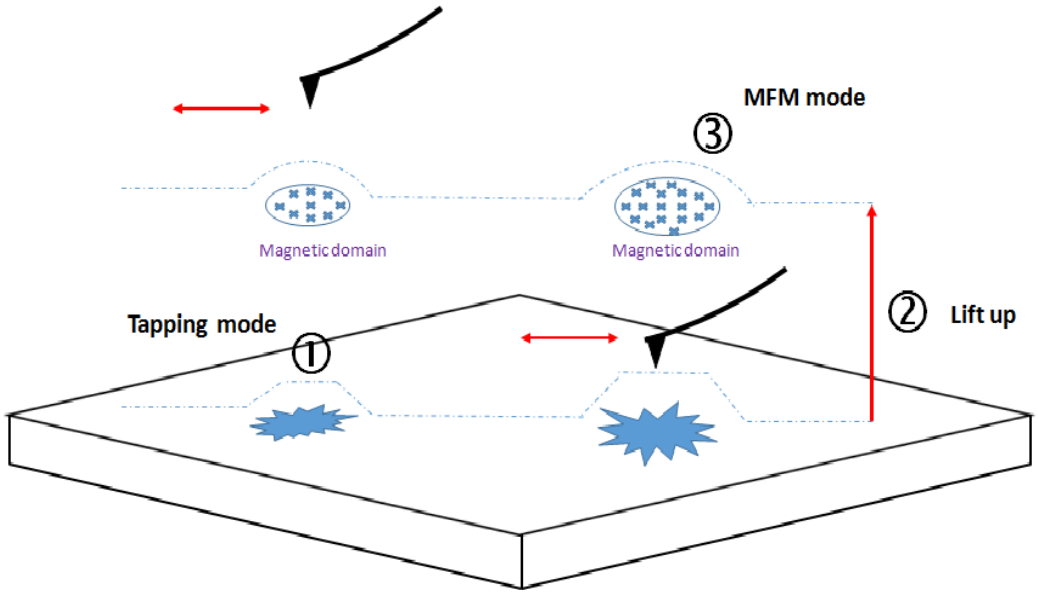

Scheme IV: In MFM mode, a magnetized tip will scan above the sample two times. On the first pass, the tip is brought into an approaching sample for topographic profile. On the second pass, the tip is lifted further away from the sample in order to induce magnetic domain.

Schneider, et.al developed a multifunctional polymeric NP coated by dual materials which are the anti-cancer drug tetrandrine and superparamagnetic Fe_3O_4 NPs[26]. Such co-loaded NPs have been successfully observed under TEM shown in figure XVI. Then they were dropped on austenitic stainless steel in order to inflict phase separation easily, so that the magnetic region being determined can be distinguished from the steel by presenting phase contrast. The magnetic region reflected in a phase canal is clear to present the magnetic profile of the sample which is attributed to the loading of superparamagnetic NPs in the polymer. The magnetic images of MFM are shown in figure XVII. Associated with vibrating sample magnetometer which showed superparamagnetic property we thus expect the co-loaded NPs can be used for further magnetic manipulation and it has been proofed in SEM showed in figure XVIII.

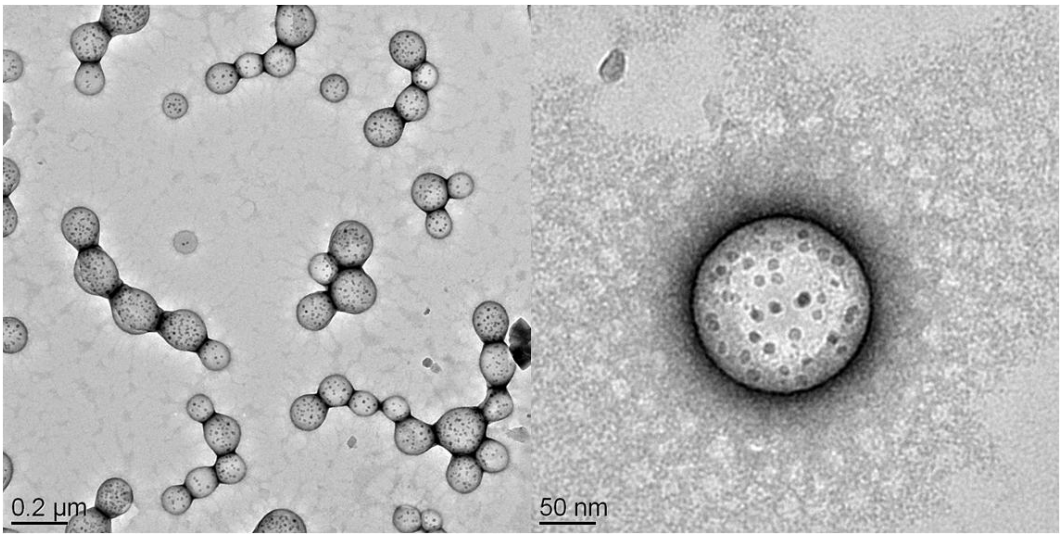

Figure XVI: TEM images of Co-loaded-PLGA-NPs. The Fe_3O_4 NPs and tetrandrine were coated with PLGA and homogenous distribute inside.

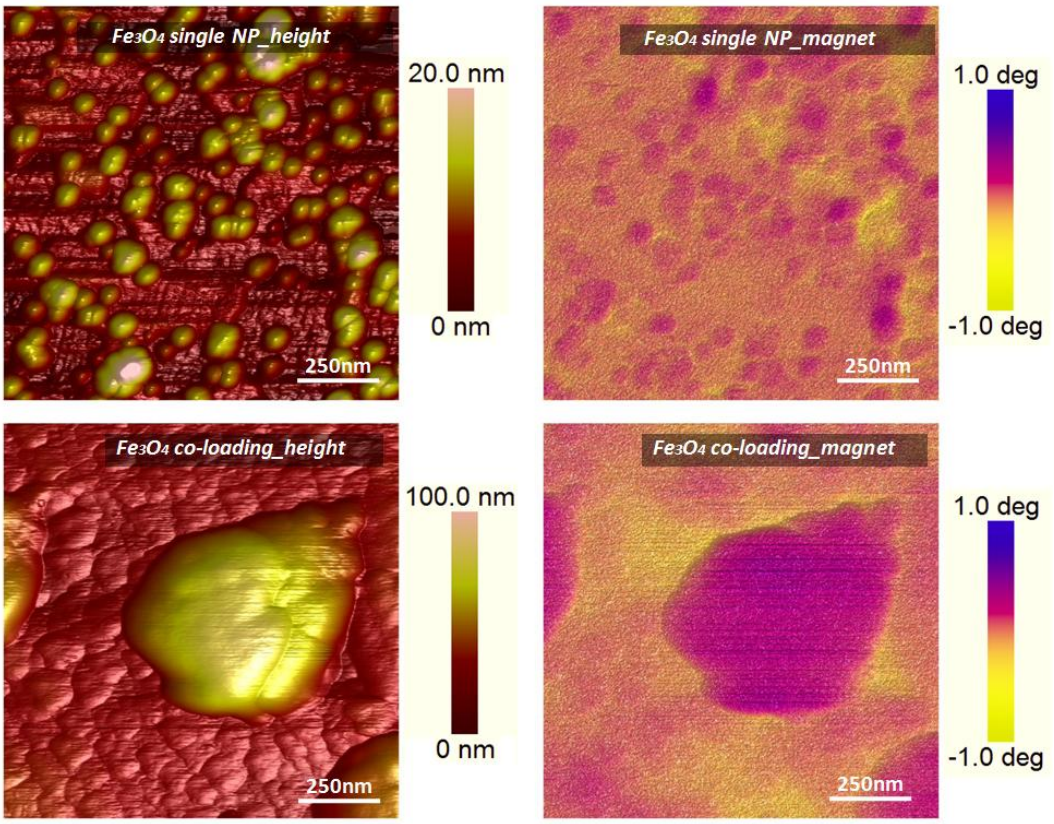

Figure XVII: The AFM topography associated with images of magnetic domain under MFM mode.

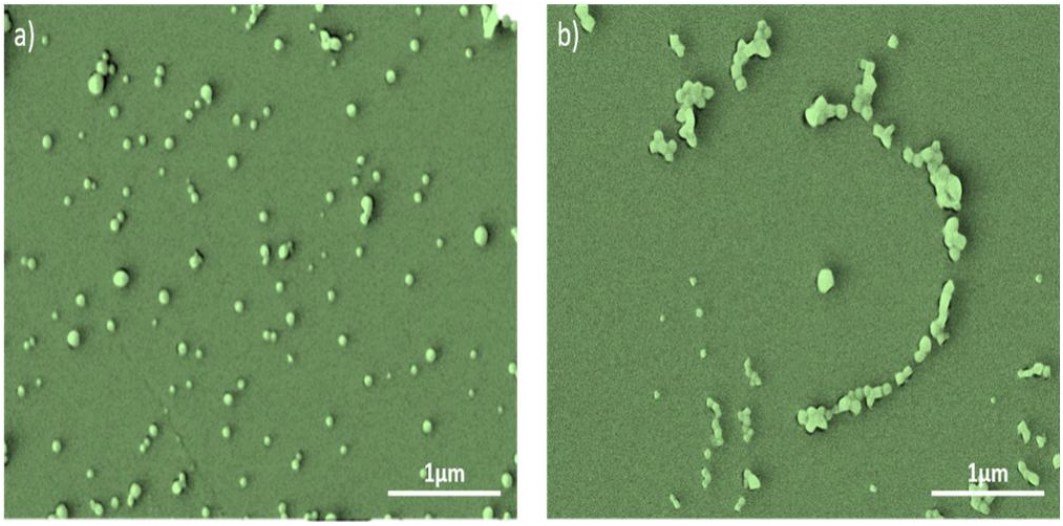

Figure XVIII: SEM images of co-loaded-PLGA NPs without rotating magnetic field (left image) and with rotating magnetic field (right image). Due to rotating magnetic interaction the NPs are moving in a circular path.

Due to superparamagnetic properties the discrete magnetic NPs are offered to target tumor cells more effectively by remote application of focused magnetic fields. An externally rotating permanent magnet will transfer a rotational magnetic movement to magnetic NPs hence inducing inter cellular break and cytotoxicity. The impact of the magnetic NPs in a rotating magnetic field (RMF) is most likely because of shear forces created by hindered rotation of the particles in the intracellular matrix (incomplete rotation). Therefore, the co-loaded NPs which consist of the superparamagnetic Fe_3O_4 NPs and Tetrandrine can enhance the harmful effect to cancer cells even tumor tissue for further biomedical applications. A549 cells are the adenocarcinomic human alveolar basal epithelial cells from cancerous lung tissue and are wildly used for modeling drug metabolism and studying the interaction effect of the NPs in vitro. Thus, the A549 cells internalized by the co-loaded PLGA NPs have been investigated. In addition, as references, the discrete superparamagnetic Fe_3O_4 NPs and a weak external rotating magnetic

field were used to compare with the co-loaded NPs. After uptake of the different NPs to cells and treatment with external rotating field, Topography of AFM in contact mode was utilized to visually observe cellular surface and morphology and quantitatively analyze the cellular surface roughness (see figure XIX). In addition, confocal laser scanning microscopy (CLSM) is used to characterize the cellular morphology as well, and in order to verify their biological harmful effect, a cell viability assay was used for comparison with different NPs and rotating magnetic NPs. Finally, according to all the results, it is proved that the superparamagnetic co-loaded PLGA NPs can be enhanced for ablation of cancer cells via a weak rotating magnetic field.

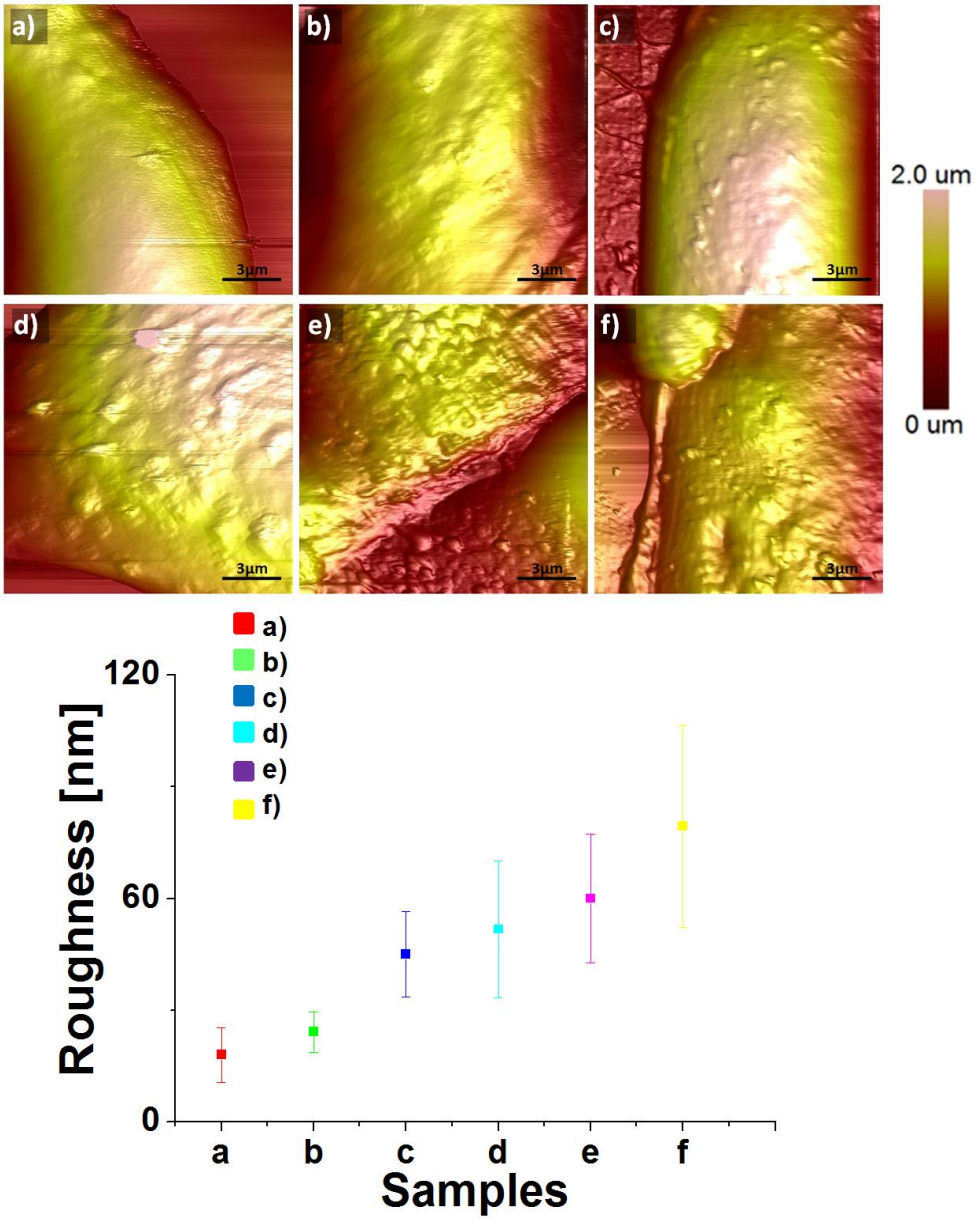

Figure XIX : The selected topography of A549 cells after uptake of the superparamagnetic polymerized NPs show above: a) A549 cells without any NPs and rotating magnetic field b) A549 cells without any NPs and with rotating magnetic field c) A549 cells with the Fe3O4-loaded PLGA NPs but without rotating magnetic field d) A549 cells with the Fe3O4-loaded PLGA NPs and rotating magnetic field e) A549 cells with the co-loaded PLGA NPs but without rotating magnetic field f) A549 cells with the co-loaded PLAG NPs and rotating magnetic field. The diagram below shows the quantitative results of the cellular surface roughness.

Electrostatic force microscope towards mutant purple membrane modified by nanoparticles

EFM is a secondary imaging mode derived from AFM. It measures the surface electrostatic potential distribution above the sample based on electrostatic interaction between a conductive tip and a sample. A voltage is applied in lift mode and the bias is used to create and modulate an electrostatic field between the tip and sample surface. In measurement the surface potential can be adjusted from the voltage on the tip. In order to maintain the feedback, this voltage will be maintained from the constant deflection or constant amplitude which is based on two different applied modes: direct current (DC) by recording deflection and alternating current (AC) by recording amplitude or phase. According to cantilever's phase shift or deflection change with the strength of the electric field gradient an EFM image can be constructed, so that difference between conductive and insulating regions can be distinguished (scheme V). Therefore, in principle EFM is an effective and useful tool for confirming conductive properties of a sample.

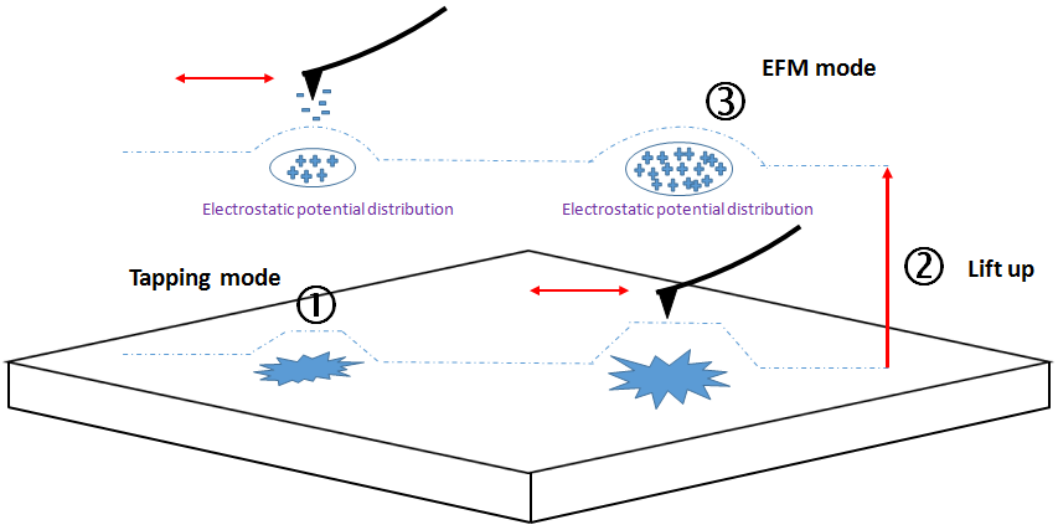

Scheme V: In EFM mode, a conductive tip scan above sample on the first pass for topographic profile, and then the cantilever is held up such that it only senses with electrostatic forces, so that Phase shift of the cantilever in response to the electrostatic force gradient. Therefore, the electrostatic potential signal is extracted.

So far some scientists need to map electronic biological materials to characterize their surface electrostatic potential distribution and analyze their electronic properties for further applications. Most of the samples are of sub-micron scale even several nanometers, whereby EFM is an optimal tool for imaging them. As mentioned above some mutant PM is normally negatively charged on its surface attributed to the genetically introduced amino acid sequence. A new class of purple membrane was successfully described for its surface distribution of electrostatic potential[45]. In addition, attachment of nanoparticles to a biomembane, which serves as a collective carrier for the nanoparticle, is a novel approach opening new application possibilities. It is simple to realize and can take advantage of the fact that NPs with the functional organic molecule connect the amino acid-appended biomembrane utilizing well established metal-affinity interaction. A versatile approach is reported where Au NP-NTA are immobilized to the

surface of a mutated purple membrane (PM) carrying a C-terminal His-tag based on NTA-Ni^{2+}-His coordination complex. Herein, EFM was contributed for interpretation of distribution of electrostatic potential. In figure XX it is clearly indicated that the Au NP-NTA-Ni^{2+} covered on the top of Histidine mutant PM (HisPM) but not covered on wild type PM (PM-WT) as well as the Au NP-EtOH did not covered to the HisPM. In the experimental section Electrostatic force microscopy (EFM) was conducted in air using SCM-PIT tips (antimony (n) doped Si, k= 1 – 5 N/m, f0= 70 – 83 kHz, 0.01 – 0.025 Ω/cm, Veeco, Santa Barbara, CA).

In order to characterize the hybrid bioconjugation with comparison the images of SEM were performed in figure XXI. All the samples were mounted on stainless steel where they can be observed with high contrast comparing with native biological PM. In order to get high resolution images they were presented under vacuum condition using YAG ($Y_3Al_5O_{12}$:Ce^{3+}; Yttrium Aluminum Garnet activated by Ce^{3+}) and BSE (backscattered electron) to distinguish PM and the NPs clearly. It is obviously indicated that HisPM can only be successfully assembled by Au NP-NTA-Ni^{2+}. In addition, to analyze the composition at a level of single membrane, all the samples were characterized using TEM described in figure XXII. It revealed that the C-His-PM is covered with Au NP-NTA-Ni^{2+} but not with the Au NP-Et-OH.

The hybrid conjugation based on HisPM covered by functional Au NPs can be investigated for creating a novel functional biomembrane shown in figure XXIII. Due to magnetic property of Ni^{2+} and diverse properties of the Au NPs, such functional biomaterial can promote further study towards oriented array of PM in order to conduce to explore more biometric applications and optical storage and security system.

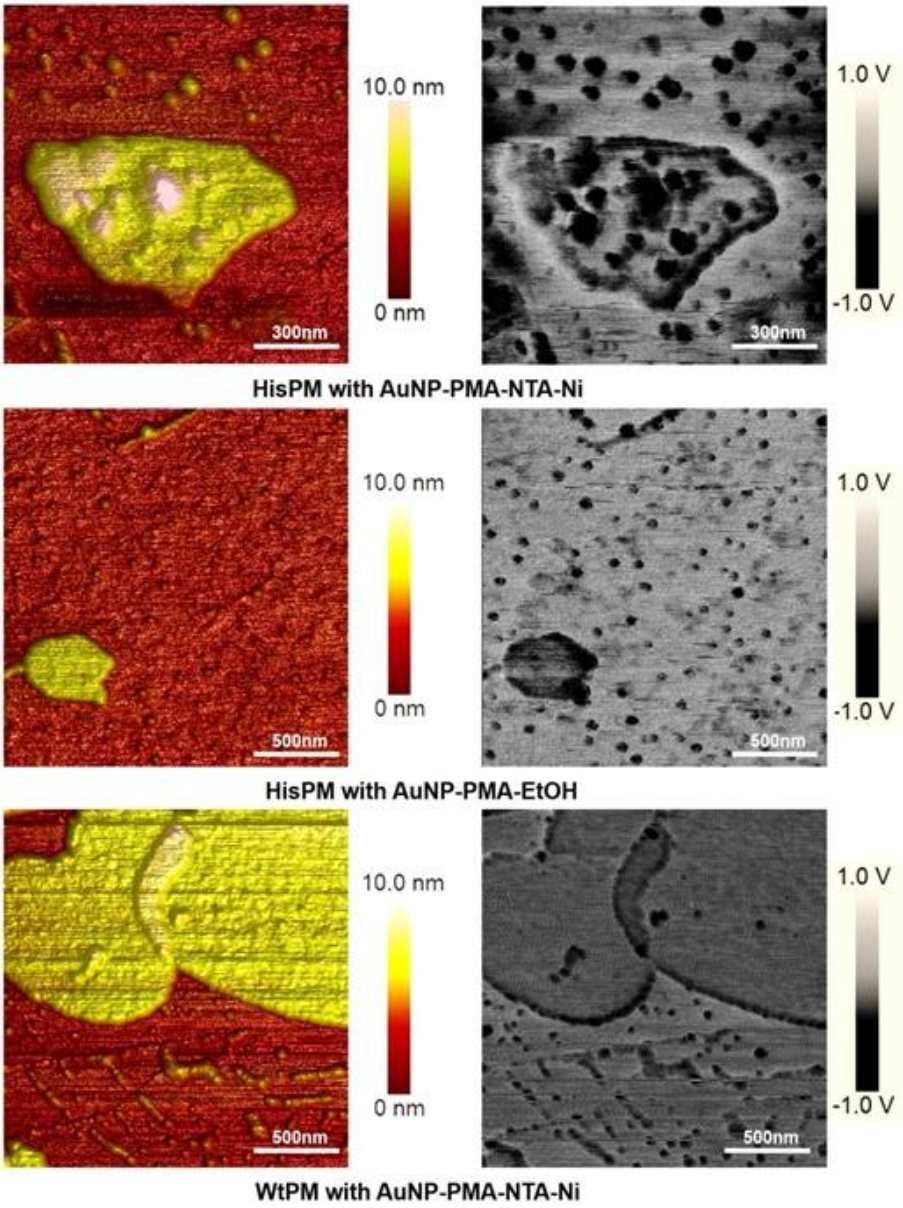

Figure XX: EFM images for characterization of hybrid bioconjunction and the reference mixtures. The height image reveals topological membrane patches covered by NPs or not covered by NPs. In the corresponding EFM image, low negatively charged PM and high negatively charged NPs were observed, which face cytoplasmatic surface of HisPM side up and WtPM as well. In comparison of the samples NPs with –NTA group were stabilized on HisPM cytoplasmatic surface and NPs with -OH were just spread

around HisPM. The elongating WtPM was attached by several NPs-NTA. The corresponding scale bar in both canals reveals height and electric potential difference between membranes and the NPs, respectively.

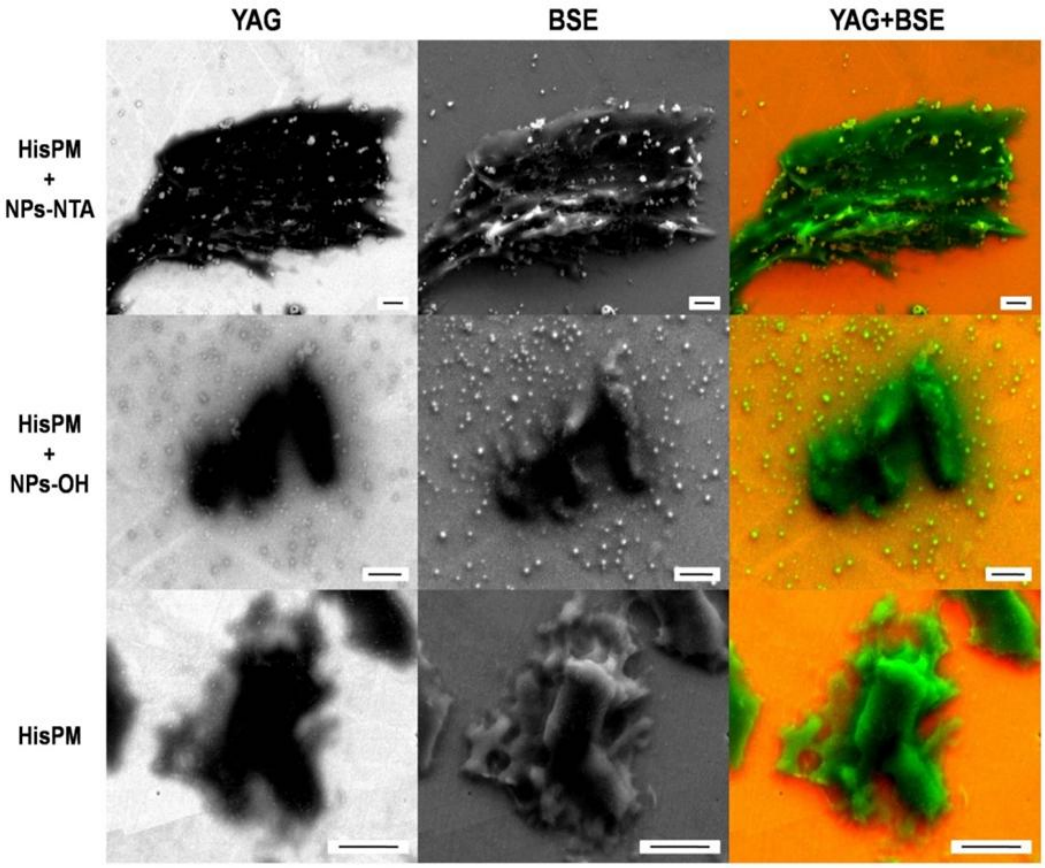

Figure XXI: The image shows SEM images for characterization of hybrid bioconjunction and the reference mixtures (a) YAG ($Y_3Al_5O_{12}:Ce^{3+}$; Yttrium Aluminum Garnet activated by Ce^{3+}) images, BSE (backscattered electron) images and overlay of YAG and BSE images were described for all three samples which are C-His-PM with Au NPs-NTA, C-His-PM with NPs-OH and native C-His-PM. It is clearly to see that only C-His-PM and NPs-NTA have connection establishment. The NPs without NTA but -OH group were spread around C-His-PM. The pure C-His-PM was observed as reference. Scale bars correspond to 1 µm.

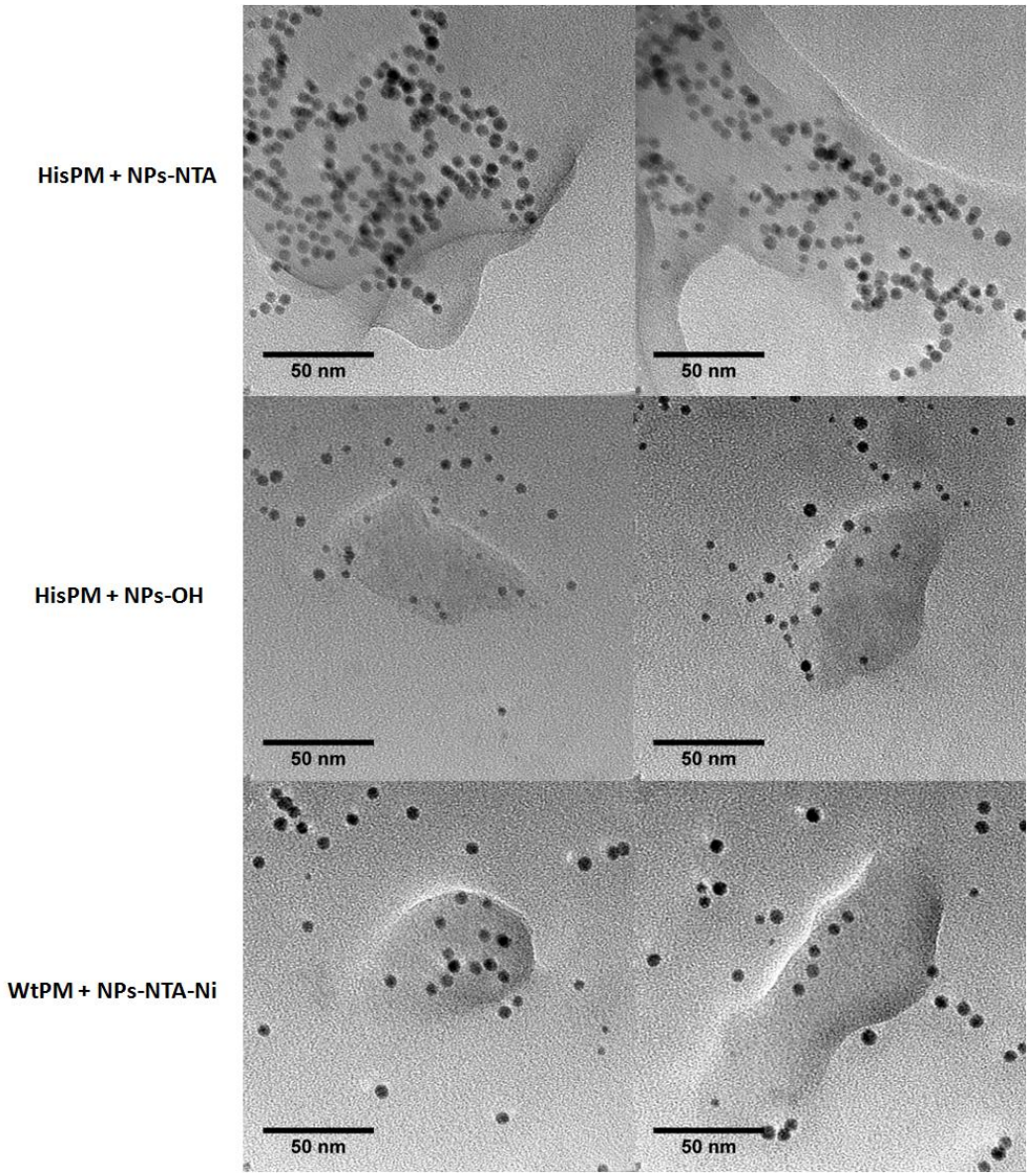

Figure XXII: The image shows high-resolution TEM images for characterization of hybrid bioconjunction and the reference mixtures. Multi-layers of HisPM assembled by Au NPs-NTA can be clearly seen. In contrast NPs only with –OH group were just dispread around HisPM without any connection. WtPM were adherent with several NPs-NTA by chance.

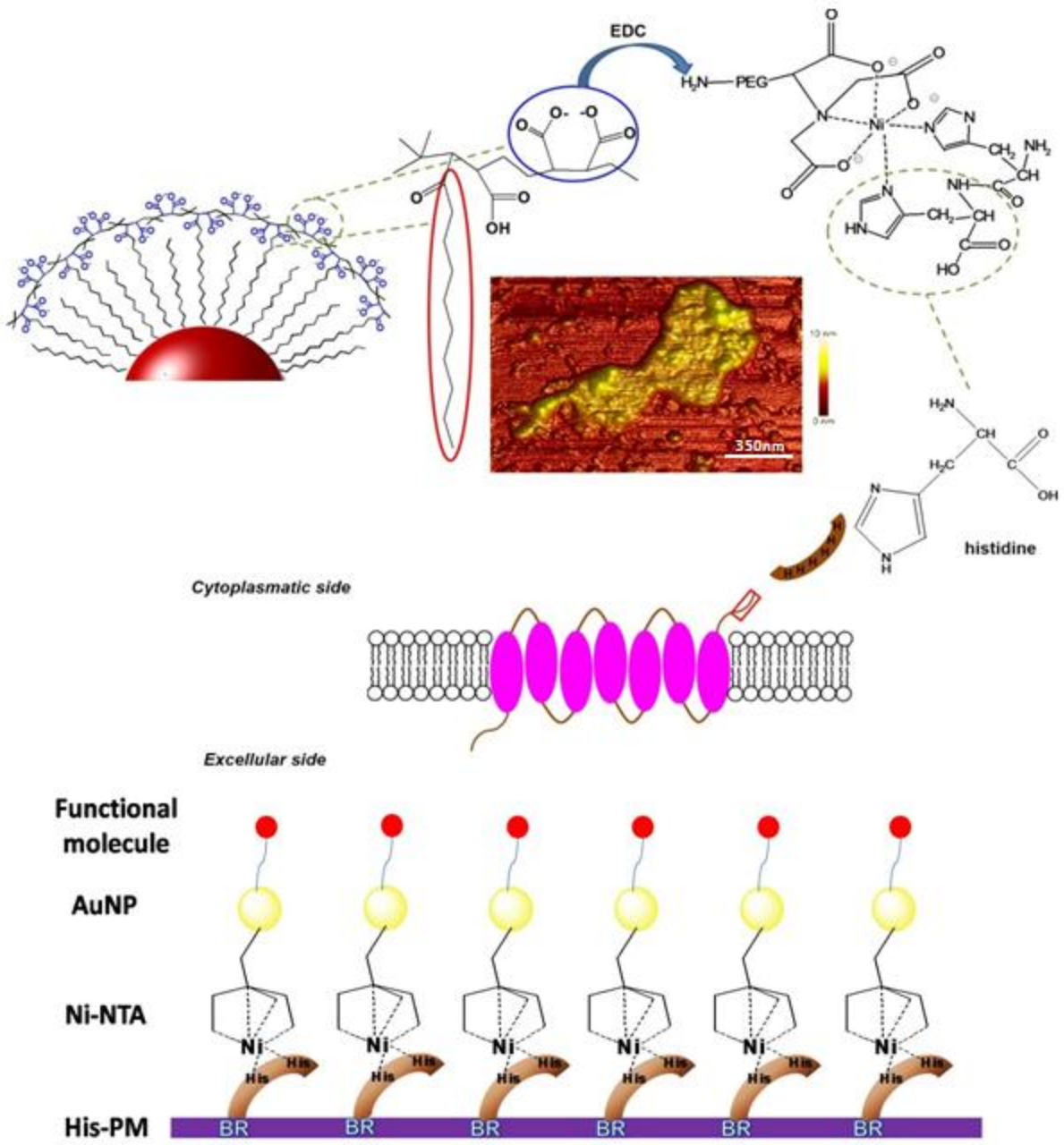

Figure XXIII: Schematic fabrication process for modification of Au NP-PMA with NTA-Ni^{2+} and combining the NPs onto the cytoplasmatic surface of C-His-PM and the illustration using AFM height image. The functionalized Au NPs attached to C-His-PM via NTA-Ni^{2+}-histidine coordination complex.

Oscillation system towards real-time monitoring cell viability

In the last 20 years scanning probe microscope has been wildly used as a powerful tool for characterizing and mapping materials because of its high resolution. Particularly, AFM has given huge contributions on biological researches and applications in nano field. Nevertheless its great potential has not been tapped yet. In this chapter the intention is to describe a novel quantitatively real-time cell viability detection based on cell adhesion property via an AFM oscillating system which is beyond the conventional functions of AFM. A cantilever is oscillating by a given frequency and in its oscillating state the amplitude is highly depending on the mass of the cantilever and its attachments. It can be clearly derived from Bernoulli Theory[46, 47]. The flexural strength of a cantilever is proportional to the force loading on the cantilever according to Hook's law:

$$\boldsymbol{\Delta z = k_f^{-1} F} \qquad (1)$$

Where Δz is the bending deflection, k_f is the spring constant and F is a force as known as loading force. Upon that the cantilever was forced to oscillate harmonically by a piezo element with a given frequency. Herein deflection in harmonic oscillation can be described by equation (2).

$$\boldsymbol{\Delta z = A \cos(\omega t + \varphi)} \qquad (2)$$

Where A is the maximal deflection, ω is the angular frequency and φ is the phase. The frequency υ describes the number of oscillations within a certain period, mostly per second. It is related to the angular frequency according to equation (3).

$$\boldsymbol{\omega = 2\pi\nu} \qquad (3)$$

While a force is applied on a harmonically oscillating cantilever, the total energy of the oscillation is affected which is proportional to the square of amplitude A^2. Hence, while the frequency remains constant, the amplitude is highly depending on the loading force.

As scheme VI shows, a force that is vertically applied to a bar makes it bending, resulting in compressive strain at the lower part of the bar and elongation at its upper part. The middle part of the bar remains constant in length and is called “neutral fiber”. Variation of length increases linearly with increasing vertical distance of the bar shifted to the neutral fiber. Further calculations proposed several assumptions: while the bar was initially bending up, the weight of the bending bar can be ignored since the cross sectional area remains constant and the perpendicular loading force remains orthogonal to neutral fiber before and after bending. The distance between two adjacent cross-sectional areas is considered to be dx before bending. After bending, the curvature angle $d\phi$ can be approximated by dx/R, where R is the curvature radius of the neutral fiber in x-y plane and L is the length of the bar.

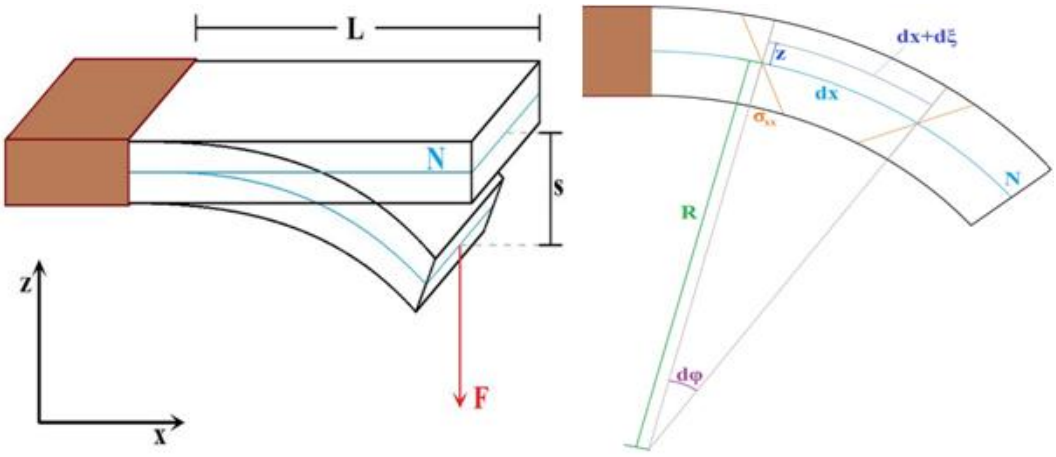

Scheme VI: schematic description of the bending of a cantilever. A loading force applied to a bar fixed at one end describes the bending theoretically.

Thus the relative elongation ε_{xx} of a single shift parallel to the neutral fiber and with a distance z to the neutral fiber can be described by equation 4.

$$\frac{d\xi}{dx} = \varepsilon_{xx} = \frac{(R+z)d\varphi - Rd\varphi}{dx} = z\frac{d\varphi}{dx} = \frac{z}{R} \tag{4}$$

Equation 5 defines the Young's modulus.

$$E = \frac{\sigma_{xx}}{\varepsilon_{xx}} \tag{5}$$

Combining equation 4 and equation 5 results in equation 6.

$$\sigma_{xx} = E\varepsilon_{xx} = E\frac{z}{R} \tag{6}$$

Integration of all shifts leads to equation 7.

$$\int \sigma_{xx} dA = \frac{E}{R}\int z dA = 0 \tag{7}$$

Nonetheless they exert an angular momentum to the bar, which is called "bending moment" M.

$$M = Fx = \int z\sigma_{xx} dA \tag{8}$$

Combining equation 7 with 8 leads to equation 9.

$$M = \int z\sigma_{xx} dA = \frac{E}{R}\int z^2 dA = \frac{E}{R}I \tag{9}$$

Where I is called „moment of inertia of area“, which equates $\int z^2 dA$. The angular momentum tries to cancel the external force:

$$\boldsymbol{M = -F(L - x)} \tag{10}$$

The lever arm can be considered to be L-x since bending is low. Hence:

$$\boldsymbol{\frac{1}{R} = -\frac{F}{EI}(L - x)} \tag{11}$$

Using the following equation from differential geometry:

$$\boldsymbol{\frac{1}{R} = \pm \frac{z''}{(1 + z'^2)^{\frac{3}{2}}}} \tag{12}$$

The sign (±) is negative in this case and Z´ ≈ 0 for low bending. Thus, for the neutral fiber:

$$\boldsymbol{\frac{d^2 z}{dx^2} = \frac{F}{EI}(L - x)} \tag{13}$$

Double integration leads to:

$$\boldsymbol{z = \frac{F}{EI}\left(\frac{Lx^2}{2} - \frac{x^3}{6}\right) + k_1^x + k_2} \tag{14}$$

A boundary condition is that at the fixed end of the bar (x = 0) both Z and Z ´equal zero. Thus the integration constants k and k ´equal zero. This results in equation 15.

$$\boldsymbol{z = \frac{F}{EI}\left(\frac{Lx^2}{2} - \frac{x^3}{6}\right)} \tag{15}$$

or:

$$z = \frac{Fx^2(3L - x)}{6EI} = \frac{gx^2(3L - x)}{6EI} m \quad (16)$$

Where the deflection of the bar depends on L, E and I, which are characterizing properties of the bar, as well as F, which is a loading force to the bar, in this situation, highly dependent on the mass of cells (m) on the cantilever, and the position x where the force applied on the bar. This theory is appropriated to the cell attached on cantilever whereby deflection can be varied depending on different loading force.

Cell adhesion to surfaces related to cell viability has been presented in literature[48]. Inspired by this, cells are allowed to attach to the surface of a triangular cantilever. For a given frequency the cantilever amplitude is highly depending on the mass of the cantilever[49], in current case, on the mass of the attached cells. Then after injection of some toxic agents the cells can be negatively influenced and cause amplitude decreasing. Therefore, a process of cytotoxicity towards agents can be real-time observed by dynamic deflection variation. Herein, a new experimental setup based on the AFM oscillation system was successfully built as scheme VII shows below. A monitoring system is connected to a fluid chamber where a cantilever oscillates, so that a dynamic deflection signal can be recorded by a multimeter (Kathely mode 2000) Cells suspension was stored in an incubation box at standard cell condition (37.5 ℃ and 5% CO_2) and was injected using a plastic syringe into a reservoir based on the fluid chamber with cantilever. In the chamber, a laser beam was focused on the cantilever and reflected to a photodiode. The deflection of the cantilever leads to displacement of the laser on the photodiode depending on the loading force of the cantilever. After calculating "deflection sensitivity" a dynamic amplitude change can be real-time recorded quantitatively.

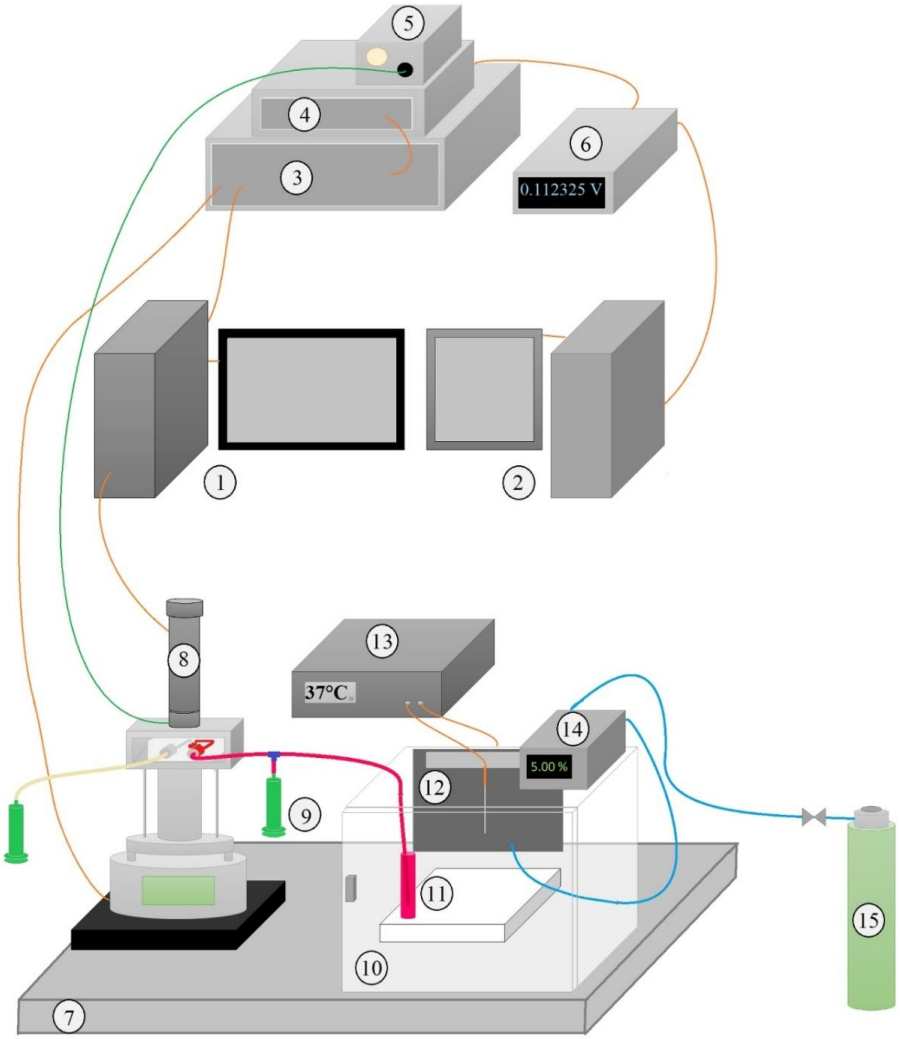

Scheme VII: Complete schematic experimental setup. (1) Computer with software for demonstrating visual images from AFM device (2)Monitoring system for recording measurement data. (3) Multimode Controller, which is an electric device for analysing feedback from AFM. (4) Picoforce-spectrometer for activating deflection recoding (5) Light source for optical camera (2). (6) Keithley 2000 Multimeter for converting data from Pico force spectrometer into device (7) Laser table for keeping steady dynamic balance. (8) Light microscope with camera for visually observing cantilever (9) input syringe (10) Incubation box for cells. (11) Cells storage tubes. (12) Heating plate with circulation fan for keeping homogeneous atmosphere. (13) Temperature controller for regulating heating plate and measuring incubation box temperature. (14) CO_2 controller. (15) Gas container storing.

In order to verify that this method can work with any adhesive cells and toxic agents HeLa (human cervical cancer cells from Mrs. Henrietta Lacks) and MCF7 (a breast cancer cell, Michigan cancer foundation-7) cells were detected with the following three types of AuNPs, respectively. 1) Au(5)-PMA which have a core diameter of 5 nm and were coated by PMA. 2) Au(13)-PMA which have a core diameter of 13 nm and were coated by PMA. 3) Au(13)-PEG which have a core diameter of 13 nm and were coated by PEG. A concentration range from 3 to 400 nM was tested. Besides the NPs other common toxic agents were detected for comparison, that is, ethanol (70%), $CdCl_2$ and staurosporine (3 nM to 1 µM). Firstly, figure XIX a) depicts the method schematically and b) demonstrated an example of HeLa cells with Au NPs by following successive steps: 1) the mounted cantilever started oscillating in air and then the cell medium was injected into the chamber. Meanwhile, the amplitude was increasing. 2) A cell suspension (120 µL of a solution of HeLa cells at 10^5 cells/mL) was injected into the chamber. Meanwhile, the cantilever kept resting for ca. 10 minutes, so that the cells can successfully attach on the cantilever successfully. Then oscillation was started. The deflection amplitude increased due to the attached cells. 3) After 1 hour the Au NPs suspension was injected into the sealed and thermostated (37.5 ℃) sample chamber. Because the cells uptake the NPs by endocytosis, they were expected to cause huge variation of deflection till decreasing. After a lag-phase which is derived from the relatively slow endocytosis process, a diminishing amplitude is observed. In this process, they change their adhesion properties and are gradually detached from the oscillating cantilever accompanied by a decrease of the cantilever amplitude. 4) 70% ethanol and PBS (phosphate buffered saline) were successively injected to kill the remaining cells until the amplitude reduces to a minimal value, just as before the measurements and in particular, before

new series of cells are injected to the measuring chamber, and to clean the cantilever. This process should be repeated several times so that measurements from the same batch of agents may be accomplished during a single session afterwards. The cell medium was then flushed again in order to keep the chamber in condition of cell culture. These processes can be proved by the selected optical images of cells attached to the cantilever in figure XXV.

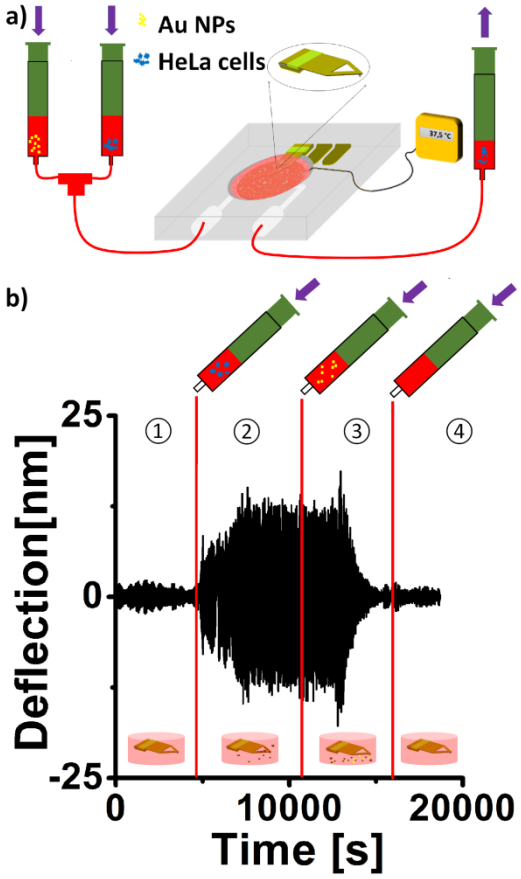

Figure XIX: Setup of the analytical system and the measurement principle. (a) A thermostatic controlled and sealed chamber with a cantilever stage of the AFM. It is connected with in and outlet for liquids where syringes are used as reservoirs for cells and Au NPs. (b) A triangle cantilever is oscillating at a given frequency and the deflection is traced. During the measurements the sample cell is fully filled. At first medium is injected and then cells are injected. Till the cells are saturated on the cantilever

nanoparticles were injected. After a while, the time the cells need to uptake the nanoparticles, the signal decreases because more and more cells detach from the cantilever. Finally the cantilever is washed with ethanol and PBS to clean the debris of cells. Then the cantilever followed by cell medium supplemented and returns to the initial amplitude.

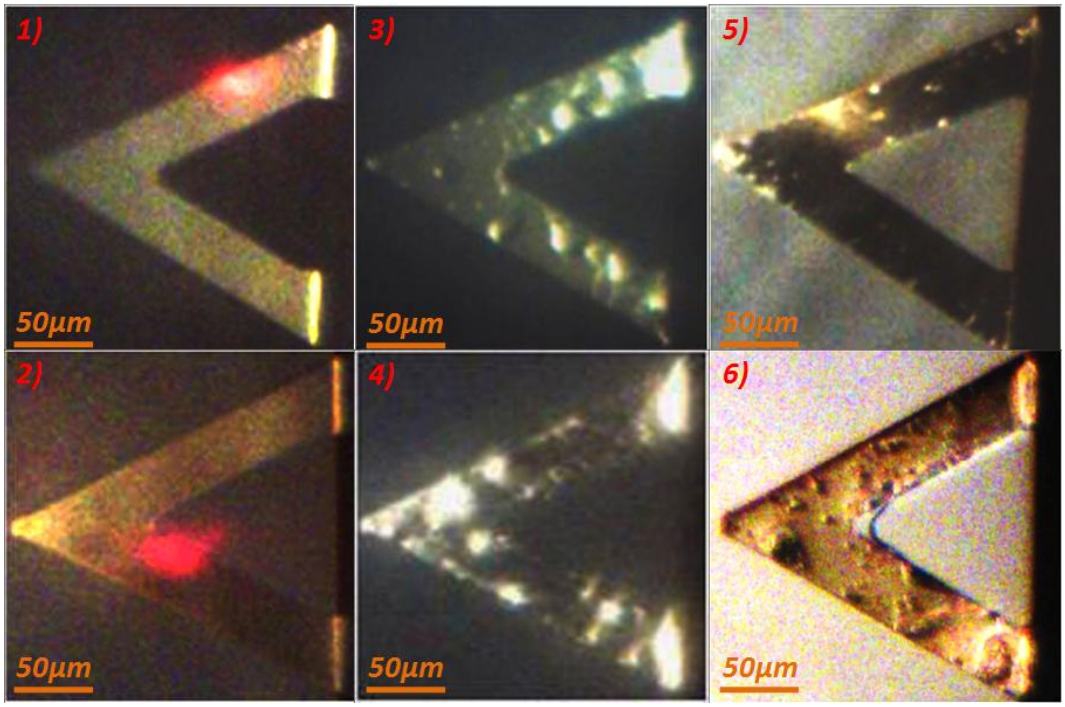

Figure XXV: The optical images of the cantilever. 1) The oscillating cantilever in air before. 2) The oscillating cantilever in cell medium solution. 3) Cells attached to the cantilever. 4) The cantilever with cells after injecting Au NPs. 5) The cantilever after cells detachment and washing with EtOH (70%) and PBS. 6) The cantilever in air after measurement with cells and Au NPs incubation without washing.

Such a mass-sensing platform for label-free measurement of cell viability by using an oscillating cantilever of AFM real-time monitored the whole intoxication for 4-5 hours. The diagrams of deflection variation versus time are presented in figure XXVI for HeLa cells and figure XXVII for MCF7 cells. Agents were injected into the chamber (red line indicates) after 1 hour injection

of HeLa cells. The Cells start to detach from cantilever were indicated from diminishing deflection amplitude. Comparing results it is pronounced that Au (13)-PMA NPs caused cells detachment faster than Au (5)-PMA NPs, PMA caused cells detachment faster than PEG, and high concentration caused cells detachment faster than low concentration. As expected, ethanol (70%) and $CdCl_2$ as necrosis-trigger were used for describing faster detachment of cells. In addition staurosporine was used as reference to underline the general apoptosis for cells whereas the deflection decreased slower than the other agents.

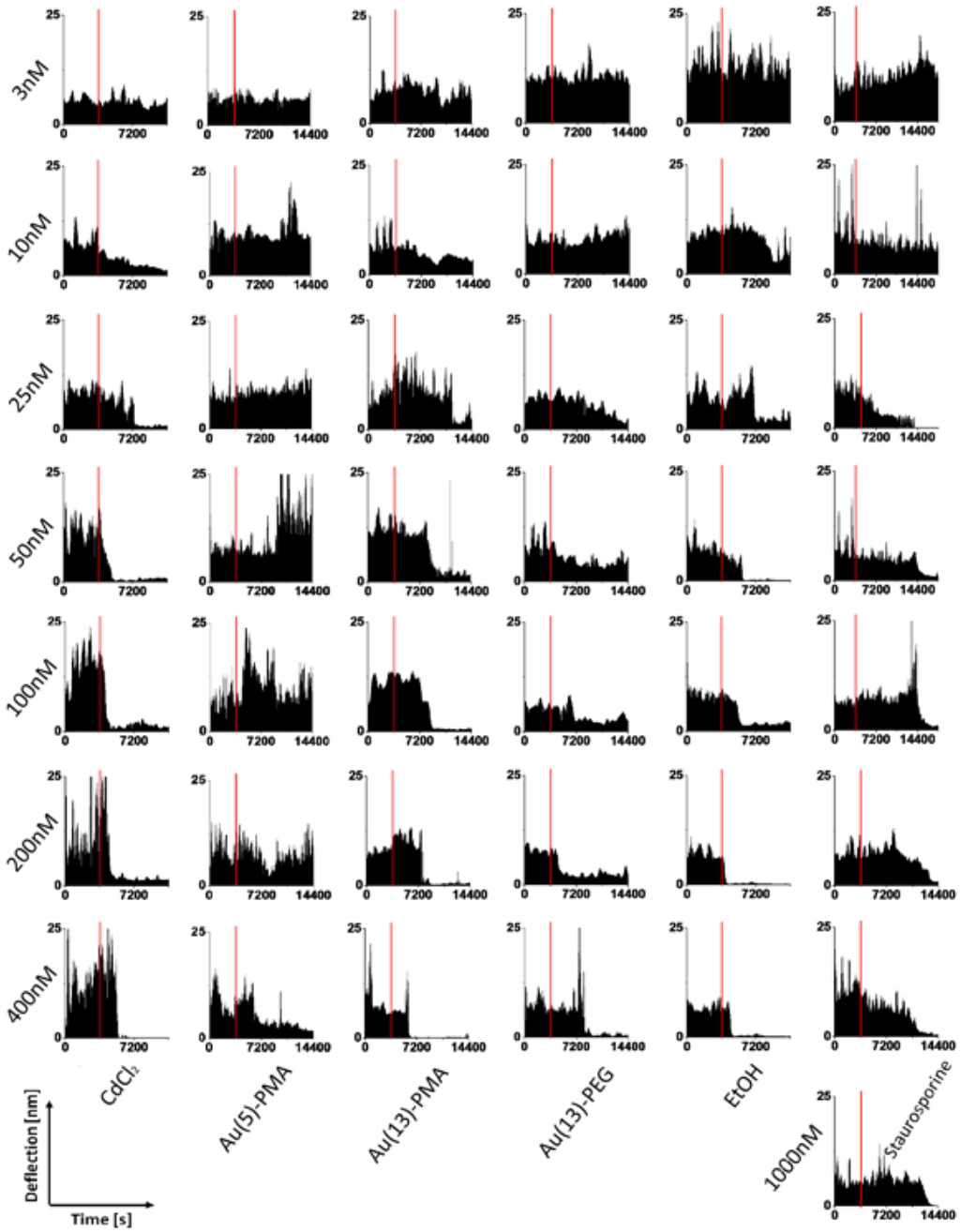

Figure XXVI: Real-time record of HeLa cells with different agents based on diagram of deflection vs time.

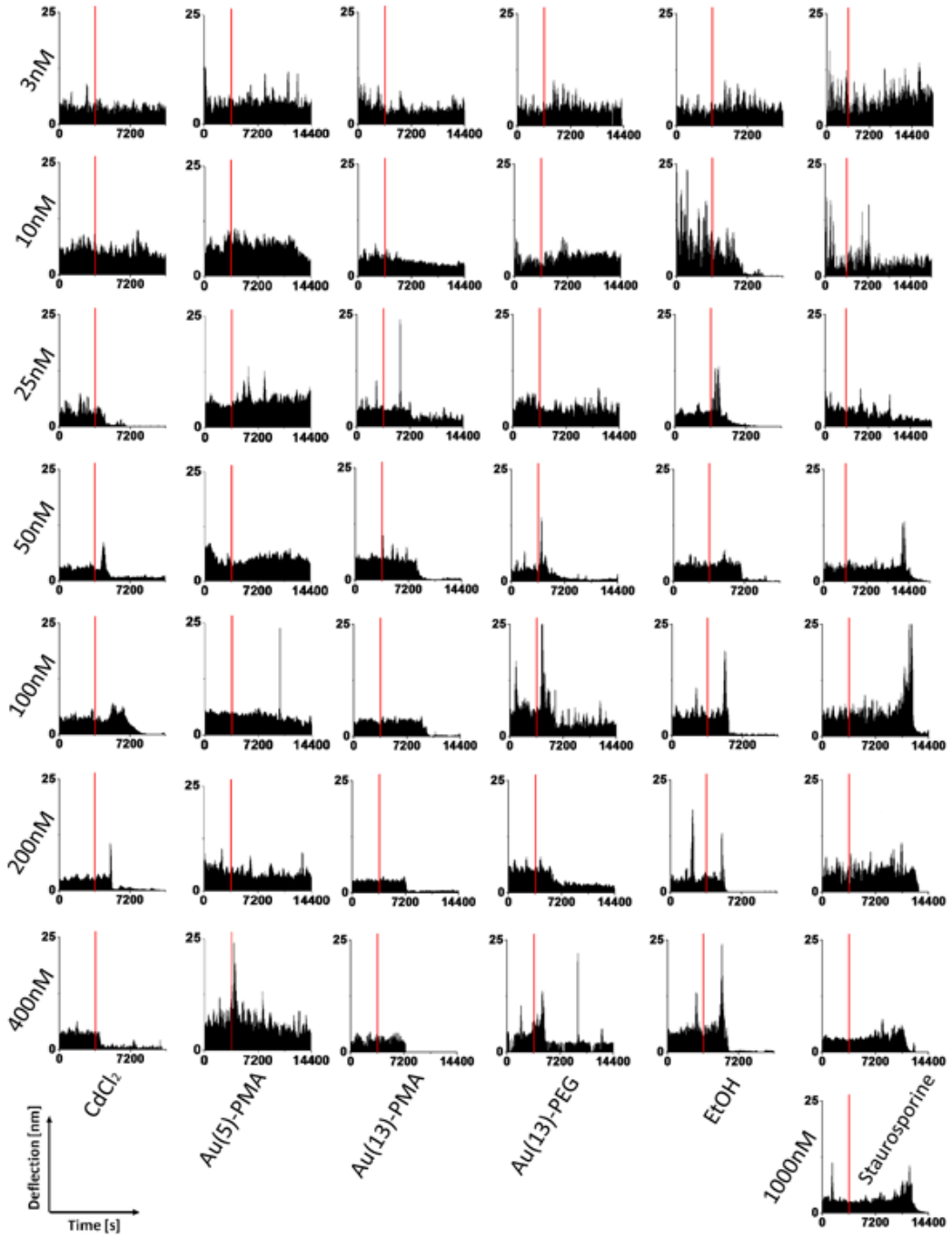

Figure XXVII: Real-time record of MCF7 cells with different agents based on diagram of deflection versus time.

The amplitude increases for increasing numbers of cells attached to the cantilever. When a cell detached from the cantilever the amplitude decreases. The damping constant of the oscillation is linked to the detachment rate of the cells, which is scenario measure for the cell viability. All measurements are finished in real-time. In order to minimize noise not related to the cantilever deflection a sliding average was calculated for each absolute value for a time interval of -1800 s to +1800 s. The values higher than the curve of the sliding average were not considered for further calculations. After the noise canceling the measurements comprise several parts for further analysis. The first part is from $t_{1,S}$ = 0 s to $t_{1,E}$ = 3600 s. During this period HeLa cells in medium were measured without added Au NPs. After injecting gold nanoparticles (red line) a certain lack-phase is observed, then the amplitude rose because of an increased metabolism activity of the cells accompanied by an increasing mass of the cells due to incorporated gold nanoparticles. This increases the loading force to the cantilever (Region 1 in Figure XXVIII). Soon after Au NP uptake the harmful effect of the Au NPs is observed. Cells begin to detach and the deflection decrease (Region 2 in Figure XXVIII) till a minimum is reached.

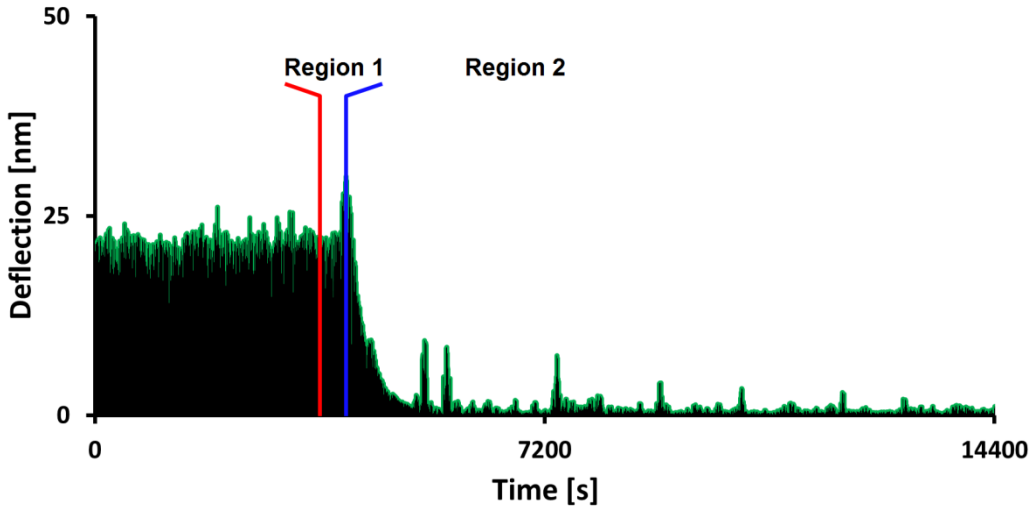

Figure XXVIII: The data (without the outliers) are divided into two parts for further processing. Region 1 (from red to blue line) starts with the addition of the toxic agent, followed by an increment of the

deflection due to the increase of cell mass (i.e., NP's uptake). Region 2 (from blue line) shows the detachment of cells and the accompanied decrease of the amplitude until a constant value is reached.

The damping of the oscillation was approximated by an exponential function (region 2), where A_0 is the amplitude at t = 0 , and e^{-Bt} describes the time-dependent damping of the oscillation.

$$A(t) = A_0 e^{-Bt} \tag{17}$$

Resolving this equation for B leads to equation:

$$\mathrm{B} = -\frac{1}{\mathrm{t}} \ln\left(\frac{\mathrm{A}}{\mathrm{A_0}}\right)$$

B is the damping coefficient which characterizes the detachment and decrease rate, respectively. The B value describes the negative logarithmic ratio of the amplitude at point t and the original amplitude (t= 0 s), divided by the time. Keeping in mind that $A/A_0 \leq 1$, The B-value is thus an indication for the amplitude damping grade, whereas the damping increases with an increase of B. Thus, a high positive B value stands for a high toxic effect to the cells. The B values were calculated using a least square fit of the data points to the function given in eq. (17).

According to the self-written software, all B-values of the agents were calculated. For each serie of agents, at least 2 times measurements were detected with same conditions. Therefore, the mean of B-values of the cell lines were collected in a table shown in figure XXIV below.

		HeLa			MCF7	
	Con[nM]	B-value [1/s]	Deviation [1/s]	Con[nM]	B-value [1/s]	Deviation [1/s]
$CdCl_2$	3	8,01E-05	1,46E-04	3	9,27E-05	1,26E-05
	10	1,63E-04	5,22E-05	10	2,21E-04	7,17E-05
	25	2,70E-04	1,52E-04	25	9,39E-04	2,06E-04
	50	1,60E-03	7,90E-04	50	1,28E-03	2,40E-04
	100	1,90E-03	5,97E-04	100	1,74E-03	7,12E-04
	200	1,90E-03	7,08E-04	200	2,05E-03	4,70E-04
	400	2,20E-03	4,21E-04	400	1,96E-03	1,24E-04
EtOH	3	-1,40E-04	3,80E-05	3	5,41E-05	4,04E-05
	10	9,75E-05	5,30E-05	10	3,10E-04	4,74E-05
	25	6,94E-05	1,25E-05	25	3,68E-04	6,79E-05
	50	8,35E-05	4,10E-05	50	3,20E-05	1,26E-04
	100	2,80E-04	8,10E-05	100	5,71E-04	1,04E-04
	200	2,48E-04	1,10E-04	200	4,09E-04	1,51E-04
	400	5,92E-04	2,80E-04	400	4,54E-04	6,65E-05
Au(5)-PMA	3	1,32E-04	1,05E-04	3	3,58E-05	1,43E-06
	10	9,23E-05	9,26E-05	10	8,14E-05	2,50E-05
	25	2,08E-04	3,86E-05	25	4,04E-04	3,17E-04
	50	6,08E-04	3,23E-04	50	6,50E-04	8,54E-05
	100	1,87E-03	3,86E-04	100	7,63E-04	1,93E-04
	200	1,56E-03	2,48E-04	200	6,88E-04	1,89E-04
	400	1,59E-03	2,74E-06	400	1,12E-03	1,54E-04
Au(13)-PMA	3	5,10E-05	4,27E-06	3	-6,97E-06	6,16E-05
	10	2,50E-05	2,24E-05	10	4,84E-05	5,98E-05
	25	1,99E-04	4,39E-05	25	3,85E-05	4,95E-05
	50	1,76E-04	1,05E-04	50	1,98E-04	2,15E-04
	100	1,93E-04	5,62E-06	100	3,15E-04	2,55E-04
	200	5,79E-04	2,72E-04	200	6,08E-04	2,71E-04
	400	7,91E-04	2,61E-04	400	9,21E-04	3,74E-04
Au(13)-PEG	3	7,10E-05	9,77E-05	3	7,51E-05	3,68E-05
	10	2,27E-04	3,85E-05	10	5,27E-04	3,78E-04
	25	1,46E-03	4,30E-04	25	1,17E-03	3,43E-04
	50	1,12E-03	7,07E-05	50	1,61E-03	6,63E-04
	100	3,37E-03	1,93E-03	100	1,67E-03	3,28E-04
	200	4,76E-03	2,25E-03	200	2,09E-03	4,12E-04
	400	4,99E-03	2,41E-03	400	2,34E-03	1,02E-03
Staurosporine	3	-2,81E-05	4,96E-07	3	3,20E-05	9,07E-05
	10	9,85E-05	2,33E-05	10	9,07E-05	1,40E-05
	25	1,68E-04	4,12E-05	25	3,22E-04	3,13E-04
	50	1,98E-04	4,66E-06	50	3,46E-04	2,60E-04
	100	2,31E-04	1,05E-05	100	5,64E-04	2,38E-04
	200	3,76E-04	2,93E-06	200	7,12E-04	2,65E-04
	400	3,80E-04	9,54E-05	400	9,50E-04	2,96E-04
	1000	5,42E-04	1,00E-04	1000	1,14E-03	1,22E-04

Figure XXIV: All mean B-values out of measurements for each agent and respective standard deviations.

The toxic grad can be demonstrated by a damping value (so called B value) which was accurately calculated from the dynamic deflection by a self-written program in figure XXX a) and b) for HeLa cells and MCF7 cells, respectively. All B values of two different cell lines with different agents in dependence of concentrations were summarized as a heat-map in part c)-d) for HeLa cells and MCF7 cells, respectively.

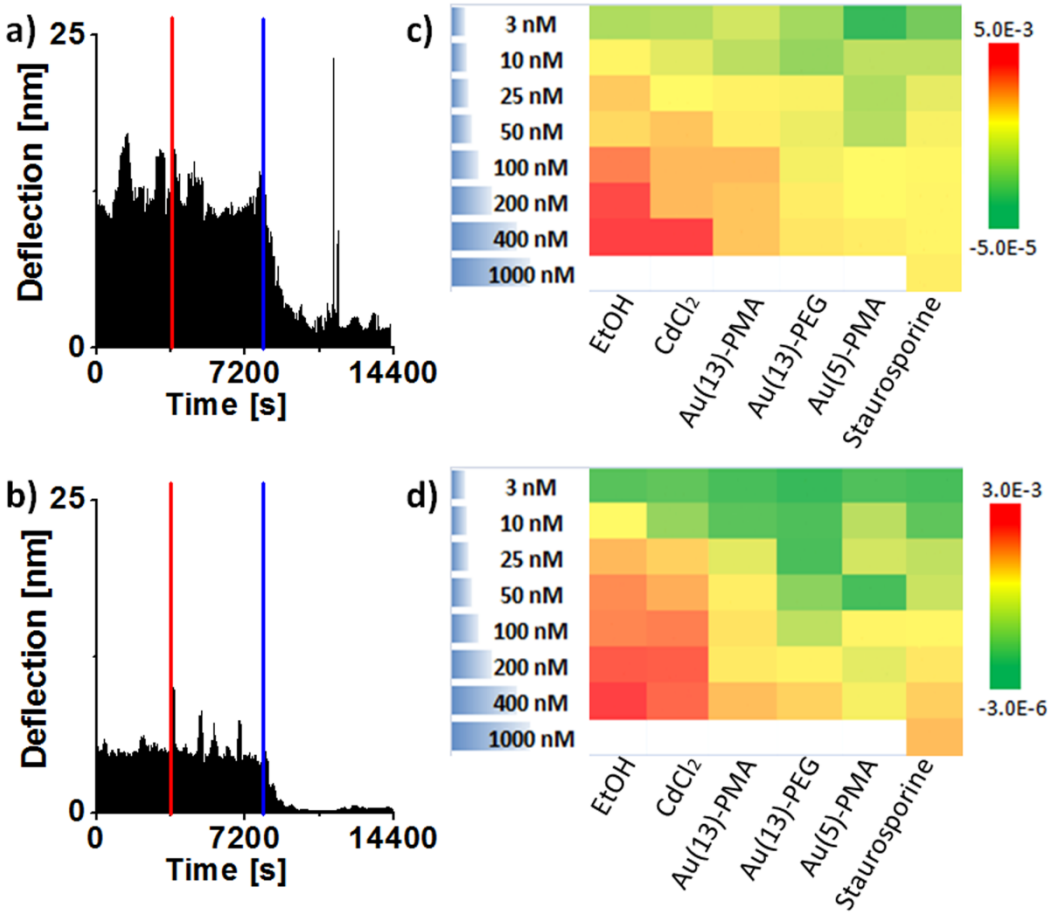

Figure XXX: Real-time recorded deflection of cantilever oscillation and analytic results of HeLa cells and MCF7 cells exposed to agents depending on different concentrations. a)-b) Amplitude trace of cantilever oscillation based on time with HeLa cells and MCF7 cells, respectively. The time of injection of agent after 3600 seconds is indicated by red line and start of the cell detachment is indicated by blue line. Each damping constant based on the curve is taken as a measure. c)-d) Heatmaps toward

Summarized analytic damping values for HeLa cells and MCF7 cells in dependence on agents with different concentrations.

According to the 3D-diagrams in figure XXXI, B-values were fitted with logistic curves for both cell lines, yielding "half-detachment" dose values to extract the trends. In order to verify that this method can quantitatively measure toxicity, resazurin assay is used as a control for comparison.

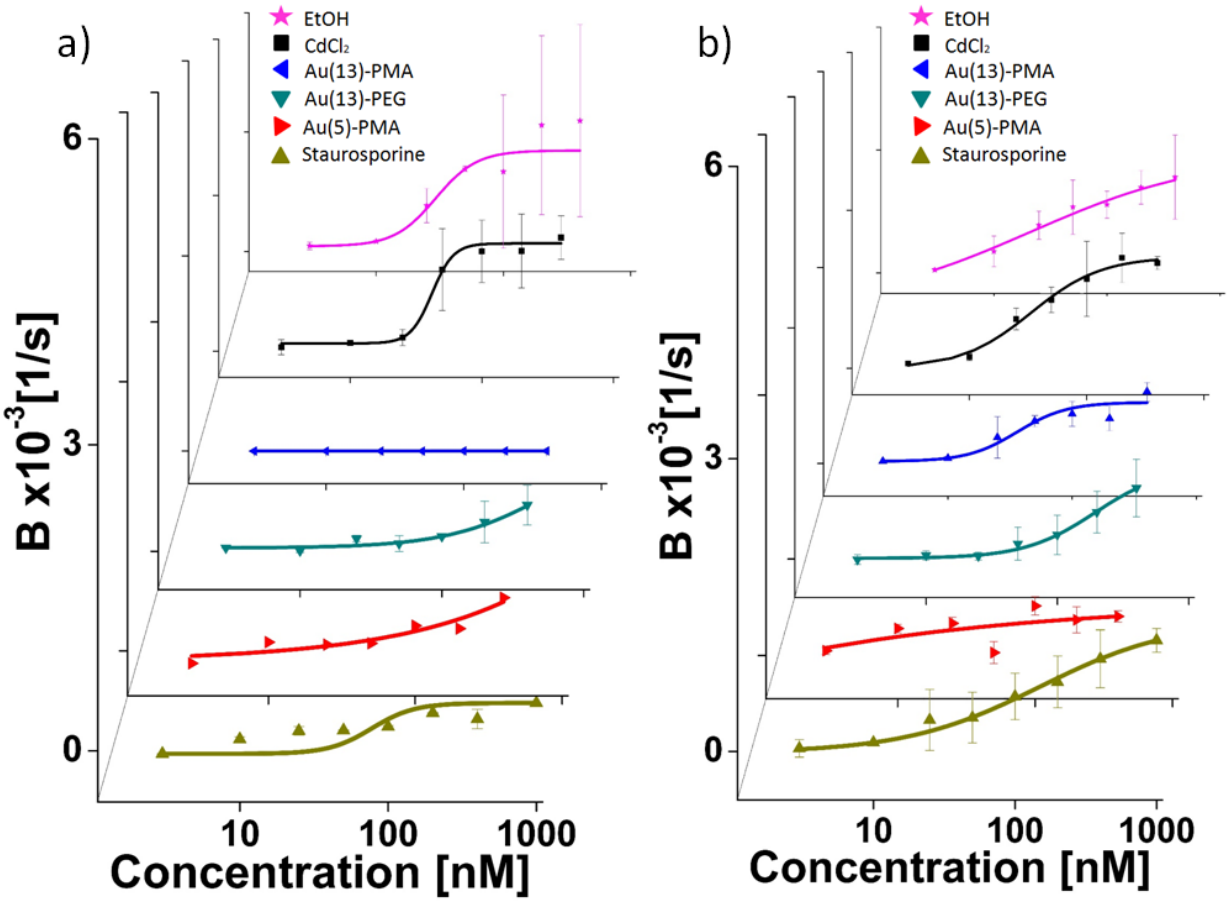

Figure XXXI: B-values for different agents and the corresponding logistic fit curves. a) Results for HeLa cells are presented, from which based on the respective logistic fit curves, "half-detachment" dose values can be extracted, i.e., 29.33 nM (EtOH), 41.80 nM ($CdCl_2$), 53.03 nM (Au(13)-PMA), 637.09 nM (Au(13)-PEG), 97.66 nM (Au(5)-PMA), and 77.54 nM (staurosporine). b) Results for MCF7 cells are presented,

from which based on the respective logistic fit curves, "half-detachment" dose values can be extracted, i.e., 21.15 nM, 32.78 nM ($CdCl_2$), 53.03 nM (Au(13)-PMA), 193.84 nM (Au(13)-PEG), 81.02 nM (Au(5)-PMA), and 150.63 nM (staurosporine).

This method is a generally applicable quantitative real-time cell viability monitoring system which indicates cell intoxication based on cell adhesion properties on an oscillating cantilever. From the detachment rate, an early harmful influence to cells for metabolism by endocytosis can be analyzed as well as the quantitative uptake of a single cell or a primary cell.

Conclusion and outlook

In the past years a lot of scientists pointed out that AFM would be a valuable tool for probing nano-materials in different way at high resolution and would be wildly used in biological applications. In order to satisfy multiple measuring requirements AFM was innovating many times. Hence the advent of multi-mode AFM made the dream come true. In fact, by now it is becoming a fascinating tool which has recently gained increased attention as nanomaterials continue to gain popularity. With rapid development of nanotechnology more multifunctional and diverse nanomaterials need to be characterized and analyzed for further biological and biomedical applications. For NPs, multi-mode AFM plays an important role in the characteristic aspect which offers the topological information as well as electric distribution and magnetic domain. In order to better understand NPs tapping mode associated with lift mode was normally utilized for further physical observation. The cantilever tapped on a sample for describing its surface and morphology and repeatedly scanned on it for secondary imaging more physical description. Herein, a biomembrane known as PM covered by NPs have emerged under EFM to reveal different electric distributions between native membrane and NPs modified membrane.

Such promising functional PM was successfully described from an electrical aspect. On the other hand, a multifunctional polymerized NP was successfully synthesized in order to ablate cancer cells under a weak rotating magnetic field. It comprised anti-cancer drugs and superparamagnetic NPs. The characterization of morphology and magnetic property was realized by MFM. Besides visual observation evaluating physical properties of NPs was realized by SMFS. The force spectroscopy recorded numerous force-distance curves for calculating the young's modulus of the NPs which is highly related to their stiffness. In order to satisfy scientific calculations, the software Nanoscope analysis was used for data processing. Behind the truth of exploring the nano-world we should speculate about mechanisms of NPs at first. Hence, mechanical properties of NPs are primary jobs we have to do. According to investigation about NPs we can probe their contribution for biological applications.

AFM is well known as one of the greatest inventions of the 20th century, because it has no limitation for measuring condition and has varied measuring function modes. Besides NPs, for cells, it is significant in magnitude compared with optical microscopy and electron microscopy. High resolution enables the detailed analysis of cellular morphology. According to this filopodia which occur on the surface of cells can be detected for ensuring its number and volume depending on NPs uptake. This classic observation system satisfied scientific visual characterization, so that cellular morphology can be correctly interpreted. In addition the surface roughness change can also be analyzed via topological mode as well. In situ of magneto-poration the polymerized functional co-loading NPs which obtain anti-cancer drugs and superparamagnetic NPs were internalized into cancerous cells. After treatment under weak rotating magnetic field the cells roughness has been changed, because the negative influence of the NPs reflect to cellular surface shrinking. It is due to shear force from magnetic moment under

induced rotating magnetic field destroyed cellular inner structure to generate cellular membrane tight. Inner cellular pressure balance was broken and huge pressure difference in- and outside will cause cell dehydration. Therefore cellular surface drape fold can be revealed from roughness analysis. Multi-mode AFM realized visual observation associated with analytic calculation can be advanced in development of nanomaterials in biological and biomedical applications. It will be a great start for leading magnetoperation into further clinic cancer therapy. Moreover, the oscillation system of AFM was modified to build a new real-time live cells monitoring system. It also offered a great opportunity to quantitatively investigate the cellular mechanisms. An oscillating cantilever by a given frequency was seen as a cell stage. Its amplitude is dependent on the mass of the cantilever with the attached cells, as the cell adhesion property is directly related to cell viability. Therefore, when cells uptake any toxicants, it will make a diminishing amplitude. According to the trend of the decreasing amplitude a real-time toxicity process can be recorded. Furthermore, it is realized that toxicity can be quantitatively realized. In future, even a single cell can be operated in such a system.

Publications

This thesis is written in a cumulative way, so the studies mentioned above are all related to publications towards application of multi mode AFM. An abstract demonstrates an overview about motivations and results of the publications, some of which are still in preparation. They are ordered thematically and some extra notes present the specific contributions by the author. A list of publications can be found in appendix. More details and experimental process are described in supporting information which are omitted here but available online following the respective journal web.

Topological image towards cellular surface characterization

(i) Colloidal nanoparticles (NPs) with different concentrations can harm cells differently. Mostly such harmful effects can be determined by biochemical assays or probed from molecular biology like viability assays, gene expression profiles, etc., but these methods still neglect that nanoparticles can affect the morphology of cells to a certain degree. In the case of uptake of polymer coated Au NPs, some intracellular organelle are changed, i.e., lysosomes are full of inner cellular spaces due to swelling of these organelles, the morphology of mitochondria changes from thread-like elongated to smaller spherical structures, the actin and tubulin network are disturbed, and the contact area of focal adhesion points is reduced, as the number of filopodia decreases. HeLa cell line and Huvec cell line are chosen for experiments. In the study of filopodia, contact mode of AFM with small bearing force is utilized for scanning the cell surface. The topological images record changes in morphology that occur at NP concentrations as the onset of reduced cellular viability. According to further counting and analyzing the images, volume of filopodia is proved as one of the indicators to verify the harmful effects of nanoparticles to cells. In addition, in order to realize the other quantitative determinations, some visual images with label and stain from different techniques will be used for analyzing these concentration-dependent changes in cellular morphology features. As one of the important co-authors I utilized AFM to observe surface change and morphology of the HeLa cells and Huvec cells which uptake different concentrations of the Au NPs, respectively. Afterwards each serie includes 30 images and each image has been modified via NanoScope analysis software for further quantitative calculation towards filopodia. At the end I wrote the part of AFM in this paper and commented on the manuscript.

(i) Xiaowei Ma[#], Raimo Hartmann[#], Dorleta Jimenez de Aberasturi, Fang Yang, Stefaan J. Soenen, Bella Manshian, Jonas Franz, Daniel Valdeperez, Beatriz Pelaz, Norbert Hampp, Christoph Riethmüller, Henning

Vieker, Natalie Freese, Armin Gölzhäuser, Michael Simonich, Robert Tanguay, Xing-Jie Liang, Wolfgang J. Parak* , Colloidal nanoparticles induce changes in cellular morphology ,, Nanotoday, submittd (#contribute equally; *corresponding author)

(ii) A polymeric nanoparticle based on PLGA loaded with a natural anticancer drug tetrandrine and superparamagnetic iron oxide NPs is developed. Such multifunctional magnetic nanoparticles can be used for ablation of cancer cells because of their potential on physical treatment. After cells finished uptake of the magnetic NPs, due to magnetism controllable property a rotating permanent magnet outside of the cells will transfer a rotational movement to intracellular magnetic NPs. The influence of multifunctional NPs in rotating magnetic field (RMF) is most likely because of shear forces created by hindered rotation of the particles in the intracellular matrix (incomplete rotation). Such mechanical action leads to harmful effects to cells. In addition, cellular morphology change which is a quantitative indicator to verify cell apoptosis and toxicity can't be neglected as well. In this study, roughness analysis serves as a reference point for morphology change and the results were calculated from topological images of AFM with contact mode without lack of any scanning data. And besides, the other assays based on labeling and imaging techniques determinate cell viability and cellular morphology changes as well. According to this, it is proved that a dual anti-cancer drug with tetrandrine and magnetic NPs can not only be exerted for determination of toxic effect by cellular morphology but also can be used for the multi-therapeutic effect against tumor cells in biomedical and clinical applications via controllable rotation. As one of the key authors I designed cell membrane poration using weak rotating magnetic field. In addition I performed topological images of cell membranes as well as quantitative analysis of cell membrane surface roughness.

(ii) Chen Shi[#], Fang Yang[#], Qian Zhang, Sandra Neitemeier, CarolinThum, Norbert Hampp, Carsten Culmsee, Wolfgang Parak and Marc Schneider*, Enhancing cellular morphological changing and ablation of cancer cells via interaction of multifunctional magnetic co-loaded NPs in rotating magnetic fields, in preparation.

Single molecule force spectroscopy towards determining stiffness of gold nanoparticles

(i) SMFS is a useful tool for measuring and analyzing intermolecular forces and is setup based on AFM utilizing binding force between tip and sample. Therefore some physical properties, i.e., stiffness, adhesion force, dissipation, and deformation, can be studied according to calculation of the force versus distance. Au NPs coated with polyethylene glycol, whereby the diameter of the gold cores as well as the thickness of the shell of polyethylene glycol, were employed to explore basic physicochemical parameters of this two-dimensional NP library, such as size, ζ-potential, hydrophilicity, elasticity, and catalytic activity. Young's modulus serves as a good factor for evaluating elasticity. Due to a conical tip penetrating a single Au NP, Sneddon's equation was used for calculating huge statistic data. In addition, exposure of cells to the NPs and their effect on basic structural and functional cell parameters were determined. Increased incorporation of the PEG coated NPs relates to significant effects on the parameters. As one of the key authors I performed all AFM images and quantitative analysis about elasticity of all different Au NPs-PEGs. At the end I commented the manuscript and wrote the part of AFM and elasticity.

(i) Pablo del Pino[#*], Fang Yang[#], Beatriz Pelaz[#], Qian Zhang, KarstenKantner, Raimo Hartmann, Natalia Martinez de Baroja, Marta Gallego, Marco Möller, Bella Manshian, StefaanSoenen, Norbert Hampp, Wolfgang J. Parak*. Basic Physicochemical Properties of Polyethylene Glycol Coated Gold Nanoparticles that Determine Their Interaction with Cells, Angewandte Chemie international edition**,** 128**,** 2016

Magnetic force microscopy towards magnetic domains of mNPs

(i) A multifunctional co-loading magnetic NP with superparamagnetic Fe_3O_4 NPs and tetrandrine is successful synthesized. In further study we demonstrate that such magnetic NPs by virtue of their superparamagnetic nature, rotate when exposed to a rotating magnetic field and cause them to tend to rotationally migrate. The shear forces produced by the rotation thus disrupt the cell membrane integrity when the cells are internalized by NPs subjected to the rotating magnetic field, by which harmful effects of the NPs are directly visible by magneto-cell-poration. These results indicate the possibility of magneto-cell-lysis as a means in situ ablation of tumors. In order to realize the remote application of magnetic control, MFM is a powerful tool to characterize magnetic property and visually observe magnetic domains of the NP. Including the drug tetrandrine as a dual enhanced multifunctional anti-cancer NP will offer an attractive alternative methodology for cancer therapeutics and clinical applications. As one of the key authors I designed experiment towards magnetic domain observation of the samples using MFM and performed MFM images.

(i) Chen Shi[#], Fang Yang[#], Qian Zhang, Sandra Neitemeier, CarolinThum, Norbert Hampp, Carsten Culmsee, Wolfgang Parak and Marc Schneider*, Enhancing cellular morphological changing and ablation of cancer cells via interaction of multifunctional magnetic co-loaded NPs in rotating magnetic fields, in preparation.

Electrostatic force microscopy towards electrostatic potential of PM modified by functional NPs

(i) Biomineralization of inorganic materials formed by self-assembled proteins is a widespread phenomenon in nature. So far molecular mechanism especially the morphogenesis, has not been elucidated. Nevertheless more and more researchers give concern about silicate cell walls of diatoms in biomineral structure area. In this manuscript a new class of PM will be described

which is genetically modified on the extracellular side, were seven amino acids starting from E234 were replaced by arginine. Due to this exchange the cytoplasmatic surface charge of the PM changes from negative to positive. The introduced arginine sequence catalyses silica biomineralization and investigate process of in diatoms as well. Hence, It is demonstrated and analyzed that the biomineralization of silicic acid at room temperature form membrane attached spherical silica nanoparticles which then fuse to form 2-dimensional silica nano-flakes selectively on the cytoplasmic side of this mutated PM variant. As one of the authors I performed topological images and EFM images. I wrote the part of AFM and commented on the manuscript at the end.

(i) Annegret P. Busch, Daniel. Rhinow, Fang. Yang, Hendrik. Reinhardt, Andr é Beyer, Armin. G ölzh äuser**,** Norbet. Hampp, Site-Selective Biomineralization of Native Biological Membranes. *J. Mat. Chem. B*, 2 (**2014**) 6924-6930.

(ii) One new functional biomaterial is a greatly promising strategy to form hybrid biosystem based on integration of NP and biomembrane. Attachment of NPs to a biomembrane, which serves as a collective carrier for the NP, is a novel approach opening new application possibilities. It is simple to realize and can take advantage of the fact that NPs with the functional organic molecule connect the amino acid-appended biomembrane utilizing well established metal-affinity interaction. In this paper a versatile approach is reported where nitrilotriacetate-modified gold NPs are immobilized to the surface of a mutated purple membrane carrying a C-terminal His-tag. NH and I conceived the idea. I designed all the experiments and developed the framework. I performed all the AFM images and EFM images. I analyzed all the data and wrote the manuscript.

(ii) Fang Yang, Beatriz Pelaz, Xiang Yu, René Riedel, Qian Zhang, Bo Zhang, Pablo del Pino, Wolfgang J. Parak, Norbert A Hampp*, Hybrid bioconjugation based on assembly of functional gold nanoparticles on mutant purple membrane via Ni-NTA and histidine interaction, in preparation.

Oscillation system towards real-time monitor cell viability

Multi-mode AFM has emerged as a powerful tool to measure small force and has proved advantages in probing bio-nanotechnology. With the strong foundation to build on, a generally applicable quantitative real-time cell viability monitoring system which uses cell adhesion based on the AFM oscillation system will be successfully set up, whereby a cantilever at a given frequency is highly dependent on the mass of the cantilever, in this situation, the mass of cells on the cantilever. In our method, a dynamic toxic process can be observed and analyzed even at early stage of intoxication, so that more toxic mechanism in the presence of different agents will be studied. Apart from this, single stem cells can be analyzed as well. As the key author I designed the experiment and built the most parts of the monitoring system. I analyzed the most of data and performed all figures. At the end WJP, NH, PDP and I wrote the paper and commented on the manuscript.

(i) Fang Yang, René Riedel, Pablo del Pino, Beatriz Pelaz, Alaa Hassan Said, Mahmoud Soliman, Shashank R. Pinnapireddy, Neus Feliu, Wolfgang J. Parak, Udo Bakowsky, Norbert Hampp*, Real-time, label-free monitoring of cell viability based on cell adhesion measurements with an atomic force microscope, submitted.

Equipments and materials

AFM: Multi mode atomic force microscopy with Nanoscope V system (Brucker. Ltd, Karlsruhe, Germany)

EFM: Electrostatic force microscope with Nanoscope V system (Brucker. Ltd, Karlsruhe, Germany)

MFM: Magnetic force microscope with Nanoscope V system (Brucker. Ltd, Karlsruhe, Germany)

SMFM: Single molecule force sprectoscopy with Nanoscope V system (Brucker. Ltd, Karlsruhe, Germany)

SEM: JEOL JSM-7500F with high resolution

TEM: JEOL JEM 3010, Japan with high-resolution maximal magnification: 1,500,000

CLSM: Confocal laser scanning microscope (Carl Zeiss, Germany)

UV-Vis spectroscopy: Lambda 35, PerkinElmer Instruments, USA

DLS: Dynamic light scattering spectroscopy (Delsa® Nano C particle analyzer, Beckman Coulter, Krefeld, Germany)

Digital Multimeter: Keithley Digital multimeter 2000/E

SNL cantilever: Silicon-tip on nitride lever, k = 0.32 N/m, f = 40-75 kHz.

SCM-PIT cantilever: tip antimony (n) doped Si, k= 1 - 5 N/m, f_0= 70 - 83 kHz, 0.01 – 0.025 Ω/cm, (Brucker Ltd, Karlsruhe, Germany)

MESP cantilever: tip

Mica: Plano, Wetzlar, Germany

HOPG: highly oriented pyrolytic graphite (Plano, Wetzlar, Germany).

Stainless steel plate: 1cm*1cm (Plano, Wetzlar, Germany) with a smooth surface

Abbreviation and explanation of words

Au	gold
AFM	atomic force microscope
A549	a carcinomic human alveolar basal epithelial cell
AC	alternative current
Arg7PM	arginine mutant purple membrane
BR	bacteriorhodopsin
DS	deflection sensitivity
DLS	dynamic light scattering spectroscopy
DC	direct current
EFM	electrostatic force microscope
HeLa	human cervical cancer cells from Mrs. Henrietta Lacks
Huvec	human umbilical vein endothelial cell
HIM	helium ion microscope
HisPM	histidine mutant purple membrane
LDA	laser doppler anemometry
MFM	magnetic force microscope
MRI	magnetic resonance imaging
NPs	nanoparticles
PMA	poly(isobutylene-alt-maleic anhydride
PEG	polyethylene glycol
PBS	phosphate buffered saline
PM	purple membrane
PLGA	poly(lactic-co-glycolic acid)
PM-WT	wild type purple membrane
RMF	rotating magnetic field
SMFM	single molecule force spectroscopy
SEM	scanning electron microscope
STM	scanning transmission microscope
TEM	transmission electron microscope

TM	tapping mode

Reference

1. Binnig, G.; Quate, C. F.; Gerber, C. *Phys Rev Lett* **1986,** 56, (9), 930-933.
2. Roiter, Y.; Minko, S. *J Am Chem Soc* **2005,** 127, (45), 15688-9.
3. Unsay, J. D.; Cosentino, K.; Garcia-Saez, A. J. *J Vis Exp* **2015**, (101), e52867.
4. Hamon, L.; Pastre, D.; Dupaigne, P.; Le Breton, C.; Le Cam, E.; Pietrement, O. *Nucleic Acids Res* **2007,** 35, (8), e58.
5. Lyubchenko, Y. L.; Shlyakhtenko, L. S. *Methods* **2009,** 47, (3), 206-13.
6. Erdmann, M.; David, R.; Fornof, A.; Gaub, H. E. *Nat Nanotechnol* **2010,** 5, (2), 154-9.
7. Geisler, M.; Balzer, B.; Hugel, T. *Small* **2009,** 5, (24), 2864-2869.
8. Moskalenko, A. V.; Yarova, P. L.; Gordeev, S. N.; Smirnov, S. V. *Biophys J* **2010,** 98, (3), 478-87.
9. Kaiser, U.; Schwarz, A.; Wiesendanger, R. *Nature* **2007,** 446, (7135), 522-5.
10. Lyuksyutov, S.; Vaia, R.; Paramonov, P.; Juhl, S.; Waterhouse, L.; Ralich, R.; Sigalov, G.; Sancaktar, E. *Nat Mater* **2003,** 2, (7), 468-472.
11. Srikanth, M.; Kessler, J. A. *Nat Rev Neurol* **2012,** 8, (6), 307-18.
12. Sonkaria, S.; Ahn, S. H.; Khare, V. *Recent Pat Food Nutr Agric* **2012,** 4, (1), 8-18.
13. Dreaden, E. C.; Austin, L. A.; Mackey, M. A.; El-Sayed, M. A. *Ther Deliv* **2012,** 3, (4), 457-78.
14. Osorio, H.; Cea, P.; Ballesteros, L.; Gascon, I.; Marques-Gonzalez, S.; Nichols, R.; Perez-Murano, F.; Low, P.; Martin, S. *J Mater Chem C* **2014,** 2, (35), 7348-7355.
15. Saxena, U.; Goswami, P. *J Nanopartic Res* **2012,** 14, (4).
16. Del Pino, P.; Yang, F.; Pelaz, B.; Zhang, Q.; Kantner, K.; Hartmann, R.; Martinez de Baroja, N.; Gallego, M.; Moller, M.; Manshian, B. B.; Soenen, S. J.; Riedel, R.; Hampp, N.; Parak, W. J. *Angew Chem Int Ed Engl* **2016,** 55, (18), 5483-7.
17. Du, S.; Kendall, K.; Toloueinia, P.; Mehrabadi, Y.; Gupta, G.; Newton, J. *J Nanopartic Res* **2012,** 14, (3).
18. Han, X.; Liu, Y.; Yin, Y. *Nano Lett* **2014,** 14, (5), 2466-70.
19. Gao, Y.; Li, X.; Li, Y.; Li, T.; Zhao, Y.; Wu, A. *Chem Commun (Camb)* **2014,** 50, (49), 6447-50.

20. Miao, L.; Xin, J.; Shen, Z.; Zhang, Y.; Wang, H.; Wu, A. Sens *Actuator B Chem* **2013,** 176, 906-912.

21. Lin, C. A.; Sperling, R. A.; Li, J. K.; Yang, T. Y.; Li, P. Y.; Zanella, M.; Chang, W. H.; Parak, W. J. *Small* **2008,** 4, (3), 334-41.

22. Kantner, K.; Ashraf, S.; Carregal-Romero, S.; Carrillo-Carrion, C.; Collot, M.; Del Pino, P.; Heimbrodt, W.; De Aberasturi, D. J.; Kaiser, U.; Kazakova, L. I.; Lelle, M.; de Baroja, N. M.; Montenegro, J. M.; Nazarenus, M.; Pelaz, B.; Peneva, K.; Gil, P. R.; Sabir, N.; Schneider, L. M.; Shabarchina, L. I.; Sukhorukov, G. B.; Vazquez, M.; Yang, F.; Parak, W. J. *Small* **2015,** 11, (8), 896-904.

23. Zhang, F.; Lees, E.; Amin, F.; Rivera Gil, P.; Yang, F.; Mulvaney, P.; Parak, W. J. *Small* **2011,** 7, (22), 3113-27.

24. Perez-Hernandez, M.; Del Pino, P.; Mitchell, S. G.; Moros, M.; Stepien, G.; Pelaz, B.; Parak, W. J.; Galvez, E. M.; Pardo, J.; de la Fuente, J. M. *ACS Nano* **2014,** 9, (1), 52-61.

25. Soenen, S. J.; Manshian, B.; Montenegro, J. M.; Amin, F.; Meermann, B.; Thiron, T.; Cornelissen, M.; Vanhaecke, F.; Doak, S.; Parak, W. J.; De Smedt, S.; Braeckmans, K. *ACS Nano* **2012,** 6, (7), 5767-83.

26. Shi, C.; Thum, C.; Zhang, Q.; Tu, W.; Pelaz, B.; Parak, W. J.; Zhang, Y.; Schneider, M. *J Control Release* **2016,** 237, 50-60.

27. Felton, C.; Karmakar, A.; Gartia, Y.; Ramidi, P.; Biris, A.; Ghosh, A. *DRUG Metab. Rev* **2014,** 46, (2), 142-154.

28. Zeng, L.; Ren, W.; Xiang, L.; Zheng, J.; Chen, B.; Wu, A. *Nanoscale* **2013,** 5, (5), 2107-13.

29. Attar, M. M.; Haghpanahi, M. *Electromagn Biol Med* **2016**, 1-16.

30. Liu, D.; Wang, L.; Wang, Z.; Cuschieri, A. *Nano Lett* **2012,** 12, (10), 5117-21.

31. Vasilakaki, M.; Trohidou, K. N.; Nogues, J. *Sci Rep* **2015,** 5, 9609.

32. Zhang, Q.; Castellanos-Rubio, I.; Munshi, R.; Orue, I.; Pelaz, B.; Gries, K.; Parak, W.; del Pino, P.; Pralle, A. *Chem Mater* **2015,** 27, (21), 7380-7387.

33. Liepins, A. *Immunopharmacol Immunotoxicol* **1989,** 11, (4), 539-58.

34. Mattila, P. K.; Lappalainen, P. *Nat Rev Mol Cell Biol* **2008,** 9, (6), 446-54.

35. Busch, A.; Rhinow, D.; Yang, F.; Reinhardt, H.; Beyer, A.; Golzhauser, A.; Hampp, N. *J Mater Chem B* **2014,** 2, (40), 6924-6930.

36. Soliman, M.; Pelaz, B.; Parak, W.; del Pino, P. *Chem Mater* **2015,** 27, (3), 990-997.

37. Mignani, A.; Fazzini, S.; Ballarin, B.; Boanini, E.; Cassani, M.; Maccato, C.; Barreca, D.; Nanni, D. *Rsc Adv* **2015,** 5, (13), 9600-9606.

38. Huhn, D.; Kantner, K.; Geidel, C.; Brandholt, S.; De Cock, I.; Soenen, S. J.; Rivera Gil, P.; Montenegro, J. M.; Braeckmans, K.; Mullen, K.; Nienhaus, G. U.; Klapper, M.; Parak, W. J. *ACS Nano* **2013,** 7, (4), 3253-63.

39. Rivera-Gil, P.; De Aberasturi, D.; Wulf, V.; Pelaz, B.; Del Pino, P.; Zhao, Y.; De La Fuente, J.; De Larramendi, I.; Rojo, T.; Liang, X.; Parak, W. *Acc Chem Res* **2013,** 46, (3), 743-749.

40. Cao, G., *Nanostructures & Nanomaterials: Synthesis, Properties & Applications*. ed.; Imperial college press: London, **2004**; 'Vol.' p 265.

41. Zhang, L.; Cao, Z.; Li, Y.; Ella-Menye, J.; Bai, T.; Jiang, S. *ACS NANO* **2012,** 6, (8), 6681-6686.

42. Qin, S.; Yin, H.; Yang, C.; Dou, Y.; Liu, Z.; Zhang, P.; Yu, H.; Huang, Y.; Feng, J.; Hao, J.; Hao, J.; Deng, L.; Yan, X.; Dong, X.; Zhao, Z.; Jiang, T.; Wang, H.; Luo, S.; Xie, C. *Nat Mater* **2016,** 15, (2), 217-+.

43. Giustini, A. J.; Petryk, A. A.; Cassim, S. M.; Tate, J. A.; Baker, I.; Hoopes, P. J. *Nano Life* **2013,** 1, (1n02).

44. Cho, H. S.; Chang, S. H.; Chung, Y. S.; Shin, J. Y.; Park, S. J.; Lee, E. S.; Hwang, S. K.; Kwon, J. T.; Tehrani, A. M.; Woo, M.; Noh, M. S.; Hanifah, H.; Jin, H.; Xu, C. X.; Cho, M. H. *J Vet Sci* **2009,** 10, (1), 23-8.

45. Baumann, R. P.; Busch, A. P.; Heidel, B.; Hampp, N. *J Phys Chem B* **2012,** 116, (14), 4134-40.

46. Budó, A., *Theoretische Mechanik*. 11 ed.; VEB Deutscher Verlag der Wissenschaften: Berlin, 1987; 'Vol.' p.

47. Han, S.; Benaroya, H.; Wei, T. *J Sound Vibration* **1999,** 225, (5), 935-988.

48. Perillo, N. L.; Marcus, M. E.; Baum, L. G. *J Mol Med (Berl)* **1998,** 76, (6), 402-12.

49. Longo, G.; Alonso-Sarduy, L.; Rio, L. M.; Bizzini, A.; Trampuz, A.; Notz, J.; Dietler, G.; Kasas, S. *Nat Nanotechnol* **2013,** 8, (7), 522-6.

Acknowledgement

I would like to express my sincere thanks to my supervisor Prof. Dr. Norbert Hampp for offering me opportunities to work in his group and always supporting me to attempt my scientific ideas with his kind attitude and suggestions. Moreover he always encourages me and gives me personal advices about future career.

As well I would like to address many thanks to Prof. Dr. Wolfgang Parak who led me to a right way towards science. I would express deep thanks to him for giving me scientific suggestions and personal advices. Without his help and advices it would not have been possible to have such achievements today.

In particular I am very grateful for Dr. Pablo del Pino to give me some nice suggestions and help me with improving scientific abilities. Hence I want to express my deepest gratitude to him.

I am very gratefully acknowledging Dr. Beatriz Pelaz for the open and interminable discussion, valuable hints and reviewing my doctoral thesis.

I would especially thank to Prof. Dr. Aiguo Wu (NIMTE, Chinese Academy of Sciences, China) for personal encouragement and crucial suggestions. In addition I will thank him to offer me a great chance for doing research.

I am so glad and appreciated that I have such nice supervises even friends in my life.

For collaborated works I would love to thank Prof. Dr. Udo Bakowsky and Mr. Shashank Readdy Pinnapireddy (AG Bakowsky, Pharmacy department, Marburg, Germany), Dr. Neus Feliu Torres, Mr. Alaa Hassan said Abdelkarim, Dr. Sumaira Ascharf (AG Biophotonic, Physical department, Marburg, Germany) for preparing cells and cellular measurements towards toxicity assay, and thank Dr. Mahmoud Soliman, Dr. Pablo del Pino, Dr. Beatriz Pelaz, and Dr. Qian Zhang (AG Biophotonic, physical department, Marburg, Germany) for preparing NPs as well as

Prof. Dr. Mac Schneider and Dr. Chen Shi (AG Schneider, Pharmacy department, Marburg, Germany)for preparing co-loading magnetic NPs. In addition I want to thank Dr. Xiaowei Ma (National center for nanoscience and technology, China) for preparing cells plate towards AFM.

I also would like to thank Mr. René Riedel for helping me with some experiments and computer programs during his time as lab student.

I would be grateful for all my colleagues in my group and former group for their technical and non-technical help, advice, and support.

In the end I express my deep thanks to my family and friends, especially to my parents and Yuwen who are always standing by my side and motivate me over and over.

Appendix

1. Xiaowei Ma#, Raimo Hartmann#, Dorleta Jimenez de Aberasturi, Fang Yang, Stefaan J. Soenen, Bella Manshian, Jonas Franz, Daniel Valdeperez, Beatriz Pelaz, Norbert Hampp, Christoph Riethmüller, Henning Vieker, Natalie Freese, Armin Gölzhäuser, Michael Simonich, Robert Tanguay, Xing-Jie Liang, Wolfgang J. Parak* , *Colloidal nanoparticles induce changes in cellular morphology* ,, Nano today, submitted (#contribute equally; *corresponding author)
2. Pablo del Pino#*, Fang Yang#, Beatriz Pelaz#, Qian Zhang, KarstenKantner, Raimo Hartmann, Natalia Martinez de Baroja, Marta Gallego, Marco Möller, Bella Manshian, StefaanSoenen, Norbert Hampp, Wolfgang J. Parak*. *Basic Physicochemical Properties of Polyethylene Glycol Coated Gold Nanoparticles that Determine Their Interaction with Cells*, Angewandte Chemie international edition, 128, 2016
3. Annegret P. Busch, Daniel. Rhinow, Fang. Yang, Hendrik. Reinhardt, André. Beyer, Armin. Gölzhäuser, Norbet. Hampp, *Site-Selective Biomineralization of Native Biological Membranes*. J. Mat. Chem. B, 2 (2014) 6924-6930.
4. Fang Yang, René Riedel, Pablo del Pino, Beatriz Pelaz, Alaa Hassan Said, Mahmoud Soliman, Shashank R. Pinnapireddy, Neus Feliu, Wolfgang J. Parak, Udo Bakowsky, Norbert Hampp*, *Real-time, label-free monitoring of cell viability based on cell adhesion measurements with an atomic force microscope*, Nano Letters, submitted.

Colloidal nanoparticles induce changes in cellular morphology

Xiaowei Ma[1,2*], Raimo Hartmann[1*], Dorleta Jimenez de Aberasturi[1,3], Fang Yang[4,5], Stefaan J. Soenen[6], Bella Manshian[6], Jonas Franz[7], Daniel Valdeperez[1], Beatriz Pelaz[1], Norbert Hampp[4,5], Christoph Riethmüller[8], Henning Vieker[9], Natalie Freese[9], Armin Gölzhäuser[9], Michael Simonich[10], Robert Tanguay[10], Xing-Jie Liang[2#], Wolfgang J. Parak[1,3#]

[1] Fachbereich Physik, Philipps Universität Marburg, Marburg, Germany
[2] Chinese Academy of Sciences (CAS) Key Laboratory for Biological Effects of Nanomaterials and Nanosafety, National Center for Nanoscience and Technology, Beijing, China
[3] CIC Biomagune, San Sebastian, Spain
[4] Fachbereich Chemie, Philipps Universität Marburg, Marburg, Germany
[5] Material Science Center, Philipps Universität Marburg, Marburg, Germany
[6] Biomedical MRI Unit/MoSAIC, Catholic University of Leuven, Leuven, Belgium
[7] nAnostic Institute, Center for Nanotechnology, University of Münster, Germany
[8] Serend-ip GmbH, Center for Nanotechnology, Münster, Germany
[9] Fakultät für Physik, Universität Bielefeld, Bielefeld, Germany
[10] OSU Sinnhuber Aquatic Research Laboratory (SARL), Oregon, USA
* both authors contributed equally to this work
# corresponding authors: liangxj@nanoctr.cn; wolfgang.parak@physik.uni-marburg.de

Abstract

Exposure of cells to colloidal nanoparticles (NPs) can have concentration-dependent harmful effects. Mostly, such effects are monitored with biochemical assays or probes from molecular biology, *i.e.* viability assays, gene expression profiles, *etc.*, neglecting that the presence of NPs can also drastically affect cellular morphology. In the case of polymer-coated Au NPs we demonstrate that upon NP internalization, cells undergo lysosomal swelling, alterations in mitochondrial morphology, disturbances in actin and tubulin cytoskeleton and associated signaling, and reduction of focal adhesion contact area and number of filopodia. Appropriate imaging and data treatment techniques allow for quantitative analyses of these concentration-dependent changes. Abnormalities in morphology occur at similar (or even lower) nanoparticle concentrations as the onset of reduced cellular viability. Cellular morphology is thus an important quantitative indicator to verify harmful effects of NPs to cells, without requiring biochemical assays but relying on appropriate staining and imaging techniques.

Keywords: nanoparticles, Au NPs, cellular morphology, cytotoxicity, viability, cellular response

1. Introduction

Colloidal nanoparticles (NPs) are incorporated by living cells, regardless of whether this is intended for certain delivery applications (*i.e.* tumor targeting), or not due to leakage of NPs into the environment (*i.e.* air, water pollution)[1]. Once in contact with cells, the typical uptake scenario involves endocytosis[2-4]. Proteins adsorbed to the surface of the NPs hereby play a major role[5, 6]. Interaction of NPs with cells has been demonstrated to trigger dose-dependent effects in cells (which obviously strongly depend on the nature of NPs and on the type of cells), which can ultimately lead to cell death. Details about the uptake mechanisms of NPs by cells, as well as the molecular signaling cascades which are being triggered [7], in particular involving molecular mechanisms for toxic effects, are well described in the literature[8-10]. Most of these studies aim at understanding the interaction of NPs with cells at a molecular level. However, effects of the NPs on cells are also manifested at the level of cell morphology. Due high-throughput microscopy and high content screening of the acquired data the assessment of morphological parameters is becoming more and more feasible allowing for multiparametric response- and cytotoxicity studies to be carried out [11-13].

In multiple studies the disruption of organelles and other subcellular structures caused by NPs have been reported. Gold NPs for example (as well as other NPs) have been described to have a profound effect on several intracellular organelles/structures and functions associated with morphological changes. First, this applies to mitochondria. Mitochondria are one of the most important organelles in cells. Damage/disruption of mitochondria can result in a wide range of diseases and disorders. It has been reported that the decrease of mitochondrial activity reflects acute cytotoxicity of colloidal NPs [14]. Many studies have found that exposure of cells to Au NPs was accompanied by an increased level of reactive oxygen species (ROS), which is associated with malfunctioned mitochondria. Pan *et al.* observed that Au NPs of an average diameter of 1.4 nm induce cytotoxicity by oxidative stress, which is indicated by endogenous ROS production, compromised mitochondrial potential, integrity, and mitochondrial substrate reduction[15]. Interestingly, Chompoosor *et al.* reported that 2 nm Au NPs with different hydrophobic alkyl tails could generate significant amounts of ROS at concentrations that do not even affect mitochondrial activity[16]. Wang *et al.* speculated that the selective targeting and damaging effects of Au nanorods to the mitochondria of cancer cells could be used in tumor therapy, while normal cells maintain intact mitochondria[17]. For NPs of other materials and sizes even mitochondrial permeabilization and fragmentation was observed [18]. Second, effects on lysosomes have been reported. Most NPs will eventually be accumulated inside acidic organelles after following their endocytic pathway. Being the major degradative compartment of eukaryotic cells, the lysosome is a high capacity organelle responsible for macromolecular homeostasis. Previous work has shown that large amounts of Au NPs aggregated in the lysosomes can lead to lysosome alkalinization. This is associated with the impairment of vacuolar V-ATPases, which regulate lysosome acidification. Consequently, the lysosome-based degradative autophagy-pathway is affected, which leads to a disruption of cellular homeostasis[19]. Swelling of lysosomes upon NP enrichment has also been reported[14, 20, 21]. Third, NPs have been shown to interfere with the cellular cytoskeleton. The cytoskeleton is responsible for anchoring organelles, maintaining cell morphology, and intercellular connections. Previous findings by Pernodet *et al.* indicate that the diameter, the

stretching state, and the density of actin filaments in human dermal fibroblasts were affected in a concentration-dependent manner upon treatment with Au NPs. These effects might cause major changes in cell shape, cell spreading, cell adhesion, and cell growth[22-24]. The same group also found that different sized Au NPs (13 or 45 nm) can induce cytoskeletal filament disruption to a different extent, without changing actin or beta-tubulin protein levels[25]. A further study by Yang *et al*. showed that the actin F-fibers were disrupted to various extents depending on the aggregation state of Au NPs. The authors reported varying decrease in F-actin fiber intensity and thickness and the appearance of actin dots. The lack of actin-fiber formation and the appearance of actin dots rather than long fibers were correlated with the presence of Au NPs in the cytosol which were thought to cause depolymerization of actin[26]. Furthermore, the morphology of cell junctions may be subject to changes[27] following NP exposure. The intracellular disruption of the cytoskeletal network caused by Au NPs has been found to be associated with the disruption of cell-cell adhesion. It was found that exposure to highly concentrated Au NPs will significantly reduce the area of focal adhesion complexes (FACs) which leads to an increase in the amount of free vinculin, a major structural component of FACs[12]. Lin *et al.* also found different sized Au NPs could cause loosening of the intercellular tight junctions that are joining individual cells[28]. Finally, NP impact on the cytoskeleton may influence cellular migration. Rafailovich's group found that the presence of Au NPs in human adipose-derived stromal cells could result in a concentration-dependent increase in population doubling times, a decrease in cell motility, and cell-mediated collagen contraction[29]. Considering that cell migration plays a crucial role in tumor growth and metastasis, therefore, NPs that can impede the mobility of tumor cells are of great interest in preclinical research. In summary, there is clear evidence that the uptake of Au NPs by cells has a (concentration-dependent) effect on their morphology.

In the present work, we provide a comprehensive study on how *in vitro* uptake of Au NPs affects cellular morphology and intracellular organelles/structures. Thus, the focus of this work is not on signal pathways, but rather on morphological changes. Polymer-coated, anionic Au NPs (Au-PMA* NPs) with a fluorescent label were chosen for this study[12, 30-32]. These NPs have been fully characterized for their colloidal properties and interaction with cells within the last 10 years. They are colloidally stable with a narrow size distribution (4.8 ± 0.7 nm core diameter)[33, 34]. These NPs are incorporated by cells *via* endocytic pathways and accumulated inside acidic intracellular vesicles, in particular lysosomes[35-37]. In contrast to other NPs such as cadmium selenide (CdSe) or silver (Ag) NPs the Au NPs are not composed of an intrinsically toxic material, yet several concentration-dependent cytotoxic responses such as production of ROS have been described *in vitro*[12, 38]. Reported IC_{50} concentration values for Au NPs of similar size distribution vary between a few hundred nM[12, 39] and a few µM or even mM[40, 41] depending on surface coating, the cell types used and incubation conditions. The NPs used in the present study are bigger than the ultra-small clusters of 1.3 nm core size Au NPs for which size-specific effects have been reported[15]. In the case of the here used *ca.* 4.8 nm core diameter NPs toxic effects do not only originate from their surface coating, but also due to the Au core[38], which possesses some catalytic activity. For this study two well established and commonly used mammalian cell lines were used. These were the human umbilical vein endothelial cells (HUVECs) and the human cervical cancer cell line (HeLa). As control the same Au NP cores, but with different surface coating (*i.e.* PMA without a fluorescence label,

mercaptoundecanoic acid (Au-MUA NPs [42]) and polyethylene glycol (Au-PEG NPs [42, 43]) were used. In addition Au^{3+} (as obtained from hydrogen tetrachloroaurate (III) hydrate,$HAuCl_4 \cdot xH_2O$) and Cd^{2+} (as obtained from $CdCl_2$) was used as reference [44].

2. Materials and Methods

Polymer-coated Au NPs (Au-PMA* NPs)[12, 30-32] with a core diameter of $d_c = 4.8 \pm 0.7$ nm (as determined by transmission electron microscopy (TEM)), a hydrodynamic diameter of $d_h = 12 \pm 3$ nm (as determined from the number distribution of dynamic light scattering (DLS) in water), and a zeta-potential of $\zeta = -30 \pm 2$ nm (as determined from laser Doppler anemometry (LDA) in water) were used, *cf.* the Supporting Information for the raw data. Due to a fluorophore which is located inside the inner hydrophobic polymer shell[45], and thus in first order not present at the NP surface, these NPs are fluorescent and thus can be visualized with confocal microscopy. Also the control NPs (Au-PMA NPs (without fluorescence label in the polymer shell), Au-MUA NPs [42], Au-PEG NPs [39, 42, 46]) were synthesized according to previously published protocols, *cf.* the Supporting Information for more details. HUVECs and HeLa cells were exposed to the NPs at NP concentrations ranging from 0.1 - 100 nM (in serum containing medium, for details *cf.* the Supporting Information). In parallel, Au^{3+} and Cd^{2+} ions were added at the same amount of total Au atoms for the Au NPs (0 – 35 mM). Their uptake was quantified by confocal microscopy and standard viability and proliferation assays (Live/Dead viability assay[47], cell proliferation assay[48], resazurin assay[49-51], and MTT assay[52]). Different cellular structures (lysosomes, mitochondria, actin and microtubule network, vinculin, and filopodia) were optionally labeled by immunostaining or transfection, and changes in their geometry, as well as changes in the morphology of the whole cell (*i.e.* cell spreading) were analyzed from fluorescence or atomic force microscopy (AFM) images by digital image analysis tools. In addition, the effects of the NPs on expression of genes related to the cytoskeleton, as well as actin- and tubulin polymerization assays were carried out[53, 54].

3. Results and Discussion

3.1. Au-PMA* NP location and internalization rate

As expected the Au NPs were internalized by both HeLa cells and HUVECs. While we did not make attempts to unravel the detailed uptake pathways (*i.e.* by blocking of certain pathways by specific inhibitors or by colocalization experiments with objects of known pathways of internalization) it is known from previous experiments with NPs of similar surface chemistry that they are endocytosed by cells[12]. Experiments have shown contribution of macropinocytosis (see for example the formation of macropinocytic cups upon NP internalization, *cf.* TEM images in the Supporting Information) as well as caveolin-mediated endocytosis[36]. Presence of the Au NPs in the lysosomes after cellular internalization was proven by colocalization of the fluorescence-labeled NPs with green fluorescent protein (GFP)-labeled lysosomal associated protein 1 (LAMP1), employing confocal laser scanning microscopy [55]. LAMP1 which was expressed in HUVEC and HeLa cells as a marker for lysosomal membranes (*cf.* the Supporting Information for data). Quantification of internalized

NPs demonstrate that the uptake rate was higher and that transport of the Au NPs into the lysosomes (25, 50, 100 nM) by HUVECs (in 2% serum supplemented medium) was faster than by HeLa cells (in 10% serum supplemented medium). In case of HUVECs saturation of cells with NPs was already seen after less than 5 hours, whereas in HeLa cells the amount of internalized NPs still increased after 15 hours. After 24 hours of incubating cells with NPs at concentrations $c_{NP} > 5$ nM (at lower concentrations the signal of the fluorescently-labeled Au NPs was too weak for reliable quantitative analysis, *i.e.* in the range of the auto-fluorescence of cells). In the case of HUVECs incubation with the double amount of NPs (from 25 to 50 nM) resulted also in more or less the double amount of internalized NPs, while this was not observed for HeLa cells where the internalization rate slightly decreases with increasing concentration of NPs. This again points out that internalization of the Au NPs by HeLa cells is less effective. Even within 24 hours of exposure HeLa cells were not saturated with Au NPs at the used concentrations. Uptake of the Au NPs by HeLa cells thus follows a much slower kinetics compared to the HUVECs (all raw data are shown in the Supporting Information). We have also noted that differences in the amount of serum in the culture medium may play a role in the NP uptake, as serum in general reduces NP uptake [34].

3.2. Effect of Au-PMA* NPs on cell viability, proliferation, and other indicators

It is well known that even inert Au NPs can cause cytotoxic effects on cells at elevated exposure concentrations and times. In order to investigate a useful range of concentrations we took into account two considerations. First, in case of biological *in vitro* labeling experiments NP concentrations are typically chosen in the range of a few to a few tens of nM, in order to provide sufficient effect. Second, as according to Paracelsus everything at high enough concentration is toxic, we performed *in vivo* toxicity experiments with zebra fish embryos. Exposure of zebrafish embryos to NP concentrations up to 700 nM was not significantly associated with mortality or any morphological abnormality (data are presented in the Supporting Information), which demonstrates the relatively low toxic profile of the here used Au NPs. Guided by these two considerations we decided to investigate NP concentrations in the range from 0.1 to 100 nM, which covers the range of typical *in vitro* applications, but does not cause any acute abnormality *in vivo*. Using this range of concentrations we performed several standard biochemical assays to investigate the concentration-dependent effect of Au NPs on HUVECs and HeLa cells. As exposure time for all following experiments we chose 24 h. In a first set of assays effects on cellular enzymatic activity were probed: i) oxidation of resazurin (Alamar blue) by cellular dehydrogenases (Resazurin assay/Alamar blue assay) likely inside mitochondria, ii) reduction of 3-(4,5-dimethylthiazol-2-yl)-2,5-diphenyltetrazolium bromide (MTT) by oxidoreductases (MTT assay), and iii) conversion of cell permeable calcein acetoxymethyl (AM) by esterases (first part of a commercial Live/Dead assay). In order to probe for interlaboratory variation, the resazurin assay was carried out as well in the Marburg as in the Ghent laboratory according to the local standard protocols. In HUVECs the resazurin ("Marburg") as well as the MTT assays showed reduction of cell viability at around $c_{NP,50} \approx 10$ nM (all raw data can be found in the Supporting Information, a summary of all effects is shown in Table 1), whereas in case of the resazurin ("Ghent") and the “Live” assay these effects were detected at slightly higher concentrations of NPs. Comparison of the results for the resazurin assay as carried out with the local protocols of different laboratories

demonstrates that absolute values have to be interpreted with care, and variation between different laboratories may occur. In the case of HeLa cells the effect of the Au NPs on cell viability was much lower, and exposure with NPs up to concentrations of 100 nM could in most assays not reduce viability to its half. Still, also in HeLa cells concentration-dependent reduction in cell viability was observed. In a second assay format cellular proliferation was probed in terms of measuring DNA synthesis (see the Supporting Information for the details and the data). For both cell lines inhibition of proliferation was already caused by NP concentrations well below 1 nM. Cellular proliferation thus is at least sensitive to one order of magnitude lower NP concentrations than cellular viability. In a third assay we probed for direct damage: In the "Live/Dead" assay a cell-impermeable ethidium homodimer only stains cellular nuclei in case their membrane is damaged in the form of perforation. Altogether the $c_{NP,50}$ values obtained from the Live/Dead assay were in the range of a few tens of nM. Images of the outer cell membrane with Helium Ion Microscopy also show disruption of the cellular plasma membrane at high NP concentrations (see the Supporting Information for images). In a fourth assay type we probed for the generation of ROS, which are typically associated with cytotoxic effects, using CellROX Green as the probe. For both cell types we found $c_{NP,50}$ values of around 10 nM. First, these data (*cf.* Table 1) show that significant reduction in cellular proliferation starts already at least at one order of magnitude lower Au NP concentrations, which corresponds to the concentration at which cellular viability is affected. Second, viability of HeLa cells is less influenced by the exposure to Au NPs than HUVECs. Onset of oxidative stress (production of ROS) starts at similar NP concentrations as required to reduce cell viability. More dramatic effects such as permeation of nuclear membranes occur at even higher NP concentrations. Summing up, these data indicate that first toxic effects of Au NPs can be already noted at NP concentrations well below 1 nM (proliferation), whereas typical onset of drastic reduction in cell viability requires exposure concentrations in the order of 10 nM.

3.3. Lysosomal swelling caused by endocytosed Au-PMA* NPs

Staining of the lysosomes (yellow stain in the corresponding image in Figure 1) as well as of the cytoskeleton allows for relating the average sectional area of lysosomes A_{lyso} to the cell cross-section area A_{cell} in a defined intracellular plane. Thereby, a useful measure, the fraction of cell area which is occupied by lysosomes A_{lyso}/A_{cell} can be derived. The results clearly indicate that lysosomes start to swell, *i.e.* increase their size, upon exposure of cells to NPs, whereby the effect was higher for HUVECs than for HeLa cells (*cf.* Table 1). Just looking at the size of lysosomes already allows for pre-estimating whether NPs are present. $c_{NP,50}$ values, *e.g.* the required NP concentration at which half of the effect is observed, are in the order of 10 nM. In summary, exposure of cells to NPs causes swelling of lysosomes and thus leading to an increased fraction of intracellular space which is occupied by lysosomes.

3.4. Loss of mitochondrial structure caused by Au-PMA* NPs

Staining of the mitochondria (green stain in the corresponding image in Figure 1) allowed for observing changes in the morphology of the mitochondria upon cellular exposure to Au NPs. Data show that upon presence of NPs there is a significant shape change from more thread-like elongated to smaller spherical structures. This can be quantified by calculating the form factor

F_{mito} and the Zernike moment of 0^{th} order Z^0_{mito}, *cf.* Table 1 and the Supporting Information. Both measures describe the transition from an indefinitely extended object (F, $Z_0 = 0$) to a spherical object (F, $Z_0 = 1$)[56], *cf.* the Supporting Information. The results clearly indicate dramatic changes in mitochondrial morphology upon exposure to NPs. As mitochondria are the "power plant" of cells thus energy availability might be affected. For both investigated cell types the $c_{NP,50}$ values were between 1 and 10 nM, and therefore well below NP concentrations in which reduction of cellular viability was detected. Thus, reduction in cellular viability might be interpreted as a consequence of mitochondrial impairment.

3.5. Distortion of the cytoskeleton caused by Au-PMA* NPs

Staining of several components of the cytoskeleton was performed, *cf.* Figure 1. Actin was stained with fluorescence-labeled phalloidin, while specific antibodies were used for tubulin and vinculin staining procedures. Even by microscopic inspection with the naked eye striking effects of the NPs on the morphology of the cells were visible. Presence of NPs strongly reduced the cellular cross-section area A_{cell}. In the case of HeLa cells NP exposure induced a more elongated, stretched cell shape, manifested by a reduction in the form factor F_{cell}, *cf.* Table 1. Actin fibers were directly affected by exposure to the NPs. In the case of HUVECs the elongated actin fiber bundles shortened and rounded up. In the case of HeLa cells the actin fibers appeared smoother, indicated by a decreasing texture contrast $T_{act,cont}$[57]. For tubulin an increase in texture contrast $T_{tub,cont}$ and decrease in texture correlation $T_{tub,corr}$ was observed in case of HUVECs. Under high NP doses tubulin fibers were arranged less compactly and became thinner and longer. Visual inspection with the naked eye however leads to the conclusion that the tubulin network is less affected than the actin network by the presence of NPs. The cytoskeleton stabilizes cells in a dynamic way, based on continuous polymerization and depolymerization of fibers. For this reason control experiments without involving cells were performed, in which reduction of actin and tubulin polymerization upon presence of NPs was determined with biochemical assays. Data indicate that already NP concentrations below 1 nM significantly reduce polymerization of both, actin and tubulin, *cf.* the Supporting Information. Staining of vinculin indicated a reduction in focal adhesion contact areas A_{vinc}. Additionally, atomic force microscopy (AFM) data showed that, in particular, for HUVECs the number N_{filo} and area A_{filo} of filopodia decreased upon exposure to NPs. Here again a clear difference between both cell types could be seen. Accompanying gene expression assays revealed the upregulation of several genes which are related to the cellular cytoskeleton, *cf.* Table 1. Taken together the data demonstrate that NPs clearly have an impact on the cellular cytoskeleton, whereby detailed effects and in particular related NP doses vary between the investigated cell lines. In general HUVECs seem to be more affected than HeLa cells. Morphology changes occur at NP concentrations around $c_{NP,50} \approx 10$ nM, though this number can be seen only as an indicator for the order of magnitude. In contrast, it is safe to suggest that changes in gene expression are detected only at much higher NP concentrations than changes in morphology.

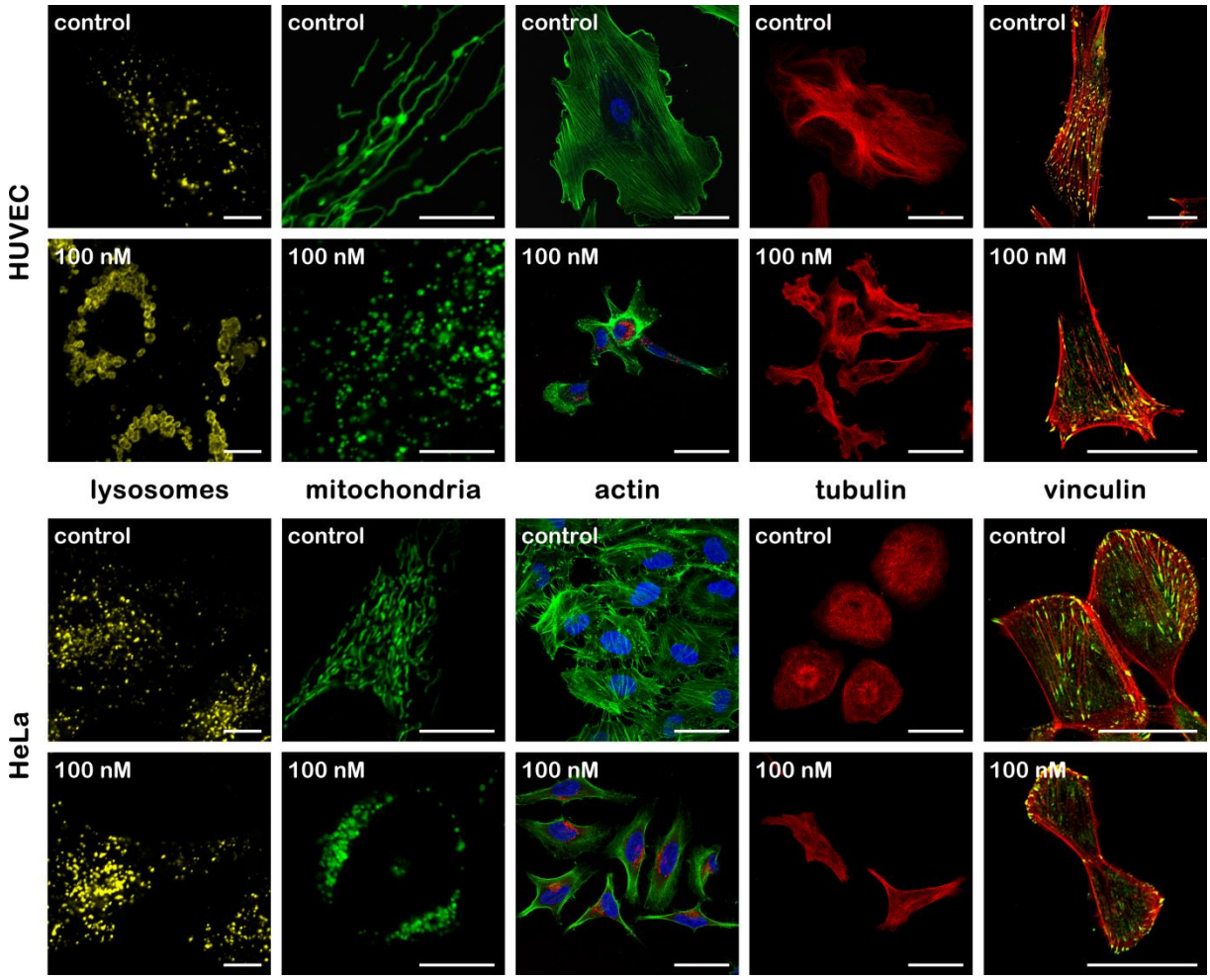

Figure 1: Morphological changes of different cellular structures without and after c_{NP} = 100 nM Au-PMA NP treatment in HUVECs and HeLa cells. All scale bars correspond to 50 µm except for lysosomes and mitochondria (10 µm). Lysosomes were stained with anti-lysosomal associated protein 1 (LAMP1) antibodies (shown here in yellow false colors). Mitochondria were stained by expressing green fluorescent protein GFP-labeled E1 alpha pyruvate dehydrogenase in the cells (shown in green). Actin fibers were stained by phalloidin (shown in green), nuclei stained with DAPI (shown in blue), together with the red fluorescence of incorporated NPs. Tubulin was stained using an anti-alpha tubulin antibody (shown here in red). Vinculin was stained with an anti-vinculin mouse monoclonal antibody (shown in green), together with actin staining with phalloidin (shown in red).*

Feature	Parameter	Variable	Derived from	Trend		$c_{NP,50}$ range [nM]	
				HUVEC	***HeLa***	***HUVEC***	***HeLa***
NP uptake	Integrated intensity	I_{NP}	NP fluorescence	+++	+		
Viability	Viability	V_{res}	Resazurin ("Maburg")	--	-	3.5-**11**-33	
		V_{AB}	Resazurin ("Ghent")	--	o	55-**65**-77	
		V_{MTT}	MTT	--	-	2.7-**8.4**-27	
	Dead/Live	D	Live/Dead stain	+	+	30+	80+
	Proliferation rate	p	DNA synthesis	--	--	0.49-**0.54**-0.59	0.073-**0.12**-0.20
	ROS	R	Pyocyanin/N-acetyl-L-cysteine	++	+	10+	10+
Cell morphology	Area	A_{cell}	CellMask blue	--	-	18-**26**-37	39-**49**-61
			Actin (phalloidin)	--	-	2+	10+
		A_{nuclei}	DAPI	o	o		
	Form factor	F_{cell}	Actin (phalloidin)	o	-		8+
Lysosomes	Area	A_{lyso}	LAMP1 (Ab)	+++	o	5+	
	Fraction of cell area	A_{lyso}/A_{cell}	LAMP1 (Ab) / actin (phalloidin)	++	++	30+	10+
	Intensity	I_{lyso}	LAMP1 (Ab)	o	+		10+
Mitochondria	Form factor	F_{mito}	CellLight - mitochondria	++	++	3.0-**4.7**-7.3	2.0-**2.5**-3.1
	Zernike 0^{th} order	Z^0_{mito}		+++	++	2.9-**4.4**-6.8	1.8-**2.3**-2.9
Cytoskeleton	Filopodia: Area	A_{vinc}	Vinculin (Ab)	--	-	50+	50+
		A_{filo}	AFM	--	o/-	2+	25+
	Filopodia: Number	N_{filo}		--	-	2+	50+
	Filopodia: Volume	V_{filo}		-	-	2+	25+
	Filopodia: Height	h_{filo}		o	o		
	Actin: Texture contrast	$T_{act,cont}$	Actin (phalloidin)	+	--	5+	1.7-**3.3**-6.3
	Actin: Texture correlation	$T_{act,corr}$		+	-	5+	5+
	Tubulin: Texture contrast	$T_{tub,cont}$	Tubulin (Ab)	+	/	50+	/
	Tubulin: Texture correlation	$T_{tub,corr}$		-	/	10+	/
	Gene expression	CALD1	RT-PCR array	+	+	12+	25+
		CCNA1		+	+	50+	25+
		CYFIP2		++	++	25+	25+
		IQGAP2		+	++	50+	12+
		MAPK13		+++	+	25+	50+
		MAPT		++	o	25+	
		PPP1R12A		+	o	50+	
		PPP1R12B		+	++	50+	12+
		TIAM1		+	++	50+	12+
		VASP		o	+		(50+)

Table 1: Summary of the experimental results, in which cellular reaction to exposure to Au-PMA NPs was probed. Reactions are shown in the trend column. $c_{NP,50}$ describes the NP concentration at which half of the maximum effect was obtained. If a sigmoidal fit could be applied to the data the uncertainty is given in addition. The full data sets corresponding to this table are shown in the supporting information. Ab = antibody.*

3.6. Deviation of results due to aging of the Au-PMA NPs

Batch-to-batch variations were upon carrying out the assays used for assembling Table 1. In the Supporting Information therefore data obtained with different batches are labelled. However, also variation over time within the same batch was found. As general observation regarding cell viability results obtained from the resazurin assay ("Marburg"), Au-PMA* NPs older than one year were found to be more toxic than the ones coated immediately before exposure of cells. One may speculate that part of the protecting PMA* shell may be lost over time, thus allowing a closer contact of exposed cells to the Au surface. This demonstrates that NPs may change their toxicity over time.

3.7. Comparison of the effects of Au-PMA NPs to the effects of Au NPs with different surface chemistry

For comparison the effects on selected cellular parameters were investigated for Au NPs with different surface chemistry, *cf.* Table 2. Similarly to Au-PMA* NPs, strong effects on cellular viability in terms of proliferation and metabolic activity and the morphology of mitochondria were observed for Au-PMA NPs without a fluorescence label. In terms of cell viability comparably strong impairments were only observed for Cd^{2+} ions at similar equivalent doses. MUA-coated NPs and Au salt seem to be less cytotoxic. In case of PEG NPs HUVECs are more affected than HeLa cells regarding cytotoxicity, inhibited proliferation and changes in mitochondrial morphology. Data indicate that for example the effect of Au-PMA and Au-PMA* NPs on mitochondria seems to be specific, as in comparison to the other NPs and the Cd and Au salts a much stronger damage was observed. Also swelling of the lysosomes seems to be trigger more by NPs than by Cd and Au salts. In this way these observed changes in cell morphology are likely related to NP-induced toxicity, which can be different to the effects of other toxic agents. This may be related to the particular intracellular distribution of the NPs, which accumulate inside endosomes/lysosomes.

	Feature	Parameter	Variable	Derived from	Trend		$c_{NP,50}$ range [nM]	
					HUVEC	*HeLa*	*HUVEC*	*HeLa*
Au-PMA	*Viability*	Viability	V_{res}	Resazurin ("Maburg")	-	--	73-**82**-92	
		Proliferation rate	p	DNA synthesis	--	--	0.8-**1.0**-1.2	0.67-**1.3**-2.6
	Cell morphology	Area	A_{cell}	Actin (phalloidin)	-	o	50+	
			A_{nuclei}	DAPI	o	o		
	Lysosomes	Fraction of cell area	A_{lyso}/A_{cell}	LAMP1 (Ab) / actin (phalloidin)	++	++		
	Mitochondria	Zernike 0^{th} order	Z^0_{mito}	CellLight - mitochondria	+++	+++	0.13-**0.29**-0.64	0.10-**0.21**-0.44
Au-PEG	*Viability*	Viability	V_{res}	Resazurin ("Maburg")	---	o	2.6-**3.6**-5.1	
		Proliferation rate	p	DNA synthesis	-	o	35-**60**-100	
	Cell morphology	Area	A_{cell}	Actin (phalloidin)	-	o		
			A_{nuclei}	DAPI	o	o		
	Lysosomes	Fraction of cell area	A_{lyso}/A_{cell}	LAMP1 (Ab) / actin (phalloidin)	++	o		
	Mitochondria	Zernike 0^{th} order	Z^0_{mito}	CellLight - mitochondria	+	+	4.7-**7.4**-12	45-**46**-48
Au-MUA	*Viability*	Viability	V_{res}	Resazurin ("Maburg")	o	o		
		Proliferation rate	p	DNA synthesis	-	-	13-**19**-28	47-**80**-140
	Cell morphology	Area	A_{cell}	Actin (phalloidin)	-	o		
			A_{nuclei}	DAPI	o	o		
	Lysosomes	Fraction of cell area	A_{lyso}/A_{cell}	LAMP1 (Ab) / actin (phalloidin)	++	+		
	Mitochondria	Zernike 0^{th} order	Z^0_{mito}	CellLight - mitochondria	o	o		
Au ions*	*Viability*	Viability	V_{res}	Resazurin ("Maburg")	-	o	64-**72**-81	
		Proliferation rate	p	DNA synthesis	-	-	10-**18**-34	36-**96**-250
	Cell morphology	Area	A_{cell}	Actin (phalloidin)	o	o		
			A_{nuclei}	DAPI	-	o	50+	
	Lysosomes	Fraction of cell area	A_{lyso}/A_{cell}	LAMP1 (Ab) / actin (phalloidin)	o	o		
	Mitochondria	Zernike 0^{th} order	Z^0_{mito}	CellLight - mitochondria	o/+	+	52-**55**-58	42-**51**-63
Cd ions*	*Viability*	Viability	V_{res}	Resazurin ("Maburg")	-	--	21-**24**-26	4.3-**13**-42
		Proliferation rate	p	DNA synthesis	-	--	3-**6**-13	0.37-**0.60**-0.96
	Cell morphology	Area	A_{cell}	Actin (phalloidin)	--	--	22-**28**-35	0.6-**2.3**-9.9
			A_{nuclei}	DAPI	-	-	50+	10+
	Lysosomes	Fraction of cell area	A_{lyso}/A_{cell}	LAMP1 (Ab) / actin (phalloidin)	o	o		
	Mitochondria	Zernike 0^{th} order	Z^0_{mito}	CellLight - mitochondria	o/+	++	27-**29**-30	1.8-**4.0**-8.9

Table 2: Summary of the experimental results, in which cellular reaction to exposure to Au NPs with different surface chemistry was probed. Reactions are shown in the trend column. $c_{NP,50}$ describes the NP concentration at which half of the maximum effect was obtained. If a sigmoidal fit could be applied to the data the uncertainty is given in addition. The full data sets corresponding to this table are shown in the supporting information. (*) For Au and Cd ions the indicated concentrations correspond to equivalent NP concentrations (cf. § 2).

4. Conclusions

There are many published records in which cytotoxic effects of NPs on cells have been observed. Many of these reports focus on biochemical assays, probing cell viability or measuring gene expression levels. In this work we demonstrate that effects are also directly visible by changes in cellular morphology. Though there is an impressive amount of studies available in literature, quantitative comparison is hindered by the fact that on the one hand toxicity strongly depends on the type of NPs and on the other hand the type of cells which have been used. In our study we performed many different assays with the same type of NP on two different types of cells, which allows for a quantitative comparison. In general, first effects upon exposure to NPs can be seen by a reduction in cellular proliferation rates. This effect is already clearly visible at NP concentrations one or two orders of magnitude lower than the effects can be observed with standard cell viability assays. Also, changes in mitochondrial morphology can be measured which are an early indicator of NP induced cellular damage. Then again lysosomal swelling and changes in cytoskeleton morphology occur at the same order of NP concentrations that cause significant reduction in cell viability. On the contrary, ROS production sets-on prominently only at even higher concentrations. These data suggest that not all indicators for NP toxicity have the same sensitivity. Cellular proliferation and alterations in mitochondrial morphology are clearly early indicators. Prior to changes in cellular viability are observable there are already detectable changes in (sub-) cellular morphology. Geometrical changes in certain cellular compartments occur already at surprisingly low NP concentrations, in particular in mitochondria. Most likely these effects can be linked to the surface chemistry of the used Au NPs as the observed changes vary among the different surface coatings which were being tested.

In this way, just by visual inspection of cells (upon appropriate immunostaining) NP-related toxicity can be observed *via* morphological analysis. In our case of polymer-coated Au NPs, even at NP concentrations where no significant oxidative stress (ROS production) can be detected morphology can already be altered significantly. These morphological changes provide a reliable assessment for the effect of NPs on the cellular homeostasis. Therefore, the determination of toxic effects of NP exposure based on morphological features may be an attractive alternative methodology for situations in which fixed samples, such as tissue sample from a biopsy have to be inspected, and in which case the use of biochemical assays can no longer be applied. Morphology changes seem to be in particular in the case of mitochondria and lysosomes related to NP-induced toxicity, and are different to changes observed upon exposure of cells to toxic metal salts.

Acknowledgements

This work was supported by the European Commission (project FutureNanoNeeds to WJP). The authors are grateful to Andre Beyer for technical assistance with helium ion microscopy.

Contributions

X. M. was responsible for cell culture and involved in CLSM and TEM imaging. R. H. performed parts of the microscopic imaging and the major part of the image processing, data

analysis, and assembly of figures and graphs. D. J. de A., D.V. and B. P. prepared and characterized the nanoparticles. D. V. conducted the actin/tubulin polymerization assays. S. J. S. and B. A. performed several cyto-/genotoxocity assays. F. Y., J. F. and C. R. did AFM imaging while H. V. and N. F. performed HIM imaging. M. S. and R. T. did the *in vivo* zebrafish experiments. N. H., A. G., X.-J. L., and W. J. P. designed the experiments. R. H. and W. J. P. wrote the major part of the manuscript. All authors discussed the results and implications and commented on the manuscript at all stages.

References

[1] M. Auffan, J. Rose, J.-Y. Bottero, G.V. Lowry, J.-P. Jolivet, M.R. Wiesner, Nature Nanotechnology, 4 (2009) 634-641.
[2] A. Alkilany, C. Murphy, Journal of Nanoparticle Research, 12 (2010) 2313-2333.
[3] I. Canton, G. Battaglia, Chemical Society Reviews, 41 (2012) 2718-2739.
[4] M. Nazarenus, Q. Zhang, M.G. Soliman, P. del Pino, B. Pelaz, S. Carregal_Romero, J. Rejman, B. Rothen-Ruthishauser, M.J.D. Clift, R. Zellner, G.U. Nienhaus, J.B. Delehanty, I.L. Medintz, W.J. Parak, Beilstein Journal of Nanotechnology, 5 (2014) 1477-1490.
[5] F. Bertoli, G.L. Davies, M.P. Monopoli, M. Moloney, Y.K. Gun'ko, A. Salvati, K.A. Dawson, Small, 10 (2014) 3307-3315.
[6] A. Lesniak, F. Fenaroli, M.R. Monopoli, C. Aberg, K.A. Dawson, A. Salvati, ACS Nano, 6 (2012) 5845-5857.
[7] M. Perez-Hernandez, P. Del Pino, S.G. Mitchell, M. Moros, G. Stepien, B. Pelaz, W.J. Parak, E.M. Galvez, J. Pardo, J.M. de la Fuente, ACS nano, 9 (2015) 52-61.
[8] A.E. Nel, L. Madler, D. Velegol, T. Xia, E.M.V. Hoek, P. Somasundaran, F. Klaessig, V. Castranova, M. Thompson, Nature Materials, 8 (2009) 543-557.
[9] T. Xia, L. Rome, A. Nel, Nature Materials, 7 (2008) 519-520.
[10] M.I. Setyawati, P.K.S. Khoo, B.H. Eng, S. Xiong, X. Zhao, G.K. Das, T.T.-Y. Tan, J.S.C. Loo, D.T. Leong, K.W. Ng, Journal of Biomedical Materials Research Part A, 101A (2012) 633-640.
[11] S. Anguissola, D. Garry, A. Salvati, P.J. O'Brien, K.A. Dawson, PLoS ONE, 9 (2014) e108025.
[12] S.J. Soenen, B. Manshian, J. M.Montenegro, F. Amin, B. Meermann, T. Thiron, M. Cornelissen, F. Vanhaecke, S. Doak, W.J. Parak, S.D. Smedt, K. Braeckmans, ACS Nano, 6 (2012) 5767-5783.
[13] E. Jan, S.J. Byrne, M. Cuddihy, A.M. Davies, Y. Volkov, Y.K. Gun'ko, N.A. Kotov, ACS Nano, 2 (2008) 928-938.
[14] F. Wang, M.G. Bexiga, S. Anguissola, P. Boya, J.C. Simpson, A. Salvati, K.A. Dawson, Nanoscale, 5 (2013) 10868-10876.
[15] Y. Pan, A. Leifert, D. Ruau, S. Neuss, J. Bornemann, G. Schmid, W. Brandau, U. Simon, W. Jahnen-Dechent, Small, 5 (2009) 2067-2076.
[16] A. Chompoosor, K. Saha, P.S. Ghosh, D.J. Macarthy, O.R. Miranda, Z.J. Zhu, K.F. Arcaro, V.M. Rotello, Small, 6 (2010) 2246-2249.
[17] L. Wang, Y. Liu, W. Li, X. Jiang, Y. Ji, X. Wu, L. Xu, Y. Qiu, K. Zhao, T. Wei, Y. Li, Y. Zhao, C. Chen, Nano Letters, 11 (2011) 772-780.
[18] M.G. Bexiga, C. Kelly, K.A. Dawson, J.C. Simpson, Nanomedicine, 9 (2014) 1651-1664.
[19] X. Ma, Y. Wu, S. Jin, Y. Tian, X. Zhang, Y. Zhao, L. Yu, X.-J. Liang, ACS Nano, 5 (2011) 8629-8639.
[20] M. Mahmoudi, A.M. Abdelmonem, S. Behzadi, J.H. Clement, S. Dutz, M.R. Ejtehadi, R. Hartmann, K. Kantner, U. Linne, P. Maffre, S. Metzler, M.K. Moghadam, C. Pfeiffer, M.

Rezaei, P. Ruiz-Lozano, V. Serpooshan, M.A. Shokrgozar, G.U. Nienhaus, W.J. Parak, ACS Nano, 7 (2013) 6555-6562.
[21] A. Ott, X. Yu, R. Hartmann, J. Rejman, A. Schütz, M. Ochs, W.J. Parak, S. Carregal-Romero, Chemistry of Materials, 27 (2015) 1929−1942.
[22] N. Pernodet, X.H. Fang, Y. Sun, A. Bakhtina, A. Ramakrishnan, J. Sokolov, A. Ulman, M. Rafailovich, Small, 2 (2006) 766-773.
[23] Y.-L. Wu, N. Putcha, K.W. Ng, D.T. Leong, C.T. Lim, S.C.J. Loo, X. Chen, Accounts of Chemical Research, 46 (2013) 782-791.
[24] L.T. Allen, E.J.P. Fox, I. Blute, Z.D. Kelly, Y. Rochev, A.K. Keenan, K.A. Dawson, W.M. Gallagher, Proceedings of the National Academy of Sciences of the United States of America, 100 (2003) 6331-6336.
[25] T. Mironava, M. Hadjiargyrou, M. Simon, V. Jurukovski, M.H. Rafailovich, Nanotoxicology, 4 (2010) 120-137.
[26] J.A. Yang, S.E. Lohse, C.J. Murphy, Small, 10 (2013) 1642-1651.
[27] M.I. Setyawati, C.Y. Tay, S.L. Chia, S.L. Goh, W. Fang, M.J. Neo, H.C. Chong, S.M. Tan, S.C.J. Loo, K.W. Ng, J.P. Xie, C.N. Ong, N.S. Tan, D.T. Leong, Nature Communications, 4 (2013) 1673.
[28] I.C. Lin, M. Liang, T.-Y. Liu, Z.M. Ziora, M.J. Monteiro, I. Toth, Biomacromolecules, 12 (2011) 1339-1348.
[29] T. Mironava, M. Hadjiargyrou, M. Simon, M.H. Rafailovich, Nanotoxicology, 8 (2014) 189-201.
[30] T. Pellegrino, L. Manna, S. Kudera, T. Liedl, D. Koktysh, A.L. Rogach, S. Keller, J. Rädler, G. Natile, W.J. Parak, Nano Letters, 4 (2004) 703-707.
[31] C.-A.J. Lin, R.A. Sperling, J.K. Li, T.-Y. Yang, P.-Y. Li, M. Zanella, W.H. Chang, W.J. Parak, Small, 4 (2008) 334-341.
[32] F. Zhang, E. Lees, F. Amin, P. Rivera_Gil, F. Yang, P. Mulvaney, W.J. Parak, Small, 7 (2011) 3113-3127.
[33] G. Charron, D. Hühn, A. Perrier, L. Cordier, C.J. Pickett, T. Nann, W.J. Parak, Langmuir, 28 (2012) 15141-15149.
[34] D. Hühn, K. Kantner, C. Geidel, S. Brandholt, I. De Cock, S.J.H. Soenen, P. Rivera Gil, J.-M. Montenegro, K. Braeckmans, K. Müllen, G.U. Nienhaus, M. Klapper, W.J. Parak, ACS Nano, 7 (2013) 3253-3263.
[35] S. Harakeh, R.M. Abdel-Massih, P. Rivera_Gil, R.A. Sperling, A. Meinhardt, A. Niedwiecki, M. Rath, W.J. Parak, E. Baydoun, Nanotoxicology, 4 (2010) 177-185.
[36] B. Rothen-Rutishauser, D.A. Kuhn, Z. Ali, M. Gasser, F. Amin, W.J. Parak, D. Vanhecke, A. Fink, P. Gehr, C. Brandenberger, Nanomedicine, 9 (2014) 607-621.
[37] C. Schweiger, R. Hartmann, F. Zhang, W.J. Parak, T. Kissel, P. Rivera Gil, J. Nanobiotechnol., 10 (2012) 28.
[38] A.D. Lehmann, W.J. Parak, F. Zhang, Z. Ali, C. Röcker, G.U. Nienhaus, P. Gehr, B. Rothen-Rutishauser, Small, 6 (2010) 753-762.
[39] S.J. Soenen, B.B. Manshian, A.M. Abdelmonem, J.-M. Montenegro, S. Tan, L. Balcaen, F. Vanhaecke, A.R. Brisson, W.J. Parak, S.C.D. Smedt, K. Braeckmans, Particle & Particle Systems Characterization, 31 (2014) 794-800.
[40] Y. Pan, S. Neuss, A. Leifert, M. Fischler, F. Wen, U. Simon, G. Schmid, W. Brandau, W. Jahnen-Dechent, Small, 3 (2007) 1941-1949.
[41] R. Shukla, V. Bansal, M. Chaudhary, A. Basu, R.R. Bhonde, M. Sastry, Langmuir, 21 (2005) 10644-10654.
[42] E. Caballero-Díaz, C. Pfeiffer, L. Kastl, P. Rivera-Gil, B. Simonet, M. Valcárcel, J. Jiménez-Lamana, F. Laborda, W.J. Parak, Particle and Particle Systems Characterization, 30 (2013) 1079-1085.

[43] P. del_Pino, F. Yang, B. Pelaz, Q. Zhang, K. Kantner, R. Hartmann, N.M.d. Baroja, M. Gallego, M. Möller, B.B. Manshian, S.J. Soenen, R. Riedel, N. Hampp, W.J. Parak, Angew Chem Int Ed Engl, 55 (2016) 5483–5487.
[44] C. Kirchner, L. T., S. Kudera, T. Pellegrino, A. Muñoz Javier, H.E. Gaub, S. Stölzle, N. Fertig, W.J. Parak, Nano Letters, 5 (2005) 331-338.
[45] F. Amin, D.A. Yushchenko, J.M. Montenegro, W.J. Parak, ChemPhysChem, 13 (2012) 1030-1035.
[46] R.A. Sperling, T. Pellegrino, J.K. Li, W.H. Chang, W.J. Parak, Advanced Functional Materials, 16 (2006) 943-948.
[47] N.G. Papadopoulos, G.V.Z. Dedoussis, G. Spanakos, A.D. Gritzapis, C.N. Baxevanis, M. Papamichail, Journal of Immunological Methods, 177 (1994) 101-111.
[48] A. Salic, T.J. Mitchison, Proceedings of the National Academy of Sciences, 105 (2008) 2415-2420.
[49] J. O'Brien, I. Wilson, T. Orton, F.o. Pognan, European Journal of Biochemistry, 267 (2000) 5421-5426.
[50] K. Van_Hoecke, K.A.C. De Schamphelaer, Z. Ali, F. Zhang, A. Elsaesser, P. Rivera_Gil, W.J. Parak, G. Smagghe, C.R. Janssen, Nanotoxicology, 7 (2013) 37-47.
[51] M.P. Singh, T.M. Atkins, E. Muthuswamy, S. Kamali, C. Tu, A.Y. Louie, S.M. Kauzlarich, ACS Nano, 6 (2012) 5596-5604.
[52] A. Magrez, L. Horvath, R. Smajda, V. Salicio, N. Pasquier, L. Forro, B. Schwaller, ACS Nano, 3 (2009) 2274-2280.
[53] T. Kouyama, K. Mihashi, European Journal of Biochemistry, 114 (1981) 33-38.
[54] D. Bonne, C. Heuséle, C. Simon, D. Pantaloni, Journal of Biological Chemistry, 260 (1985) 2819-2825.
[55] W.G. Kreyling, A.M. Abdelmonem, Z. Ali, F. Alves, M. Geiser, N. Haberl, R. Hartmann, S. Hirn, D.J. de Aberasturi, K. Kantner, G. Khadem-Saba, J.M. Montenegro, J. Rejman, T. Rojo, I.R. de Larramendi, R. Ufartes, A. Wenk, W.J. Parak, Nat Nanotechnol, 10 (2015) 619-623.
[56] M.V. Boland, M.K. Markey, R.F. Murphy, Cytometry, 33 (1998) 366-375.
[57] R.M. Haralick, Proceedings of the IEEE, 67 (1979) 786-804.

Colloidal nanoparticles induce changes in cellular morphology

Xiaowei Ma[1,2*], Raimo Hartmann[1*], Dorleta Jimenez de Aberasturi[1,3], Fang Yang[4,5], Stefaan J. Soenen[6], Bella Manshian[6], Jonas Franz[7], Daniel Valdeperez[1], Beatriz Pelaz[1], Norbert Hampp[4,5], Christoph Riethmüller[8], Henning Vieker[9], Natalie Freese[9], Armin Gölzhäuser[9], Michael Simonich[10], Robert Tanguay[10], Xing-Jie Liang[2#], Wolfgang J. Parak[1,3#]

[1] Fachbereich Physik, Philipps Universität Marburg, Marburg, Germany
[2] Chinese Academy of Sciences (CAS) Key Laboratory for Biological Effects of Nanomaterials and Nanosafety, National Center for Nanoscience and Technology, Beijing, China
[3] CIC Biomagune, San Sebastian, Spain
[4] Fachbereich Chemie, Philipps Universität Marburg, Marburg, Germany
[5] Material Science Center, Philipps Universität Marburg, Marburg, Germany
[6] Biomedical MRI Unit/MoSAIC, Catholic University of Leuven, Leuven, Belgium
[7] nAnostic Institute, Center for Nanotechnology, University of Münster, Germany
[8] Serend-ip GmbH, Center for Nanotechnology, Münster, Germany
[9] Fakultät für Physik, Universität Bielefeld, Bielefeld, Germany
[10] OSU Sinnhuber Aquatic Research Laboratory (SARL), Oregon, USA
* both authors contributed equally to this work
[#] corresponding author: liangxj@nanoctr.cn; wolfgang.parak@physik.uni-marburg.de

SUPPORTING INFORMATION

I) Nanoparticle synthesis

I.1) Synthesis of gold nanoparticles (Au NPs)

I.2) Synthesis of amphiphilic polymer, optionally functionalized with TMR-cadaverine

I.3) Polymer coating of Au NPs (Au-PMA* and Au-PMA NPs)

I.4) Ligand exchange of Au NPs with 11-mercaptoundecanoic acid (Au-MUA NPs)

I.5) Ligand exchange of Au NPs with polyethyleneglycol (Au-PEG NPs)

I.6) Au salt

I.7) Cd salt

I.1) Synthesis of gold nanoparticles (Au NPs)

Gold nanoparticles (Au NPs) were synthesized following the Brust method[1] according to previously published protocols[2, 3]. Briefly, 0.300 g (0.9 mmol) of hydrogen tetrachloroaurate (III) (99.9 %, Alfa Aesar, #12325) was dissolved as aqueous gold precursor in 25 mL of Milli-Q water. This solution was mixed with a solution of 2.170 g (3.9 mmol) of tetraoctylammonium bromide (TOAB, Sigma-Aldrich, #294136) dissolved in 80 mL of toluene (Fluka, #89682). The mixture of both solutions was shaken vigorously for about 5 min. Hereby $AuCl_4^-$ ions were gradually transferred from the aqueous into the organic phase (toluene) through the formation of tetraoctylammonium-gold tetrachloroaurate ion pairs.

$$AuCl_4^- (aq) + N(C_8H_{17})_4^+ (tol) \rightarrow N(C_8H_{17})_4^+AuCl_4^- (tol)$$

Afterwards, the aqueous solution was discarded and the toluene solution containing the $AuCl_4^-$ ions was transferred to a 250 mL round bottom flask. A solution of 0.334 g (8.8 mmol) sodium borohydride ($NaBH_4$, Sigma-Aldrich, #452882) in 25 mL of Milli-Q water was added drop-wise to the vigorously stirred solution of gold precursor in toluene. The gold started to be reduced after a few seconds by sodium borohydride resulting in a change of color from orange to violet.

$$nAuCl_4^- (tol) + 3ne^- \rightarrow 4nCl^- (aq) + Au_n$$

Then the growth of NPs was mediated by the residue of sodium borohydride, which reduced the remaining gold ions. After one-hour stirring, the solution was transferred to a separation funnel and the NPs were washed several times. The first washing step was performed with 25 mL of 0.01 M HCl, in order to remove the excess sodium borohydride. The second step was done with 25 mL of 0.01 M NaOH to remove the excess acid. Finally, four times washing with 25 mL of Milli-Q water was performed to remove salt residues from the HCl and NaOH washing steps. The resulting organic solution was transferred to a 250 mL round-bottomed flask and was stirred overnight to allow the NPs to reach a thermodynamically stable size distribution (Ostwald ripening process[4]). Next day, a ligand exchange was carried out by adding 10 mL (8.450 g, 41.7 mmol) of 1-dodecanethiol (Sigma-Aldrich, #471364) and heating the solution up to 65 °C for 3 hours. Hereby the dodecanethiol displaces the Br^- ions from the NP surface due

to the high binding affinity of thiol groups to gold[5]. Large agglomerates were first removed by centrifugation at 700 rcf whereby the supernatant was collected, and the precipitate containing the agglomerates was discarded. Then the obtained NPs were precipitated with methanol undergoing a selective size precipitation process by centrifugation. After discarding the supernatant the NP precipitate containing the hydrophobic Au NPs was dissolved in chloroform to a final concentration of 4 µM.

I.2) Synthesis of amphiphilic polymer, optionally functionalized with TMR-cadaverine

First, following the previously reported synthesis procedure[6-9], an amphiphilic polymer, poly(isobutylene–*alt*–maleic anhydride)–*graft*–dodecylamine (PMA), was prepared. The amphiphilic polymer is not only useful to transfer the hydrophobic NPs to aqueous solution[6, 10], but it also allows the attachment of other molecules containing free amino groups directly *via* amide bonds to its maleic anhydride rings[7, 9, 11]. The polymer consists of a polyisobutylene-*alt*-maleic anhydride hydrophilic backbone ($M_w \approx 6$ kDa, Sigma-Aldrich, #531278) modified with dodecylamine hydrophobic side chains. 75 % of the anhydride rings of the polymer backbone are covalently linked *via* amide bonds to the amine groups of hydrophobic chains. Figure SI-I.1 shows the structure of the polymer in detail. The synthesis is described in detail in Lin *et al.*[7]

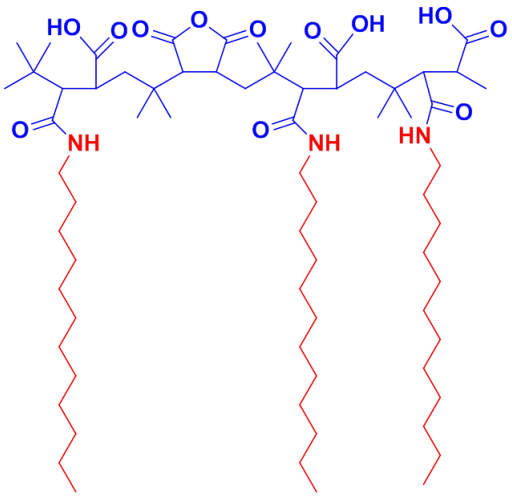

Figure SI-I.1: Structure of the synthesized amphiphilic polymer (PMA). Polyisobutylene-alt-maleic anhydride hydrophilic backbone (blue) modified with dodecylamine hydrophobic side chains (red).

In order to attach the tetramethylrhodamine cadaverine dye (TMR-cadaverine, λ_{ex} = 544 nm, λ_{em} = 571 nm, Molecular Probes, #A1318) to the polymer, 2 % of the total anhydride rings of the amphiphilic polymer were modified by the reaction of the maleic anhydride rings with the amino group of the dye, leaving in total 23 % of the anhydride rings free (75 % are occupied by the linked dodecylamine side chains). Briefly, 2 mg of the dye dissolved in chloroform were mixed with 400 µL of 0.5 M (in terms of monomer concentration[7]) of the prepared amphiphilic polymer solution. The reaction mixture was refluxed overnight at room temperature. Then, the solvent mixture was evaporated and the dye-modified polymer was

redissolved in anhydrous chloroform to obtain a final (monomer) concentration of c_P = 0.05 M (*cf.* Figure SI-I.2).

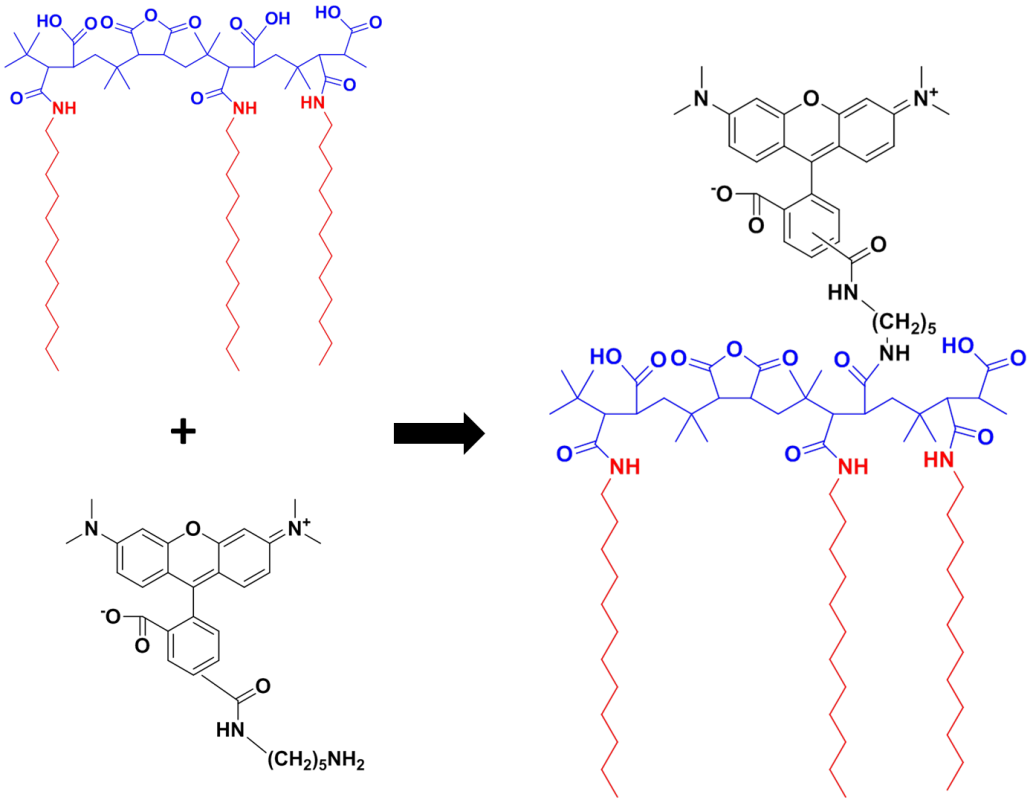

Figure SI-I.2: Scheme of the linkage of the TMR-cadaverine dye 590 (black) via amide bonds to the anhydride rings of the hydrophilic backbone of the amphiphilic polymer (blue). The -NH_2 group of the dye is used for linkage to the PMA backbone and the fluorescence-labelled polymer is referred to as PMA.*

I.3) Polymer coating of Au NPs (Au-PMA* and Au-PMA NPs)

To calculate the amount required to coat the synthesized NPs with the prepared amphiphilic polymer Equation SI-I.1 was used[7, 12, 13].

$$V_p = \frac{\pi \cdot c_{NP} \cdot V \cdot d_{eff}^2 \cdot R_{p/area}}{c_p} \qquad \text{Equation SI-I.1}$$

The variable c_{NP} corresponds to the NP concentration and V corresponds to the volume of the NP solution. c_p is the monomer concentration of the amphiphilic polymer dissolved in chloroform while V_p represents the volume of the polymer solution. d_{eff} corresponds to the effective diameter of the NPs: $d_{eff} = d_c + 2 \cdot l_{surfactant}$, which is the sum of the diameter of the inorganic core (d_c) plus two times the assumed thickness of the surfactant shell that corresponds to $l_{surfactant} \approx 1.2$ nm. $R_{p/area}$ is the number of polymer monomers which need to be added per surface area $A_{eff} = 4\pi \cdot (d_{eff}/2)^2$ of NP in monomer units/nm^2.

Thus, for all the experiments, several batches of polymer coated NPs were prepared with the

following procedure: Au NPs (d_c = 4.8 nm ⇒ d_{eff} = 4.8 nm + 2·1.2 nm = 7.2 nm; V = 1,000 µL, c_{NP} = 4 µM in chloroform) were mixed with PMA functionalized with TMR cadaverine dye (PMA*) in chloroform (V_P = 515 µL, c_P = 0.05 M, $R_{p/area}$ = 50 nm^{-2}) in a 10 mL round-bottomed flask. The mixture was stirred and the solvent was slowly evaporated. Then the NP powder was dissolved in 50 mM sodium borate buffer at pH 12 (SBB 12). The basic pH of the buffer opens the remaining anhydride rings, leading to negatively charged carboxyl groups at that pH, which increases the surface charge and renders the NPs water-soluble. As control, Au NPs were also coated with PMA without any dye modification (Au-PMA NPs).

Gel electrophoresis was used after the polymer coating procedure in order to purify the sample and to eliminate empty polymer micelles[6]. For this purpose, a 2 % agarose gel was prepared by mixing the agarose (2 g) with Tris-Borate-EDTA buffer (TBE; 0.5x, 98 mL corresponding to 98 g). In addition, the polymer-coated Au NPs were mixed with glycerol (in order to increase the density of the sample) and with Orange G dye (in order to label the sample mixture which is loaded on the gel)[14]. The mixture was then placed into the cavity of the prepared gel. Applying an electric field of 15 $V \cdot cm^{-1}$, the negatively charged NPs will move to the plus pole. After one hour, the polymer-coated NPs form a band which can be distinguished from empty micelles and free dye molecules that move faster, as they are smaller[6]. The band which contains the NPs was cut and placed into a dialysis membrane (50 kDa molecular weight cut-off (MWCO)) filled with TBE buffer. Applying again an electric field of 10 $V \cdot cm^{-1}$ for *ca.* 20 min, which caused the NPs to move out of the gel, whereby they stayed trapped inside the dialysis membrane. In order to be sure that all empty micelles were removed this procedure was applied twice. Examples are shown in Figure SI-I.3.

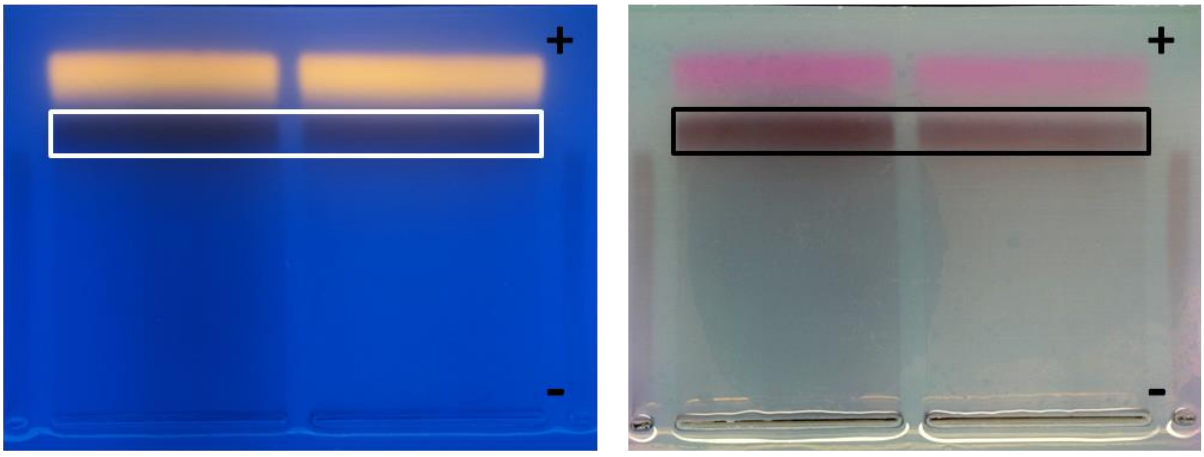

Figure SI-I.3: Images of agarose gels on which the Au-PMA NPs with TMR-cadaverine in their polymer shell had been run for 1 h in an electric field of 15 $V \cdot cm^{-1}$ under white-light (left) and UV (right) illumination. Images of the gels were taken after 60 min. "+" and "-" indicate the direction of the electric field. The marked sections correspond to the NP-containing bands that were cut to extract the Au NPs.*

I.4) Ligand exchange of Au NPs with 11-mercaptoundecanoic acid (Au-MUA NPs)

A ligand exchange procedure replacing the initial ligand (dodecanethiol) from the synthesis on the Au NP surface with 11-mercaptoundecanoic acid (MUA) was performed [13]. First, 1.6 g MUA was added in a glass vial with 130 mL Tris-borate-EDTA buffer pH=8.3 (TBE 0.5x). The mixture was sonicated for 30 minutes at room temperature. Then, 20 mL of Au NP dispersion (0.5 mg/mL, *cf.* § I.1) in chloroform was poured into the MUA solution and the resulting mixture was vigorously shaken for 4 days. During this time the ligand exchange takes place, allowing the MUA to attach onto the Au NPs' surface, and therefore transferring the Au NPs from chloroform to the aqueous solution. After this, the sample was centrifuged at 720 rcf for 30 minutes with the aim of removing the excess of ligands from the MUA coated Au NPs. The aqueous phase was taken and poured into centrifuge filters with 100 kDa MWCO membranes. The sample was five times concentrated at 1,600 rcf for 15 minutes and resuspended in Milli-Q water, being filtered with syringe filters (0.2 μm pore diameter) and finally stored in Milli-Q water. Two batches were synthesized for this study, which are denoted as Au-MUA_1 and Au-MUA_2 NPs.

I.5) Ligand exchange of Au NPs with polyethyleneglycol (Au-PEG NPs)

PMA-coated Au NPs were coated with CH_3O-PEG-NH_2 of 10 kDa molecular mass (1210000-2, Rapp Polymere) [13, 15, 16]. First, 1 mL PMA-coated AuNPs (0.62 μM) in Milli-Q water was taken and mixed with 306 μL CH_3O-PEG-NH_2 in 10 mM in Sodium borate buffer of pH = 9 (SBB9) in a ratio of 5,000 PEG molecules per PMA-coated Au NP. Then 61 μL 1 M EDC in SBB9 were added to the sample (100,000 molecules of EDC per Au NP) and the mixture was adjusted to a final volume of 3 mL with SBB9. The resulting sample was incubated for 4 h at room temperature and moderate stirring. The NPs were then washed five times with centrifuge filters (100 kDa MWCO) at 1,600 rcf for 15 minutes. The PEG-coated Au NPs were finally filtered with syringe filters (0.2 μm pore diameter) and stored in Milli-Q water for further use. Two batches were synthesized for this study, which are denoted as Au-PEG_1 and Au-PEG_2 NPs.

I.6) Au salt

Au ions (in the form of hydrogen tetrachloroaurate(III) hydrate (99 %, $HAuCl_4 \cdot xH_2O$ were used as control. The concentration of Au ions C_{Au} (in terms of mg ions per mL) was converted to a virtual concentration of Au NPs c_{NP} (in terms of mol NPs per L). As conversion factor the number of Au atoms per Au NP as synthesized in § I.1, together with Avogadro's constant was used. The (mass) concentration C_{Au} of Au atoms in a solution of c_{NP} = 1 μM Au NPs was determined with inductively coupled plasma mass spectrometry (ICP-MS). By knowing the core diameter (d_c) of Au NPs from the histogram of the TEM pictures (*cf.* § II), the volume of a single Au NP can be obtained as $V_{NP} = (4/3)\cdot\pi\cdot(d_c/2)^3$. The mass of a single Au NP (m_{NP}) can be calculated as $m_{NP} = \rho_{Au}\cdot V_{NP}$, with gold metal density ρ_{Au} at room temperature (19.3 g/cm^3). The molar concentration of the Au NPs can then be calculated by dividing the Au atom concentration (C_{Au}, measured by ICP-MS) by the mass of one mole of NPs (set as the Avogadro's number, N_A multiplied by m_{NP}):

$$c_{NP} = \frac{C_{Au}}{m_{NP} \cdot N_A} \qquad \text{(Equation SI-I.2)}$$

This leads to the relation between Au atoms and Au NPs in a solution. The total amount of $c_{Au} = 3.41 \cdot 10^{-3}$ M Au ions in solution corresponds to a solution of $c_{NP} = 1$ µM Au NPs. Or vice versa, $c_{Au} = 1$ mM of Au ions corresponds to a solution of $c_{NP} = 0.29$ µM Au NPs.

I.7) Cd salt

Also the concentration of Cd ions was renormalized into a virtual concentration of NPs. As described in § I.6, $c_{Cd} = 1$ mM of Cd ions corresponds to a solution of $c_{NP} = 0.29$ µM Au NPs.

II) Nanoparticle characterization

The polymer-coated Au NPs (Au-PMA* NPs) were characterized with different methods. First, the inorganic core diameter d_c was derived from transmission electron microscopy (TEM) images, *cf.* Figure SI-II.1. For this purpose a drop of the NP solution was dried on a TEM grid, and low resolution TEM images were recorded. Note that only the Au core, but not the organic molecules around the NP surface (dodecanethiol, amphiphilic polymer) provide contrast[17, 18]. A histogram of the NP diameter d_c was generated from these images using a standard image analysis software. The average diameter of the inorganic core d_c of the Au-PMA* NPs obtained was determined to be 4.79 ± 0.70 nm (*cf.* Figure SI-II.1).

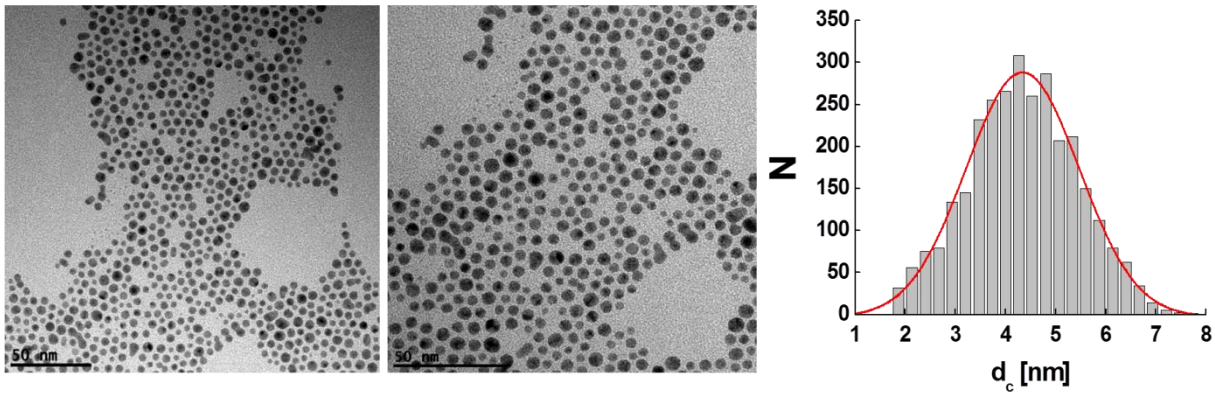

Figure SI-II.1: TEM images of a solution of dried polymer coated NPs (Au-PMA NPs). The scale bar corresponds to 50 nm. From these images a histogram of the distribution N(d_c) of the Au core diameter of the NPs was obtained.*

For measuring the hydrodynamic diameter d_h with dynamic light scattering (DLS; d_h = 12.2 ± 0.7 nm, *cf.* Figure SI-II.2) and the zeta-potential ζ with laser Doppler anemometry (LDA; ζ = -20 ± 3 mV, *cf.* Figure SI-II.3) a Malvern Zetasizer Nano ZS with a red laser (632.8 nm) as light source was used in 173° backscatter detection mode. All the Au-PMA* NP samples were measured in Milli-Q water using polystyrene cuvettes as described previously[13].

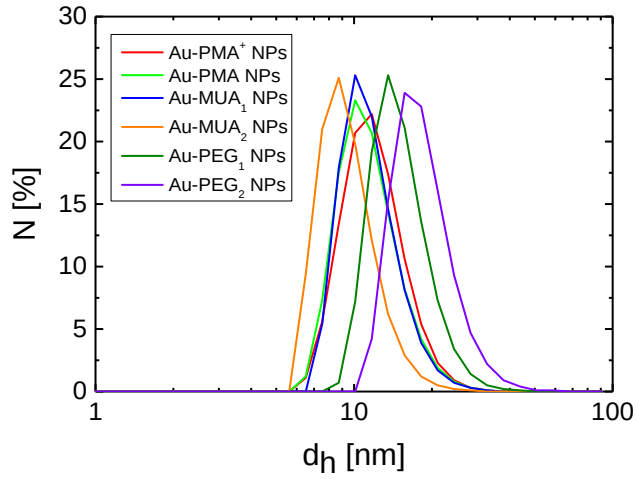

Figure SI-II.2: Number distribution N(d_h) of the hydrodynamic diameter of Au NPs dispersed in water.

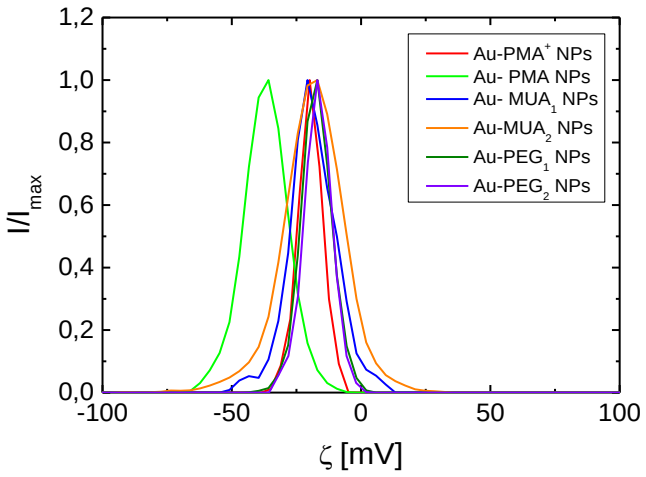

Figure SI-II.3: Distribution of the zeta potential I(ζ) of Au NPs dispersed in water.

UV/vis absorption (*cf.* Figure SI-II.4) and fluorescence (in case of Au-PMA* NPs, *cf.* Figure SI-II.5) spectra of the Au NP samples dispersed in water were recorded. From the absorption spectra A(λ) the NP concentration c_{NP} was calculated using the Lambert Beer law:

$$A_{max} = c_{NP} \cdot \varepsilon_{NP} \cdot l \qquad \text{(Equation SI-II.1)}$$

Hereby, A_{max} is the absorption maximum at the surface plasmon resonance peak of the Au NPs, c_{NP} the NP concentration, l is the path length of the cuvette in which measurements were performed, and ε_{NP} is the molar extinction coefficient of the NPs at the wavelength of the absorption peak, which was assumed to be $\varepsilon_{NP} = 8.7 \cdot 10^6\ M^{-1}cm^{-1}$. The fluorescence of the NPs was measured with a Horiba FluoroLog fluorometer upon excitation at λ_{ex} = 544 nm.

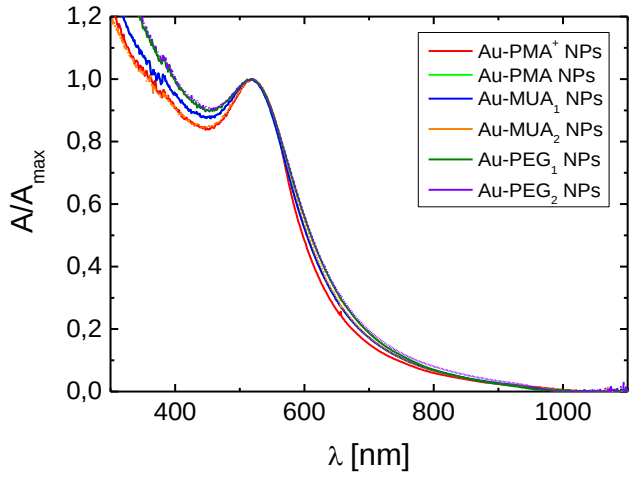

Figure SI-II.4: Normalized UV/vis absorption spectra as recorded in aqueous solution of polymer-coated Au-PMA NPs without ("Au-PMA NPs"), and with TMR-cadaverine ("Au-PMA NPs") in their polymer shell, respectively. Different batches of Au NPs modified with MUA (Au-MUA$_1$ NPs and Au-MUA$_2$ NPs) and Au NPs coated with PMA and modified with 10 kDa PEG (Au-PEG$_1$ NPs and Au-PEG$_2$ NPs) are also shown.*

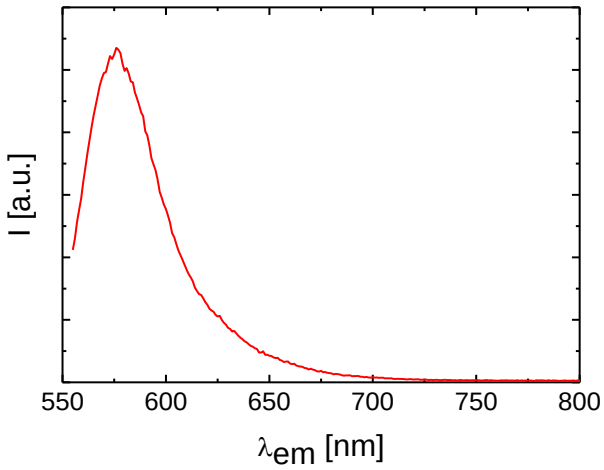

Figure SI-II.5: Fluorescence emission spectrum of Au-PMA NPs with TMR-cadaverine in their polymer shell.*

III) Cell culture and nanoparticle exposure

HeLa cells (derived from cervical cancer cells) were cultured in Minimum Essential Medium (MEM, Sigma-Aldrich, #M4655) and Human Umbilical Vein Endothelial Cells (HUVECs) were cultured in Endothelial Cell Growth Medium (ECGM, PromoCell, Germany, #C-22010). MEM medium was supplemented with 10 % fetal bovine serum (Biochrom, Germany, #S0615), and 1 % penicillin/streptomycin (P/S, Sigma-Aldrich, #P4333). ECGM was supplemented with ECGM supplement mix (PromoCell, #C-39215), and 1 % P/S. HeLa cells or HUVECs were added to 8 well µ-slides (1 cm^2 per well, Ibidi, Germany, #80826) and incubated at 37 °C and 5 % CO_2 (all incubation steps are at 37 °C; only pre-warmed media were added to the cells). After 24 h, the particular growth medium was replaced by Au NP-containing medium for additional 24 h unless otherwise stated.

IV) Transmission electron microscopy of cells

Cells (grown on 35 mm corning culture dishes, #ym-2011A) were rinsed in phosphate buffered saline (PBS) for 3 times and then fixed in 2.5 % glutaraldehyde (8 %, EMS, USA, #16010) in 0.1 M 3-(N-morpholino)propanesulfonic acid (MOPS) buffer (pH 7.0) for 10 h at room temperature. This was followed by secondary fixation with 1 % osmium tetraoxide for 1 h. Then, the specimens were dehydrated through a graded ethanol series (50 %, 70 %, 80 %, 90 % and 100 %), and infiltrated through propylene oxide, and embedded in epoxy resin. Ultrathin sections (80 nm) were cut with a diamond knife using a Leica Ultracut UCT microtome (Leica EM UC6, Stockach, Germany). The sections were placed on 300 mesh copper grids and post-stained with uranyl acetate and lead citrate for observation under the transmission electron microscope (Hitachi, H-7650B).

Transmission electron microscopy (TEM) images of HUVECs and HeLa cells with incorporated Au-PMA* NPs are shown in Figure SI-IV.1. As Figure SI-IV.1 shows, in HUVECs as well as HeLa cells, Au-PMA* NPs along with some other substances outside the cells form loose clusters around 200 nm in diameter. Presumably macropinocytosis plays a role in internalization of the Au-PMA* NPs, as it can be seen from the pictures that a macropinocytic cup wraps the Au-PMA* NP cluster. After Au-PMA* NPs are taken up into the cells, they appear to accumulate in lysosomes (*cf.* Figure SI-IV.1, yellow arrows, as well the discussion in § XI.1).

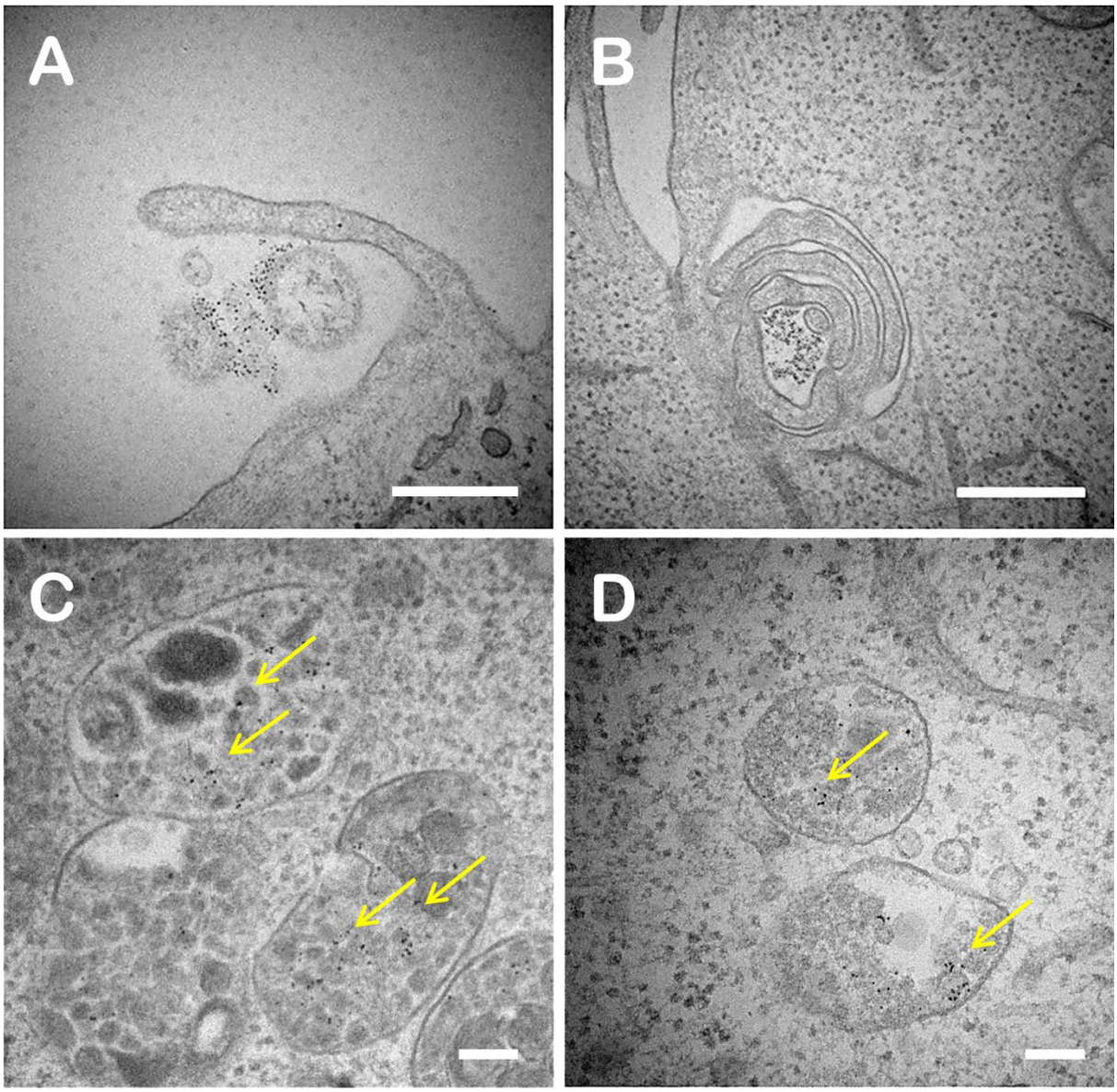

Figure SI-IV.1: TEM images of HUVECs and HeLa cells after having been incubated with Au-PMA NPs at a final NP concentration of c_{NP} = 25 nM for 24 h. The scale bars correspond to 500 nm for A and B, 100 nm for C and D. Yellow arrows indicate Au-PMA* NPs present in lysosomes.*

V) Atomic force microscopy of cells

After incubation with Au-PMA* NPs, cells were imaged with atomic force microscopy (Nanoscope IV, Veeco, Santa Barbara, CA). Contact Mode (CM) was utilized for topological imaging, which was performed in phosphate buffered saline (PBS), using a silicon-tip on nitride lever cantilever (SNL, spring constant $k = 0.08\ N \cdot m^{-1}$, resonance frequency $f = 12\text{-}24$ kHz, Bruker, Karlsruhe, Germany). The deflection set point was adjusted to 0.8 V. The scanning area was chosen to be $40x40\ \mu m^2$ for imaging the whole cell, and the scan angle was set to 90^o.

VI) Helium ion microscopy

For helium ion microscopy (HIM) cells were seeded on glass cover slips (d = 15 mm, Roth, Germany, #P231.1). After 24 h the cells were exposed to the Au-PMA* NPs at concentrations between 0 and 100 nM. After additional 24 h the cells were fixed with 1 % glutaraldehyde (8 %, EMS, USA, #16010), which was added directly to the cell medium for 10 min, followed by three washing steps with PBS. Subsequently, the samples were treated with 2 % glutaraldehyde and 4 % paraformaldehyde (8 %, EMS, USA, #157-8-100) in 0.1 M sodium cacodylate buffer (pH 7.2, Sigma-Aldrich, #20840) for 90 min and dehydrated in ethanol-water mixtures with increasing ethanol content (30 %, 50 %; 70 %, 95 %, and 3 x 100 %) for 10 min per step. Finally critical point drying was performed using a Polaron E3000 (Quorum Technologies, UK). The samples were imaged with a HIM ORION PLUS from Zeiss at a working distance of 19.5 mm, with an accelerating voltage of 36.5 keV, and a beam current of 0.8-0.9 pA. A flood gun was used to compensate charging. Images show the distribution of secondary electrons or Rutherford backscattered helium ions. The latter images highlight materials with high atomic numbers such as Au.

As visible in Figure SI-VI.1 local membrane disruptions occur in case of HUVECs, which may be attributed to the exposure to Au-PMA* NPs. In addition, this interpretation is strengthened by Rutherford backscattering images of such structures (*cf.* Figure SI-VI.2) which show an increased level of backscattered ions probably due to the presence of Au-PMA* NPs.

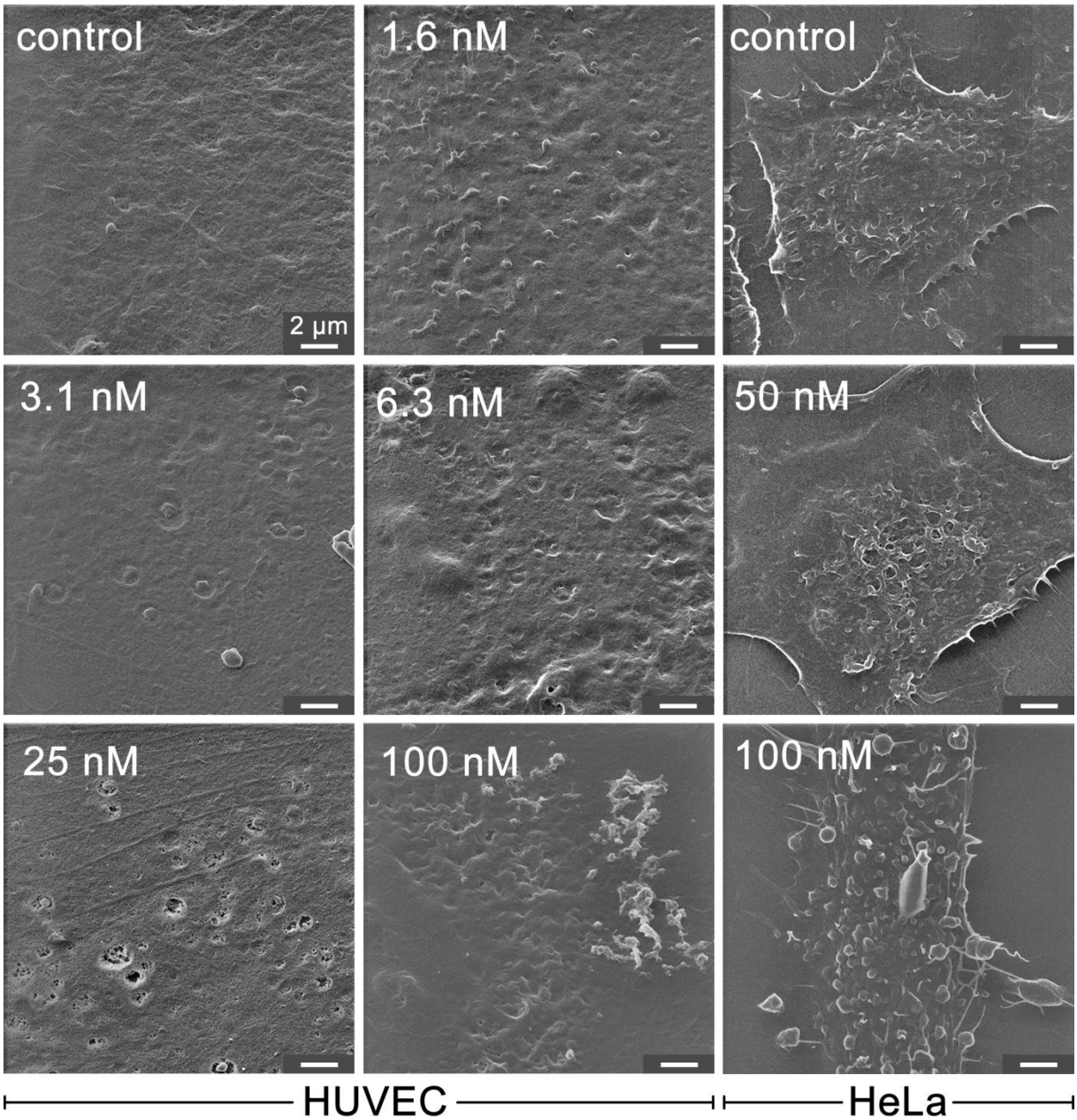

Figure SI-VI.1: HIM images (secondary electrons) of HUVEC and HeLa cells after exposure to Au-PMA NPs. In case of HUVECs the surface becomes locally disrupted.*

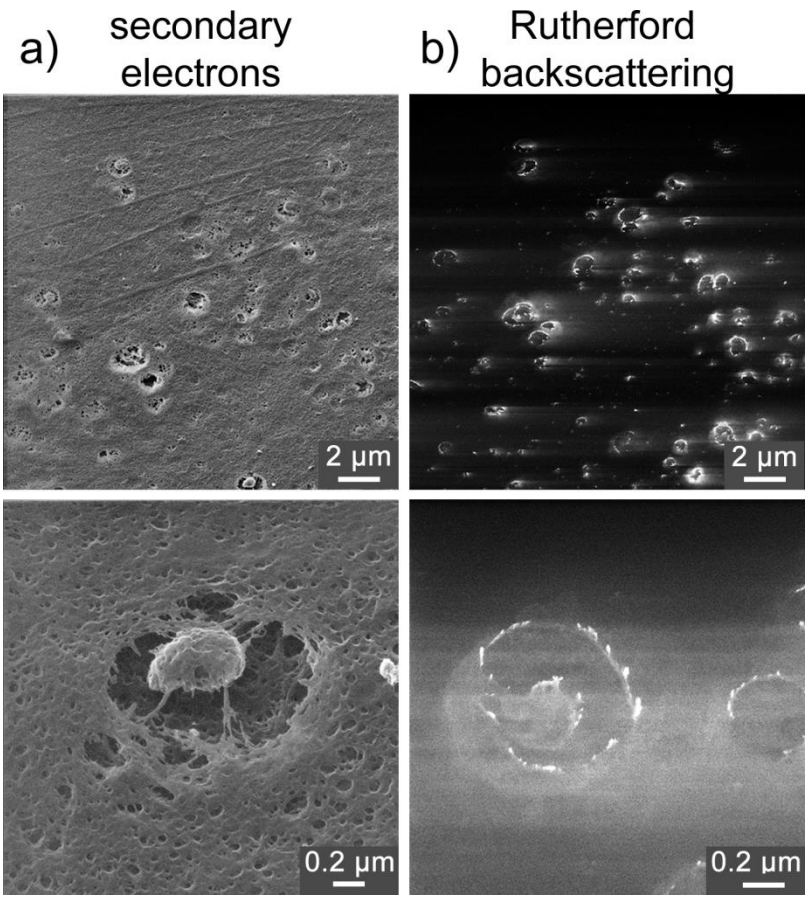

Figure SI-VI.2: Rutherford backscattering at membrane disruptions (HUVECs, c_{NP} = 25 nM, Au PMA NPs).*

VII) Confocal microscopy of cells

Imaging was performed with a confocal laser scanning microscope (CLSM 510 Meta) from Zeiss, equipped with lasers allowing excitation at 405, 488, 543, and 633 nm. Details regarding the imaging are given in the descriptions of the corresponding assays.

VIII) Data analysis of geometrical features from fluorescence images

VIII.1) Cells

VIII.2) Subcellular structures (mitochondria/lysosomes)

VIII.3) Geometrical features

VIII.4) NP uptake

To extract geometrical features, texture information and NP uptake from fluorescence images in a high throughput manner CellProfiler[19] and Matlab (Mathworks) were used.

VIII.1) Cells

To quantify the effect of NP exposure on cell morphology several geometrical features were calculated, based on cross-sections of hundreds of individual cells. Cells were automatically identified from 2D fluorescence images in low magnification, based on the fluorescence pattern of the cytoskeleton and nuclei. Therefore, nuclei (primary objects) were identified first, in order to obtain the outlines of the whole cells (secondary objects) more easily in a second step[19]. Thus, image processing was performed as follows: First, cell nuclei were segmented based on their DAPI-staining pattern (Figure SI-VIII.1.1, a) by thresholding and identified as primary objects. Around each nucleus the corresponding cell body (secondary object) was derived from actin or cell membrane staining (Figure SI-VIII.1.1, b), by using the "propagation"-algorithm[20] provided by CellProfiler. Manual post-processing (removal of dead cells and correction of erroneous segmentation results) was performed with a graphical user interface written in Matlab (Mathworks). The obtained shapes were converted into binary images and several geometrical parameters were calculated (listed below) (Figure SI-VIII.1, c-d).

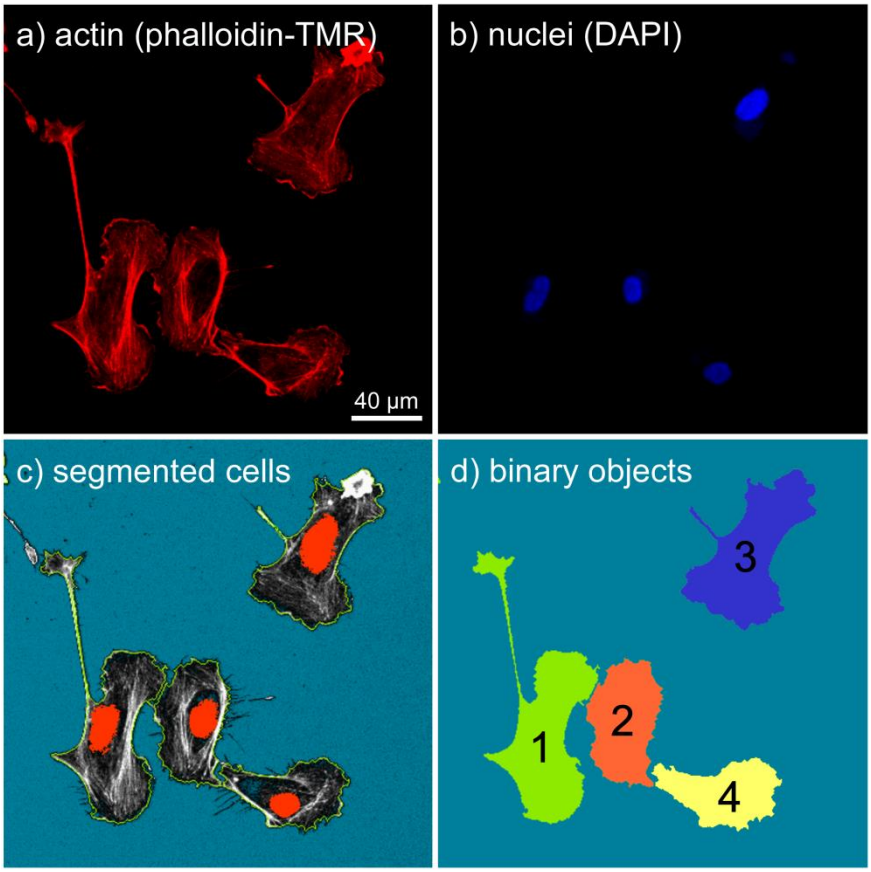

Figure SI-VIII.1: Cell segmentation example. Fluorescence image of non-treated HUVECs, showing (a) the cytoskeleton (phalloidin-TMR) in the red channel and (b) the nuclei (DAPI) in the blue channel. (c) The outcome of the segmentation procedure is shown. (d) The resulting objects which were used to derive all geometrical features are shown.

VIII.2) Subcellular structures (mitochondria/lysosomes)

The segmentation of subcellular structures was difficult, as shapes can vary from spindle like objects (*e.g.* mitochondria of untreated cells) over polliwog shaped forms (*e.g.* mitochondria of cells exposed to increasing concentration of NPs) to simple round objects (*e.g.* lysosomes, damaged mitochondria). Object identification was performed based on fluorescence confocal microscopy 2D slices (*cf.* Figure SI-VIII.2, a). In case of mitochondria the image quality was enhanced by employing a classical maximum likelihood estimation deconvolution algorithm, using a theoretical point spread function. Apart from being able to cope with different shapes, the segmentation routine should be able to handle staining intensity variations. In addition the background in an intracellular region is not dark (unfocussed structures), especially in the perinuclear region, where the lysosomal and mitochondrial density is significantly higher than in outer regions of the cell. To obtain satisfactory results multiple thresholding steps were performed: First, the image was roughly segmented by adaptive two-class thresholding following the Otsu-method[21] (*cf.* Figure SI-VIII.2, b). This step was applied to separate scattered structures in the outer region of the cell from clumpy structures in the perinuclear region. The obtained objects were processed again with an object based thresholding approach using the MoG (Mixture of Gaussian) algorithm provided by CellProfiler[19] (*cf.* Figure SI-

VIII.2c). Third, to indentify objects which were still including more than one structure, the objects were classified with respect to texture entropy and area (*cf.* Figure SI-VIII.2, d). Correctly segmented objects with only one structure of interest are smaller and show a much lesser texture entropy than objects including more than one or clumpy structures. Fourth, objects which showed a high texture entropy were segmented a third time, again following the adaptive two-class thresholding approach using the Otsu-method[21], which was used already for the initial segmentation step (*cf.* Figure SI-VIII.2, e). Fifth, the size distribution of all resulting objects was analyzed and large objects very excluded from the analysis. Finally, texture and intensity of all individual objects was determined and several geometrical features were calculated based on their shape (features are listed below) (*cf.* Figure SI-VIII.2, f).

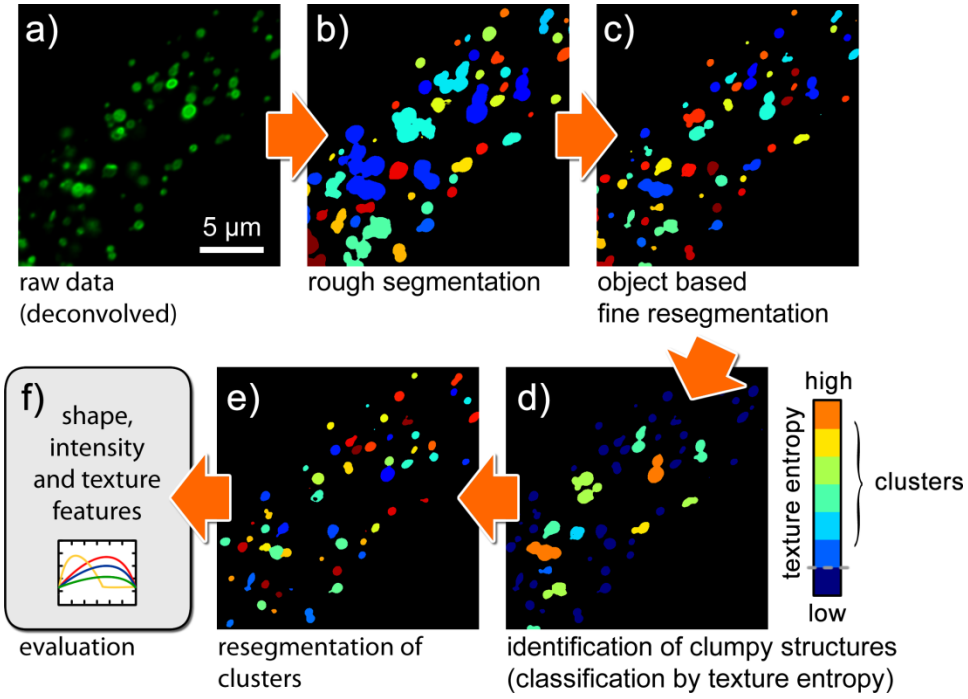

Figure SI-VIII.2: Segmentation of mitochondria. An example of a fluorescence image of HUVECs treated with Au-PMA NPs at 12.5 nM is depicted, showing mitochondria (CellLight Mitochondria-GFP) in the green channel (a) after deconvolution and (b-f) after subsequent segmentation procedure steps .*

VIII.3) Geometrical features

Form factor: For the identified objects their area A [µm^2], as well as their perimeter P [µm] was determined. From these parameters the form factor F was calculated. Examples are given in Table SI-VIII.1.

$$F = 4 \cdot \pi \cdot A/P^2 \qquad \text{(Equation SI-VIII.1)}$$

Zernike moments: Zernike moments are commonly used for automatic recognition of pattern characteristics in fluorescence imaging[22]. They describe the decomposition of an image object onto an orthogonal set of polynomials similar to the way that Fourier coefficients are used to decompose a time series. In this work only the 0th moment Z^0 was used to describe

whether a shape is similar to a disk ($Z^0 = 1$) or more spindle like ($Z^0 = 0$). Examples are given in Table SI-VIII.1.

Feature	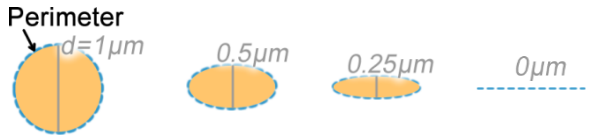			
A [µm²]	0.78	0.39	0.2	0
P [µm]	3.1	2.5	2.2	2
F	1	0.76	0.5	0
Z^0	1	0.5	0.25	0

Table SI-VIII.1: Features used to describe cell, mitochondria, and lysosomal shapes upon exposure to NPs. A = area, P = perimeter, F = form factor, Z^0 = Zernike moment of order 0, d corresponds to the semi-minor axis of the example shapes, if being represented by an ellipse.

Lysosomal fraction: To investigate lysosomal swelling upon exposure to NPs the total area A_{lyso} of all lysosomes in a confocal 2D-slide was divided by the cell area A_{cell}, *cf.* Figure SI-VIII.3. The area occupied by lysosomes was obtained by binarizing the image containing the fluorescence information of stained lysosomes using manual thresholding. Along the obtained shape of each cell (as described in § VIII.1) the number of positive pixels in the corresponding binary image was determined and divided by the total cell area.

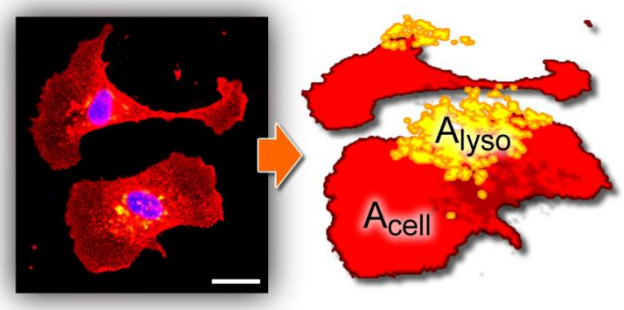

Figure SI-VIII.3: The lysosomal fraction is calculated by dividing the area occupied by lysosomes (A_{lyso}) by the area of the whole cell (A_{cell}). Left image: blue: nuclei, red: plasma membrane, scale bar: 20 µm.

Texture: To quantify the texture of actin or tubulin staining, several Haralick texture features were calculated[23]. These features are derived from the co-occurrence matrix, containing information about how pixel intensities or correlated spatially in horizontal orientation. Examples are given in Table SI-VIII.2.

Texture					
T_{cont} [a.u.]	36	4.2	0.6	0	7.8
T_{corr} [a.u.]	-0.5	-0.6	0.3	0	0.7

Table SI-VIII.2: Features used to describe the texture of actin and tubulin staining of cells treated with NPs. T_{cont} = texture contrast, T_{corr} = texture correlation.

VIII.4) NP uptake

The relative amount of fluorescent NPs taken up by individual cells was estimated from fluorescence images. In addition to the fluorescence information of nuclei and cytoskeleton the signal of the NPs was recorded in a third channel. Along the area of each cell obtained in § VIII.1 the fluorescence intensity of the internalized NPs was summed up, yielding the integrated intensity I_{NP} per cell[24].

IX) Cell viability, proliferation, etc.

IX.1) Resazurin assay (as carried out in Marburg)

IX.2) Resazurin assay (as carried out in Ghent)

IX.3) MTT assay

IX.4) Live/dead assay

IX.5) Proliferation assay

IX.6) Oxidative stress

A selection of standard assays used for analysis of cytotoxic effects of NPs on cells in vitro was applied. These data show the different concentration ranges at which effects occur.

IX.1) Resazurin assay (as carried out in Marburg)

First, cell viability in the presence of NPs was investigated with resazurin assays. HUVECs and HeLa cells were seeded in 96-well plates (Sigma Aldrich, #CLS3603) at a density of 5,000 cells in 300 µL medium per well (each well had an area of 0.3 cm^2), and were grown for 24 h in cell growth medium. Then the cells were rinsed with PBS and supplemented cell growth medium containing Au NPs at different resulting concentrations c_{NP} was added to the wells (100 µL medium per well). Concentrations were adjusted in a way that a wide range of concentrations was covered. The cells were incubated at 37 °C and 5 % CO_2 for 24 h. After that, the cells were rinsed with PBS and a freshly prepared solution of 90 % medium and 10 % resazurin (Sigma-Aldrich, #TOX8) was added to the wells. The cells were incubated for 3 h at 37 °C and 5 % CO_2.

Non-fluorescent resazurin (Almar blue) is oxidized by living cells to fluorescent resorufin. Therefore, the fluorescence intensity is a measure of the viability of the cells. After incubation, the fluorescence emission spectrum $I(\lambda, c_{NP})$ of the solution was recorded with a fluorometer (Fluorolog-3, Horiba Jobin Yvon). Hereby, the wells were excited at $\lambda_{ex} = 560$ nm, and fluorescence emission was recorded from 572 to 650 nm, *cf.* Figure SI-IX.1.

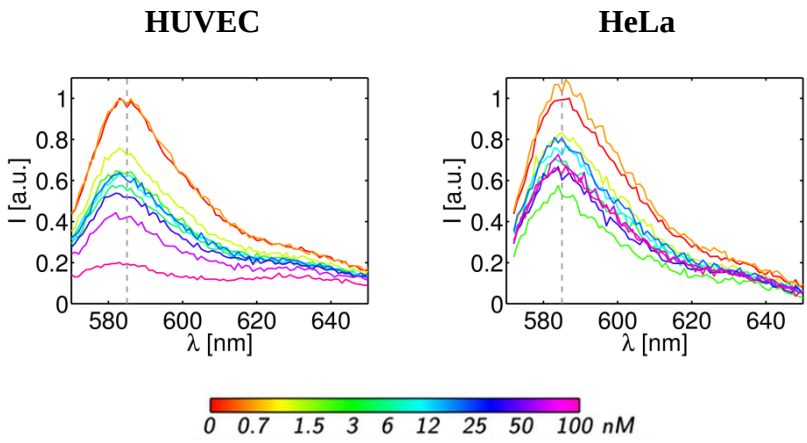

Figure SI-IX.1: Resorufin fluorescence spectra as recorded on cells incubated with different concentrations c_{NP} of Au-PMA NPs and resazurin for (a) HUVECs, and (b) HeLa cells.*

The intensities between 640 to 650 nm were averaged and subtracted as background from the intensity average between 583 to 587 nm, which was the maximum of the emission spectrum. The background corrected averaged intensity maxima $I(c_{NP})$ were plotted versus the concentration c_{NP}, *cf.* Figure SI-IX.2**Fehler! Verweisquelle konnte nicht gefunden werden.**. The cell viability V_{res} was hereby defined as normalized intensity maxima, *cf.* Equation SI-IX.1.

$$V_{res}(c_{NP}) = I(c_{NP}) / I(c_{NP} = 0) \qquad \text{(Equation SI-IX.1)}$$

The concentration-dependent fluorescence intensities $I(c_{NP})$ were then fitted using the sigmoidal function shown in Equation SI-IX.2, with the fit parameters $c_{NP,50}$, I_{min}, I_{max}, and p. Hereby, $c_{NP,50}$ is the NP concentration at which viability of cells has been reduced to half of its activity, and are I_{min} and I_{max} the minimum and the maximum of the concentration-dependent intensity maxima $I(c_{NP})$.

$$I(c_{NP}) = \frac{I_{max} - I_{min}}{1 + \left(\frac{c_{NP}}{c_{NP,50}}\right)^{p}} + I_{min} \qquad \text{(Equation SI-IX.2)}$$

The resulting viability data are shown in Figure SI-IX.2**Fehler! Verweisquelle konnte nicht gefunden werden.**. As expected, upon a certain NP concentration cell viability is reduced. HUVECs are more sensitive than HeLa cells to incubation with the NPs.

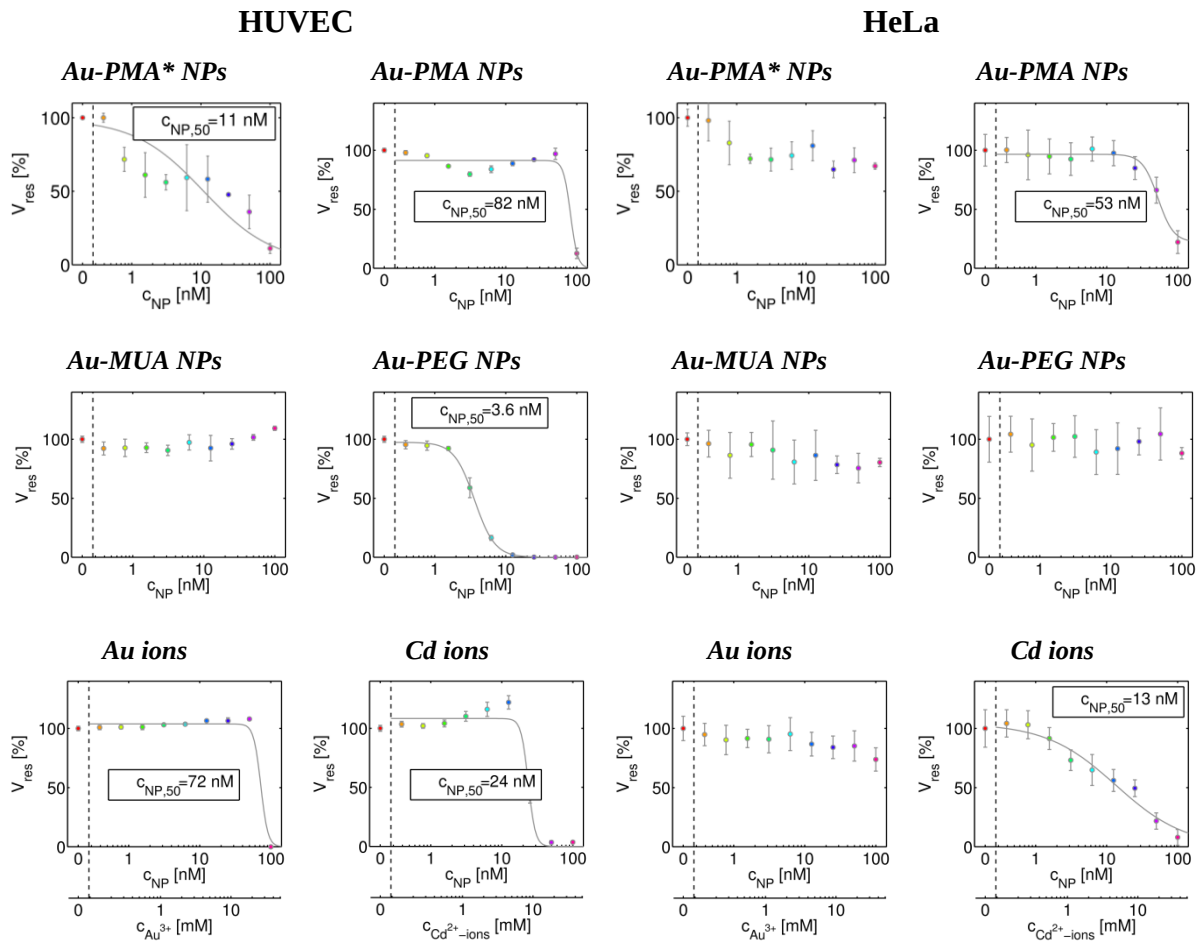

Figure SI-IX.2: Cell viability V_{res}, as determined with the resazurin test, in dependence of the NP concentration c_{NP}. Different types of NPs were used. In the case of HUVECs the batches Au-MUA$_2$ and Au-PEG$_2$ were used, in case of HeLa cells the batches Au-MUA$_1$ and Au-PEG$_1$ were used. The results are presented as mean value ± standard deviation (SD). Differences for Au-PEG NPs acting on HUVECs and HeLa cells are ascribed to potential differences betwen the two NP batches (Au-PEG$_2$, Au-PEG$_1$)

IX.2) Resazurin assay (as carried out in Ghent)

Second, the same resazurin (Almar blue) assay [25] was carried out in a different laboratory with a slightly modified protocol.

HeLa cells or HUVECs were seeded at 5,000 cells/well in black, clear-bottom 96-well plates and were allowed to settle overnight. Cells were then incubated for 24 h with the Au NPs at the indicated concentrations (from c_{NP} = 0 to 100 nM), after which the Alamar Blue assay (Molecular Probes, #DAL1025) was performed according to the manufacturer's protocol. Fluorescence readouts were performed using an Optima FluoStar plate reader instrument (λ_{ex} = 560 nm; λ_{em} = 590 nm). Data analysis was performed as described in § IX.1. Data are expressed as mean ± SD (n = 4).

The results of the Alamar blue test are reported in Figure SI-IX.3. For the HUVECs, the NPs

resulted in a reduction of cell viability at high NP concentrations, with the cell viability being significantly reduced at c_{NP} = 100 nM. For the HeLa cells, no significant toxic effects were observed for NP concentrations up to 100 nM.

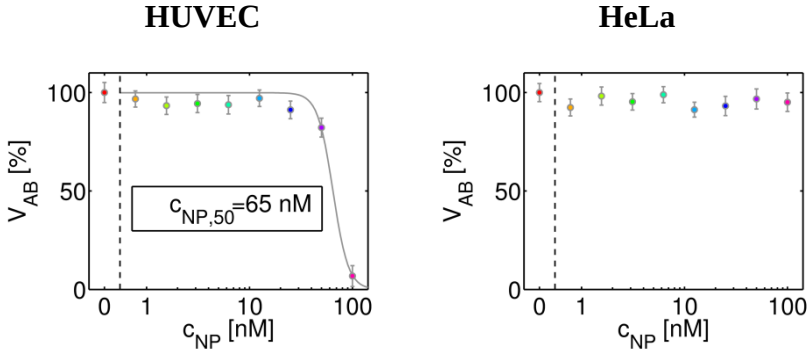

Figure SI-IX.3: Cell viability V_{AB}, as determined with the Alamar blue test, in dependence of the concentration c_{NP} of Au-PMA NPs The results are presented as mean ± SD for 4 independent measurements.*

IX.3) MTT assay

Third, cell viability was probed with the 3-(4,5-dimethylthiazol-2-yl)-2,5-diphenyltetrazolium bromide (MTT) assay. For the assay HUVECs and HeLa cells were seeded in 24-well plates (Greiner Bio-One, #662160) at a density of 50,000 cells per well (1 mL/well, 1.9 cm^2 area per well) one day prior the planed experiments. Cells were then incubated with the Au NPs for 24 h at the indicated concentrations (from 0 to 200 nM). After extensive washing an MTT cell proliferation assay (Roche, #11465007001) was performed according to the manufacturer´s instructions. Briefly, 500 µL of regular cell media were added to the cells and then supplemented with 50 µL MTT1 solution. After 4 hours 500 µL of solubilization solution (MTT2) were added. An analysis of the absorbance maximum A_{max} at 590 nm wavelength in an Agilent Technologies 8453 UV-Vis spectrophotometer was done after an overnight incubation. The MTT test is based on the cleavage of the yellow tetrazolium salt MTT in the presence of an electron-coupling reagent[26]. NAD(P)H-dependent cellular oxidoreductase enzymes are capable of reducing the tetrazolium salt MTT to insoluble formazan, that has a purple color, which can be analyzed by measuring absorbance at 590 nm. This bioreduction occurs only in viable cells, and is related to NAD(P)H production through glycolysis. Therefore, the amount of formed formazan dye, directly correlates to the number of metabolically active cells in the culture. The cell viability was defined as

$$V_{MTT}(c_{NP}) = A_{max}(c_{NP})/A_{max}(c_{NP} = 0) \qquad \text{(Equation SI-IX.3)}$$

The cell viability V_{MTT} was plotted against the NP concentration c_{NP}, *cf.* Figure SI-IX.4. The resulting viability data $V_{MTT}(c_{NP})$ as obtained from the MTT test are displayed in Figure SI-IX.4. The data demonstrate that HUVECs are more sensitive to exposure with NPs than HeLa cells.

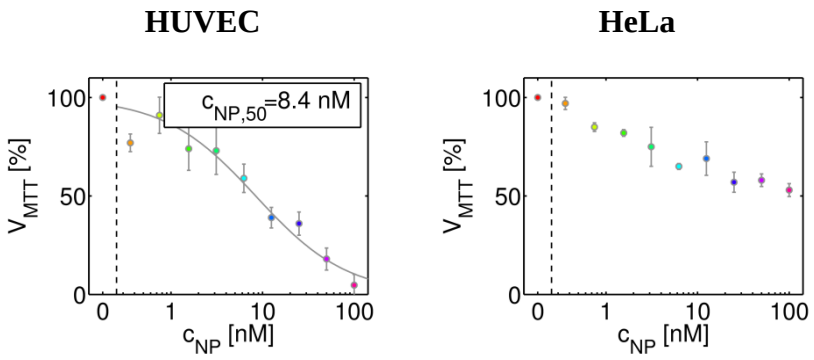

Figure SI-IX.4: Cell viability V_{MTT}, as determined with the MTT test, in dependence of the Au-PMA NP concentration c_{NP}. The results are presented as mean ± SD for n = 3 independent measurements.*

IX.4) Live/dead assay

Forth, a commercially available live/dead assay was performed. Cell viability upon exposure to NPs was assessed by discriminating live and dead cells in fluorescence micrographs, using the LIVE/DEAD Viability/Cytotoxicity Kit (Molecular Probes, #L3224). The kit contains two dyes: i) non-fluorescent cell-permeant calcein acetoxymethyl (AM) which enters live cells and is enzymatically converted into fluorescent calcein by intracellular esterases. ii) upon binding to DNA the fluorescence of live cell-impermeant ethidium homodimer (EthD-1) is strongly increased. The latter stains dead cells. Additionally, the nuclei of all cells (live and dead) were stained with Hoechst 33342 which is specific to DNA to allow automatic segmentation to simplify the readout of the assay.

Briefly, cells were seeded into an 8-well Ibidy µ-slide (12,500 cells/well). After 24 h NPs were added at various concentrations (c_{NP} = 0 - 100 nM). After an additional 24 h incubation cells were washed twice with PBS and stained referring to the instructions of the kit. Living cells were stained with calcein AM at a concentration of 12.5 µM, while EthD-1 was used at 40 µM (HeLa cells) and 200 µM (HUVECs) to stain dead cells. In addition, all nuclei were counterstained by Hoechst 33342 (Molecular Probes, life technology, #H1399) at 30 µg/mL. After 10 min incubation time imaging was started while the staining solution remained on the sample.

Imaging was performed with a fluorescent widefield microscope (Zeiss, Axiovert 200M). Calcein was excited at λ_{ex} = nm (30 nm width band-pass filter) and emission was recorded at λ_{em} = 535 nm (40 nm width band-pass filter: green channel). Excitation of EthD-1 was performed at λ_{ex} = 555 nm (50 nm width band-pass filter) while emitted photons were detected using a λ_{em} = 615 nm long-pass filter (red channel). Hoechst 33342 was excited around λ_{ex} = 365 nm and the emission was detected at λ_{em} = 440 nm (20 nm width band-pass filter: blue channel).

A total area of 10 mm^2 was imaged for each well, allowing the analysis of 3,000-6,000 cells (*cf.* Figure SI-IX.5). For evaluation the micrographs were processed using MATLAB (Mathworks) and CellProfiler[19] in the following way: To identify whether a cell was stained green or red all nuclei were segmented based on the Hoechst stain. Along the area of each nucleus the corresponding mean intensities in the green and red channel were calculated. For live *vs.* dead cells two distinct populations appear when the mean intensity of calcein ($I_{Calcein}$) is plotted against the mean intensity of EthD-1 (I_{EthD-1}) in logarithmic scale (*cf.* Figure SI-IX.5, b-c). Those scatter plots allowed gating of individual populations and simplified the calculation of the ratio D of dead to living cells, defined as the ratio of the average number of red fluorescent cells to the average number of green fluorescent cells. The resulting data (mean values of three individual experiments ± SD) is given in Figure SI-IX.6.

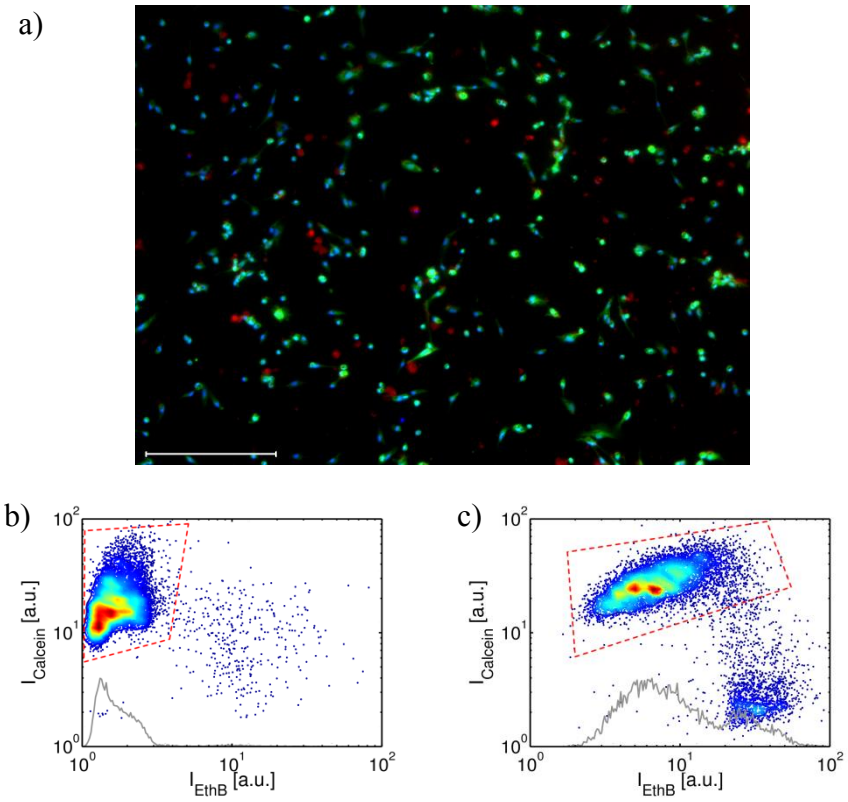

Figure SI-IX.5: Cell viability assessed by calculating the ratio of dead/live cells. In a) a typical fluorescence image is shown after staining live cells with calcein AM (green), dead cells with EthD-1 (red), and nuclei with Hoechst 33342 in blue. The scale bar corresponds to 50 µm. The scatter plots are showing gated populations of living (surrounded by red dashed line), and dead cells for HUVECs (b) in growth medium only, and (c) exposed to Au-PMA NPs at a concentration of c_{NP} = 100 nM for 24 h (c).*

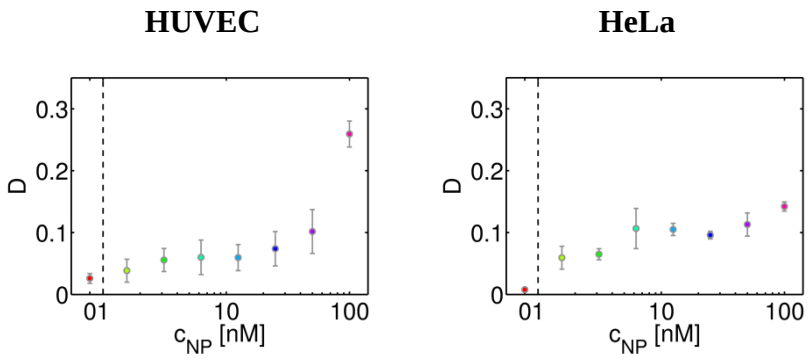

Figure SI-IX.6: Rate of dead vs. live cells D upon exposure to Au-PMA NPs, as derived from a fluorescence cell staining specific for live and dead cells, respectively. The results are presented as mean ± SD for 3 independent measurements.*

IX.5) Proliferation assay

The effect of the Au NPs on cell proliferation was investigated by directly measuring DNA synthesis, as monitored by the incorporation of the thymidine-analog EdU (5-ethynyl-2´-deoxyuridine). EdU can be detected by a copper-catalyzed click-reaction between its alkyne group and an azide group-containing fluorescent dye[27].

Briefly, cells were seeded into 96 well plates (6,000 cells/well). After 24 h, the growth medium was exchanged with medium containing NPs at various concentrations (c_{NP} = 0 - 100 nM). As a negative control colchicine (Sigma Aldrich, #C3915) was added at a concentration of 5 µM (HUVECs) and 10 µM (HeLa cells). Cholchicine is an inhibitor of chromosome segregation during mitosis and suppresses cell proliferation. After additional 24 h of incubation, the growth medium was replaced with medium containing 10 µM EdU (Molecular Probes, #A10044) for 6 h. Subsequently, the cells were fixated and permeabilized. Incorporated EdU was labelled with AlexaFluor 488 azide (Molecular Probes, #A10266) by following the protocol of Salic *et al.*[27]. Briefly, the reaction cocktail for one 96 well plate was prepared by mixing 3360 µL Milli-Q water with 840 µL of 1.7 M Tris (Sigma Aldrich, #T1503) buffer pH 8.5, 42 µL 100 mM $CuSO_4$ (Sigma Aldrich, #61230), 15 µL 10 mM AlexaFlour azide, and 840 µL 0.5 M ascorbic acid (Sigma Aldrich, #255564) and applied for 30 min. Additionally, the nuclei of all cells were labelled with DAPI (Molecular Probes, #D1306) for 5 min at 5 µM or Hoechst 33342 (Molecular Probes, #H1399) for 30 min at 10 µg/mL.

Imaging was performed with a fluorescent widefield microscope (Zeiss, Axiovert 200M). EdU-AlexaFluor 488 was exited at λ_{ex} = 480 nm (30 nm width band-pass filter) and emission was recorded at λ_{em} = 535 nm (40 nm width band-pass filter: green channel). DAPI/Hoechst 33342 was excited around λ_{ex} = 365 nm and the emission was gated at λ_{em} = 440 nm (20 nm width band-pass filter: blue channel).

A total area of 10 mm^2 was imaged for each well, allowing for the analysis of 3,000-6,000 cells (*cf.* Figure SI-IX.7). To determine the proliferation rate p the micrographs were processed using

MATLAB (Mathworks) and CellProfiler[19] in the following way: First, the DAPI/Hoechst-stained nuclei were segmented, representing all cells (proliferated and non-proliferated) present in the current frame. Second, the mean fluorescence intensity in the blue channel ($I_{Hoechst}$) per nuclei was determined, as well as the mean intensity of EdU-AlexaFlour 488 in the corresponding green channel ($I_{EdU\text{-}AF488}$). For each nucleus the logarithm of both intensity values was plotted in a scatter plot to allow for identification and gating of proliferated cells from non-proliferated ones, similar to analyzing flow cytometry data (*cf.* Figure SI-IX.7, b-c). Finally the fraction p of proliferated cells from all cells was calculated for each image and averaged for each concentration. Figure SI-IX.8 shows the mean values ± SD resulting from three individual experiments.

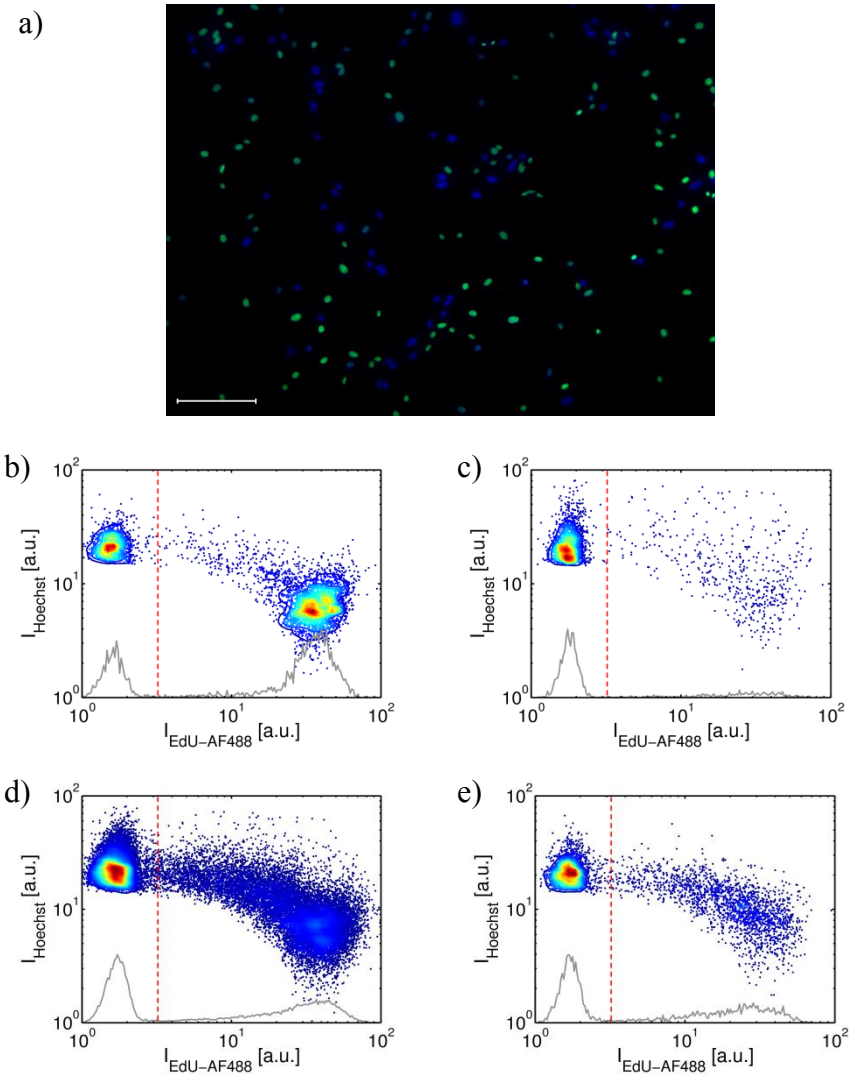

Figure SI-IX.7: Cell proliferation assay carried out with Au-PMA NPs. In a) a typical fluorescence image is shown for HUVECs used to derive quantitative results (scale bar: 100 µm). The nuclei of all cells are stained with DAPI (blue), while only proliferated cells show green fluorescence in addition. The scatter plots are showing two populations divided by a dashed red line: the left spot in each plot is representing non-proliferated cells, while the right population is generated by proliferated cells. Shown are the data for (b) the positive control, (c) the negative control, (d) all cells analyzed, and (e) cells being exposed to NPs at* c_{NP} =

0.59 nM.

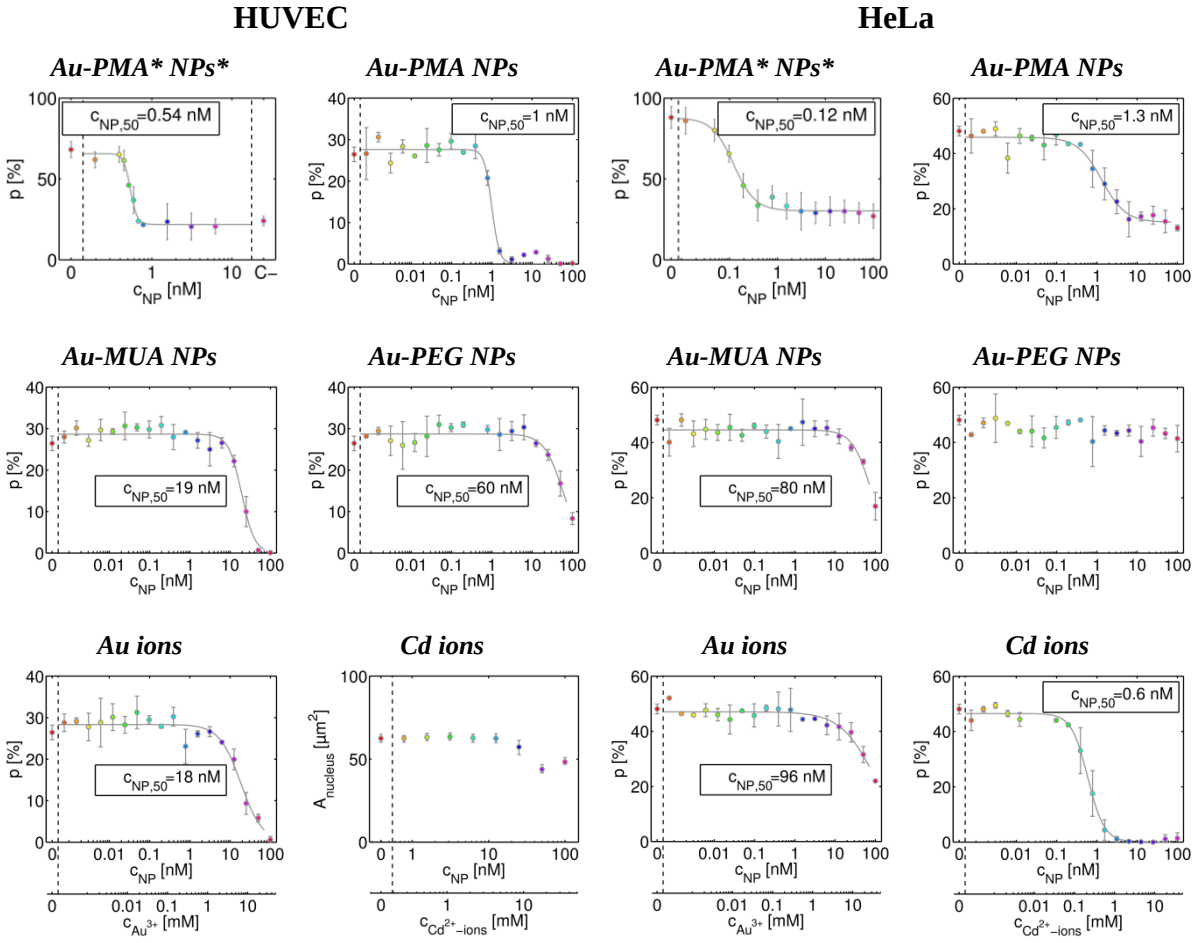

Figure SI-IX.8: Proliferation rate p, as derived from newly synthesized DNA of cells after 24 h of NP exposure to different types of NPs. The results are presented as mean ± SD for n = 3 (Au-PMA) and n = 2 (others) independent measurements. Data were obtained with the batches Au-MUA$_1$ and Au-PEG$_1$. Proliferation data for Au-PMA* NPs (indicated with an asterisk) was obtained by measuring the incorporation of EdU into the DNA while the cells were exposed to Au-PMA* NPs for 24 h and not afterwards.*

IX.6) Oxidative stress

Sixth, oxidative stress was measured using CellROX as the probe. HeLa cells and HUVECs were seeded at 20,000 cells/well in non-transparent 96 well plates (Greiner Bio One, Wemmel, Belgium) and were allowed to settle overnight, after which the cells were incubated with Au NPs at c_{NP} = 0 - 100 nM for 24 h. Then, the cells were washed 3 times with PBS and incubated with 10 µM CellROX Green (Molecular Probes, #C10444) for 45 min. Cells were then washed 3 times with PBS, followed by an additional incubation for 30 min in full culture medium. Then, the cells were washed twice with PBS, and the fluorescence signal was measured using a Wallac Envision plate reader instrument with an excitation filter at λ_{ex} = 480 nm and an emission filter at λ_{ex} = 540 nm. As a positive control, cells were incubated with 0.5 % H_2O_2 for 1 h prior to

incubation with CellROX Green. Data are expressed relative to untreated control cells (= 100 %) as mean + SD (n = 4). As toxic effects occurred, the data obtained for oxidative stress have been normalized for 20,000 cells based on the cell viability data from the Alamar Blue assay (*cf.* Figure SI-IX.3).

The relative level R of ROS as calculated from the measurements is shown in Figure SI-IX.9. For HUVECs, an increase in ROS can be seen at higher NP concentrations. For HeLa cells, the level of ROS is increasing at higher NP concentrations, but the values themselves are not very high and significantly lower than those of HUVECs. This may in part explain the lower toxicity of the NPs to HeLa cells as compared to HUVECs.

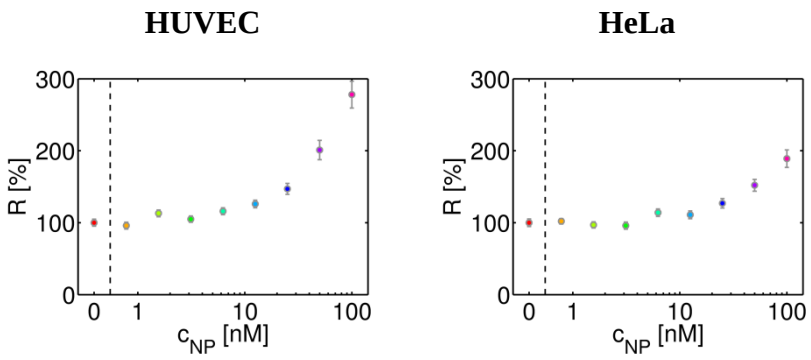

Figure SI-IX.9: ROS levels R after exposure to Au-PMA NPs. Results are presented as mean value ± SD for n = 4 independent measurements.*

X) Analysis of general cell morphology

Concerning cell morphology, the average cell and nuclear area A_{cell} and $A_{nucleus}$, respectively, were determined first. After cell exposure to the NPs for 24 h, cells were washed twice with PBS and fixed for 15 min at room temperature with 4 % paraformaldehyde. The fixative was then aspirated, cells were washed twice with PBS (500 µL/well), after which cells were permeabilized with 250 µL/well of Triton X-100 (1 %) for 10 min at room temperature. Cells were then blocked with 10 % serum-containing PBS for 30 min at room temperature, followed by the addition of primary murine anti-α-tubulin (Abcam, Cambridge, UK, #ab80779) IgG antibody (Ab, 1 µg/mL in blocking buffer) at a total volume of 200 µL/well, and were incubated in the dark for 1.5 h at room temperature. Cells were washed twice with PBS, followed by addition of the secondary AF488-coupled secondary goat anti-murine IgG Ab (Molecular Probes, #A-11029) (1/500 dilution in blocking buffer) and 15 µL (1/100 dilution) Acti-Stain 555 (Tebu-Bio, Belgium) per mL of blocking buffer to a total volume of 200 µL/well. Cells were incubated for 1 h at room temperature in the dark. The latter solution was removed and cells were washed once with PBS and incubated with CellMask Blue (Molecular Probes, #H32720) at 5 µg/mL in PBS for 10 min in the dark. Finally, cells were washed twice with PBS, 500 µL fresh PBS was added to each well, and plates were analyzed on the InCell analyser 2000, where phase contrast and fluorescence-based images for the blue (CellMask Blue), green (α-tubulin), and red (F-actin) channel were collected for a minimum of 2,000 cells/well. Images are shown in Figure SI-X.1 and Figure SI-X.2 for HUVECs and HeLa cells, respectively.

To obtain the data presented in Figure SI-X.3 data analysis was performed with the InCell Investigator software (GE Healthcare Life Sciences, Belgium) using in-house developed protocols. The size of the cells was calculated as follows: First, cell nuclei were segmented based on the blue channel (CellMask Blue stains the entire cytoplasm, but in permeabilized cells, the nucleus is preferentially stained and has a higher intensity). Using the green and red channel, cells were then segmented, where any holes in the cells were filled up and included and any cells on the border of the field of view were excluded from the analysis. The segmentation was based on the blue channel as seed channel for the nucleus. The total area of every individual cell was then determined. The data presented in Figure SI-X.5 and Figure SI-X.6 were derived as described in § VIII from another dataset .

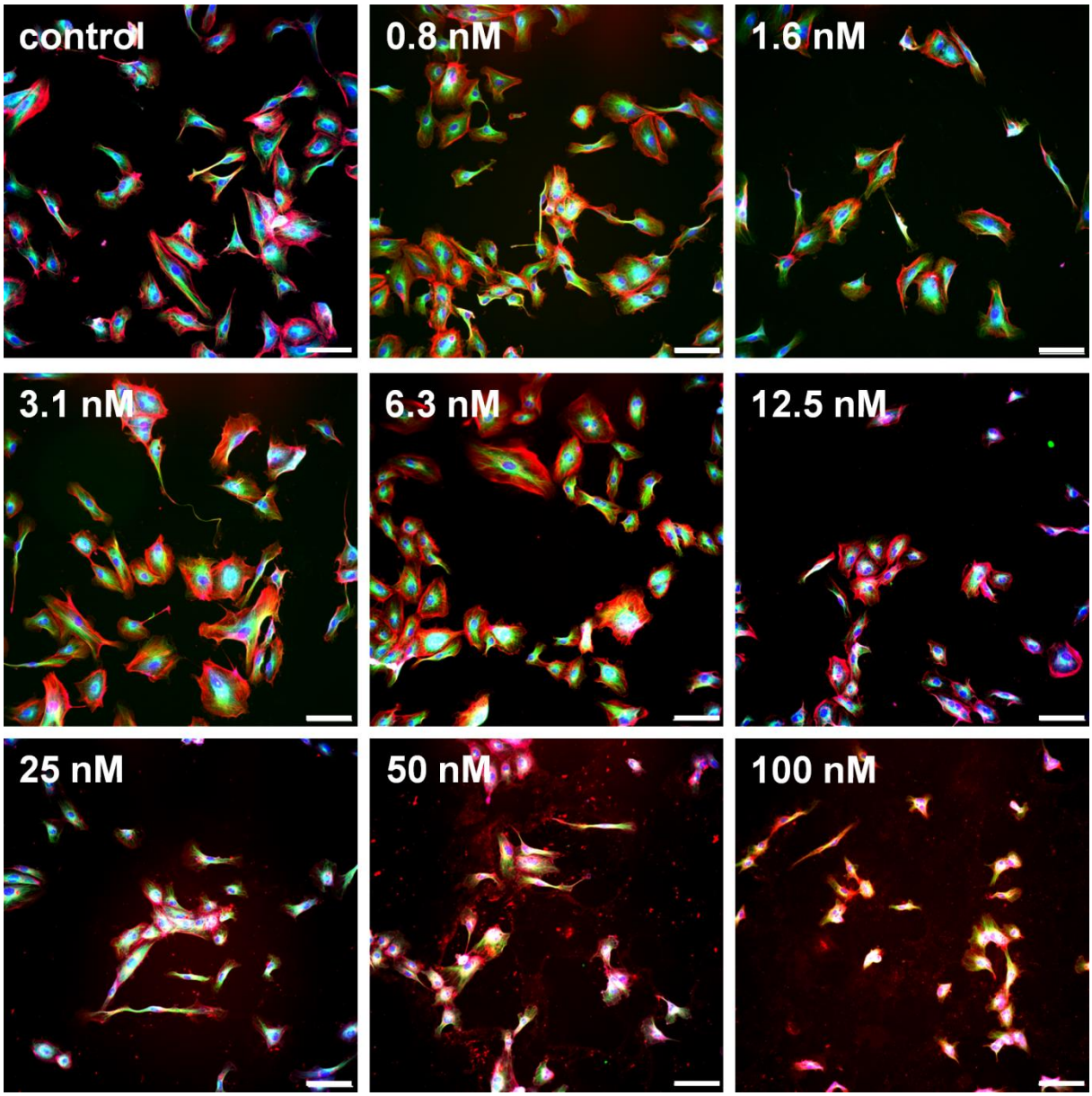

Figure SI-X.1: Representative images of HUVECs treated with Au-PMA NPs at different NP concentrations c_{NP}. Cells were stained for actin (red), tubulin (green), and CellMask (blue). The scale bar corresponds to 100 µm.*

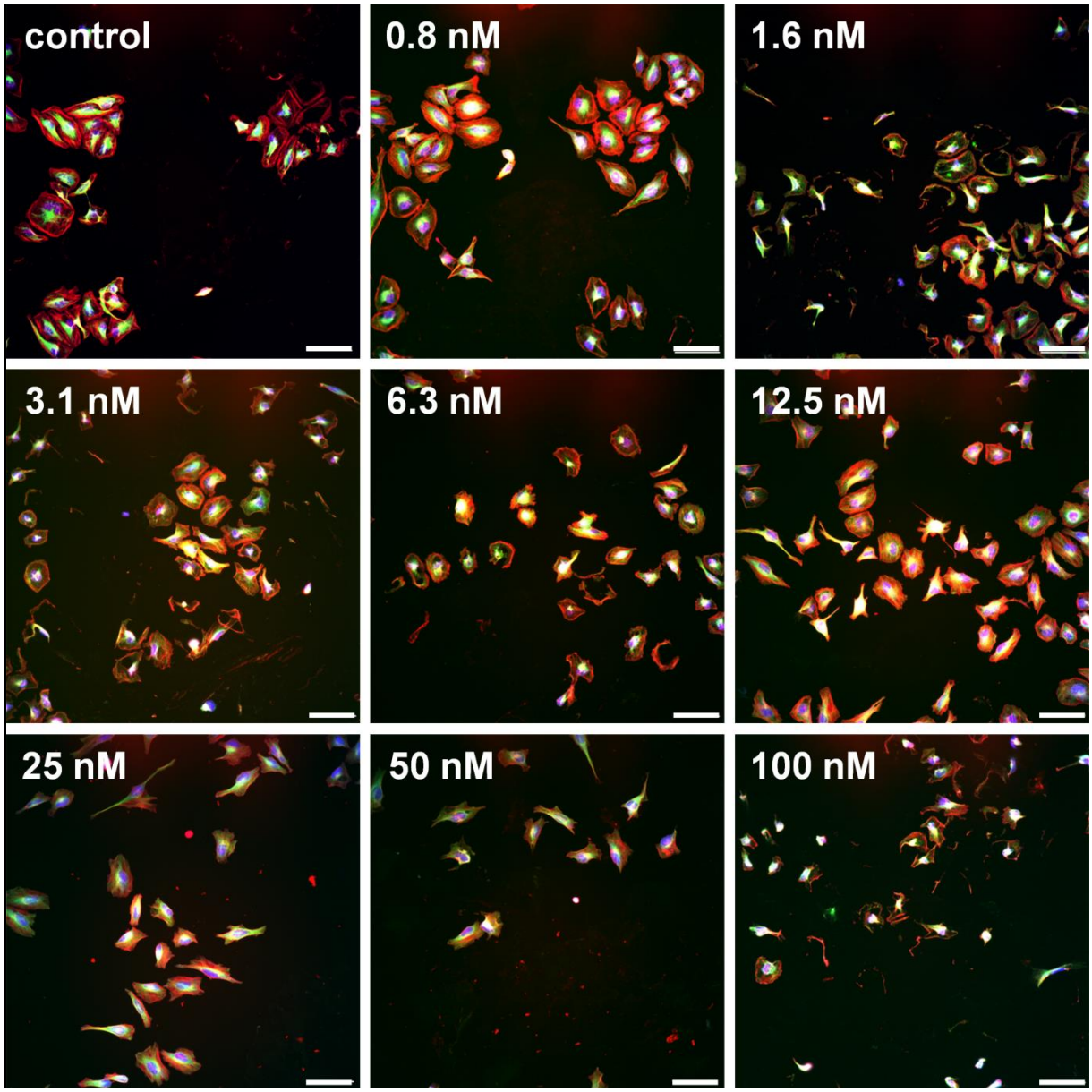

Figure SI-X.2: *Representative images of HeLa cells treated with Au-PMA* NPs at different concentrations c_{NP}. Cells were stained for actin (red), tubulin (green), and CellMask (blue). The scale bar corresponds to 100 µm.*

The results for the cell spreading experiments are summarized in Figure SI-X.3. The data demonstrate that upon exposure to NPs the cell area A_{cell} is reduced. For HUVECs the effects of the exposure to Au-PMA* NPs are far more outspoken as in comparison to HeLa cells.

Cell spreading was investigated also from an additional data set, which was derived by actin-staining, as described in § VIII.1 and § XIII. The data set shown in Figure SI-XIII.1 and Figure SI-XIII.2 was also used for estimating the area per cell, in this case in terms of area of stained actin fibers per cell. The resulting values are shown in Figure SI-X.4Figure SI-X.4 and Figure SI-X.5.

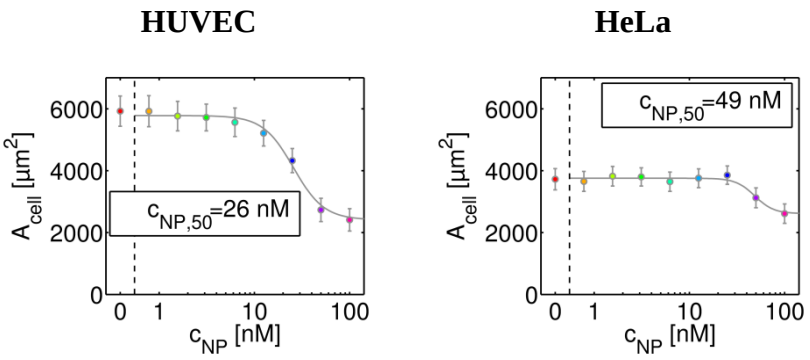

Figure SI-X.3: Mean cross section area per cell A_{cell} of HUVECs (left) and HeLa cells (right) which had been incorporated for 24 h with Au-PMA NPs at different concentrations c_{NP}. Error bars indicate standard deviation for 3 independent sets of over 2,000 cells evaluated per condition.*

In agreement with Figure SI-X.3 the data demonstrate that with increasing of the Au-PMA* NP concentration the cell area decreases concentration dependently in both of the cells. Under the highest Au-PMA* NP exposure concentration the area of HUVECs is reduced by a factor of two, whereas HeLa cells only lose 20 % of the cell area (as quantified in terms of stained actin). From the same data also the form factor F_{cell} of cells was determined, which shows that not only spreading area, but also shape of the cells upon exposure to Au-PMA* NPs changed.

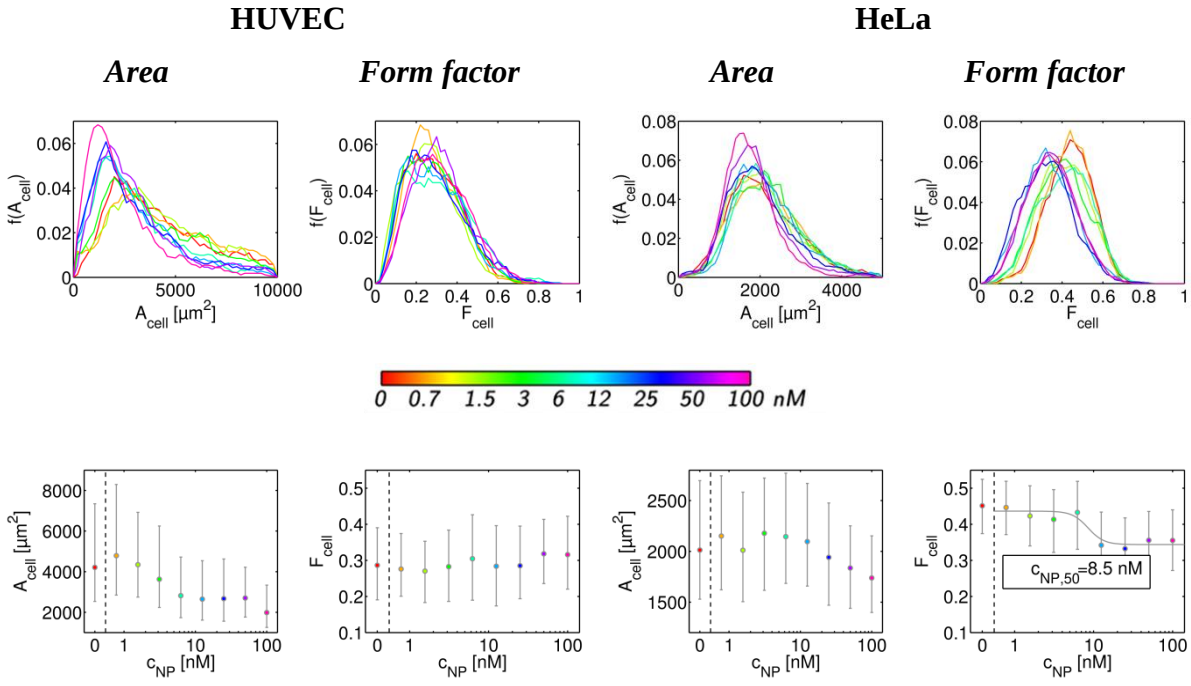

Figure SI-X.4: The normalized probability distribution $f(A_{cell})$ and $f(F_{cell})$ of the frequency of cells found with an area A_{cell} and with form factor F_{cell} , respectively, as derived from stained actin per cell, is plotted for different Au-PMA NP concentrations c_{NP}. The results are presented as normalized probability distributions (first row) and median ± lower/upper quartile for 500 - 1000 cells/condition.*

The same experiments were also carried out for the other Au NPs, *cf.* Figure SI-X.5.

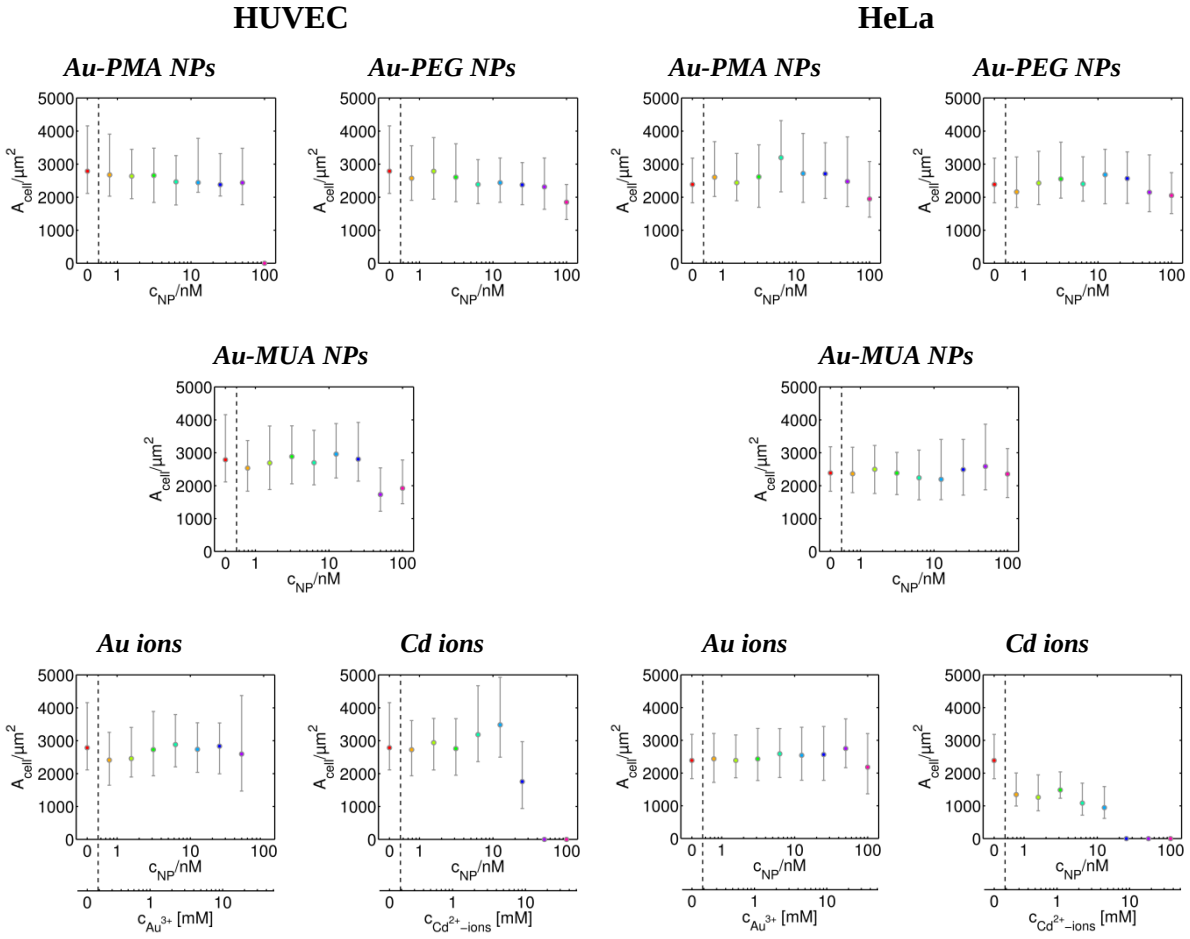

Figure SI-X.5: Cellular cross section area A_{cell}, as derived from stained actin per cell, is plotted for different Au NP concentrations c_{NP} for different types of Au NPs. The batches Au-MUA$_1$ and Au-PEG$_1$ were used. The results are presented as median ± lower/upper quartile for 500 – 1,000 cells/condition.

The nuclear area is often used as an indicator for cell viability. As displayed in Figure SI-X.6, the nuclear area A_{nuclei} is only very slightly decreased after exposure to Au NPs. Effects are only visible at concentrations were acute cytotoxicity is observed and cells start to detach. In comparison to Au and Cd ions the decrease in size is much less pronounced.

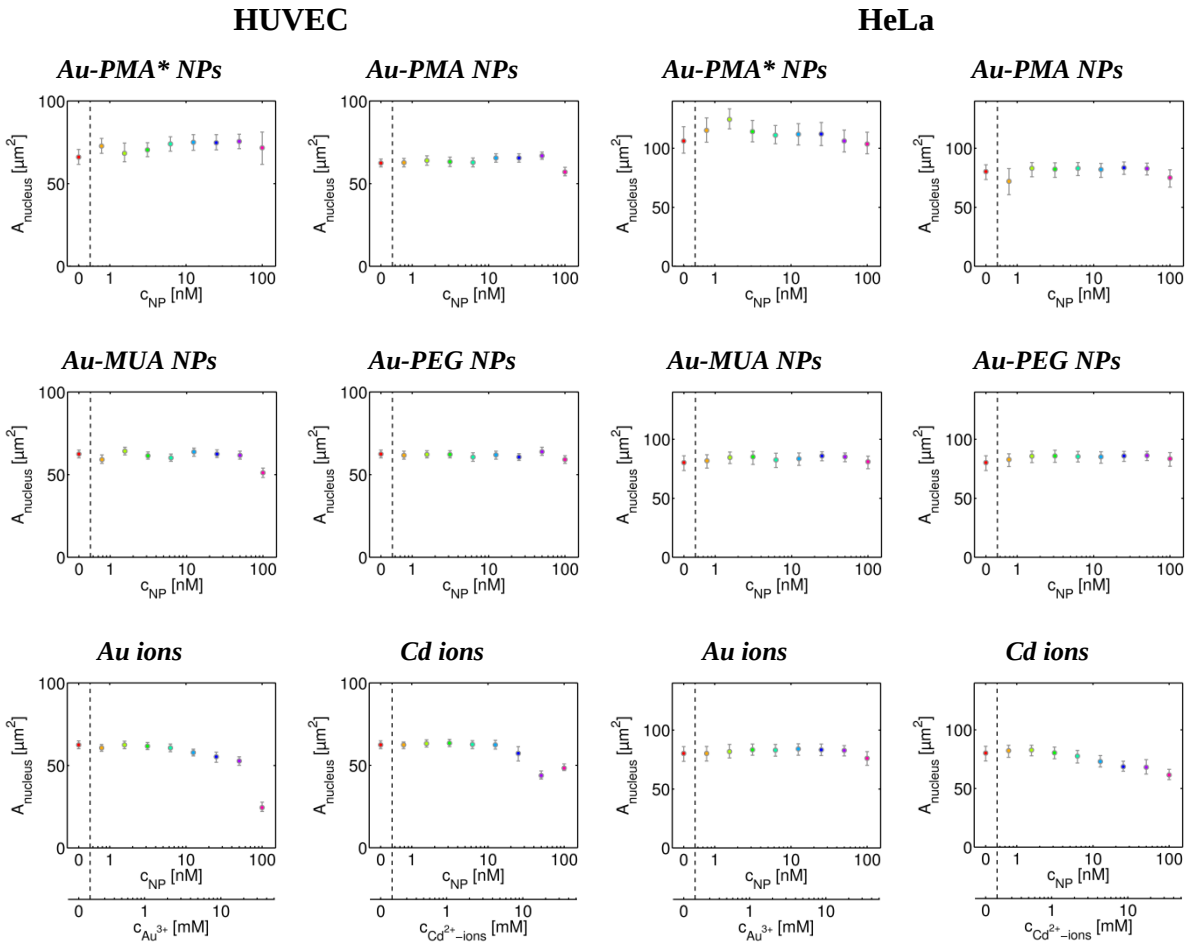

Figure SI-X.6: Nuclear cross section area A_{nuclei}, as derived from stained DNA, is plotted for different Au NP concentrations c_{NP} for different types of Au NPs. The batches Au-MUA$_1$ and Au-PEG$_1$ were used. The results are presented as median ± lower/upper quartile for 3,000 – 5,000 cells/condition.

As a second parameter describing cell morphology, filopodia of the two cell types were investigated. For this purpose, AFM analysis was performed on cells, which had been incubated for 24 h with NPs. Resulting images are presented in Figure SI-X.7**Fehler! Verweisquelle konnte nicht gefunden werden.** and Figure SI-X.8**Fehler! Verweisquelle konnte nicht gefunden werden.**.

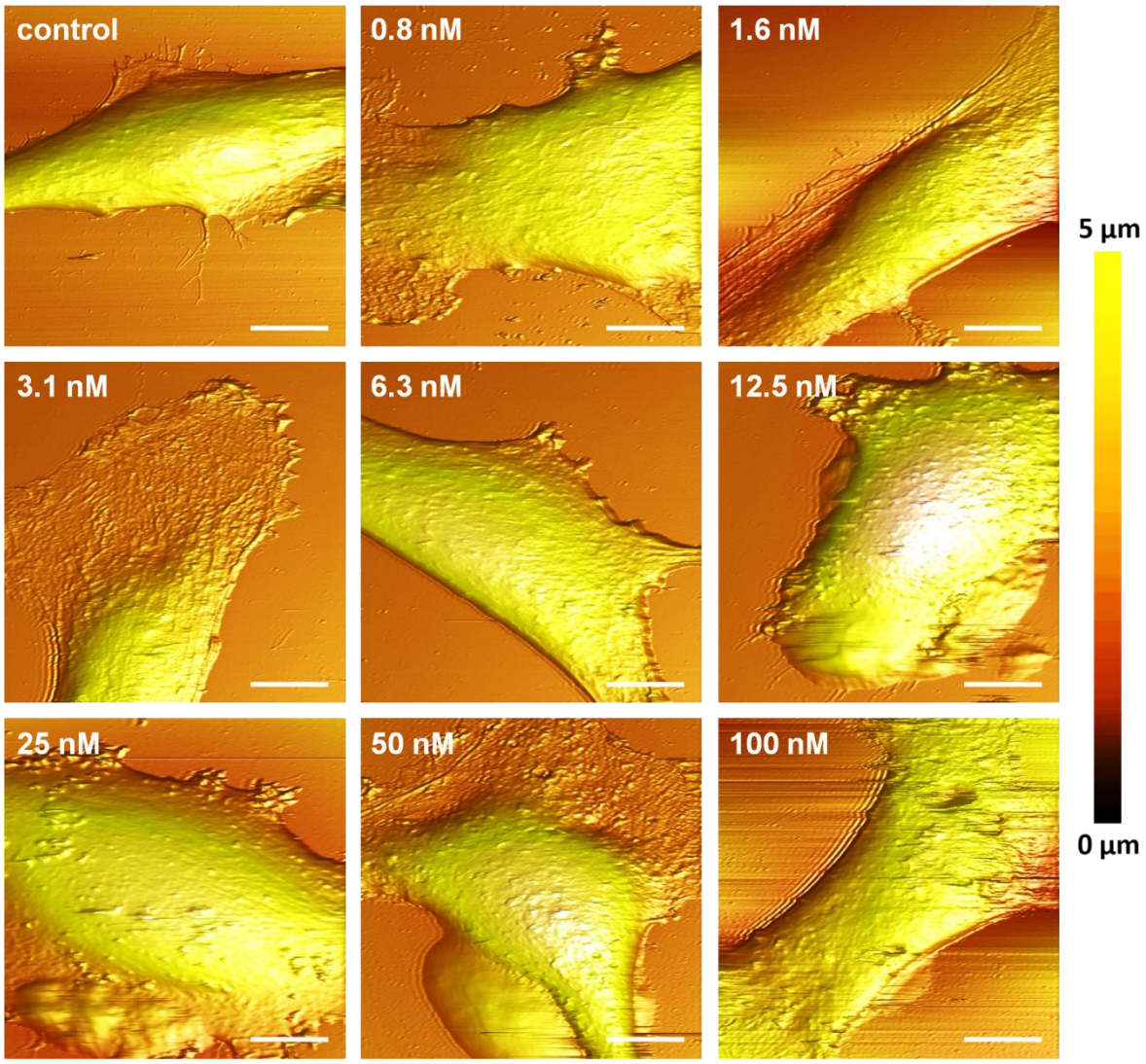

Figure SI-X.7: AFM images (contact mode) of HUVECs which have been exposed to Au-PMA NPs at different concentrations c_{NP}. All samples were imaged on a glass-slide substrate. The scale bars correspond to 10 µm.*

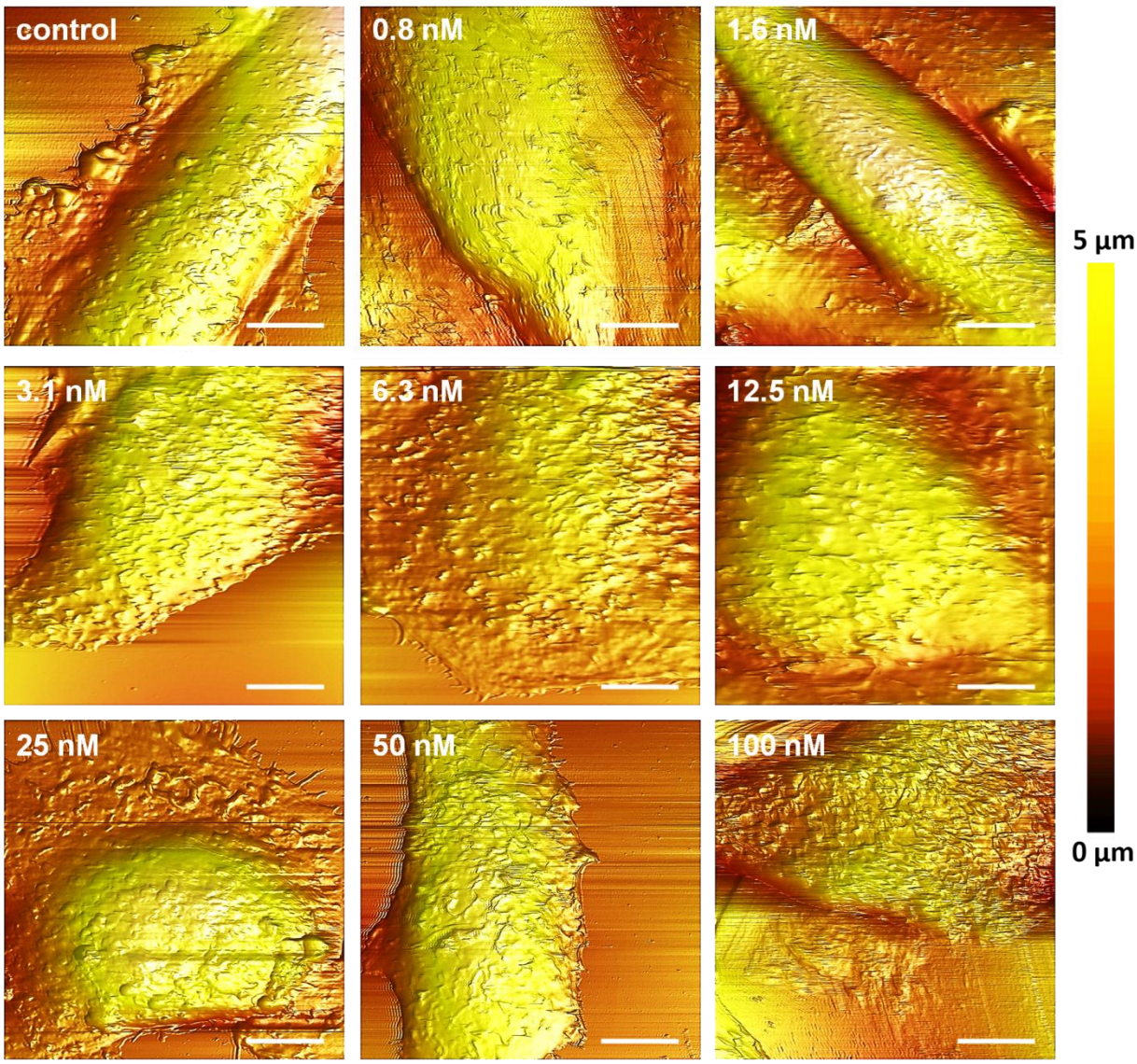

Figure SI-X.8: AFM images (contact mode) of HeLa cells which have been exposed to Au-PMA NPs at different concentrations. All samples were examined on a glass-slide substrate. The scale bars correspond to 10 µm.*

From these images quantitative data concerning filopodia were derived. Computer vision for the counting of surface objects (nAnosticTM method) was done using proprietary algorithms (Serend-ip GmbH, Münster, Germany), which are optimized for AFM-images. Basically, the experimenters label manually the objects of interest and feed an artificial neuronal network with these examples (machine learning). The computer then searches similar structures, *cf.* Figure SI-XI.7**Fehler! Verweisquelle konnte nicht gefunden werden.** and Figure SI-X.10. Of each sample 10 images at arbitrarily chosen positions were recorded. The following parameters were extracted: the number of counted filopodia N_{fiolo} found on a cell within an imaging area of 20x20 µm^2, the total area A_{filo} occupied by filopodia within an imaging area of 20x20 µm^2, the average filopodia height h_{filo}, and the sum of the local deviational volumes V_{filo} occupied by filopodia within an imaging area of 20x20 µm^2. The local deviational volume of each filopodium was calculated by summation of the height values corrected by a local plane fit for each filopodium[28]. Both cell types HUVECs and HeLa cells show a decreasing number, area

and local deviational volume of filopodia per image within an increasing concentration of Au NPs. In contrast the height increases at higher concentrations of Au-PMA* NPs. Comparing HUVECs and HeLa cells demonstrates that the morphology of HUVECs is altered at lower concentrations of Au NPs. The resulting data are presented in Figure SI-X.11.

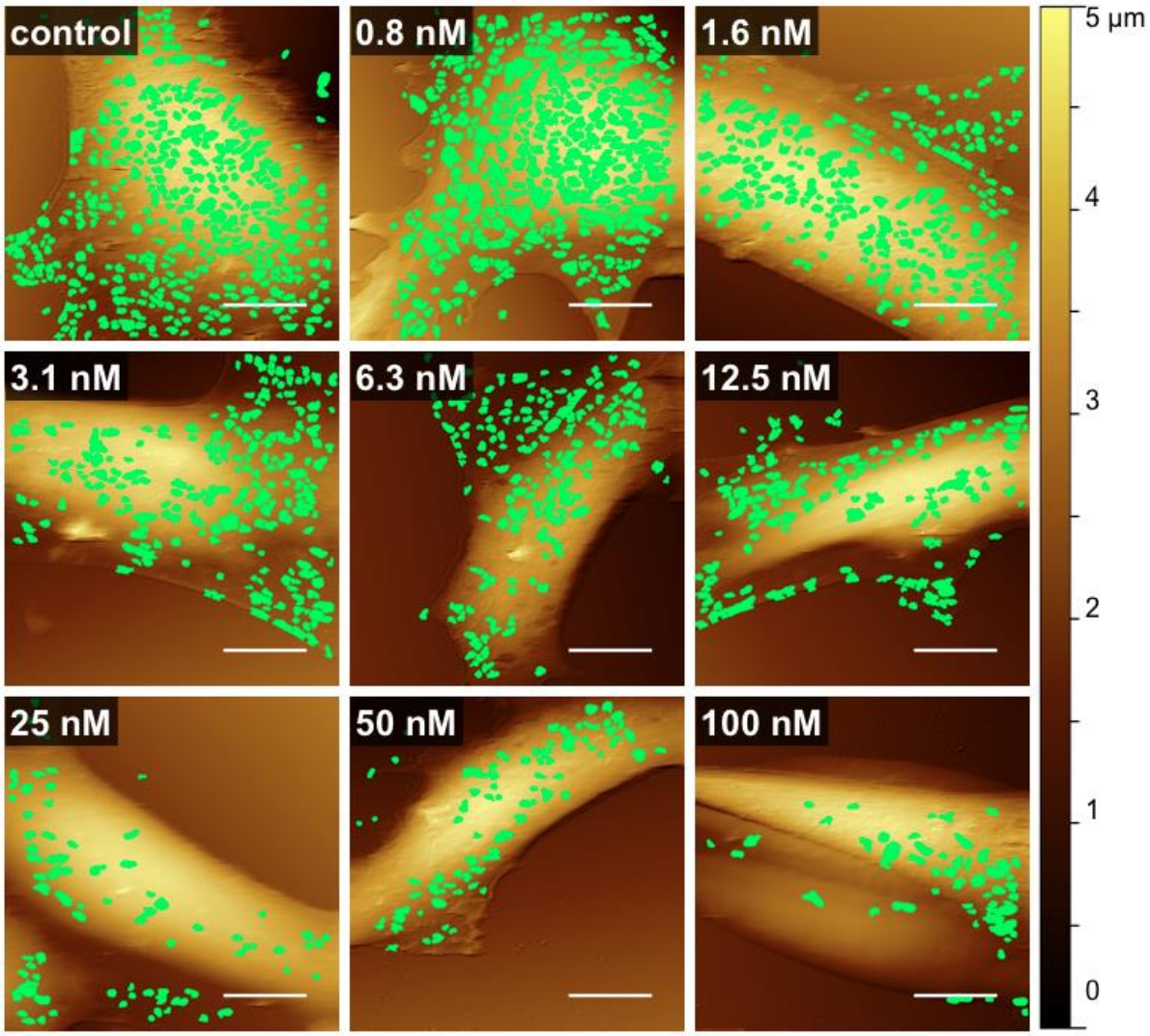

Figure SI-X.9: Results of computer vision are displayed as green overlays demonstrating the decreasing number of filopodia in HUVECs exposed to increasing concentrations of Au-PMA NPs. The scale bars correspond to 10 µm.*

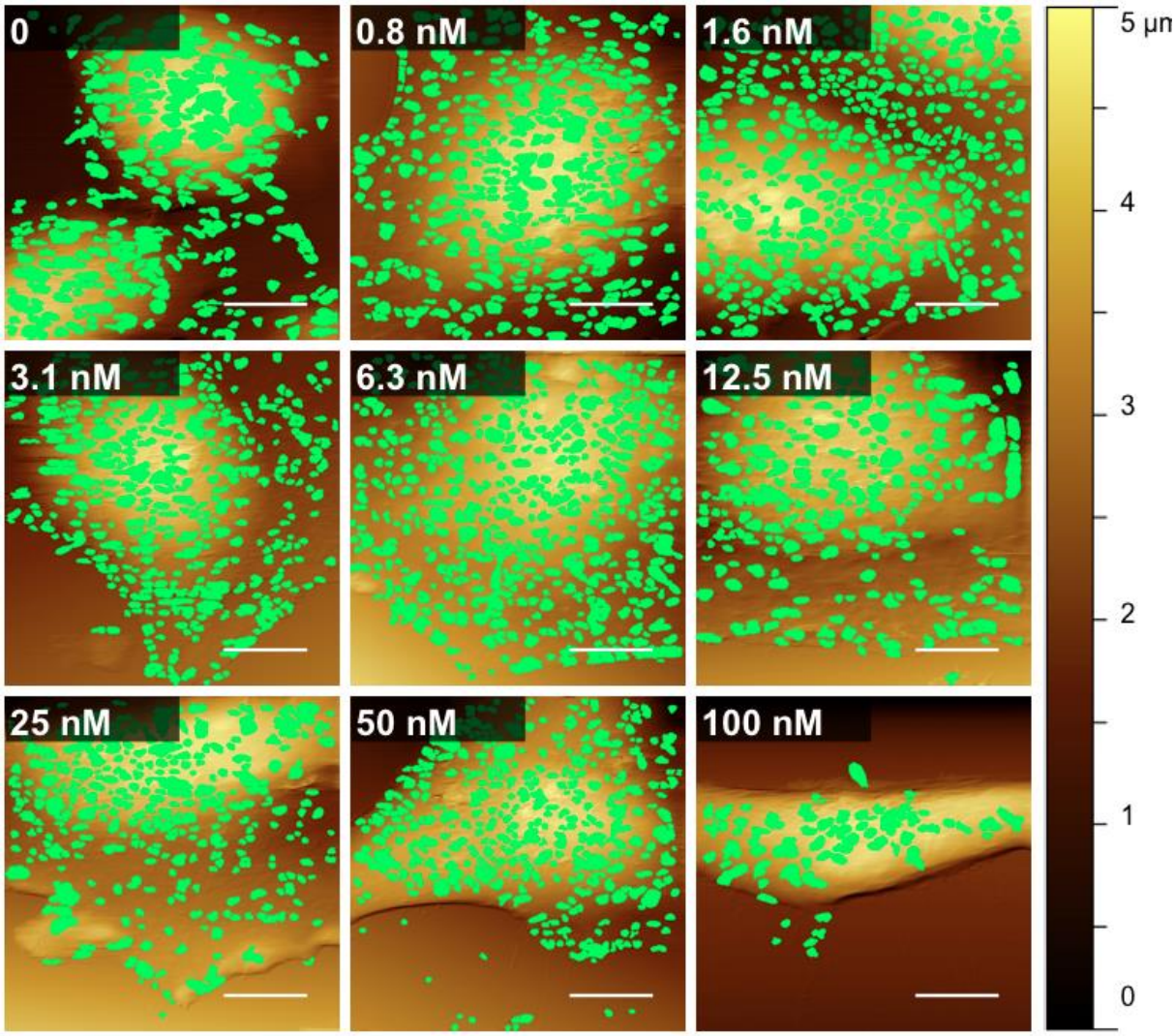

Figure SI-X.10: Results of computer vision are displayed as green overlays demonstrating the decreasing number of filopodia in HeLa cells exposed to increasing concentrations of Au-PMA NPs. The scale bars correspond to 10 µm.*

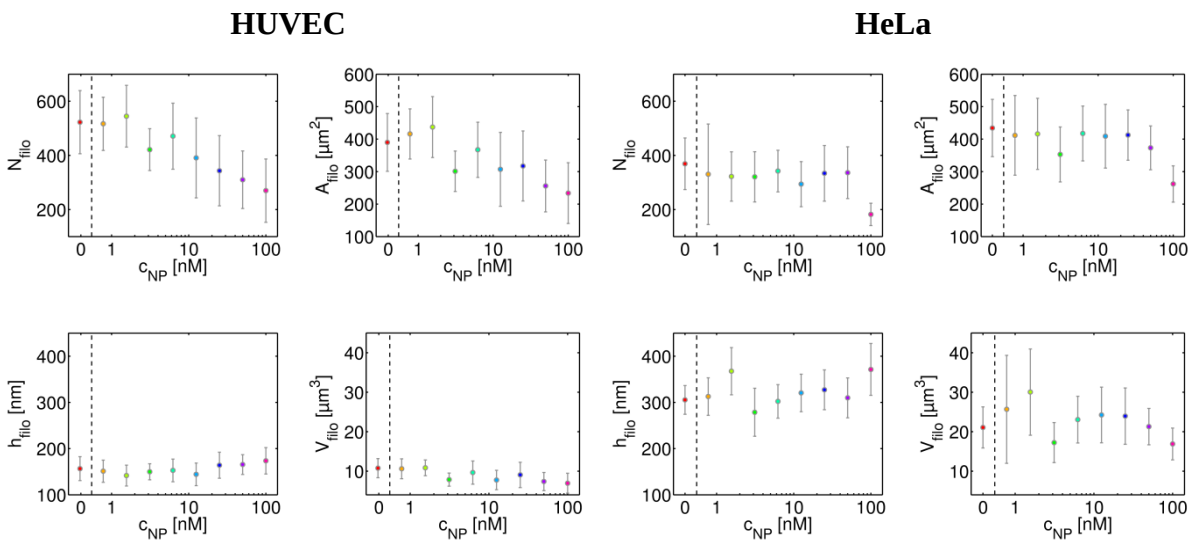

Figure SI-X.11: Mean number of counted filopodia N_{fiolo}, the total area A_{filo} occupied by filopodia, the average filopodia height h_{filo}, and the total volume V_{filo} occupied by filopodia within an imaging area of 20x20 μm^2, as determined by data analysis of AFM images, in dependence of the Au-PMA NP concentration. The results are presented as mean ± SD for 3 individual experiments.*

XI) Analysis of nanoparticle uptake and morphology of the lysosomes

XI.1) Quantification of NP uptake

XI.2) Assessment of NP-induced changes in lysosome morphology

XI.1) Quantification of NP uptake

First, we first investigated the endocytosis of Au-PMA* NPs. In agreement with previous reports we assume that macropinocytosis plays a role in the uptake pathway, as in Figure SI-IV.1 one can see a macropinocytic cup which wraps around an assembly of Au-PMA* NPs. However, studies on uptake of bigger Au NPs with similar surface chemistry showed a dominant *via* caveolin-mediated endocytosis[29].

In order to trace the intracellular location of the NPs, green fluorescent protein (GFP)-labeled lysosomal associated protein 1 (LAMP1) was expressed in HUVECs and HeLa cells to allow for simultaneous live-imaging of lysosomes and fluorescence-labeled NPs[24].

HeLa cells (2500 cells/per well, in 200 µL) or HUVECs (5,000 cells/per well, in 200 µL) were added to µ-Slide 8 well-ibiTreat chambers (1 cm^2 per well, Ibidi, Germany) and incubated over night at 37 °C. Next, the cells were transfected with CellLight lysosome-GFP (Molecular Probes, #C10596), 1 µL and 2 µL per well for HeLa cells and HUVECs, respectively. After 24 h the µ-slide was mounted into a portable microscope incubator system (PeCon, Germany) on the CLSM to allow for live cell imaging at 37 °C and 5 % CO_2. After equilibration Au-PMA* NPs were added (c_{NP} = 25 - 100 nM) and imaging was started using an Apochromat 63x/1.40 Oil DIC M27 objective. For each concentration 10 positions (2800 µm², approx. 30-50 cells) were imaged at a lateral sampling frequency of 140 µm (pinhole size: 1 AU) and a temporal resolution of 45 min. The focus position was adjusted to be 0.5 µm above the substrate. GFP was excited at λ_{ex} = 488 nm and the emission was detected between λ_{em} = 505 and 530 nm (band-pass, green channel). Fluorescence-labeled NPs were excited at λ_{ex} = 543 nm and emitted photons were gated using a long-pass filter at λ_{em} = 560 nm filter (red channel). From the obtained time image series the NP intensity inside lysosomes (density of NPs) was calculated: For each time point and for each position the fluorescence signal originating from the lysosomes (green channel) was used to mask the signal derived from the NPs (red channel) spatially. Thereto the green channel containing the signal of the lysosomes was carefully thresholded followed by median-filtering to remove background noise. Then, the signal was binarized by adjusting all pixel intensities above zero to 1. Subsequently, the obtained mask was deconvolved with the related image containing the NP intensities (red channel). In other words, only the NP signal at positions colocalizing with lysosomes was considered. Due to the high axial resolution of a CLSM almost all NP-signal which is not originating from NPs being present in structures associated with LAMP1 is suppressed. Finally for each time point the mean of the masked NP intensity I_{NP}(lyso) was calculated and plotted *versus* time (Figure SI-XI.2).

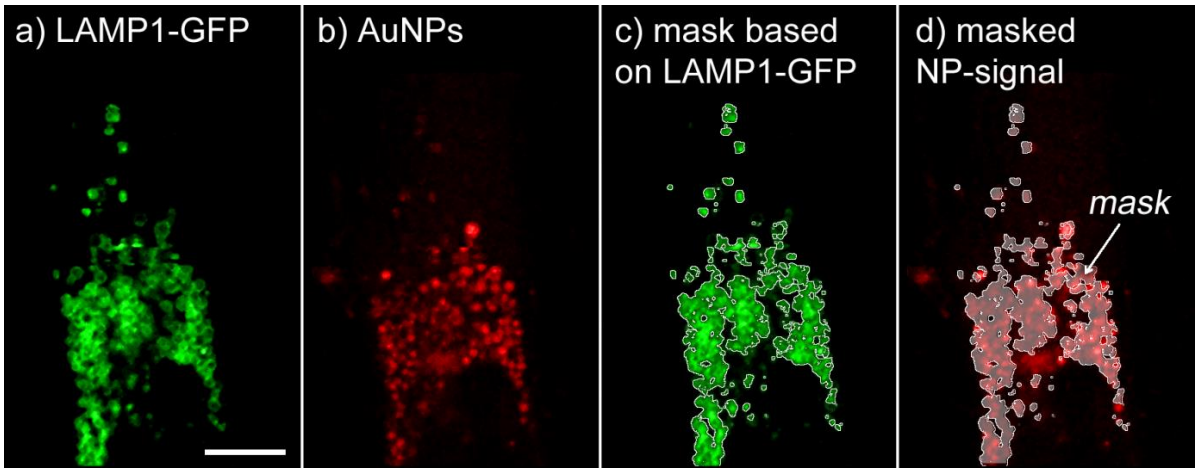

Figure SI-XI.1: Confocal micrographs of a time lapse series showing parts of a HUVEC which has been exposed to Au-PMA NPs for 16 h at c_{NP} = 50 nM. (a) The signal of stained lysosomes is used to create a mask. (b) Shows the channel of fluorescence labeled NPs. (c) Mask based on LAMP1-GFP signal. (d) Mean intensity I_{NP}(lyso) of NPs inside the lysosomal mask. The scale bar corresponds to 10 µm.*

Although the absolute intensity values cannot be compared for HUVECs and HeLa cells (the total uptake by HUVECs is much higher as compared to HeLa cells, *cf.* Figure SI-XI.3), the results highlight the different uptake/transport kinetics of the NPs in HUVECs and HeLa cells. Regarding HUVECs, the largest fraction of NPs is transported into lysosomes within the first 4 hours of incubation, while in HeLa cells the lysosomal enrichment takes place more linearly.

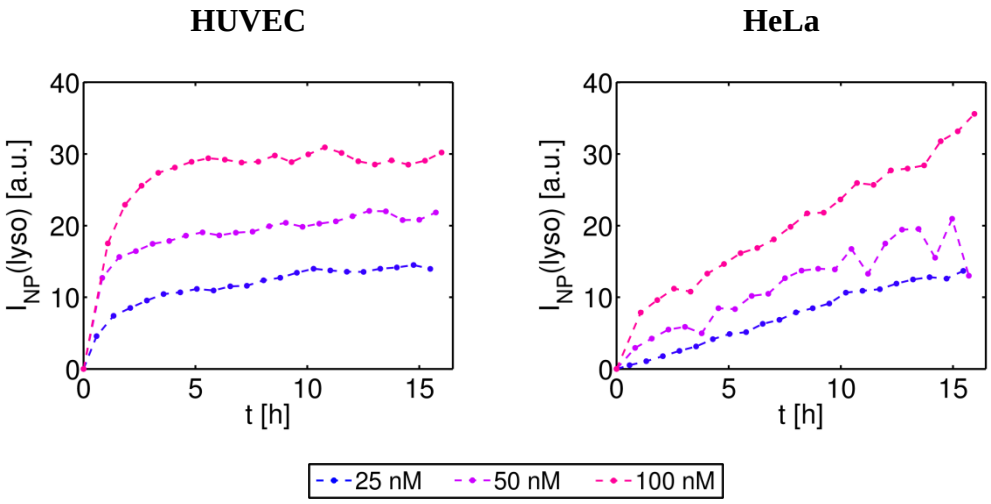

Figure SI-XI.2: Mean NP-intensity I_{NP}(lyso) measured inside lysosomal structures at different Au-PMA NP concentrations c_{NP} = 25, 50 and 100 nM. I_{NP}(lyso) is proportional to the average lysosomal Au NPs density. The intensities are not comparable between HUVECs and HeLa cells as the uptake rate of HeLa cells was much lower.*

HeLa cells (3,000 cells/per well, in 200 µL) or HUVECs (6,000 cells/per well, in 200 µL) were added to 8 well µ-Slide chambers (1 cm^2 per well, Ibidi, Germany, #80826) and incubated over

night at 37 °C. Next, the cells were incubated with Au-PMA* NPs at c_{NP} = 0-100 nM for 24 h at 37 °C and 5 % CO_2. The cells were then fixed for 20 min in 4 % paraformaldehyde, after which the cells were washed 3 times with Hank's balanced salt solution (HBSS). Cells were stained with Wheat Germ Agglutinin (WGA)-AlexaFluor 488 conjugate (Molecular Probes, USA, #W11261**)** solution (15 µg/mL in HBSS) for 15 minutes. Then the cells were washed 2 times in HBSS, followed by 2 times in PBS. Next, the cells were permeabilized (5 mg/mL glycine, Roth, Germany, #3908.1), 0.5 mg/mL saponin (Sigma-Aldrich, #S7900) in PBS for 5 min and incubated in blocking solution (PBS with 2 % BSA (bovine serum albumin, Jackson ImmunoResearch Laboratories, #001-000-161)). Afterwards, the cells were stained with murine anti-LAMP-1 antibodies (Developmental Studies Hybridoma Bank, USA, #H4A3) at 2 µg/mL at 4 °C overnight. Then, the cells were washed three times with PBS and stained with 1.25 µg/mL secondary antibody DyLight 649 donkey anti-mouse IgG (H+L) antibody (Jackson ImmunoResearch Laboratories, #715-495-150) at 37 °C for 30 minutes. After that, the cells were stained with 50 µM DAPI and incubated for 5 min at room temperature. Cells were then washed three times with PBS and stored in 200 µL PBS/well at 4 °C, followed by analysis using a CLSM.

Images were recorded using a Plan-Apochromat 20x/0.8 M27 objective and a pinhole-size of around four airy units (AU). The focus position was determined automatically 3 µm above the substrate for each position. The emission of DAPI (λ_{ex} = 405 nm) was detected using a 420-490 nm band-pass, AlexaFluor 488 was excited at λ_{ex} = 488 nm. Emission was detected at λ_{em} = 525 (with a 40 nm bandwidth band-pass filter). DyLight 649 was excited at λ_{ex} = 633 nm and emission was filtered using a λ_{em} =650 nm long-pass. Around 500 – 1,000 cells were imaged per condition.

The data shown in Figure SI-XI.1 suggest that the internalized Au-PMA* NPs accumulate inside lysosomes. The number of internalized NPs per cell (as measured in average integrated fluorescence intensity I_{NP} of the NP-signal in one cell, *cf.* § VIII.4) is display in Figure SI-XI.3.

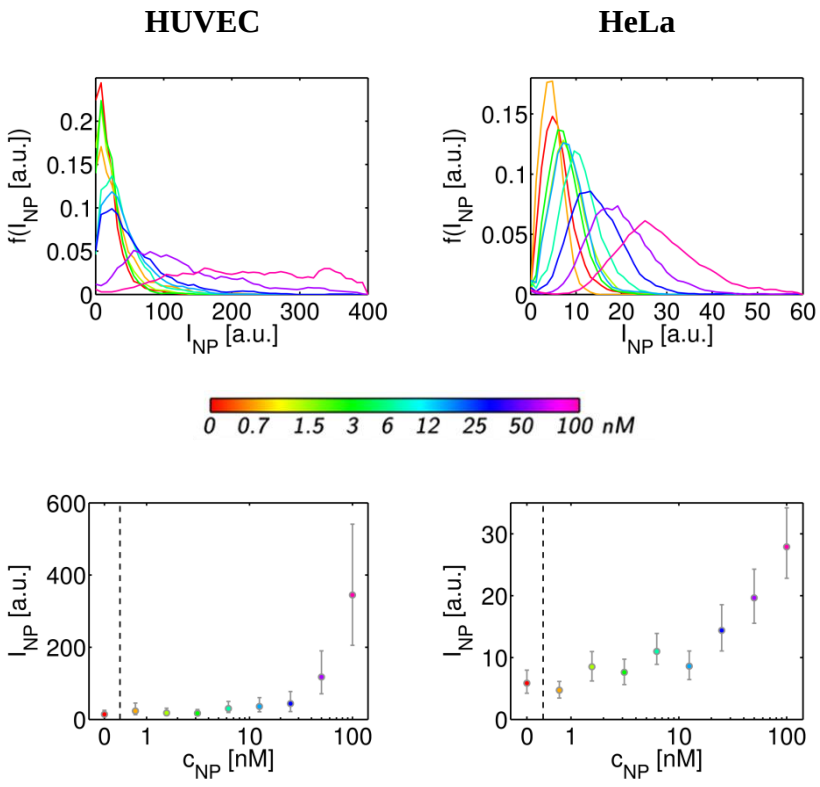

Figure SI-XI.3: Integrated fluorescence intensity of internalized Au-PMA NPs per cell (I_{NP}). The results are presented as normalized probability distributions (first row) and median ± lower/upper quartile for 500 – 1,000 cells/condition.*

XI.2) Assessment of NP-induced changes in lysosome morphology

Eventually, we investigated the effects of Au-PMA* NPs on the morphology of the lysosomes (§ VIII.3, *lysosomal fraction*). The fraction of the area within the cells, which is occupied by lysosomes A_{lyso}/A_{cell} (an example is given in Figure SI-VIII.3) as well as the amount of lysosomes in terms of lysosome fluorescence I_{lyso} per cell was determined, *cf.* Figure SI-XI.4.

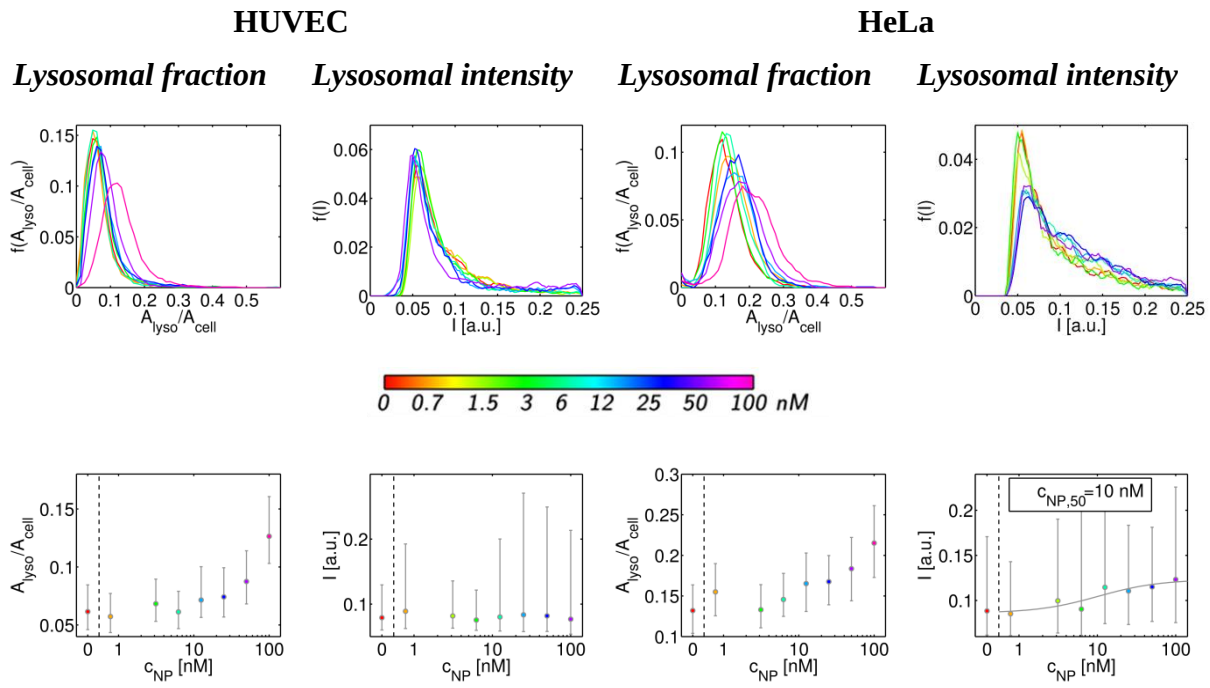

Figure SI-XI.4: Fraction of cross section area occupied by lysosomes A_{lyso}/A_{cell}, as derived by dividing the lysosome area (yellow stain in Figure SI-VIII.3) by the total area of each cell (red stain in Figure SI-VIII.3), upon exposure of cells to different concentrations of Au-PMA NPs. In addition, the amount of lysosomes per cell as determined by their fluorescence intensity I_{lyso} is depicted. The results are presented as normalized probability distributions (first row) and median ± lower/upper quartile for 400 – 1,000 cells/condition.*

In an additional set of data we investigated lysosome swelling, *i.e.* the change in size distribution of the lysosomes upon exposure to Au NPs. Imaging was performed at higher magnification, using a Plan-Apochromat 63x/1.40 Oil DIC M27 objective and a lateral sampling frequency of 90 nm. In Figure SI-XI.5 and Figure SI-XI.6 images were obtained at different exposure concentrations c_{NP} are displayed for HUVECs as well as for HeLa cells.

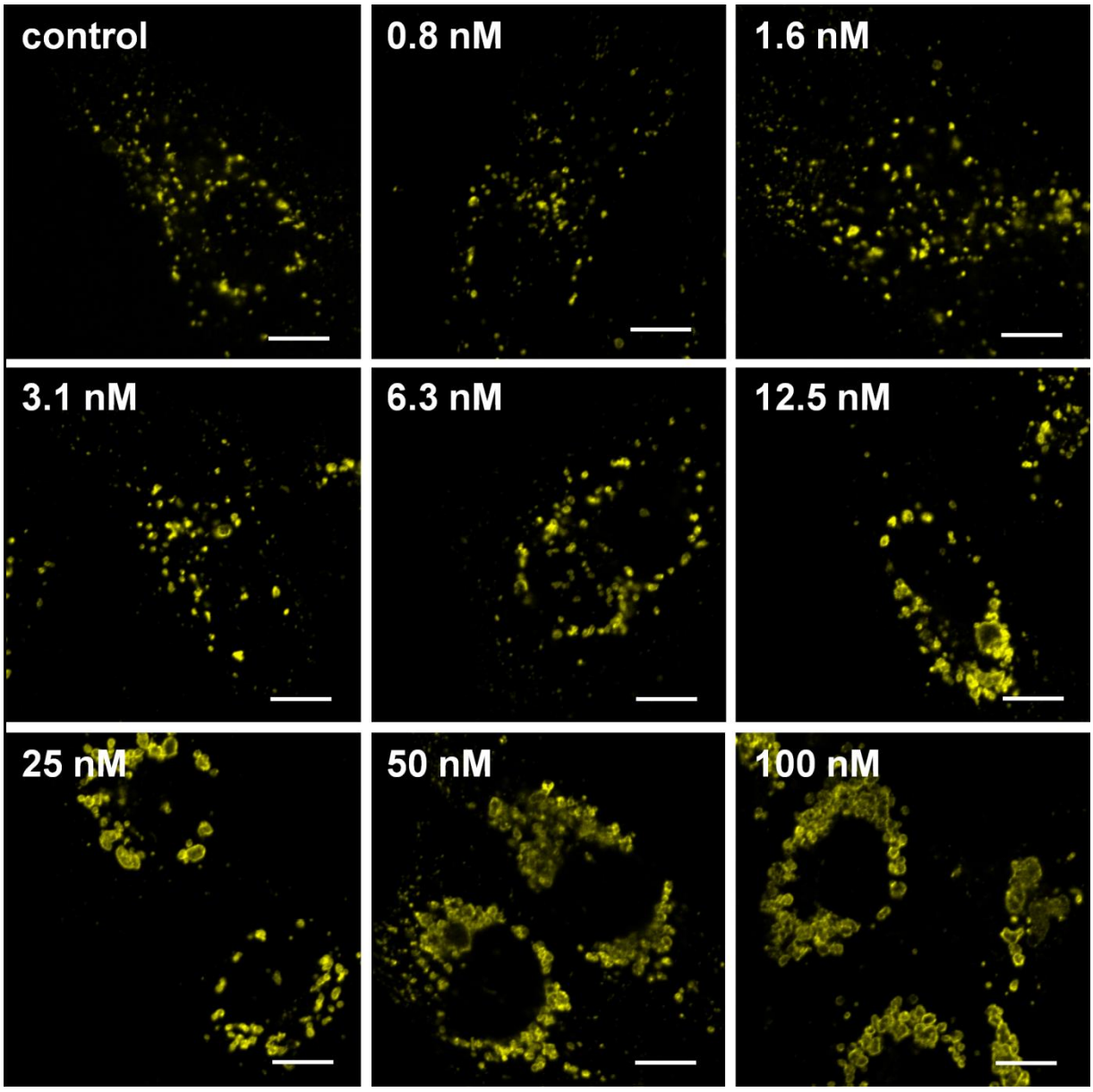

Figure SI-XI.5: Change in lysosome morphology of HUVECs exposed to c_{NP} = 1-100 nM of Au-PMA NPs (scale bar: 10 μm).*

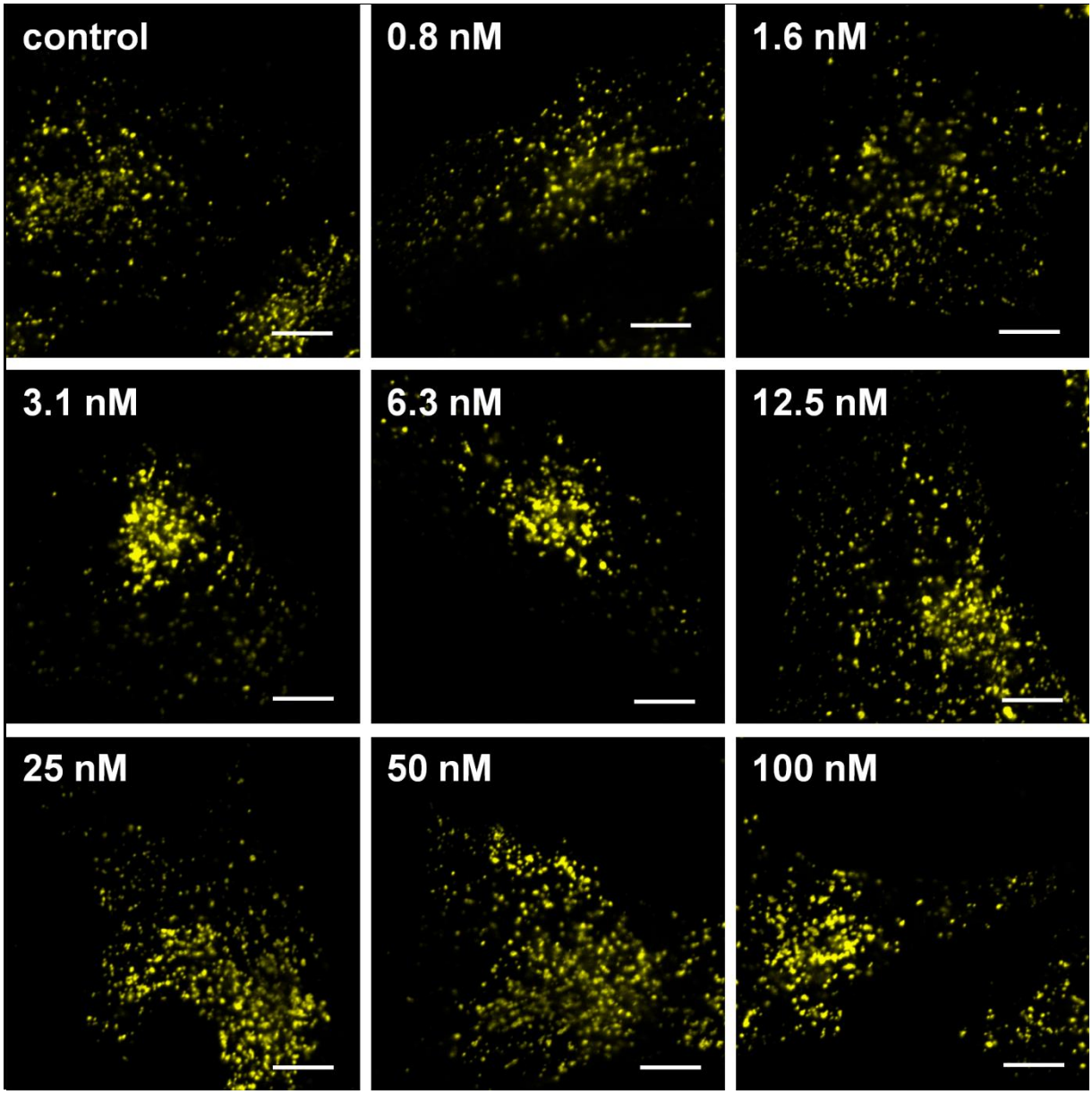

Figure SI-XI.6: Change in lysosome morphology of HeLa cells exposed to c_{NP} = 1 - 100 nM of Au-PMA NPs (scale bar: 10 µm).*

The average area of an individual lysosome A_{lyso} is shown for the different Au-PMA* NP concentrations in Figure SI-XI.7. It can be seen that lysosome swelling, *i.e.* increase of lysosome size upon increasing NP concentrations, is very intense in HUVECs, but the change of lysosome morphology is not so obvious in HeLa cells. Therefore, the increase of the fraction occupied by lysosomes A_{lyso}/A_{cell} as displayed in Figure SI-XI.4 has more relevance for indicating morphology changes of the lysosome. Anchoring organelles is an important function of cytoskeleton. Therefore, the change in lysosome occupation fraction should be also a reflection of cytoskeletal disruption, *cf.* § XIII.

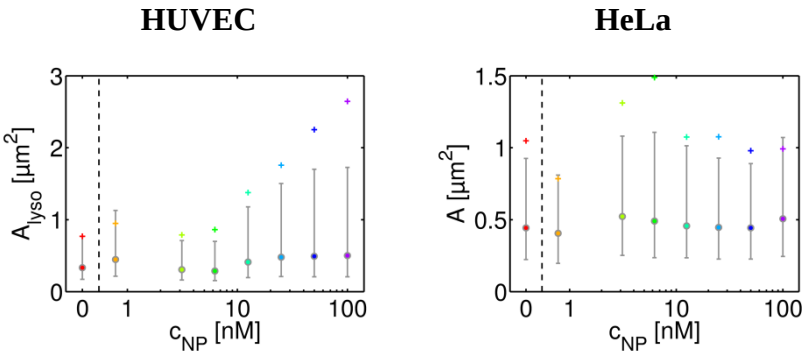

Figure SI-XI.7: Size of individual lysosomes after cells had been exposed to Au-PMA NPs at different concentration. The results are presented as median (o) ± lower/upper quartile for 1,800-4,000 lysosomes/condition. The mean values are represented as crosses (+).*

Similar experiments were also carried out for the Au NPs with different surface chemistry, *cf.* Figure SI-XI.8.

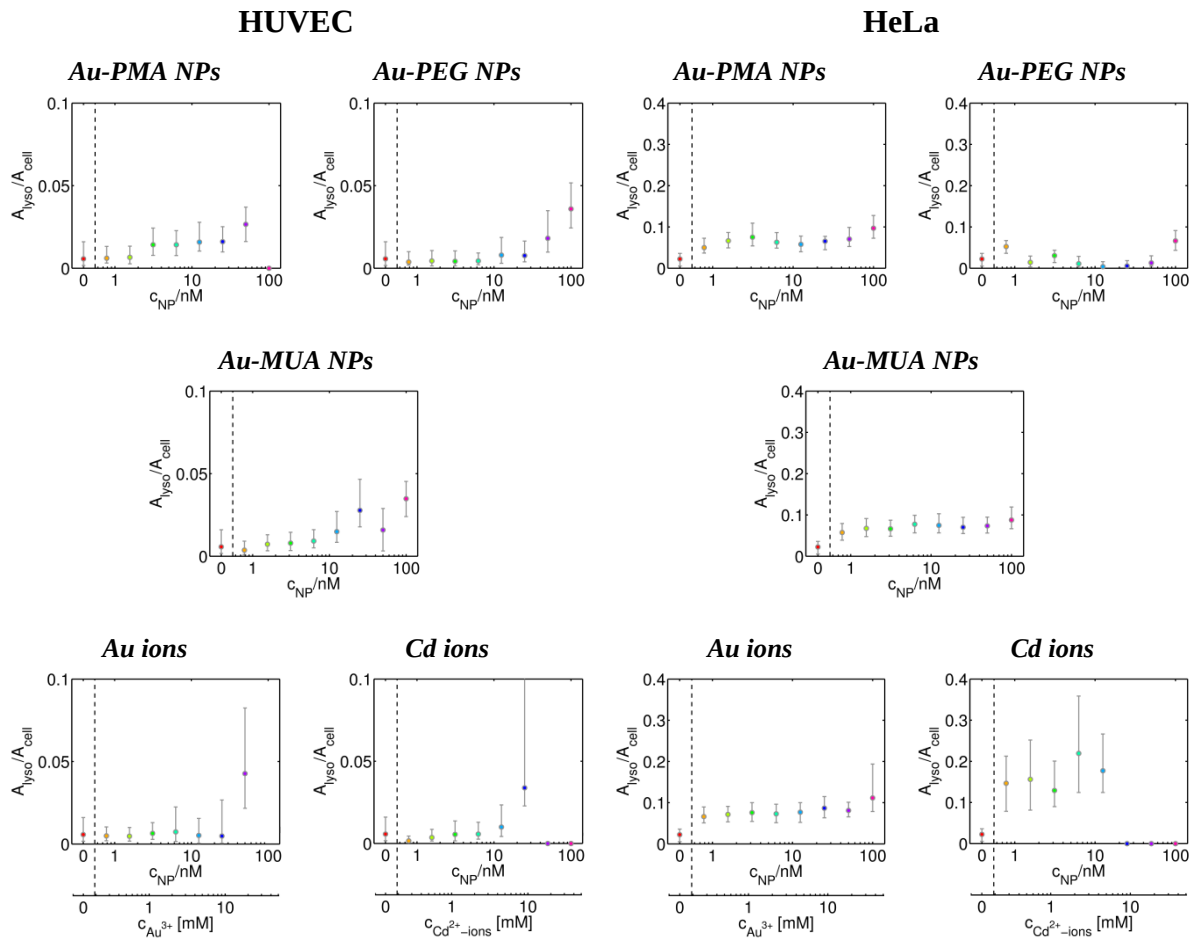

Figure SI-XI.8: Fraction of cross section area occupied by lysosomes A_{lyso}/A_{cell}, as derived by dividing the lysosome area by the total area of each cell, upon exposure of cells to Au NPs. Date were obtained with the batches Au-MUA$_1$ and Au-PEG$_1$. The results are presented as median ± lower/upper quartile.

XII) Analysis of the morphology of the mitochondria

We also investigated the effects of Au NPs on mitochondrial morphology. Mitochondrial morphology is a very sensitive parameter for cellular stress. In order to image individual mitochondria, green fluorescent protein GFP-labeled E1 alpha pyruvate dehydrogenase was expressed in HUVECs and HeLa cells, to allow for simultaneous live-imaging of mitochondria and fluorescence-labeled NPs.

HeLa cells (2,500 cells/per well, in 200 µL) or HUVECs (5,000 cells/per well, in 200 µL) were added to 8 well µ-slides (1 cm^2 per well, Ibidi, Germany, #80826) and incubated over night at 37 °C. Next, the cells were transfected with CellLight Mitochondria-GFP (Molecular Probes, #C10600), 1.5 µL and 3 µL reagent per well for HeLa cells and HUVECs, respectively. After 24 hours, the cells were exposed to Au NPs at c_{NP} = 0 - 100 nM for 24 h at 37 °C and 5 % CO_2. Then, pre-warmed paraformaldehyde was added to the cells (4 %) for 20 min while the cells remained at 37 °C and 5 % CO_2, after which they were washed three times with PBS. Cells were stored in 200 µL PBS/well at 4 °C, followed by analysis using a CLSM. The fluorescence of GFP was excited at λ_{ex} = 488 nm. Emission was detected at λ_{em} = 52 (40 nm bandwidth band-pass). Imaging was performed using a Plan-Apochromat 63x/1.40 Oil DIC M27 objective and a lateral sampling frequency of 30 nm.

In the HUVECs the mitochondria are long thread-like structures in the control group (*i.e.* without NP exposure) and at low concentrations of Au-PMA* NPs, *cf.* Figure SI-XII.1 and Figure SI-XII.2. With an increase of the Au-PMA* NP concentration the morphology of the mitochondria changed from polliwog-like structures to large dots and finally to small spots. This can be seen in the form factor F_{mito}, which would be equal to 1 in case the mitochondria had perfect spherical shape. Looking at the HeLa cells, the mitochondria without or with exposure to low NP concentrations are longer, however, not as long as the ones which can be observed in HUVECs. Thread and polliwog structures co-exist in the control group and cells exposed to low concentrations of Au-PMA* NPs, *cf.* Figure SI-XII.1 and Figure SI-XII.2. The mitochondria become smaller and smaller with the increase of the Au-PMA* NPs concentration. HeLa cells are even more sensitive at low Au-PMA* NP concentrations. The mitochondria begin to become round-shaped already at c_{NP} = 6.2 nM in HUVECs, but in HeLa cells, the change starts already at concentrations as low as c_{NP} = 3.1 nM, *cf.* Figure SI-XII.1 and Figure SI-XII.8.

The results for Au NPs with other surface chemistries are presented in Figure SI-XII.3 - Figure SI-XII.7 for HUVECs and Figure SI-XII.9 - Figure SI-XII.13 for HeLa cells. A summary is given in Figure SI-XII.14.

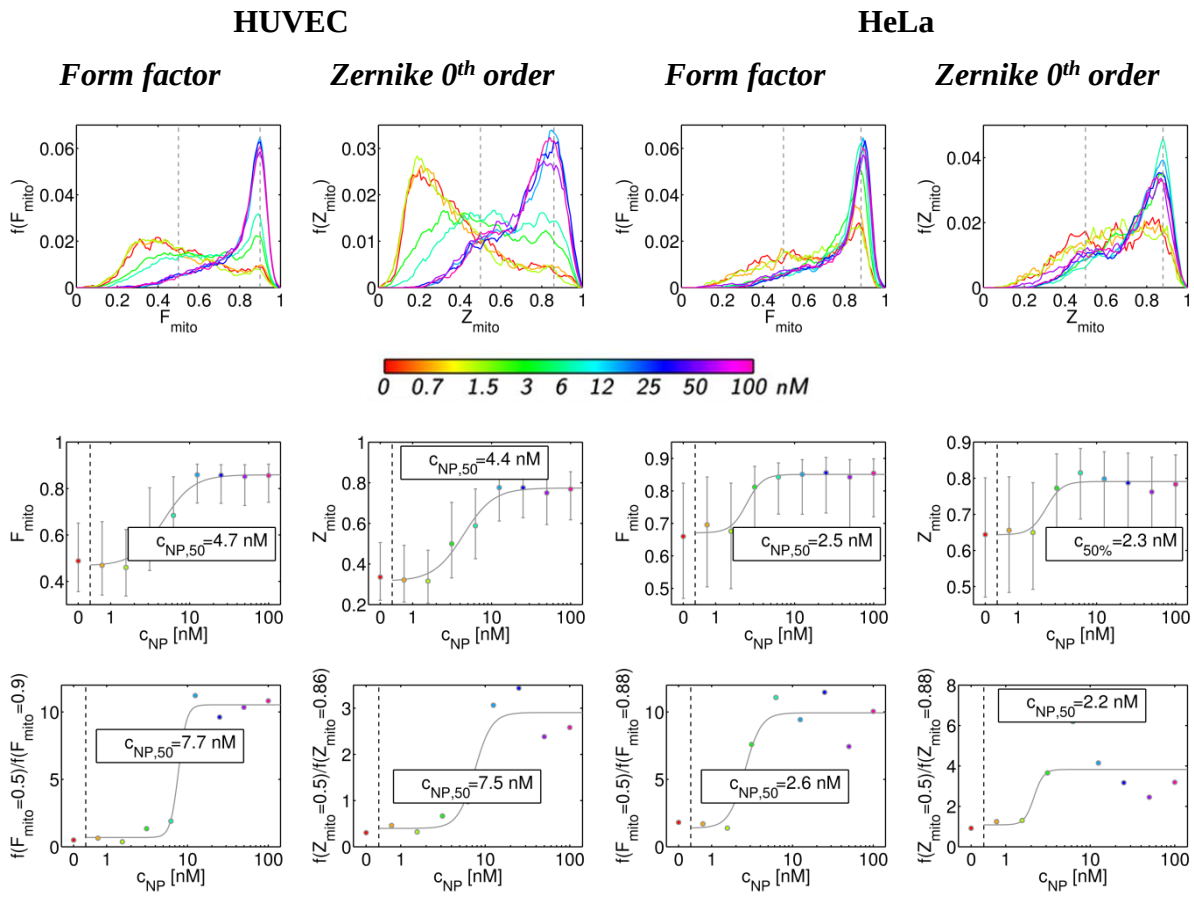

Figure SI-XII.1: Geometrical features of mitochondria upon exposure to Au-PMA NPs. The results are presented as normalized probability distributions (first row) and median ± lower/upper quartile for 1,700-5,000 mitochondria/condition (second row). In the last row the ratios of the corresponding values at the dotted lines were derived from the probability distributions.*

HUVECs, *Au-PMA* NPs*

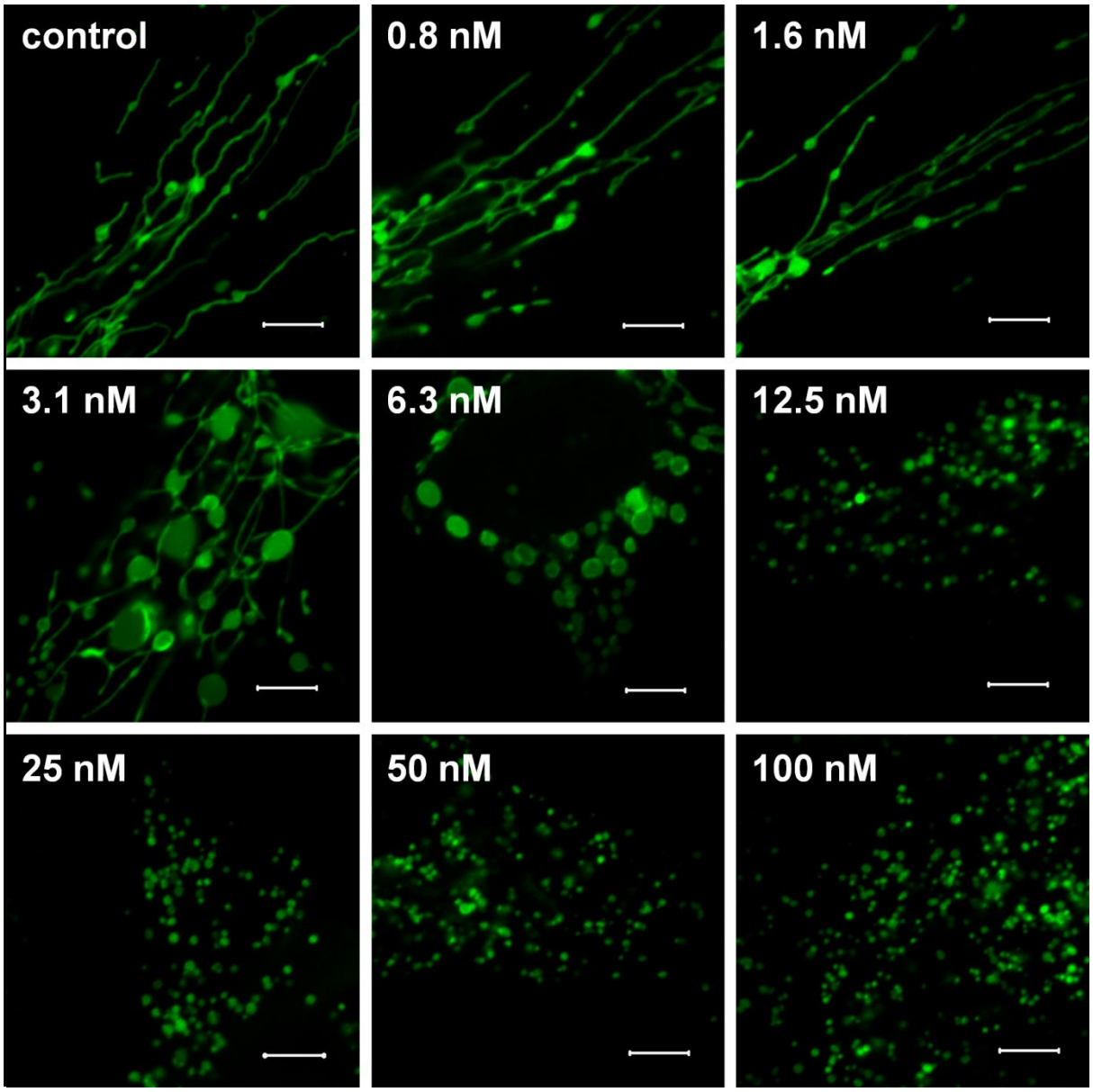

Figure SI-XII.2: Changes in mitochondrial morphology of HUVECs after exposure to Au-PMA NPs at different concentrations c_{NP} for 24 h (scale bar: 5 µm). The corresponding analysis is shown in Figure SI-XII.1.*

HUVECs, *Au-PMA NPs*

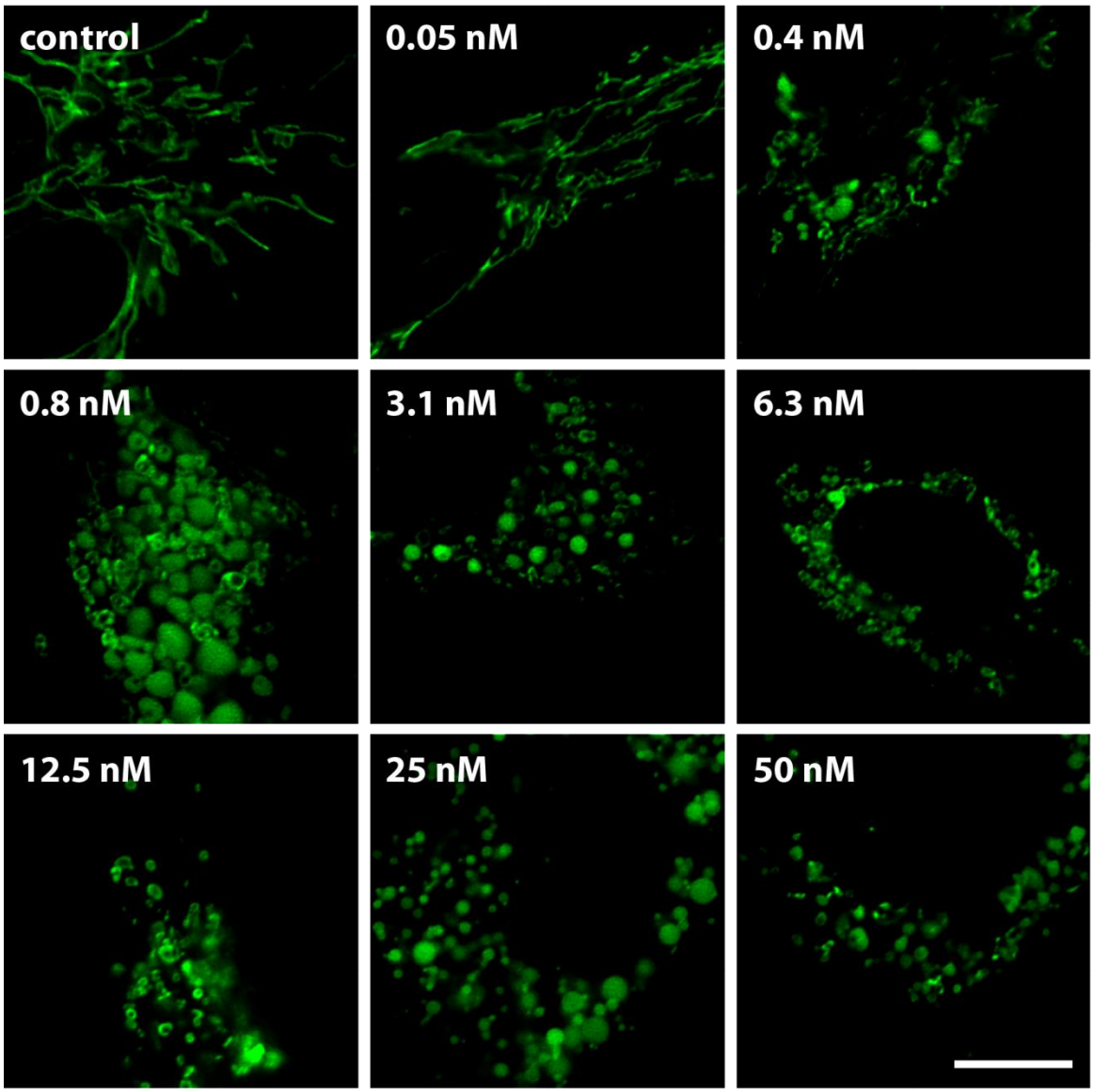

Figure SI-XII.3: Changes in mitochondrial morphology of HUVECs after exposure to Au-PMA NPs at different concentrations c_{NP} for 24 h (scale bar: 5 µm). The corresponding analysis is shown in Figure SI-XII.14.

HUVECs, *Au-PEG NPs*

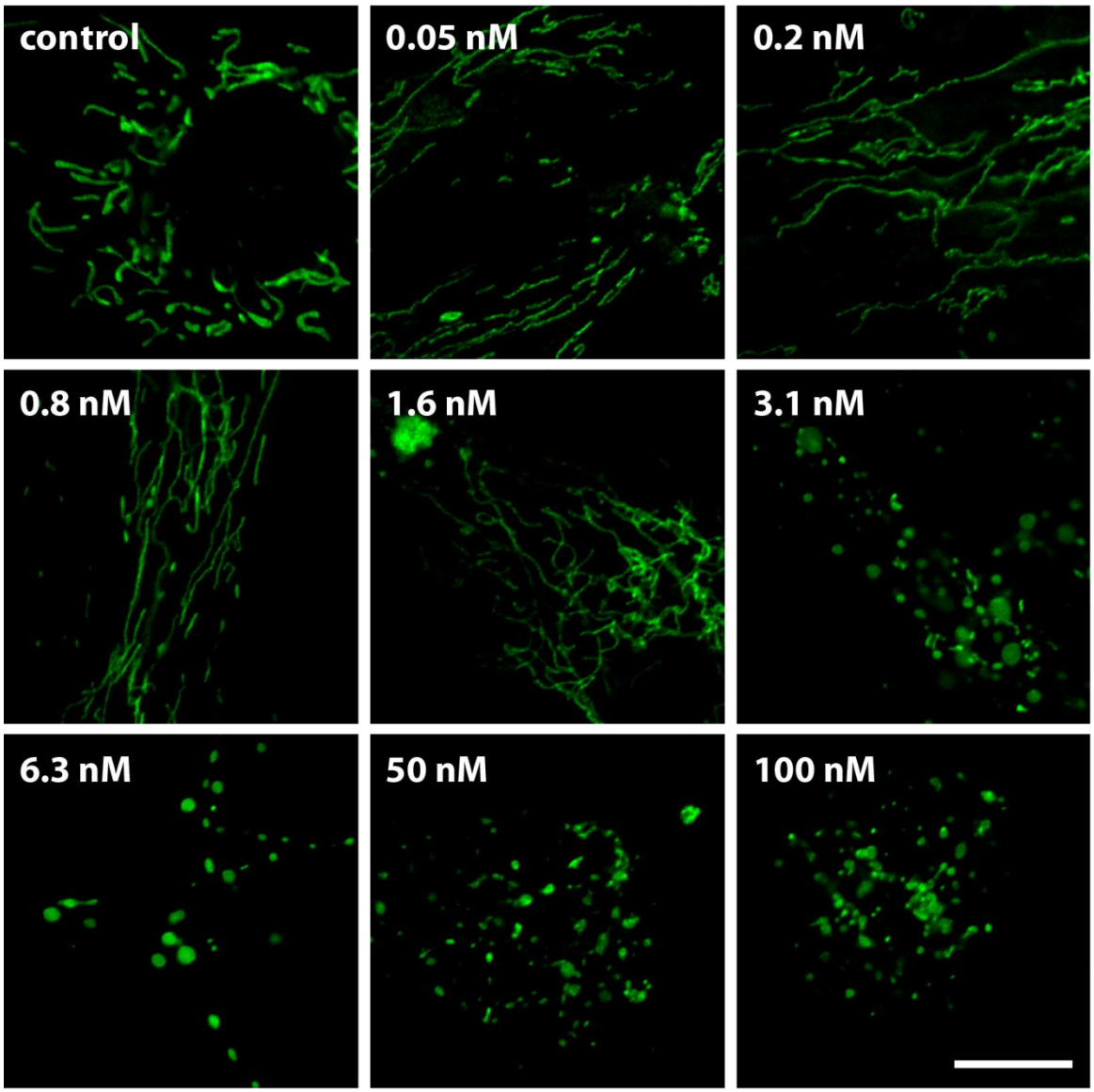

Figure SI-XII.4: Changes in mitochondrial morphology of HUVECs after exposure to Au-PEG NPs (batch Au-PEG$_2$) at different concentrations c_{NP} for 24 h (scale bar: 5 µm). The corresponding analysis is shown in Figure SI-XII.14.

HUVECs, *Au-MUA NPs*

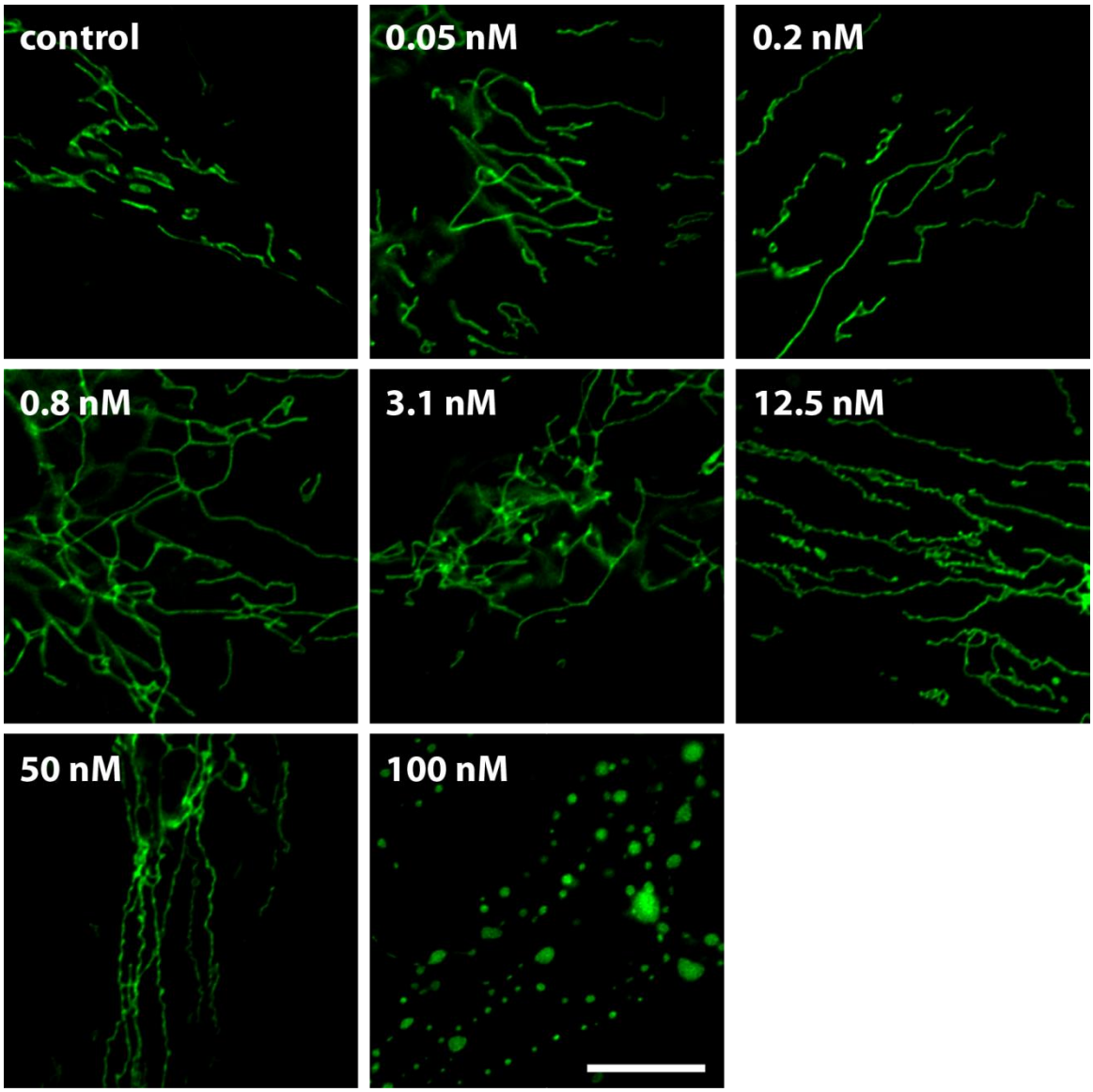

Figure SI-XII.5: Changes in mitochondrial morphology of HUVECs after exposure to Au-MUA NPs (batch Au-MUA$_2$) at different concentrations c_{NP} for 24 h (scale bar: 5 µm). The corresponding analysis is shown in Figure SI-XII.14.

HUVECs, *Au ions*

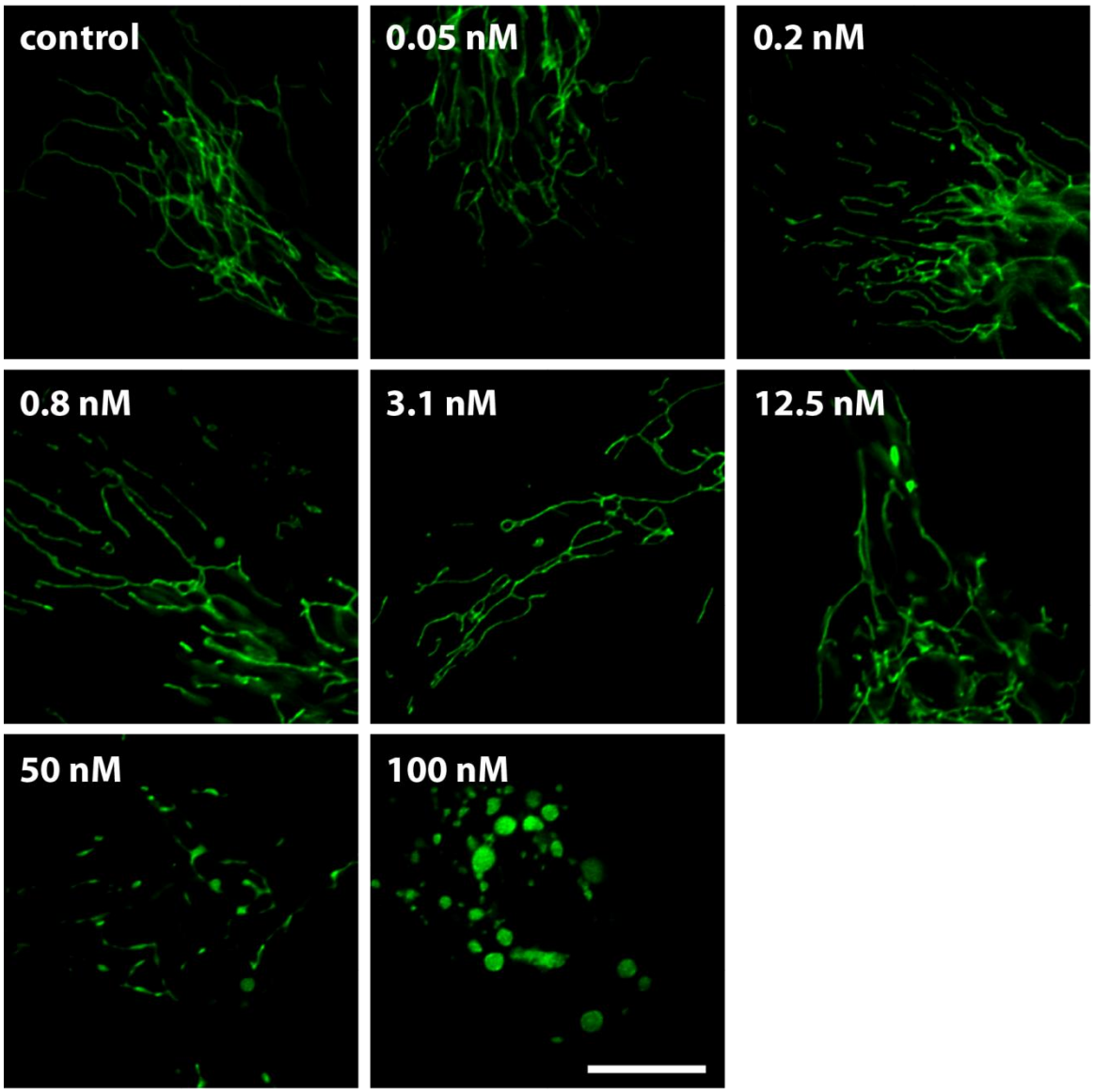

Figure SI-XII.6: Changes in mitochondrial morphology of HUVECs after exposure to Au-ions at different concentrations c_{NP} for 24 h (scale bar: 5 µm). The corresponding analysis is shown in Figure SI-XII.14.

HUVECs, *CdCl ions*

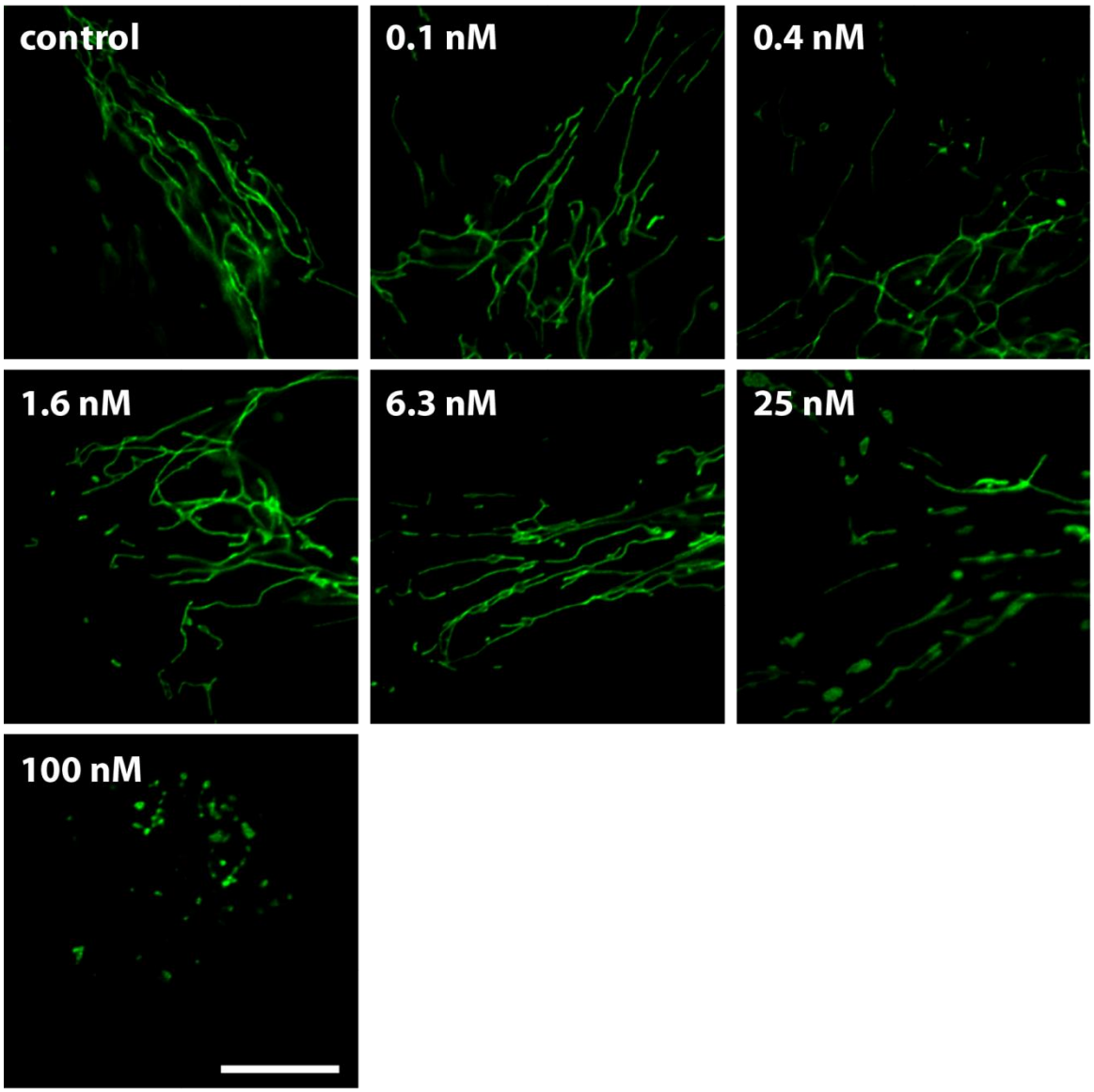

Figure SI-XII.7: Changes in mitochondrial morphology of HUVECs after exposure to CdCl ions at different concentrations c_{NP} for 24 h (scale bar: 5 µm). The corresponding analysis is shown in Figure SI-XII.14.

HeLa, *Au-PMA* NPs*

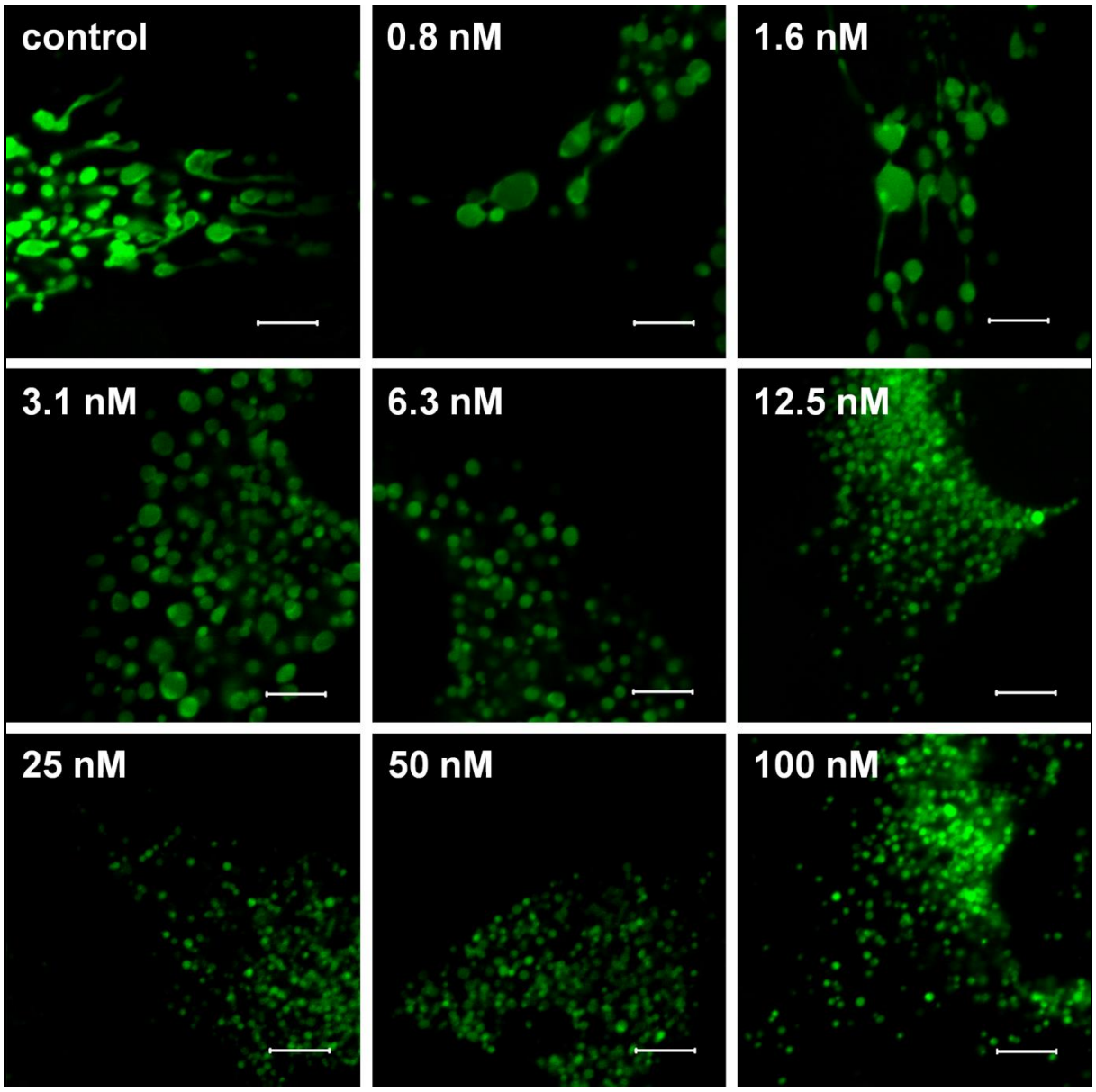

Figure SI-XII.8: Changes in mitochondrial morphology of HeLa cells after exposure to Au-PMA NPs at different concentrations c_{NP} for 24 h (scale bar: 5 µm). The corresponding analysis is shown in Figure SI-XII.1.*

HeLa, *Au-PMA NPs*

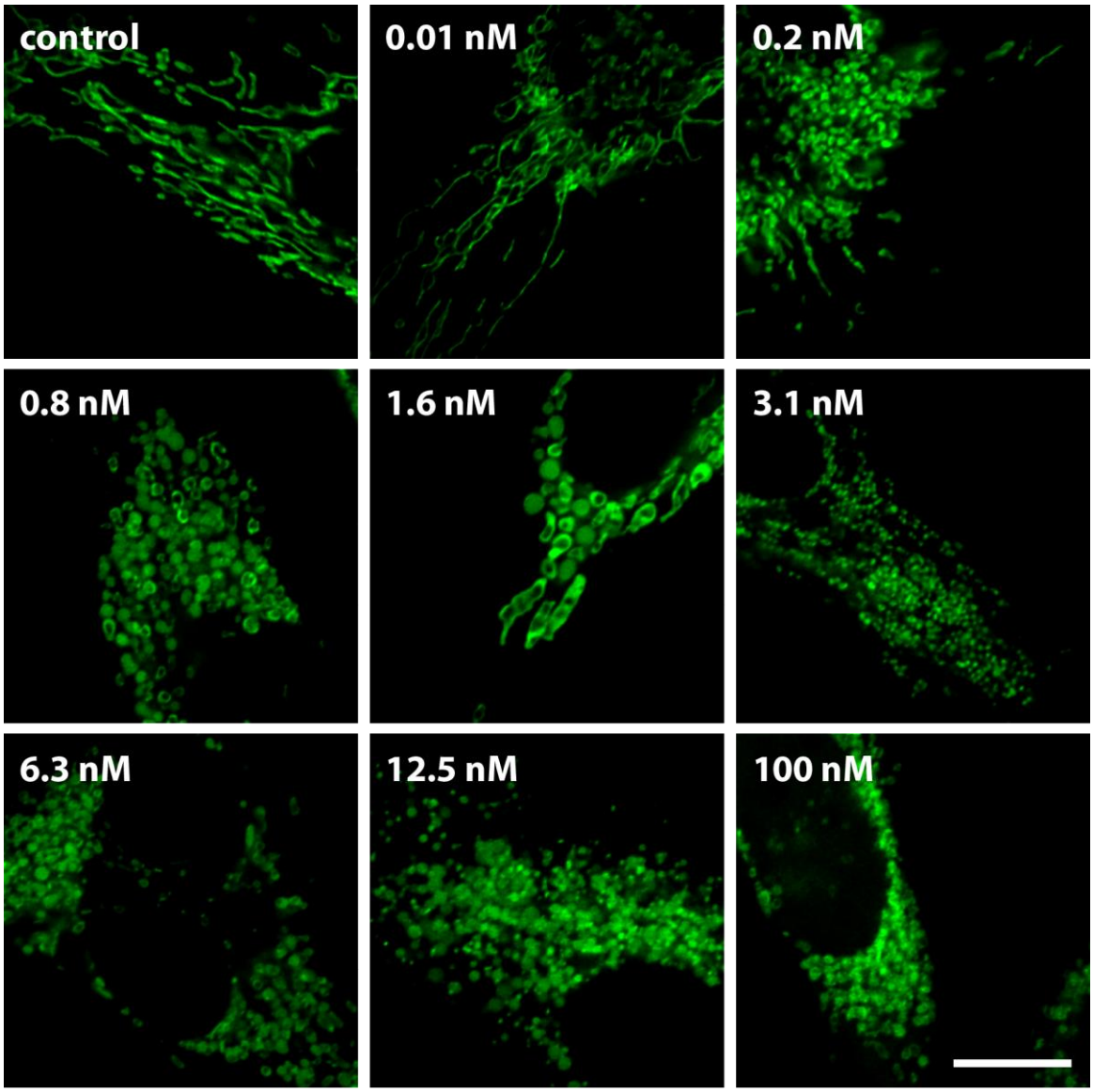

Figure SI-XII.9: Changes in mitochondrial morphology of HeLa cells after exposure to Au-PMA NPs at different concentrations c_{NP} for 24 h (scale bar: 5 µm). The corresponding analysis is shown in Figure SI-XII.14.

HeLa, *Au-PEG NPs*

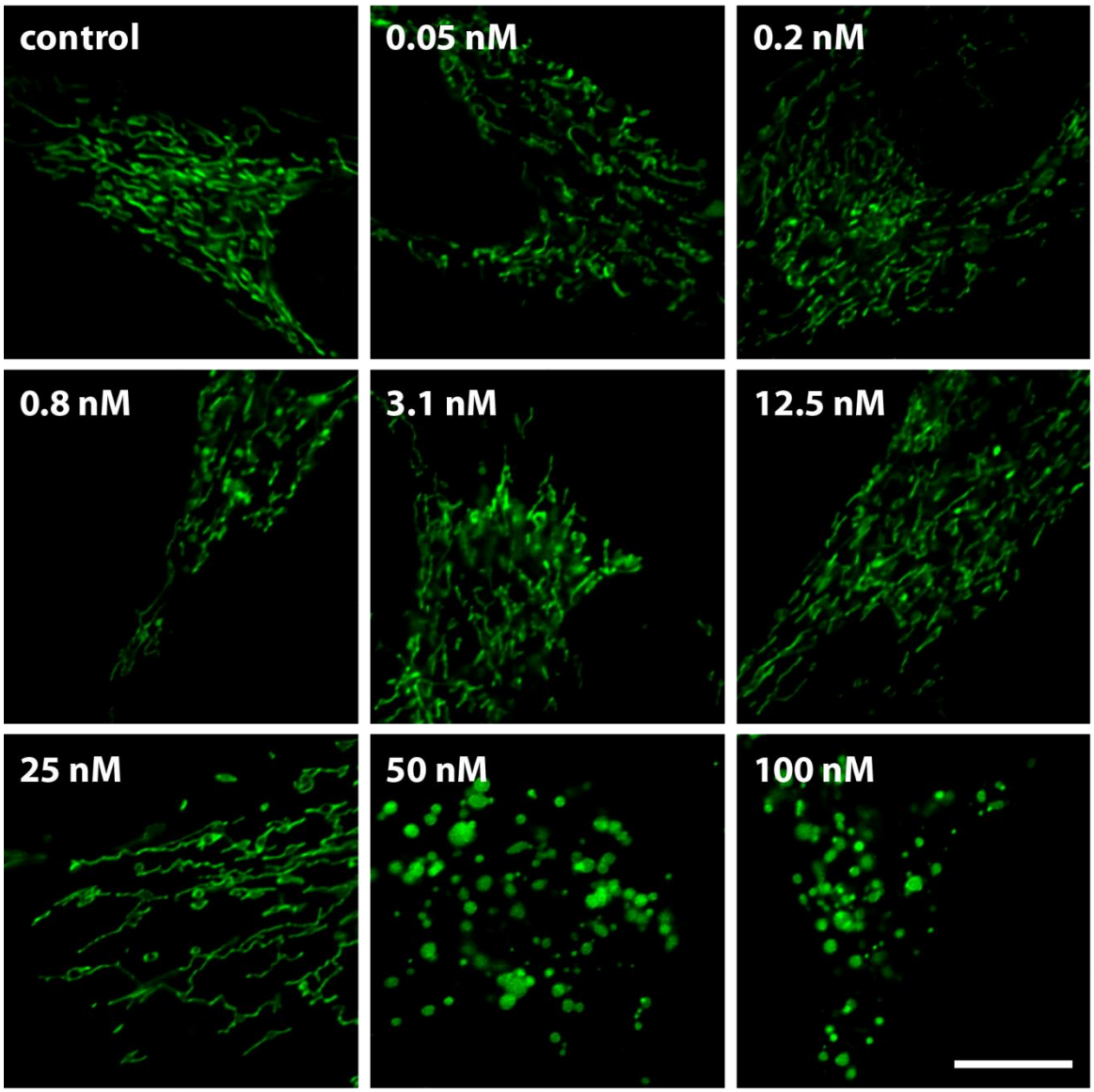

Figure SI-XII.10: Changes in mitochondrial morphology of HeLa cells after exposure to Au-PEG NPs (batch Au-PEG$_2$) at different concentrations c_{NP} for 24 h (scale bar: 5 µm). The corresponding analysis is shown in Figure SI-XII.14.

HeLa, *Au-MUA NPs*

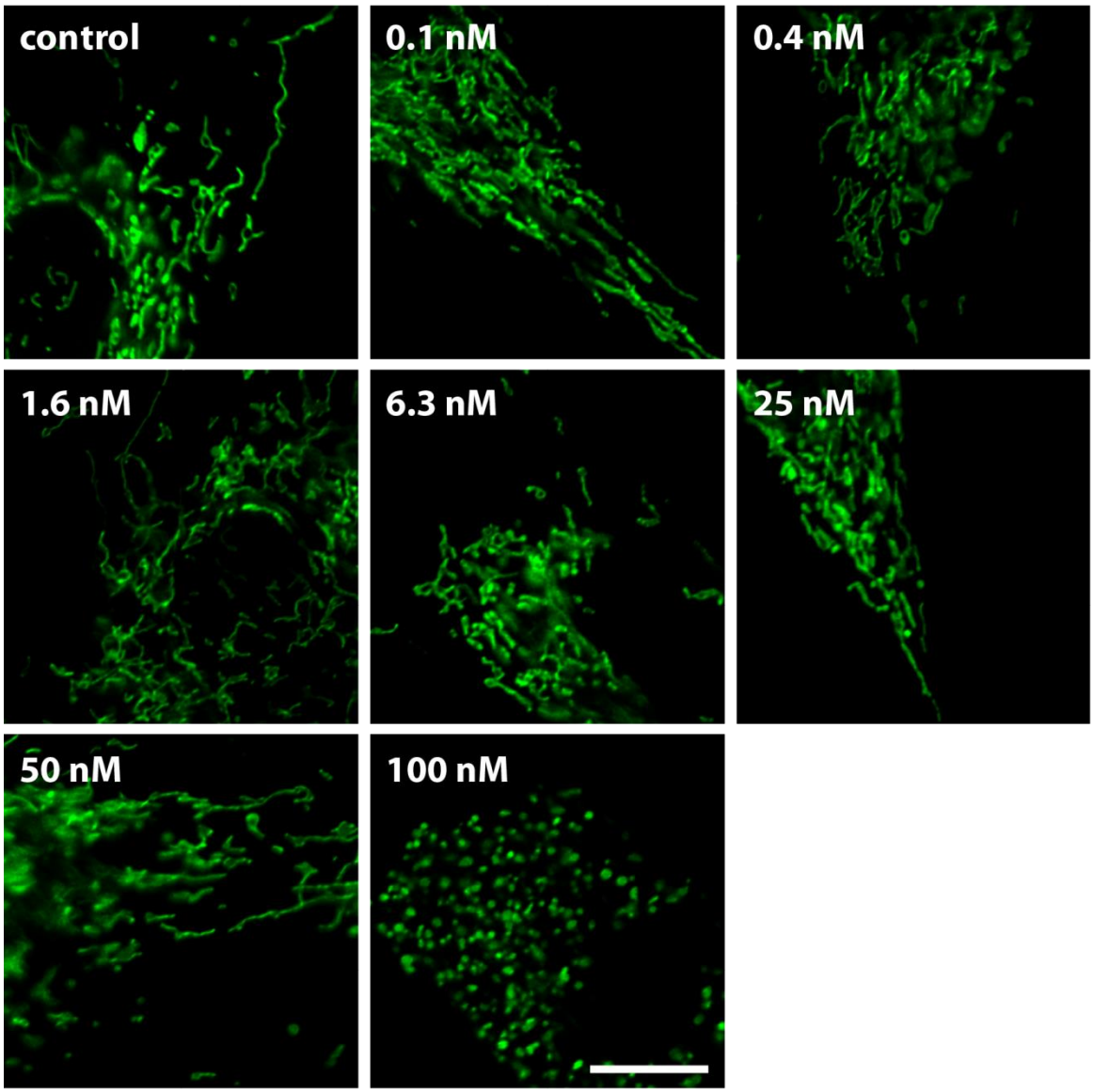

Figure SI-XII.11: Changes in mitochondrial morphology of HeLa cells after exposure to Au-MUA NPs (batch Au-MUA$_2$) at different concentrations c_{NP} for 24 h (scale bar: 5 µm). The corresponding analysis is shown in Figure SI-XII.14.

HeLa, *Au ions*

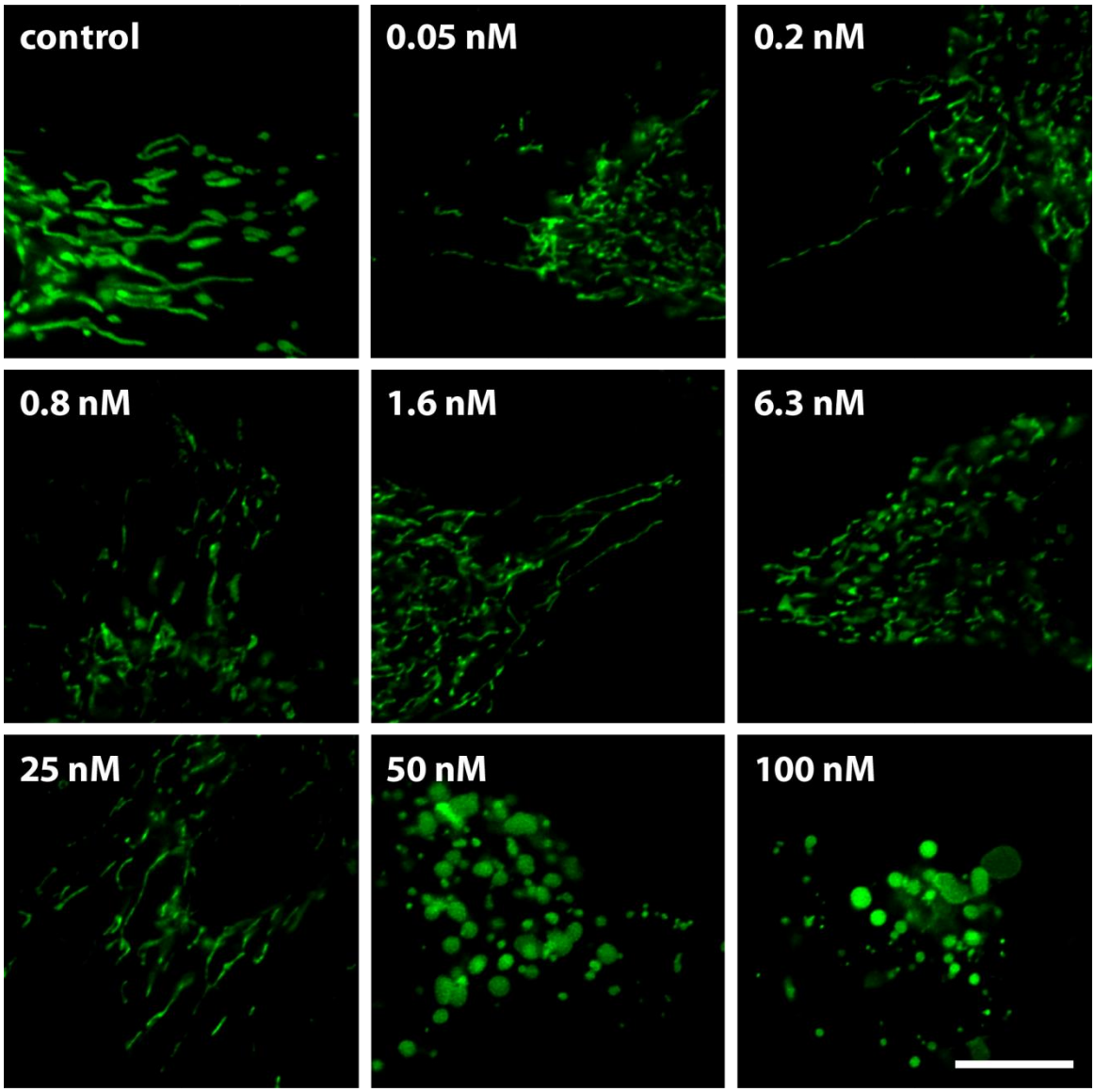

Figure SI-XII.12: Changes in mitochondrial morphology of HeLa cells after exposure to Au ions at different concentrations c_{NP} for 24 h (scale bar: 5 µm). The corresponding analysis is shown in Figure SI-XII.14.

HeLa, *CdCl ions*

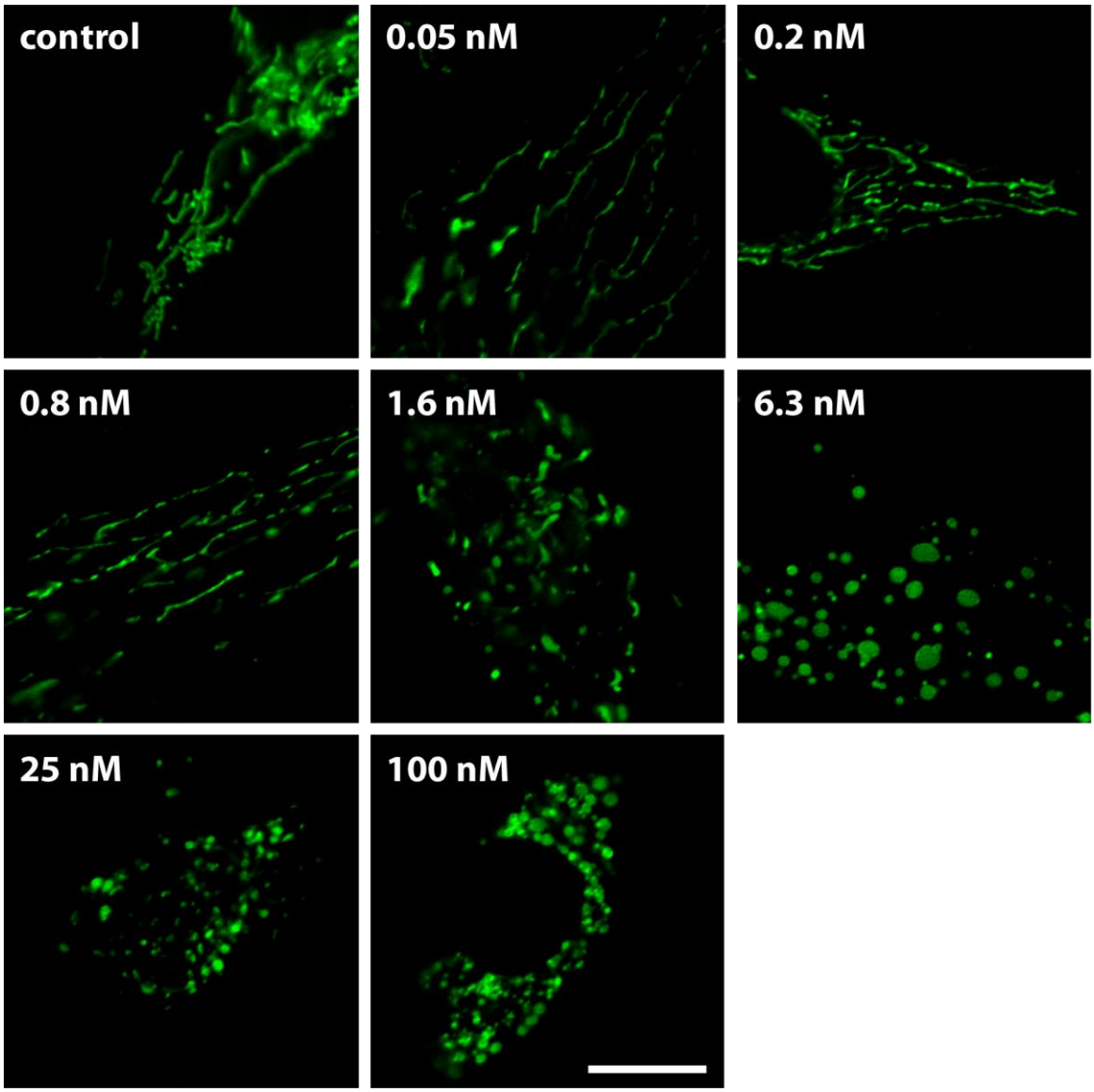

Figure SI-XII.13: Changes in mitochondrial morphology of HeLa cells after exposure to CdCl ions at different concentrations c_{NP} for 24 h (scale bar: 5 µm). The corresponding analysis is shown in Figure SI-XII.14.

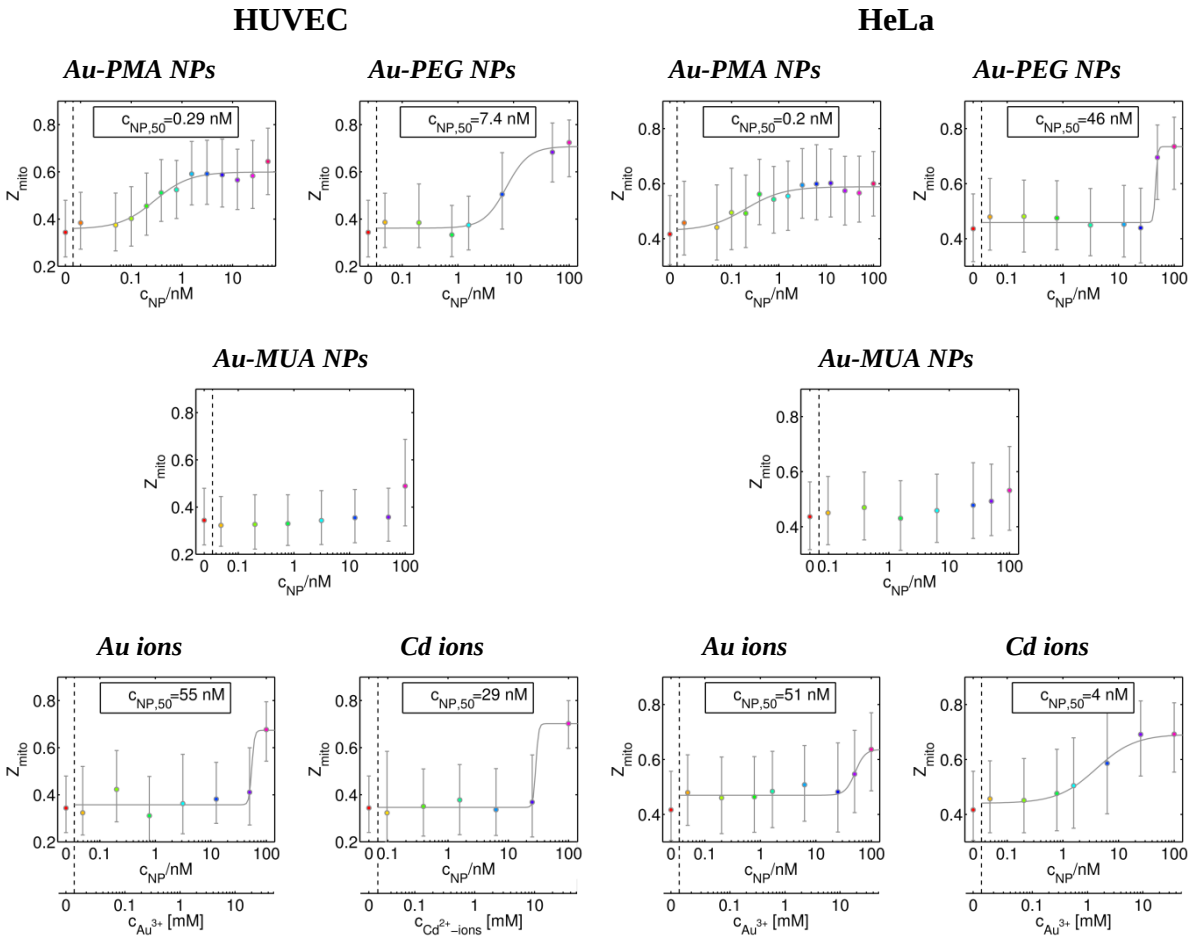

Figure SI-XII.14: Geometrical feature (Zernike coefficient of 0th order) of mitochondria upon exposure to Au NPs of different types. Experiments were carried out with the batches Au-MUA$_2$ and Au-PEG$_2$. The results are presented as median ± lower/upper quartile.

XIII) Analysis of the morphology of the cytoskeleton

XIII.1) Assessment of changes in actin morphology

XIII.2) Assessment of changes in tubulin morphology

XIII.3) Assessment of focal adhesions

The cytoskeleton provides support and shape to the cell and anchors the organelles to their designated place. It also helps in movement of materials in and out of cells. Once the solid Au NPs are endocytosed and accumulate in cells, they may occupy significant space and therefore the cytoskeleton may be affected. We investigated the change of actin and tubulin fibers.

XIII.1) Assessment of changes in actin morphology

HeLa cells (3,000 cells/per well, in 200 µL) or HUVECs (6,000 cells/per well, in 200 µL) were added to 8 well µ-Slide (1 cm^2 per well, Ibidi, Germany, #80826) and incubated over night at 37 °C. Next, the cells were incubated with Au-PMA* NPs at c_{NP} = 0 - 100 nM for 24 h at 37 °C and 5 % CO_2. The cells were then fixed for 20 min in 4 % paraformaldehyde, after which the cells were washed with PBS for 3 times. Next, the cells were permeabilized with 5 mg/mL glycine (Roth, Germany, #3908.1) and 0.5 mg/mL saponin (Sigma-Aldrich, #S7900) in PB for 5 min, followed by incubation in blocking solution (PBS with 2 % BSA (Jackson ImmunoResearch Laboratories, #001-000-161)). Then, the cells were stained with 165 nM AlexaFluor 488-phalloidin (Molecular Probes, USA, #A12379) and incubated at room temperature for 20 min. After that, the cells were stained with 50 µM DAPI (Molecular Probes, #D1306) and incubated for 5 min at room temperature. The cells were washed three times with PBS and stored in 200 µL PBS/well at 4 °C, followed by analysis using a CLSM. The emission of DAPI (λ_{ex} = 405 nm) was detected using a λ_{em} = 420 - 490 nm band-pass. The fluorescence of AlexaFluor 488-phalloidin was excited at λ_{ex} = 488 nm. Emission was detected at λ_{em} = 525 nm (40 nm width band-pass). Imaging was performed using a Plan-Apochromat 20x/0.8 M27 objective. Actin texture features were calculated as described in § VIII.3 with a correlation length of 1.8 µm.

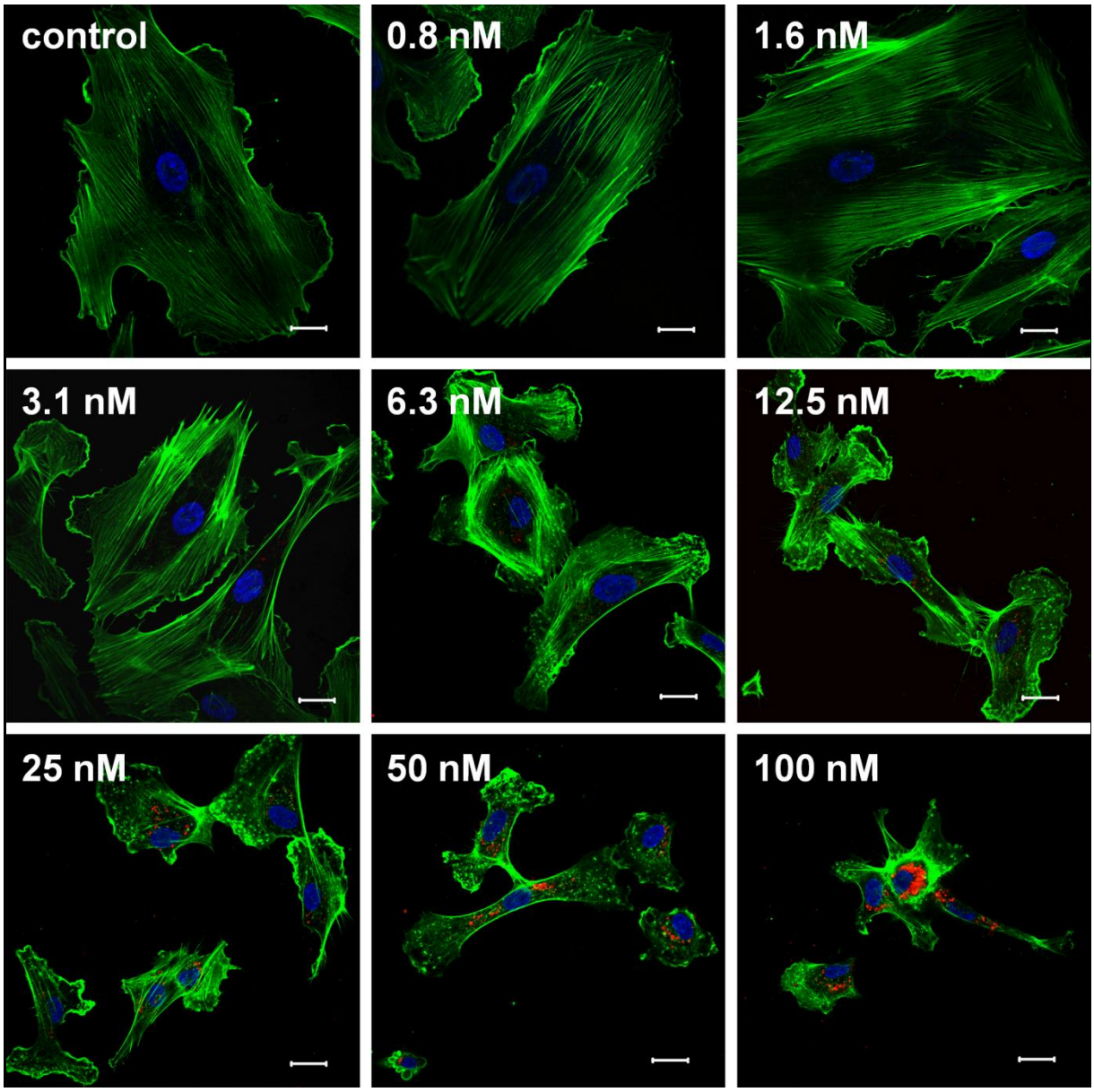

Figure SI-XIII.1: Actin morphology change of HUVECs under different concentrations of Au-PMA NPs (scale bars: 20 μm). Blue channel: nuclei, red channel: Au NPs, green channel: actin fibers.*

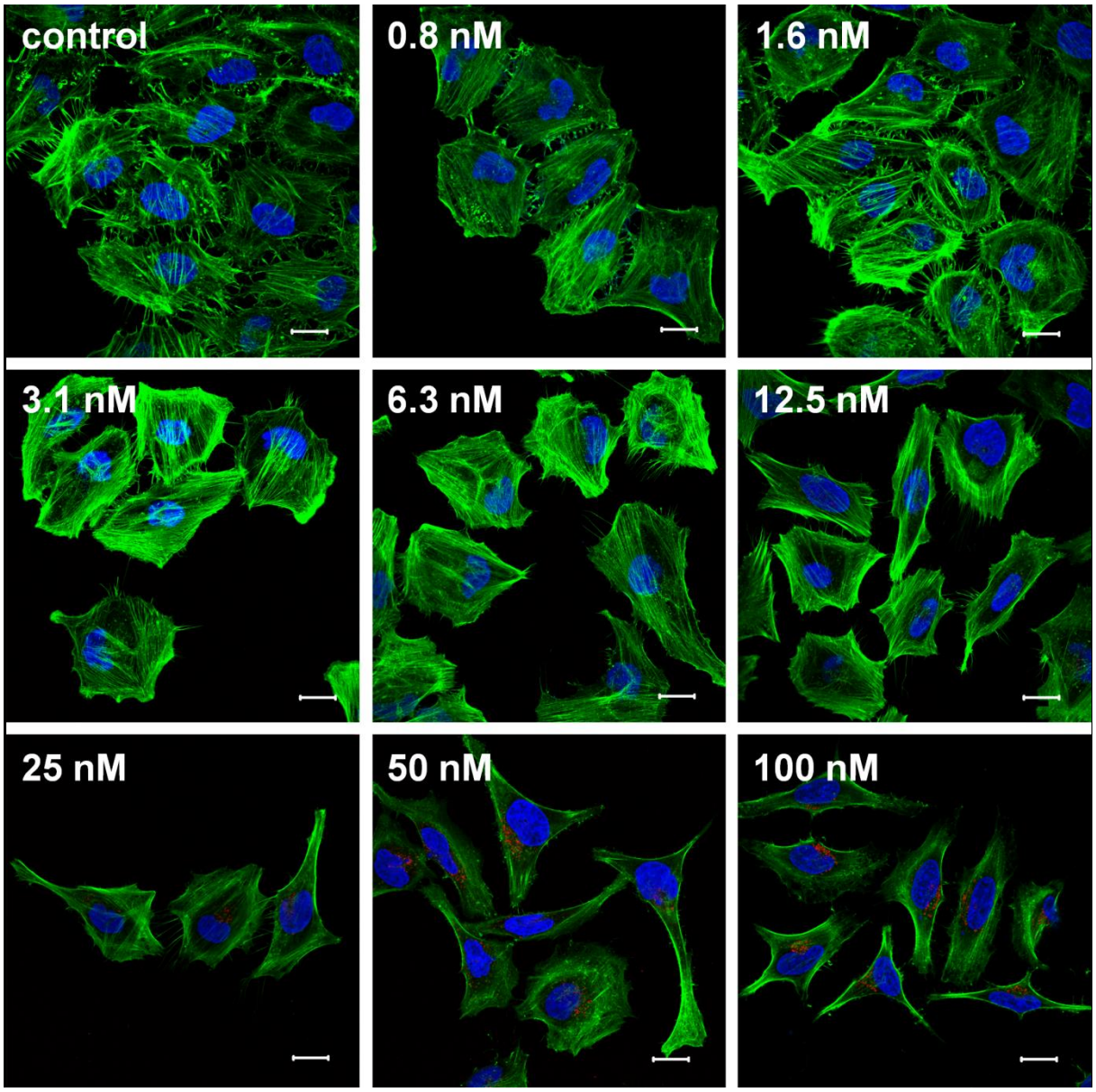

Figure SI-XIII.2: Actin morphology change of HeLa cells under different concentrations of Au-PMA NPs (scale bars: 20 μm). Nuclei are shown in blue, Au-PMA* NPs in red, and actin fibers in green.*

In the HUVECs, with increasing concentration of Au-PMA* NPs, the long thread like structure of actin was partially lost, and more and more dot-like structures appeared, *cf.* Figure SI-XIII.1. From the analysis of actin texture change, we found that in HUVECs the texture contrast increased after Au NP treatment, which is correlated with an increase of dot-like structures and a decrease of thread-like structures in HUVECs (*cf.* Table SI-VIII.2 and Figure SI-XIII.3). This is different with HeLa cells. In this case the appearing of dot-like structures was not observed, *cf.* Figure SI-XIII.2). Here the texture variance decreased after Au NP treatment. This is correlated with the cell surface actin fibers becoming smoother after Au NP treatment. In HeLa cells, the edge of the cells changed significantly, *i.e.* the edge of the cells were "kiwi"-like in the control group (c_{NP} = 0 nM), and the actin fibers tightly connect the neighboring cells. The cell surface became smoother after Au NP treatment. This involves that the cells might lose

connection and communications with each other after exposure to Au NPs. In addition, round-shaped cells became long and narrow after Au-PMA* NPs treatment, which suggests that the adhesion of the cells to the culture dish is not as tight anymore after exposure to Au NPs. High intracellular numbers of non-degradable solid Au-PMA* NPs are clustered in endosomal structures, which are located in the perinuclear region and near the microtubule organizing center, *cf.* § IX. Thus the Au-PMA* NPs may hinder existing or newly forming cytoskeletal structures.

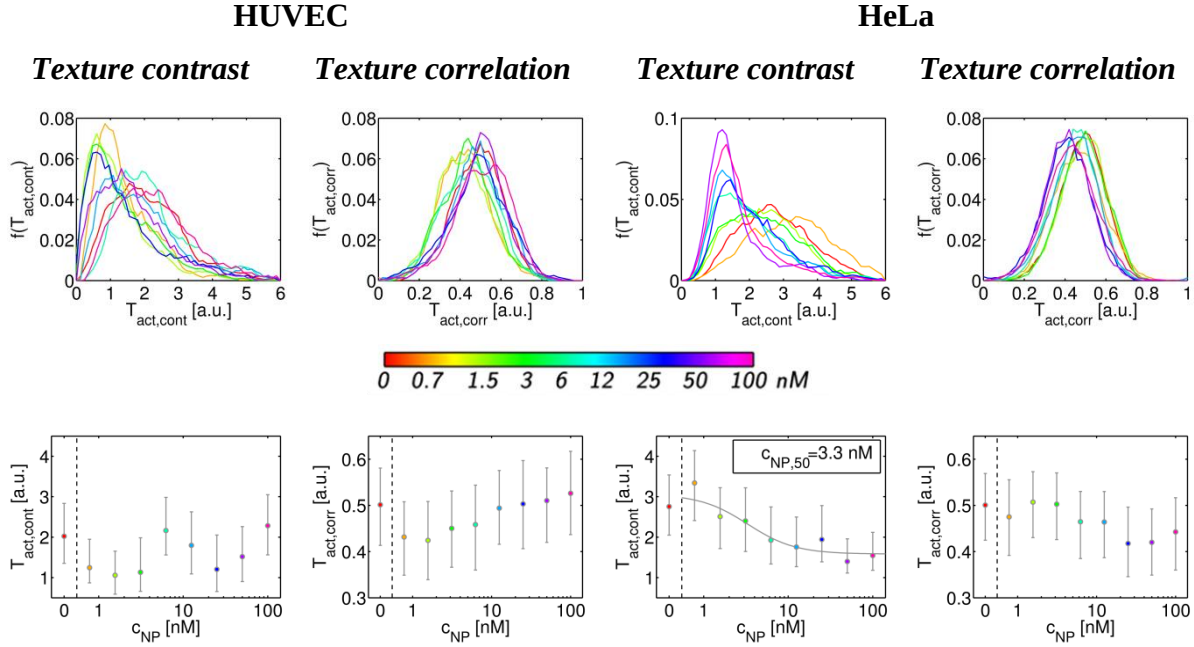

Figure SI-XIII.3: Change of actin texture features (contrast $T_{act,cont}$, correlation $T_{act,corr}$) upon exposure of cells to Au-PMA NPs. The results are presented as normalized probability distributions (first row) and median ± lower/upper quartile for 600 – 1,000 cells/condition.*

XIII.2) Assessment of changes in tubulin morphology

HeLa cells (3,000 cells/per well, in 200 µL) or HUVECs (6,000 cells/per well, in 200 µL) were added to 8 well µ-Slide chambers (1 cm^2 per well, Ibidi, Germany) and incubated over night at 37 °C. Next, the cells were incubated with Au-PMA* NPs at c_{NP} = 0 - 100 nM for 24 h at 37 °C and 5 % CO_2. Then, the cells were fixed for 20 min in 4 % paraformaldehyde, after which the cells were washed with PBS for 3 times. Next, the cells were permeabilized (5 mg/mL glycine (Roth, Germany, #3908.1), 0.5 mg/mL saponin (Sigma-Aldrich, #S7900) in PBS) for 5 min and incubated in blocking solution (PBS with 2 % BSA (Jackson ImmunoResearch Laboratories, #001-000-161)). The cells were stained with goat anti-alpha tubulin antibody (abcam, UK, #ab18251) at the concentration of 1 µg/mL at 4 °C overnight. Then, the cells were washed three times with PBS and stained with 20 µg/mL secondary antibody (Ab) AlexaFluor 430 goat anti-rabbit IgG (H+L) antibody (Molecular Probes, USA, #A11064) at 37 °C for 30 minutes. After that, the cells were washed three times with PBS and stored in 200 µL PBS/well at 4 °C, until they were analyzed using a CLSM. The fluorescence of AlexaFluor 488 was excited at λ_{ex} = 488 nm. Emission was detected at λ_{ex} = 525 nm (40 nm width band-pass). Imaging was performed using a Plan-Apochromat 63x/1.40 Oil DIC M27 objective and a lateral sampling frequency of 200 nm. Tubulin texture features were calculated as described in § VIII.3 with a correlation length of 1.2 µm.

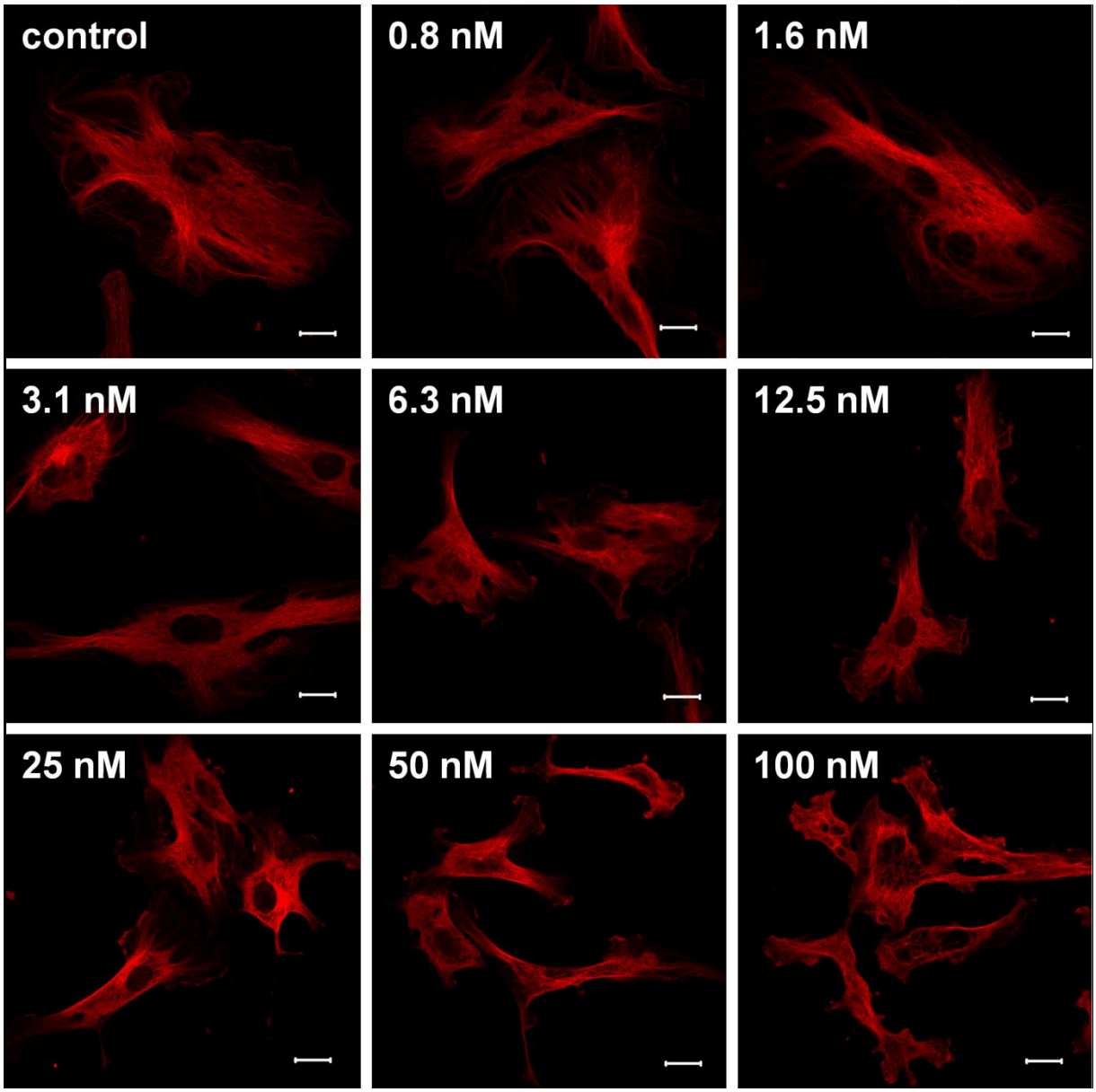

Figure XIII.4: Tubulin morphology change of HUVECs under exposure to different concentrations of Au-PMA NPs (scale bars: 20 μm)*

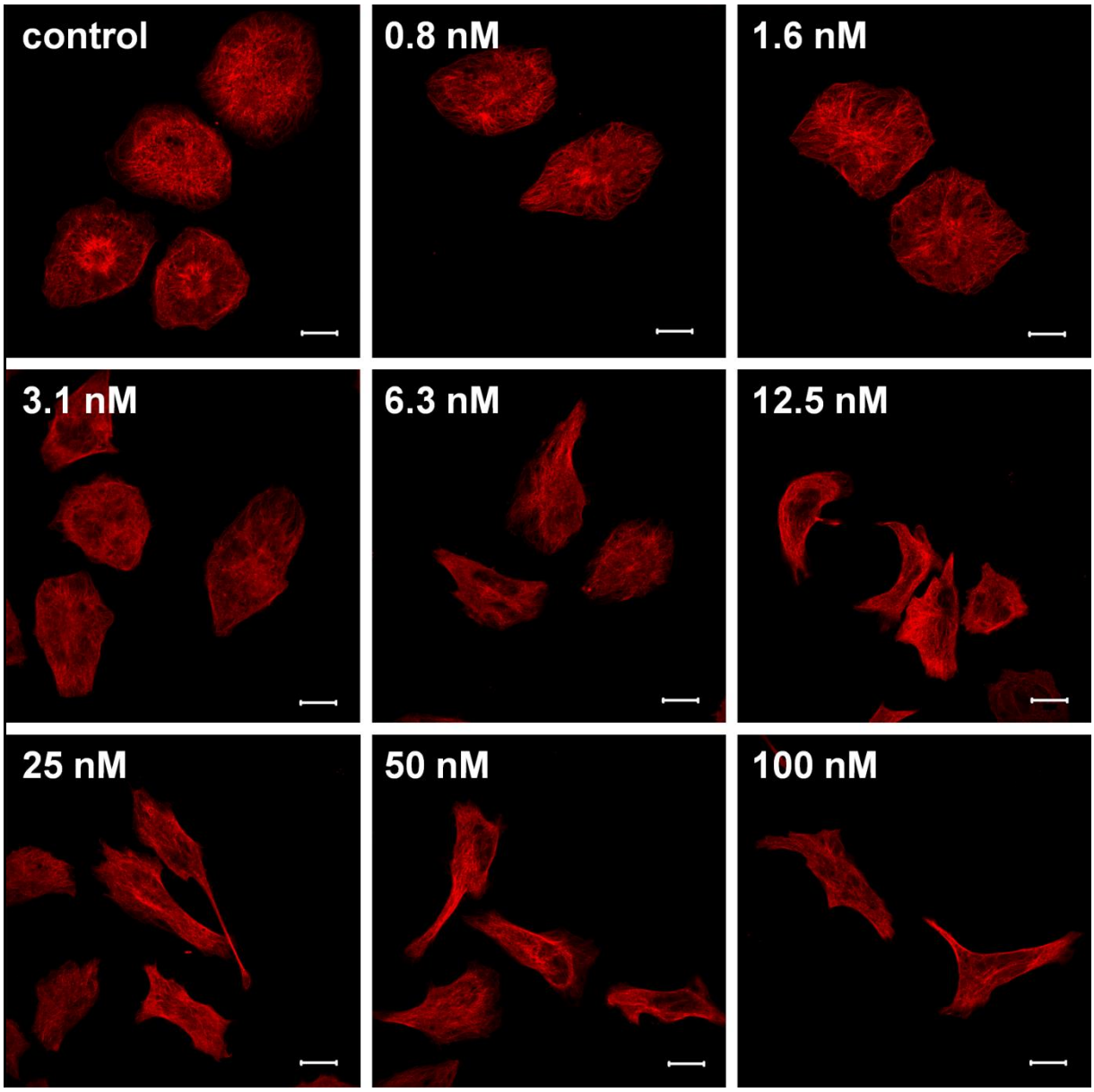

Figure XIII.5: Tubulin morphology change of HeLa cells under Au-PMA NP-treatment (scale bars: 20 µm)*

In HUVECs we found a clear loss of tubulin network at high Au-PMA* NP concentrations, *cf.* Figure XIII.4. The tubulin fibers are compactly arranged in the control group (c_{NP} = 0 nM), but big holes can be found in cells treated with c_{NP} = 100 nM. In HeLa cells, the tubulin network was originally circularly arranged in the control (c_{NP} = 0 nM) and at low concentrations of Au-PMA* NPs. Upon increasing Au-PMA* NP concentrations the tubulin network became thin and long. The deformation of the actin cytoskeleton is more serious than the one of the tubulin network, suggesting that the actin fibers are more sensitive to the Au-PMA* NP-induced deformations, *cf.* § XIV.

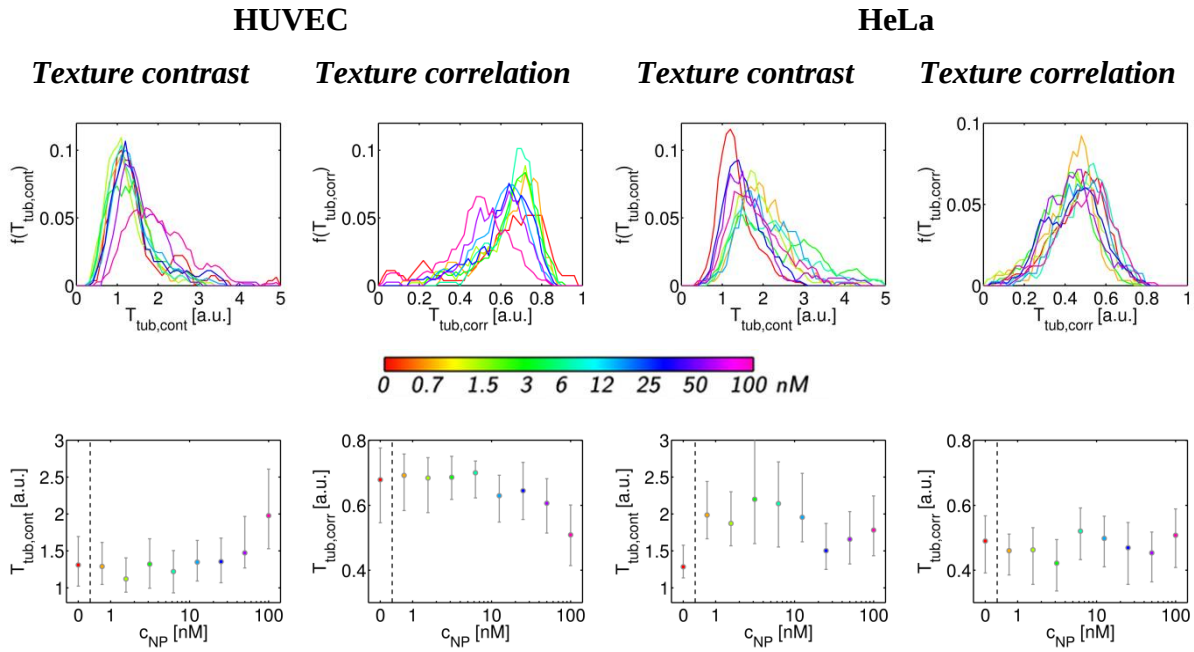

Figure XIII.6: Change of tubulin texture features (contrast $T_{tub,cont}$, correlation $T_{tub,corr}$) upon exposure of cells to Au-PMA NPs. The results are presented as normalized probability distributions (first row) and median ± lower/upper quartile for 60 - 150 cells/condition.*

XIII.3) Assessment of focal adhesions

Focal adhesions are important mediators in cell signaling along actin fibers, and represent the integrity of contact of the cell cytoskeleton with cell surface located receptors that regulates signaling. For this reason we performed a co-staining of the actin network as well as vinculin. To analyze the effects of the Au-PMA* NPs on focal adhesions, HUVECs and HeLa cells were seeded in MatTek glass bottom microscopy culture dishes (MatTek, USA, #P35G-1.5-10-C) at $2 \cdot 10^4$ cells/dish and allowed to settle overnight. Cells were then labeled with the Au NPs at c_{NP} = 0 - 100 nM for 24 h. Then, media were removed, and cells were washed 3 times with PBS (500 µL/dish). Then cells were fixed (2 % paraformaldehyde for 15 min), permeabilized (1 % Triton X-100 for 15 min), and blocked for 30 min in PBS containing 10 % goat serum (Gibco, #PCN5000) and 2 % BSA. Cells were then incubated with primary antibody in blocking solution: mouse anti-vinculin monoclonal Ab (1:200, Abcam, Cambridge, UK, #ab18058) for 2 h at ambient temperature, followed by 1 h incubation at ambient temperature with secondary AlexaFluor 488-conjugated goat anti-mouse antibody (1:250, Molecular Probes, #H32720), and AlexaFluor 546-conjugated phalloidin (Molecular Probes, #A22283). Subsequently, cells were washed three times with blocking solution and mounted on microscope slides prior to being analyzed by confocal laser scanning microscopy (LSM710, Zeiss, Germany). For analysis of focal adhesion areas, confocal images displaying vinculin were background-corrected, and thresholded. Focal adhesions were identified and the total areas per cell were calculated for 40 cells per condition. Images are shown in Figure XIII.7**Fehler! Verweisquelle konnte nicht gefunden werden.** and Figure XIII.8.

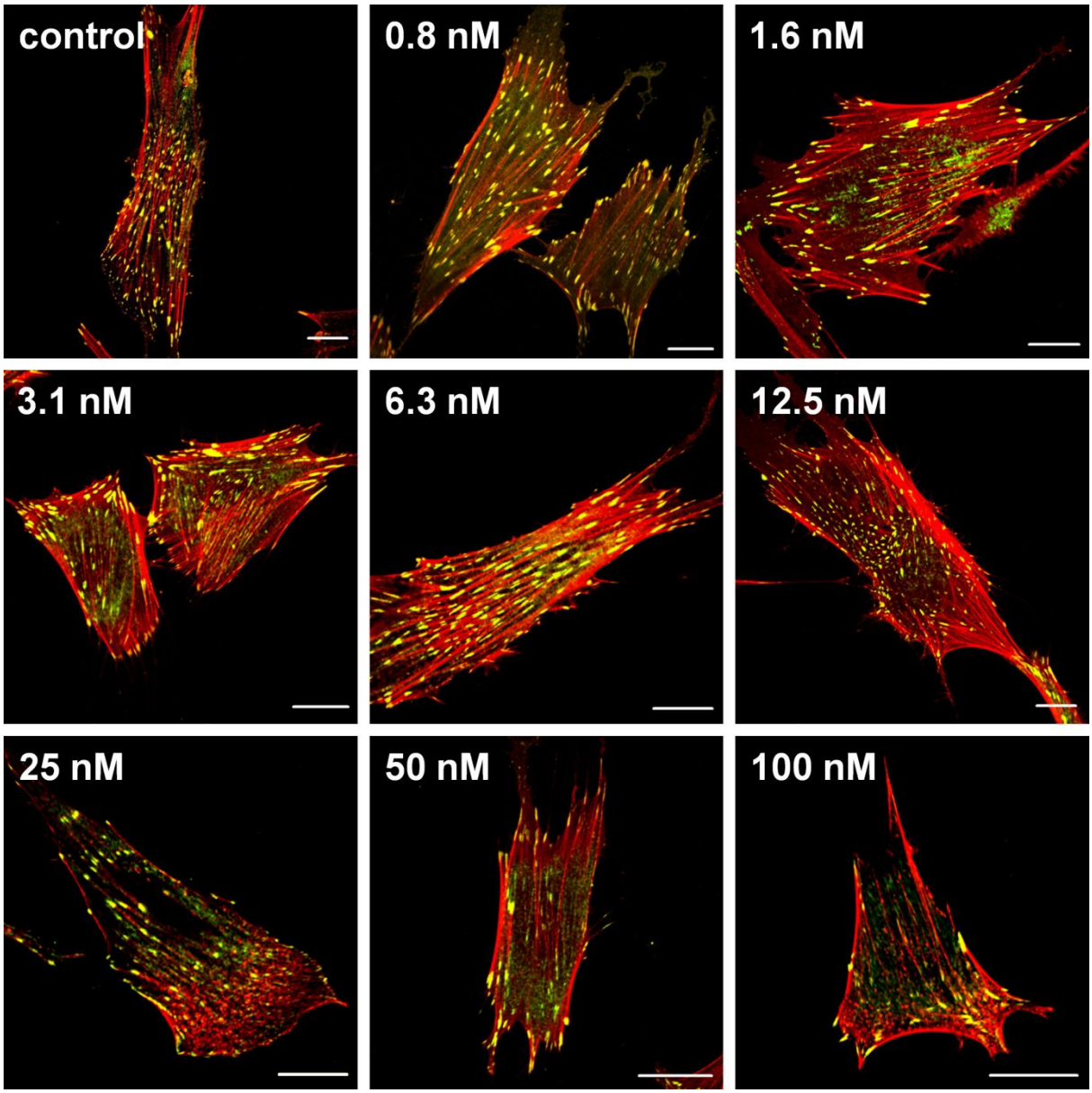

Figure XIII.7: Confocal microscopy images of HUVECs treated with Au-PMA NPs at the indicated concentrations for 24 h. Cells were then stained for F-actin (red) and vinculin (green). Scale bars: 25 µm.*

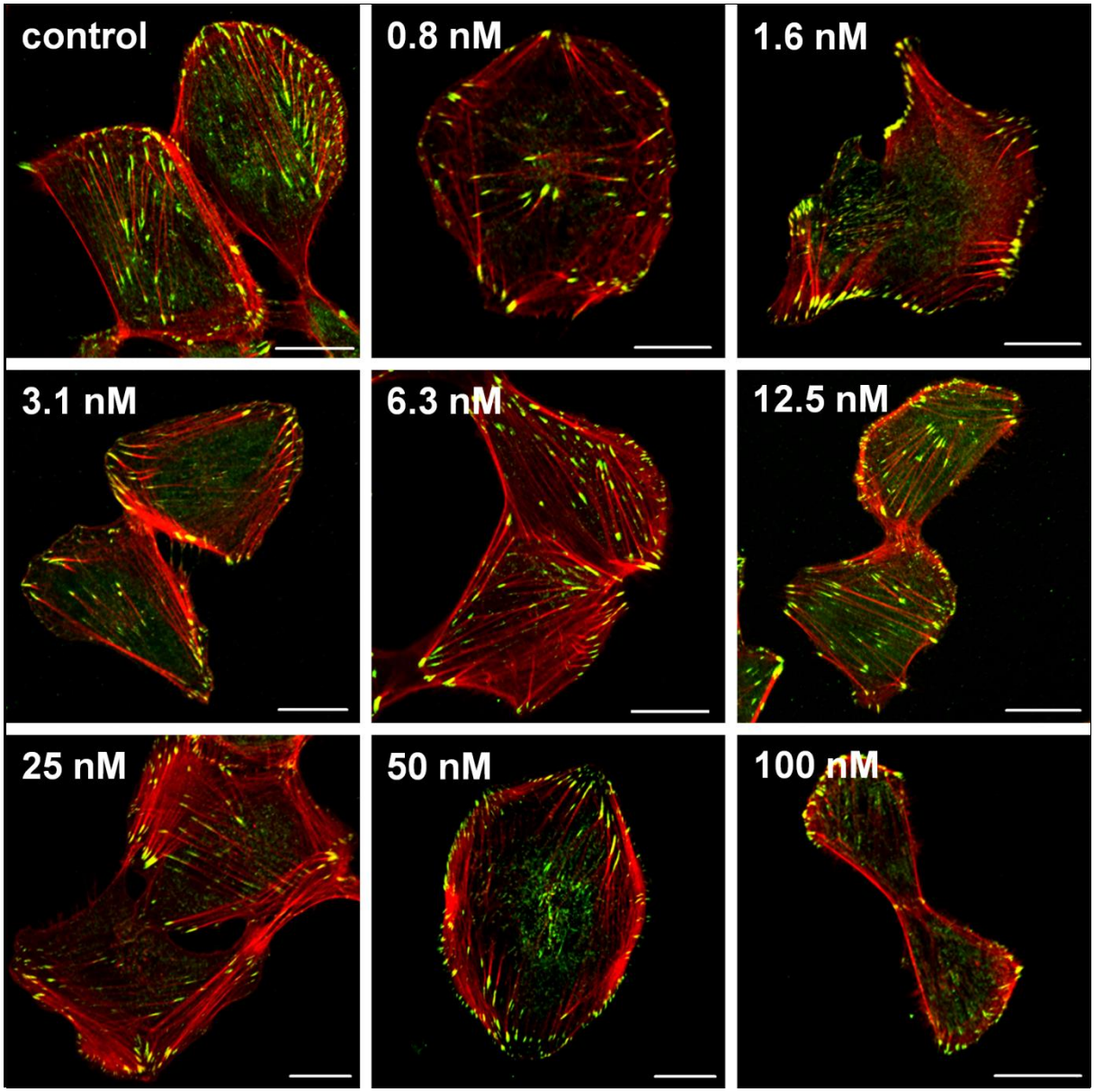

Figure XIII.8: Confocal microscopy images of HeLa cells treated with Au-PMA NPs for 24 h at different NP concentrations c_{NP}. Cells were then stained for F-actin (red) and vinculin (green). Scale bars: 25 µm.*

For HUVECs, the overall size of focal adhesions (as determined in the area of vinculin staining A_{vinc}) is much higher and the effects are much more outspoken and significant at higher Au-PMA* NP concentrations, as compared to HeLa cells, *cf.* Figure SI-XIII.9. With HeLa cells, only minor effects can be seen, but at higher Au-PMA* NP concentrations, the total vinculin area A_{vinc} per cell goes down. These results indicate that as the cell cytoskeleton is affected, as is actin-mediated signaling (which affects many different pathways such as cell division, cell death, *etc.*…).

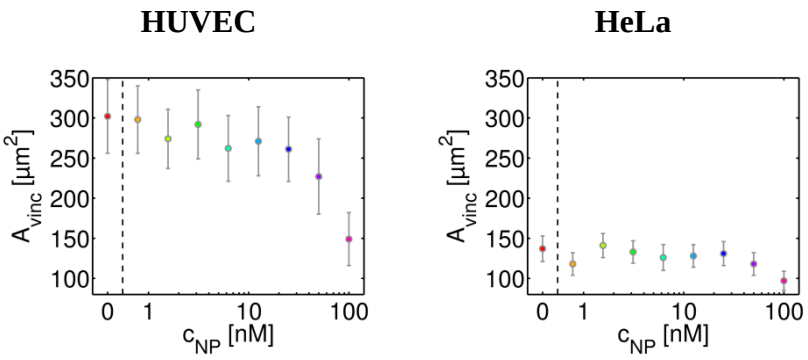

Figure SI-XIII.9: Focal adhesion area A_{vinc} after exposure of cells to Au-PMA NPs. The results are presented as mean ± SD for 30 cells/condition.*

XIV) Biochemical influence of nanoparticle exposure to the cytoskeleton

XIV.1) Gene expression assay

XIV.2) Polymerization of cytoskeletal fibers

XIV.1) Gene expression assay

To have a look into the precise mechanisms causing the effects on cell cytoskeleton, the effect of the presence of Au-PMA* NPs on gene expression related to the cytoskeleton was investigated. Real time polymerase chain reaction (RT-PCR) arrays involving the cytoskeletal regulator pathway (Qiagen Benelux BV, Netherlands, #PAHS-088Z) were run in which the expression of 84 genes involved with actin and tubulin cytoskeleton were probed. HUVECs or HeLa cells were seeded at $1.5 \cdot 10^5$ cells/mL and allowed to settle overnight. Then, cells were either left untreated (controls) or incubated for 24 h with the Au NPs at various concentrations (c_{NP} = 6.3 100 nM). Next, cells were washed twice with PBS and harvested into centrifuge tubes. RNA was extracted using the Qiagen RNeasy Mini Kit (Qiagen, Benelux BV, Netherlands, #74104) according to the manufacturer's instructions. Every RNA sample underwent DNase digestion to eliminate genomic DNA contamination using the RNase-Free DNase Set (Qiagen, Benelux BV, Netherlands). RNA samples were converted into first strand cDNA using the RT2 First Strand Kit (Qiagen Benelux BV, Netherlands), where Genomic DNA Elimination Mixture was applied according to the manufacturer's instructions and samples were amplified by PCR. First strand cDNA was then used in the RT-PCR after samples were added to the RT2 qPCR Master Mix plus Sybr Green (Qiagen Benelux BV, Netherlands). RT-PCR was performed on the iCycler iQ5 Thermal Cycler (Bio-Rad Laboratories N.V., Belgium). PCR array data were analyzed using the ΔΔCt method *via* the SABiosciences web portal (www.SABiosciences.com/ pcrarraydataanalysis.php). The data shown in Figure SI-XIV.1 reveal those genes where high levels of upregulation (> 4.5-fold increase compared to control) were noticed. Overall, there are clear NP concentration-dependent effects noticeable for several of the investigated genes. For the genes most affected (the ones shown in Figure SI-XIV.1), the effects are also clearly highest for the highest NP doses. Some genes such as MAPK13 and CCNA1 were strongly up-regulated in both cell types, indicating that these are quite essential for the general effect. The differences noted between the two cell types can then be explained by differences in intrinsic gene expression levels.

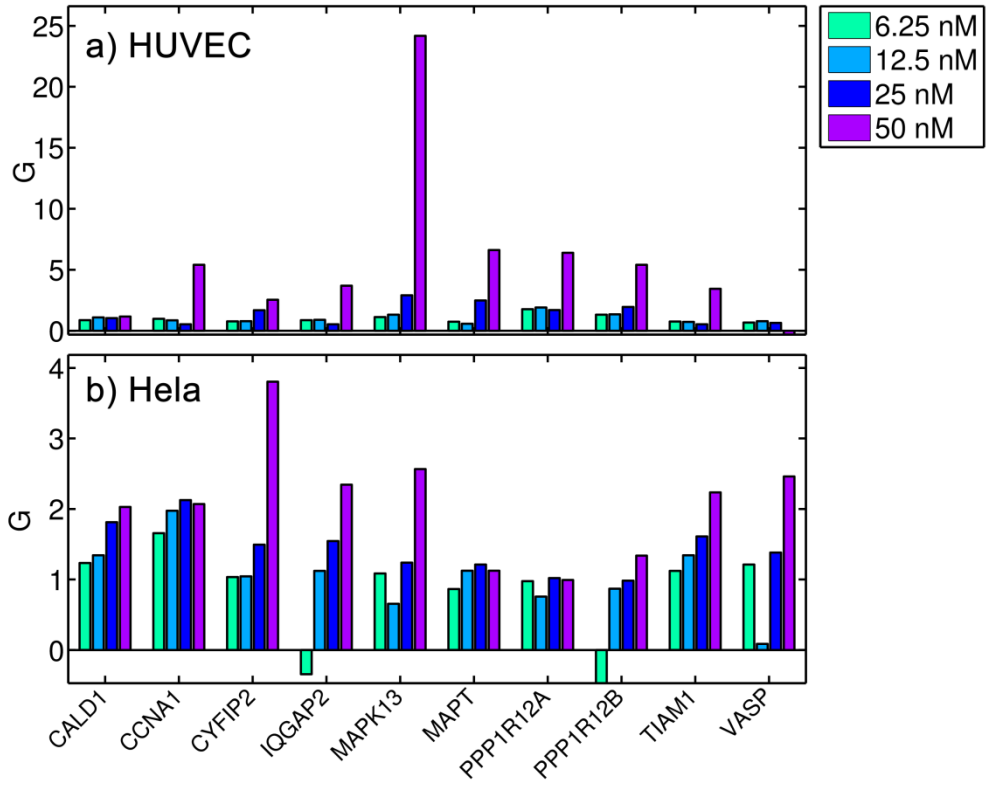

Figure SI-XIV.1: Gene expression level G (normalized to c_{NP} = 0 nM) for cytoskeleton-related genes, upon exposure of cells to Au-PMA NPs. The data shown reveal the fold-change expression level of genes in treated cells compared to the expression level of the corresponding genes in the untreated control cells. Only those genes are shown where a difference of 4.5-fold change in relative gene expression level was observed for any of the samples.*

XIV.2) Polymerization of cytoskeletal fibers

In order to unravel the effects of Au-PMA* NPs on the formation of actin and tubulin fibers, actin and tubulin polymerization assays were performed. Both proteins polymerization processes follow a polymerization curve with three different phases: nucleation (phase I), growth (phase II), and steady state equilibrium (phase III) (*cf.* Figure SI-XIV.2). Under physiological conditions inside cells, globular-actin readily polymerizes to form filamentous-actin, which in return forms double-helical filaments. Effect of Au-PMA* NPs on this polymerization was probed with a fluorescence-based commercial assay.

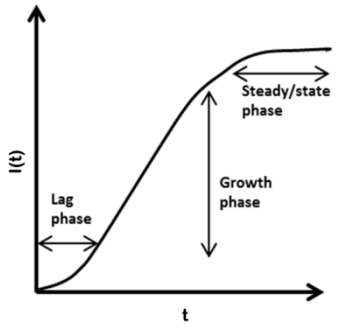

Figure SI-XIV.2: Actin/tubulin polymerization as determined by time-dependent fluorescence intensity I(t) follows three phases, divided in a lag phase, and a growth- and steady state.

To investigate the effect of Au NPs on actin fiber polymerization, the Actin Polymerization Biochem Kit (Cytoskeleton Inc., USA, #BK003) was used. The kit makes use of the enhanced fluorescence of pyrene-conjugated actin obtained during the polymerization process. This reaction is followed by an increase in fluorescence emission, λ_{em}, in the range of λ_{em} = 395 - 440 nm over a period of 60 minutes at room temperature (excitation in the range of λ_{ex} = 340 - 380 nm). Here, at physiological conditions double-helically structured actin (filamentous-actin) is obtained by the polymerization of pyrene globular-actin (monomer), involving ATP hydrolysis. Actin requires ATP and divalent cations for stability.

The experiment was performed in a 96-well plate in which triplicates of all the samples were prepared. First, an adenosine triphosphate (ATP) solution in Tris-HCl pH 7.5, was diluted in 5 mM Tris-HCl, 0.2 mM $CaCl_2$ pH 8.0 buffer to obtain a final concentration of 0.2 mM ATP (ATP-buffer). Next, lyophilized pyrene-labeled muscle actin was dissolved in this ATP-buffer at 0.4 mg/mL and left on ice to avoid the start of polymerization process. Eventually, 100 µL of actin-ATP-buffer was added into each well. As negative control, 100 µL of ATP-buffer were used. The 96-well plate was shaken for 5 seconds and placed into a fluorometer (FluoroLog, Horiba). The emission was recorded over 3 min to obtain a baseline emission signal for the samples. After this, 10 µL Au-PMA* NPs in Milli-Q water were added to obtain loading concentrations between c_{NP} = 0 - 100 nM, and the emission intensity was recorded with a temporal resolution of 60 s for about 20 min, to ensure that Au NPs themselves do not enhance actin polymerization without ATP present.

After 20 minutes, 10 µL of 10 mM ATP, 500 mM KCl, 20 mM $MgCl_2$ in 0.05 M guanidine carbonate pH 7.5 (Actin Polymerization Buffer) were added into each well to start the polymerization reaction. Fluorescence readouts were performed every 60 s. The normalized emission results I(t) are shown in Figure SI-XIV.3.

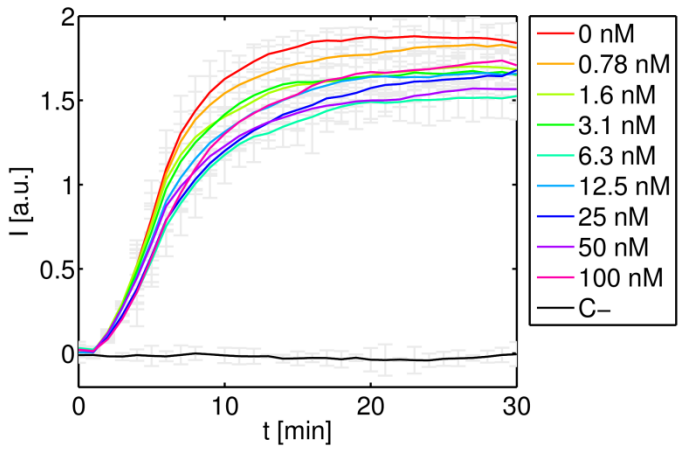

Figure SI-XIV.3: Normalized emission I(t) of pyrene-conjugated actin (λ_{ex} = 355 nm, λ_{em} = 410), indicating the amount of polymerized fibers upon addition of Au-PMA NPs at c_{NP} = 0 - 100 nM.*

The data presented in Figure SI-XIV.3 show that the presence of high Au-PMA* NP-concentration slightly affected the polymerization process of actin. This is probably due to the binding of actin monomers to the Au-PMA* NPs, hampering actin polymerization. These results correlate with the changes in actin morphology of HUVECs and HeLa cells exposed to high concentrations of Au-PMA* NPs (*cf.* Figure SI-XIII.1 and Figure SI-XIII.2). For quantitative evaluation the I(t) values were from Figure SI-XIV.3 were fitted with the following function: $I(t) = 1 - \exp(-k_{act} \cdot t)$, with the actin polymerization rate k_{act} as fit parameter. The NP-exposure dependent actin polymerization rate is shown in Figure SI-XIV.4.

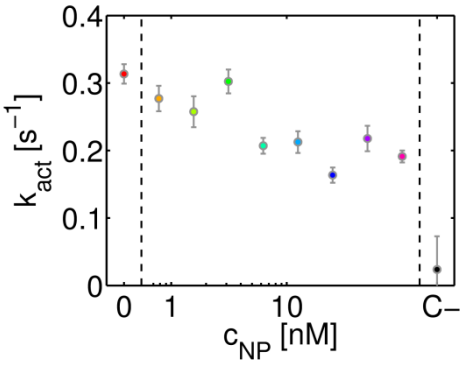

Figure SI-XIV.4: Actin polymerization rate k_{act} during actin growth in the presence of Au-PMA NPs at indicated concentrations c_{NP}.*

It can be stated that Au-PMA* NPs influence the actin polymerization growth phase, since different maximum slope values are shown in Figure SI-XIV.3. The higher the Au-PMA* NP concentration in the media, the higher the obtained k_{act}. No influence was observed on the other process phases.

The effect of Au-PMA* NPs on tubulin fiber polymerization was investigated using the Tubulin Polymerization Assay Kit (Cytoskeleton Inc., USA, #BK006P). Tubulin polymerizes forming microtubules. During the polymerization process, fluorescence is increased due to the

incorporation of a fluorescent dye into microtubules. Au-PMA* NPs may alter any of the three phases of polymerization described earlier. During polymerization, fluorescence is increased due to the incorporation of a fluorescent reporter dye into microtubules. Au NPs may alter any of the three phases of polymerization.

As positive control, the anti-mitotic drug paclitaxel was used at a final concentration of 0.03 mM in Milli-Q water, since this compound removes the nucleation process (phase I) and enhances the maximum slope of the growth phase (phase II). In addition to this, 5 mM $CaCl_2$ solution in working buffer was used as negative control, since the calcium inhibits tubulin polymerization. First, a 96 well plate was pre-warmed to 37 °C. 972 µL of buffer 1, composed of 80 mM piperazine-N,N'-bis[2-ethanesulfonic acid] sesquisodium salt, 2 mM $MgCl_2$, 0.5 mM ethylene glycol-bis(b-amino-ethyl ether) N,N,N',N'-tetra-acetic acid, pH 6.9, and 10 µM fluorescence reporter were mixed with 448 µL of the tubulin glycerol buffer, composed of 80 mM piperazine-N,N'-bis[2-ethanesulfonic acid] sesquisodium salt, 2 mM $MgCl_2$, 0.5 mM ethyleneglycol-bis(b-amino-ethyl ether) N,N,N',N'-tetra-acetic acid in 60 % v/v glycerol at pH 6.9. Quickly, 17.7 µL of 100 mM guanosine triphosphate (GTP), required for tubulin polymerization, dissolved in Milli-Q water, and 340 µL of 10 mg/mL tubulin stock solution in buffer 1 were added to the previous mixture. The obtained "Tubulin Reaction Mix" was placed on ice to avoid the start of the reaction at room temperature.

Once prepared, 5 µL of the Au-PMA* NP samples at a 10x concentration (0-1 µM) were added to their respective wells, leading to final NP concentrations c_{NP} = 0 - 100 nM. Paclitaxel and $CaCl_2$ solutions were also added in control wells. Then, the plate was placed at 37 °C for 1 min. After this, 50 µL of the Tubulin Reaction Mix were added to every well of the plate and fluorescence emission I(t) (λ_{ex} = 360 nm, λ_{em} = 420 nm) was recorded at a temporal resolution of 60 s for 2 h. Normalized results are shown in Figure SI-XIV.5.

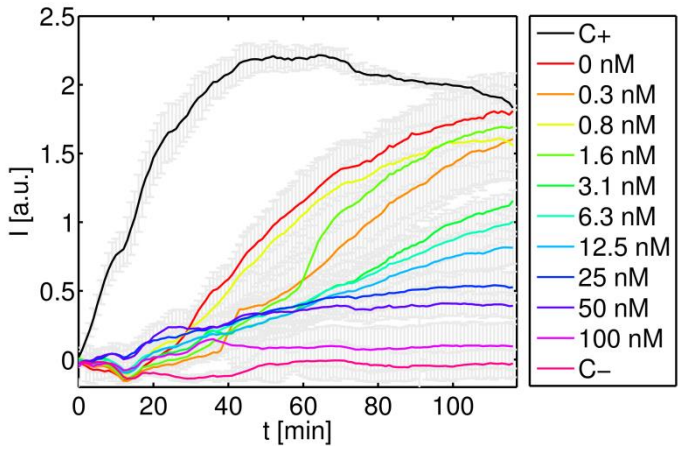

Figure SI-XIV.5: Normalized emission I(t) of the tubulin polymerization process (λ_{ex} = 360 nm, λ_{em} = 420 nm) upon exposure to Au-PMA NPs. The reaction starting point values have been taken for normalization. C+ is the positive control (paclitaxel), and C- is the $CaCl_2$ solution acting as negative control.*

Obviously, Au-PMA* NPs do not only clearly inhibit tubulin polymerization in the growth phase (phase II), but also influence the steady state phase (phase I). The increase in Au-PMA* NP-concentration leads to a diminution of the maximum slope of the microtubules formation and thus, having a clear effect on the polymerization process. For quantification we defined the normalized amount of polymerized tubulin as $N_{tub} = I(c_{NP}, t = 110\ min)/I(c_{NP} = 0\ nM, t = 110\ min)$, as shown in Figure SI-XIV.6.

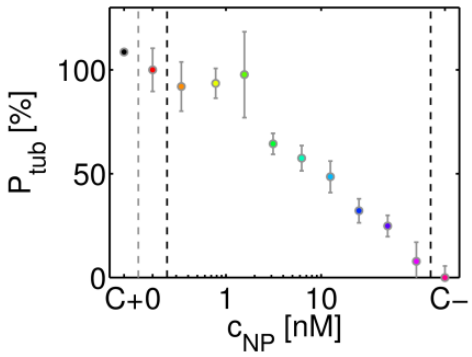

Figure SI-XIV.6: Normalized amount of polymerized tubulin N_{tub} after 110 min of reaction in the presence of Au-PMA NPs. C+ is the positive control (paclitaxel) and C- is the $CaCl_2$ solution acting as negative control.*

The tubulin polymerization process was clearly inhibited as the concentration of Au-PMA* NPs was increased, indicating Au-PMA* NPs might destabilize microtubules. This correlates with the appearance of big holes among the tubulin network in HUVECs and HeLa cells at high concentration of Au-PMA* NPs (*cf.* **Fehler! Verweisquelle konnte nicht gefunden werden.** and **Fehler! Verweisquelle konnte nicht gefunden werden.**).

XV) In vivo cytotoxic effects using a zebrafish model

To assess the developmental hazard potential of the Au-PMA* NPs *in vivo*, a toxicity study in zebrafish embryo was carried out. For the experiments the sterile Au-PMA* NPs in water were diluted in E3 medium (5 mM NaCl, 0.17 mM KCl, 0.33 mM $CaCl_2$, 0.33 mM $MgSO_4$) to form a 1:10 serial dilution series corresponding to c_{NP} = 700, 70, 7, 0.7, 0.07 and 0 nM. At 4 hours post fertilization, zebrafish embryo chorions were removed enzymatically, and the embryos were transferred to individual wells of a 96-well plate with 100 µL of the prepared test compound dilutions[30]. Exposure plates were sealed to prevent evaporation and wrapped with aluminum foil for photoprotection. The dilution series above was duplicated on each plate (columns 1-6 duplicated in columns 7-12) and 2 plates were run for the test compound. Thus, 32 embryos were exposed to each concentration. The static exposures were maintained at 28 °C until 24 hours post fertilization (hpf) when developmental progress, mortality, and photo-induced tail flexion were assessed. At 120 hpf, embryos were assessed for their photo-induced locomotor activity and their escape response to a gentle touch with a blunt probe to the head and tail region. Then they were euthanized by ricaine overdose and scored for mortality and morphological malformations. For malformation statistics, only embryos that survived until 120 hpf were included. 22 morphological endpoints were evaluated[31, 32]. Exposure to Au NPs was not associated with altered activity in the 24 hpf photo-response test as it can be observed in Figure SI-XV.1.

a)

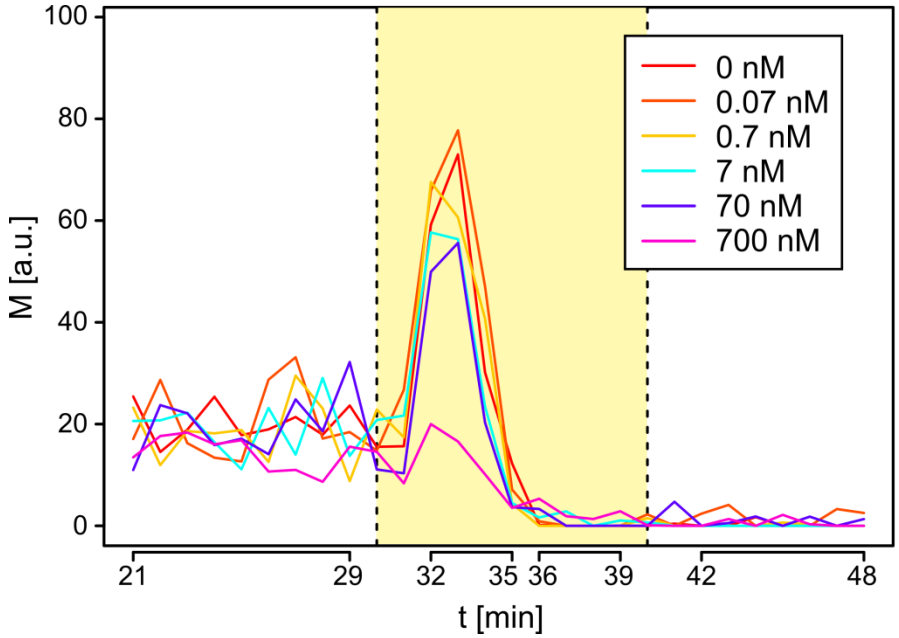

b)

c_{NP} [nM]	0	0. 07	0.7	7	70	700
Baseline phase	1	0.425	0.464	0.578	0.800	0.073
Excitatory phase 1	1	0.586	0.889	0.211	0.209	0.000031
Excitatory phase 2	1	1	1	1	1	0.730
Refractory phase	1	1	1	1	1	1

Figure SI-XV.1: Photo-induced tail flexion at 24 hpf associated with Au-PMA NPs exposure: a) The yellow area indicates the time of a single bright, visible light flash. The y-axis values are a unit less index of motion M (tail flexion) recorded as pixel changes between successive video frames. Embryos were placed 1 per well of a 96 well plate. b) P values indicate significant differences where P < 0.01(Kolmogorov-Smirnov test) in tail flexions per unit time from the vehicle (E3 medium) control group. No significant differences from the control group were observed. Dead or malformed embryos at 24 hpf were excluded from the analysis.*

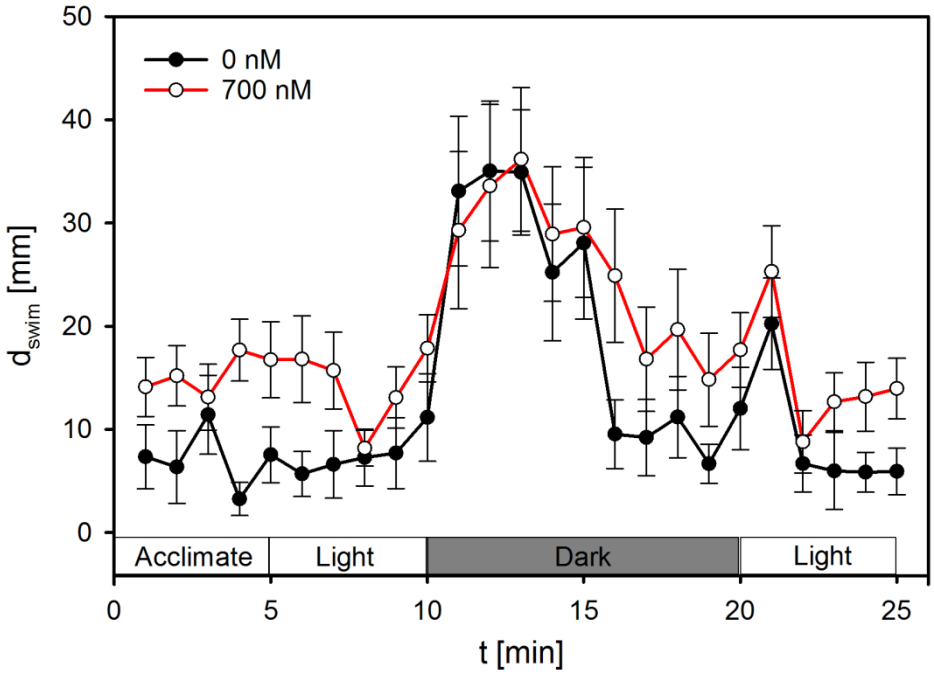

Figure SI-XV.2: Total locomotor activity in terms of total swim distance d_{swim} under light/dark stimulation measured in 5 days post fertilization (dpf) zebrafish exposed from 6 hpf to 5 dpf to Au-PMA NPs. Data were analyzed using a Mann-Whitney Rank Sum comparison of activity between treatment and control in each phase of the test (t =1-5 min = acclimation, minutes 6-10 = visible light, minutes 11 - 20 = dark (IR light), minutes 21-25 = visible light. The threshold for statistical significance was $p < 0.05$. Only the highest dose was reported because no other endpoints were significantly affected in the dose range used.*

Other concentrations were not associated with behavioral abnormality at 120 hpf. Exposure to Au-PMA* NPs was not significantly associated with mortality or any morphological abnormality, *cf.* Figure SI-XV.3.

The results indicate that the Au-PMA* NPs were not overtly toxic in the developmental zebrafish under the reported laboratory conditions and practices and, with the exception of the hyperactivity observed at 120 hpf, the hazard potential of this compound appears to be low.

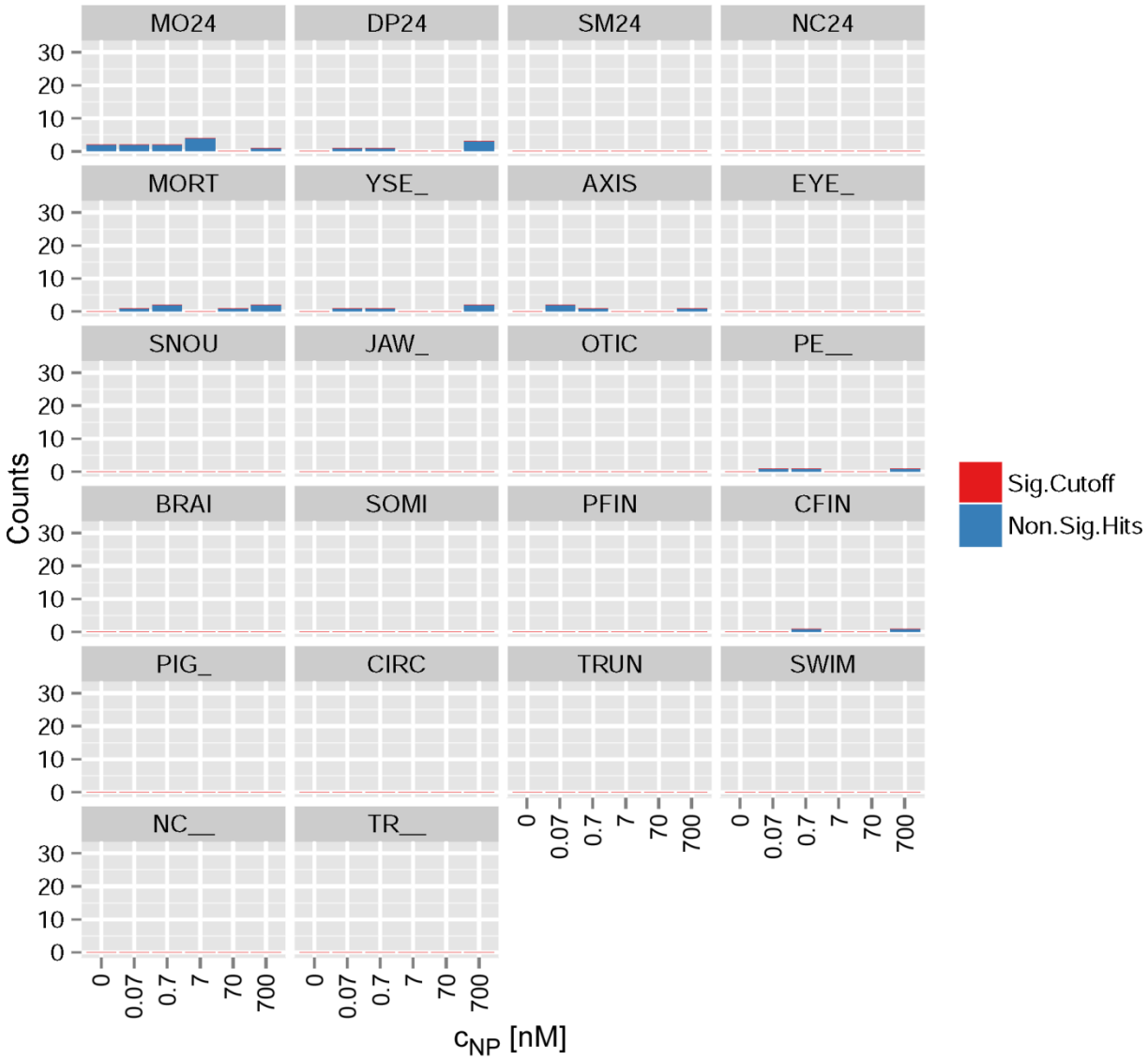

Figure SI-XV.3: Endpoint incidence (binomial, presence/absence data) across all 24 replicates was plotted as stacked points, one point per observation. Any points at or above the threshold for statistical binomial significance would appear in red. The control incidence of all morphological and touch response endpoints was insignificant and within the 10 % tolerance limit. No significant responses were associated with exposure to Au-PMA NPs. Endpoint Key: Yolk sac edema (YSE), bent body axis (AXIS), eye defect EYE), snout malformed (SNOU), jaw malformed (JAW), ear malformed (OTIC), pericardial edema (PE), brain malformed (BRAI), muscle somite defect (SOMI), caudal fin defect (CFIN), pectoral fin(s) abnormal (PFIN), circulation slower/faster or less prevalent than normal (CIRC), pigmentation abnormal (PIG), body trunk length shorter than normal (TRUN), swim bladder not present or not inflated (SWIM), notochord curvy or otherwise abnormal (NC), and response to blunt probe gently touched to head or tail region without characteristic escape response (TR).*

XVI) References

[1] M. Brust, M. Walker, D. Bethell, D.J. Schiffrin, R. Whyman, J. Chem. Soc., Chem. Commun., 1 (1994) 801-802.

[2] F. Amin, D.A. Yushchenko, J.M. Montenegro, W.J. Parak, ChemPhysChem, 13 (2012) 1030-1035.

[3] D. Hühn, K. Kantner, C. Geidel, S. Brandholt, I. De Cock, S.J.H. Soenen, P. Rivera Gil, J.-M. Montenegro, K. Braeckmans, K. Müllen, G.U. Nienhaus, M. Klapper, W.J. Parak, ACS Nano, 7 (2013) 3253-3263.

[4] C.J.J. den Ouden, R.W. Thompson, Journal of Colloid and Interface Science, 143 (1991) 77-84.

[5] J. Fink, C.J. Kiely, D. Bethell, D.J. Schiffrin, Chemistry of Materials, 10 (1998) 922-926.

[6] M.T. Fernández-Argüelles, A. Yakovlev, R.A. Sperling, C. Luccardini, S. Gaillard, A.S. Medel, J.-M. Mallet, J.-C. Brochon, A. Feltz, M. Oheim, W.J. Parak, Nano Letters, 7 (2007) 2613-2617.

[7] C.-A.J. Lin, R.A. Sperling, J.K. Li, T.-Y. Yang, P.-Y. Li, M. Zanella, W.H. Chang, W.J. Parak, Small, 4 (2008) 334-341.

[8] T. Pellegrino, L. Manna, S. Kudera, T. Liedl, D. Koktysh, A.L. Rogach, S. Keller, J. Rädler, G. Natile, W.J. Parak, Nano Letters, 4 (2004) 703-707.

[9] F. Zhang, E. Lees, F. Amin, P. Rivera_Gil, F. Yang, P. Mulvaney, W.J. Parak, Small, 7 (2011) 3113-3127.

[10] U.I. Tromsdorf, N.C. Bigall, M. Kaul, O.T. Bruns, M.S. Nikolic, B. Mollwitz, R.A. Sperling, R. Reimer, H. Hohenberg, W.J. Parak, S. Förster, U. Beisiegel, G. Adam, H. Weller, Nano Letters, 7 (2007) 2422-2427.

[11] Z. Ali, A.Z. Abbasi, F. Zhang, P. Arosio, A. Lascialfari, M.F. Casula, A. Wenk, W. Kreyling, R. Plapper, M. Seidel, R. Niessner, J. Knoll, A. Seubert, W.J. Parak, Analytical Chemistry, 83 (2011) 2877-2882.

[12] U. Kaiser, D.J.d. Aberasturi, R. Malinowski, F. Amin, W.J. Parak, W. Heimbrodt, Applied Physics Letters, 104 (2014) 41901-41904.

[13] E. Caballero-Díaz, C. Pfeiffer, L. Kastl, P. Rivera-Gil, B. Simonet, M. Valcárcel, J. Jiménez-Lamana, F. Laborda, W.J. Parak, Particle and Particle Systems Characterization, 30 (2013) 1079-1085.

[14] T. Pellegrino, R.A. Sperling, A.P. Alivisatos, W.J. Parak, J. Biomed. Biotechnol., Article ID 26796 (2007) 1-9.

[15] R.A. Sperling, T. Pellegrino, J.K. Li, W.H. Chang, W.J. Parak, Advanced Functional Materials, 16 (2006) 943-948.

[16] S.J. Soenen, B.B. Manshian, A.M. Abdelmonem, J.-M. Montenegro, S. Tan, L. Balcaen, F. Vanhaecke, A.R. Brisson, W.J. Parak, S.C.D. Smedt, K. Braeckmans, Particle & Particle Systems Characterization, 31 (2014) 794-800.

[17] R.A. Sperling, T. Liedl, S. Duhr, S. Kudera, M. Zanella, C.-A.J. Lin, W.H. Chang, D. Braun, W.J. Parak, J. Phys. Chem. C, 111 (2007) 11552-11559.

[18] P. Rivera Gil, D. Jimenez de Aberasturi, V. Wulf, B. Pelaz, P. del Pino, Y. Zhao, J. de la Fuente, I. Ruiz de Larramendi, T. Rojo, X.-J. Liang, W.J. Parak, Accounts of Chemical Research, 46 (2013) 743-749.

[19] A. Carpenter, T. Jones, M. Lamprecht, C. Clarke, I. Kang, O. Friman, D. Guertin, J. Chang, R. Lindquist, J. Moffat, P. Golland, D. Sabatini, Genome Biology, 7 (2006) R100.

[20] Y. Liu, T. Jiang, C. Zhang, T.R. Jones, A. Carpenter, P. Golland, Voronoi-Based Segmentation of Cells on Image Manifolds, Computer Vision for Biomedical Image Applications, Springer Berlin Heidelberg2005, pp. 535-543.

[21] M. Sezgin, B.l. Sankur, Journal of Electronic Imaging, 13 (2004) 146-168.

[22] M.V. Boland, M.K. Markey, R.F. Murphy, Cytometry, 33 (1998) 366-375.

[23] R.M. Haralick, Proceedings of the IEEE, 67 (1979) 786-804.

[24] M. Mahmoudi, A.M. Abdelmonem, S. Behzadi, J.H. Clement, S. Dutz, M.R. Ejtehadi, R. Hartmann, K. Kantner, U. Linne, P. Maffre, S. Metzler, M.K. Moghadam, C. Pfeiffer, M. Rezaei, P. Ruiz-Lozano, V. Serpooshan, M.A. Shokrgozar, G.U. Nienhaus, W.J. Parak, ACS Nano, 7 (2013) 6555-6562.

[25] J. O'Brien, I. Wilson, T. Orton, F.o. Pognan, European Journal of Biochemistry, 267 (2000) 5421-5426.
[26] T. Mosmann, Journal of Immunological Methods, 65 (1983) 55-63.
[27] A. Salic, T.J. Mitchison, Proceedings of the National Academy of Sciences, 105 (2008) 2415-2420.
[28] G. Thoelking, B. Reiss, J. Wegener, H. Oberleithner, H. Pavenstaedt, C. Riethmuller, Nanotechnology, 21 (2010).
[29] B. Rothen-Rutishauser, D.A. Kuhn, Z. Ali, M. Gasser, F. Amin, W.J. Parak, D. Vanhecke, A. Fink, P. Gehr, C. Brandenberger, Nanomedicine, 9 (2014) 607-621.
[30] D. Mandrell, L. Truong, C. Jephson, M.R. Sarker, A. Moore, C. Lang, M.T. Simonich, R.L. Tanguay, Journal of Laboratory Automation, 17 (2012) 66-74.
[31] L. Truong, S.L. Harper, R.L. Tanguay, Evaluation of embryotoxicity using the zebrafish model, Drug Safety Evaluation, Springer2011, pp. 271-279.
[32] L. Truong, D.M. Reif, L. St Mary, M.C. Geier, H.D. Truong, R.L. Tanguay, Toxicological Sciences, 137 (2014) 212-233.

Nanoparticle Uptake

International Edition: DOI: 10.1002/anie.201511733
German Edition: DOI: 10.1002/ange.201511733

Basic Physicochemical Properties of Polyethylene Glycol Coated Gold Nanoparticles that Determine Their Interaction with Cells

Pablo del Pino[+], Fang Yang[+], Beatriz Pelaz[+], Qian Zhang, Karsten Kantner, Raimo Hartmann, Natalia Martinez de Baroja, Marta Gallego, Marco Möller, Bella B. Manshian, Stefaan J. Soenen, René Riedel, Norbert Hampp, and Wolfgang J. Parak**

Abstract: *A homologous nanoparticle library was synthesized in which gold nanoparticles were coated with polyethylene glycol, whereby the diameter of the gold cores, as well as the thickness of the shell of polyethylene glycol, was varied. Basic physicochemical parameters of this two-dimensional nanoparticle library, such as size, ζ-potential, hydrophilicity, elasticity, and catalytic activity ,were determined. Cell uptake of selected nanoparticles with equal size yet varying thickness of the polymer shell and their effect on basic structural and functional cell parameters was determined. Data indicates that thinner, more hydrophilic coatings, combined with the partial functionalization with quaternary ammonium cations, result in a more efficient uptake, which relates to significant effects on structural and functional cell parameters.*

The role of basic physicochemical parameters of the NPs towards their interaction with cells is still not fully unraveled.[1] The manifold final composition of the NPs makes it hard to define and measure in terms of physicochemical properties.[1] It even is complicated to synthesize a series of model NPs in which only one physicochemical property is varied, while the others are kept constant. Yet, some examples can be found in the literature, for instance, regarding size,[2] shape,[3] stiffness,[4] or surface charge.[5]

In the present study, an array of NPs was synthesized, which takes into account the hybrid nature of NPs. Au NPs and polyethylene glycol (PEG) were used as main constituents of a series of PEGylated colloids, whereby the diameter of the inorganic Au cores d_C as well as the thickness of the PEG shell $1/2\,d_S$ was varied (Figure 1). In detail, differently sized citrate-capped Au NPs ($d_C \approx 14$, 18, 23, and 28 nm[6]) were saturated with four different HS-PEG-COOH polymers with increasing molecular weight (ca. 1, 3, 5, and 10 kDa), thereby providing NPs with increasing shell thickness $1/2\,d_S$.

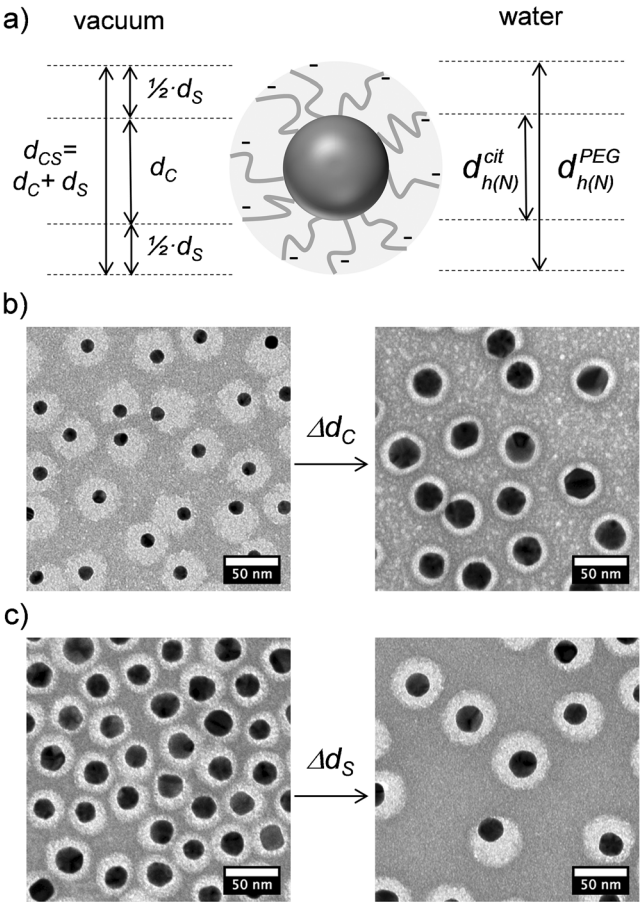

Figure 1. a) PEGylated Au NPs, showing different properties in vacuum and in solution. d_C and d_{CS} refer to the diameters of the Au cores and of the cores with the PEG shell (the core–shell system), respectively, as determined by transmission electron microscopy (TEM). $d^{cit}_{h(N)}$ and $d^{PEG}_{h(N)}$ refer to the hydrodynamic diameters as obtained from the number distribution with dynamic light scattering (DLS) of the originally citric acid stabilized Au NPs before PEGylation and of the PEGylated NPs, respectively. b) Negative staining TEM images of two types of PEGylated NPs are shown, in which d_C increases, while d_{CS} is kept constant at ca. 38 nm. c) Negative staining TEM images of two types of PEGylated NPs are shown, in which d_{CS} increases while d_C is kept constant at ca. 23 nm. Scale bar: 50 nm.

[*] Dr. P. del Pino,[+] Dr. B. Pelaz,[+] Dr. Q. Zhang, K. Kantner, R. Hartmann, Prof. Dr. W. J. Parak
Fachbereich Physik, Philipps Universität Marburg
Marburg (Germany)
E-mail: wolfgang.parak@physik.uni-marburg.de
Dr. P. del Pino,[+] Dr. N. Martinez de Baroja, M. Gallego, M. Möller, Prof. Dr. W. J. Parak
CIC biomaGUNE, San Sebastian (Spain)
E-mail: pdelpino@cicbiomagune.es
F. Yang,[+] R. Riedel, Prof. Dr. N. Hampp
Fachbereich Chemie, Philipps Universität Marburg
Marburg (Germany)
Dr. B. B. Manshian, Dr. S. J. Soenen
Radiology Department, KULeuven Campus Gasthuisberg
Leuven (Belgium)
[+] These authors contributed equally to this work.
Supporting information and the ORCID identification number(s) for the author(s) of this article can be found under http://dx.doi.org/10.1002/anie.201511733.

This in total provides an array of $4 \times 4 = 16$ samples in which each core was combined with each PEG (see the Supporting Information). In this way, a size range d_{CS} from ca. 20 to 60 nm, widely used in cell studies (50 nm has been suggested as optimal for cell uptake[7]), was studied in detail.

A large set of basic physicochemical properties was determined for all NPs of the NP library. As measurements were carried out upon variation of two parameters (d_C and d_{CS}), dependencies in a two-dimensional parameter space can be systematically analyzed. This involves analysis of the NPs properties upon α) keeping the whole size d_{CS} of the NP constant ($\Delta d_{CS} = 0$), by increasing the size of the Au core ($\Delta d_C > 0$) and decreasing the thickness of the PEG shell ($\Delta d_S < 0$); β) simultaneously increasing the diameter of the NP core ($\Delta d_C > 0$) and the thickness of the PEG shell ($\Delta d_S > 0$); χ) keeping the core diameter constant ($\Delta d_C = 0$) and increasing the thickness of the PEG shell ($\Delta d_S > 0$); and δ) increasing the thickness of the PEG shell ($\Delta d_S > 0$) and reducing the core diameter ($\Delta d_C < 0$; Figure 2).

The degree of PEGylation is expressed in terms of the parameter $R_{PEG}^{TEM} = \frac{d_S}{d_C + d_S}$ (Figure 2b). R_{PEG}^{TEM} equals 0 or 1 if the whole size (d_{CS}) comes from the Au core or the PEG shell, respectively. It is increased upon increasing the thickness of the PEG shell or by reducing the core diameter. As the first parameter, the meso-equilibrium interfacial tension γ_m of the NPs is analyzed (Figure 2c and the Supporting Information). A high γ_m indicates a more hydrophilic NP surface, whereas a low γ_m indicates more hydrophobic NP surfaces.[8] γ_m almost does not depend on the size of the Au NP core, but strongly increases (that is, hydrophilicity increases) upon decreasing the contribution of the amphiphilic PEG shell to d_{CS}, which is opposite to the increase in R_{PEG}^{TEM}. This indicates that surface tension and thus hydrophilicity of the Au NPs are influenced by the thickness of the PEG shell. The amphiphilic character of PEG motivates this apparently counterintuitive trend. Notice also that for the carboxylic-terminated PEGs used here, the higher the molecular weight, the smaller the ratio of ethylene glycol units to the carboxylic groups per NP results.

The Young's modulus E of the NPs is only mildly affected upon variation of d_C (direction α) in the explored range, either in air (E_A) or water (E_W; Figure 2d,e). Surprisingly, E increases upon increasing d_{CS} (direction χ). That is, thicker PEG coatings result in stiffer colloids. This can actually be explained by the high PEG packing density achieved, as deduced from the similar values of R_{PEG}^{TEM} and R_{PEG}^{DLS} (see the Supporting Information). Notice that smaller values of R_{PEG}^{TEM} (inferred from negative staining TEM, vacuum) than of R_{PEG}^{DLS} (inferred from DLS, water) could have been expected due to hydration; however, they are very similar. Yet, for any of the samples studied, E_W values are significantly larger than the equivalent ones in air E_A (that is, GPa vs. MPa), which suggests that water molecules stiffen inter-PEG interactions. This is actually in contradiction with a previous report about the mechanical properties of PEGylated surfaces.[9] Yet, PEG packing density plays a determining role with respect to the mechanical properties of PEGylated surfaces. E_W values obtained here are in the same order of magnitude than E_W reported for viruses (ca. 0.12–2 GPa[10]) or those reported for BSA-coated Au NPs (ca. 1–2 GPa[11]), and clearly above those reported for natural vesicles or liposomes (ca. 0.01–0.1 GPa[12]).

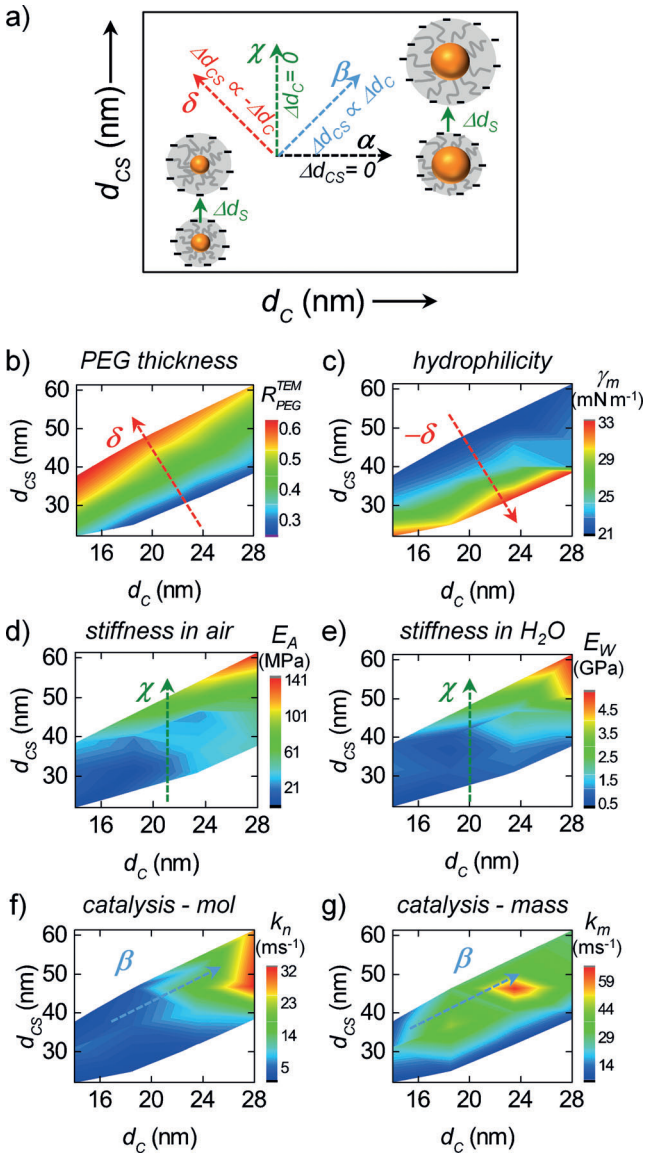

Figure 2. a) Different variables related to the size of the PEGylated Au NPs. b)–g) Heatmaps of different physicochemical properties of the NPs in dependence of d_{CS} and d_C. The color code refers to b) the proportion of PEG in the NP size R_{PEG}^{TEM}, c) the meso-equilibrium interfacial tension γ_m (that is, hydrophilicity), d) the Young's modulus (modulus of elasticity) in air E_A, e) the Young's modulus in water E_W, f) the catalytic activity k_n at equal number of NPs, and g) the catalytic activity at equal mass of gold k_m. The parameters α, β, χ, and δ are used to describe variations of d_C and/or d_S when $\Delta d_{CS} = 0$, $\Delta d_{CS} \propto \Delta d_C$, $\Delta d_C = 0$ and $\Delta d_{CS} \propto -\Delta d_C$, respectively. In panels (b)–(g), the dashed arrows point at the main variation in each case (that is, δ, −δ, χ, or β).

Catalytic activity of the NPs was assayed towards their capability to trigger the reduction of methylene blue (Figure 2f,g). Here results depend on the metrics. In case the same amount of Au NPs (ca. 0.2 nM) is used, catalytic activity scales with both the core size (d_C) and the core–shell size (d_{CS}), that is, in direction β (Figure 2f). At the same number

of NPs, the NPs with bigger cores have a much higher surface area S_{NP} ($S_{NP} \propto d_C^2$), which typically will result in higher catalytic activity. On the other hand, in case the number of Au atoms (ca. 30 mg L^{-1}) is kept constant (Figure 2g), for smaller cores there are more NPs in solution as compared to NPs with bigger d_C. For this reason it would be expected that an increase of surface reactivity should scale antiproportionally to d_C, as for smaller cores there are more NPs in solution. While this was found to be true for medium- to large-sized Au NPs (d_C from 24–28 nm at $d_{CS} \approx 45$ nm), for smaller NPs (d_C from 14–24 nm at $d_{CS} \approx 45$ nm) the opposite behavior is observed. We speculate that this is due to the presence of the PEG shell. Along the direction α the relative contribution of the PEG shell decreases. Very small cores are coated by a very thick shell of PEG, which may hinder diffusion of the methylene blue to the NP surface, and thus the thicker the PEG shell and the smaller the Au cores, the lower the catalytic activity.

In a next step we wanted to investigate the effect of these NPs on basic cellular parameters. From the 16 samples evaluated, we choose 4 samples with a fixed overall diameter $d_{CS} \approx 38$ nm, from "small" Au cores with thick PEG shell towards "large" Au cores with thin PEG shell. Thus, 4 samples with approximately equal d_{CS} and E_W, but varying γ_m and catalytic activity (k), were selected. As for observing NP uptake with fluorescence microscopy terminal carboxylic groups of the PEGs at the NP surface were partially covalently cross-linked with an amino-modified NIR dye (dyomics dy647P1) via EDC (1-ethyl-3-(3-dimethylaminopropyl)carbodiimide) chemistry (Figure 3a). Also, as internalization of NPs by cells highly depends on charge,[5] optionally, a quaternary ammonium group (2-aminoethyl trimethylammonium chloride hydrochloride, positive in all of the pH range) was also covalently attached to the surface of the NPs. In this way two sets of four different fluorescence-labeled Au NPs were created, in which the overall NP diameter $d_{CS} \approx 38$ nm was kept constant, but the proportion of PEGylation was reduced in direction α (Figure 3b). ζ-potential measurements as shown in Figure 3c demonstrate that attachment of a fluorescence label, and optionally quaternary ammonium groups, can modify the surface properties of NPs by partially neutralizing the net negatively charge of the NPs.

The two series of fluorescently labeled NPs (2 × 4 samples) were incubated with two cell lines, murine C17.2 neural progenitor and primary human umbilical vein endothelial cells (HUVECs). Following previously described protocols,[13] the following cellular parameters were analyzed: autophagy (*LC3*), cell area (*A*), endosome size (S_E), membrane damage (*MD*), mitochondrial health (*MH*), reactive oxidative species (*ROS*), cell skewness (*SK*), cell viability (*V*), and focal adhesion (*FA*). For cellular exposure studies, cells were incubated with the NPs at an equal number of NPs (1.25, 2.5, or 5 nM) or at equal mass of gold (62.5, 125, or 250 μg mL^{-1}; see the Supporting Information). The NP uptake (N_i) was determined by ICP-MS. First, the NPs with the added quaternary ammonium groups were incorporated by cells to a higher extend than the quaternary ammonium non-modified NPs (Figure 3e). Upon exposing cells to the same number of NPs, with the same overall diameter d_{CS} but different contribution of the PEG shell, NP uptake differs along direction α. Uptake seems to be correlated with the presence of quaternary ammonium groups, as in every case the presence of this group significantly enhances NP uptake. Interestingly, uptake is not directly related to the ζ-potential, as can be observed by comparing the middle and right panels in Figure 3c and 3e, that is, samples with the same ζ-potential present quite different uptakes (for example, $d_C \approx 14$ in the middle panel compared to $d_C \approx 24$ in the right panel). NP

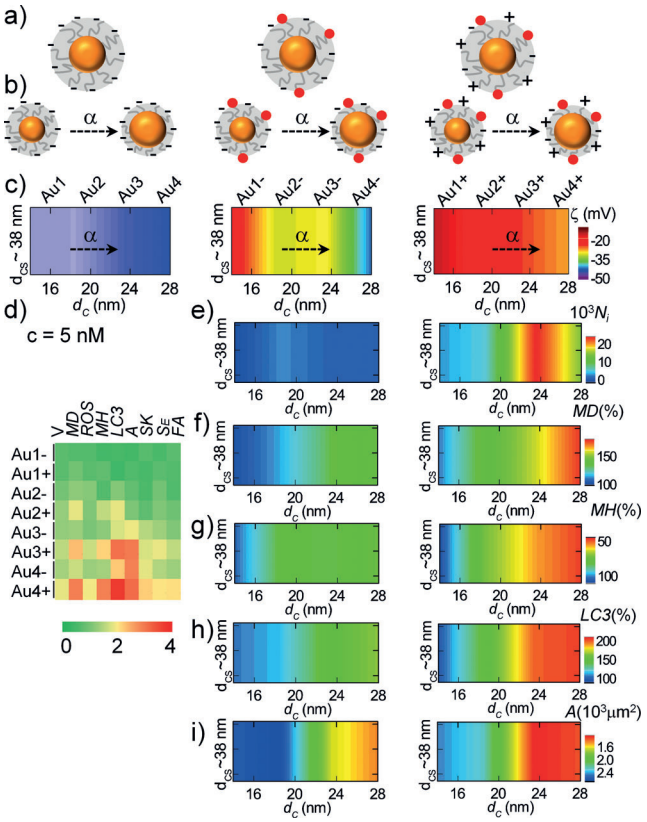

Figure 3. a) The NP geometry: bare (left) and fluorescence-labeled (middle, right) PEGylated NPs. In the case of the NPs shown on the right, additional quaternary ammonium groups (+) were coupled to some of the negatively charged carboxyl termini (−) of the PEG molecules. b) For each type of NP a series of 4 samples with the same NP size d_{CS}, but variable core diameter (Au1, Au2, Au3, Au4) and thickness of the PEG shell along direction α was prepared. c) ζ-potential heatmaps for Au1 to Au4 (left), Au1− to Au4− (middle), and Au1 + to Au4 + (right), respectively. d) Heatmaps for various reporters related to structural and functional cell parameters (*V*: viability; *MD*: membrane damage; *ROS*: production of reactive oxidative species; *MH*: mitochondrial health; *LC3*: autophagy; *A*: cell area; *SK*: cell skewness; S_E: endosomal size; *FA*: focal adhesion) for the NPs given at equal number (5 nM) to C17.2 cells, where Au1, Au2, Au3 and Au4 represent Au NPs with ca. the same d_{CS} (ca. 38 nm) yet PEGylated with ca. 10, 5, 3, and 1 kDa HS-PEG-COOH, respectively; the signs − and + stand for without and with addition of quaternary ammonium groups, respectively. e) Heatmaps for NPs internalized per cell (N_i). f)–i) Heatmaps for selected parameters, that is, more affected *MD*, *MH*, *LC3*, and *A*, related to basic cellular parameters for the NPs given to C17.2 cells, for the fluorescence labeled NPs without (middle column) and with addition of quaternary ammonium groups (right column).

uptake does not seem to directly depend on only one of the physicochemical parameters studied here (see Figure 2). It could be speculated that hydrophilicity (γ_m along α at $d_{CS} \approx 38$ in Figure 2c) plays a role on NP uptake; however, quaternary ammonium non-coupled and coupled equivalent colloids present very different NP uptake profiles, although γ_m is only mildly affected by functionalization with the dye and the quaternary ammonium group (see the Supporting Information for a comparison of γ_m for Au3− and Au3+, the most internalized species).

The impact of PEGylation along direction χ on NP uptake has been already investigated in previous work,[14] which concluded that NP uptake decreases in the direction χ due to the molecular weight of the PEG. Here in the direction α, we do not observe a linear trend with respect to the length of the PEG. Clearly, the architecture used in each case as a profound impact on the results, which illustrates how challenging is to draw general conclusions, even when comparing a model system such PEGylated NPs. We can conclude that the combination of more hydrophilic and partial coupling of quaternary ammonium groups results in a more efficient NP uptake, which is probably due to the interaction with negatively charged heparan proteoglycan sulfate receptors on the cell membrane.[15] The data with regard to cell function and structural parameters are intimately related to NP uptake. That is, when NPs are given at equal number of NPs, more NP uptake has a clear negative effect on membrane damage (Figure 3f), mitochondrial health (Figure 3g), autophagy (Figure 3h), and cell area (Figure 3i), whereas the other parameters are less affected compared to the control cells (Figure 3d). Gene expression (for a total of 84 genes involved in cytoskeletal signaling and regulation) results for C17.2 cells also indicate highest levels of upregulation in more internalized NPs, indicating clear alterations in cytoskeletal architecture and regulation, which is in line with the imaging results (see the Supporting Information).

The same cell study was also carried out with HUVEC cells, yielding similar results. Likewise, when cells (either C17.2 or HUVEC) were incubated with NPs at equal mass of gold similar trends were found (see the Supporting Information), although in general cells were less and slightly differently affected (for example, viability is more affected), which is probably due to less NP uptake. Notice that, however, in case of equal mass of gold, NPs with smaller d_C (direction α) were more efficiently internalized. This is due to the metrics, that is, a concentration of 250 μg mL^{-1} correspond to a relative number of NPs of ca. 8.5:3.5:1.7:1, with diameter of ca. 14, 18, 23, and 28 nm, respectively. Nevertheless, even though more "small" NPs were added and thereby were more internalized, the amount of gold found in the cells (mass of gold per cell) was bigger for the "larger" NPs, which however did not negatively affect the cells.

The fundamental problem in correlating the interaction of PEGylated NPs with cells with their physicochemical properties is that many basic physicochemical parameters of the NPs, such as size, ζ potential, hydrophilicity, elasticity, and catalytic activity depend on the "type" of PEGylated Au NP (Figure 2). To account for changes in size, which may be as well due to differences in core diameter as in thickness of the PEG shell, a two-dimensional array of NPs had been synthesized in this work. In contrast to previous studies found in literature, in the present work thus a homologous NP library had been created, in which not only one parameter (that is, one dimension), but two parameters (that is, two dimensions) had been varied. Analysis of the dependence of physicochemical properties of the NPs due to PEGylation as shown in Figure 2 suggests that hydrophilicity (as quantified here in terms of γ_m) is the parameter most directly influenced by PEGylation. R_{PEG}^{TEM} and γ_m increase in opposite directions as indicated in Figure 2a. In contrast to other NP libraries,[16] PEGylation does not largely influence NP elasticity (E_A and E_W) and catalytic activity (k_n), where only thick PEG shells may reduce diffusion of reagents to the NP core.

Concerning interaction with cells, in previous work we had investigated the effect of the thickness of the PEG shell with the NP core size kept constant, that is, variation in direction χ.[14] In the present work we focused on variation in direction α, that is, variation of the PEG shell contribution upon keeping the total NP diameter constant. In direction α, γ_m clearly increases (Figure 2c), that is, reduction in PEGylation (R_{PEG}^{TEM} decreases in direction α) makes NPs more hydrophilic. PEG on the other hand is amphiphilic, that is, soluble in aqueous solution as in some less polar solvents such as chloroform. More hydrophilic NPs are incorporated best by cells (Figures 2c and Figure 3e), yet not in a linear fashion. Comparing Figures 3c and 3e suggests that the presence of quaternary ammonium groups combined with hydrophilicity is the more direct parameter, as changes in ζ potential (Figure 3c) are not directly translated into changes in NP internalization (Figure 3e). Note that we are referring here to the number of the incorporated NPs (Figure 3e), which forms a different metrics than the volume of incorporated NPs (Supporting Information). Reduction of cellular function and structure goes directly hand-in-hand with increased uptake of NPs (compare Figures 3f–i with Figure 3e). While PEGylation can have some effect on catalytic activities of NPs, the data from Figures 2f,g and Figure 3e rather suggest that reduction in cellular function and structure of cells is not directly an effect of changes of catalytic activity upon PEGylation, but rather due to changes of the amount of incorporated NPs.

In summary, the data obtained in this study indicate that PEGylated Au NPs may be designed to present many different physicochemical properties ("faces") and thus interact differently with cells, even when keeping the size d_{CS} constant. Effects of NPs on cellular function and structure for these NPs mainly scale with the amount of incorporated NPs, highly dependent on both partial functionalization with quaternary ammonium groups and the thickness of the PEG shell (lower for NPs with "thick" PEG coatings).

Acknowledgements

Parts of this work were supported by the European Commission (project FutureNanoNeeds, grant to W.J.P.), and by the MINECO (project MAT2013-48169-R to W.J.P. and P.d.P.). B.P. acknowledges a postdoctoral fellowship from the

Alexander von Humboldt Foundation. Q.Z. acknowledges a graduate student fellowship for the Chinese Scholarship Council (CSC). S.J.S. is a post-doctoral fellow from the FWO Vlaanderen. B.B.M. acknowledges the FWO Vlaanderen (Krediet aan Navorsers 1514716N).

Keywords: gold nanoparticles · nanoparticle uptake · physicochemical properties · polyethylene glycol · toxicity

[1] P. Rivera-Gil, D. Jimenez de Aberasturi, V. Wulf, B. Pelaz, P. del Pino, Y. Zhao, J. de la Fuente, I. Ruiz de Larramendi, T. Rojo, X.-J. Liang, W. J. Parak, *Acc. Chem. Res.* **2013**, *46*, 743.
[2] K. Li, M. Schneider, *J. Biomed. Opt.* **2014**, *19*, 101505.
[3] B. D. Chithrani, W. C. W. Chan, *Nano Lett.* **2007**, *7*, 1542.
[4] L. Zhang, Z. Cao, Y. Li, J.-R. Ella-Menye, T. Bai, S. Jiang, *ACS Nano* **2012**, *6*, 6681.
[5] D. Hühn, K. Kantner, C. Geidel, S. Brandholt, I. De Cock, S. J. H. Soenen, P. Rivera Gil, J.-M. Montenegro, K. Braeckmans, K. Müllen, G. U. Nienhaus, M. Klapper, W. J. Parak, *ACS Nano* **2013**, *7*, 3253.
[6] N. G. Bastús, J. Comenge, V. Puntes, *Langmuir* **2011**, *27*, 11098.
[7] B. D. Chithrani, A. A. Ghazan, C. W. Chan, *Nano Lett.* **2006**, *6*, 662.
[8] S. Rana, X. Yu, D. Patra, D. F. Moyano, O. R. Miranda, I. Hussain, V. M. Rotello, *Langmuir* **2012**, *28*, 2023.
[9] X. Wang, R. N. Sanderson, R. Ragan, *J. Phys. Chem. C* **2014**, *118*, 29301.
[10] M. G. Mateu, *Virus Res.* **2012**, *168*, 1.
[11] H. P. Wampler, A. Ivanisevic, *Micron* **2009**, *40*, 444.
[12] A. Calò, D. Reguera, G. Oncins, M.-A. Persuy, G. Sanz, S. Lobasso, A. Corcelli, E. Pajot-Augy, G. Gomila, *Nanoscale* **2014**, *6*, 2275.
[13] a) B. B. Manshian, D. F. Moyano, N. Corthout, S. Munck, U. Himmelreich, V. M. Rotello, S. J. Soenen, *Biomaterials* **2014**, *35*, 9941; b) B. B. Manshian, S. Munck, P. Agostinis, U. Himmelreich, S. J. Soenen, *Sci. Rep.* **2015**, *5*, 13890.
[14] B. Pelaz, P. Del Pino, P. Maffre, R. Hartmann, M. Gallego, S. Rivera-Fernandez, J. M. de la Fuente, G. U. Nienhaus, W. J. Parak, *ACS Nano* **2015**, *9*, 6996.
[15] H.-B. Pang, G. B. Braun, E. Ruoslahti, *Sci. Adv.* **2015**, *1*, e1500821.
[16] R. Hartmann, M. Weidenbach, M. Neubauer, A. Fery, W. J. Parak, *Angew. Chem. Int. Ed.* **2015**, *54*, 1365; *Angew. Chem.* **2015**, *127*, 1382.

Received: December 18, 2015
Revised: February 8, 2016
Published online: ■■ ■■, ■■■■

Communications

Nanoparticle Uptake

P. del Pino,* F. Yang, B. Pelaz, Q. Zhang, K. Kantner, R. Hartmann, N. Martinez de Baroja, M. Gallego, M. Möller, B. B. Manshian, S. J. Soenen, R. Riedel, N. Hampp, W. J. Parak* _____ ■■■■–■■■■

Basic Physicochemical Properties of Polyethylene Glycol Coated Gold Nanoparticles that Determine Their Interaction with Cells

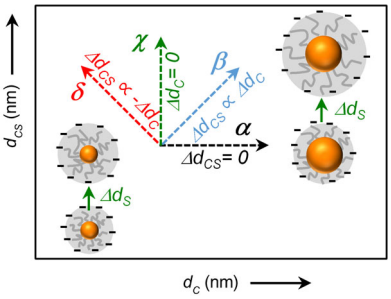

A homologous library of gold nanoparticles coated with polyethylene glycol was synthesized, whereby the diameter of the gold cores, as well as the thickness of the shell of polyethylene glycol, was varied. Basic physicochemical parameters of this two-dimensional nanoparticle library were determined. Cell uptake of selected nanoparticles and their effect on basic structural and functional cell parameters were determined.

Angewandte Chemie
Eine Zeitschrift der Gesellschaft Deutscher Chemiker

Supporting Information

Basic Physicochemical Properties of Polyethylene Glycol Coated Gold Nanoparticles that Determine Their Interaction with Cells

Pablo del Pino[+], Fang Yang[+], Beatriz Pelaz[+], Qian Zhang, Karsten Kantner, Raimo Hartmann, Natalia Martinez de Baroja, Marta Gallego, Marco Möller, Bella B. Manshian, Stefaan J. Soenen, René Riedel, Norbert Hampp, and Wolfgang J. Parak**

anie_201511733_sm_miscellaneous_information.pdf

Table of Contents:		**Page**

I) Synthesis of citrate-capped gold nanoparticles (NPs), i.e., Au cores

Five batches of Au NPs of increasing sizes (i.e., inorganic diameters – d_C) were produced using a modified protocol of the seeded growth method reported by Bastus et al.,[1] cf. Figure S.II-1. The synthesis starts with the production of NPs with diameter of ca. 9 nm (~ 6.3 nM), in the following referred to as seeds. Next, seeds were grown to produce NPs with a diameter of ca. 14 nm (~ 3.8 nM, Au1). Then, Au1, Au2 and Au3 were grown to produce NPs with diameters of ca. 19 nm (~ 2.5 nM, Au2), ca.23 nm (~ 1.3 nM, Au3) and ca. 27 nm (~ 0.8 nM, Au4), respectively. The NPs' size (d_C) was characterized by transmission electron microscopy (TEM, JEOL JEM-1400PLUS) to check the size distribution and their monodispersity, cf. Figures S.II-2, -3, -4, -5, -6. Synthetic details for the production of seeds, Au1, Au2, Au3 and Au4 are given in the following:

Synthesis of Seeds: A solution of 2.0 mM sodium citrate (Sigma Aldrich, #W302600) in ultrapure water (150 mL) was heated with a heating mantle in a 250 mL three-necked round-bottomed flask under vigorous stirring. A condenser was utilized to prevent the evaporation of the solvent. 20 min after boiling had started 1 mL of $HAuCl_4$ (25 mM, Strem Chemicals, #16903-35-8) was injected. The color of the solution changed from yellow to bluish gray and then to soft pink in 10 min.

Synthesis of Au1: Immediately after the synthesis of the seeds and in the same reaction vessel, the reaction was cooled until the temperature of the solution reached 90 °C. Then, 1 mL of a $HAuCl_4$ solution (25 mM) was injected. After 30 min, the reaction was finished. This process was repeated twice to yield Au1, i.e., two injections of $HAuCl_4$ into the seeds solution.

Synthesis of Au2: After that, the sample was diluted by extracting 55 mL of sample (Au1, ~ 3.8 nM) and adding 53 mL of ultrapure water and 2 mL of 60 mM sodium citrate. This solution was then used as a seed solution, and the growth process was repeated again, which required 2 sequential injections of 1 mL of $HAuCl_4$ solution (25 mM) into Au1, separated by 30 min time intervals at 90 °C, to produce Au2.

Synthesis of Au3: After that, the sample Au2 was diluted by extracting 55 mL of sample (Au2, ~ 2.5 nM) and adding 53 mL of ultrapure water and 2 mL of 60 mM sodium citrate. This solution was then used as a seed solution, and the process was repeated again, which required 2 sequential injections of 1 mL of $HAuCl_4$ solution (25 mM), separated by 30 min time intervals at 90 °C, to produce Au3.

Synthesis of Au4: After that, the sample Au3 was diluted by extracting 55 mL of sample (Au3, ~ 1.3 nM) and adding 53 mL of ultrapure water and 2 mL of 60 mM sodium citrate. This solution was then used as a seed solution, and the process was repeated again, which required 2 sequential injections of 1 mL of a $HAuCl_4$ solution (25 mM), separated by 30 min time intervals at 90 °C, to produce Au4 (~ 0.8 nM).

II) Characterization of NPs

Figure S.II-1 shows a photograph of colloidal solutions of NPs as prepared in aqueous solutions of citric acid (A), and the corresponding UV-Vis spectra (B). Notice that for comparison, spectra are shown normalized to 1 OD (OD: optical density) at 450 nm. The localized surface plasmon band (LSPR) is blue-shifted as the size of the NPs increases (from seeds to Au4), which also influences the maximum scattering intensity (I_{MAX}), i.e., the greater the size of the NPs, the greater the scattering intensity, cf. Table S.II-1.

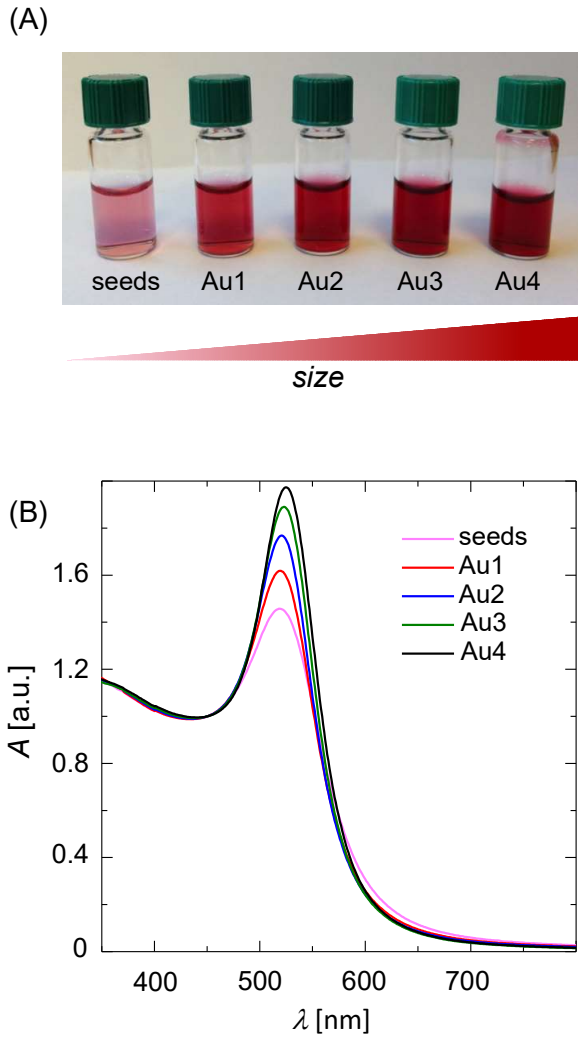

Figure S.II-1. (A) Photograph of colloidal solutions of Au NPs as synthesized in an aqueous solution of citric acid. (B) Normalized absorbance spectra A(λ) (normalization at 450 nm, maximum peak values I_{MAX}) for citrate capped NPs after different growth steps. The localized surface plasmon resonance (LSPR) peaked at λ_{LSPR} = 518, 519, 521, 523 and 525 nm after 4 growth steps.

The size distribution and mean diameter of NP's inorganic core (d_C) was determined by analyzing > 300 NPs in TEM micrographs with the free software ImageJ. Samples were prepared by deposition of a drop (3 µL) of NP solution on top of a copper grid coated with a layer of carbon. The NPs were characterized by TEM (JEOL JEM-1400PLUS) to check the size distribution and their monodispersity. In the Figures S.II-2 to S.II-6 selected TEM images and the corresponding histograms for the core diameters d_C of all the NPs are presented.

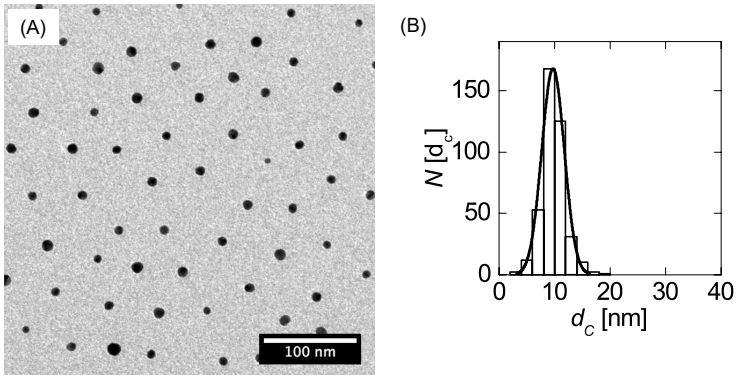

Figure S.II-2. A) TEM image of citrate capped Au seeds. B) Histogram of the size distribution of the Au cores with diameter d_C = 9.7 ± 1.9 nm. N[d_C] refers to the total counts and the scale bar corresponds to 100 nm.

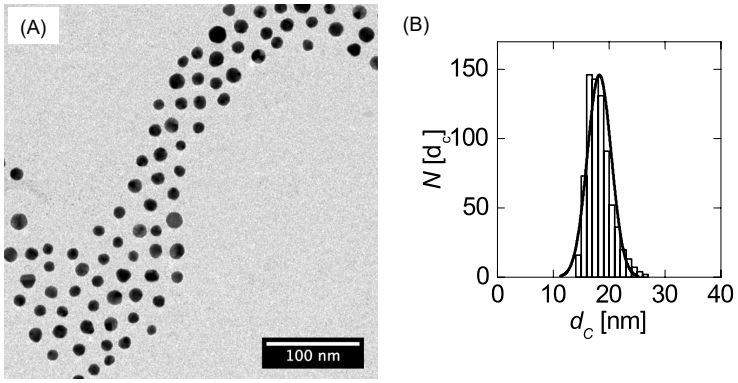

Figure S.II-3. A) TEM image of Au1. B) Histogram of the size distribution of the Au1 cores with diameter d_C = 13.8 ± 1.7 nm. N[d_C] refers to the total counts and the scale bar corresponds to 100 nm.

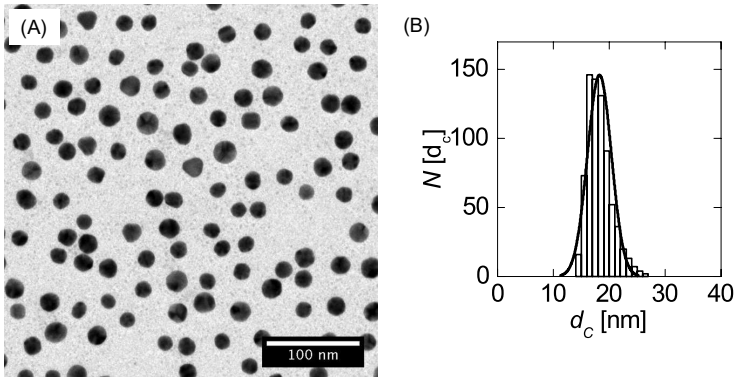

Figure S.II-4. A) TEM image of Au2. B) Histogram of the size distribution of the Au2 cores with diameter d_C = 18.5 ± 2.1 nm. N[d_C] refers to the total counts and the scale bar corresponds to 100 nm.

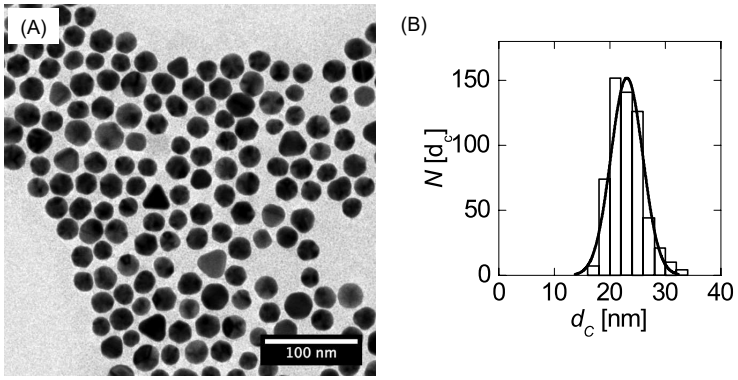

Figure S.II-5. A) TEM image of Au3. B) Histogram of the size distribution of the Au3 cores with diameter d_C = 23.5 ± 2.5 nm. N[d_C] refers to the total counts and the scale bar corresponds to 100 nm.

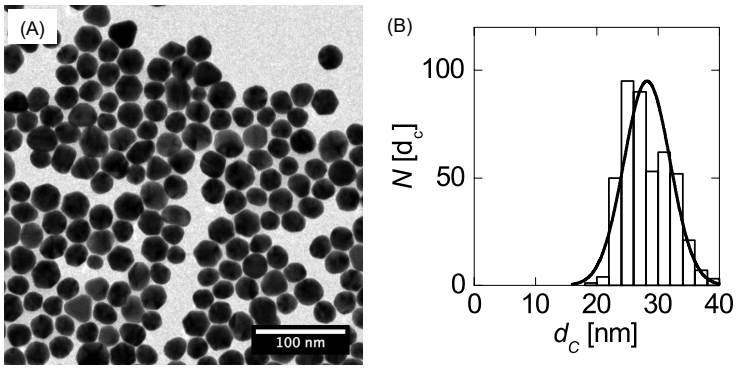

Figure S.II-6. A) TEM image of Au4. B) Histogram of the size distribution of the Au4 cores with diameter d_C = 28.0 ± 3.5 nm. N[d_C] refers to the total counts and the scale bar corresponds to 100 nm.

The concentration of the NPs was determined via UV/Vis spectroscopy (Cary 5000 Varian spectrometer) using the Beer-Lambert law, the molar extinction coefficient (ε_{450}),[2] and the absorbance values measured at 450 nm, cf., Table S.II-1. A Malvern Zetasizer was used to measure the average intensity, volume and number distribution of the hydrodynamic diameter $d_{h(I)}$, $d_{h(V)}$ and $d_{h(N)}$ (with dynamic light scattering, DLS), respectively, in the aqueous solutions of citric acid in which the NPs had been prepared. All the samples were equilibrated for 5 min at 25 °C to ensure that the changes belong to the Brownian motion and not to any thermal conversion. The NPs were measured at 173° backscatter settings, and using a 633 nm laser. The hydrodynamic diameter is a good indicator to assess the monodispersity and colloidal stability of the NPs.

Table S.II-1. Diameter of the NPs' core as determined by TEM (d_C), data from the UV-Vis spectra (λ_{LSPR} and I_{MAX}), NP's concentration values (C_{NP}, as determined by Haiss et al. [2]), mean hydrodynamic diameter in intensity ($d_{h(I)}$), volume ($d_{h(V)}$) and number ($d_{h(N)}$).

Sample	d_C [nm]	λ_{LSPR} [nm]	I_{MAX} [a.u.]	ε_{450} [$M^{-1}\cdot cm^{-1}$]	C_{NP} [nM]	$d_{h(I)}$ [nm]	$d_{h(V)}$ [nm]	$d_{h(N)}$ [nm]
seeds	9.7 ± 1.9	518	1.50	$5.6\cdot10^{7}$	6.3	–	–	–
Au1	13.8 ± 1.7	519	1.61	$1.8\cdot10^{8}$	3.8	39 ± 24	19 ± 9	14 ± 4
Au2	18.5 ± 2.1	521	1.76	$4.0\cdot10^{8}$	2.5	38 ± 19	23 ± 10	18 ± 5
Au3	23.5 ± 2.5	523	1.88	$8.8\cdot10^{8}$	1.3	36 ± 9	31 ± 8	27 ± 6
Au4	27.8 ± 3.5	525	1.98	$1.4\cdot10^{9}$	0.8	71 ± 34	43 ± 21	30 ± 9

III) PEGylation of NPs

The goal of this section is to illustrate the preparation of a series of PEGylated Au NPs with about the same $d_{h(N)}$ by DLS. We used Au1, Au2, Au3 and Au4 (increasing core size) with PEG molecules of 10, 5, 3 and 1 kDa (decreasing molecular weight $\rightarrow$ size), respectively. The selected heterofunctional chains bear a thiol group in one end, which binds to the NPs, and a carboxyl group in the other end. All of the different polyethylene glycol polymers (PEG) were obtained from Rapp-Polymere.

III.1) Saturation experiments: in order to estimate how many thiolated chains of PEG can be anchored onto citrate-capped NPs, increasing ratios of PEG per NP were added, i.e. 50, 500, 1000, 3000 and 5000 PEGs per NP (see Table S.III-1 for the concentration of the stocks). In a typical experiment, selected amounts of PEG molecules were added to a solution of 15 mL of citrate-capped NPs, to which after 2 minutes of stirring, NaOH was added to increase the pH value to 8-9 (aiming to increase the reactivity of the thiol group of the PEG). Samples were stirred overnight, and then, samples were precipitated by centrifugation (three steps). Therefore, excess of PEG and other chemicals can be washed out. Also, poorly PEGylated NPs (non saturated with PEG) would typically irreversibly agglomerate after adding NaOH and/or during centrifugation, which can be clearly seen in the UV-Vis spectra of the washed samples, cf. Figure S.III-1.

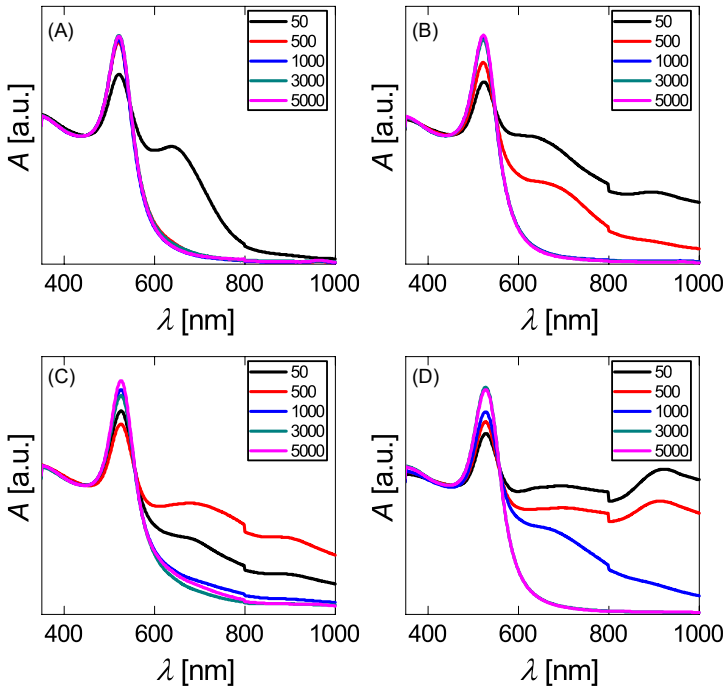

Figure S.III-1. Normalized UV-Vis absorption spectra $A(\lambda)$ of PEGylated Au NPs after three washing steps by centrifugation (12100 x g) recorded in water. A) Au1@PEG-10kDa; B) Au2@PEG-5kDa; C) Au3@PEG-3kDa; D) Au4@PEG-1kDa. The colors indicate for the number of PEG molecules added per NP.

The saturation steps clearly show that 50 and 500 chains per NPs are insufficient to produce stable colloids after precipitation, whereas 3000 and 5000 chains seems to produce stable colloids with equivalent optical features, cf. Figure S.III-1.

The different NPs were run in a 2% agarose gel at 5 $V \cdot cm^{-1}$ for 1 h in Tris-Borate-EDTA buffer (TBE 0.5x), aiming to see differences in their electrophoretic mobility which could be related to saturation by PEG chains. Please notice that PEG chains employed in this work are heterofunctional molecules with a thiol group in one end (to bind to gold) and a carboxylic group in the other end, which will be used for coupling other molecules and provide the colloids with negative charge. The gel indicated that 5000 PEG molecules per NP added confer colloidal stability to the respective NPs; furthermore NPs are saturated with 5000 PEG per NP, cf. Figure S.III-2A. Figure S.III-2B shows that Au NPs with less than 1000 PEG molecules added per NP were agglomerated, which can be clearly seen in the loading wells of the gel.

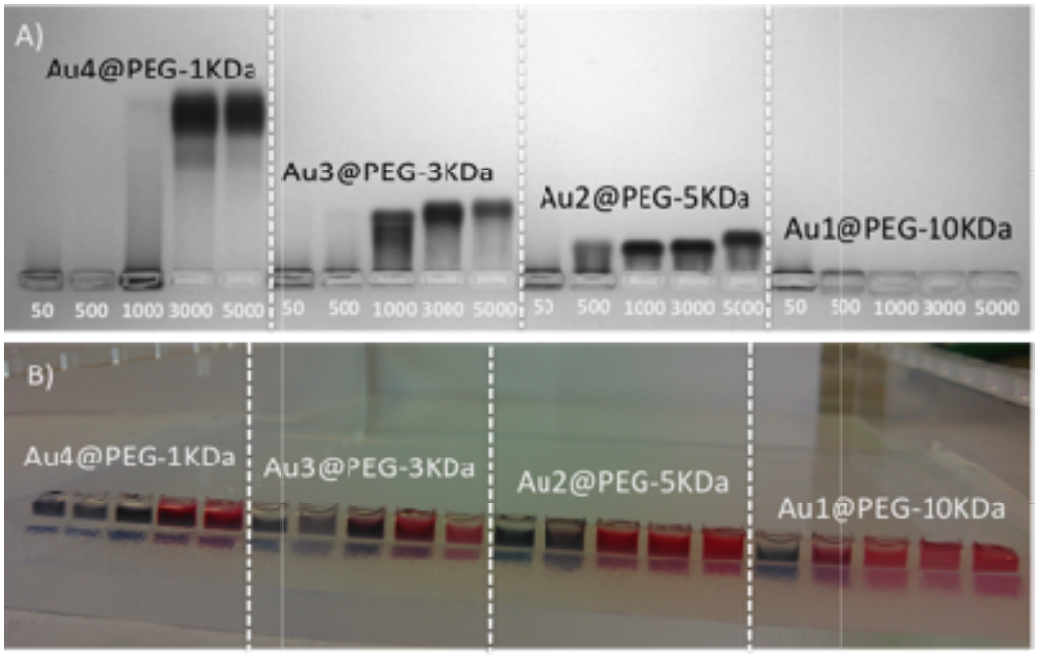

Figure S.III-2. A) Gel of PEGylated Au NPs with increasing number of PEG molecules added per NP. B) Colors of the samples in the loading wells. Agarose 2%; 5 $V \cdot cm^{-1}$; 90 min.

These samples then were analyzed by DLS in water, with the following results, as shown in Figure S.III-3 and Table S.III-1 (raw data).

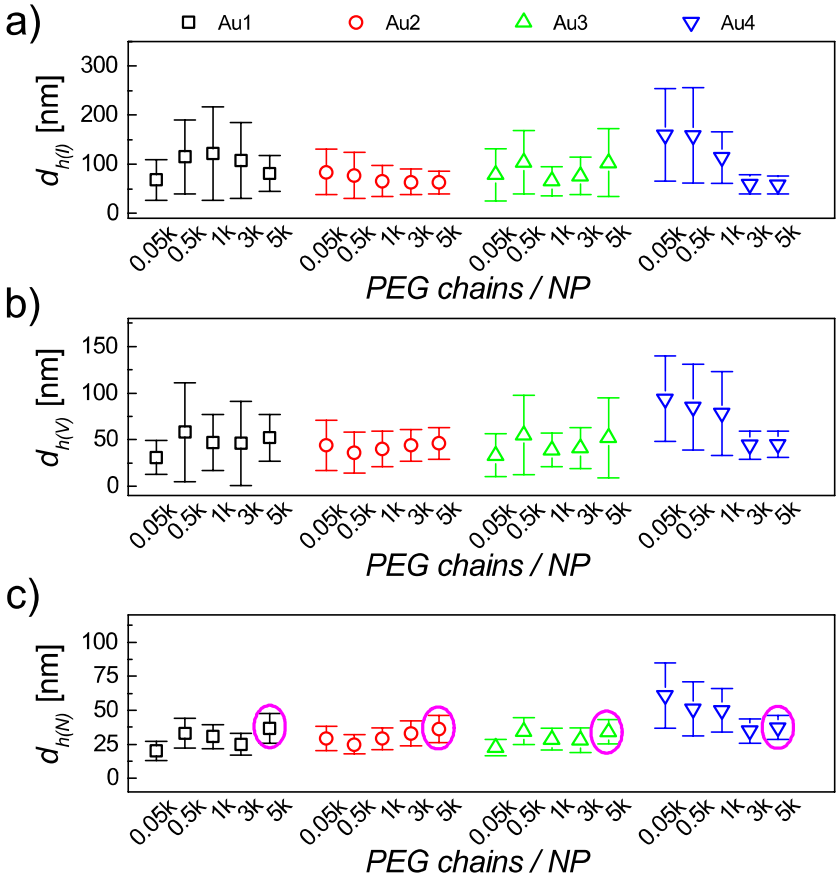

Figure S.III-3. a) Intensity, b) Volume and (b) number mean values of the hydrodynamic diameters ($d_{h(I)}$, $d_{h(V)}$ and $d_{h(N)}$, respectively) for Au1 (black squares), Au2 (red circles), Au3 (green triangles) and Au4 (blue inverted triangles), with increasing number PEG molecules added per NP. Pink open circles highlight that cores with increasing size (Au1, Au2, Au3, and Au4) PEGylated with polymer with decreasing molecular weight (10, 5, 3 and 1 kDa), respectively, result in colloids with ca. the same hydrodynamic size.

PEG saturation of Au1, Au2, Au3 and Au4 with -10kDa, -5kDa, -3kDa and PEG-1kDa, respectively, resulted in the formation of PEGylated NPs with ca. the same hydrodynamic diameter (i.e., 37 nm), yet with different size of Au cores (d_C from ca.14 to 28 nm).

Table S.III-1. Ratio of PEG chains added per NP, number of PEG chains added per nm^2 of NP. Mean hydrodynamic diameter in number ($d_{h(N)}$), volume ($d_{h(V)}$) and intensity ($d_{h(I)}$), and polydispersity index (*PDI*) for all of the PEGylated NPs as recorded in water. Notice that for low saturation (typically 50 and 500 PEG chains added per NP) the given d_h values represent the main DLS peak.

sample	*Ratio PEG:NP*	*PEG/nm²*	$d_{h(I)}$ [nm]	$d_{h(V)}$ [nm]	$d_{h(N)}$ [nm]	*PDI*
Au1@PEG-10k	50	0.08	68 ± 41	31 ± 18	20 ± 7	0.59
	500	0.84	115 ± 75	58 ± 53	33 ± 11	0.34
	1000	1.67	122 ± 95	47 ± 30	31 ± 9	0.33
	3000	5.01	108 ± 77	46 ± 45	25 ± 8	0.36
	5000	8.36	81 ± 37	52 ± 25	**37** ± 11	0.22
Au2@PEG-5k	50	0.05	84 ± 46	84 ± 27	29 ± 9	0.51
	500	0.47	78 ± 47	78 ± 22	25 ± 7	0.46
	1000	0.93	66 ± 32	68 ± 19	29 ± 8	0.25
	3000	2.79	64 ± 26	66 ± 17	33 ± 9	0.21
	5000	4.65	63 ± 23	65 ± 17	**36** ± 10	0.12
Au3@PEG-3k	50	0.03	79 ± 53	33 ± 23	23 ± 6	0.55
	500	0.29	104 ± 65	55 ± 43	35 ± 10	0.53
	1000	0.58	66 ± 30	39 ± 18	29 ± 8	0.46
	3000	1.73	76 ± 38	41 ± 22	28 ± 9	0.44
	5000	2.88	103 ± 69	52 ± 43	**34** ± 9	0.51
Au4@PEG-1k	50	0.02	160 ± 94	94 ± 46	61 ± 24	0.46
	500	0.21	159 ± 97	85 ± 46	51 ± 20	0.49
	1000	0.41	114 ± 52	78 ± 45	50 ± 16	0.41
	3000	1.24	59 ± 20	44 ± 15	35 ± 9	0.13
	5000	2.06	58 ± 18	45 ± 14	**37** ± 9	0.10

III.2. PEGylation experiments using different PEGs for the same core: Having in mind the saturation's experiments, in which by using 5000 added PEG molecules per NP all the NPs show ca. the same $d_{h(N)}$, in the following all the PEGylation experiments were performed by using 10^4 PEG molecules added per NP, thereby assuring full saturation of the PEG shell, and ca. the same $d_{h(N)}$. We combined each inorganic core, i.e., Au1-Au4, with all the different PEG shells, i.e., saturated shells of PEG with 1k, 3k, 5k, 10k Da molecular mass. Two parameters were thereby varied: the size of the core d_C and the thickness of the PEG shell $1/2d_S$ (as the PEG shell contributes to all NP surface a shell with thickness $1/2d_S$ increases the diameter by d_S). Figure S.III-4 shows a gel in which the different electrophoretic mobilities for all the different combinations are apparent. Figure S.III-5 shows the corresponding UV-Vis absorption spectra, in which it can be seen that attachment of the different PEG molecules did not affect the optical properties of the PEGylated NPs within the accuracy of the spectrometer. Figure SIII-6, -7, -8, -9 show the DLS histograms for Au1, Au2, Au3 and Au4, respectively, with all the PEG combinations.

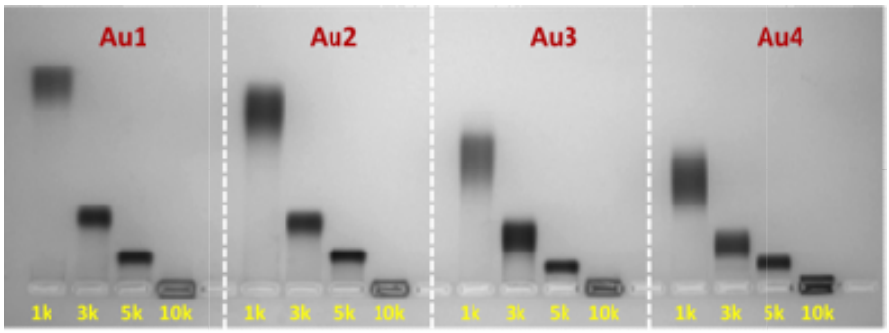

Figure S.III-4. Migration due to gel electrophoresis of Au NPs with different PEG molecule attached through a 2% agarose gel to which an electric field of $5 \cdot V\ cm^{-1}$ had been applied for 90 min. The bands of the NPs are clearly visible on the photo of the gel. Due to their negative charge the NP migrated from the wells (on the bottom of the photo) towards the plus pole (on the top of the photo).

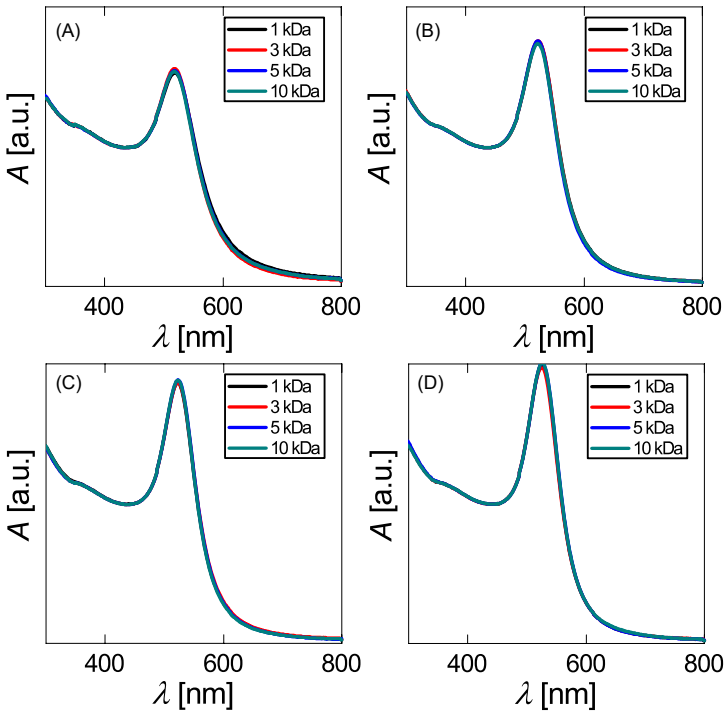

Figure S.III-5. Normalized UV-Vis absorption spectra *A(λ)* of PEGylated Au NPs after three washing steps by centrifugation (12100 x g) recorded in water. A) Au1@PEG; B) Au2@PEG; C) Au3@PEG; D) Au4@PEG. The colors indicate the molecular weight of the PEG molecules added to the NPs.

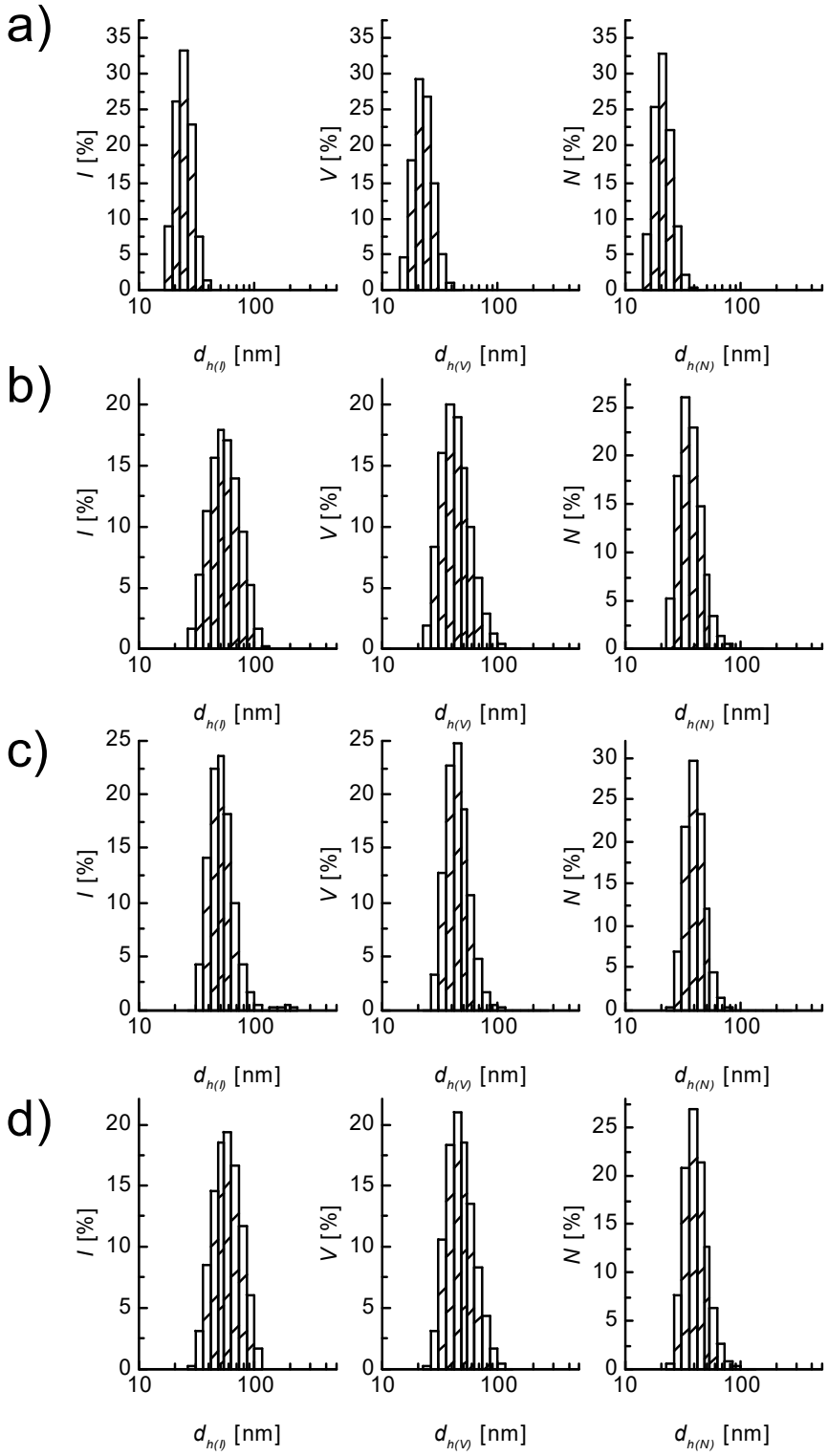

Figure SIII-6. DLS histograms for Au1 (left: Intensity; middle: Volume; right: Number) modified with a) PEG-1k, b) PEG-3k, c) PEG-5k and d) PEG-10k.

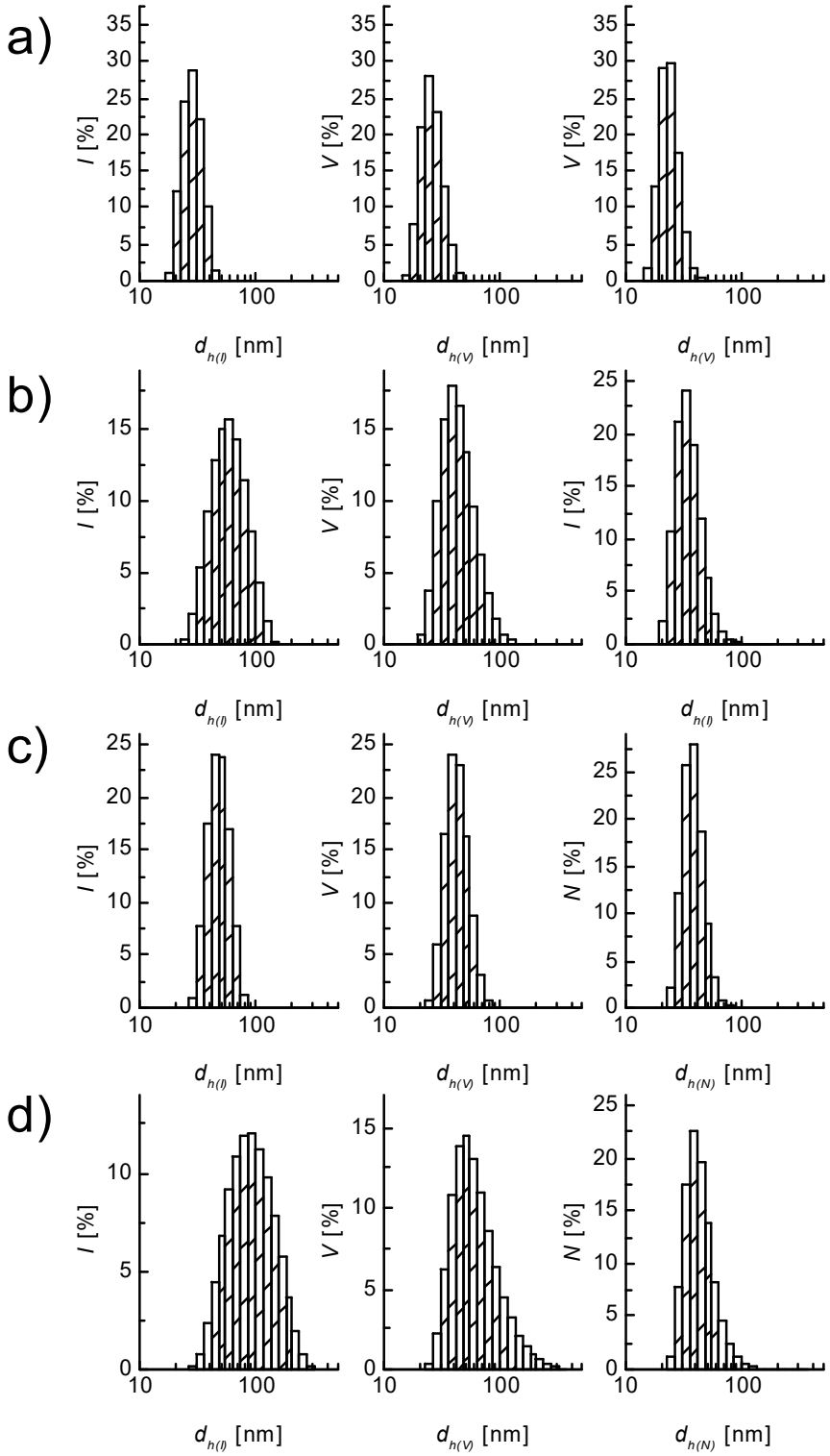

Figure SIII-7. DLS histograms for Au2 (left: Intensity; middle: Volume; right: Number) modified with a) PEG-1k, b) PEG-3k, c) PEG-5k and d) PEG-10k.

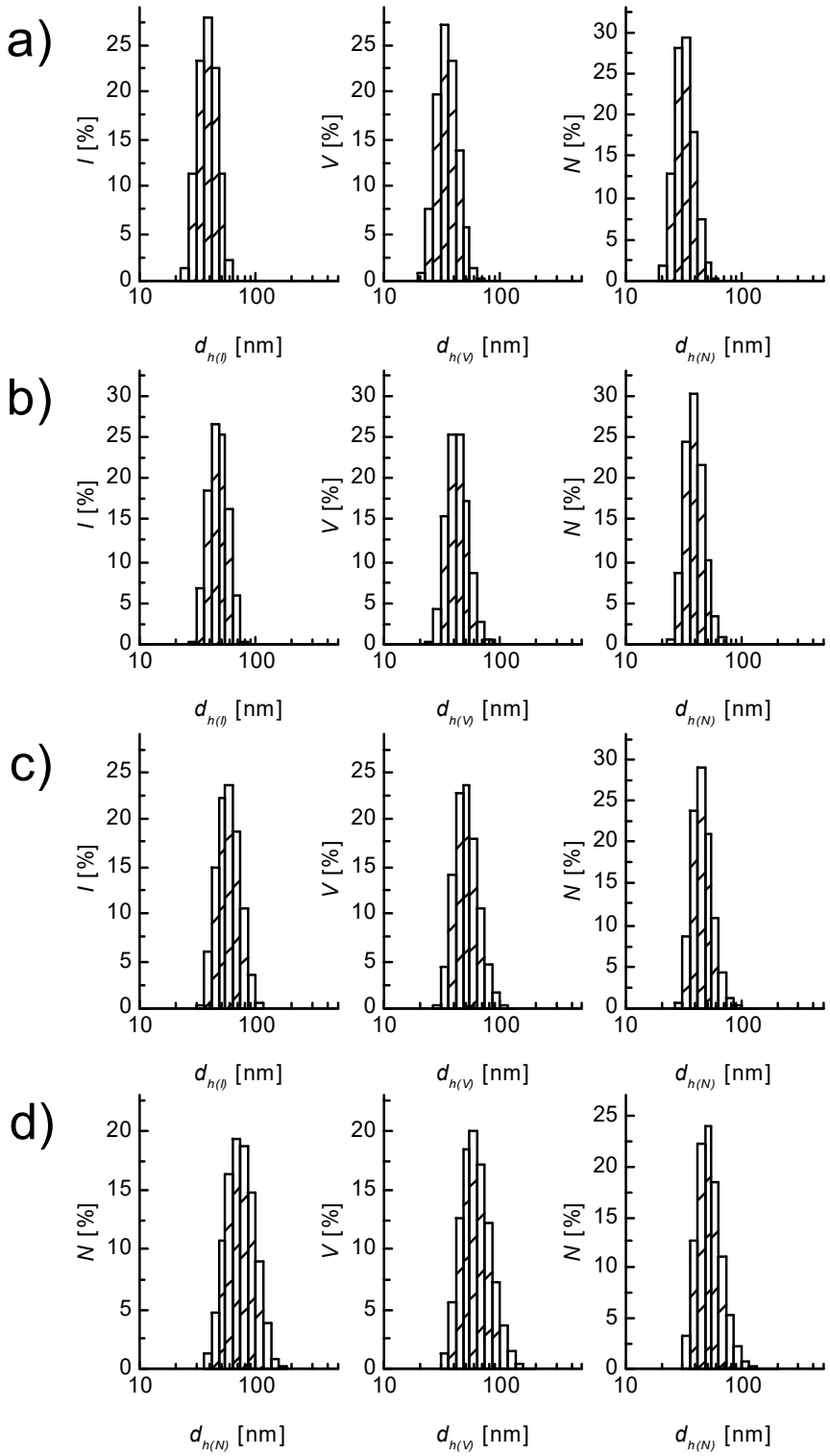

Figure SIII-8. DLS histograms for Au3 (left: Intensity; middle: Volume; right: Number) modified with a) PEG-1k, b) PEG-3k, c) PEG-5k and d) PEG-10k.

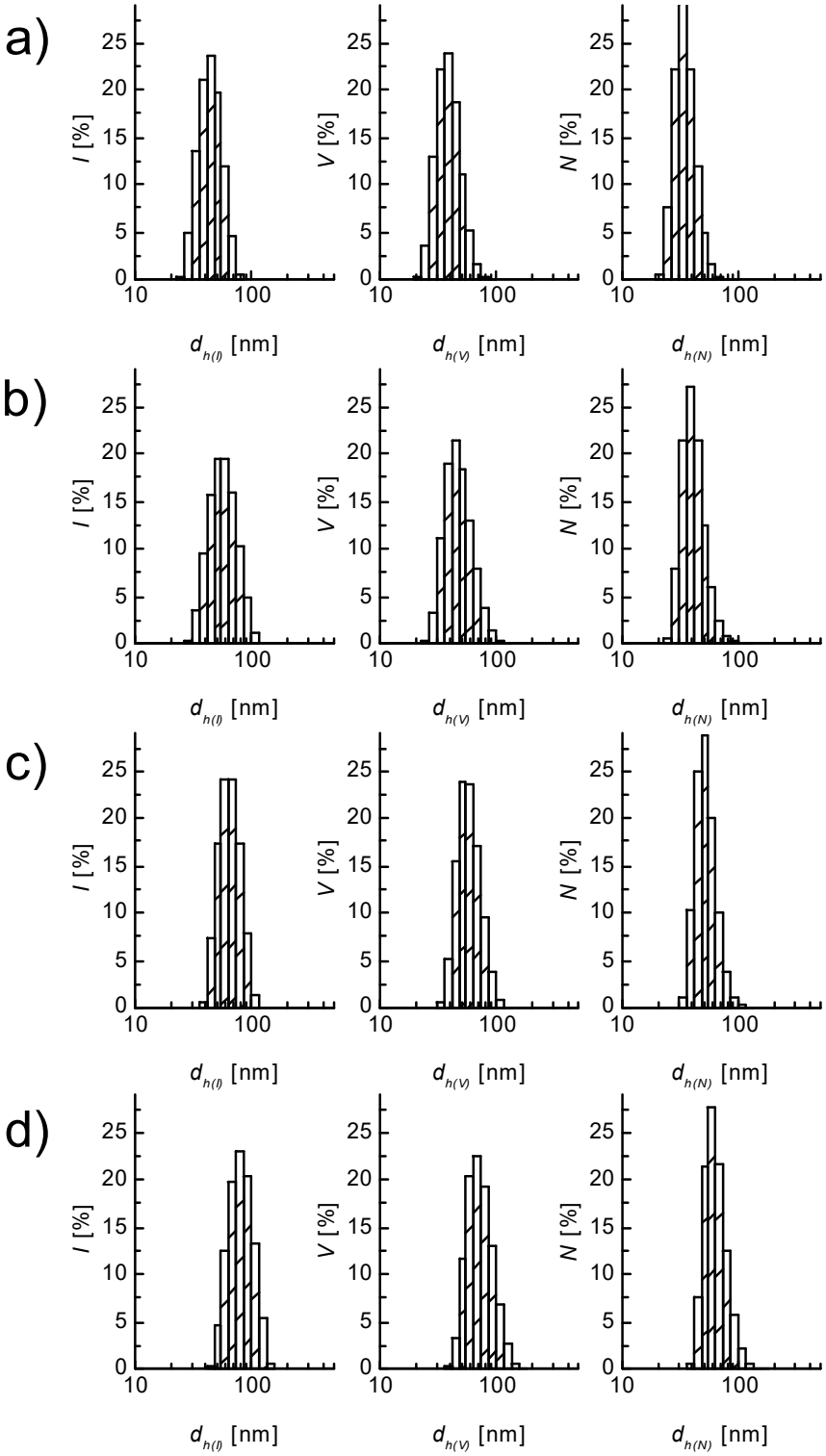

Figure SIII-9. DLS histograms for Au4 (left: Intensity; middle: Volume; right: Number) modified with a) PEG-1k, b) PEG-3k, c) PEG-5k and d) PEG-10k.

III.3. Experimental determination of the concentration of PEGylated NPs: As previously mentioned, the extinction coefficients of samples listed in Table S.II-1 were calculated using the tables from Haiss et al.,[2] and confirmed by ICP-MS, cf., Figure S.III-6. The concentration determination for the PEGylated Au NPs was accomplished using inductively coupled plasma mass spectrometry (ICP-MS, Agilent 7700 Series) in comparison with UV-vis tables from Haiss *et al.* ICP-MS measures the atomic gold concentration in solution. First 5 µL of the NP suspension was transferred from the transport tubes (5 mL, VWR, #216-0153) into 6 mL perfluoroalkoxy alkane tubes (PFA) prefilled with freshly prepared 395 µL aqua regia, consisting of 1 part HNO_3 (67 wt%, ultra pure, Fisher Chemical, #7697372) and 3 parts HCl (35 wt%, ultra pure, Fisher Chemicals, #7647010) and mixed for at least 4 hours under constant agitation. During this period the gold core as well as the polymer shell were digested and broken down to small basic components. In the second step 4.6 mL of 2% HCl solution as low matrix was introduced to each digested sample to prevent the acid from digesting the ICP-MS machinery as well as to provide an ion stable environment with constant background conditions for the samples. The overall dilution factor for these types of sample is therefore 1000 times. Measurements were done using 3 repetitions per sample, 100 sweeps, and a peak pattern of 3 peaks. The diluted samples were introduced to the ICP-MS set-up through an integrated autosampler, coupled to a peltier cooling spray chamber where the sample was nebulized and taken up by the argon gas flow at a speed of ½ m/s. The concentration determination was performed using a calibration curve consisting of 9 measurement points (2500 to 0 µg/L) of freshly prepared, consecutive gold concentrations derived from a gold standard solution from Agilent (1000 mg/L). Results are always the mean of all three measurements and are presented in parts per billion (ppb = µg/L).

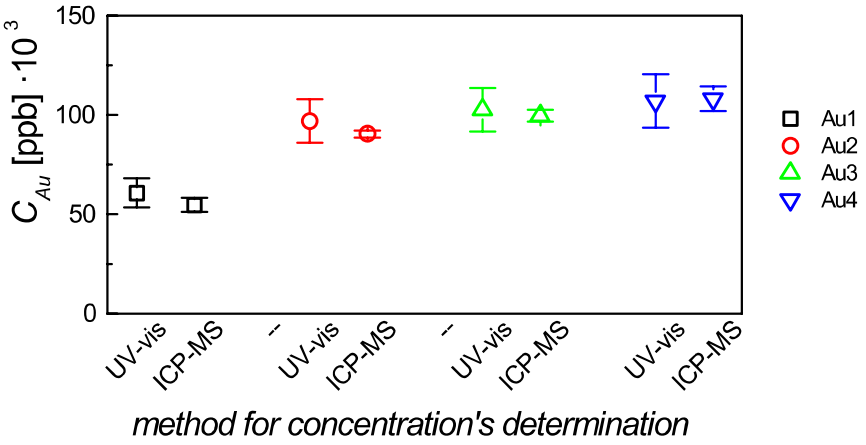

Figure S.III-6. Comparison of Au concentration (C_{Au}) in samples Au1-Au4 as determined by tables from Haiss et al.[2] (i.e., combining size by TEM and absorbance by UV-Vis, that from the NP concentrations the concentration of elemental gold C_{Au} was obtained) and as determined by ICP-MS. Error bars in UV-Vis and ICP-MS measurements are calculated by the standard deviation on size (TEM) and by various measurements, respectively.

In order to derive the concentration of NPs in mass units (c_m [ppb]) from the UV-Vis absorption spectra, we used the molar concentration values (c_{NP} [M]) obtained by using the extinction coefficients at 450 nm (ε_{450}) reported by Haiss *et al.*, the diameters of the inorganic cores

obtained by TEM (d_C), and the density of bulk gold (ρ =19.3 g/cm^3). For instance, for sample Au1, TEM gives a diameter of ca. 14 nm, for which the Haiss tables[2] reports ε_{450} [M^{-1}·cm^{-1}] = 1.8·10^8. Then, using ε_{450} and the absorbance of the samples at 450 nm (A_{450}) in a cuvette of pathlength = 1 cm, $c_{NP} = A_{450}/\varepsilon_{450}$ = 3.8·10^{-9} M. Then, the mass of one Au1 NP (m_{NP}) can be deduced from the volume of the NP (V_{NP} [cm^3] = $\pi \cdot d_C^3/6$) and ρ[g·cm^{-3}], *by* $m_{NP} = \rho \cdot V_{NP}$ [g]. The molecular weight of the NPs ($M_{W,NP}$) can be obtained by $M_{W,NP} = m_{NP}\, N_A$ [g·mol^{-1}], where N_A is the Avogadro number. Finally, the theoretical mass concentration c_m [ppb], which can be extracted from the absorbance of the NPs and compared with the experimental ICP measurements, is obtained by $c_m = M_{W,NP} \cdot c_{NP}$, cf.Table S.III-2.

Table S.III-2. Mean hydrodynamic diameter in number ($d_{h(N)}$) and intensity ($d_{h(I)}$), and polydispersity index (*PDI*) for all of the PEGylated NPs. Notice that for low saturation (typically 50 and 500 PEG chains added per NP) the given d_h represent the main DLS peak.

sample	d_C[nm]	ε_{450} [M^{-1}·cm^{-1}]	c_{NP} [nM]	V_{NP} [cm^3]	m_{NP} [g]	c_m [ppb]
Au1	13.8 ± 1.7	1.8·10^8	3.8	1.3·10^{-18}	2.6·10^{-17}	6.1·10^4
Au2	18.5 ± 2.1	4.0·10^8	2.5	3.3·10^{-18}	6.4·10^{-17}	9.7·10^4
Au3	23.5 ± 2.5	8.8·10^8	1.3	6.8·10^{-18}	1.3·10^{-16}	1.0·10^4
Au4	27.8 ± 3.5	1.4·10^9	0.8	1.1·10^{-17}	2.2·10^{-16}	1.1·10^4

IV) Negative staining of the PEGylated NPs

In order to estimate the thickness of the PEG shell (i.e., $1/2d_S$) on NPs (i.e., PEGylation on Au cores), the NP samples were analyzed by negative staining TEM. Ideally this technique allows to resolve the true solvent-excluded surface and shape of the core-shell system, which remains after samples have been dried for TEM imaging.[3] All of the combinations of Au cores (Au1 – Au4) and PEGs (PEG-1k – PEG-10k) were analyzed by negative staining (a total of 16 samples). Uranyl acetate was used as negative stain, which allows the formation of a uniform, consistent, and high contrast staining, cf. Figure S.IV-1 – SIV-4.

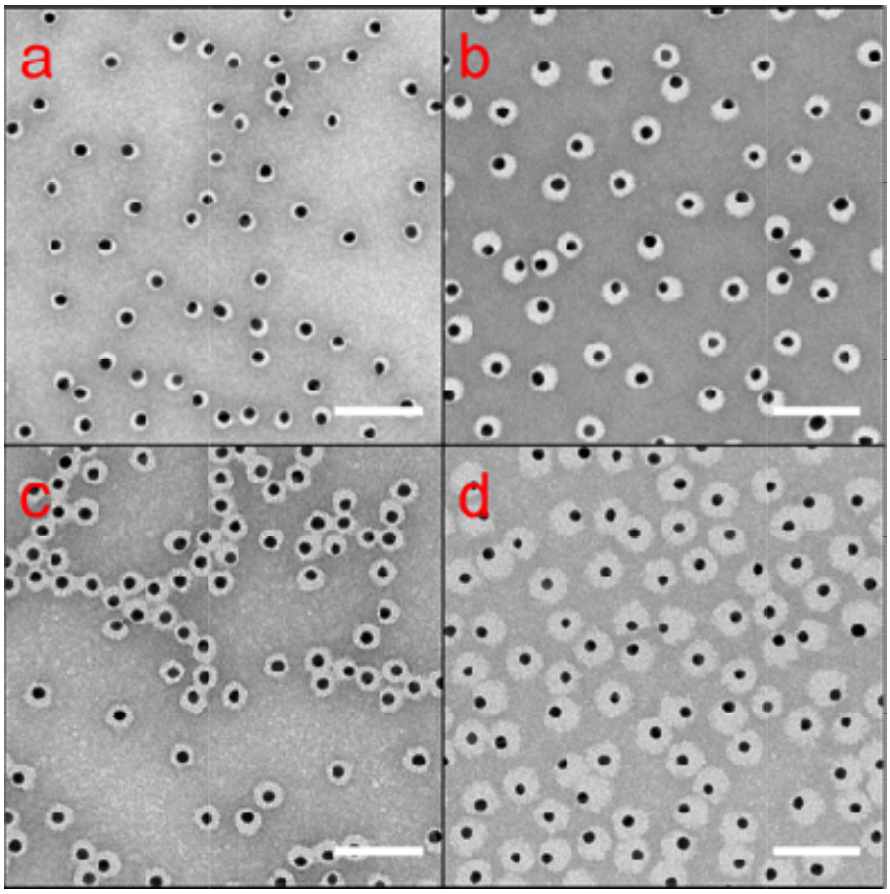

Figure S.IV-1. Selected negative staining TEM micrographs for PEGylated Au1 cores. a) Au1@PEG-1k; b) Au1@PEG-3k; c) Au1@PEG-5k; d) Au1@PEG-10k. Scale bar is 100 nm.

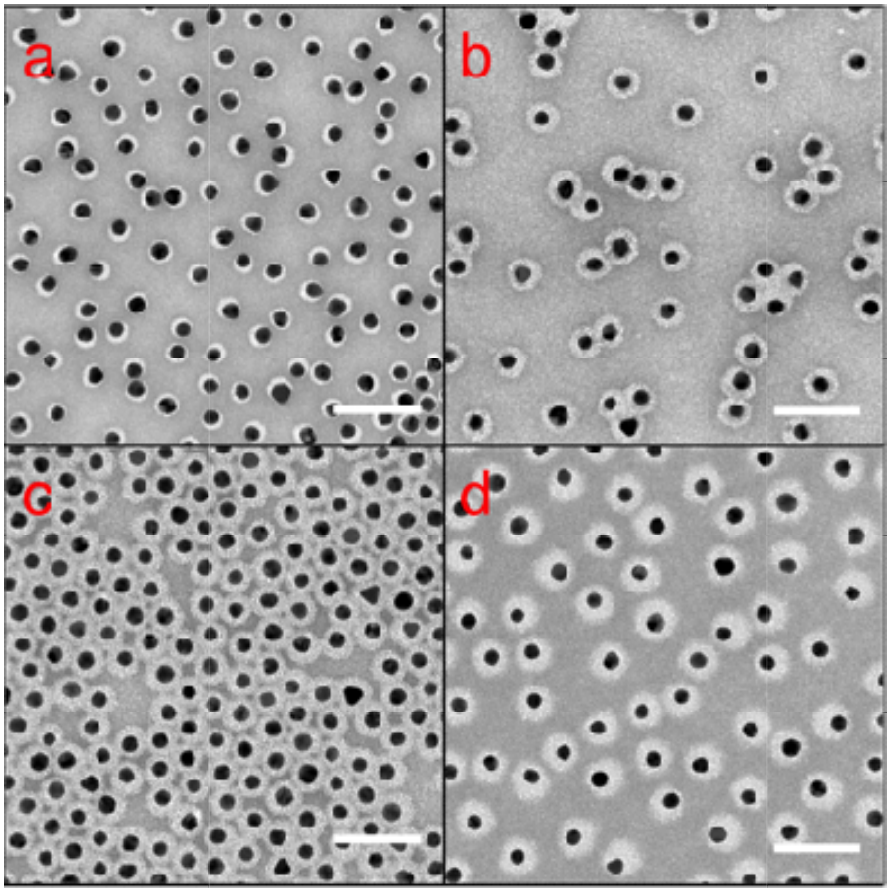

Figure S.IV-2. Selected negative staining TEM micrographs for PEGylated Au2 cores. a) Au2@PEG-1k; b) Au2@PEG-3k; c) Au2@PEG-5k; d) Au2@PEG-10k. Scale bar is 100 nm.

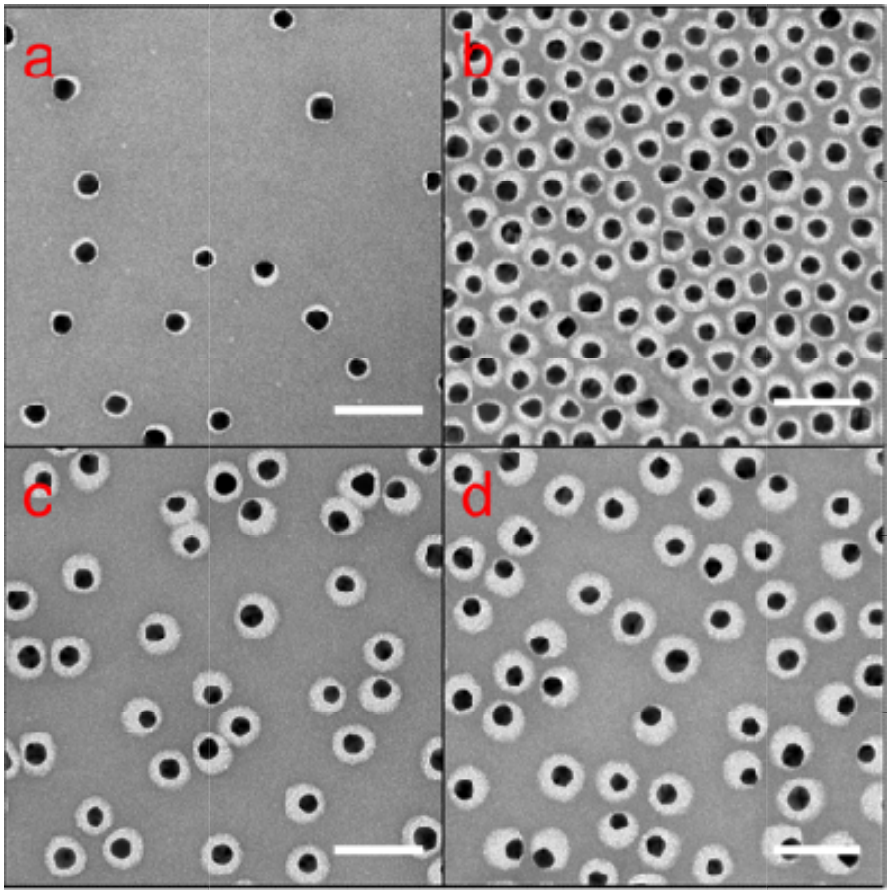

Figure S.IV-3. Selected negative staining TEM micrographs for PEGylated Au3 cores. a) Au3@PEG-1k; b) Au3@PEG-3k; c) Au3@PEG-5k; d) Au3@PEG-10k. Scale bar is 100 nm.

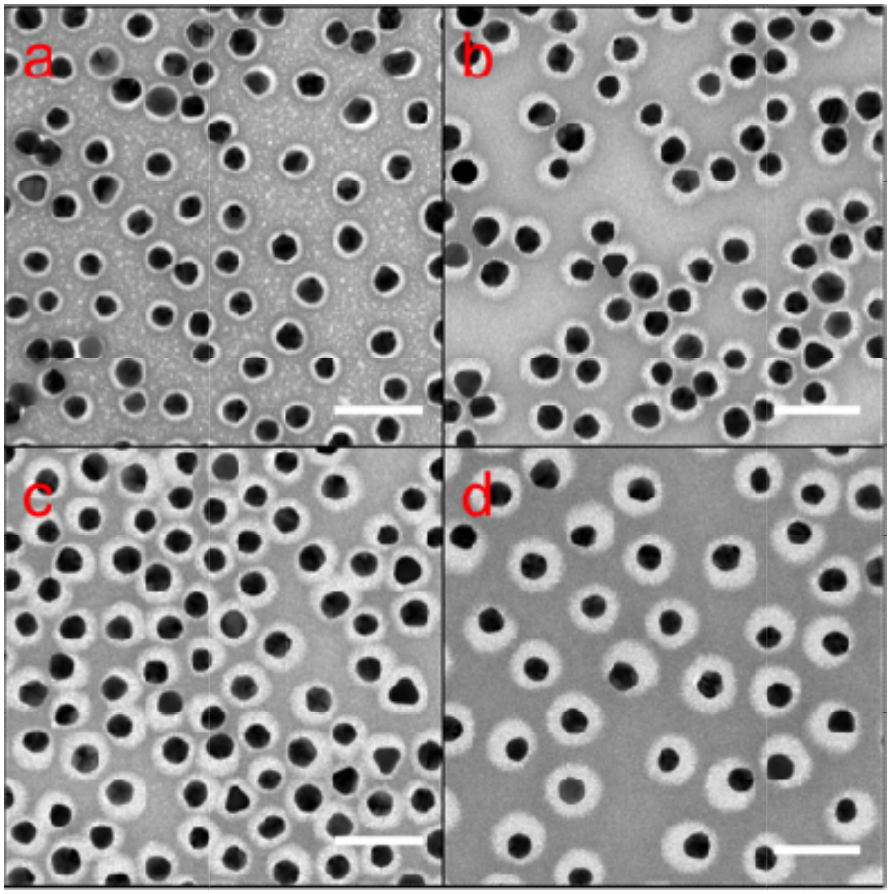

Figure S.IV-4. Selected negative staining TEM micrographs for PEGylated Au4 cores. a) Au4@PEG-1k; b) Au4@PEG-3k; c) Au4@PEG-5k; d) Au4@PEG-10k. Scale bar is 100 nm.

The transmission electron microscopy bright field (TEM) images were taken at a JEM-1400PLUS HC (JEOL) transmission electron microscope, equipped with a LaB6 filament and operated at 120 kV acceleration voltage, with a U-1000 CCD camera (GATAN) mounted to the high resolution position and controlled by the Digital Micrograph V1 Software.

Negative stained TEM samples have been prepared from aqueous NP and uranyl acetate solutions on air plasma treated, hydrophilized, carbon film-coated copper grids in a droplet technique, following a concept as described in more detail by Robin Harris.[3]

It is to be expected that strong electron-scattering material, such as the gold cores in the studied nanoparticles, maps to TEM images as an amplitude contrast dominated dark representation, while marginal electron-scattering materials, like the PEG shell in the studied nanoparticles, do not show such significant appearing contrast and stay more or less invisible in the bright color of the (unstained) image background. The heavily electron-scattering uranium acts as a negative staining contrast agent by mainly adsorbing everywhere on the sample-supporting carbon film, except in places which already became occupied by protruding matter. Ideally it deposits as a monolayer on the unoccupied carbon film surface and slightly accumulates along topographical edges of the sample. It thus in the TEM image would render the formerly by sample unoccupied area grayish and line topographical edges of the sample darker.

In our successfully negative stained TEM images the Au cores of the nanoparticles therefore appear almost black and the PEG shell appears contrasted against the finally grayish background as a bright rim around the particle cores. We in our preparation achieved that the topographical edges stay unpronounced, which facilitates the subsequent, automatized image analysis.

The image analysis of several negative staining TEM micrographs (>1000 NPs) for each of the 16 samples provides a quantitative characterization of the diameter of the core-shell system (i.e. $d_{CS} = d_C + 2\cdot(1/2d_S)$). For morphological characterization of the NPs and their corresponding shells, TEM images, such as shown in Figure S.IV-5 – SIV-8, were segmented using Matlab (Mathworks) and Cellprofiler [4]. Firstly, NP cores were identified and characterized regarding size and shape. Secondly, for determination of the thickness ($1/2d_S$) and the shape of the corresponding polymer shells, the area of the NP core objects was extended based on the negative shell staining without including regions of background. For image enhancement unsharp masking and morphological image processing was applied. Obtained objects (core + shell) comprising several touching NPs were identified based on their circularity and subsequent declumping was performed using Cellprofiler.

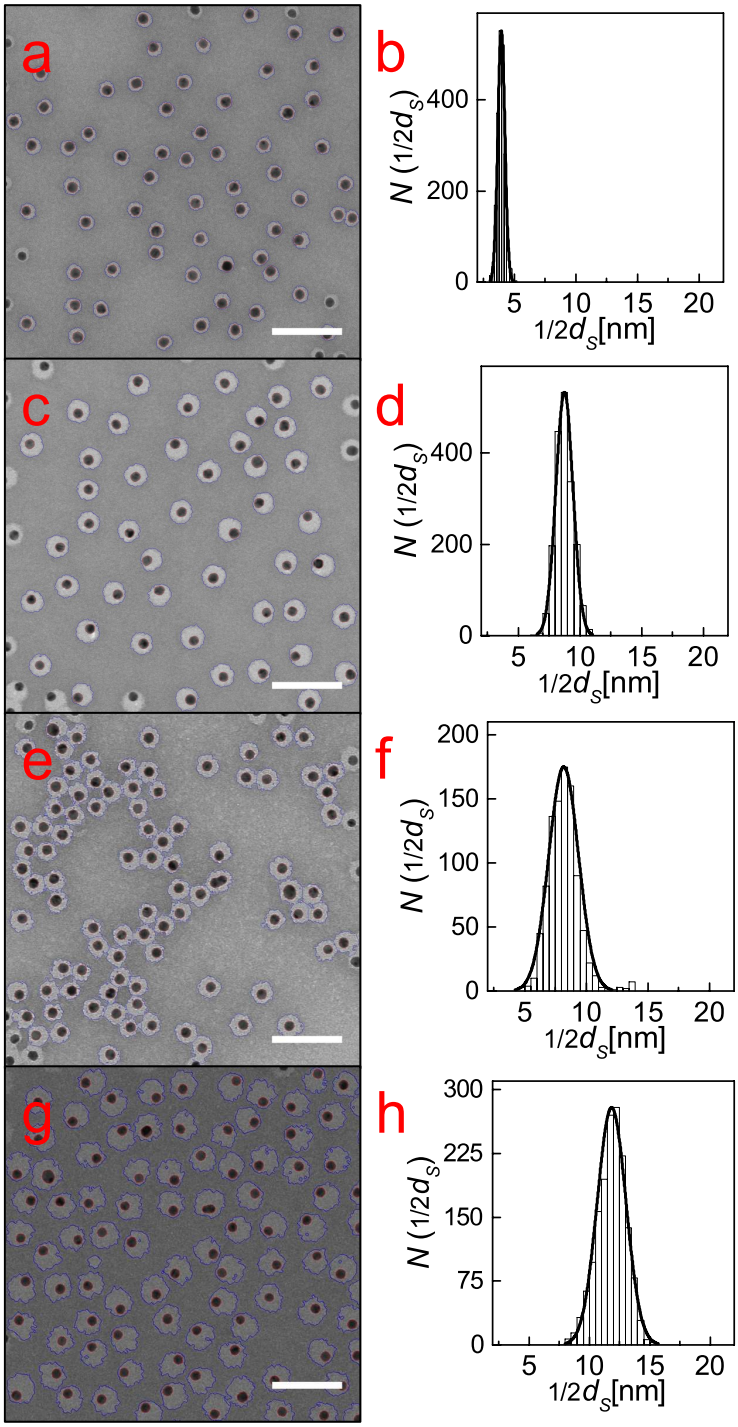

Figure S.IV-5. Selected segmented images for PEGylated Au1 cores. a) Au1@PEG-1k; c) Au1@PEG-3k; e) Au1@PEG-5k; g) Au1@PEG-10k. Panels c, d, f and h represent the corresponding $1/2d_S$ histograms. The red and blue outlines are drawn around the Au cores and the PEG shell, respectively. Scale bar is 100 nm.

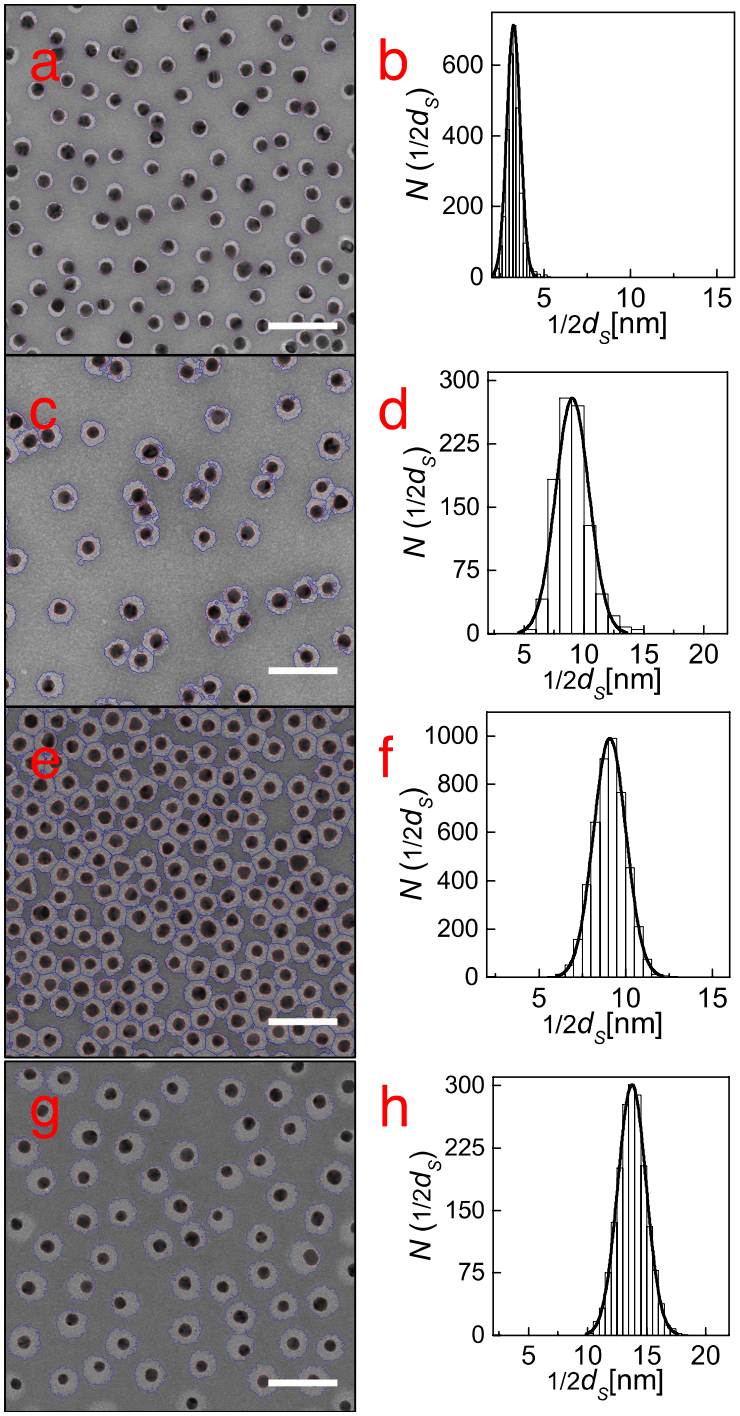

Figure S.IV-6. Selected segmented images for PEGylated Au2 cores. a) Au2@PEG-1k; c) Au2@PEG-3k; e) Au2@PEG-5k; g) Au2@PEG-10k. Panels c, d, f and h represent the corresponding $1/2d_S$ histograms. The red and blue outlines are drawn around the Au cores and the PEG shell, respectively. Scale bar is 100 nm.

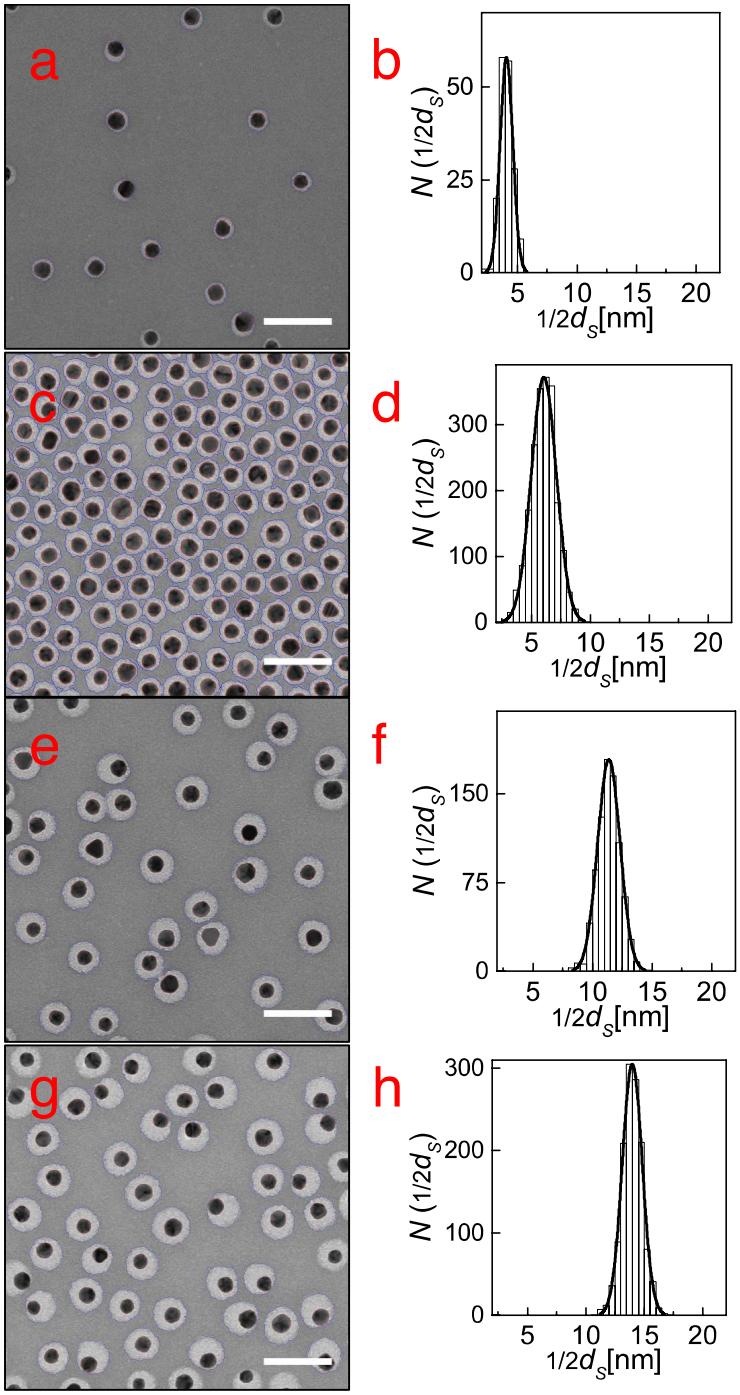

Figure S.IV-7. Selected segmented images for PEGylated Au3 cores. a) Au3@PEG-1k; c) Au3@PEG-3k; e) Au3@PEG-5k; g) Au3@PEG-10k. Panels c, d, f and h represent the corresponding $1/2d_S$ histograms. The red and blue outlines are drawn around the Au cores and the PEG shell, respectively. Scale bar is 100 nm.

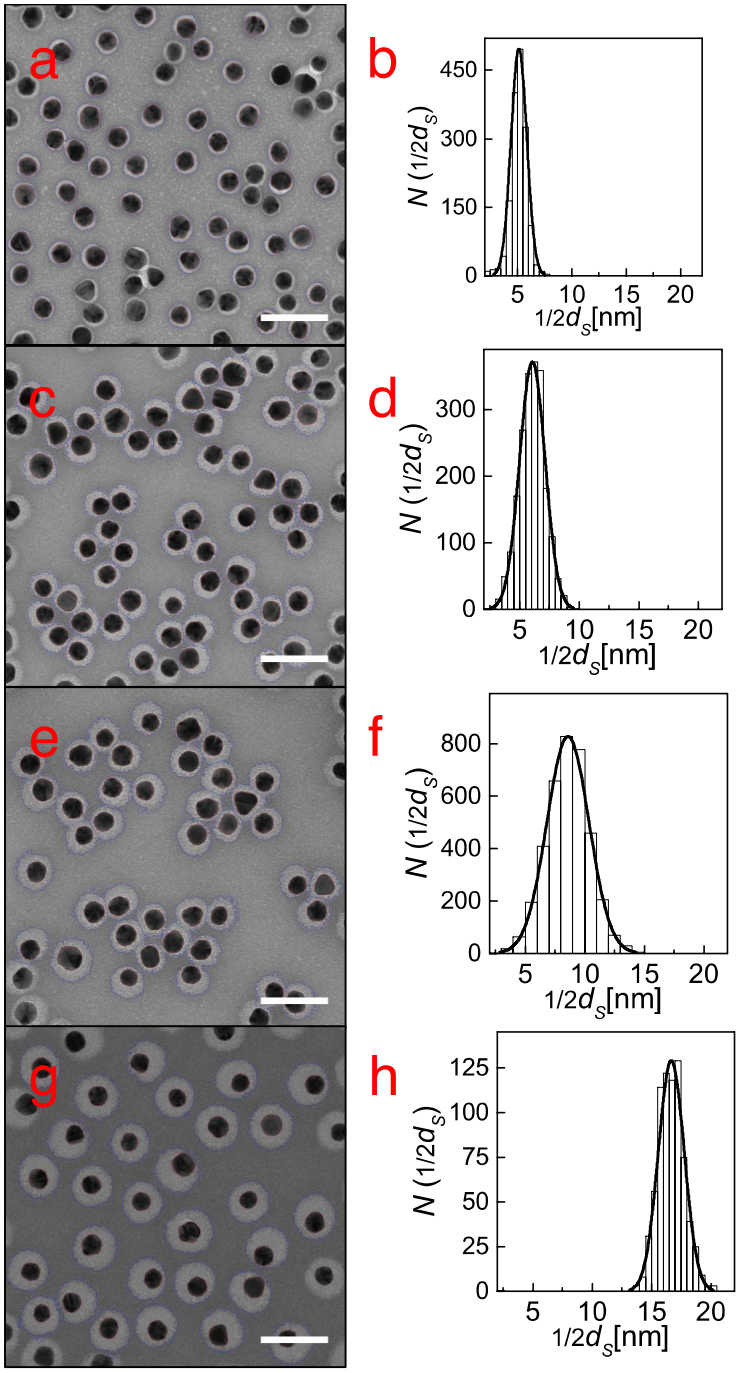

Figure S.IV-8. Selected segmented images for PEGylated Au4 cores. a) Au4@PEG-1k; c) Au4@PEG-3k; e) Au4@PEG-5k; g) Au4@PEG-10k. Panels c, d, f and h represent the corresponding $1/2d_S$ histograms. The red and blue outlines are drawn around the Au cores and the PEG shell, respectively. Scale bar is 100 nm.

Figure S.VI-9 summarizes and compares the size of the core-shell system ($d_{CS} = d_C + d_S$), as analyzed by negative staining TEM analysis.

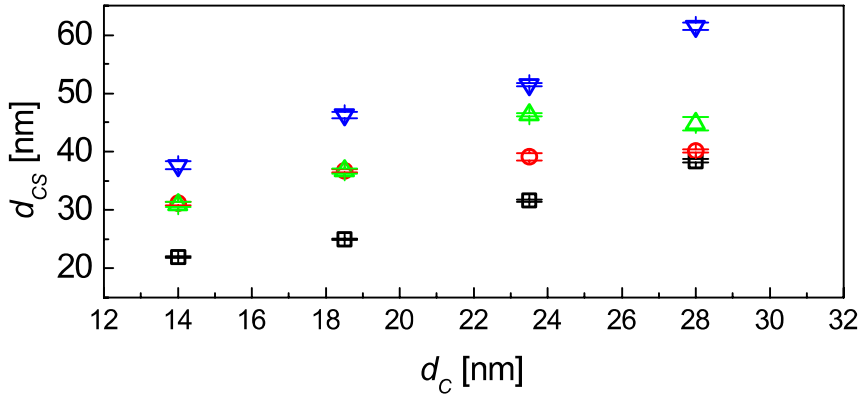

Figure S.IV-9. Comparison of the sizes determined by negative staining analysis of the 16 samples (4 cores with different core diameters: Au1 /14 nm, Au2 /18.5, Au3 /23.5 and Au4 /28 nm; 4 PEG saturated PEG shells with increasing molecular weight: 1 kDa / black squares, 3 kDa /red circles, 5 kDa /green triangles, and 10 kDa /inverted blue triangles).

Likewise, hydrodynamic diameter results obtained by DLS of the cores (citrate capped Au NPs) and the 16 PEGylated samples can be represented similarly as in Figure S.IV-9, cf. Figure S.IV-10.

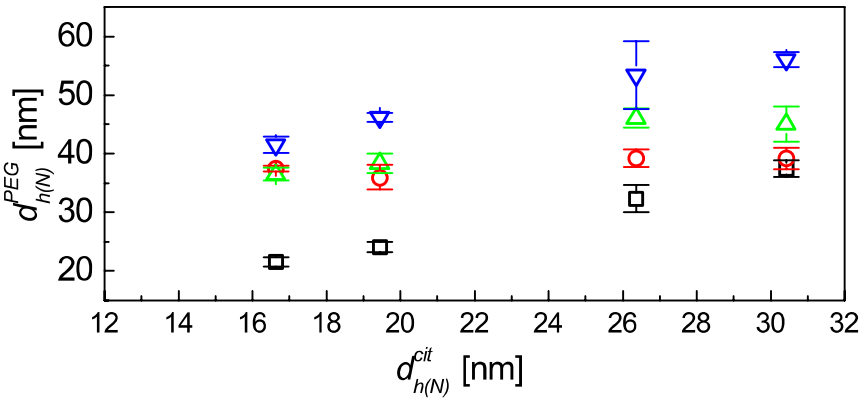

Figure S.IV-10. Comparison of the sizes (hydrodynamic diameter $d_{h(N)}$) determined by DLS of the 16 PEGylated samples $d^{PEG}_{h(N)}$ (4 citrate capped cores of different hydrodynamic diameters $d^{cit}_{h(N)}$: Au1 /16.6 nm, Au2 /19.4, Au3 /26.4 and Au4 /30.4 nm; 4 saturated shell of PEG with increasing molecular weight: 1 kDa / black squares, 3 kDa /red circles, 5 kDa /green triangles, and 10 kDa /inverted blue triangles).

In the following we introduce two dimensionless parameters, i.e., R^{TEM}_{PEG} and R^{DLS}_{PEG}, which represent the contribution of PEG to the resulting size as determined by TEM (vacuum) and

DLS (solution); R_{PEG}^{TEM} or R_{PEG}^{DLS} equals 0 or 1 if the whole core-shell size comes from the Au core or the PEG shell, respectively. Notice that although TEM are DLS are experimental techniques, which in principle should provide different numbers due to hydration of the samples in solution (DLS), the thickness of the PEG shells was observed to be similar for each sample, both in vacuum and in solution. This observation indicates that the PEG chains are very efficiently packed onto the Au NPs. The explicit equations used to calculate these parameters are:

$$R_{PEG}^{TEM} = \frac{d_S}{d_C + d_S} \qquad \text{(Equation S.IV-1)}$$

$$R_{PEG}^{DLS} = \frac{d_{h(N)}^{PEG} - d_{h(N)}^{cit}}{d_{h(N)}^{PEG}} \qquad \text{(Equation S.IV-2)}$$

Table S.IV-1. Thickness of the PEG shell as determined by negative staining TEM analysis (½d_S) in vacuum, and DLS (½($d_{h(N)}^{PEG} - d_{h(N)}^{cit}$) in solution. The dimensionless parameters R_{PEG}^{TEM} and R_{PEG}^{DLS} represent the contribution of PEG to the resulting size as determined by TEM and DLS, respectively.

Sample	½d_S [nm]	R_{PEG}^{TEM}	½($d_{h(N)}^{PEG} - d_{h(N)}^{cit}$) [nm]	R_{PEG}^{DLS}
Au1@PEG-1k	4.0 ± 0.1	0.36	2.5 ± 0.8	0.23
Au1@PEG-3k	8.6 ± 0.3	0.55	10.4 ± 0.5	0.56
Au1@PEG-5k	8.5 ± 0.5	0.55	9.9 ± 1.1	0.54
Au1@PEG-10k	11.9 ± 0.7	0.63	12.4 ± 1.4	0.60
Au2@PEG-1k	3.2 ± 0.1	0.26	2.3 ± 0.9	0.19
Au2@PEG-3k	9.1 ± 0.2	0.50	8.3 ± 2.0	0.46
Au2@PEG-5k	9.1 ± 0.4	0.50	9.4 ± 1.7	0.49
Au2@PEG-10k	13.9 ± 0.5	0.60	13.4 ± 0.8	0.58
Au3@PEG-1k	4.1 ± 0.2	0.26	3.0 ± 2.3	0.19
Au3@PEG-3k	7.8 ± 0.6	0.40	6.5 ± 1.5	0.33
Au3@PEG-5k	11.4 ± 0.2	0.49	9.9 ± 1.7	0.43
Au3@PEG-10k	14.0 ± 0.2	0.54	13.5 ± 5.8	0.51
Au4@PEG-1k	5.2 ± 0.2	0.27	3.5 ± 1.4	0.19
Au4@PEG-3k	6.1 ± 0.2	0.30	4.4 ± 1.8	0.22
Au4@PEG-5k	8.4 ± 1.1	0.37	7.3 ± 3.1	0.32
Au4@PEG-10k	16.7 ± 0.6	0.54	12.8 ± 1.3	0.46

Figure S.IV-11 summarizes and compares the mean $1/2d_S$ for the sixteen samples studied by image analysis. Clearly, the $1/2d_S$ values increase as the molecular weight of the PEGs ($M_{W,PEG}$) increases for each type of Au core, cf.panel a. In principle, for each molecular weight of the PEG, $1/2d_S$ remains very similar, cf. panel b, which points out that increasing the radius of curvature (i.e., increasing the value d_C) does not significantly influence the polymer's thickness ($1/2d_S$). Additionally, Figure S.IV-12 shows a heatmap for $1/2d_S$, in which we can observe how $1/2d_S$ increases with R_{PEG}^{TEM}. Alternatively, Figure S.IV-13 shows a 3d surface plot.

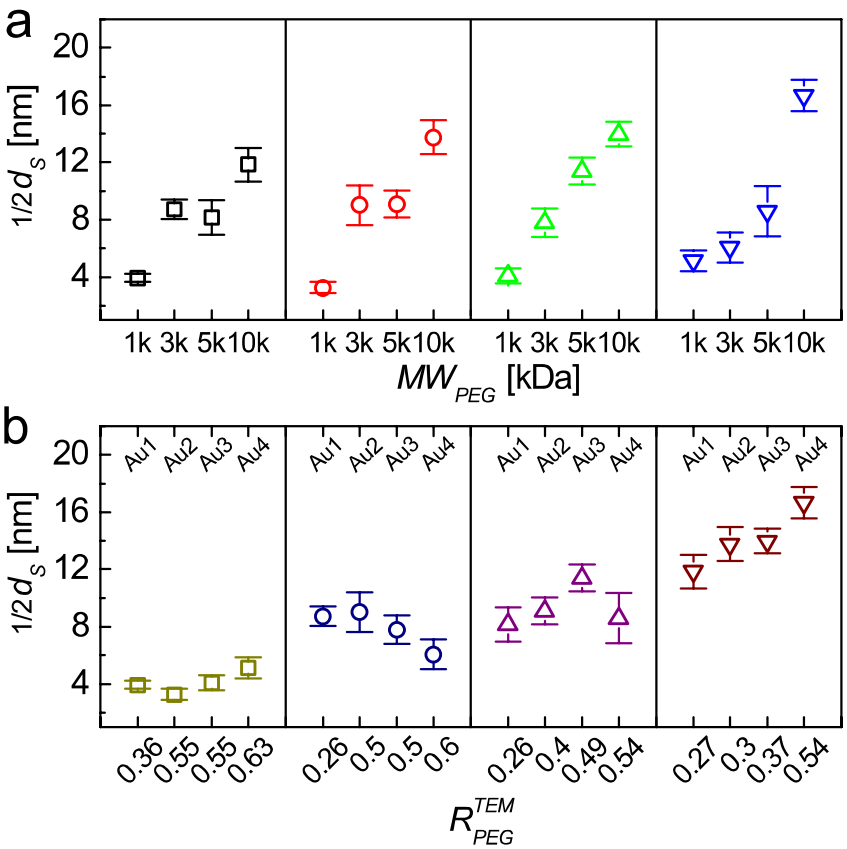

Figure S.IV-11. Comparison of the mean PEG shell thickness $1/2d_S$ of the PEGylated samples, as determined by negative staining TEM analysis. a) Influence of increasing molecular weight ($M_{W,PEG}$) of PEG for the same Au core, i.e., Au1 (black squares), Au2 (red circles), Au3 (green triangles) and A4 (blue inverted triangles). b) Influence of increasing the diameter of the inorganic core (d_C) for the same PEG coating, PEG-1k (olive squares), PEG-3k (dark blue circles), PEG-5k (magenta triangles) and PEG-10k (brown inverted triangles).

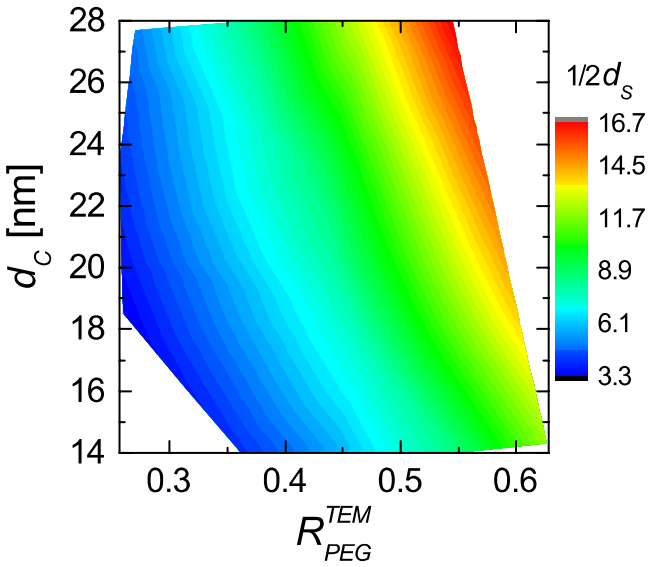

Figure S.IV-12. 1/2d_S heatmap in a diagram d_C versus R_{PEG}^{TEM}. Increasing R_{PEG}^{TEM} (at $\Delta d_C = 0$) thus is reflected by increase in 1/2d_S. Likewise, increasing d_C (at $\Delta R_{PEG}^{TEM} = 0$) leads to increase in 1/2d_S (seen on trajectories parallel to the d_C axis). As only two of the three parameters (d_C, 1/2d_S, R_{PEG}^{TEM}) are independent, this curve is directly given by the definition of R_{PEG}^{TEM}, cf. Equation S-IV-3.

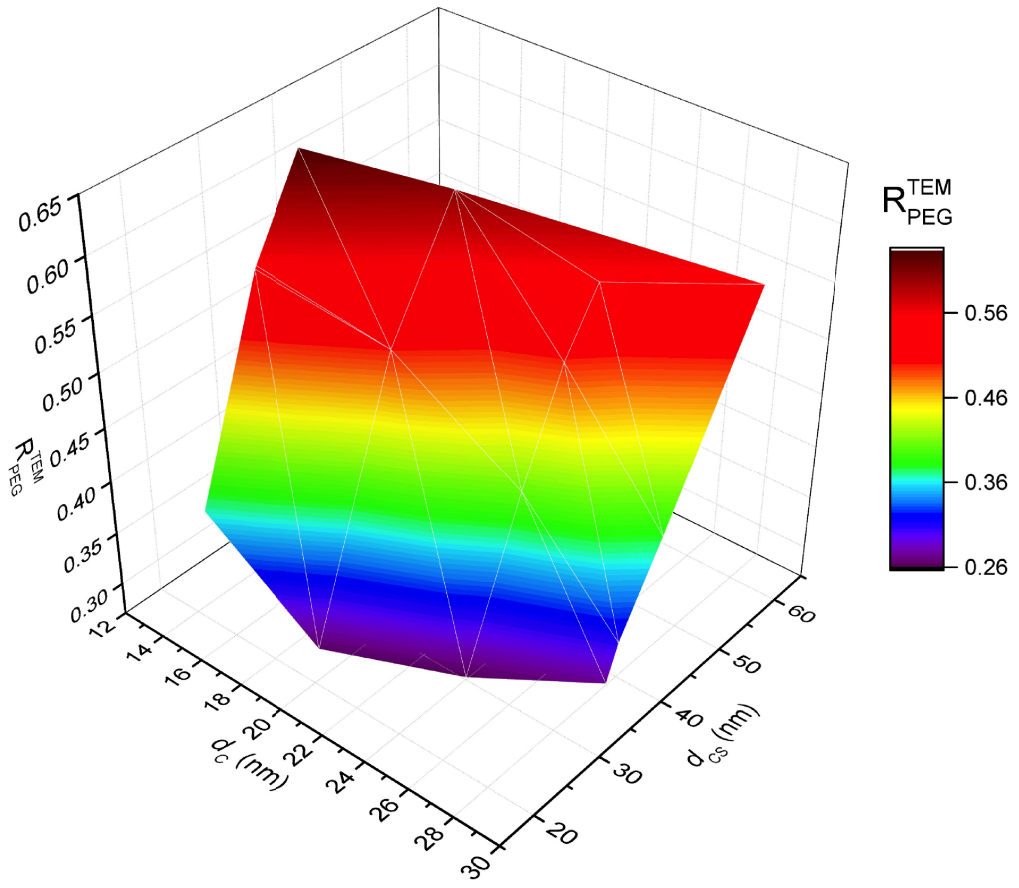

Figure S.IV-13. 3d surface plot for d_C, d_{CS} and R_{PEG}^{TEM}.

V) Characterization of the NPs' dynamic interfacial tension (IFT)

The dynamic interfacial tension was determined by pendant drop tensiometry at the toluene-water interface using a Drop Shape Analysis System (DSA100, Krüss, Germany). A Hamilton syringe plugged to a stainless steel needle (diameter 1.85 mm) immersed in the toluene phase was used to produce a 50 μL sample droplet at 200 μL·min^{-1} dosing rate. The sample concentration varied with the Au core used, being 3.0 nM for A1, 1.3 nM for Au2, 0.66 nM for Au3 and 0.41 nM for Au4. The series measurement of the droplet profile upon time was recorded using an ultra fast camera (Krüss). The interfacial tension ($\gamma_{\square}$) was estimated using the analysis software package DSA3 (Krüss) fitting the droplet profile with the Young-Laplace equation:

$$\gamma_t = \frac{\Delta\rho \cdot g \cdot d_e}{H} \qquad \text{(Equation S.V-1)}$$

where $\Delta\rho = 0.128\,\mathrm{g/mL}$ is the density difference between the liquid drop (water) and its surrounding medium (toluene), g = 9.81 m/s^2 is the gravitational acceleration, d_e is the largest horizontal diameter of the drop, and H is a function of $S_n\ (= d_n/d_e)$, in which d_n is the horizontal diameter at a distance equal to d_e (n/10) from the bottom of the drop. All experiments were performed at room temperature.

Figure S.V-1 presents the dynamic surface tension (γ_t) plots for all of the combinations of Au cores (Au1 – Au4) and PEG shells (PEG-1k – PEG-10k) (a total of 16 samples), where the interfacial tension decreases with time, approaching an equilibrium value. In the early stage, the interfacial tension drops because of instantaneous self-assembly of the NPs at the interface. Once the droplet is mostly covered by NPs, the decrease in interfacial tension reaches a dynamic equilibrium where the rate of adsorption of NPs at the interface equals the rate of desorption. It can be observed that the experimental meso-equilibrium γ (γ_m) value decreases equivalently for all of the different cores. The variation in interfacial tension with different PEG shells (PEG-1k to PEG-10k) can be explained by the effect of their polymer length on the assembly at the toluene−water interface. For any type of Au core (Au1-Au4), PEGylation with PEG-10k resulted in the maximum reduction in the equilibrium γ_m values, followed by PEG-5k, PEG-3k and PEG-1k. Therefore, although the amphiphilic behavior of PEG is known, the thickness of the PEG shell (*1/2*Δd_S) determines the hydrophilic behavior of the PEGylated NPs, that is, increasing the *1/2*Δd_S results in a increment of the NP's hydrophobicity. The kinetic behavior of the surface tension of the NP stabilized water-in-toluene emulsions was obtained using $\gamma_t$versus time plots fitted to the empirical Hua and Rosen equation,[5]cf. Equation S.V-2.

$$\gamma_t = \gamma_m + \frac{\gamma_0 - \gamma_m}{1 + (t_D/t^*)^n} \qquad \text{(Equation S.V-2)}$$

where γ_t is the surface tension at any time t_D, γ_0 is the surface tension of the pure solvent (water in toluene), γ_m is the surface tension at mesoequilibrium, *t** is the half-time in reaching γ_m, and *n* is a dimensionless exponent. Assuming that the value of γ_0 is held constant (ca. 36 nN/m, the value of the pure buffer surface tension), there are three adjustable parameters: γ_m, *t**, and *n*. These parameters were estimated by computer fitting (with the software OriginLab) of the measured dynamic surface tension data.

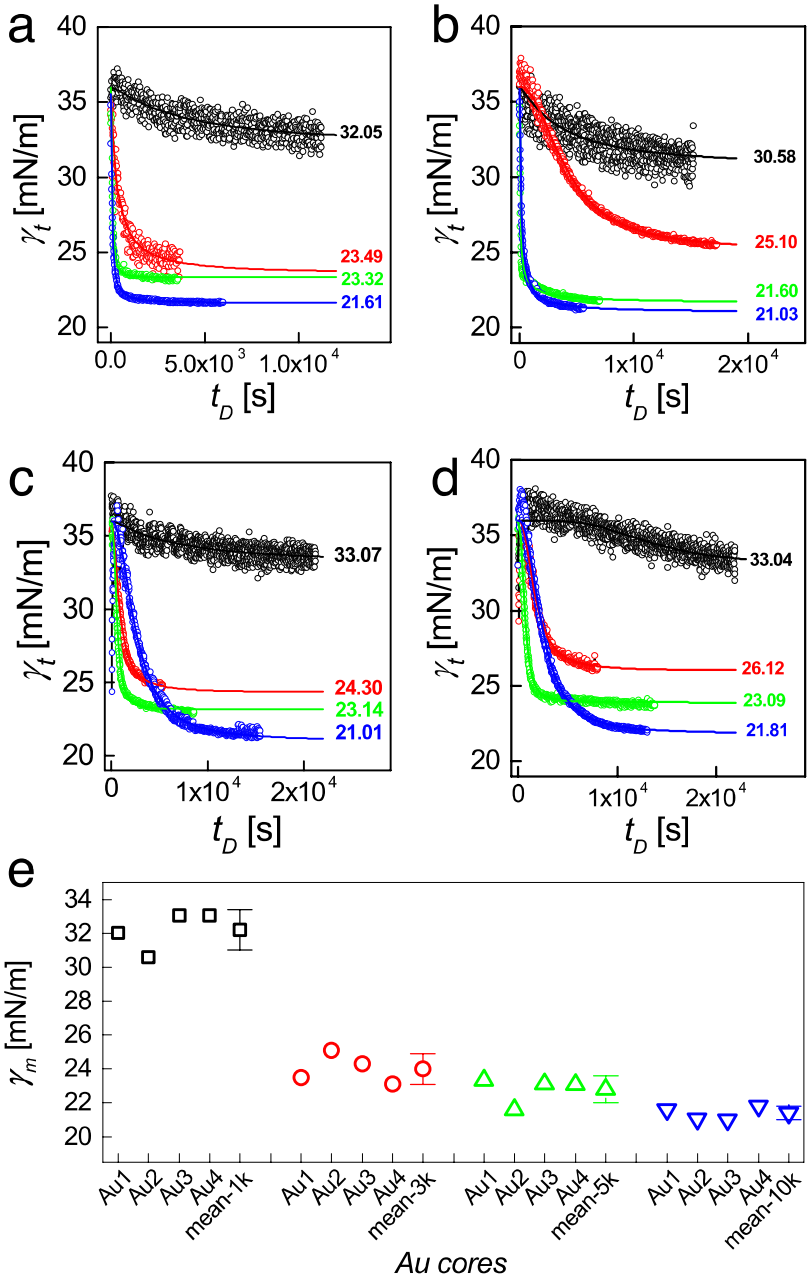

Figure S.V-1. a-d) $\gamma_t$versus time (t_D) plots for Au1, Au2, Au3, and Au4, respectively, PEGylated with different PEG shells (1 kDa: black, 3 kDa: red, 5 kDa: green, 10 kDa: blue); experimental data and the respective fitting lines are represented by hollow circles and solid lines, respectively. e) Summary of the γ_m values for all the 16 samples and the mean γ_m for each PEG shell of different molecular weight (i.e., mean-1k, -3k, -5k and -10k, for PEG shells of 1, 3, 5 and 10 kDa, respectively).

Additionally, Figure S.V-2 shows a heatmap for γ_m, which decreases (i.e., less hydrophilic/more hydrophobic) as R_{PEG}^{TEM} increases. Alternatively, Figure S.V-3 shows a 3d surface plot for the parameters d_C , d_{CS} and γ_m.

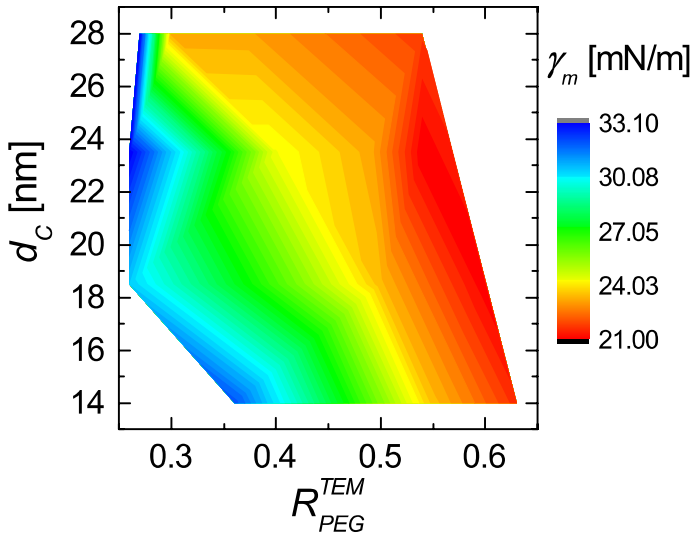

Figure S.V-2. Heatmap for γ_m in a diagram d_C versus R_{PEG}^{TEM}. γ_m almost does not depend on size of the Au NPs (seen on trajectories parallel to the d_C axis), but is strongly reduced with higher amount of PEG molecules, which makes the NPs more hydrophobic (seen on trajectories parallel to the R_{PEG}^{TEM} axis).

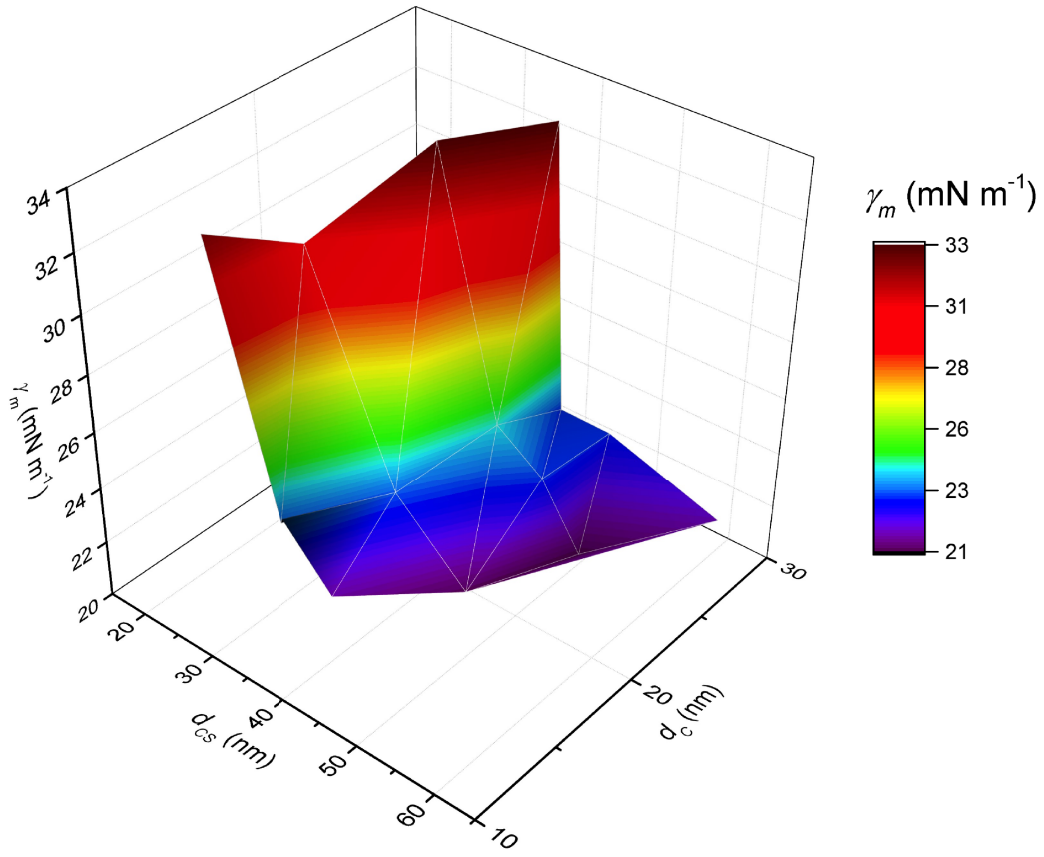

Figure S.IV-13. 3d surface plot for d_C , d_{CS} and γ_m.

VI) AFM measurements on PEGylated NPs: stiffness

Sample patch preparation: diluted samples of NP solutions were dropped on a 1x1 cm piece of stainless steel with smooth surface (roughness ca.1 nm). Before use, all stainless steel patches were cleaned with aceton and chloroform and then, dried at 180 °C in vacuum. After dropping of each sample, the NPs were left to adsorb on the substrate for ca. 20-10 min. Considering that the water content in the PEG shell can influence the results of stiffness, all the samples were measured in solution (water) as well as in air (water content lower than 2%). For measurements in air, all the samples were dried naturally for 8 hours and then, treated with vacuum for 1 hour prior to AFM measurements. For the AFM measurements in water, samples were immersed and measured immediately.

AFM measurements: Multi-mode IV (Veeco, Santa Barbara, CA) atomic force microscopy (AFM) was used for the measurements. A silicon-tip on nitride lever probe (spring constant k = 0.32 N/m, oscillation frequency f = 40-75 kHz) was utilized, with an initial drive amplitude of 0.499 V (tip oscillation amplitude 1.5 V). Single molecule force spectrometry (SMFS)[6] was employed to measure indentation depth (d_i) of the AFM tip into the PEG shell of the NPs, cf. Scheme S.VI-1. Several force F versus d_i curves were collected in each NP, as shown in Scheme S.VI-2, which were used to calculate the Young's Modulus (E) of single NPs. Note that for all the samples, more than 15 NPs were analyzed, and each NP was tapped at least 60 times. Overall more than 1000 curves for each sample were evaluated with NanoScope Analysis 1.5 (Brucker Corporation 2013). A calibration was performed in order to analyze the area covered by the conical tip used for all measurements.[7] Since a conical tip was used, the Sneddon[8] conical indenter model was used for calculating the Young's modulus, cf. Equation S.VI-1 and Scheme S.VI-3.

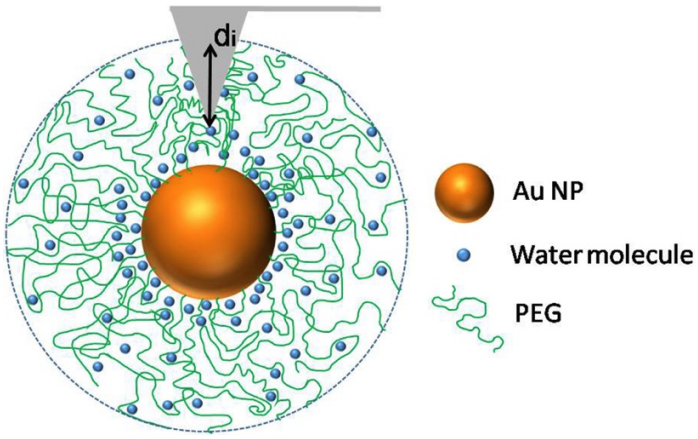

Scheme S.VI-1. Schematic of the indentation process of a PEGylated Au NP in aqueous solution. The indentation depth (d_i [nm]) is shown (arrow). During a typical nano indentation test, force and displacement are recorded as the tip is pressed into the PEGylated surface.

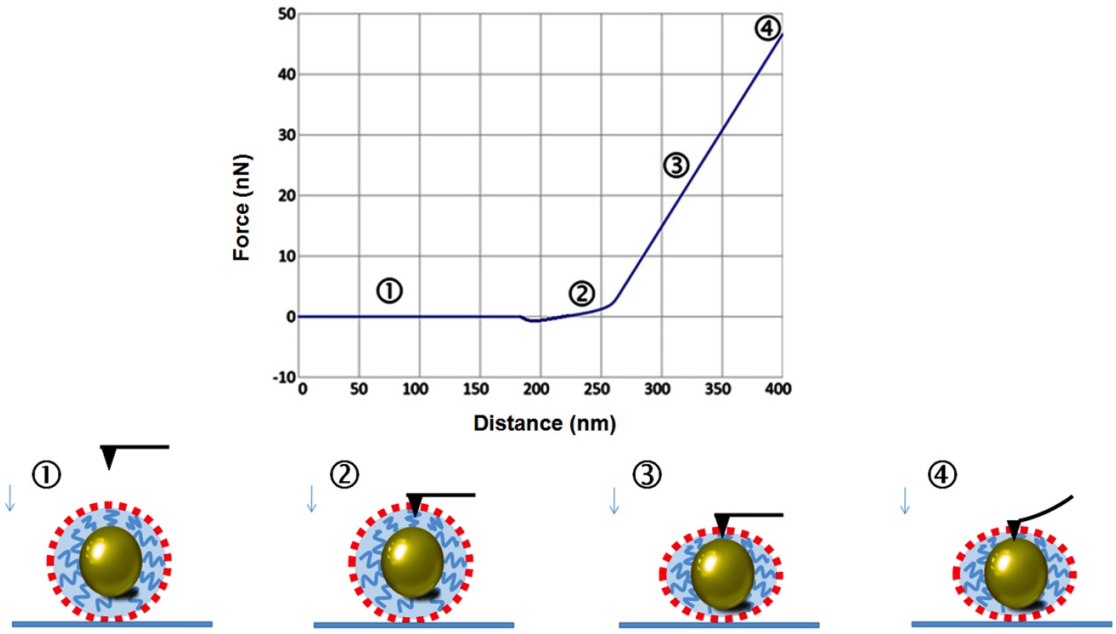

Scheme S.VI-2. $F(d_i)$ nanoindentation loading curve with the following regions: 1) The tip approaches the PEGylated surface, yet there is no "touching"; 2) The tip presses the PEG coating, yet it does not "touch" the Au core; 3) The tip reaches the core; 4) The tip keeps pressing the core.

$$F = \frac{2}{\pi} \cdot \frac{E}{1-\nu^2} \cdot tan\,\alpha \cdot d_i \qquad \text{(Equation S.VI-1)}$$

Where F, E, ν, α and d_i are loading force, the Young's modulus, the Poison's ratio, the half angle of the conical tip and the indentation displacement, respectively.

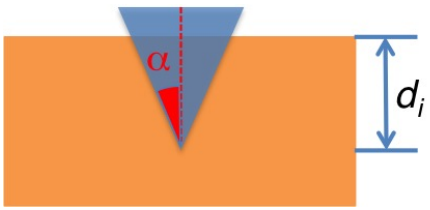

Scheme S.VI-3. Schematic of the Sneddon conical indenter model, where α and d_i are the half angle of an ideal indenter conical tip and the indentation displacement.

Results and discussion: In order to obtain the distribution frequency of the Young's modulus (i.e., N(*E*)) for each single NP investigated, more than 60 force-indentation curves (i.e., *F* versus d_i) were collected, thereby assuring that each NP is tapped in different parts of its surface. One has to keep in mind that the hardness represented by the Young's modulus is highly dependent on the radius of the tip, the deflection sensitivity, the spring constant of the tip, tip half angle and the Poisson's ratio.[9] Figure S.VI-1 and S.VI-4 show the stiffness diagrams for individual NPs (one arbitrary NP for each of the 16 samples) in air (E_A) and in water (E_W), respectively. Figures S.VI-2 and VI-3, and VI-5 and VI-6 summarize the average values extracted for each sample. From these diagrams/heatmaps, one can see that in general the Young's modulus depends on the NPs' size and the molecular weight of PEG molecules. The Young's modulus increased with increasing core size (for the same molecular weight of PEG). Likewise the Young's modulus increased with increasing molecular weight of PEG for the same NP size. In addition, the Young's modulus in water (E_W) is significantly higher than in air (E_A). Thus the water content in PEG plays an important role for the hardness of the NPs, which can be explained due to crosslinking of PEG ligands with water molecules.[10]

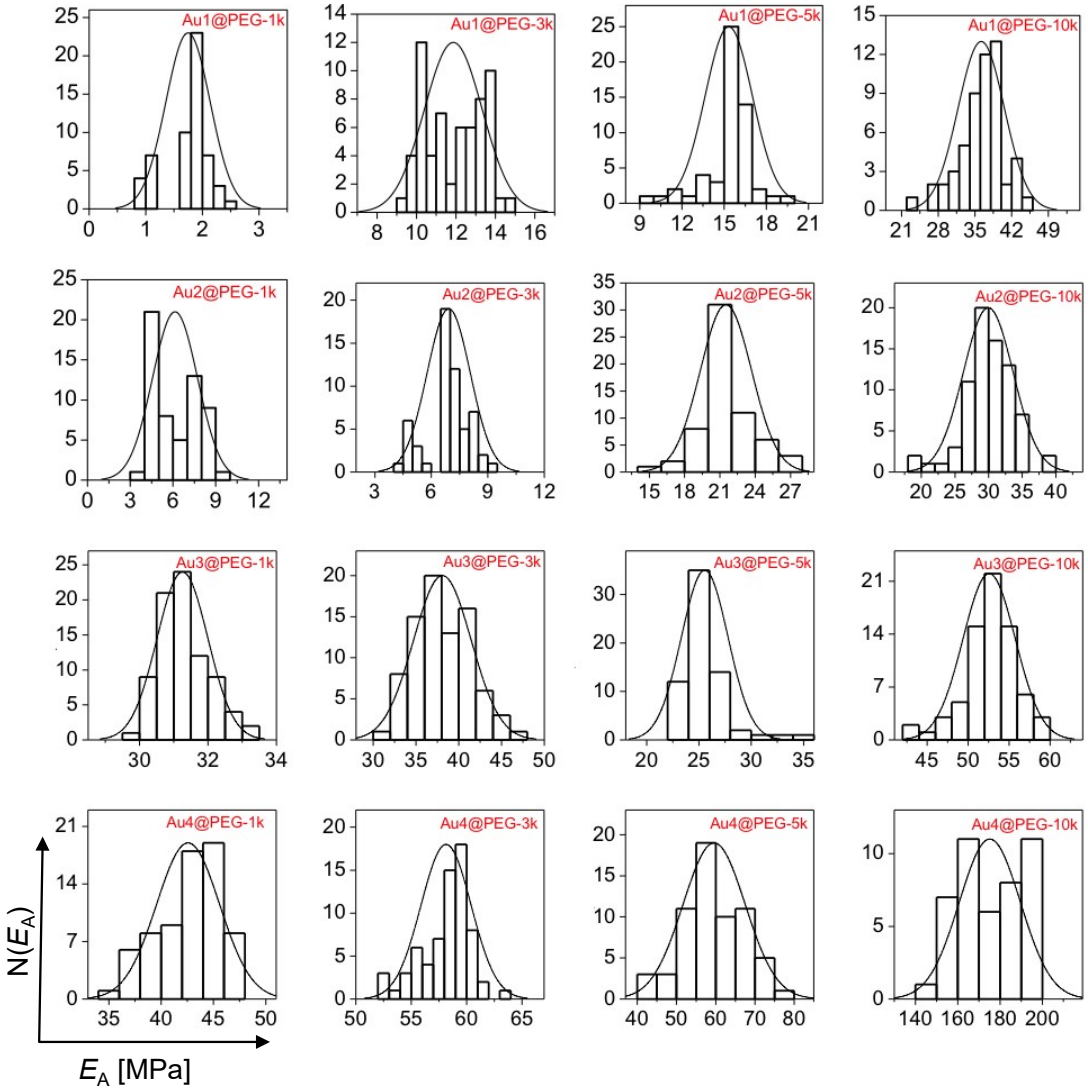

Figure S.VI-1. Stiffness measurements in air (E_A). The distribution frequency N(E_A) of the Young's modulus is plotted.

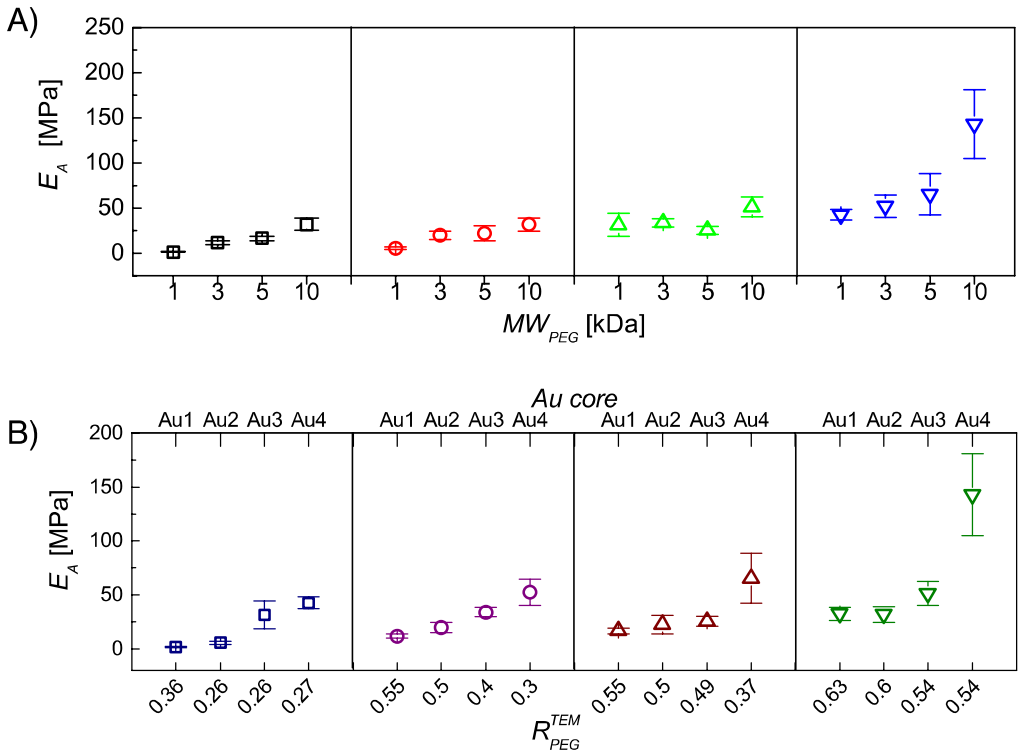

Figure S.VI-2. *E* values in air (E_A). A) Dependence of the Young's modulus on PEGylation for Au1 (black), Au2 (red), Au3 (green) and Au4 (blue); B) Role of the dimensionless parameter R_{PEG}^{TEM} for PEG-1k (dark blue), PEG-3k (magenta), PEG-5k (brown) and PEG-10k (olive).

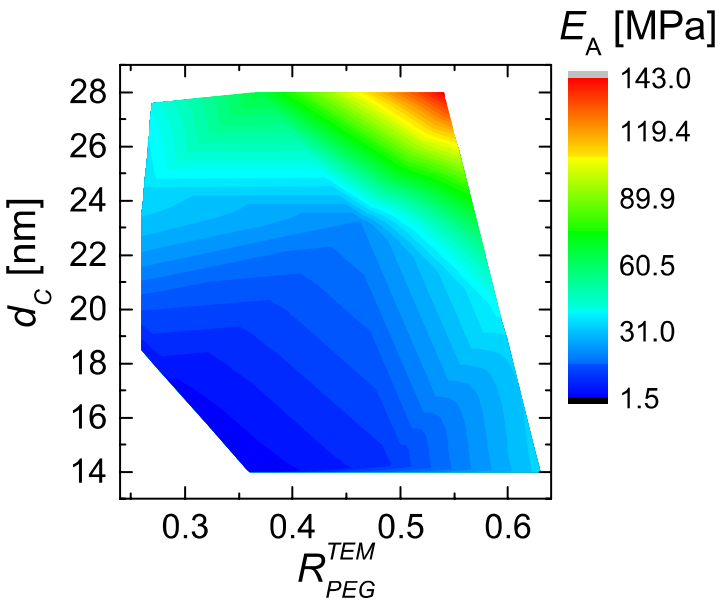

Figure S.VI-3. E_A heatmap in a diagram d_C versus R_{PEG}^{TEM}.

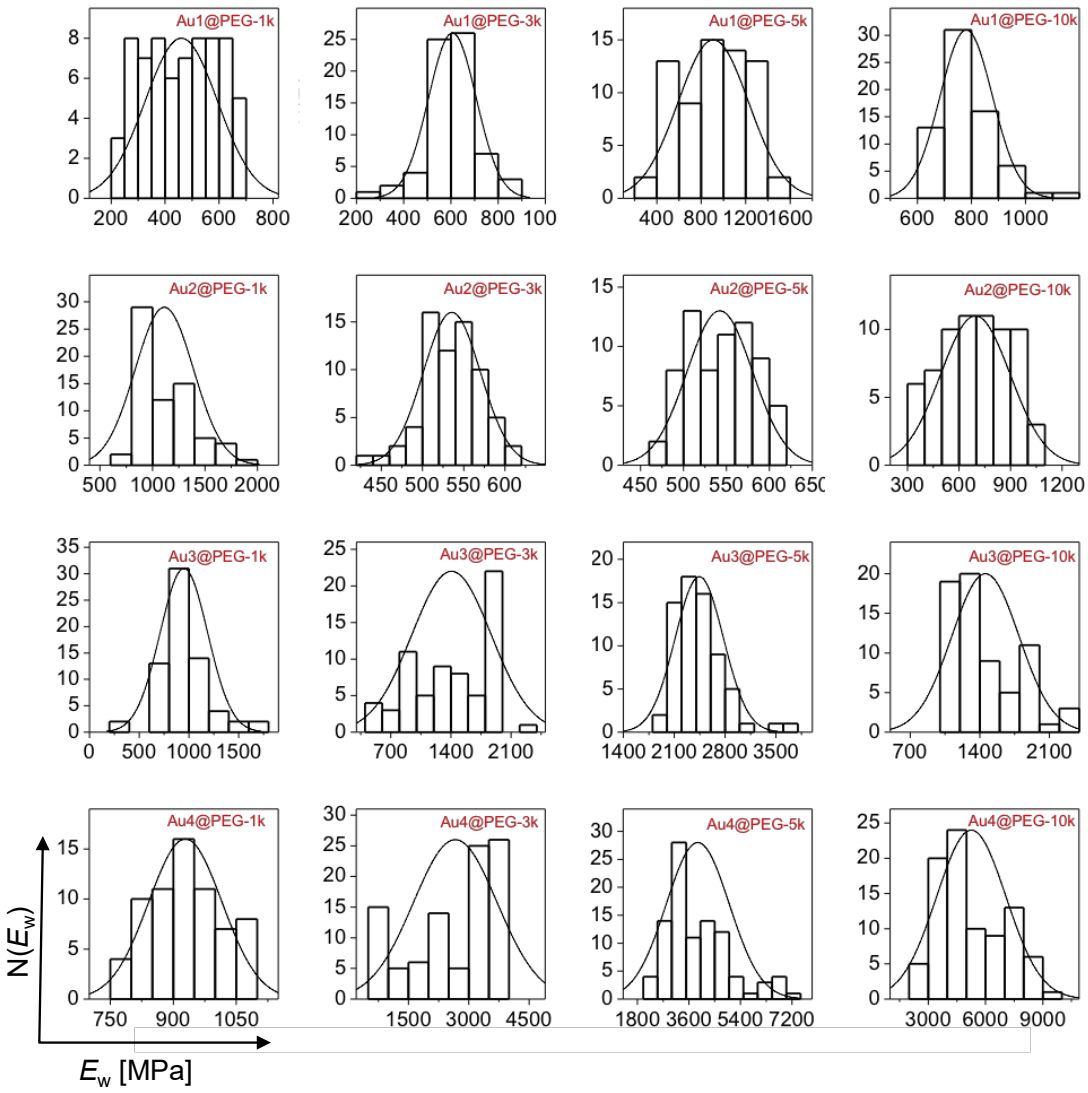

Figure S.VI-4. Stiffness measurements in water (E_W). The distribution frequency N(E_W) of the Young's modulus is plotted.

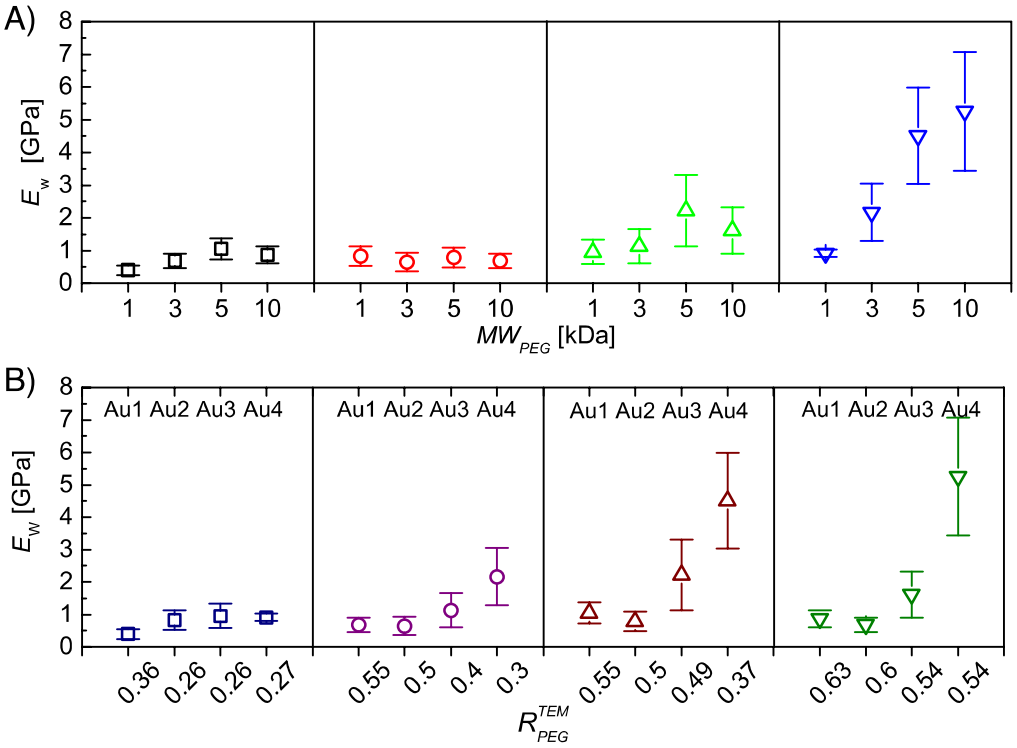

Figure S.VI-5. E values in water (E_W). A) Dependence of the Young's modulus on PEGylation for Au1 (black), Au2 (red), Au3 (green) and Au4 (blue); B) Role of the dimensionless parameter R_{PEG}^{TEM} for PEG-1k (dark blue), PEG-3k (magenta), PEG-5k (brown) and PEG-10k (olive).

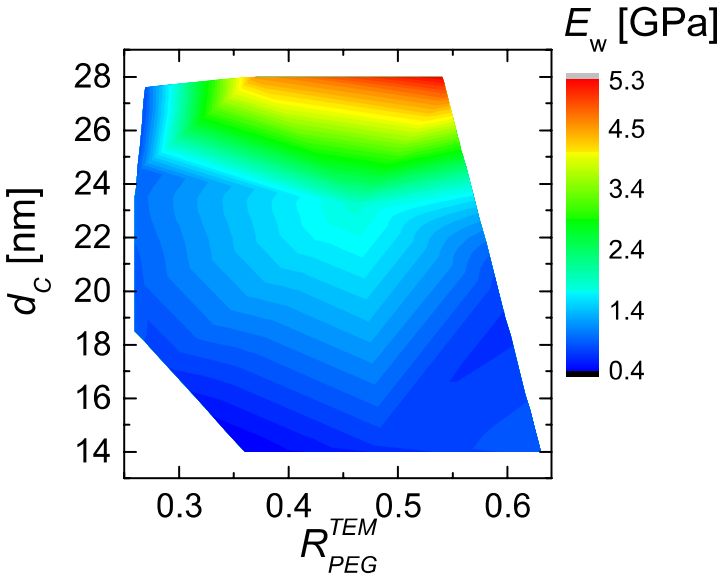

Figure S.VI-6. E_W heatmap in a diagram d_C versus R_{PEG}^{TEM}.

Alternatively, the heatmaps for E_A and E_W can be represented as 3d surface plots as follows:

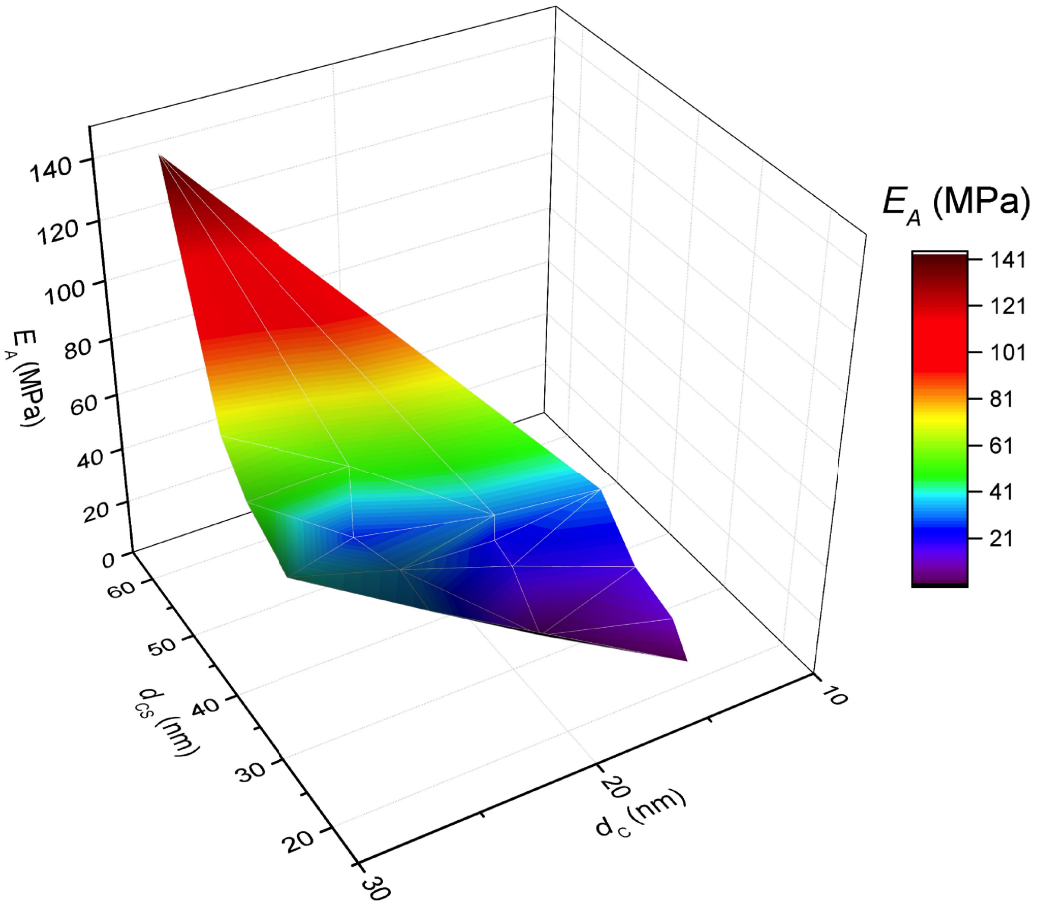

Figure S.VI-7. 3d surface plot for d_C, d_{CS} and E_A.

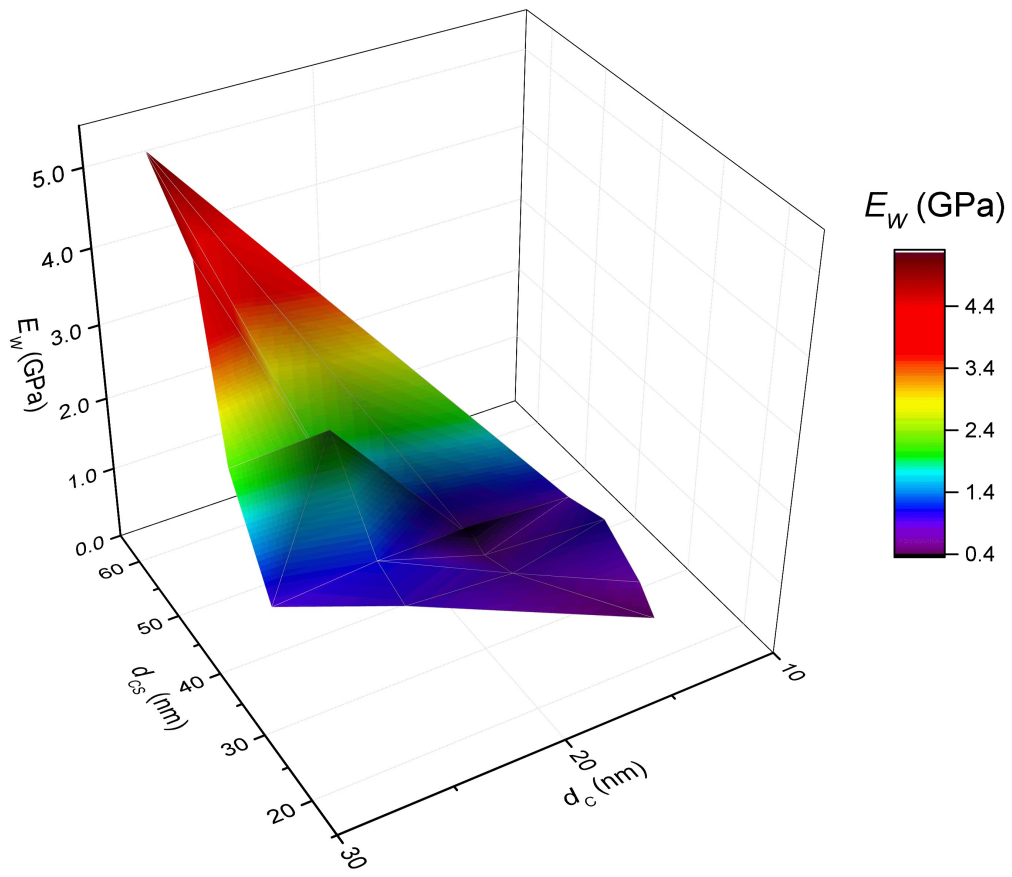

Figure S.VI-8. 3d surface plot for d_C, d_{CS} and E_W.

VII) Catalytic properties of PEGylated NPs

Description of the experiment:

The catalytic activity of Au@PEG NPs towards the reduction of methylene blue (MB, blue color) to leucomethylene blue (LMB, colorless), in the presence of an excess of $NaBH_4$ at room temperature (ca. 25 ºC), was followed by UV-vis absorption measurements (Agilent 8453 UV/Vis absorbance spectrometer) in a 1.25 cm plastic cuvette (Sarstedt #67.758.001).[11]

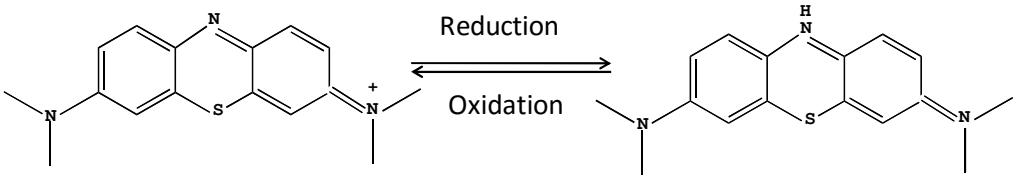

Methylene blue (Blue)

Leucomethylene blue (Colorless)

Scheme S.VII-1: Reduction reaction of MB to LMB.

VII.1. Catalysis using the same concentration of the Au@PEG NPs:In a plastic cuvette, 400 µL of MB ($9.37 \cdot 10^{-4}$ M) was mixed with 10 µL of Au NPs (0.22 nM; corresponding to $1.3 \cdot 10^{9}$NPs). Then 120 µL of freshly prepared $NaBH_4$solution ($5.28 \cdot 10^{-2}$ M, Aldrich #452874) was added immediately. The catalytic properties of the Au@PEG NPs were monitored for the first 90 s of the reaction by collecting UV-Vis spectra(400 - 800 nm) automatically (one spectrumevery3.6 s), cf.Figure S.VII-1. The evolution of the absorbance at the maximum (λ_{max} = 664 nm) over time is shown in Figure S.VII-2. Finally, the NPs' catalytic properties were calculated by kinetics (*k*, Ln (A/A_0)) taking into account the first 30 s at λ_{max}(Table S.II-1). That is, *k* [s^{-1}] is obtained from the slope of the curves Ln (A/A_0) versus time. The blank absorption (A_0) was measured with the same parameters but using H_2O instead of NP solution.

VII.2. Catalysiswith same gold amount: In our experiment, given an equal number of Au@PEG NPs with different inorganic core (Au1 to Au4) and different PEGylation (PEG-1k, PEG-3k, PEG-5k and PEG-10k), the mass of gold depends on the diameter of the NPs (Au1-Au4), i.e., 1 nM Au@PEG NPs would be equivalent to 16 mg/L of Au1 ($1 \cdot 10^{-9}$ mol/L · $6.023 \cdot 10^{23}$ NPs/mol · $2.6 \cdot 10^{-17}$ g/NP); 32 mg/L of Au2 ($1 \cdot 10^{-9}$ mol/L · $6.023 \cdot 10^{23}$ NPs/mol · $6.4 \cdot 10^{-17}$ g/NP); 79 mg/L of Au3 ($1 \cdot 10^{-9}$ mol/L · $6.023 \cdot 10^{23}$ NPs/mol · $1.3 \cdot 10^{-16}$ g/NP); and 134 mg/L of Au4 ($1 \cdot 10^{-9}$ mol/L · $6.023 \cdot 10^{23}$ NPs/mol · $2.2 \cdot 10^{-16}$ g/NP). In order to prove whether the gold mass plays any role on the catalyticefficiency of the NPs, equal gold amounts of AuNP solution of different concentration wasused for the study. Using the same conditions as described above, 10 µL of the Au@PEG NPs (29.4 mg/L, with the four PEG coatings) were used, which is equivalent to 1.96 nM, 0.76 nM, 0.37 nM and 0.22 nM for Au1, Au2, Au3 and Au4, respectively. These values can be also compared in terms of concentration of surface atoms. Given that Au1, Au2, Au3 and Au4 present ca.8900, 16100, 26200 and 37400 surface atoms, respectively, we can express the mass concentration in terms of surface atoms per L as follows: c[mol/L]·N_A·N_{SA} [surface atoms/NP], which gives for Au1, Au2, Au3 and Au4: $1.1 \cdot 10^{-19}$, $7.4 \cdot 10^{-18}$, $5.8 \cdot 10^{-18}$ and $4.9 \cdot 10^{-18}$ surface atoms/L, where N_A is the Avogadro's number ($6.023 \cdot 10^{23}$). The absorption spectra of the catalytic reactions at equal Au mass and plots of λ_{max} over time are shown in Figure S.VII-3

and Figure S.VII-4, respectively. The catalytic parameters extracted from the plots are enlisted in Table S.VII-2.

Results and discussion:

From Figure S.VII-1, Figure S.VII-2, and Table S.VII-1 we can see that under the same concentration of Au@PEG NPs, the size of the inorganic core (i.e., different number of surface atoms) has an impact ontheir catalytic properties: the bigger the NPs are (more surface atoms), the more efficient catalysts the NPs are. On the other hand, the molecular weight of the PEG used for PEGylation also influences their catalytic properties. Our data show that 5 kDa PEGylated NPs show always the highest catalytic values comparedto 1 kDa, 3 kDa and 10 kDa equivalent colloids. From all 16 samples we can see that the best sample in terms of catalytic efficiency is Au4@PEG-5k (k = $33.0 \cdot 10^{-3}$ s^{-1}). This might be due to a more efficient surface accessibility of MB molecules in the case of 5 kDa PEGylation. Possibly PEG shell of PEG molecules with 1 kDa and 3 kDa are better packed due to their smaller length, whereas the 10 kDa PEG is long enough to wrap the NPs more efficiently than the 5 kDa PEG.

With the same gold amount (29 mg/L) the catalytic behavior of the 16 samples is indeed significantly marked for the type of PEGylation, cf.Figure S.VII-3, Figure S.VII-4, and Table S.VII-2. For each type of core (Au1-Au4), again, the PEG-5kDasamples present the fastest kinetic constants compared to the other PEGylations. If we now look at one type of PEGylation with different Au core (i.e., different number of NPs: 1.96 nM, 0.76 nM, 0.37 nM, and 0.22 nM for Au1, Au2, Au3 and Au4, respectively), the combinations Au2@PEG-5k and Au3@PEG-3k present the highest catalytic rates (k = $66.3 \cdot 10^{-3}$ s^{-1} and $64.7 \cdot 10^{-3}$ s^{-1}, respectively), although they present less concentration of surface atoms than the Au1 samples ($7.4 \cdot 10^{-18}$/ $5.8 \cdot 10^{-18}$ vs. $1.1 \cdot 10^{-19}$ for Au2/Au3 vs. Au1).

Overall, these measurement confirm that this type of PEGylated AuNPs presents fast kinetic constants for the reduction of MB, in the same range of other systems like Ag NPs.[11] However, the catalytic response is significantly affected by the type of PEGylation. In addition the electronic band structure of the Au cores will change upon reduction in core diameter. Extrapolation to a solution with only gold atoms as “NPs” of minimum size justifies this speculation, as catalytic activity of gold atoms is different from the one of gold surfaces.[12] At any rate, comparison of the heatmaps shown in Figure S.VII-5 and VII-6 emphasizes the importance of the NP metrics.

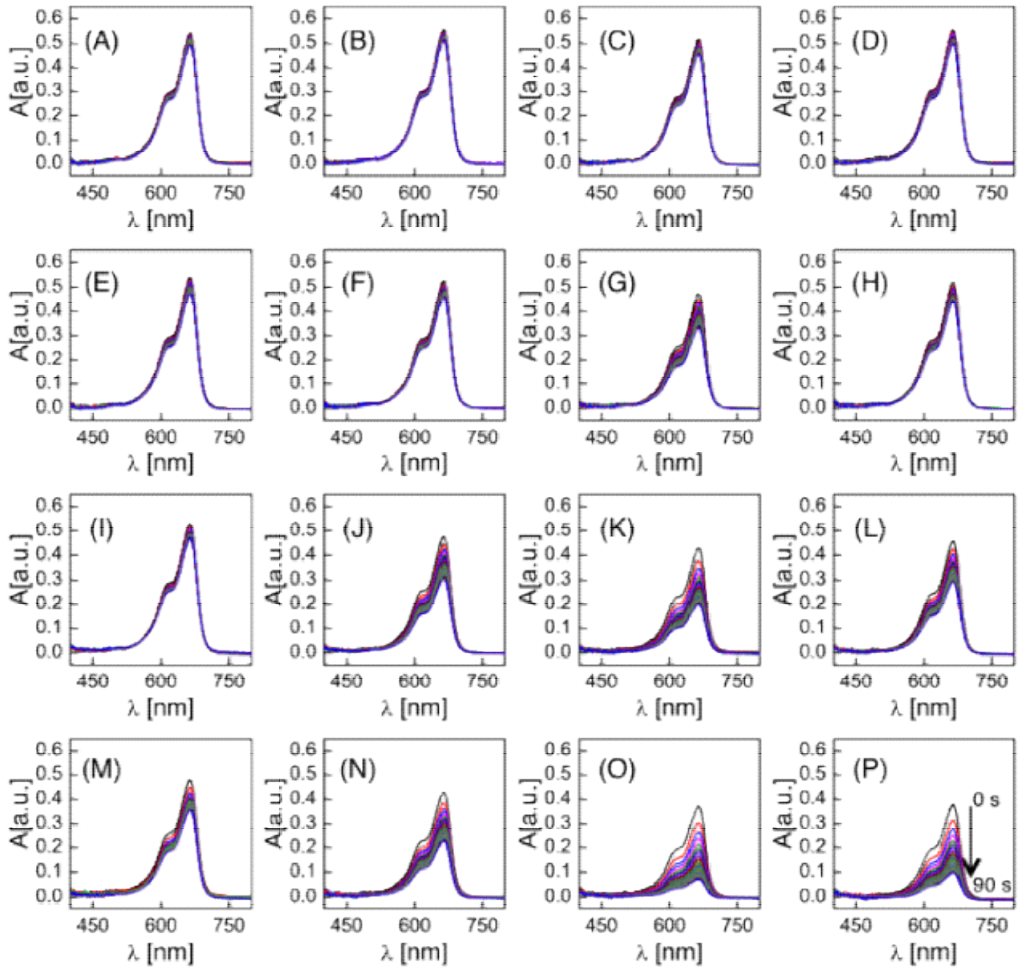

Figure S.VII-1. Absorption spectra collected over 90 s for the reduction of MB to LMB catalyzed by Au@PEG NPs at equal number of particles. (A-D) the spectra of Au1 with different PEGs (1 kDa, 3 kDa, 5 kDa and 10 kDa); (E-H) the spectra of Au2 with1 kDa, 3 kDa, 5 kDa and 10 kDa; (I-L) the spectra of Au3 with1 kDa, 3 kDa, 5 kDa and 10 kDa; and (M-P) the spectra of Au4 with 1 kDa, 3 kDa, 5 kDa and 10 kDa. The arrow in panel P shows the evolution to the spectra from 0-90 s.

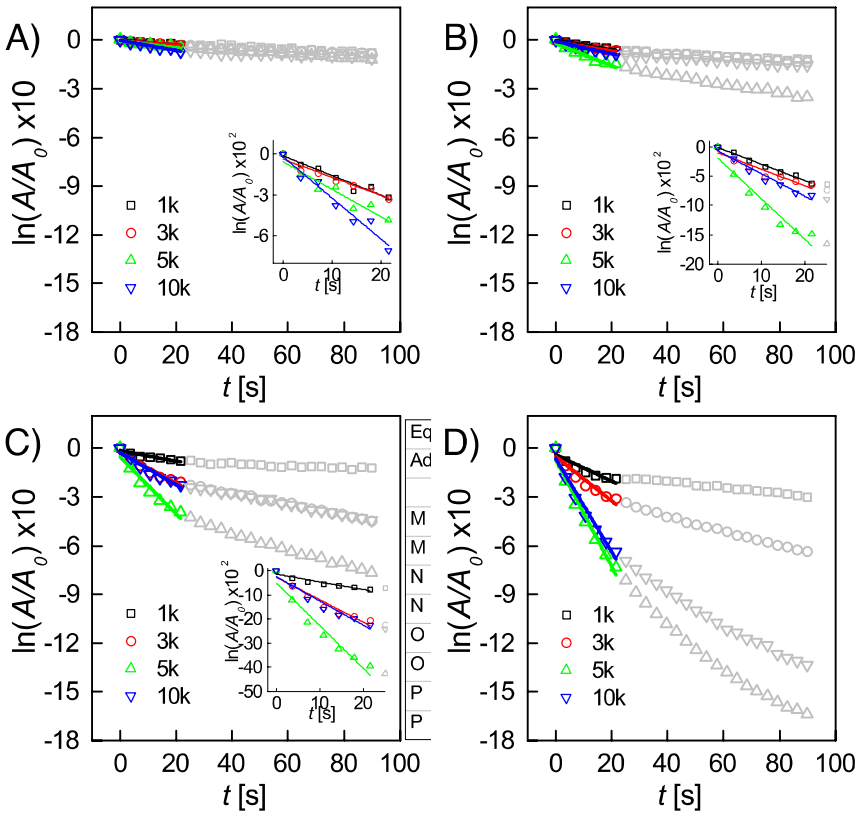

Figure S.VII-2. (A-D) Absorption at λ_{max} (A)versus time for equal number of NPs, i.e., Au1, Au2, Au3, and Au4, respectively, PEGylated with different PEG shells (1 kDa: black; 3 kDa: red; 5 kDa: green; and 10 kDa: blue). Data considered for the kinetic fitting (first order) are coloured (initial 22 s). Inserts show zoom areas of the fitting regions for selected samples.

Table S.VII-1. Kinetic constant values k_n [s^{-1}] for the 16 samples (equal molar NP concentration – 0.22 nM). A first-order catalytic behavior was considered,i.e., $\ln(A/A_0) = -k_n \cdot t$, during the initial 22 s of the reaction.

PEG / core	PEG-1k	PEG-3k	PEG-5k	PEG-10k
Au1	$1.5 \cdot 10^{-3}$ s^{-1}	$3.9 \cdot 10^{-3}$ s^{-1}	$5.7 \cdot 10^{-3}$ s^{-1}	$2.2 \cdot 10^{-3}$ s^{-1}
Au2	$1.5 \cdot 10^{-3}$ s^{-1}	$2.8 \cdot 10^{-3}$ s^{-1}	$6.8 \cdot 10^{-3}$ s^{-1}	$3.8 \cdot 10^{-3}$ s^{-1}
Au3	$3.2 \cdot 10^{-3}$ s^{-1}	$9.2 \cdot 10^{-3}$ s^{-1}	$17.6 \cdot 10^{-3}$ s^{-1}	$9.9 \cdot 10^{-3}$ s^{-1}
Au4	$8.2 \cdot 10^{-3}$ s^{-1}	$13.7 \cdot 10^{-3}$ s^{-1}	$33.0 \cdot 10^{-3}$ s^{-1}	$28.7 \cdot 10^{-3}$ s^{-1}

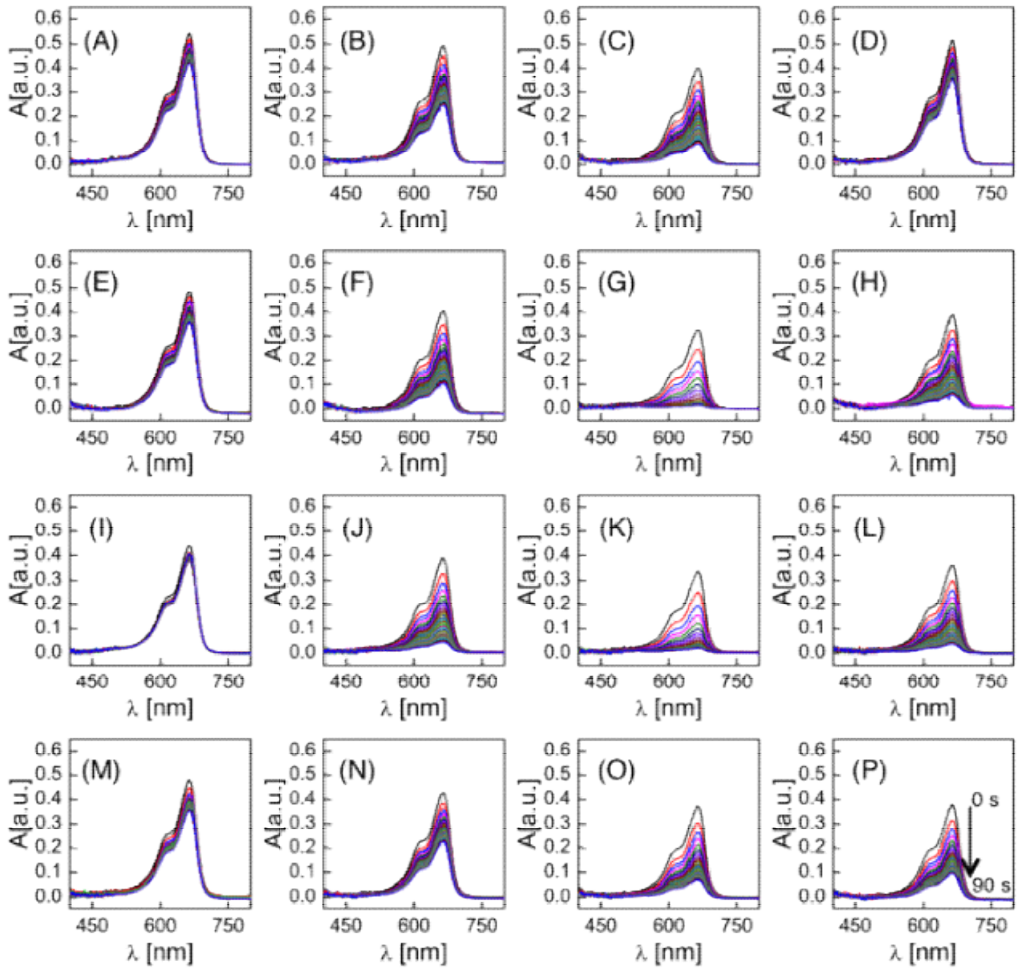

Figure S.VII-3. Absorption spectra A(λ) collected over 90 s for the reduction of MB to LMB catalyzed by Au@PEG NPs at equal mass of elemental gold. (A-D) the spectra of Au1 with different PEGs (1 kDa, 3 kDa, 5 kDa and 10 kDa); (E-H) the spectra of Au2 with1 kDa, 3 kDa, 5 kDa and 10 kDa; (I-L) the spectra of Au3 with1 kDa, 3 kDa, 5 kDa and 10 kDa; and (M-P) the spectra of Au4 with 1 kDa, 3 kDa, 5 kDa and 10 kDa. The arrow in panel P shows the evolution to the spectra from 0-90 s.

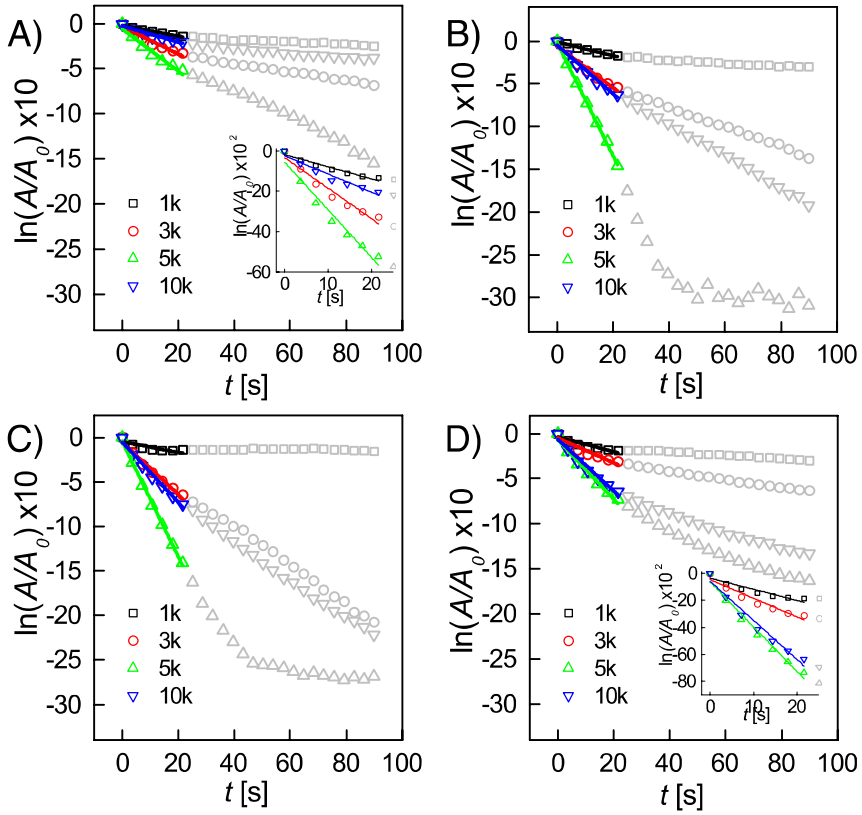

Figure S.VII-4.Absorption (A) at λ_{max} versus time for equal mass of gold, i.e., Au1, Au2, Au3, and Au4, respectively, PEGylated with different PEG shells (1 kDa: black; 3 kDa: red; 5 kDa: green; and 10 kDa: blue). A_0 is the absorption at λ_{max} at time 0 s. Data considered for the kinetic fitting (first order) are coloured (initial 22 s). Inserts show zoom areas of the fitting regions for selected samples.

Table S.VII-2.Summary of the kinetic constant values k [s^{-1}] for the 16 samples (equal Au mass concentration – 29 mg/L). A first-order catalytic behavior was considered, i.e., $\ln(A/A_0) = -k \cdot t$, during the initial 22 s of the reaction

PEG / core	PEG-1k	PEG-3k	PEG-5k	PEG-10k
Au1	$6.0 \cdot 10^{-3}$ s^{-1}	$15.0 \cdot 10^{-3}$ s^{-1}	$23.4 \cdot 10^{-3}$ s^{-1}	$8.9 \cdot 10^{-3}$ s^{-1}
Au2	$8.1 \cdot 10^{-3}$ s^{-1}	$24.3 \cdot 10^{-3}$ s^{-1}	$66.3 \cdot 10^{-3}$ s^{-1}	$28.5 \cdot 10^{-3}$ s^{-1}
Au3	$6.0 \cdot 10^{-3}$ s^{-1}	$29.3 \cdot 10^{-3}$ s^{-1}	$64.7 \cdot 10^{-3}$ s^{-1}	$34.0 \cdot 10^{-3}$ s^{-1}
Au4	$8.2 \cdot 10^{-3}$ s^{-1}	$13.7 \cdot 10^{-3}$ s^{-1}	$33.0 \cdot 10^{-3}$ s^{-1}	$28.7 \cdot 10^{-3}$ s^{-1}

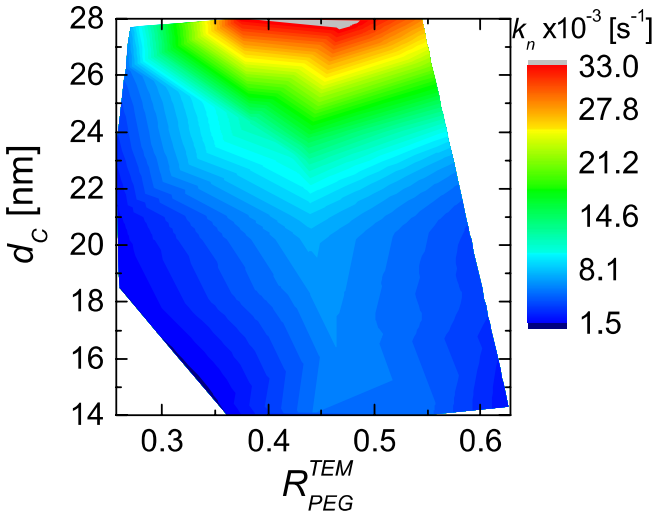

Figure S.VII-5. k_n heatmap for an equal number of NPs in a diagram d_C versus R_{PEG}^{TEM}.

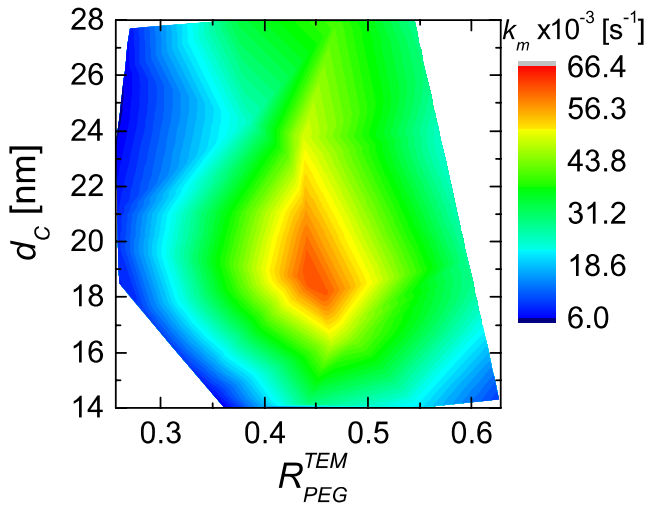

Figure S.VII-6. k_m heatmap for an equal mass of elemental gold in a diagram d_C versus R_{PEG}^{TEM}.

Alternatively, heatmaps Figure.SVII-5 and -6 can be represented as 3d surface maps as follows:

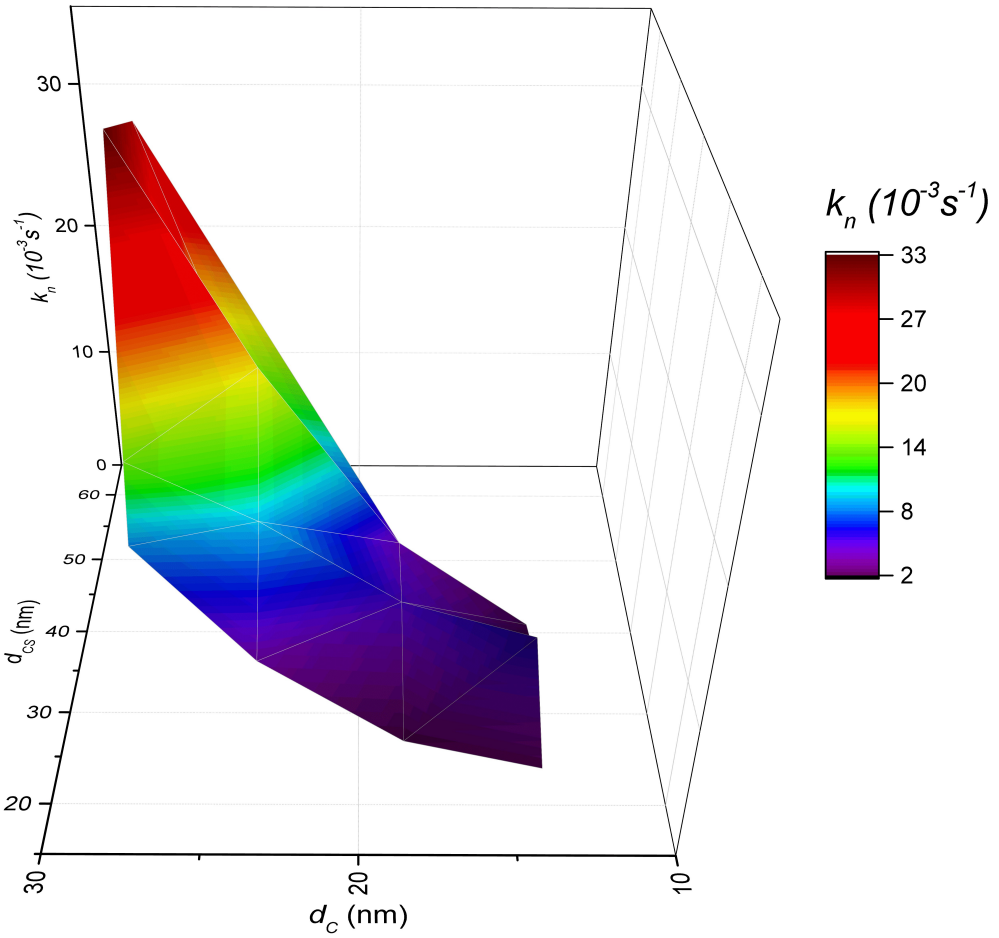

Figure S.VI-7. 3d surface plot for d_C, d_{CS} and k_n.

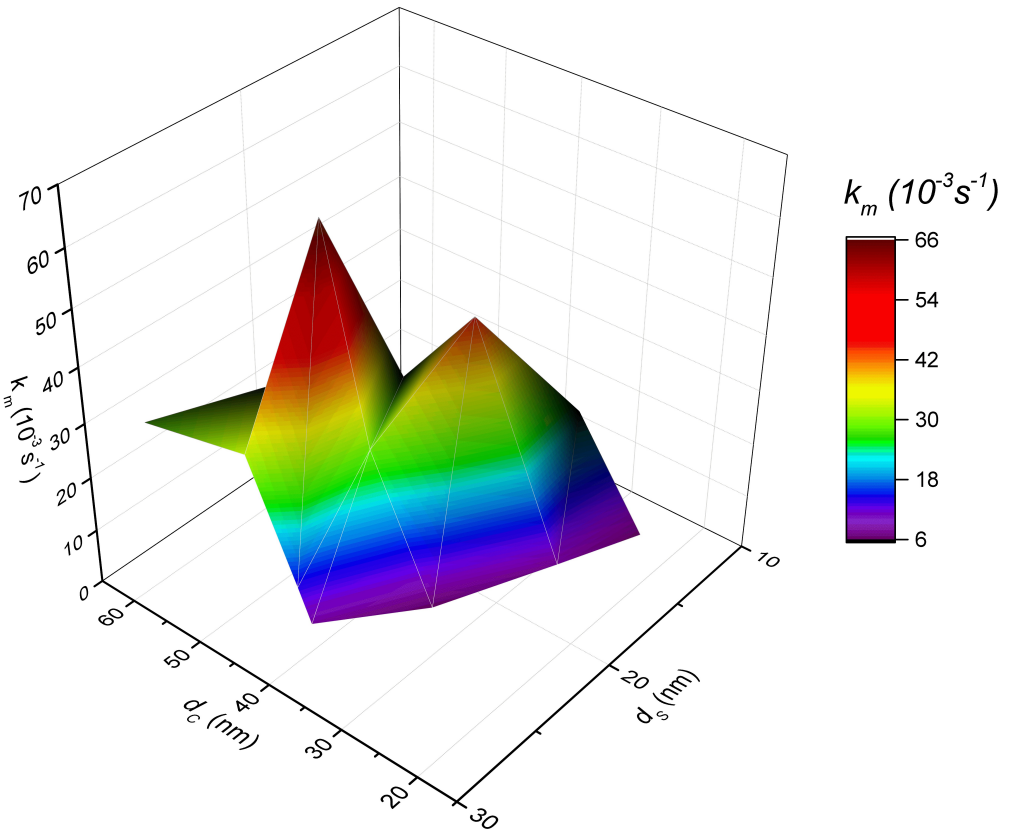

Figure S.VI-8. 3d surface plot for d_C, d_{CS} and k_m.

VIII) Functionalization of PEGylated NPs

The goal of this section is to derivatize the PEGylated samples previously discussed, i.e., Au1@PEG-10KDa, Au2@PEG-5KDa, Au3@PEG-3KDa, Au4@PEG-1KDa, with a near-infrared (NIR) dye (dyomics dy647P1, amino derivative, in the following referred to as Dye) and a quaternary ammonium group (positive in all of the pH range, 2-aminoethyl trimethylammonium chloride hydrochloride, in the following referred to as N+). To do so, we used EDC (1-Ethyl-3-(3-dimethylaminopropyl)carbodiimide) chemistry to covalently bind these molecules to the end terminal carboxylic groups of the PEG molecules, which are present in all of the samples. NPs were activated in milli-Q water with EDC and sulfo-NHS (N-hydroxysulfosuccinimide) at pH 5, with the following molar ratios (NP:EDC:sulfo-NHS) $1{:}10^6{:}2.5{\cdot}10^6$. After 20 minutes the dye was added with a NP:dye molar ratio of 1:1000. The reaction was then stirred for 1 min and then the quaternary ammonium compound (N+) was added with a NP:N+ molar ratio of $1{:}5{\cdot}10^4$. The reaction was stirred for 5 min, and then the pH was raised to 8 with a concentrated solution of NaOH. The reaction was stirred overnight, and then the NPs were washed by centrifugal precipitation. By this method we prepared Au@PEG-dye-N+; equivalently, we prepared Au@PEG-dye in which the N+ was not added.

Figure S.VIII-1 shows a gel with the different samples produced, where one can clearly see the differences in terms of functionalization. The goal of this section is to produce colloids with the same hydrodynamic size but different PEG shells and Au cores, which also are labeled with a suitable dye for cellular studies, and also with different net surface charge (by using the –N+).

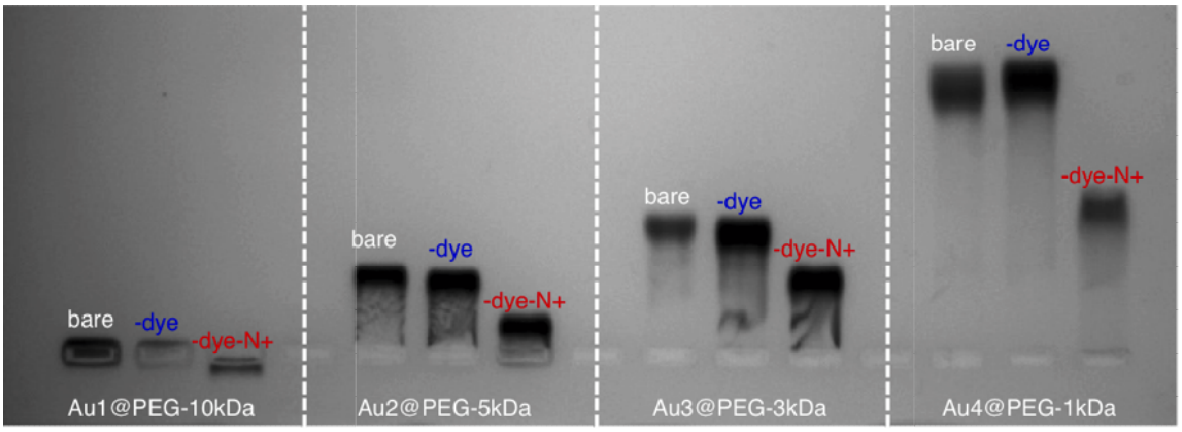

Figure S.VIII-1. Different functionalizations with dye and NR+ of Au NPs. The Au NPs were run on an agarose gel. They migrated from the well to which they were loaded (seen in the bottom part of the photo) towards the positive electrode (located above the top part of the photo).

Indeed the electrophoretical mobilities correlate very well with the ζ-potential of the samples, which were determined in water with Laser Doppler Anemometry (LDA), cf. Figure S.VIII-2 and the raw data in Table S.VIII-1.

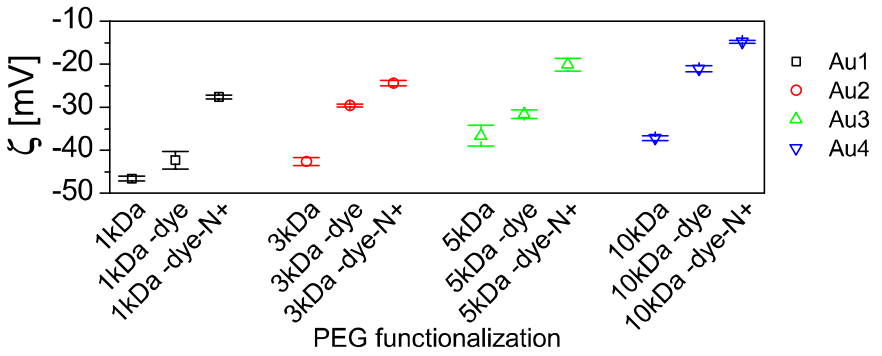

Figure S.VIII-2. ζ-potential values for different functionalization steps with dye and NR+ of Au NPs.

Table S.VIII-1.ζ-potential values for each PEGylated core in each step of their functionalization.

Samples	ζ-potential [mV]
Au1@PEG-10kDa	-37.2 ± 0.6
Au1@PEG-10kDa –dye	-21.1 ± 0.7
Au1@PEG-10kDa –dye–N+	-14.8 ± 0.3
Au2@PEG-5kDa	-36.6 ± 2.4
Au2@PEG-5kDa –dye	-31.6 ± 1.0
Au2@PEG-5kDa –dye–N+	-20.1 ± 1.5
Au3@PEG-3kDa	-42.6 ± 1.0
Au3@PEG-3kDa –dye	-29.6 ± 0.3
Au3@PEG-3kDa –dye–N+	-24.4 ± 0.6
Au4@PEG-1kDa	-46.6 ± 0.6
Au4@PEG-1kDa –dye	-42.3 ± 2.0
Au1@PEG-1kDa –dye–N+	-27.6 ± 0.4

Addition of quaternary ammonium groups, as expected, further reduces the negative ζ-potential of the NPs and makes them less negatively charged, leading to two NP series with different surface charge.

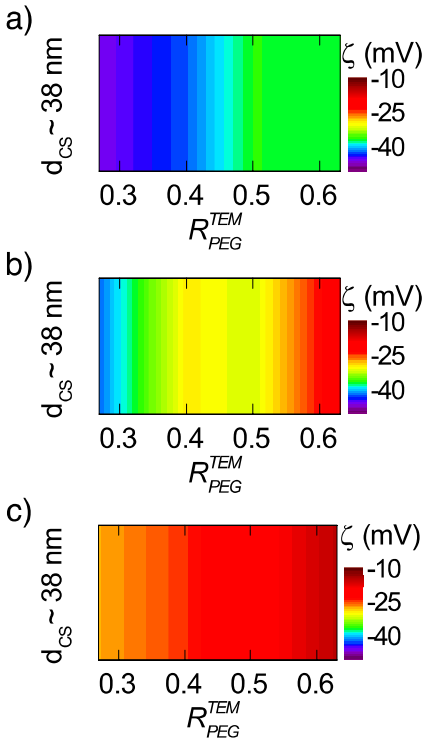

Figure S.VIII-3. Heatmaps for ζ-potential values with a) PEGylated NPs with ca. equal $d_{CS} \approx 38$ nm, as determined by negative staining TEM; b)-dye; c)-dye-N+.

The hydrophilicity of the PEGylated NPs, i.e., γ_m, cf. section V) Characterization of the NPs' dynamic interfacial tension (IFT), is only mildly affected by functionalization with the dye and the quaternary ammonium group and thus, mainly determined by the molecular weight of the PEG chains attached. As example, Figure S.VIII-4 shows the dynamic surface tension (γ_t) plots for Au3@PEG-3kDa (Au3, black open circles), Au3@PEG-3kDa-Dye (Au3-, red open red circles) and Au3@PEG-3kDa-Dye-N+ (Au3+, green open circles), where the interfacial tension decreases with time, approaching andan equilibrium value (γ_m) in each case, which do not vary significantly among samples. In case of Au3, Au3- and Au3+, γ_m is 23.14, 24.24 and 22.52, respectively.

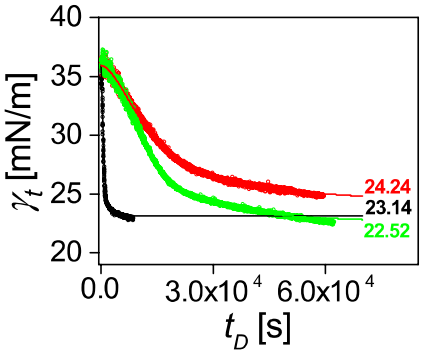

Figure S.VIII-4. γ_t versus time (t_D) plots for Au3 (black circles), Au3- (red circles) and Au3 (green circles); experimental data and the respective fitting lines are represented by hollow circles and solid lines.

9) Cell Studies

The effect of the previously described functionalized NPs on basic cellular parameters is described here. From the 16 samples evaluated, we choose 4 samples with a fixed overall diameter d_{CS} ≈ 38 nm, from "small" Au cores with thick PEG shell towards "big" Au cores with thin PEG shell. In other words, the others parameters vary in direction α, i.e., hydrophilicity and catalytic activity. We chose variation in direction α, as in a previous study we performed already a detailed investigation for variation in direction χ,[13] which is perpendicular to direction α.

Experimental setup: The data shown here are acquired using high-content imaging, where for every condition, several hundreds of images were taken and automated analysis was performed, resulting in minimal 3000 cells per condition that were analyzed. The following parameters related to cell function and morphology were analyzed (cf., Figure S.IX-1, -2. -3, -4): autophagy (in the following referred to as LC3), cell area (in the following referred to as A), endosome size (in the following referred to as S_E), membrane damage (in the following referred to as MD), mitochondrial health (in the following referred to as MH), reactive oxidative species (in the following referred to as ROS), cell skewness (in the following referred to as SK), viability (in the following referred to as V), and focal adhesion (in the following referred to as FA).

Cell culture: Cell-NP interaction studies were carried out with the following two cell types, being murine C17.2 neural progenitor cells and primary human umbilical vein endothelial cells (HUVECs). The C17.2 cells were cultured in high glucose containing Dulbecco's modified Eagle's medium (DMEM), supplemented with 10% fetal calf serum, 5% horse serum, 1 mM sodium pyruvate, 2 mM L-Glutamine and 1% penicillin/streptomycin (Gibco, Invitrogen, Belgium). The cells were passaged every 48 h and split 1/5 in uncoated culture flasks.

HUVECs were purchased from Tebu-Bio (Tebu-Bio, Belgium). The cells were cultured in endothelial basal/growth culture medium (EBM-2/EGM-2, Clonetics, San Diego, CA) with medium changes every 48 h. Cells were passaged when reaching near 80% confluency by lifting the cells with 0.05% trypsin (Gibco) followed by plating (1/5) onto tissue-culture flasks coated with collagen.

Cell-nanoparticle interaction studies: For high-content imaging studies, all cell types were seeded at 5000 cells/well in 24 well plates (Nunc, Belgium). Cells were allowed to attach overnight in a humidified atmosphere at 37 °C and 5% CO_2, after which the cells were incubated with the Au NPs for 24 h in the full growth medium (0.5 mL) respective for the cells. For cellular exposure studies, cells were incubated with the NPs at equal mass of gold (62.5, 125 or 250 µg/mL) or equal number of NPs (1.25, 2.5 or 5 nM). Every condition was performed in triplicate, after which the high-content imaging setup was ran using an InCell 2000 High-Content Imaging System (GE Healthcare Life Sciences, Belgium) for a minimum of 3000 cells per well/condition. Data analysis was then performed on the InCell Investigator software (GE Healthcare Life Sciences, Belgium) using in-house developed protocols, using a minimum of 3000 cells/condition, as described elsewhere.[14] Detailed protocols for the specific steps are outlined in the different sections below.

Cell viability (V) and membrane damage (MD): Following cellular exposure to the Au NPs, the cells were washed twice with phosphate buffered saline (PBS; Gibco, Invitrogen, Belgium) and

treated with 2 µM fixable Live-Dead Green dead cell stain (Molecular Probes, Life Technologies Europe, BV, Belgium) in 250 µL/well of PBS (with Ca^{2+} and Mg^{2+}) and incubated in the dark for 30 min at room temperature. Next, the staining media was aspirated, cells were washed gently with PBS (3x) fixed with 4% paraformaldehyde (PFA) for 15 min at room temperature. The fixative was aspirated and cells were washed three times with PBS. Cells were then counterstained using Hoechst 33342 Nuclear stain (20 µg/mL PBS in 250 µL/well) for 15 min at ambient temperature in the dark. The nuclear counterstain was then removed, cells were washed three times with PBS and 500 µL of PBS was added to every well, after which the plates were analyzed using the InCell 2000 analyzer (GE Healthcare Life Sciences, Belgium). During acquisition, a minimum of 1000 cells per well were imaged using a 20x objective for the following channels: UV/blue for Hoechst nuclear stain, FITC/FITC for the Live-Dead Green dead cell stain. Data analysis was then performed on the InCell Investigator software (GE Healthcare Life Sciences, Belgium) using in-house developed protocols, using a minimum of 3000 cells/condition. The level of cell viability was calculated as follows: First, cells were segmented based on the Hoechst stain and the perinuclear region was determined by enlarging the nuclear stain 2.5-fold and using the original Hoechst stain images as seed images. For cell viability based on cellular exposure concentrations, cell viability was calculated by determining the number of total cells minus the number of dead cells (dead cells are defined as cells with clear green nuclei, where the intensity is minimally 3-fold above noise level and having an area of minimally 2 µm²). These values were then normalized to control values (100%) to indicate the degree of cell viability.

For membrane damage, the analysis occurred similarly. All green dots in the perinuclear area with a minimum intensity of 3-fold above the noise level and with a size of minimally 0.1 µm², but smaller than 2 µm² were selected. The ratio of this value with the value obtained for control cells was then given to indicate the level of membrane damage.

Oxidative stress (ROS): After labeling the cells, they were washed (3x) with 500 µL PBS/well, after which the cells were incubated with 500 µL full media containing 5 µM CellROX Green (Molecular Probes, Invitrogen, Belgium) for 30 min at 37 °C. The staining solution was aspirated, cells were washed with 500 µL PBS/well (3x) and fixed with 4% PFA for 15 min at room temperature. The fixative was removed, cells were washed (3x) with PBS (500 µL/well) after which 500 µL of PBS was added per well and plates were kept at 4 °C in a dark container until they were needed for analysis using the InCell 2000 high-content imaging system. For acquisition, the following channels were selected: UV/blue for Hoechst nuclear stain and FITC/FITC for the CellROX Green stain. Data analysis was then performed on the InCell Investigator software (GE Healthcare Life Sciences, Belgium) using in-house developed protocols, using a minimum of 3000 cells/condition. The level of oxidative stress was then calculated as follows: First, cell nuclei were segmented based on the blue channel (Hoechst). As CellROX Green localizes in the nucleus upon oxidation, the intensity of light emitted in the green channel was then determined for every area of the corresponding nuclei. The intensity of every nucleus was then calculated for the green channel and normalized to the intensity level of untreated control cells (100%).

Endosomal size (S_E): After labeling the cells, they were washed (3x) with 500 µL PBS/well, after which the cells were stained in 250 µL PBS (containing Ca^{2+} and Mg^{2+}) containing 75 nM

Lysotracker Red (Molecular Probes, Invitrogen, Belgium) and incubated for 30 min at room temperature. The staining solution was then aspirated, cells were washed with 500 µL PBS/well (3x) and fixed with 4% PFA for 15 min at room temperature. The fixative was removed, cells were washed (3x) with PBS (500 µL/well) after which 500 µL of PBS was added per well and plates were kept at 4 °C in a dark container until they were needed for analysis using the InCell 2000 high-content imaging system. For acquisition, the following channels were selected: UV/blue for Hoechst nuclear stain and DsRed/DsRed for the Lysotracker Red stain. Data analysis was then performed using the InCell Investigator software (GE Healthcare Life Sciences, Belgium) using in-house developed protocols, analyzing a minimum of 3000 cells/condition. The size of the lysosomal network was then calculated as follows: First, cell nuclei were segmented based on the blue channel (Hoechst). Then, the DsRed/DsRed channel was segmented, using the nuclear target channel as seed images. Based on the segmented lysosomal images, the overall area of cellular lysosomes were calculated, for any dot in the lysosomal channel that had an intensity of minimum 3-fold higher than the background noise level. The total area of cellular lysosomes was then normalized to the area of lysosomes in untreated control cells (100%).

Mitochondrial health (MH): After labeling the cells, they were washed (3x) with 500 µL PBS/well, after which the cells were stained in 250 µL PBS (containing Ca^{2+} and Mg^{2+}) containing 200 nM MitoTracker Red CMXRos (Molecular Probes, Invitrogen, Belgium) and incubated for 30 min at room temperature. The staining solution was then aspirated, cells were washed with 500 µL PBS/well (3x) and fixed with 4% PFA for 15 min at room temperature. The fixative was removed, cells were washed (3x) with PBS (500 µL/well) after which 500 µL of PBS was added per well and plates were kept at 4 °C in a dark container until they were needed for analysis using the InCell 2000 high-content imaging system. For acquisition, the following channels were selected: UV/blue for Hoechst nuclear stain and DsRed/DsRed for the MitoTracker Red CMXRos stain. Data analysis was then performed using the InCell Investigator software (GE Healthcare Life Sciences, Belgium) using in-house developed protocols, analyzing a minimum of 3000 cells/condition. The mitochondrial stress and ROS were then calculated as follows: First, cell nuclei were segmented based on the blue channel (Hoechst). Then, the DsRed/DsRed channel was segmented, using the nuclear target channel as seed images. For mitochondrial viability, the level of fluorescence intensity of the segmented mitochondria was determined. The intensity of the mitochondrial signal was then normalized to the intensity level of untreated control cells (100%).

Cell area (A), skewness (SK) and NP uptake: After cellular exposure to the Au NPs, cells were washed (3x) with 500 µL PBS/well and fixed for 15 min at room temperature with 4% PFA. The fixative was then aspirated, cells were washed (3x) with PBS (500 µL/well) after which cells were permeabilised with 250 µL/well of Triton X-100 (1%) for 10 min at room temperature. Cells were then blocked with 10% serum-containing PBS for 30 min at room temperature. Next, cells were stained using 200 µL of staining solution per well first with primary murine anti-α-tubulin antibody for 90 min followed by secondary AF-488-conjugated goat anti-murine antibody for 60 min in the dark at room temperature. The staining solution was aspirated, cells were washed (3x) with PBS (500 µL/well) after which 500 µL fresh PBS was added to each well and the plates were kept at 4 °C in a dark container until analyzed using the InCell 2000 high-content

imaging system. For acquisition, the following channels were selected: UV/blue for Hoechst nuclear stain and FITC/FITC for the α-tubulin stain. Data analysis was then performed on the InCell Investigator software (GE Healthcare Life Sciences, Belgium) using in-house developed protocols, using a minimum of 3000 cells/condition. The size of the cells was calculated as follows: First, cell nuclei were segmented based on the blue channel. Cells were then segmented using the FITC channel, where any holes in the cells were filled up and included. Cells on the border of the field of view were excluded from the analysis. The segmentation was based on the blue channel as seed channel for the nucleus. The total area of every individual cell was then determined. For determination of skewness (i.e., the shape of the cells, being the ratio of cell width over cell length), the same approach was used. After segmentation, the "form factor" was calculated which provides the ratio of the cell width over cell length. This value will always be between 0 (straight line) and 1 (perfect circle). For both parameters, the values obtained were then normalized to the values obtained for untreated control cells (100%).

For NP uptake, a third channel was selected being Cy5/Cy5, which could then be used for visual confirmation of NP uptake. These data were not quantified as ICP-MS was chosen to present a more fair comparison of the level of Au rather than the fluorescence levels.

Autophagy (LC3): After cellular exposure to the Au NPs, cells were washed (3x) with 500 µL PBS/well and fixed for 15 min at room temperature with 4% PFA. The fixative was then aspirated, cells were washed (3x) with PBS (500 µL/well) after which cells were permeabilised with 250 µL/well of Triton X-100 (1%) for 10 min at room temperature. Cells were then blocked with 10% serum-containing PBS (blocking buffer) for 30 min at room temperature. Next, cells were stained using 200 µL of staining solution per well consisting out of primary mouse anti-LC3 antibody (1/400 dilution in blocking buffer; Cell Signalling Technologies, Belgium) and incubated for 90 min in the dark at room temperature. The primary antibody solution was aspirated, cells were washed (3x) with blocking buffer (500 µL/well) after which 200 µL of secondary AF488-conjugated goat anti-mouse IgG antibody (1/250 dilution in blocking buffer; Molecular Probes, Belgium) was added to each well and plates were incubated in the dark for 60 min at room temperature. Following this, the incubation media was aspirated, cells were washed (3x) with PBS (500 µL/well), after which 500 µL fresh PBS was added to each well and the plates were kept at 4 °C in a dark container until analyzed using the InCell 2000 high-content imaging system. For acquisition, the following channels were selected: UV/blue for Hoechst nuclear stain and FITC/FITC for the LC3 stain and. Data analysis was then performed on the InCell Investigator software (GE Healthcare Life Sciences, Belgium) using in-house developed protocols, using a minimum of 5000 cells/condition.

The level of autophagy was calculated as follows: First, cell nuclei were segmented based on the blue channel. Using the FITC channel, the cell cytoplasm was then selected, and cells were segmented, where any holes in the cells were filled up and included and any cells on the border of the field of view were excluded from the analysis. The segmentation was based on the blue channel as seed channel for the nucleus. Using the original FITC/FITC channel, any green dots having an intensity of minimum twice that of the noise level and that were localized within the cytoplasm were segmented, where multiple green dots could be localized within a single cell cytoplasm. Then, the cellular intensity of the green channel was measured for every cell, after which this value was normalized to the control value (100%).

Focal adhesions (FA): To analyze the effects on focal adhesion formation, C17.2 and HUVECs were seeded in collagen-coated MatTek glass bottom confocal dishes (MatTek, USA) at 10,000 cells/dish and allowed to attach overnight after which the cells were labelled with the different Au NPs for 24 h. Then, cells were fixed (2% PFA for 15 min), permeabilized (1% Triton X-100 for 15 min) and blocked for 30 min in PBS containing 10% goat serum (Gibco, Invitrogen, Belgium) and 2% bovine serum albumin (BSA). Cells were then incubated with primary antibody in blocking solution: anti-vinculin mouse monoclonal (no. ab18058, 1:200; Abcam, Cambridge, UK) for 2 h at ambient temperature followed by 1 h incubation at ambient temperature with secondary Alexa Fluor 488-conjugated goat anti-mouse antibody (1:250; Molecular Probes, Leiden, Netherlands) and Alexa Fluor 546-conjugated phalloidin (Molecular Probes, Leiden, Netherlands). Subsequently, cells were washed three times with blocking solution prior to being analysed by confocal laser scanning microscopy. To get quantitative data, images were also collected at a 40x magnification by epifluorescence microscopy using a Nikon A1R confocal microscope (Nikon, Belgium). For analysis of focal adhesion areas, confocal images displaying vinculin were background-corrected, thresholded, focal adhesions were identified and the total areas per cell were calculated for 50 cells per condition.

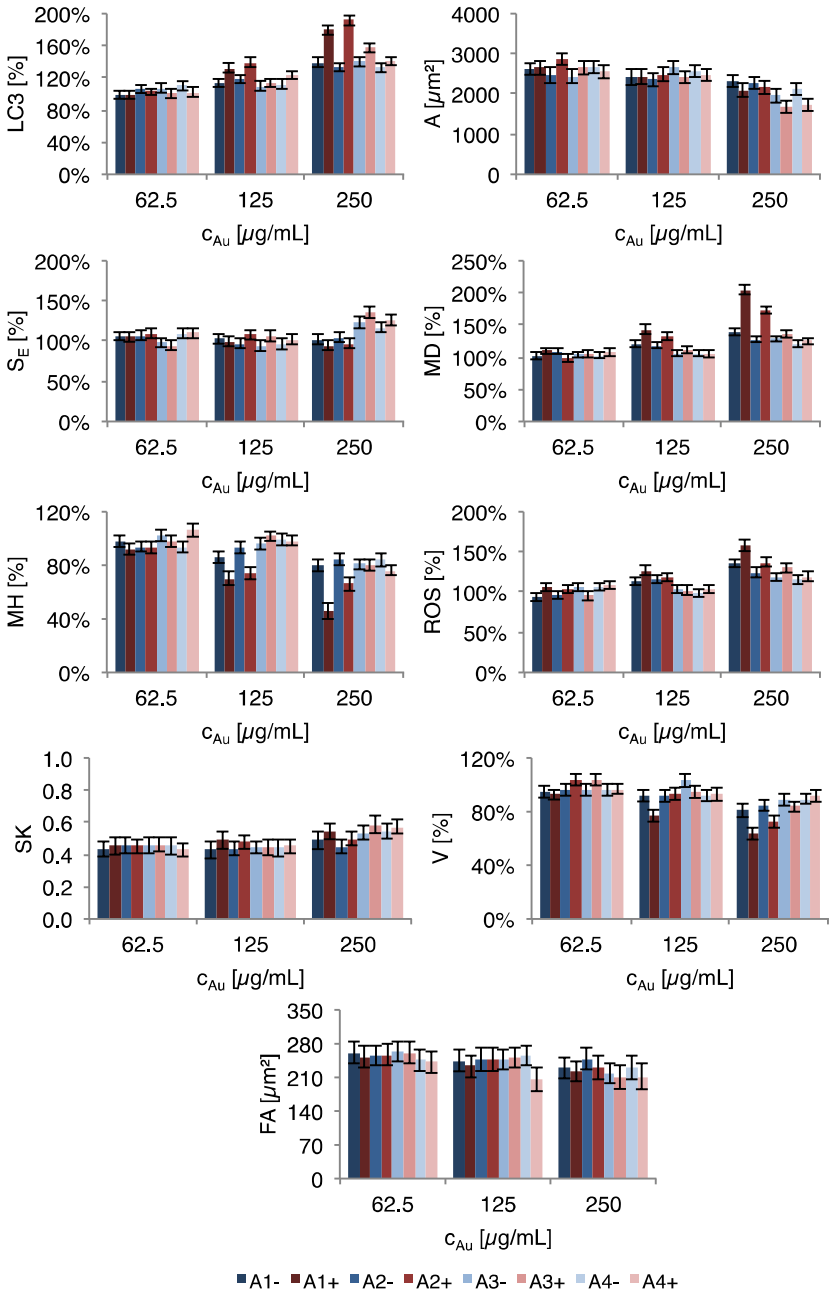

Figure S.IX-1. Overview of the data obtained by high-content imaging and confocal microscopy (focal adhesion size) for C17.2 cells treated with the various Au NPs (i.e., Au1-: Au1@PEG-10kDa–dye; Au1+: Au1@PEG-10kDa–dye–N+, Au2-: Au2@PEG-5kDa–dye; Au2+: Au2@PEG-5kDa–dye–N+, Au3-: Au3@PEG-3kDa–dye; Au3+: Au3@PEG-3kDa–dye–N+, Au4-: Au4@PEG-1kDa–dye; Au4+: Au4@PEG-1kDa–dye–N+) at equal Au mass (i.e., 62.5, 125 and 250 µg/mL).

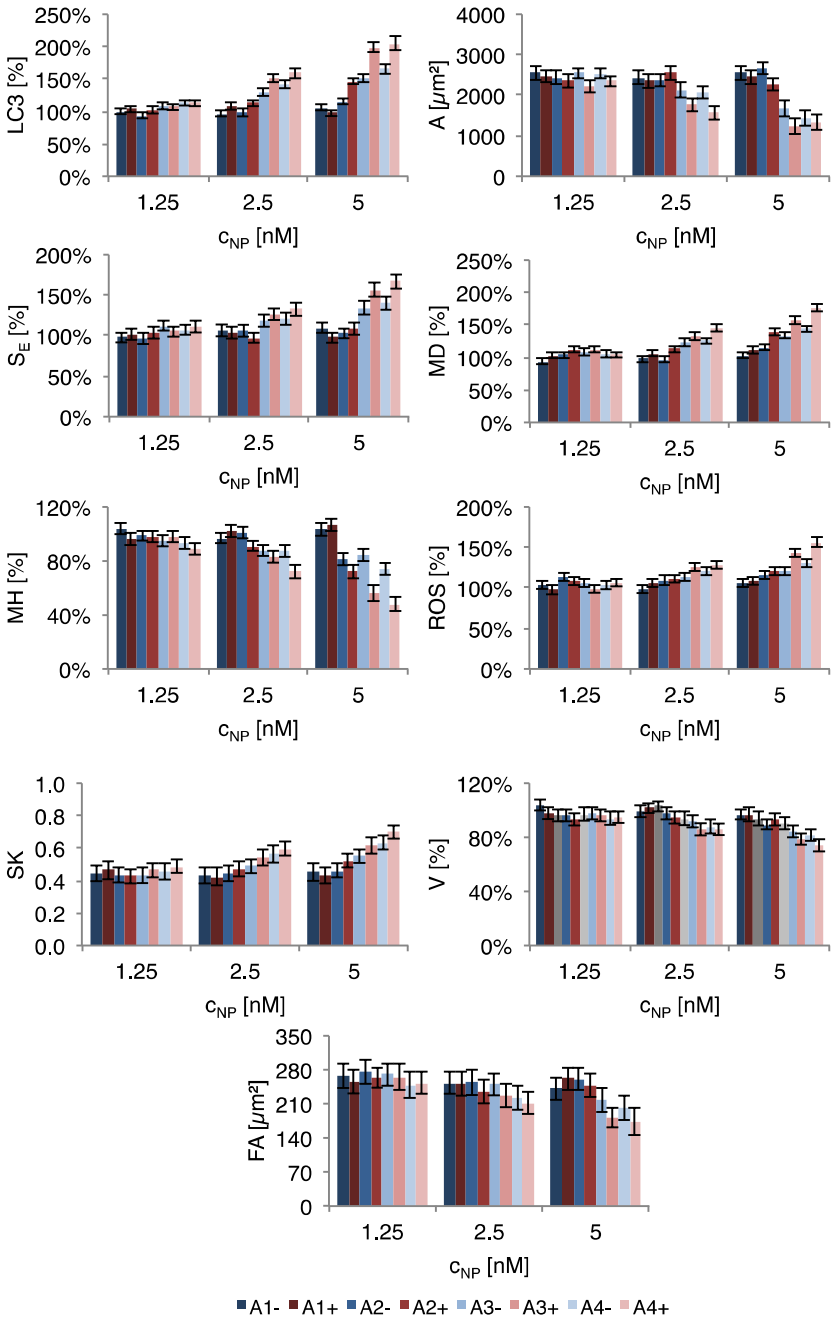

Figure S.IX-2. Overview of the data obtained by high-content imaging and confocal microscopy (focal adhesion size) for C17.2 cells treated with the various Au NPs (i.e., Au1-: Au1@PEG-10kDa–dye; Au1+: Au1@PEG-10kDa–dye–N+, Au2-: Au2@PEG-5kDa–dye; Au2+: Au2@PEG-5kDa–dye–N+, Au3-: Au3@PEG-3kDa–dye; Au3+: Au3@PEG-3kDa–dye–N+, Au4-: Au4@PEG-1kDa–dye; Au4+: Au4@PEG-1kDa–dye–N+) at equal NP number (i.e., 1.25, 2.5 and 5 nM).

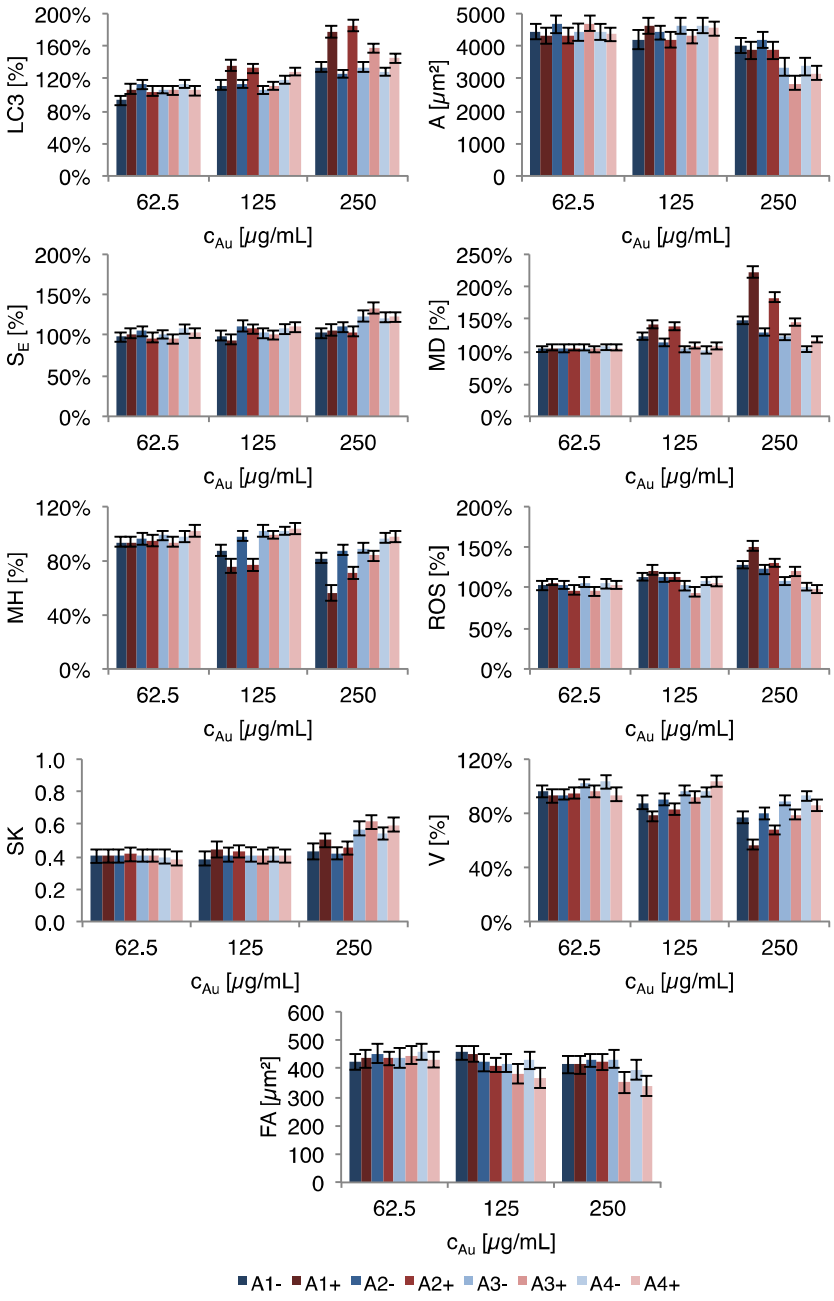

Figure S.IX-3. Overview of the data obtained by high-content imaging and confocal microscopy (focal adhesion size) for HUVEC cells treated with the various Au NPs (i.e., Au1-: Au1@PEG-10kDa–dye; Au1+: Au1@PEG-10kDa–dye–N+, Au2-: Au2@PEG-5kDa–dye; Au2+: Au2@PEG-5kDa–dye–N+, Au3-: Au3@PEG-3kDa–dye; Au3+: Au3@PEG-3kDa–dye–N+, Au4-: Au4@PEG-1kDa–dye; Au4+: Au4@PEG-1kDa–dye–N+) at equal Au mass (i.e., 62.5, 125 and 250 μg/mL).

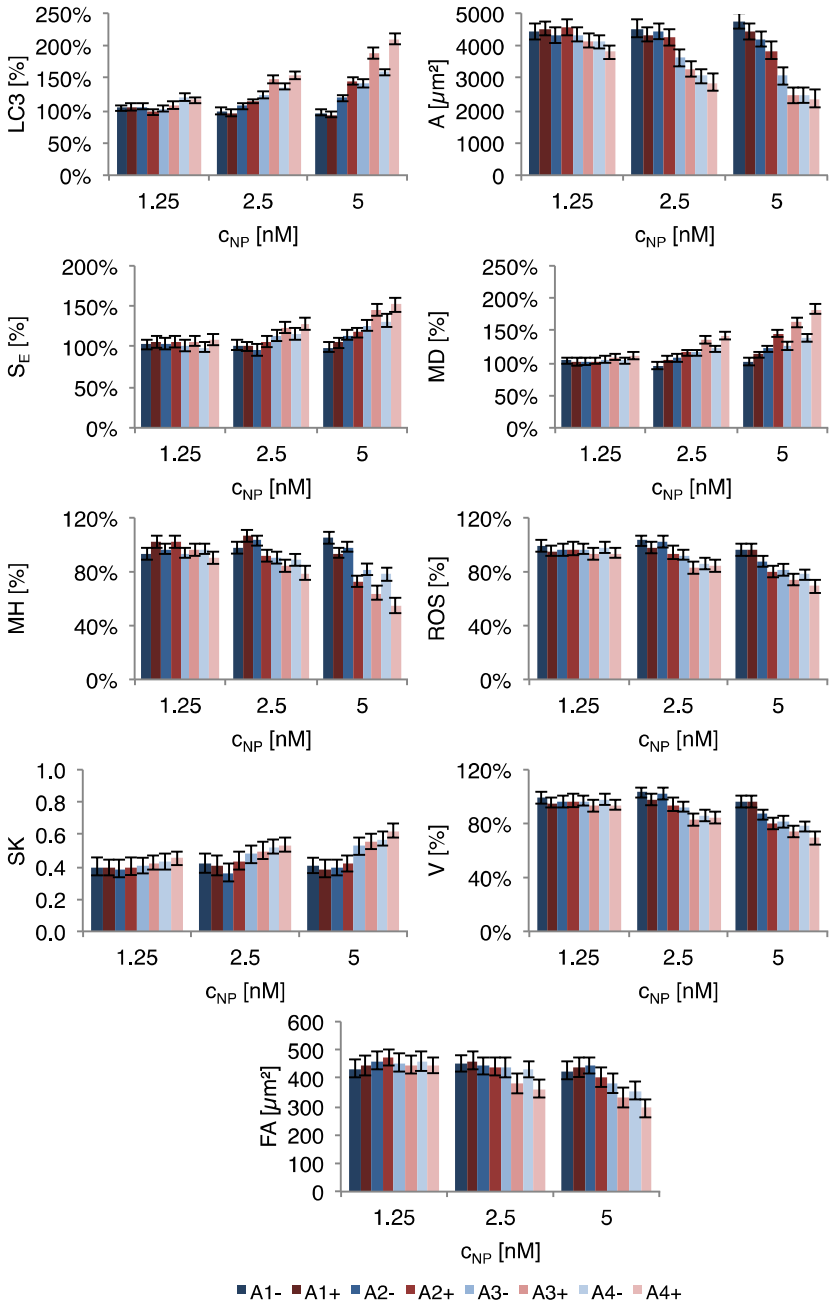

Figure S.IX-4. Overview of the data obtained by high-content imaging and confocal microscopy (focal adhesion size) for HUVEC cells treated with the various Au NPs (i.e., Au1-: Au1@PEG-10kDa–dye; Au1+: Au1@PEG-10kDa–dye–N+, Au2-: Au2@PEG-5kDa–dye; Au2+: Au2@PEG-5kDa–dye–N+, Au3-: Au3@PEG-3kDa–dye; Au3+: Au3@PEG-3kDa–dye–N+, Au4-: Au4@PEG-1kDa–dye; Au4+: Au4@PEG-1kDa–dye–N+) at equal NP number (i.e., 1.25, 2.5 and 5 nM).

Figure S.IX-5 shows an overview of the data discussed in the form of heatmaps.

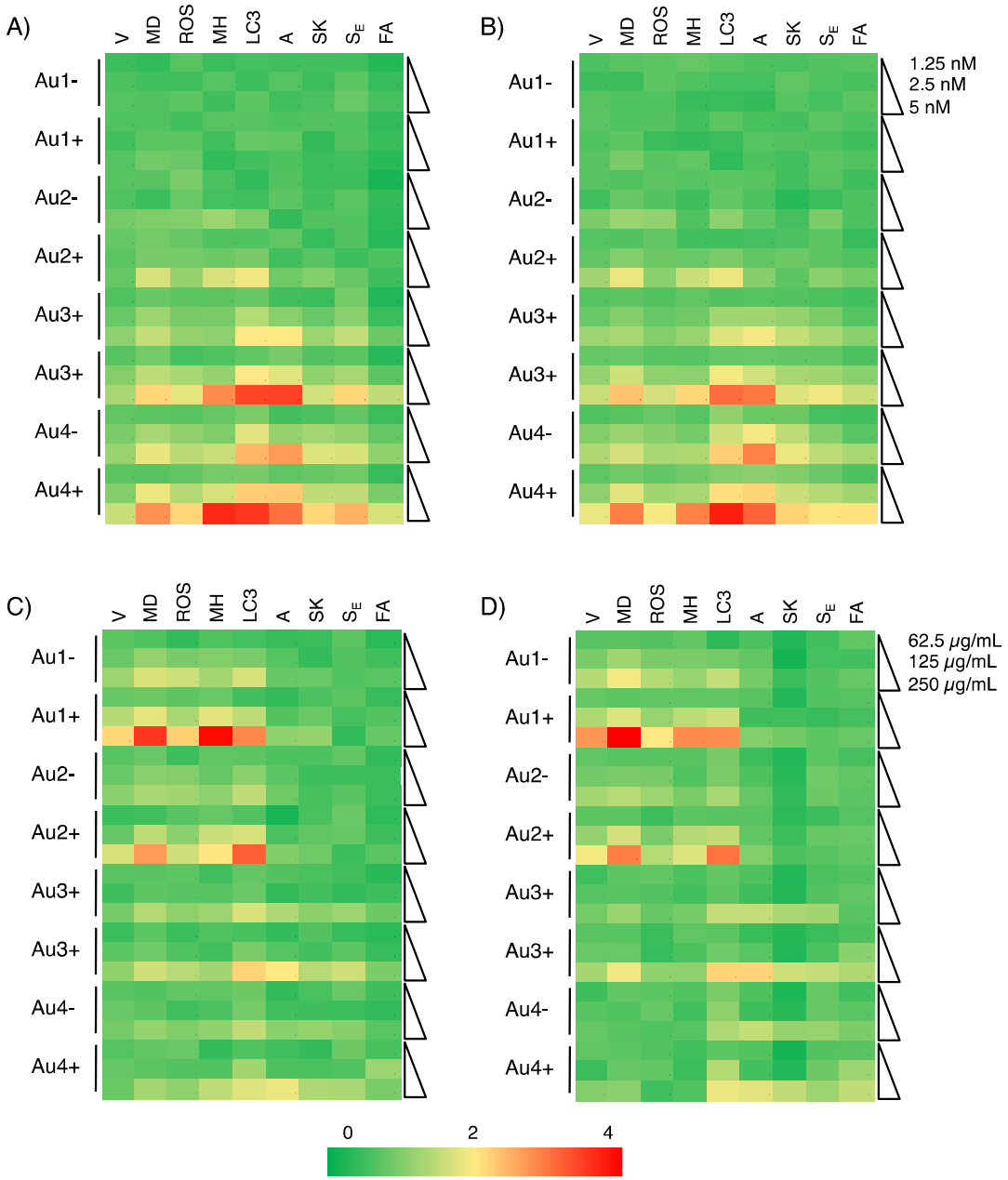

Figure S.IX-5 Overview of the data obtained by high-content imaging and confocal microscopy (focal adhesion size) for HUVEC cells (left) or C17.2 cells (right), treated with the various Au NPs at equal NP numbers/NP concentrations (A, B) and equal mass of Au (C, D).

Figures S.IX-6 and S.IX-7 show representative images of HUVEC cells incubated with NPs. Figure S.IX-8 shows control cells that have not been exposed to NPs.

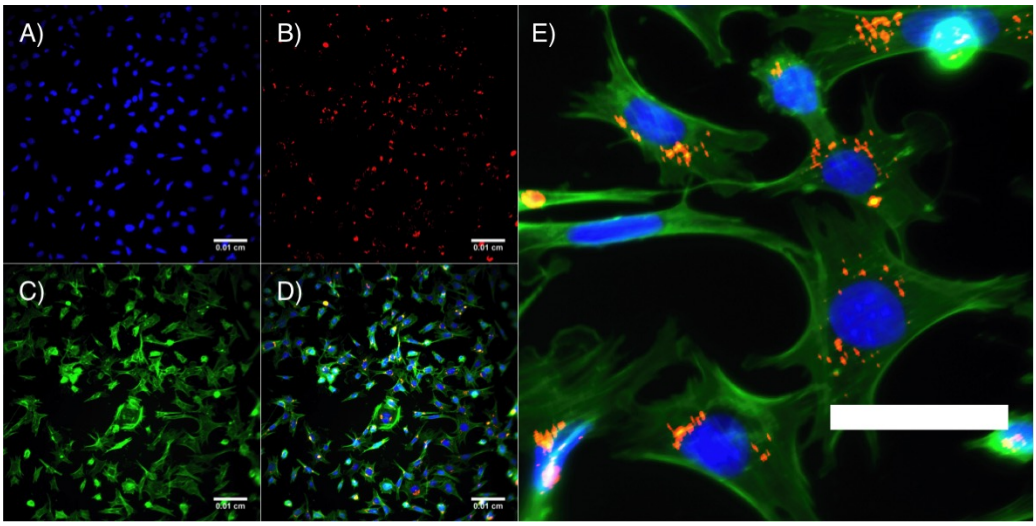

Figure S.IX-6. Representative InCell images of HUVEC cells stained with Au1+ NPs for 24 h at 5 nM. The different channels shown are: A) the cell nuclei counterstained with DAPI (blue), B) Au4+ NPs (red) and C) α-tubulin (green). A merged image of all three channels is displayed in D). E) shows a magnified view of a section of D) displaying a clear perinuclear localization of the NPs. In A-D, scale bar is 100 µm; in E, scale bar is 50 µm.

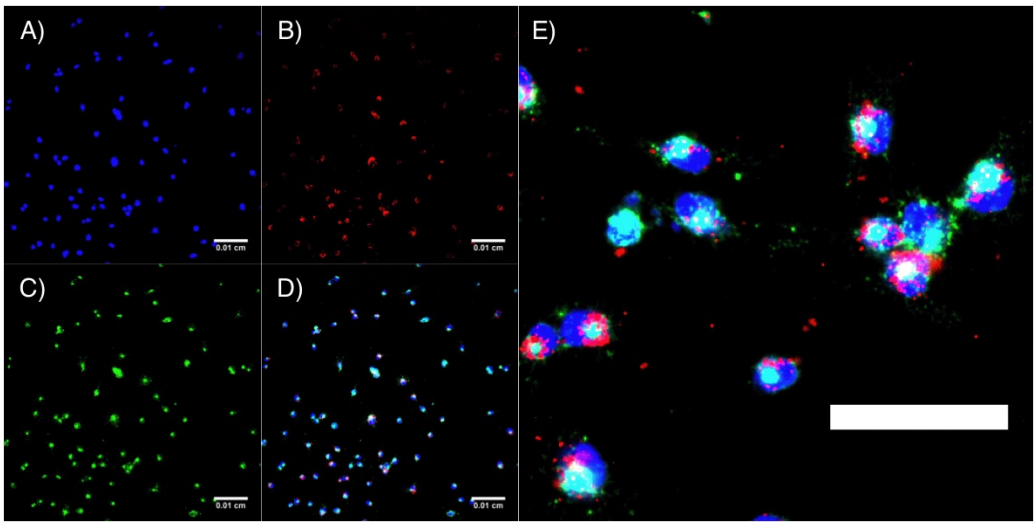

Figure S.IX-7. Representative InCell images of HUVEC cells stained with Au4+ NPs for 24 h at 5 nM. The different channels shown are: A) the cell nuclei counterstained with DAPI (blue), B) Au1+ NPs (red) and C) α-tubulin (green). A merged image of all three channels is displayed in D). E) shows a magnified view of a section of D) displaying a clear perinuclear localization of the NPs. In A-D, scale bar is 100 µm; in E, scale bar is 50 µm.

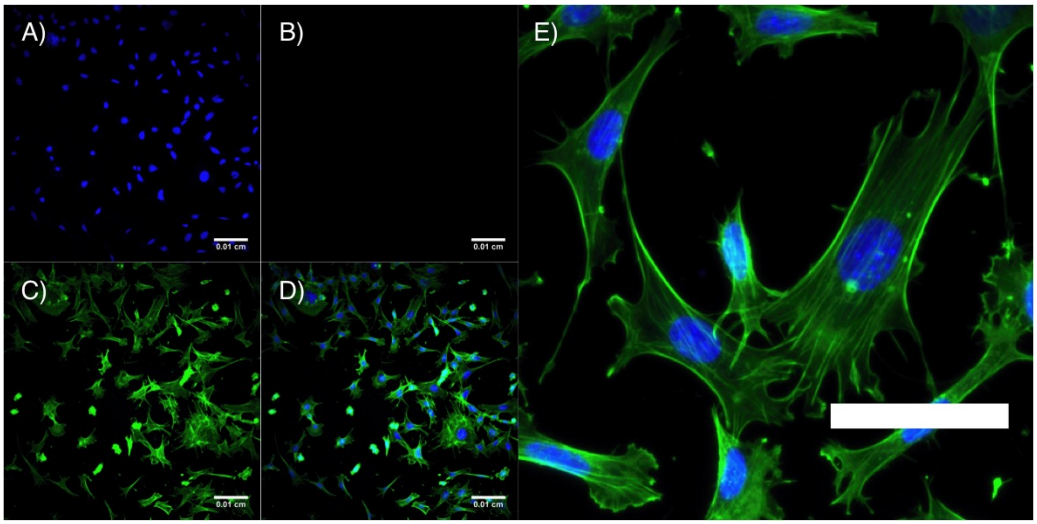

Figure S.XI-8. Representative InCell images of control HUVEC cells. The different channels shown are: A) the cell nuclei counterstained with DAPI (blue), B) lack of any NPs (red) and C) α-tubulin (green). A merged image of all three channels is displayed in D). E) shows a magnified view of a section of D) displaying a stretched morphology of the control cells not exposed to any NPs. In A-D, scale bar is 100 µm; in E, scale bar is 50 µm.

Gene Expression analysis: Gene expression (for a total of 84 genes involved in cytoskeletal signaling and regulation) results for C17.2 cells incubated with 5 nM nanoparticles. Only the genes where significant changes were found in the expression level compared to untreated control cells are shown. The level of upregulation is shown by a color-code as indicated above. The data clearly shows highest levels of upregulation in A4+, A4-, A3+, and A3-, indicating clear alterations in cytoskeletal architecture and regulation for the more internalized NPs, which is in line with the imaging results,cf. Figure S.IX-9.

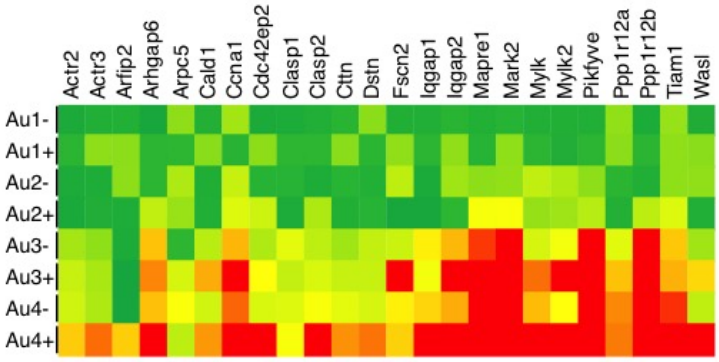

Figure S.IX-9. Heatmap of the genes affected by the NPs. *Actr2*: ARP2 actin-related protein 2 homolog (yeast); *Actr3*: ARP3 actin-related protein 3 homolog (yeast); *Arfip2*: ADP-ribosylation factor interacting protein 2; *Arhgap6*: Rho GTPase activating protein 6; *Arpc5*: Actin related protein 2/3 complex, subunit 5; *Cald1*: Caldesmon 1; *Ccna1*: Cyclin A1; *Cdc42ep2*: CDC42 effector protein (Rho GTPase binding) 2; *Clasp1*: Cyclin A1; *Clasp2*: Cyclin A2; *Cttn*: Cortactin; *Dstn*: Destrin; *Fscn2*: Fascin homolog 2, actin-bundling protein, retinal (Strongylocentrotus purpuratus); *Iqgap1*: IQ motif containing GTPase activating protein 1; *Iqgap2*: IQ motif containing GTPase activating protein 2; *Mapre1*: Microtubule-associated protein, RP/EB family, member 1; *Mark2*: MAP/microtubule affinity-regulating kinase 2; *Mylk*: Myosin, light polypeptide kinase; *Mylk2*: Myosin, light polypeptide kinase 2, skeletal muscle; *Pikfyve*: Phosphoinositide kinase, FYVE finger containing; *Ppp1r12a*: Protein phosphatase 1, regulatory (inhibitor) subunit 12A; *Ppp1r12b*: Protein phosphatase 1, regulatory (inhibitor) subunit 12B; *Tiam1*: T-cell lymphoma invasion and metastasis 1; *Wasl*: Wiskott-Aldrich syndrome-like (human).

ICP-MS uptake studies

In case of cell suspension samples the procedure requires nearly the same procedure as for the NPs. The cells with the internalized Au NPs were digested as described previously with *aqua regia*, but with a difference in volume. 50 µL of sample and 150 µL of *aqua regia* were mixed and then agitated for at least 4 hours. The number of cells was predetermined and afterwards the number of internalized Au NPs per cell could be calculated with the known core radius, the density, the molar weight of the gold sample and the results determined by the ICP-MS measurements in µg/L of atomic gold content in the digested cells.

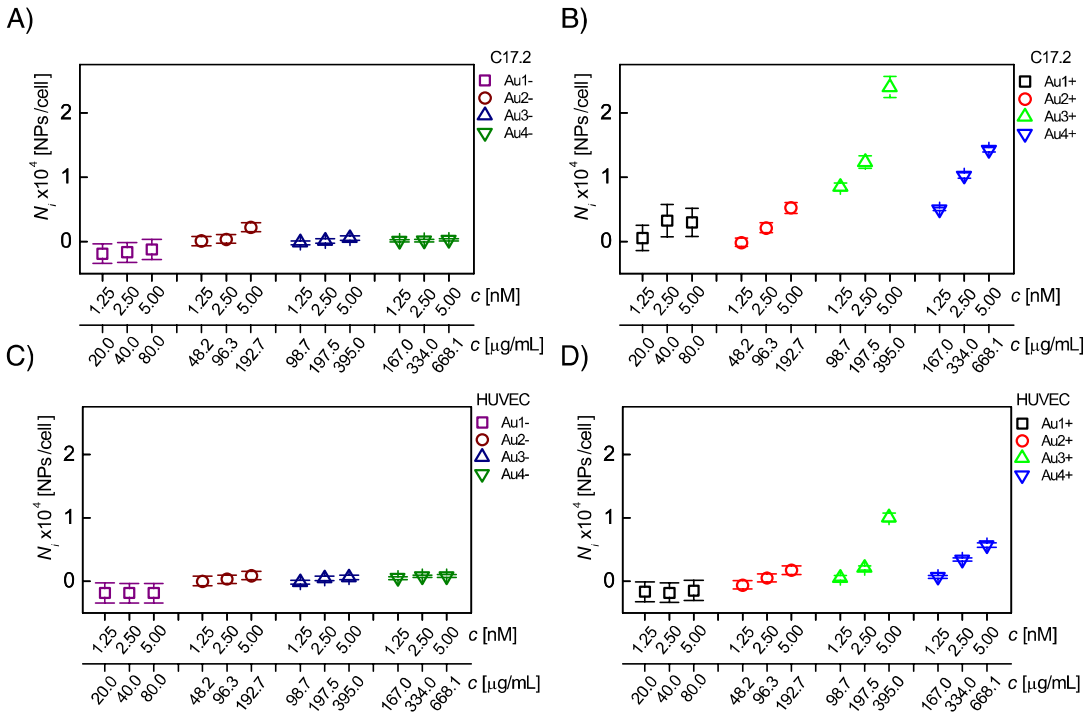

Figure S.IX-10. Overview of NPs internalized (N_i) by C17.2 cells (A, B) and HUVEC cells (C, D). A, C) Cells were exposed to three molar concentrations (1.25, 2.5 and 5 nM) of Au@PEG NPs modified with –Dye (i.e., Au1-, Au2-, Au3- and Au4-). B, D) Alternatively, Au@PEG NPs modified with –Dye and –NR+ (i.e., Au1+, Au2+, Au3+ and Au4+) were used.

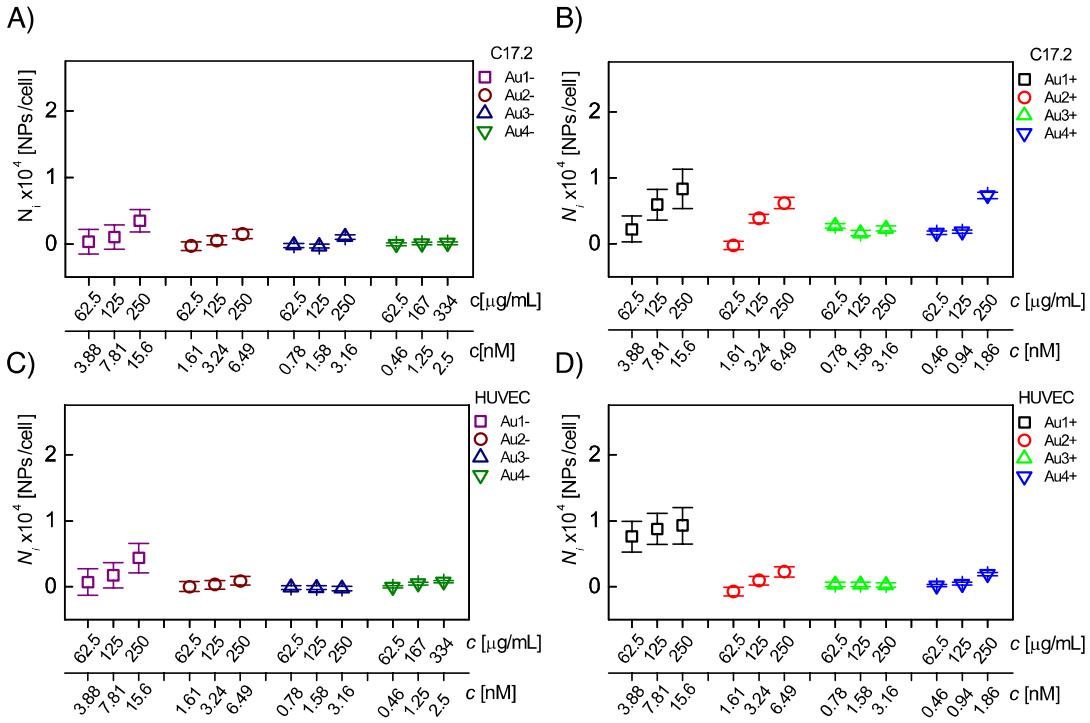

Figure S.IX-11. Overview of NPs internalized (N_i) by C17.2 cells (A, B) and HUVEC cells (C, D). A, C) Cells were exposed to three mass concentrations (i.e., 62.5, 125 and 250 μg/mL, unless otherwise specified) of Au@PEG NPs modified with –Dye (i.e., Au1-, Au2-, Au3- and Au4-). B, D) Alternatively, Au@PEG NPs modified with –Dye and –NR+ (i.e., Au1+, Au2+, Au3+ and Au4+) were used. Notice that in the case of Au4- in C), we used 167 and 224 μg/mL instead of 125 and 250 μg/mL, respectively, which in any case did not impact on a greater internalization.

Equivalently, these results can be expressed in dependence with the parameter R_{PEG}^{TEM}, cf., Figures S.IX-12 and IX-13.

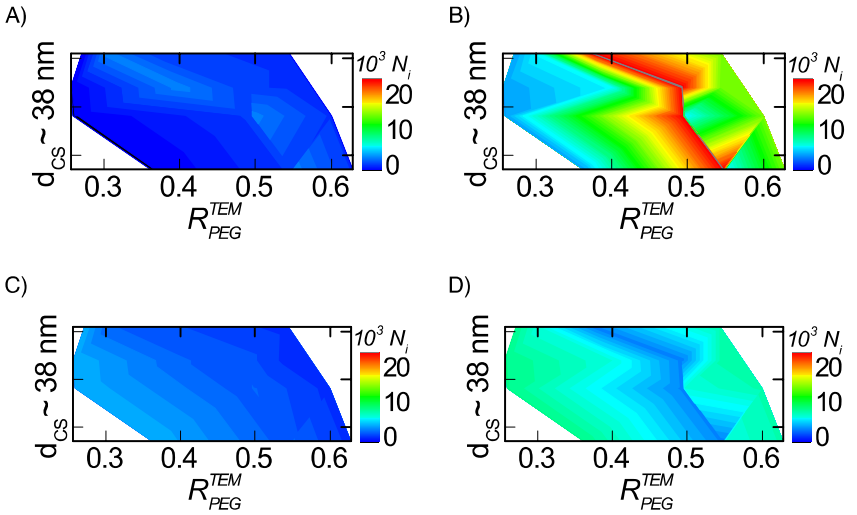

Figure S.IX-12. Internalized NPs per cell (N_i) heatmaps for C17.2 cells. a,b) equal number (5nM) ; c,d) equal mass (250 μg/mL); notice in panel C that we used for Au4- 334 μg/mL instead of 250 μg/mL, respectively, which in any case did not impact on a greater internalization.

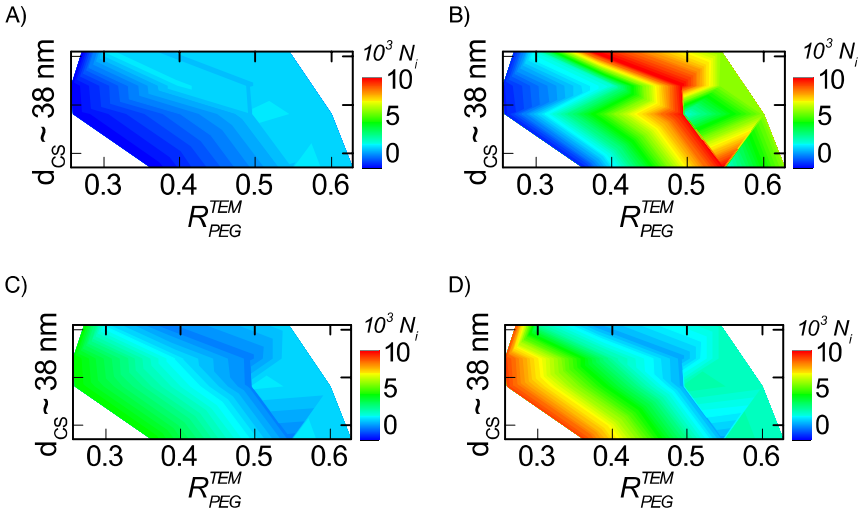

Figure S.IX-13. Internalized NPs per cell (N_i) heatmaps for HUVEC cells. Cells were exposed to a,b) equal number (5nM) ; c,d) equal mass (250 μg/mL) of NPs.

Summary of cell parameters. Figures S.IX-14 and IX-15 show a summary of heatmaps for HUVEC cells, which relate internalization (N_i) and the other parameters of cell function and morphology, when NPs are given at equal number of NPs and mass of gold, respectively.

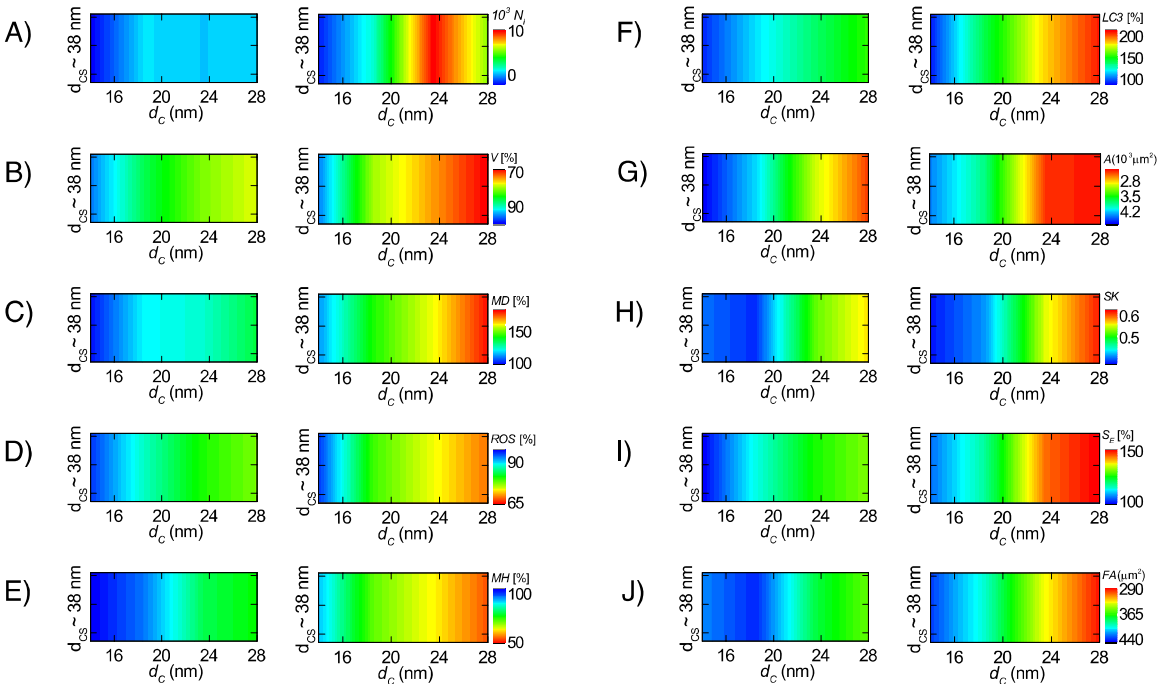

Figure S.IX-14. HUVEC at 5 nM (equal number of NPs) NP exposure. In each panel, left heatmap: Au1-, Au2-, Au3-, Au4- and right heatmap: Au1+, Au2+, Au3+, Au4+. From A) to J): number of NPs per cell (N_i), viability (V), membrane damage (MD), reactive oxidative species (ROS), mitochondrial health (MH), autophagy ($LC3$), cell area (A), cell skewness (SK), endosomal size (S_E) and focal adhesion (FA).

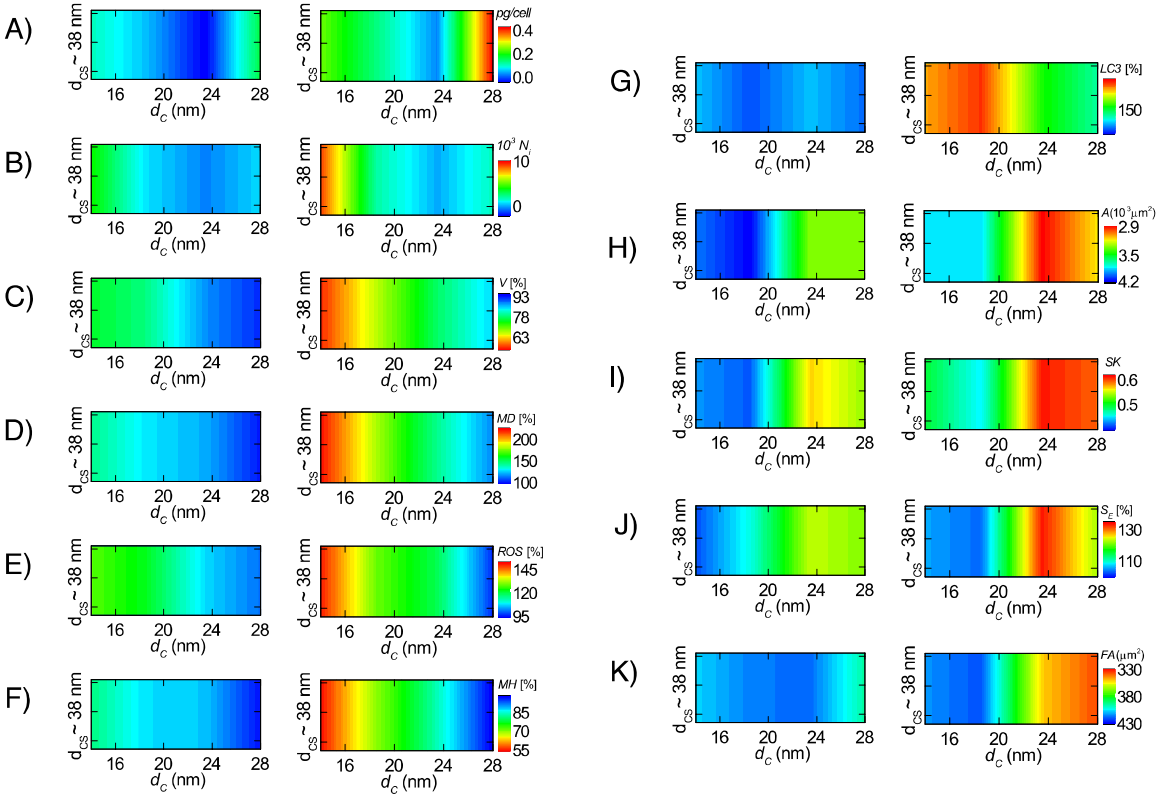

Figure S.IX-15. HUVEC at 250 μg/mL (equal mass of gold) NP exposure. In each panel, left heatmap: Au1-, Au2-, Au3-, Au4- and right heatmap: Au1+, Au2+, Au3+, Au4+. From A) to K): NP internalization expressed in terms of mass of gold (pg) per cell, number of NPs per cell (N_i), viability (V), membrane damage (MD), reactive oxidative species (ROS), mitochondrial health (MH), autophagy ($LC3$), cell area (A), cell skewness (SK), endosomal size (S_E) and focal adhesion (FA).

Equivalent heatmaps are shown for C17.2 cells, cf., Figures S.IX-16 and IX-17.

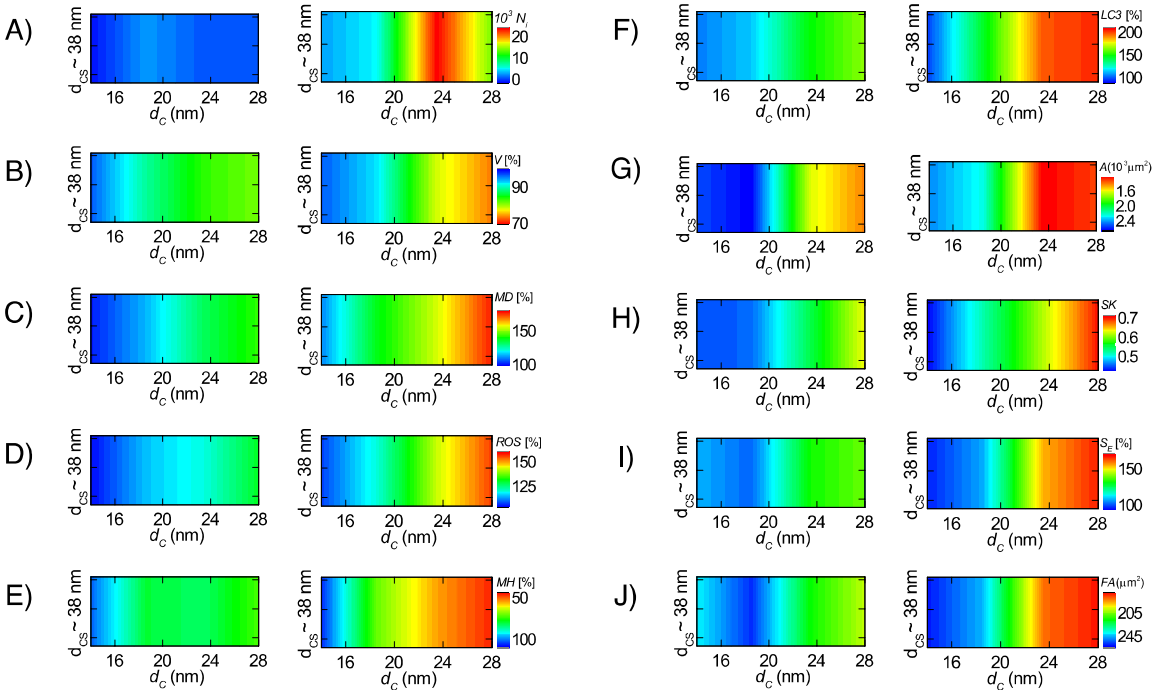

Figure S.IX-16. C17.2 at 5 nM (equal number of NPs) NP exposure. In each panel, left heatmap: Au1-, Au2-, Au3-, Au4- and right heatmap: Au1+, Au2+, Au3+, Au4+. From A) to J): number of NPs per cell (N_i), viability (*V*), membrane damage (MD), reactive oxidative species (*ROS*), mitochondrial health (*MH*), autophagy (*LC3*), cell area (*A*), cell skewness (*SK*), endosomal size (S_E) and focal adhesion (*FA*).

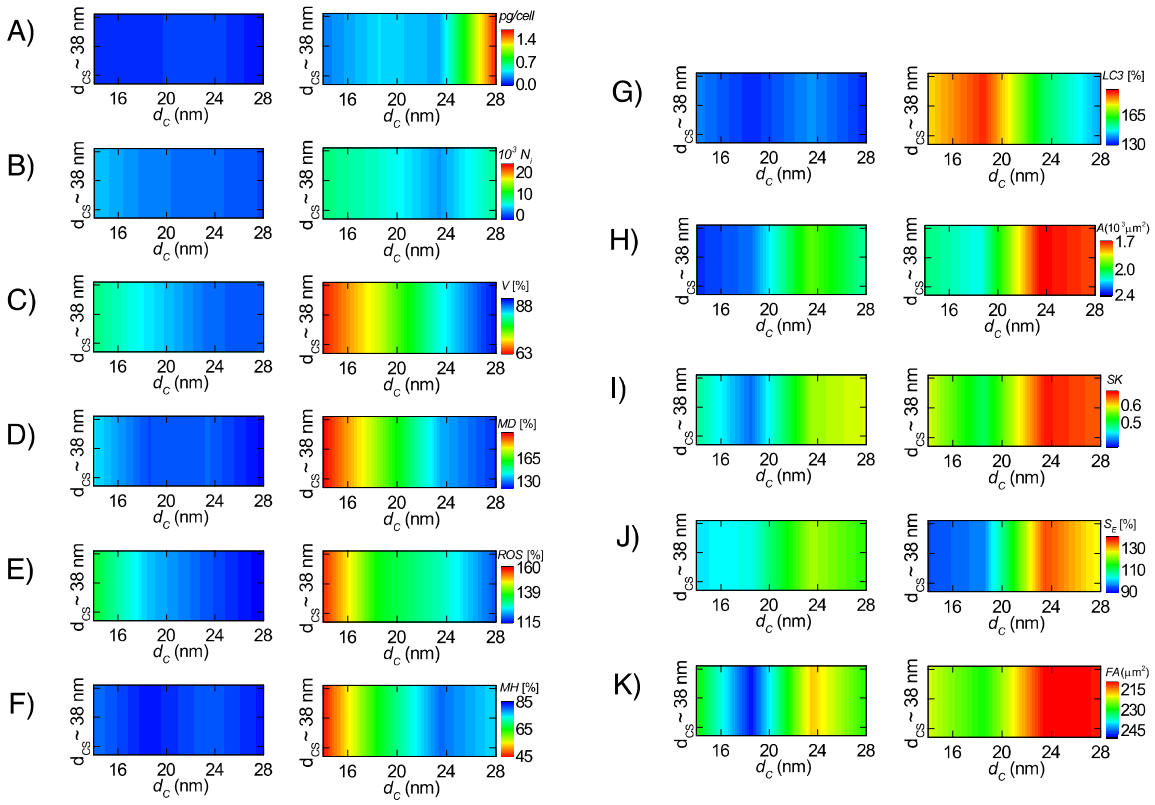

Figure S.IX-17. C17.2 at 250 μg/mL (equal mass of gold) NP exposure. In each panel, left heatmap: Au1-, Au2-, Au3-, Au4- and right heatmap: Au1+, Au2+, Au3+, Au4+. From A) to K): NP internalization expressed in terms of mass of gold (pg) per cell, number of NPs per cell (N_i), viability (V), membrane damage (MD), reactive oxidative species (ROS), mitochondrial health (MH), autophagy ($LC3$), cell area (A), cell skewness (SK), endosomal size (S_E) and focal adhesion (FA).

10) References

[1] N. G. Bastus, J. Comenge, V. Puntes, *Langmuir* **2011**, *27*, 11098.
[2] W. Haiss, N. T. K. Thanh, J. Aveyard, D. G. Fernig, *Anal. Chem.* **2007**, *79*, 4215.
[3] J. Robin Harris, in *Electron Microscopy Methods and Protocols, Vol. 117*, Humana Press, **1999**.
[4] A. Carpenter, T. Jones, M. Lamprecht, C. Clarke, I. Kang, O. Friman, D. Guertin, J. Chang, R. Lindquist, J. Moffat, P. Golland, D. Sabatini, *Genome Biology* **2006**, *7*, R100.
[5] H. Xi Yuan, M. J. Rosen, *J. Colloid Interface Sci.* **1988**, *124*, 652.
[6] M. Ludwig, M. Rief, L. Schmidt, H. Li, F. Oesterhelt, M. Gautel, H. E. Gaub, *Applied Physics A - Materials Science & Processing* **1999**, *68*, 173.
[7] a) W. Ni, Y.-T. Cheng, *J. Mater. Res.* **2005**, *20*, 521; b) X. Li, H. Gao, C. J. Murphy, L. Gou, *Nano Lett.* **2004**, *4*, 1903.
[8] I. N. Sneddon, *International Journal of Engineering Science* **1965**, *3*, 47.
[9] H.-J. Butt, B. Cappella, M. Kappl, *Surf. Sci. Rep.* **2005**, *59*, 1.
[10] S. J. Bull, *J. Phys. D: Appl. Phys.* **2005**, *38*, R393.
[11] A. Mignani, S. Fazzini, B. Ballarin, E. Boanini, M. C. Cassani, C. Maccato, D. Barreca, D. Nanni, *RSC Advances* **2015**, *5*, 9600.
[12] B. Hvolbæk, T. V. W. Janssens, B. S. Clausen, H. Falsig, C. H. Christensen, J. K. Nørskov, *Nano Today* **2007**, *2*, 14.
[13] B. Pelaz, P. Del Pino, P. Maffre, R. Hartmann, M. Gallego, S. Rivera-Fernandez, J. M. de la Fuente, G. U. Nienhaus, W. J. Parak, *ACS Nano* **2015**, *9*, 6996.
[14] B. B. Manshian, D. F. Moyano, N. Corthout, S. Munck, U. Himmelreich, V. M. Rotello, S. J. Soenen, *Biomaterials* **2014**, *35*, 9941.

Journal of Materials Chemistry B

Accepted Manuscript

This article can be cited before page numbers have been issued, to do this please use: A. P. Busch, D. Rhinow, F. Yang, H. Reinhardt, A. Beyer, A. Goelzhaeuser and N. Hampp, *J. Mater. Chem. B*, 2014, DOI: 10.1039/C4TB00468J.

ROYAL SOCIETY OF CHEMISTRY

www.rsc.org/materialsB

View Article Online
DOI: 10.1039/C4TB00468J

Journal Name

RSCPublishing

ARTICLE

Site-selective biomineralization of native biological membranes

Cite this: DOI: 10.1039/x0xx00000x

Annegret P. Busch[a], Daniel Rhinow[b], Fang Yang[a], Hendrik Reinhardt[a], André Beyer[c], Armin, Gölzhäuser[c], Norbert Hampp[a,d]

Received 00th January 2012,
Accepted 00th January 2012

DOI: 10.1039/x0xx00000x

www.rsc.org/

Biomineralization of silica precursors, mediated by self-assembled proteins, is performed by many organisms. The silica cell walls of diatoms are perhaps the most stunning biomineral structures. Although the mechanisms of biomineralization are still not fully understood, template-assisted formation of silica nanostructures has gained much attention in the materials science community. Precise control of the location and the shape of structures obtained by biomineralization remains a challenge. This paper introduces a versatile biotechnological process that enables site-selective biomineralization of native biological membranes using genetically modified purple membrane (PM) from *Halobacterium salinarum* as a template. PM is a two-dimensional crystal consisting of bacteriorhodopsin (BR) and lipids. In this work we study PM-E234R7, a genetically modified PM containing mutated BR, where seven amino acids, starting from E234, were replaced by arginine in the C-terminus. The arginine sequence catalyzes silica formation from a tetraethylorthosilicate (TEOS) precursor. Silification of the mutated PM variant starts with initial formation of membrane-attached spherical silica nanoparticles, which then fuse to form 2D silica nanoflakes, selectively, on the cytoplasmic side of the PM. Genetical modification of membrane proteins with poly-arginine sequences may be a general route for site-selective biomineralization of native biological membranes.

Introduction

Template-assisted biomineralization of inorganic precursors enables organisms to build a variety of well-defined nanostructures, such as bones, teeth, and diatoms.[1-12] Some organisms use silica as a construction material, e.g. diatoms, radiolarian, synophytes as well as multicellular sponges, and some plants like rice.[10] Diatoms are the most prominent examples of biological structures obtained by silification. Their skeletons are tough structures generated from silica precursors by catalysis of amine-rich peptide sequences, referred to as silaffins.[1,2] Silaffins are proteins post-translationally modified with long-chain oligo-N-methly-propylamines. They were identified as the main organic components of diatom biosilica.[1] *In vitro* studies have demonstrated that silaffins induce polycondensation of silicic acid under physiological conditions and also act as a framework for silica biomineralization.[1,2,13-15] Bio-inspired silicification of suitable templates has been studied by many research groups.[3,4,16-20] Only a few studies reported silicification of biological membranes.[17,21,22] Most studies refer to conditions where membranes, organelles or whole cells are nonspecifically entrapped in a silica matrix to protect the biomaterial from environmental stress.[17,22-24] However, building functional biohybrid devices from silicified membranes requires site-selective biomineralization. It is known that small cationic peptides facilitate nucleation of silica precursors.[16,20] In this work we study site-selective silicification of a genetically modified variant of the purple membrane (PM) from *Halobacterium salinarum.* PM is a native two-dimensional (2D) crystal consisting of the integral membrane protein bacteriorhodopsin (BR) and lipids only.[25,26] The 20-amino acid long C-terminus, located at the cytoplasmic side of the membrane, is easily modified by genetic tools and interacts freely with the surrounding medium. We demonstrate that substituting 7 cytoplasmic amino acids, starting from E234, by seven arginines converts PM into a template with densely packed cationic residues enabling selective silicification of the cytoplasmic side of PM-E234R7. Biomineralization of PM-234R7 is studied by a variety of physical techniques. Micrometer-scaled PM-E234R7 patches represent a perfectly ordered nano-patterned array of functional groups suitable as templates for directed silicification. Inserting poly-arginine sequences in the C-terminus of membrane proteins may be a general approach to accomplish site-selective silicification of biological membranes.

ARTICLE View Article Online
DOI: 10.1039/C4TB00463D Journal Name

Experimental

Materials

Chemicals were purchased from Sigma-Aldrich (Taufkirchen, Germany), Fisher Scientific (Leicestershire, United Kingdom), and Fluka (Buchs, Switzerland) and were used as received.
Mica and highly oriented pyrolytic graphite (HOPG) substrates for the AFM/EFM experiments were purchased from Plano (Wetzlar, Germany). Both substrates were extensively washed with doubly distilled water before use.

Preparation of PM

PM variant PM-E234R7 was prepared as described earlier.[27] Purified PM-E234R7 was lyophilized and stored at -20 °C until further use.

UV/Vis spectroscopy

UV/Vis absorption spectra of light-adapted BR were recorded on a Lambda 35 spectrometer (PerkinElmer Instruments, USA). Spectra were normalized to an optical density (OD) = 0 at 800 nm to compensate for scattering effects.

General procedure for silicification of PM-E234R7

Experiments were carried out in 10 mM ethylamine-citrate buffer of pH = 5. PM was suspended in 3 ml of the reaction buffer and tetraethylorthosilicate (TEOS) was carefully added within 5 -10 minutes until the desired ratio was obtained. The concentration of PM was measured by UV/Vis spectroscopy, using a decadic molar extinction coefficient of ε_{570nm} = 63,000 mol l^{-1}·cm^{-1}. TEOS was added relative to the molar amount of PM in the sample ranging from 0.2 to 10.0 equivalents. BR-E234R7 has a molar mass of 27281 Da. The molar mass of BR-E234R7 and TEOS is 27.172 g mol^{-1} and 208.32 g mol^{-1}, respectively. Addition of 1 molar equivalent of TEOS means that 7.66 µg of TEOS were added per mg of PM-E234R7. After 24 h of incubation at 4°C under slight agitation, silicified PM was removed from the solution by centrifugation (15 min, 13,000 rpm, room temperature, Biofuge 13, Heraeus) and suspended in water. The silicified material was stored in suspension at -20°C until further use.

Analytical density gradient centrifugation

The buoyant density of silicified PM-E234R7 was analyzed by ultracentrifugation on a five-step sucrose density gradient. (D+)-sucrose solutions with concentrations of 39 %, 41%, 50 %, 55 %, and 60 % were used. Starting with the highest density, 2.2 mL of each solution was funneled into an ultra-centrifugation tube (12.5 mL; Kontron 9091-90200) by a peristaltic pump to form density layers. 200 µL of PM material (PM-E234R7: OD_{570} = 21, silicified PM-E234R7: OD_{570} = 18) were placed onto sucrose density gradients, tared with Millipore water and were centrifuged in a Sorvall® WX ultra 80 centrifuge in a Sorvall® Surespin 630/36 rotor at 4°C and 25,000 rpm for 19 h.

Determination of zeta potential

The zeta potential was measured with a Delsa™ Nano C particle analyzer (BeckmanCoulter). For these measurements suspensions of PM-E234R7 and silificated PM-E234R7 (each OD = 10) in Millipore water were used.

Transmission electron microscopy

Silicified PM-E234R7 was analyzed in a FEI Tecnai Polara microscope operating at 300 kV, equipped with a post-column energy filter and a 2k x 2k CCD camera (Gatan). Elemental maps were obtained using the three-window method. Si maps were acquired at the Si L edge (119 eV, slit width 20 eV, 20 s acquisition time), S maps were acquired at the S L edge (180 eV, slit width 20 eV, 40 sec acquisition time).

Scanning electron microscopy (SEM)

Silicified PM-E234R7 was suspended in distilled water and dropped onto carbon coated copper grids (Plano, Wetzlar, Germany). SEM analysis was performed using a JEOL JSM-7500F SEM. Energy dispersive X-ray spectroscopy (EDX) was done with a CamScan CS 4 SEM operated at 20 keV. For this purpose the samples were trickled on carbon-coated copper grids and fixed on aluminium SEM sample holders with conductive tabs (both Plano, Wetzlar, Germany).

Helium Ion Microscopy (HIM)

Silicified PM-E234R7 was suspended in distilled water and dripped on stainless steel carriers. Helium Ion Microscopy (HIM) was done with a Carl Zeiss Orion Plus. The helium ion beam was operated at 30 kV acceleration voltage at a current of 0.5 pA. A 10 µm aperture at spot control 5 was used. Secondary electrons were collected by an Everhart-Thornley detector at 500 V grid voltage. The working distance was about 10 mm. A dwell time per pixel of 2 µs at 16 lines averaging was used. All HIM micrographs were recorded with a pixel size of 0.49 nm.

Atomic force microscopy (AFM)

Tapping mode (TM) atomic force microscopy (AFM) was chosen for topological imaging. Imaging was performed in liquid with a Nanoscope IV system (Veeco, Santa Barbara, CA). Images were acquired using TM-AFM with constant amplitude attenuation. The cantilever approach (Silicon-tip on nitride cantilever, k = 0.32 N/m, f = 40-75 kHz) was performed with an initial drive amplitude of 0.499 V (tip oscillation amplitude 1.5 V). Electrostatic force microscopy (EFM) was conducted in air using SCM-PIT tips (antimony (n) doped Si, k = 1 - 5 N/m, f_0= 70 - 83 kHz, 0.01 – 0.025 Ω/cm, Veeco, Santa Barbara, CA) and utilizing the Nanoscope´s LiftMode feature.

Results and Discussion

In this work BR-E234R7 molecules, bearing a hepta-Arg (Scheme 1) sequence in the C-terminus, serve as a template for selective biomineralization of the cytoplasmic side of PM-E234R7.

Journal Name

View Article Online
DOI: 10.1039/C4TB00468B

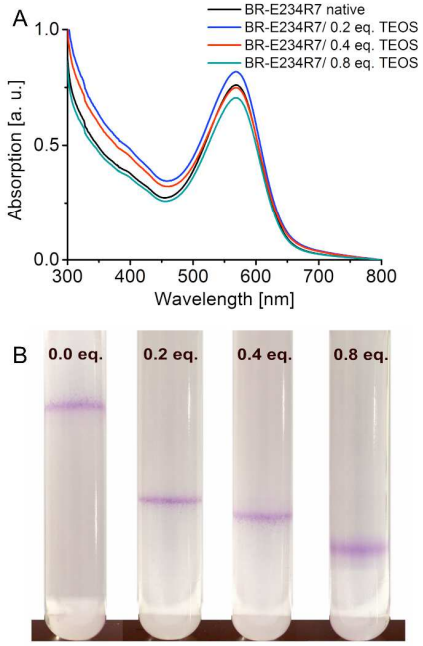

Figure 1. Physico-chemical properties of purple membrane PM-E234R7 in dependence on the degree of silicification. (A) The absorption spectra of silicified PM-E234R7 show a maximum at 570 nm indicating preservation of the retinal chromophore. (B) Density gradient centrifugation of native (0.0 eq.) and silificated PM, i.e. 0.2 eq., 0.4 eq., and 0.8 eq. of TEOS. All materials show sharp bands but with significantly different buoyant densities caused by the increasing amount of nano-silica formed on the cytoplasmic side.

The buffer system contains ethylamine which acts as a stabilizing agent for the initially formed polysilicic acid or silica nanoparticles, thus preventing uncontrolled aggregation of primary silica in solution.[17] In this buffer system, neither visible aggregation nor gel-formation occurs for more than one day in the presence of the silicic acid precursor tetraethylorthosilicate (TEOS) without PM-E234R7. The silicification of PM-E234R7 has no effect on the absorption spectrum (Figure 1A) indicating that the BR chromophore is preserved. Analytical sucrose density gradients of PM-E234R7 before and after silicification to various degrees, are shown in Figure 1B. The buoyant density of PM-E234R7 increases with increasing ratios of TEOS/PM.

Zeta potentials of silicified PM-E234R7 were measured by dynamic light scattering (DLS). The zeta potential of PM-E234R7 is -39.6 mV, significantly more positive than that of wild-type PM, which has a zeta potential of -52 mV.[28] This difference can be attributed to the genetically introduced hepta-Arg sequence. With increasing amounts of TEOS equivalents, the zeta potential of PM-E234R7 decreases proportionally, indicating increasing silicification (Table 1). Increasing silicification causes neutralization of the positively charged hepta-Arg sequence by negatively charged silica nanoparticles.

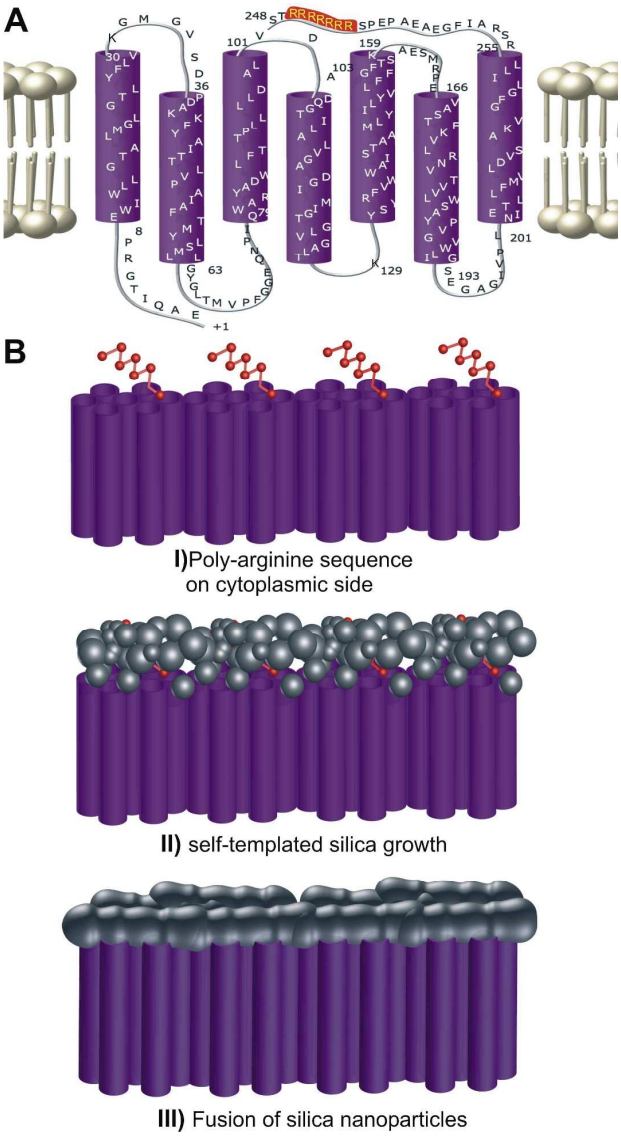

Scheme 1: PM-E234R7 as a template for site-selective biomineralization. (A) In the cytoplasmatic C-terminus of wild-type PM, a sequence of amino acids, geginning with E234, was replaced by seven arginine residues (red). This renders the cytoplasmic side of PM positively charged. (B) I) – III) Densely packed poly-arginine sequences in PM-E234R7 serve as a template for the formation silica nanoparticles. Ripening of the silica layer leads to a dense nanosized silica layer.

PM mutant / eq. TEOS	Zeta potential [mV]	Si EDX (1.74 keV) [counts]
E234R7 native	-39.6	-
E234R7 / 0.2	-50.3	1578
E234R7 / 0.4	-55.7	3725
E234R7 / 0.8	-61.0	6614

Table 1 Physico-chemical properties of silicified PM-E234R7. (middle column) The Zeta potential of PM-E234R7 decreases with increasing silicification (right column) EDX signal of silicon acquired from silicified PM-E234R7.

ARTICLE View Article Online
DOI: 10.1039/C4TB00460D Journal Name

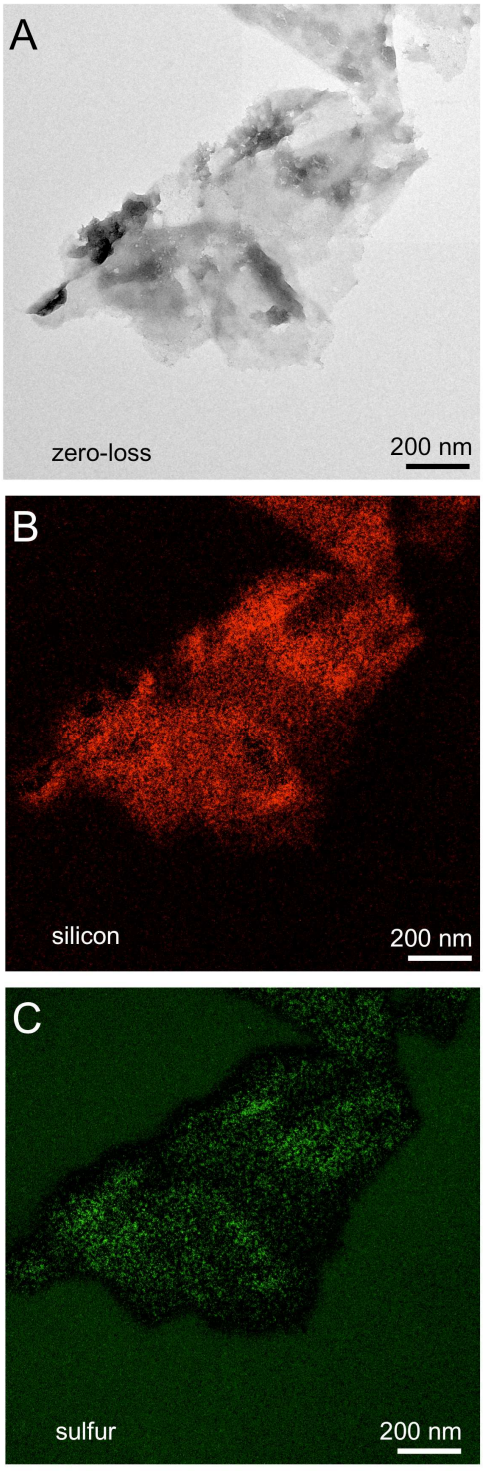

Figure 2 Energy-filtered TEM analysis of silicified PM-E234R7 (a) Zero-loss TEM image of a single silicified PM. (b) Silicon map of the same PM. (c) Sulfur map of the same PM. The sulfur signal is generated by sulfur-containing amino acids in BR. Owing to the strong absorption of the silica layer, the background of the support film appears brighter than the membrane rims.

To analyze silicification of PM-E234R7 at the level of single membranes we performed energy-filtered transmission electron microscopy (EFTEM) of biomineralized PM-E234R7. Fig. 2A shows a zero-loss EFTEM image of silicified PM-E234R7. Elemental maps acquired from the same PM confirm that PM-E234R7 is covered with silica (Fig. 2b). Fig. 2c demonstrates that the lateral size of the silica nanolayer, covering PM-E234R7, exceeds the size of the PM patch.

Scanning electron microscopy (SEM) was used to analyze the morphology of silica formed on PM-patches as a function of TEOS equivalents in detail (Figure 3). While secondary electrons (SE) primarily give information about the topology of the sample, backscattered electrons (BSE) are particularly sensitive to the atomic number and give information about the silica distribution. Superposition of both detector images (SE = green, BSE = red) shows how the amount of silica attached to the PM patches increases in dependence of TEOS equivalents (Fig. 3). Initially, silicification leads to formation of nanosized silica spheres, which later fuse into nanoscaled silica flakes attached to the cytoplasmic side of PM (Scheme 1). Upon incubation with 0.8 eq. TEOS, the surface of PM-E234R7 is completely covered. In addition, the degree of silicification was monitored by energy dispersive X-ray spectroscopy (EDX) (Table 1).

To analyze silicified PM-234R7 under near-native conditions, we used tapping mode atomic force microscopy (TM-AFM) in liquid. Figure 4 shows PM-E234R7 samples, silicified with 0.2 and 0.8 eq. of TEOS. On top of the PM spherical silica particles, attached to the surface, are observed. Their height is about 5 nm as derived from the cross-sections taken from AFM images of the 0.2 eq. sample. We used electrostatic force microscopy (EFM) to confirm that silica nanoparticles are attached to the cytoplasmic site of PM-E234R7 (not shown). With increasing TEOS concentrations the silica nanoparticles fuse into small nanoflakes (Figure 4, right). With increasing silicification the height of the silica nanoparticles remains unchanged, whereas their lateral dimensions increase significantly. We observed silica nanoflakes with lateral dimensions up to 76 nm (Fig. 4, right). The initially formed spherical silicate nanoparticles fuse into extended silica nanoflakes (Scheme 1). In reference experiments with wild-type PM no silica nanoparticles were found attached to the PM surface (see Figure 5 and Supplementary Information, Figure S1) proving that the introduced poly-arginine sequence in PM-E234R7 is responsible for the observed biomineralization. It is known from former experiments that cationic polymers are needed to induce silica formation on wild-type PM.[17]

Journal Name

View Article Online
DOI: 10.1039/C4TB00468B

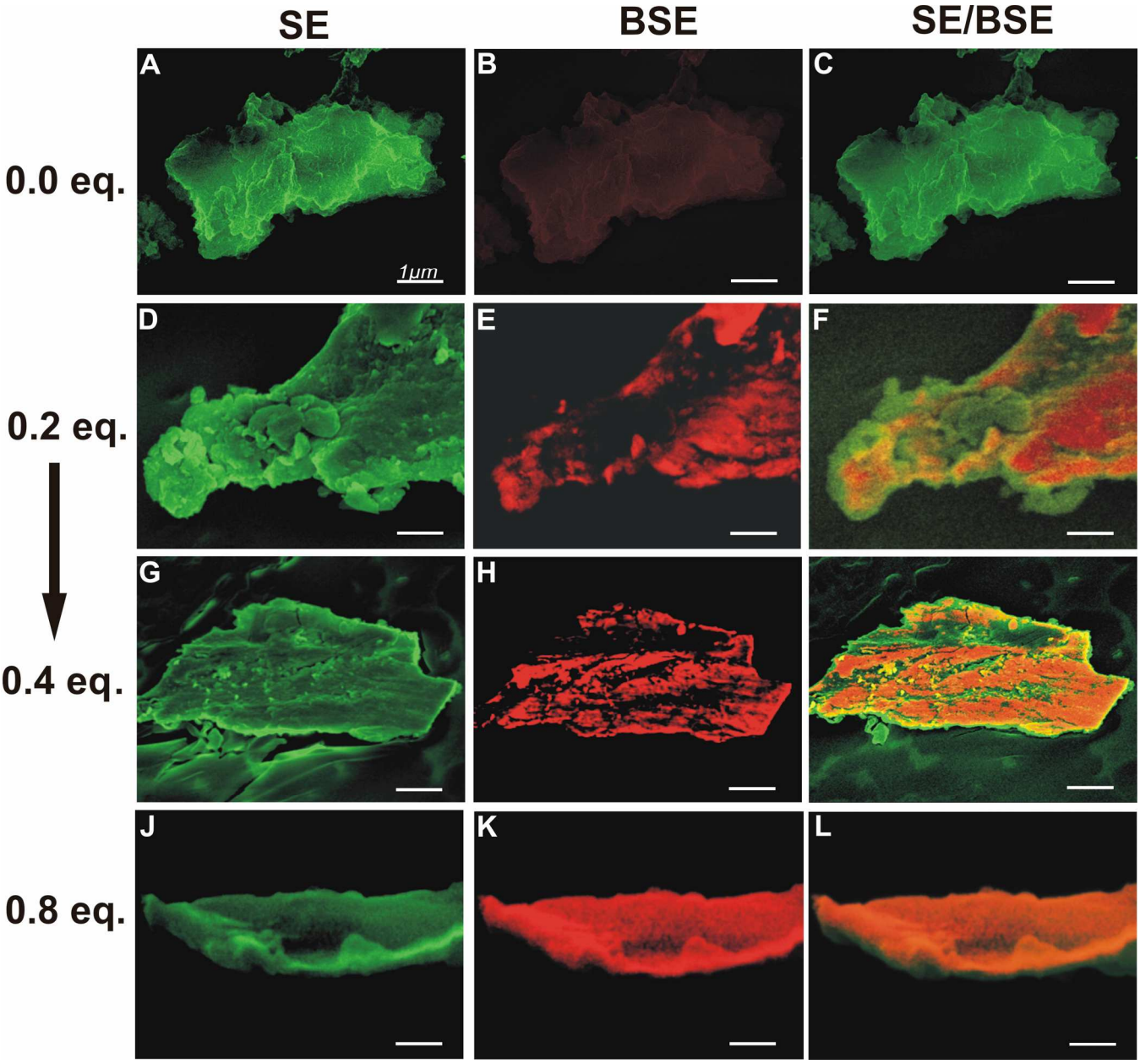

Figure 3. Gradual silicification of PM-E234R7. Characterization of the hybrid material consisting of PM and attached silica by scanning electron microscopy (SEM). From top to bottom the ratio of TEOS added to the PM is increased. In the left column, the morphology of the samples is seen as a secondary electron (SE) image shown in green. The middle column shows the corresponding backscattered electron (BSE) images in red, which reflect mainly the silica distribution. The right column shows the superposition of the SE and BSE images. With increasing amount of TEOS added, a proportionally higher degree of silicification is observed.

View Article Online
DOI: 10.1039/C4TB00460

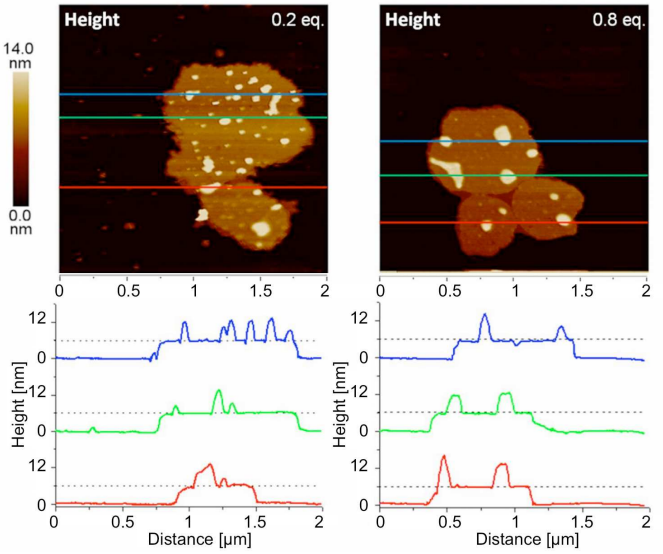

Figure 4. Topography of PM-E234R7 analyzed by AFM. (left) TM-AFM height images of PM-E234R7 with attached silica nanoparticles (0.2 eq.) on mica acquired in liquid. (right) At higher TEOS concentrations, e.g. 0.8 eq., the silica nanoparticles fuse into small islands attached to the PM patches.

We analyzed the surface of biomineralized PM-E234R7 using helium ion microscopy (HIM). We have chosen HIM to show that biomineralization occurs on one side only. SEM is not a suitable tool for this task, as the low contrast of the purple membrane does not allow to analyze on which side of the purple membrane the silica particles are located. A particular advantage of HIM is that it provides high chemical contrast for light elements making it ideal to study the structure of biohybrid materials such as silicified PM-E234R7.[29] Fig. 6 shows SE HIM images of silicified PM-E234R7. For the sake of clarity the silica particles are colored in orange and the membranes are colored in green. The only difference between PM-WT and PM-E234R7 is the replacement of amino acids in the N-terminal sequence for arginine. Biomineralization is observed with the mutated protein and not at all with PM-WT. Obviously the introduced mutation is responsible for the changed properties and the biomineralization occurs where the arginines are introduced. The HIM images confirm the model proposed in Scheme 1. First, isolated silica nanoparticles are formed, which then fuse into small 'nano-islands' (Fig. 6A), and finally form a silica flake on the PM surface (Fig. 6B). The sample shown in Figure 6B belongs to a membrane preparation, incubated with a 10-fold excess of TEOS. As a result, a silica nanoflake is observed, which is selectively formed on the cytoplasmic side of the membrane where the hepta-Arg sequences are exposed to the medium. The HIM image (Fig. 6B) shows the extracellular side of a silicified PM-E234R7, which is virtually free of any silica. Interestingly, the lateral dimensions of the silica flake exceed the size of the PM, thus resembling observations made by EFTEM (Fig. 2c).

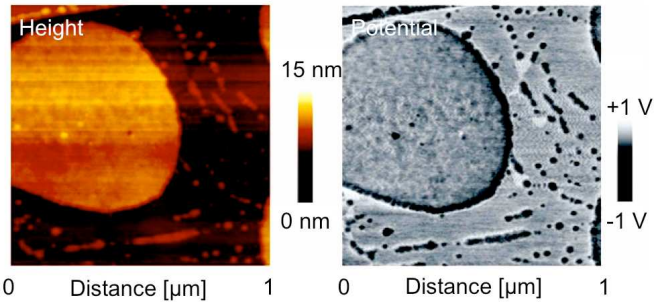

Figure 5. Control experiments with PM-Wildtype. Silicification experiments were performed with 0.4 eq. TEOS. (left) Topography of wild-type PM on highly oriented pyrolytic graphite (HOPG). (right) EFM images showing negatively charged silica nanoparticles in the vicinity of wild-type PM but not on the PM.

Conclusions

We have shown that genetical modification of integral membrane proteins enables site-selective biomineralization of native biological membranes. Polyarginine-catalyzed templated silica-biomineralization was demonstrated using PM-E234R7, a mutated purple membrane from *Halobacterium salinarum*. A hepta-arginine sequence was cloned into the C-terminus at the cytoplasmic side of PM enabling selective silicification of the cytoplasmic side of the membrane. The biosilification process was analyzed using electron and ion microscopy as well as atomic force microscopy. It was found that with increasing availability of the inorganic precursor TEOS the initially formed silica nanoparticles fuse into extended nanoflakes on the PM until it is covered with a dense layer. Poly-arginine sequences can easily be introduced in any membrane protein enabling site-selective silicification. Asymmetrically silicified biomembranes might find application as building blocks for nanobiotechnology. Furthermore, the process enables precise control over the accessibility and activity of the sides of biological membranes.

Journal Name

View Article Online
DOI: 10.1039/C4TB00468B ARTICLE

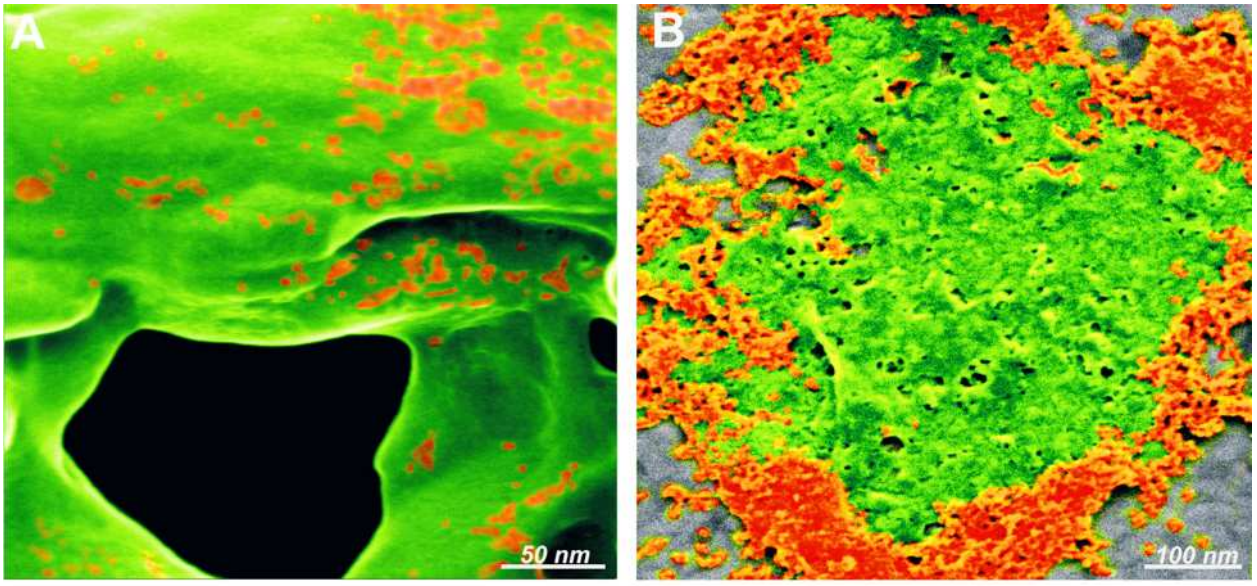

Figure 6. Helium ion microscopy of silicified PM-E234R7. (A) PM-E234R7 silicified with 0.2 eq. TEOS (B) PM-E234E7 silicified with 10.0 eq. TEOS imaged from the extracellular side. A layer of fused silica nanoparticles (orange) is attached to the cytoplasmic side of PM-E234R7 (green).

Acknowledgements

We thank Nina Schneider for preparation and purification of the PM variant, PM-E234R7. Financial support by the German Ministry of Education and Research (BMBF), through grant B-Safe plus (FKZ13N9541) is gratefully acknowledged.

Notes and references

[a] University of Marburg, Department of Chemistry, Hans-Meerwein-Str., 35032 Marburg, Germany.

[b] Max Planck Institute of Biophysics, Department of Structural Biology, 60438 Frankfurt, Germany.

[c] University of Bielefeld, Department of Physics, 33501 Bielefeld, Germany.

[d] Material Science Center, 35032 Marburg, Germany.

1 N. Kröger, R. Deutzmann and M. Sumper, *Science*, 1999, **286**, 1129.

2 M. Sumper and N. Kröger, *J. Mater. Chem.*, 2004, **14**, 2059.

3 S. Mann, *Angew. Chem. Int. Ed.,* 2000, **39**, 3392.

4 M. B. Dickerson, K. H. Sandhage and R. R. Naik, *Chem. Rev*., 2008, **108**, 4935.

5 V. C. Sundar, A. D. Yablon, J. L. Grazul, M. Ilan and J. Aizenberg, *Nature*, 2003, **424**, 899.

6 Y. Politi, T. Arad, E. Klein, S. Weiner and L. Addadi, *Science*, 2004, **306**, 1161.

7 J. Aizenberg and G. Hendlen, *J. Mater. Chem*, 2004, **14**, 2066.

8 J. Aizenberg, J. C. Weaver, M. S. Thanawala, V. C. Sundar, D. E. Morse and P. Fratzl, *Science*, 2005, **309**, 275–278.

9 J. Aizenberg, V. C. Sundar, A. D. Yablon, J. C. Weaver and G. Chen, *Proc. Natl. Acad. Sci*, 2004, **101**, 3358.

10 M. Hildebrand, Diatoms, Biomineralization Processes, and Genomics, *Chem. Rev.*, 2008, **108**, 4855.

11 L. Addadi, S. Raz and S. Weiner, *Adv. Mater.*, 2003, **15**, 959.

12 A. Veis, *Science*, 2005, **307**, 1419.

13 F. Noll, M. Sumper and N. Hampp, *Nano Lett.*, 2002, **2**, 91.

14 H. R. Luckarift, J. C. Spain, R. R. Naik and M. Stone, *Nat. Biotechnol.*, 2004, **22**, 211.

15 H. Menzel, S. Hostmann, P. Behrens, P. Bärnreuther, I. Krueger and M. Jahns, *Chem. Commun.*, 2003, **24**, 2994.

16 J. N. Cha, G. D. Stucky, D. E. Morse. and T. J. Deming, *Nature*, 2000, **403**, 289.

17 A. Schönafinger, S. Müller, F. Noll, N. Hampp, *Soft Matter* 2008, **4**, 1249.

18 J. H. Moon, J. S. Seo, Y. Xu and S. Yang, *J. Mater Sci.* 2009, **19**, 4687.

19 C. Y. Khripin, D. Pristinski, D. R. Dunphy, C. J. Brinker and B. Kaehr, *ACS Nano* 2011, **5**, 1401.

20 J. P. Hinestrosa, J. E. Sutton, D. P. Allison, M. J. Doktycz, J. M. Messman and S. T. Retterer, *Langmuir* 2013, **29**, 2193.

21 A. Bernecker, J. Ziomkowska, S. Heitmüller, R. Wieneke, A. Geyer and C. Steinem, *Langmuir* 2010, **26**, 13422.

22 R. Esquembre, S. N. Pinto, J. A. Poveda, M. Prieto and C. R. Maeto, *Soft Matter*, 2012, **8**, 408.

23 C. F. Meunier, P. van Cutsem, Y.-U. Kwon and B.-L. Su, *J. Mater. Chem.*, 2009, **19**, 1535.

24 A. Collins, D. Rhinow, N. Hampp and S. Mann, *Biomacromolecules*, 2009, **10**, 2767.

25 D. Oesterhelt and W. Stoeckenius, *Nat. New Biol.*, 1971, **233**, 149.

26 U. Haupts, J. Tittor and D. Oesterhelt, *Annu. Rev. Biophy. Biomol. Struct.*, 1999, **28**, 367.

27 R.-P. Baumann, A. P. Busch, B. Heidel and N. Hampp, *J. Phys. Chem. B*, 2012**, 116**, 4134.

28 K. C. Ng and L.-K. Chu *J. Phys. Chem B*, 2013, **117**, 6241.

29 D. C. Bell, *Microsc. Microanal.* 2009, **15**, 147.

View Article Online
DOI: 10.1039/C4TB00468J

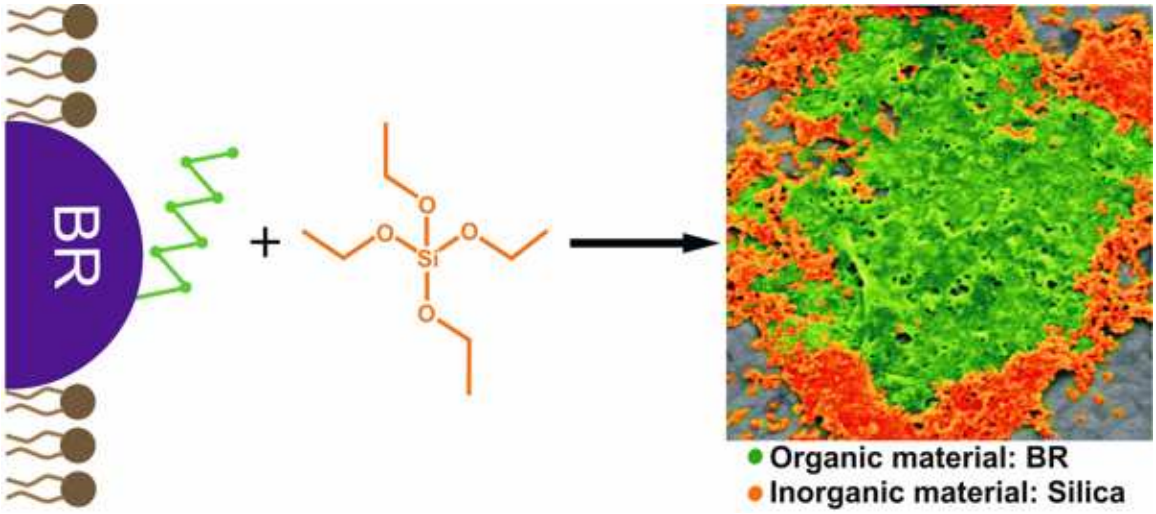

Genetical modification of integral membrane proteins with poly-arginine sequences enables site-selective silicification of a native biological membrane.

Real-time, label-free monitoring of cell viability based on cell adhesion measurements with an atomic force microscope

Fang Yang[1], René Riedel[1], Pablo del Pino[2], Beatriz Pelaz[2], Alaa Hassan Said[2], Mahmoud Soliman[2], Shashank R. Pinnapireddy[3], Neus Feliu[2], Wolfgang J. Parak[2,4], Udo Bakowsky[3], Norbert Hampp[1,5*],

[1] University of Marburg, Department of Chemistry, Marburg, Germany
[2] University of Marburg, Department of Physics, Marburg, Germany
[3]University of Marburg, Department of Pharmacy, Marburg, Germany
[4] CIC biomaGUNE, San Sebastian, Spain
[5] University of Marburg, Material Science Center, Marburg, Germany

*corresponding author: hampp@uni-marburg.de

Abstract

The adhesion of cells to an oscillating cantilever sensitively influences the oscillation amplitude at a given frequency. Even early stages of cytotoxicity cause a change in the viscosity of their membrane and morphology, both affecting their adhesion to the cantilever. We present a generally applicable method for real-time, label free monitoring and quantitative detection of early stages of cytotoxicity and viability kinetics recorded in terms of loss of cell adhesion. We present data taken from gold nanoparticles of different izes and surface coatings as well as some reference substances like ethanol, cadmium chloride, and staurosporine. Measurements were recorded with two different cell lines, HeLa cells and MCF7. The results obtained from gold nanoparticles confirm earlier findings and attest the easiness and effectiveness of the method.

Keywords

AFM, cell adhesion, cell viability, gold nanoparticles, toxicity

The cell membrane is more than just a passive lipid bilayer barrier. Of special relevance, cell membrane proteins are an integral part of the cellular machinery concerning sensing and reacting to what surrounds the cell, through different processes such as signaling, transport and immune response. In particular, cell adhesion molecules and their main function, i.e., cell adhesion, are of prime importance on cell biology and medicine, being a key player on several biological processes such as tumor invasion and metastasis[1], stem-cell fate[2] and cell death and/or growth arrest[3]. Cell detachment, or loss of anchorage in adhesive cells, is a common marker of cell death[4]. For instance, intracellular signals caused by the intracellular accumulation of exogenic agents (e.g. toxins, drugs, nanoparticles, etc.) at toxic concentrations can in general cause cell detachment[5], followed by cell death.

Most frequently employed standard methods to assess cell viability and proliferation, rely on extrinsic labeling or reporter agents which, once internalized, interact with specific cell components providing a signal, typically colorimetric, fluorescent, or bioluminescent. The measured signal can be then related to different cellular parameters such as the activity of mitochondrial enzymes, for instance the succinate dehydrogenase, the intactness of cell membranes, adenosine triphosphate production, etc[6]. The major limitation of these *in vitro* methods is that they may be affected by interferences between the compounds and the read-out signal. As example, metallic nanoparticles (NPs) may interact specifically or non-specifically with the reagent or substrate of the assay[7,8]. Fluorescent NPs may cause crosstalk with fluorescence read-out of the assay. Furthermore, some of the conventional toxicity methodologies are single endpoint assays, i.e., fail to provide real-time continuous monitoring of cell viability, as the assay itself interferes with cell viability[9]. As an alternative to the classic cytotoxicity methods, electrode-impedance-based methods have emerged as a powerful label-free analytical tool to assess cell characteristics[10, 11], including cell viability[12], adhesion, cycle, metastasis, migration, and invasion.

Mass sensors based on micro- and nanomechanical resonators represent a class of ultrasensitive sensors with enormous potential in the biomedical field[13], with the capability of weighing single cells and single nanoparticles in fluids[14]. Mechanical biosensors have been widely used for ultrasensitive detection of pathogens[15], and also some work has

attempted to dynamically inspect living cells[16-21]. There is also some recent work which addresses dynamic (>1 h) qualification of cell viability by a micromechanical mass sensor[22].

Here we report on a micromechanical mass-sensing platform for label-free continuous monitoring (4-5 hours) of intoxication in terms of loss in cell adhesion by using the oscillating cantilever of an atomic force microscope (AFM) as probe. AFM is a powerful tool to measure very small forces between a cantilever tip and a surface on the nanoscale, even if the surface to be inspected is soft and submerged in a liquid, e.g., cells in solution. With AFM binding forces between two molecules[23], adhesion of molecules to surfaces[24], adhesion of cells to surfaces[25], or cell to cell adhesion[26] can be recorded. As AFM also allows for lateral resolution also local properties of cell surfaces can be raster-scanned, such as topography[27], localization of adhesion sites[28], local electro-mechanical signaling[21], or local viscoelastic properties[29,30]. In the following, an assay will be described, in which cell detachment from the cantilever of an AFM is recorded. Hereby the loss of cell adhesion upon cellular exposure to toxic agents, e.g., NPs or chemicals, is monitored.

In our method, a triangular cantilever (SNL-10, k = 0.12 N/m, f_0 = 23 kHz, Bruker Co) is mounted in a chamber with controlled equilibrated temperature, which can be flushed with different solutions (e.g., NPs or chemical agents in different media and concentrations) through the injection system as schematically shown in **Fig. 1a.** For a given frequency the cantilever amplitude is highly dependent on the mass of the cantilever[31] or, in our case, on the mass of the cantilever with cells attached. **Fig. 1b** schematically depicts the method by showing the successive steps through which the cantilever's dynamic deflection was recorded: (1) The readily mounted cantilever started oscillating in air and then flooded with cell medium. (2) A cell suspension (120 µL of a solution of human cervical cancer HeLa cells at 10^5 cells/mL) was injected into the sample chamber and was left for ca. 1 hour to allow the cells to attach to the surface of the cantilever. During this time, the deflection amplitude increased due to the added cell mass. (3) In order to study the effect of chemical agents or NPs on cell adhesion, cells were exposed to these agents / NPs. Upon impairment of cells by these substances they lose contact to the AFM cantilever, and effects on cell adhesion could be evaluated. Cell detachment is visible as change of mass of the cantilever-cell system. (4) Finally the cell

is flushed with 70% EtOH and PBS buffer to remove all cells and prepare the system for the next measurement.

As a proof of concept, we employed differently sized and coated gold nanoparticles (Au NPs), as well as other toxic agents, such as ethanol (70%), $CdCl_2$, and staurosporine (STS) as a common agent typically used to trigger apoptosis[32]. The effects on cell adhesion upon exposure to NPs and chemical agents were evaluated using the above described setup. Au NPs were used in this study because they are interesting materials for biomedical application[33] and thus their biocompatibility needs to be studied. For instance, the metallic surface of Au NPs can trigger catalytic reactions and cause generation of reactive oxygen species (ROS)[34]. In the present study, the effects of 3 different types of Au NPs with different surface coating and size were evaluated. In general, parameters such as the organic coating around the NPs (e.g., intended as result from synthetic surface modification, or non-intended as result from the absorption of macromolecules from the cell media), size, shape, dose, among others, will affect the impact of the NPs on cell function and morphology, typically by shaping the degree and pathway(s) of NP uptake by cells[35].

In the present study we used Au NP suspension having varying NP concentrations (3 nM - 400 nM). In Fig. 1b, the AFM data after injection of 50 nM of Au NPs into the sealed and temperature-controlled (37.5 °C) sample chamber is shown. Generally, Au NPs are internalized by cells by different mechanisms, one of the most common pathway is endocytosis[36]. After a lack-phase of ca. 1 hour, a time that is typically sufficient for internalization of some amount of the Au NPs, a diminishing dynamic amplitude in the AFM signal was observed, which we ascribe to onset of cytotoxicity, resulting in loss of cell adhesion. In fact, upon exposure of cells to a potentially dose-dependent toxic agent, cells may change their adhesion properties and be gradually detached from the oscillating cantilever, which would be accompanied by the decrease of the cantilever amplitude, and in this manner recorded. In order to regenerate the cantilever *in situ* 150 mL of a solution of ethanol (70 %) and PBS buffer were injected, respectively. 70% ethanol is known to kill cells. PBS then washed the remaining cell debris away, thus clearing the cantilever, and reduced the amplitude of the cantilever oscillation to a minimal value. This process was repeated twice, so that more measurements may be accomplished during a single

session with cells from the same batch. Just before the next measurement and in particular, before cells were injected to the measuring chamber, cell medium was injected again, in order to keep the chamber in conditions suitable for cell culture.

For a more detailed and comprehensive analysis to evaluate the presented method the following three different types of Au NPs were investigated (details can be found in the SI): i) Au(5)-PMA, i.e., Au NPs having a core diameter of 5 nm which are grafted with poly(isobutylene-alt-maleic anhydride) dodecylamine (in the following referred to as PMA); ii) Au(13)-PMA, i.e., Au NPs having a core diameter of 13 nm coated with PMA[37]; iii) Au(13)-PEG, i.e., Au NPs having a core diameter of 13 nm coated with polyethylene glycol (PEG)[38]. Unless otherwise specified a concentration range from 3 to 400 nM (in terms of NP concentration) was tested. For comparison, other common toxic agents were used, such us ethanol (70 %), $CdCl_2$, and STS (3 nM to 1 μM). All of them were used with two different cells lines, the human cervical cancer cells (HeLa) and the breast adenocarcinoma cells (MCF7). The dynamic effects caused by the NPs or the chemical agents were monitored by the deflection versus time curves shown in **Fig. 2a** and **2b**. The agents were injected to the cantilever at different concentrations. Then, after about 1 h exposure, the measurement started (indicated by the red line). After a lag phase, which depended on the agent used, as well as on the dose, cells started to detach (blue line), as indicated by the diminishing deflection amplitude. Notice, that there are no significant changes before NPs have been added, i.e., during the 1 hour prior to injection of the agents. After that, the oscillation shows an exponential attenuation, described by a damping coefficient, here referred to as damping value B (details about derivation in SI). The B values extracted from the amplitude decay caused by detachment of cells in each case were quantitatively calculated by a home-made program (cf., **Fig. 2a and 2b**). All original data showing the whole dynamic process for different agents, times and doses are shown in the SI. Taken these data together, the different B values are condensed into the heatmaps shown in Fig. **2c** for HeLa cells and **2d** for MCF7 cells. The following results can be extracted from these heatmaps: 1) In case the same PMA-coating is used, bigger NPs (i.e. diameter of inorganic core of 5 nm vs. 13 nm), at the same NP concentration, induce a faster onset of cell detachment. This is understood, as the surface of big NP is bigger that then one of a small NP and thus can generate more ROS. 2) In case the NPs

had the same diameter of inorganic core (13 nm) and similar surface charge, but different organic coatings (PMA versus PEG) were used, cell detachment is less pronounced for the PEG-coated NPs, probably due to less efficient internalization, as expected from such coatings[39]. 3) Ethanol (necrosis-trigger agent), $CdCl_2$, and staurosporine (apoptosis-trigger agent) were used as references in order to underline the general applicability of the method, and to demonstrate that it is not limited to detecting cell detachment due to presence of NPs. As expected, ethanol and $CdCl_2$ show early and very fast cell detachment indicative of efficient necrotic agents, while STS shows late and slow cell detachment indicative of apoptosis[40]. The B values versus concentration data points were fitted with logistic curves for both cell lines (cf. **Fig. 3**), yielding a "half-detachment-dose" value for each agent, so that trends can be extracted. In order to verify that our method could quantitatively measure toxicity of agents to cells, we used the resazurin assay, a common cell viability assay, to evaluate the effects of NPs and compounds exposed to HeLa and MCF7 cells on their viability (see data in the SI). This cell viability assay was used as a control to compare with the cantilever measurements. As the AFM measurements were carried out without CO_2 control, the resazurin assays were carried out in the presence or absence of CO_2 (to mimic the conditions of the cantilever, i.e. without CO_2, and standard protocols, i.e. with CO_2). Indeed, the same toxicity trends were observed for the resazurin as for the AFM measurements. There is however one advantage of the AFM assays. In the resazurin assays measurements for different time points have to be carried out separately, while the AFM assays in principle allows for continuous real-time recording.

The results obtained in this work suggest that the presented method is a generally applicable label-free quantitative real-time cell viability monitoring tool, which uses cell detachment from an oscillating cantilever to measure cell intoxication. After desired exposure time, the release rate of cells (as quantified in terms of damping values B) from the cantilever was extracted. We speculate that in future, this method may be applied even to single cells or other cell types such as primary cultures.

Acknowledgements

The help of Dr. H-C. Kim in programming the calculation software is gratefully acknowledged. The authors thank Dr. S. Ashraf for help in cell culture at the initial stages of the project. This work was financially supported in part by DFG grant PA 784/25-1 to WJP.

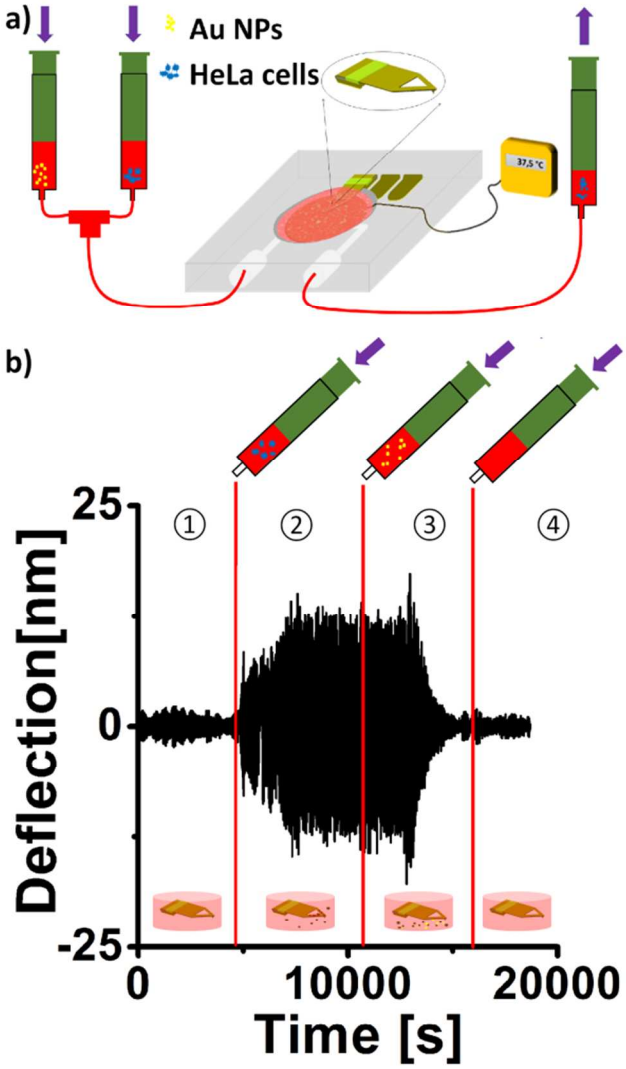

Figure 1: Sketch of the analytical system and the measurement principle. (a) The thermostatic controlled and sealed sample cell houses the AFM cantilever stage. It is equipped with in- and outlets for liquids. Syringes were used as reservoirs for cells and Au NPs. (b) (1) The cantilever oscillates at a given frequency and the deflection is recorded over time. The sample cell is fully filled with cell medium and the system is allowed to equilibrate to an approximately constant amplitude. (2) Then, cells are injected and allowed to adhere to the cantilever (deflection increases as cells attach, i.e., mass increases). (3) Then, after 3600 seconds, NPs or other chemical agents, whose effect on cell adhesion is to be tested, are injected. After a lag phase, in which NPs or other agents start interacting with cells, the deflection decreases, because more and more cells detach from the cantilever. (4) Finally the cantilever is washed with ethanol (70 %) and PBS and then, cell medium is injected to regain the initial amplitude and get ready for the next measurement cycle.

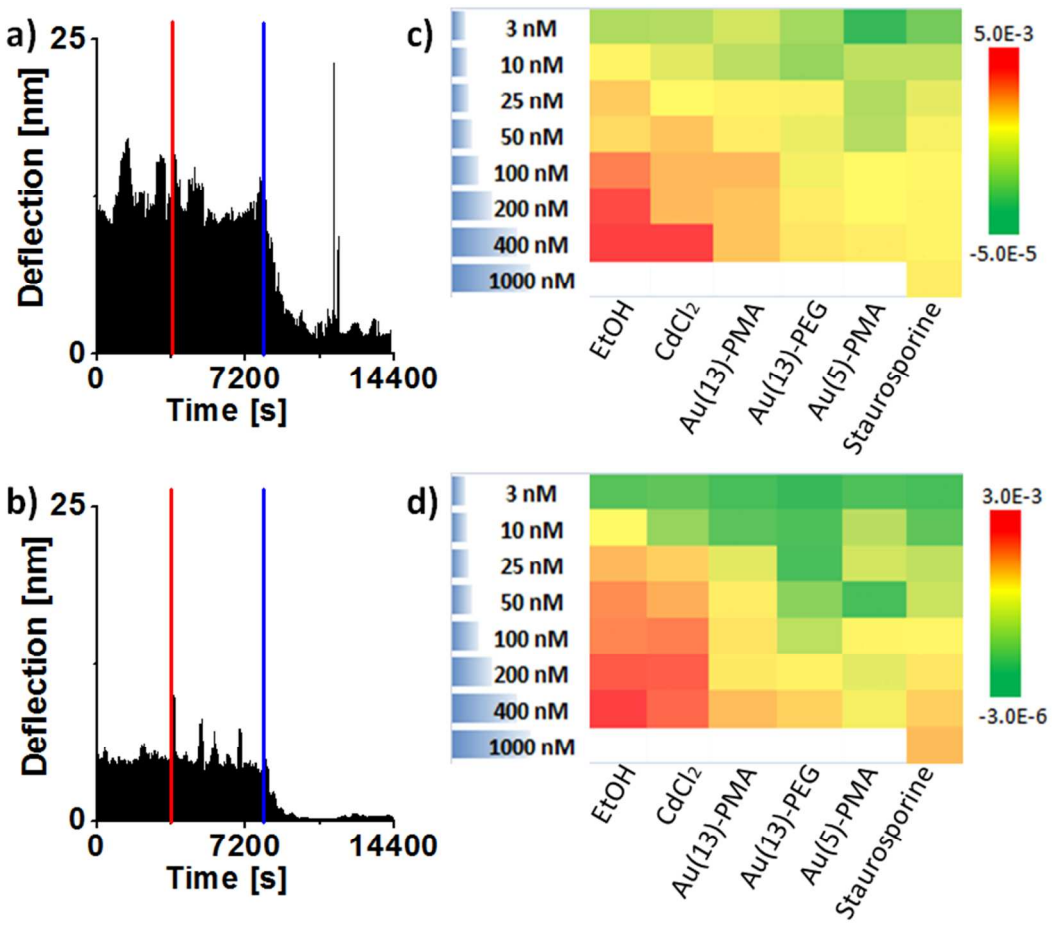

Figure 2: Real-time recorded deflection of cantilever oscillation and analytic results of a) HeLa cells and b) MCF7 cells exposed to Au-NP and other toxic chemicals. a) & b) Plotted is deflection versus time for HeLa and MCF7 cells exposed to Au(13)-PMA NPs. The time point of injection of the NPs (3600 s) is indicated by the red line, and the onset of cell detachment is indicated by the blue line, which was automatically set the time point from where the decay of oscillation amplitude was calculated for each measurement. c) & d) Heatmaps of the damping constants for HeLa and MCF7 cells as derived from the different measurements for various agents at increasing doses.

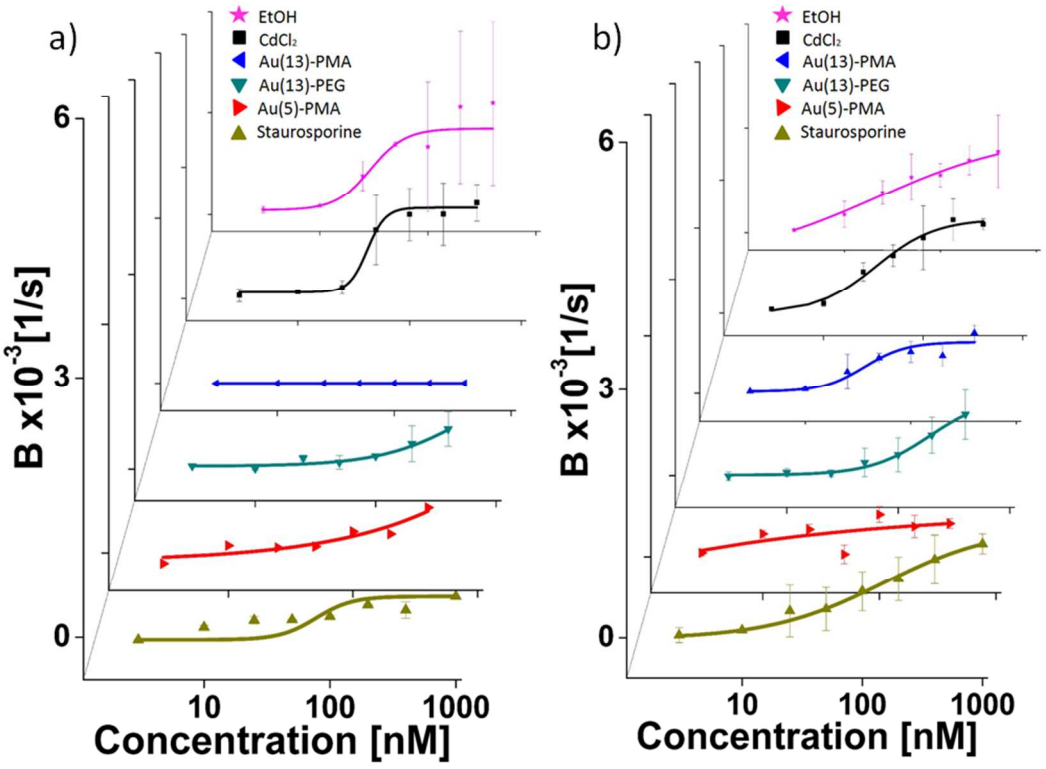

Figure 3: Damping constants B for different agents (a list of all mean values and standard deviations is presented in the supporting information) and the corresponding logistic fit curves. a) Results for HeLa cells are presented, from which based on the respective logistic fit curves the following "half-detachment-dose" values were extracted: 29 nM (EtOH), 43 nM ($CdCl_2$), 53 nM (Au(13)-PMA), 640 nM (Au(13)-PEG), 98 nM (Au(5)-PMA), and 78 nM (staurosporine). b) Results for MCF7 cells, from which based on the respective logistic fit curves the following "half-detachment-dose" values were extracted: 21 nM (EtOH), 33 nM ($CdCl_2$), 53 nM (Au(13)-PMA), 190 nM (Au(13)-PEG), 81 nM (Au(5)-PMA), and 150 nM (staurosporine).

References

1. Malanchi, I.; Santamaria-Martinez, A.; Susanto, E.; Peng, H.; Lehr, H.; Delaloye, J.; Huelsken, J. *Nature* **2012,** 481, (7379), 85-U95.
2. Trappmann, B.; Gautrot, J. E.; Connelly, J. T.; Strange, D. G.; Li, Y.; Oyen, M. L.; Cohen Stuart, M. A.; Boehm, H.; Li, B.; Vogel, V.; Spatz, J. P.; Watt, F. M.; Huck, W. T. *Nat Mater* **2012,** 11, (7), 642-649.
3. Ishikawa, F.; Ushida, K.; Mori, K.; Shibanuma, M. *Cell Death Dis* **2015,** 6.
4. Lee, M. W.; Bassiouni, R.; Sparrow, N. A.; Iketani, A.; Boohaker, R. J.; Moskowitz, C.; Vishnubhotla, P.; Khaled, A. S.; Oyer, J.; Copik, A.; Fernandez-Valle, C.; Perez, J. M.; Khaled, A. R. *Cell Death Dis* **2014,** 5, e1249.
5. Perillo, N. L.; Marcus, M. E.; Baum, L. G. *J Mol Med (Berl)* **1998,** 76, (6), 402-12.
6. Soenen, S.; Rivera-Gil, P.; Montenegro, J.; Parak, W.; De Smedt, S.; Braeckmans, K. *Nano Today* **2011,** 6, (5), 446-465.
7. Han, X.; Gelein, R.; Corson, N.; Wade-Mercer, P.; Jiang, J.; Biswas, P.; Finkelstein, J. N.; Elder, A.; Oberdorster, G. *Toxicology* **2011,** 287, (1-3), 99-104.
8. Stone, V.; Johnston, H.; Schins, R. P. *Crit Rev Toxicol* **2009,** 39, (7), 613-26.
9. Kepp, O.; Galluzzi, L.; Lipinski, M.; Yuan, J.; Kroemer, G. *Nat Rev Drug Discov* **2011,** 10, (3), 221-237.
10. Wegener, J.; Sieber, M.; Galla, H. J. *J Biochem Biophys Methods* **1996,** 32, (3), 151-70.
11. Lo, C. M.; Keese, C. R.; Giaever, I. *Biophys J* **1995,** 69, (6), 2800-7.
12. Tarantola, M.; Schneider, D.; Sunnick, E.; Adam, H.; Pierrat, S.; Rosman, C.; Breus, V.; Sonnichsen, C.; Basche, T.; Wegener, J.; Janshoff, A. *ACS Nano* **2009,** 3, (1), 213-22.
13. Tamayo, J. *Nat Nanotechnol* **2015,** 10, (9), 738-9.
14. Burg, T.; Godin, M.; Knudsen, S.; Shen, W.; Carlson, G.; Foster, J.; Babcock, K.; Manalis, S. *Nature* **2007,** 446, (7139), 1066-1069.
15. Arlett, J. L.; Myers, E. B.; Roukes, M. L. *Nat Nanotechnol* **2011,** 6, (4), 203-15.
16. Liu, Y.; Schweizer, L.; Wang, W.; Reuben, R.; Schweizer, M.; Shu, W. *Sens and Actu B-Chem* **2013,** 178, 621-626.
17. Weng, Y.; Delgado, F.; Son, S.; Burg, T.; Wasserman, S.; Manalis, S. *Lab on a chip* **2011,** 11, (24), 4174-4180.
18. Ramos, D.; Tamayo, J.; Mertens, J.; Calleja, M.; Villanueva, L. G.; Zaballos, A. *Nanotechnology* **2008,** 19, (3), 035503.
19. Ramos, D.; Tamayo, J.; Mertens, J.; Calleja, M.; Zaballos, A. *J. Appl. Phys* **2006,** 100, (10).
20. Davila, A.; Jang, J.; Gupta, A.; Walter, T.; Aronson, A.; Bashir, R. *Biosens Bioelectron* **2007,** 22, (12), 3028-3035.
21. Domke, J.; Parak, W. J.; George, M.; Gaub, H. E.; Radmacher, M. *Eur Biophys J* **1999,** 28, (3), 179-86.
22. Wu, S.; Liu, X.; Zhou, X.; Liang, X. M.; Gao, D.; Liu, H.; Zhao, G.; Zhang, Q.; Wu, X. *Biosens Bioelectron* **2016,** 77, 164-73.
23. Florin, E.-L.; Moy, V. T.; Gaub, H. E. *Science* **1994,** 264, (5157), 415-417.

24. Seitz, M.; Friedsam, C.; Jostl, W.; Hugel, T.; Gaub, H. E. *Chemphyschem* **2003,** 4, (9), 986-90.
25. Javier, A.; Kreft, O.; Alberola, A.; Kirchner, C.; Zebli, B.; Susha, A.; Horn, E.; Kempter, S.; Skirtach, A.; Rogach, A.; Radler, J.; Sukhorukov, G.; Benoit, M.; Parak, W. *Small* **2006,** 2, (3), 394-400.
26. Thie, M.; Rospel, R.; Dettmann, W.; Benoit, M.; Ludwig, M.; Gaub, H.; Denker, H. *Hum. Reprod* **1998,** 13, (11), 3211-3219.
27. Radmacher, M.; Tillamnn, R. W.; Fritz, M.; Gaub, H. E. *Science* **1992,** 257, (5078), 1900-5.
28. Benoit, M.; Gabriel, D.; Gerisch, G.; Gaub, H. E. *Nat Cell Biol* **2000,** 2, (6), 313-7.
29. Domke, J.; Dannohl, S.; Parak, W. J.; Muller, O.; Aicher, W. K.; Radmacher, M. *Colloids Surf B Biointerfaces* **2000,** 19, (4), 367-379.
30. Hofmann, U. G.; Rotsch, C.; Parak, W. J.; Radmacher, M. *J Struct Biol* **1997,** 119, (2), 84-91.
31. Longo, G.; Alonso-Sarduy, L.; Rio, L. M.; Bizzini, A.; Trampuz, A.; Notz, J.; Dietler, G.; Kasas, S. *Nat Nanotechnol* **2013,** 8, (7), 522-6.
32. Perez-Hernandez, M.; del Pino, P.; Mitchell, S.; Moros, M.; Stepien, G.; Pelaz, B.; Parak, W.; Galvez, E.; Pardo, J.; de la Fuente, J. *ACS NANO* **2015,** 9, (1), 52-61.
33. Bao, C.; Conde, J.; Polo, E.; del Pino, P.; Moros, M.; Baptista, P.; Grazu, V.; Cui, D.; de la Fuente, J. *Nanomedicine* **2014,** 9, (15), 2353-2370.
34. Soenen, S. J.; Manshian, B.; Montenegro, J. M.; Amin, F.; Meermann, B.; Thiron, T.; Cornelissen, M.; Vanhaecke, F.; Doak, S.; Parak, W. J.; De Smedt, S.; Braeckmans, K. *ACS Nano* **2012,** 6, (7), 5767-83.
35. Pelaz, B.; Charron, G.; Pfeiffer, C.; Zhao, Y.; de la Fuente, J.; Liang, X.; Parak, W.; del Pino, P. *Small* **2013,** 9, (9-10), 1573-1584.
36. Rothen-Rutishauser, B.; Kuhn, D.; Ali, Z.; Gasser, M.; Amin, F.; Parak, W.; Vanhecke, D.; Fink, A.; Gehr, P.; Brandenberger, C. *Nanomedicine* **2014,** 9, (5), 607-621.
37. Soliman, M.; Pelaz, B.; Parak, W.; del Pino, P. *Chem. Mat* **2015,** 27, (3), 990-997.
38. del Pino, P.; Yang, F.; Pelaz, B.; Zhang, Q.; Kantner, K.; Hartmann, R.; de Baroja, N.; Gallego, M.; Moller, M.; Manshian, B.; Soenen, S.; Riedel, R.; Hampp, N.; Parak, W. *Angew. Chem.,Int. Ed* **2016,** 55, (18), 5483-5487.
39. Brandenberger, C.; Muhlfeld, C.; Ali, Z.; Lenz, A.; Schmid, O.; Parak, W.; Gehr, P.; Rothen-Rutishauser, B. *Small* **2010,** 6, (15), 1669-1678.
40. Kwon, H.; Lee, J.; Shin, H.; Kim, J.; Choi, S. *Sci. Rep* **2015,** 5.

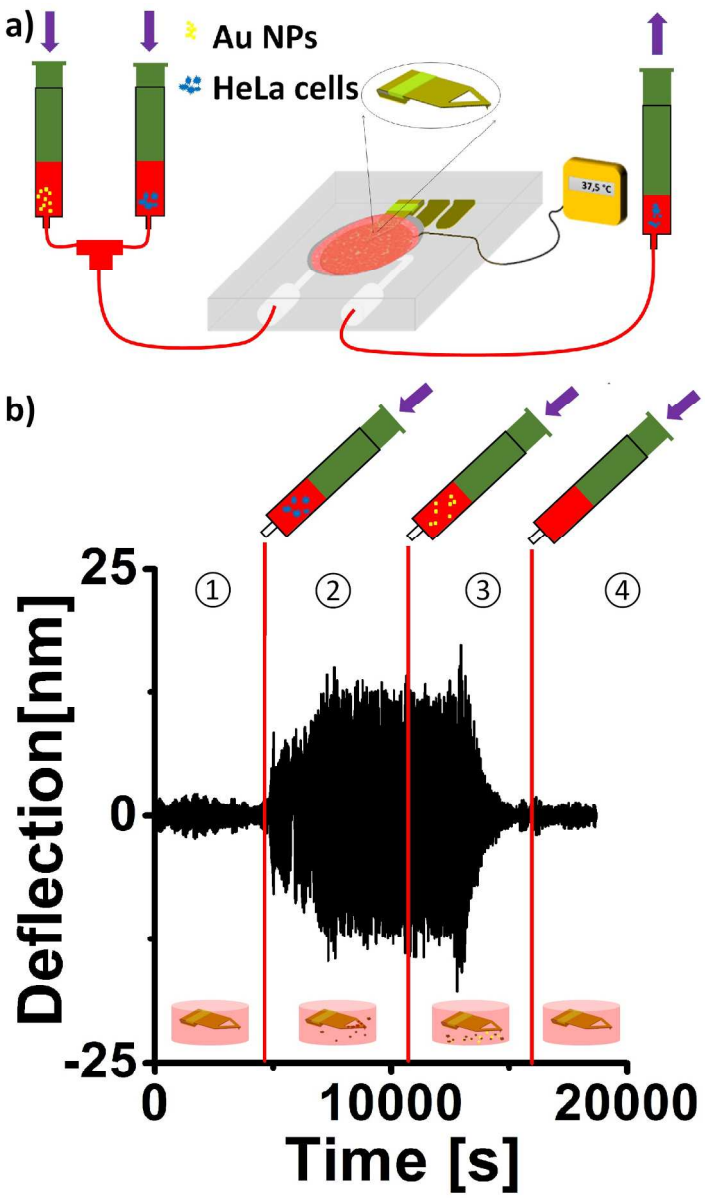

Fig. 1

444x740mm (96 x 96 DPI)

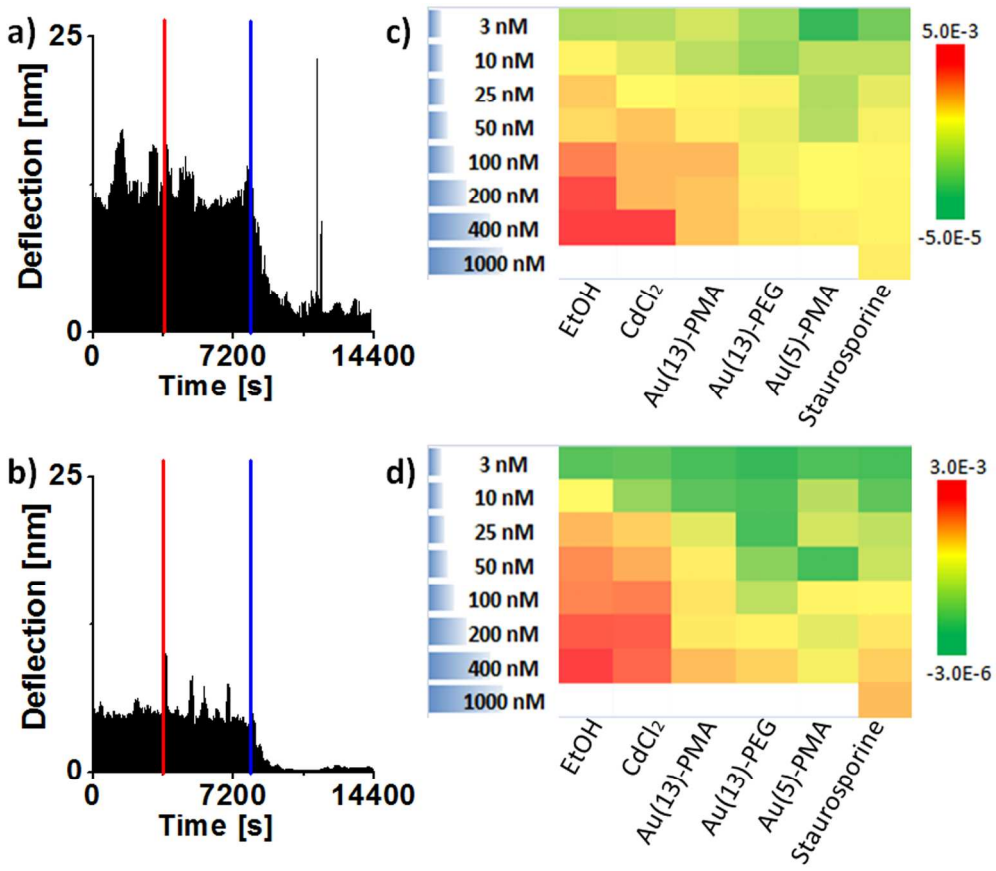

Fig. 2

184x160mm (300 x 300 DPI)

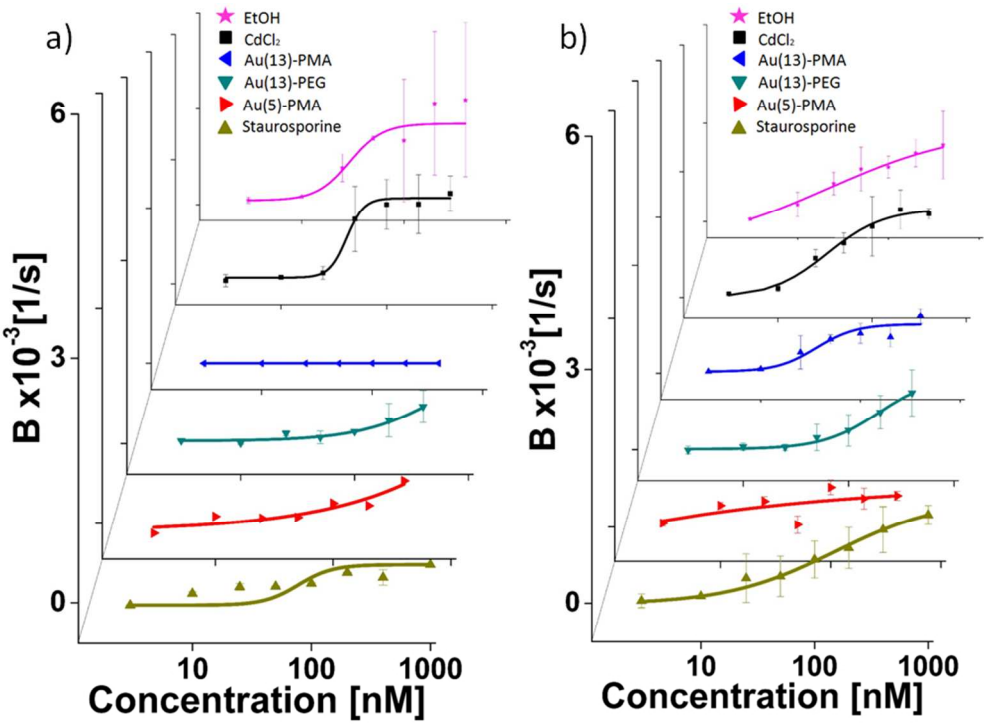

Fig. 3

267x194mm (96 x 96 DPI)

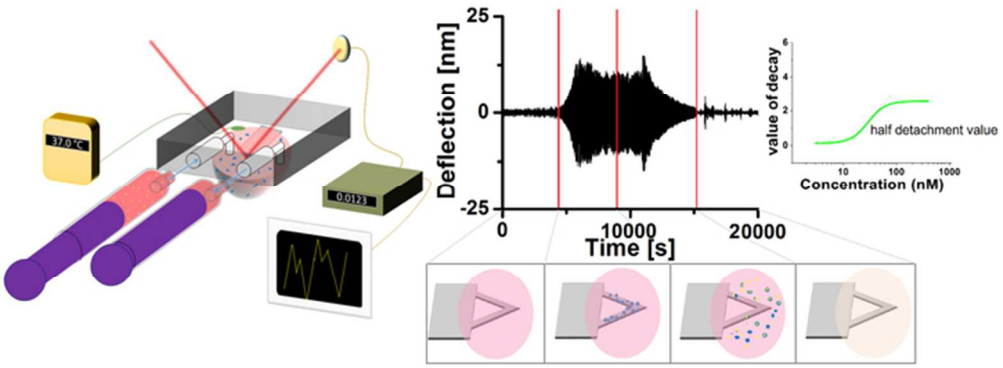

TOC graphic

61x22mm (300 x 300 DPI)

Real-time, label-free monitoring of cell viability based on cell adhesion measurements with an atomic force microscope

Fang Yang[1], René Riedel[1], Pablo del Pino[2], Beatriz Pelaz[2], Alaa Hassan Said[2], Mahmoud Soliman[2], Shashank R. Pinnapireddy[3], Neus Feliu[2], Wolfgang J. Parak[2,4], Udo Bakowsky[3], Norbert Hampp[1,5*]

[1] University of Marburg, Department of Chemistry, Marburg, Germany
[2] University of Marburg, Department of Physics, Marburg, Germany
[3]University of Marburg, Department of Pharmacy, Marburg, Germany
[4] CIC biomaGUNE, San Sebastian, Spain
[5] University of Marburg, Material Science Center, Marburg, Germany

*corresponding author: hampp@uni-marburg.de

Supporting information

I. Synthesis of Au nanoparticles

Synthesis of 13 nm Au nanoparticles: Citrate-capped Au nanoparticles (NPs) with an average inorganic diameter of 13.5 nm (± 0.8 nm), as determined by transmission electron microscopy (TEM), were synthesized by largely following the protocol reported by Schulz et al[1]. Briefly, 144 mL of Milli-Q water was added to 250 mL three-necked round-bottomed flask and heated up until boiling with a heating mantle. First, a mixture of sodium citrate (3.5 mL; 60 mM) and citric acid (1.5 ml; 60 mM) was added to the flask and kept under vigorous stirring for 30 min (450 rpm). A condenser was utilized to prevent the evaporation of the solvent. Then 100 µL of ethylene diamine tetraacetic acid (EDTA 30 mM) was added, followed by 1 mL of 25 mM hydrogen tetrachloroaurate (III) aqueous solution. After ca. 70 sec the color of the mixture changed from pale yellow to wine-red, which is indicative of the growth of the Au NPs. In this moment the heating was switched off, but not the stirring. When the temperature of the mixture had dropped down to 95 ºC, the flask with the NPs was immersed in ice in order to stop the reaction. The absorbance at 450 nm (extinction coefficient $\varepsilon(450) = 1.6 \cdot 10^8\ M^{-1} \cdot cm^{-1}$) was used to determine the concentration of the NPs, as previously described by Haiss et al[2].

Synthesis of 5 nm Au NPs: A modified protocol of the two-phase method published by Brust et al. and Holz et al. was used to produce tetraoctylammonium bromide-capped Au NPs with an inorganic diameter of 5.5 nm (± 1.0 nm), as determined by TEM [3, 4]. Briefly, at room temperature, an aqueous solution of hydrogen tetrachloroaurate-(III) (40 mM, 25 mL) and a solution of tetraoctylammonium bromide (TOAB) in toluene (50 mM, 80 mL) were mixed and vigorously shaken (ca. 5 min) in a 500 mL separation funnel. Then, once the $AuCl_4$ ions were fully transferred into the toluene phase, the organic phase was transferred into a 250 mL round bottom flask. Then, a freshly prepared aqueous solution of $NaBH_4$ (350 mM, 25 mL) was added to the solution of gold precursors in toluene under vigorous stirring and kept under stirring for 1 h. The solution was then transferred to a 500 mL separation funnel and 25 mL of 10 mM HCl was added to remove the excess of $NaBH_4$. The mixture was vigorously shaken and the aqueous phase was discarded. Then 25 mL of 10 mM NaOH were added to remove any excess of acid, followed by 4 washes with Milli-Q water (25 mL). The toluene phase containing the Au NPs was transferred to a 250 mL round bottomed flask. Then, the solution was left under stirring overnight at room temperature. Then, original TOAB coating was exchanged by 1-dodecanethiol, by mixing (65 ºC, 3 h) the original NP dispersion in toluene with a solution of 1-dodecanethiol in toluene (4.17 M,

10 mL). Then, the 1-dodecanethiol-capped Au NPs were purified from agglomerates by centrifugation at $1 \cdot 10^3$ g, whereby the NPs remained in the supernatant. To remove the excess of 1-dodecanethiol, the NPs were precipitated by addition of methanol and collected by centrifugation ($1 \cdot 10^3$g). The washing step with methanol was repeated three times to minimize the presence of free surfactant. In order to calculate the concentration of NPs, the absorbance at 520 nm (extinction coefficient $\varepsilon(520) = 8.7 \cdot 10^6\ M^{-1} \cdot cm^{-1}$) was used, as previously reported[5].

II. Surface modification of Au NPs

PEGylation of 13 nm citrate-capped Au NPs: To 150 mL of the as prepared citrate-capped NPs (NP concentration ca. 1.8 nM), 2.7 mg of α-thio-ω-carboxy poly(ethylene glycol) (HS-PEG-COOH, M_W = 987.19 Da from Iris Biotech) were added, equivalent 10^4 PEG molecules added per NP. Thus, sufficient PEG was added to ensure full PEG saturation of the NP surface. The PEGylated Au NPs were purified from PEG excess and resuspended in deionized water by centrifugal precipitation (three times at $15 \cdot 10^3$ g, 30 min).

Polymer coating poly(isobutylene-alt-maleic anhydride) dodecylamine-grafted, in the following referred to as PMA of 13 nm citrate-capped Au NPs: Citrate-capped Au NPs were transferred from aqueous media to organic solvent following the protocol of Soliman et al.[6] Briefly, $3 \cdot 10^4$ PEG molecules (M_W = 750 Da; α-Methoxy-ω-mercapto-poly(ethylene gylcol) (HS-PEG-CH_3O) from Rapp Polymere) per NP were added and kept under vigorous stirring for 2 h. Then, a 0.4 M solution of dodecylamine (DDA) in chloroform (equal volume as the aqueous solution of NPs) was mixed with the NPs under vigorous stirring, which ultimately allows to transfer the NPs from the aqueous to the chloroform phase. A small amount of NaCl (50 μL 2 M) was added to speed up the NPs' phase transfer. The NPs were then cleaned twice by centrifugal precipitation (8960 g) from excess of PEG and DDA. The precipitated NPs were collected and dispersed in chloroform, in which their concentration was determined by UV/Vis spectroscopy with the molar extinctions coefficients as provided above. Yet, to get PMA-coated Au NPs colloidally stable in aqueous solution, the Au NPs previously coated with PEG/DDA were coated with the amphiphilic polymer PMA by largely following the protocol described by Lin et al[7]. Briefly, 75% of the anhydride rings of poly (isobutylene-alt-maleic anhydride) were modified with DDA by mixing in tetrahydrofuran (THF) at 65 °C under stirring (12 h). The modified polymer (i.e., PMA) was

dried using a Rotavapor at 40 °C under reduced pressure and dispersed in 30 mL chloroform, yielding a stock solution with a final PMA concentration of 0.75 M. (Notice that 0.75 M refers to the concentration of the monomers of poly(isobutylene-alt-maleic anhydride)). Then, to efficiently achieve PMA-coating of the NPs, a specific volume of PMA, which depends on the total effective surface area (A_{eff}) of the NPs, was used as described by Soliman et al.[6] Briefly, the NPs were mixed with PMA (0.75 M in terms of monomer units; $R_{p/Area} = 3000$, where $R_{p/Area}$ refers to the number of PMA monomers added per nm^2 of A_{eff}) in a round flask and diluted with chloroform. After 25 min, the chloroform was slowly evaporated at 42 °C under reduced pressure using a Rotavapor, until the solvent was completely evaporated. This procedure was repeated twice. Finally, the dried product was dissolved in sodium borate buffer (SBB, pH= 12), which hydrolyzed the maleic anhydride groups of the PMA, yielding carboxyl groups and thereby providing the NPs with colloidal stability in aqueous solution. The PMA-coated NPs were then filtrated through a syringe membrane filter (0.22 μm pore size). Finally empty micelles formed by PMA and excess of free PMA were removed by precipitation of the PMA-coated NPs using centrifugation (8960 g; 40 minutes, twice) and the buffer was exchanged to water.

PMA coating of 5 nm Au NPs: Equivalently, PMA coating was carried out as described for the 13 nm NPs. A value $R_{p/Area} = 150$ PMA monomers per nm^2 was used instead, which was experimentally optimized to warrant for colloidal stability of NPs with about the same size of inorganic core. The PMA-coated NPs were purified first by gel electrophoresis, as described in previous works (e.g., see Lin et al.[7]) and then by ultracentrifugation (150 10^3 g; 60 min, three times).

III. Characterization of NPs

Transmission electron microscopy (TEM), UV-Vis spectroscopy, dynamic light scattering (DLS) and laser Doppler anemometry (LDA) were used to analyze the colloidal properties of the NPs.

TEM imaging: TEM images of the samples were acquired in a JEM-1230 transmission electron microscope equipped with a LaB6 cathode running at 120 kV and an ORIOUS SC1000 4008×2672 pixels CCD camera (Gatan UK, Abingdon Oxon, UK). UV-Vis spectra were obtained with an Agilent 8453 spectrometer. DLS and LDA measurements were carried out with a Malvern Zetasizer. Figure S1 (a) and (c) show TEM micrographs of PEGylated 13 nm Au NPs and PMA-coated 5 nm Au NPs with negative staining, in which a PEG layer (thickness of ca. 5

nm around cores of 13 nm) and the PMA-coating (thickness of ca. 5 nm around the 5.5 nm cores) are clearly discernible. Figure S1 (b) shows a TEM micrograph of the PMA-coated NPs (here, only the diameter of the Au core gives contrast).

TEM negative staining: Uranyl acetate was used as negative stain, which allows the formation of a uniform, consistent, and high contrast staining. The sample was prepared on carbon film 400 copper mesh grids purchased from Electron Microscopy Sciences (Hatfield, USA). The specimen grids were exposed to glow-discharge treatment under air plasma for 20 sec ($2.0 \cdot 10^{-1}$ atm and 35 mA) using a MED 020 modular high vacuum coating system (BAL-TEC AG, Balzers, Liechtenstein). Negatively charged carbon grids were used within 5 min after treatment to ensure hydrophilicity. The on-grid negative staining was performed using a slightly modified single-droplet negative-staining procedure. 1.5 μL sample droplet of NP concentration ranging from 6 to 15 nM followed by three 2.5 μL droplets of 0.25 % weight/volume (w/v) uranyl acetate aqueous solution were placed on a clean Parafilm piece. The treated grid was incubated on the sample droplet for 1 min and then on the staining droplets for 3 sec, 3 sec, and 60 sec, respectively. After each incubation step the excess fluid was nearly fully removed by touching the grid edge with Whatman filter paper. Finally the sample was fully dried for 20 min at $2.0 \cdot 10^{-1}$ atm.

UV-Vis absorption spectroscopy: The UV-Vis absorption spectra of the three polymer-coated samples are shown in Figure S1 (d), which clearly show the surface plasmon resonance band of the colloids (ca. 520 nm), more intense in the case of the 13 nm NPs, as expected.

Zetasizer measurements: DLS and ζ-potential values of the three samples are summarized in Table S1. The hydrodynamic diameter (d_h) of the PEGylated Au NPs, as determined by DLS, yielded

sample	d_{TEM} /nm	d_h(number) /nm	ζ-potential /mV
Au(13)-PEG	13.5 ± 0.8	21.9 ± 0.3	-23.0± 1.9
Au(13)-PMA	13.5 ± 0.8	16.7 ± 0.4	-20.2 ± 0.8
Au(5)-PMA	5.5 ± 1.0	15.3± 0.8	-42.7 ± 1.3

Table S1: Comparison of diameters taken from TEM and hydrodynamic diameters taken from DLS, as well as ζ-potential values of the examined NP samples. DLS and ζ-potential data were recorded in MilliQ water. The hydrodynamic diameter correspond to the mean value ± standard deviation as obtained from the number distributions.

22 nm, which matches very well the observations by negative staining TEM. Note however, that the DLS and the negative staining were obtained in aqueous solution and vacuum, respectively. The d_h values of PMA-coated 13 and 5 nm Au colloids were 17 and 11 nm, respectively. Sizes as determined by TEM (inorganic core; d_{TEM}) and DLS (d_h), and ζ-potential values of the polymer coated Au NPs are summarized in Table S1.

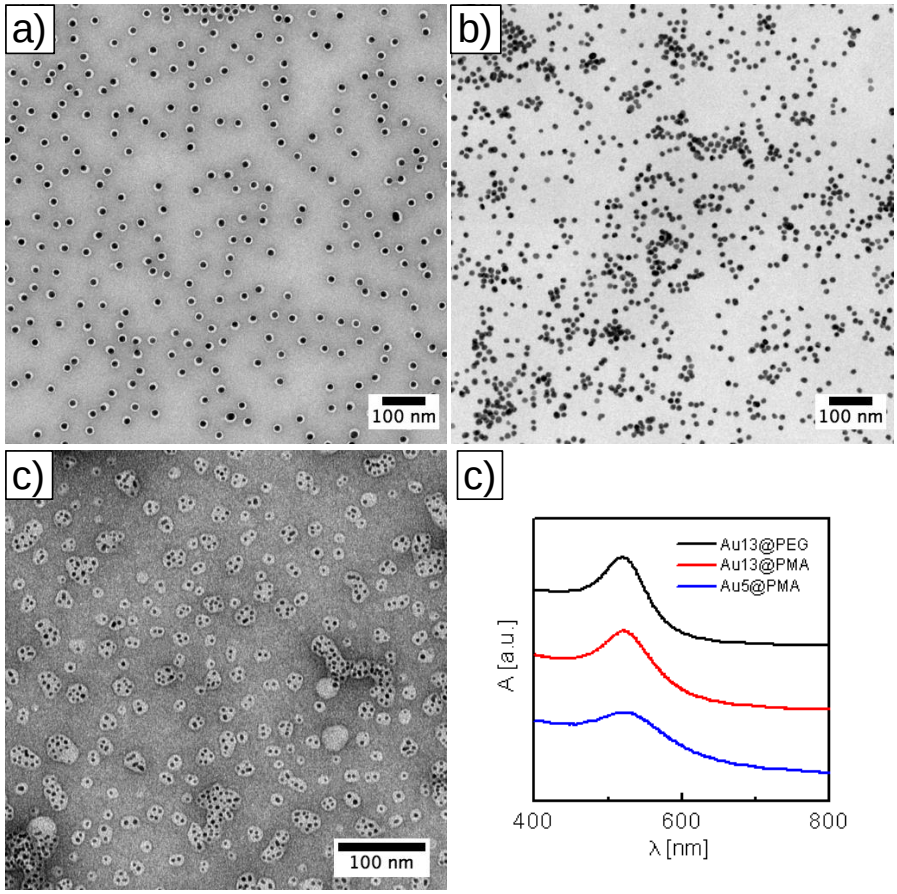

Figure S1. a,c) Negative staining TEM micrographs of samples Au(13)-PEG and Au(5)-PMA. b) TEM micrograph of sample Au(13)-PMA. d) UV-Vis absorption spectra A(λ) of Au(13)-PEG (black line), Au(13)-PMA (red line) and Au(5)-PEG (blue line).

IV. Cantilever deflection upon force loading

The deflection of a cantilever during an atomic force microscope (AFM) measurement is proportional to the force that acts on the cantilever and results from interaction of the cantilever with the sample according to Hook's law:

$$\Delta z = k_f^{-1} F \tag{1}$$

where Δz is the deflection, k_f the spring constant, and F the acting force, i.e. the loading force. In this work, the cantilever was driven to oscillate harmonically by a piezo element. The deflection of pure harmonic oscillations can be described by Equation 2

$$\Delta z = A\cos(2\pi\nu \cdot t + \varphi) \tag{2}$$

where A is the maximum deflection, ν is the frequency, and φ is the phase.

In case a force is applied on a harmonically oscillating cantilever, the total energy of the oscillation, which is proportional to the square of the amplitude A^2, is affected. Hence, the amplitude variation is highly depending on the loading force, while the oscillation frequency in first order remains constant. Equation 3 shows the dependency of the deflection z on an applied loading force F, caused by the mass of the cells attached, at loading position x within a cantilever of length L[8, 9] ($0 \leq x \leq L$).

$$z = \frac{F \cdot x^2(3L - x)}{6EI} = \frac{g \cdot x^2(3L - x)}{6EI} \cdot m_{cell} \tag{3}$$

In eq. 3 the deflection z of the bar depends on the elastic modulus E and I (the area moment of inertia), which are characteristic properties of the bar. F is the loading force, in this case due to the mass of cells, to the bar and the position x indicates where the force applies to the bar. This theory is appropriate to treat cells attached on a cantilever, whereby the deflection is varied depending on the different loading forces. Attached cells will cause an increased deflection. Due to loss of cell adhesion the number of cells remaining on the cantilever decreases, which is observed as decreasing deflection amplitude.

V. Oscillation system setup

Figure S2 shows the fluid chamber, which is the core part of the system. It comprises an inlet and an outlet for fluids and a cantilever holder. The cantilever was mounted and medium was injected through the inlet using a plastic syringe. By this way a droplet formed around the cantilever. Deflection of the cantilever was recorded by the AFM. The proportionality factor so called "deflection sensitivity", which ensures a good linear relation between the voltage applied and the deflection of the spot over the whole area of the screen, should be determined for each measurement, so that loading force of the cantilever can be quantitatively analyzed. Another syringe (Figure S2) was used to remove the fluid through the outlet (blue arrows).

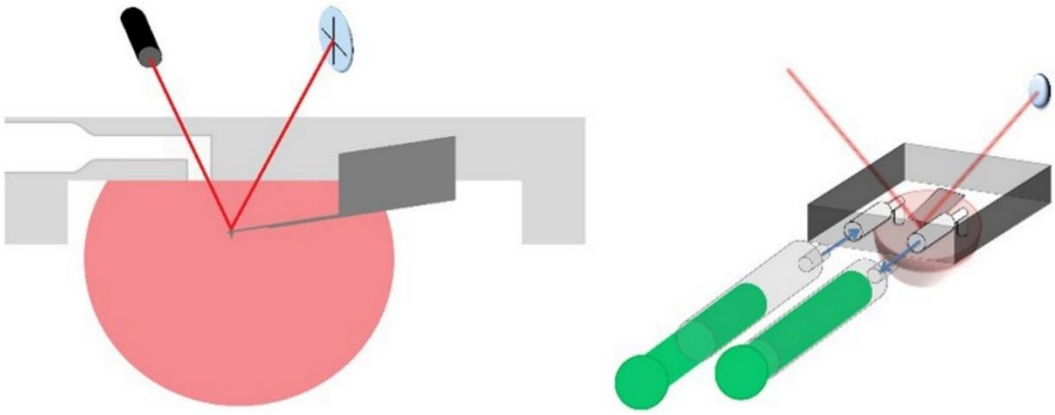

Figure S2: (left) reservoir based on fluid chamber with cantilever, laser beam and photodiode. (right) injecting system using plastic syringes connected to the reservoir.

The fluid chamber inserted into the AFM head was built as a reservoir thermostated to 37 °C. Figure S3 shows the experimental setup. An incubation chamber was used for storing the cells at 37 °C and 5% CO_2. Atmospheric conditions in the chamber were controlled by a heating plate with circulation fan and CO_2 controller. The tip deflection was recorded by the AFM picoforce spectrometer connected to a Keithley 2000 multimeter. During the whole measurement the cantilever was imaged by a camera installed on the microscope, so that the actual status of the cantilever could be correlated with the deflection dependent on the number of attached cells.

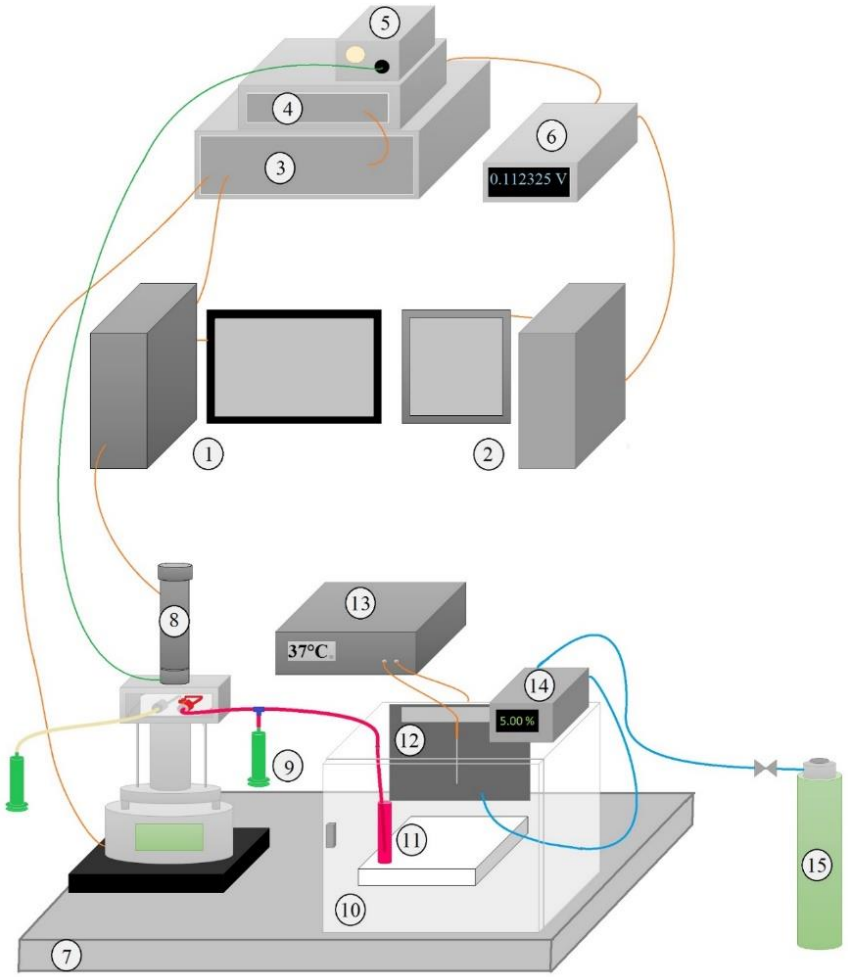

Figure S3: Scheme of the experimental setup. (1) Computer with software for recording visual images from the AFM tip. (2) Monitoring system for measurement and data recording. (3) Multimode Controller of the AFM. (4) Picoforce-spectrometer for deflection recording. (5) Fiber-coupled light source for the optical camera. (6) Keithley 2000 multimeter for recording the data from the Picoforce spectrometer. (7) Laser table. (8) Light microscope with a camera for visually obseration of the cantilever. (9) Input syringe. (10) Incubation box for cells. (11) Cell storage tubes. (12) Heating plate with circulation fan for keeping a homogeneous temperature. (13) Temperature controller for regulation of the heating inside the incubation box. (14) CO_2 controller. (15) CO_2 container.

VI. Optical images of cells attached to the cantilever

Figure S4 shows a scheme of a cantilever (SNL-10, k = 0.12 N/m, f_0 = 23 kHz, Bruker) depicting the area for the cells to attach to. In Figure S5 optical images of cantilevers are shown, which were recorded through an optical microscope. Figure S5a shows the cantilever in air. The surface was found to be clean and flat. Injecting a solution of cells leads to adsorption of cells on the cantilever (shiny spots, see Figure S5b). After washing the cantilever with ethanol and rinsing it with phosphate buffered saline (PBS), most of the cells are desorbed from the cantilever (see Figure S5c). In Figure S5d the cantilever in water is shown and Figure S5e shows the cantilever in cell medium (DMEM-HG medium, Capricorn Scientific, Ebsdorfergrund) supplemented with 10 % fetal bovine serum (Sigma Aldrich). Incubation with gold NPs, depending on the dose and their properties (e.g., size and/or coating), may trigger cell detachment from the cantilever. After removing the liquid, traces of the cells remain on the cantilever (see Figure S5f).

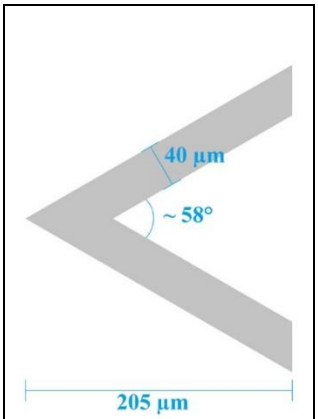

Figure S4: Scheme of cantilever SNL-10.

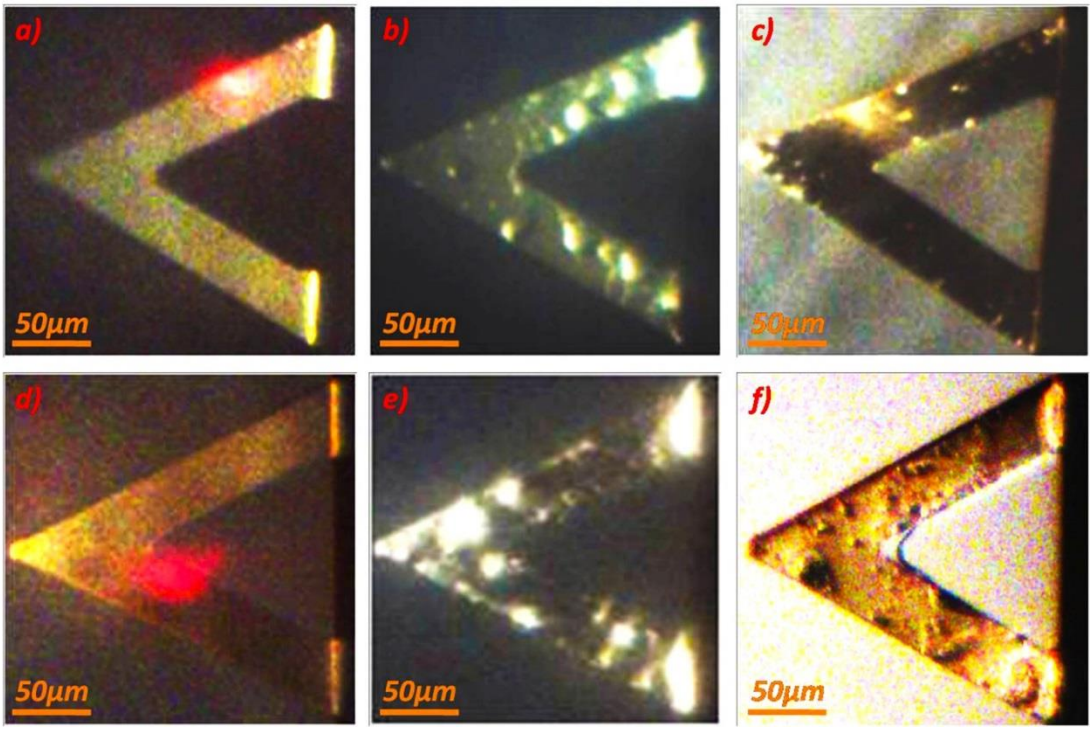

Figure S5: Optical images of one cantilever. (a) In air, before measurement. (b) In solution with cells adsorbed. (c) After cells desorbed and washing with EtOH and PBS. (d) Before measurement, in water. (e) In cell medium, after incubation with Au NPs. (f) After measurement with cells and incubation with Au NPs, without washing, in air.

VII. Baseline correction for the analysis of data

The baseline of the deflection of the cantilever showed a drift over time due to temperature fluctuations in the chamber, fluid flow in the fluid drop, etc. Thus, the baseline was flattened by subtracting a line obtained by the least square fit method (5^{th} degree function). From all data the calculated baseline was subtracted. Figure S6 shows an example of a measurement before (blue) and after (red) baseline correction.

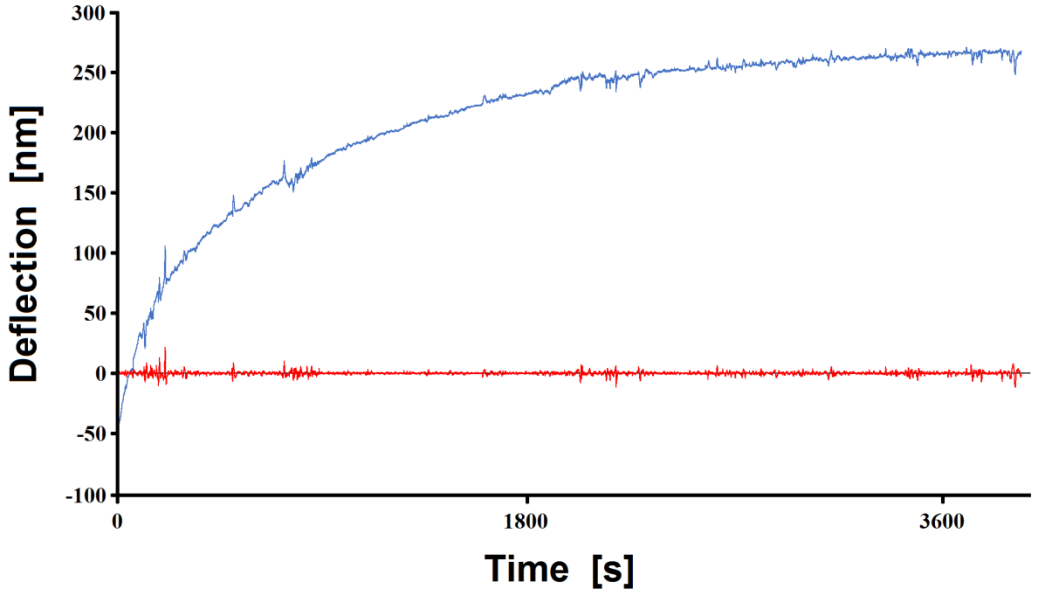

Figure S6: Example of the applied baseline correction of the cantilever deflection trace versus time. The blue data points show the raw measurement data, whereas the red curve represent the calculated data after baseline correction.

VIII. Calculation of damping curve and calculation of damping constant

The amplitude of oscillation increases for increasing numbers of cells attached to the cantilever. When a cell is desorbed from the cantilever upon intoxication the amplitude decreases. The damping constant of the oscillation is linked to the detachment rate of the cells. The detachment rate of cells here is used as measure for cell viability. These measurements are done in real-time. In order to minimize noise not related to the cantilever deflection, a sliding average was calculated for each absolute value for a time interval of -1800 s to +1800 s (see red line in Figure S7). The values higher than the curve of the sliding average were not considered for further calculations.

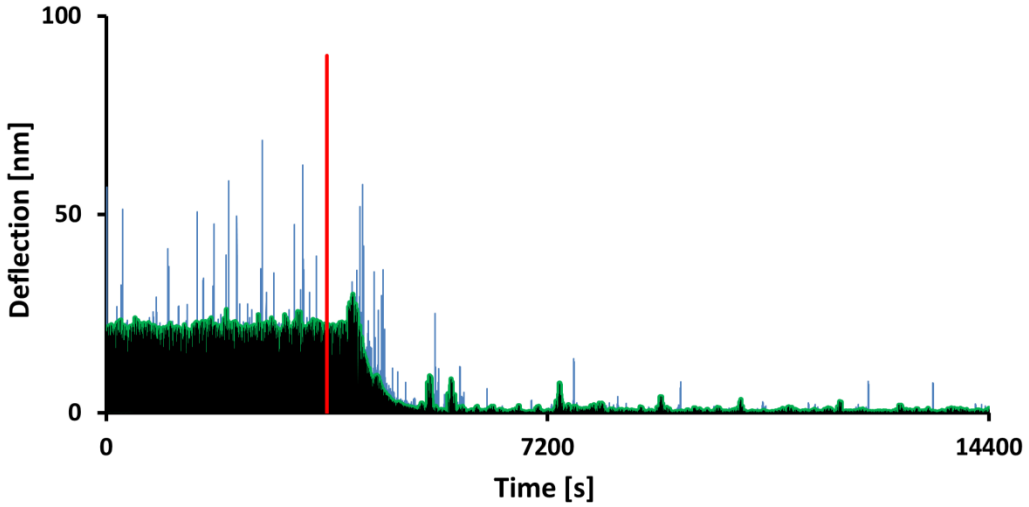

Figure S7: Absolute values of cantilever deflection versus time. HeLa cells were exposed to Au NPs after 3600 sec (vertical red line) of incubation. Outliers (showing in grey) were truncated at the green sliding average line.

The measurements comprise several parts. The first part is from $t_{1,S}$ = 0 s to $t_{1,E}$ = 3600 s. During this period HeLa or MCF7 cells in medium were measured without added Au NPs. After injection of the Au NPs (red line), a certain lack-phase is observed. One may speculate why after a while a small increase in the amplitude is observed. This is in the same range as some random peaks at higher times (e.g. at around 7200 s in Figure S7, Region 1 in Figure S8), and thus will not be further interpreted here. However, soon after Au NP uptake the harmful effect of the Au NPs (at high enough concentrations) can be observed. Cells begin to detach and the deflection decreases (Region 2 in Figure S8), until a minimum is reached.

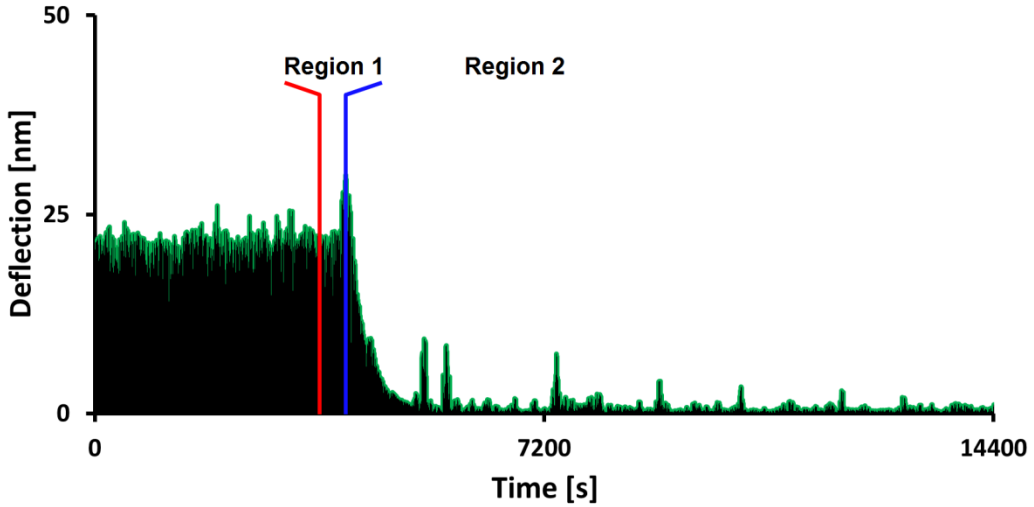

Figure S8: The data shown in Figure S7 (without the outliers) are divided into two parts for further processing. Region 1 (from red to blue line) starts with the addition of the toxic agent, followed by an increment of the deflection, which might be interpreted as an increase of the cells mass. As this is not seen in all measurement using Au NPs (see Figure S9) this is not discussed further here. The important part, region 2 shows the detachment of cells and the accompanied decrease of the amplitude until a constant value is reached.

The damping of the oscillation was approximated by an exponential function (region 2), where A_0 is the amplitude at t = 0, and e^{-Bt} describes the time-dependent damping of the oscillation.

$$A(t) = A_0 e^{-Bt} \tag{4}$$

Resolving this equation for B leads to equation (5) where B is the damping coefficient, which

$$B = -\frac{t}{\tau} ln\left(\frac{A}{A_0}\right) \tag{5}$$

characterizes the cell detachment and amplitude decrease rate, respectively. The B value describes the negative logarithmic ratio of the amplitude at point t and the original amplitude (at t = 0), divided by the time. Keeping in mind that $A/A_0 \leq 1$, the B value is thus an indication for the amplitude damping rate, whereas the damping increases with an increase of B. Thus, a high positive B value stands for a high toxic effect to the cells. The B values were calculated using a least square fit of the data points to the function given in eq. (5).

IX. Raw data of all toxicant measurements

The effect of addition of Au NPs etc. to attached cells was monitored and recorded by curves of deflection versus time. All potentially toxic agents, i.e., ethanol (EtOH) (70%), $CdCl_2$, Au(5)-PMA, Au(13)-PMA, Au(13)-PEG, and staurosporine (STS) were measured with HeLa cells and MCF7 cells respectively. The original data are presented below.

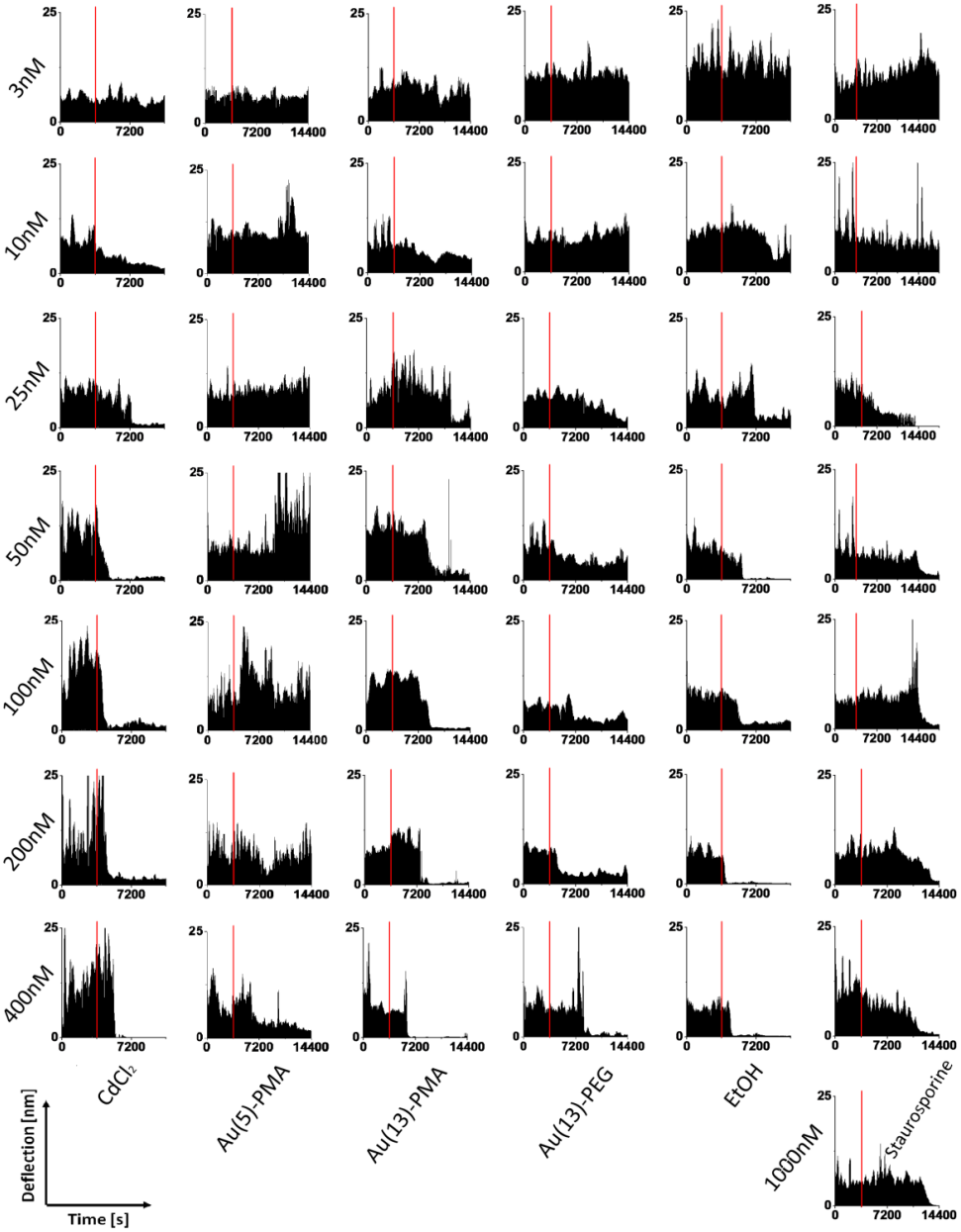

Figure S9-1: Raw data of deflection curves upon addition of all the different agents with different concentration from 3 nM to 400 nM or 1000 nM as recorded with HeLa cells. The red lines indicate the time when the agents were injected to the cells.

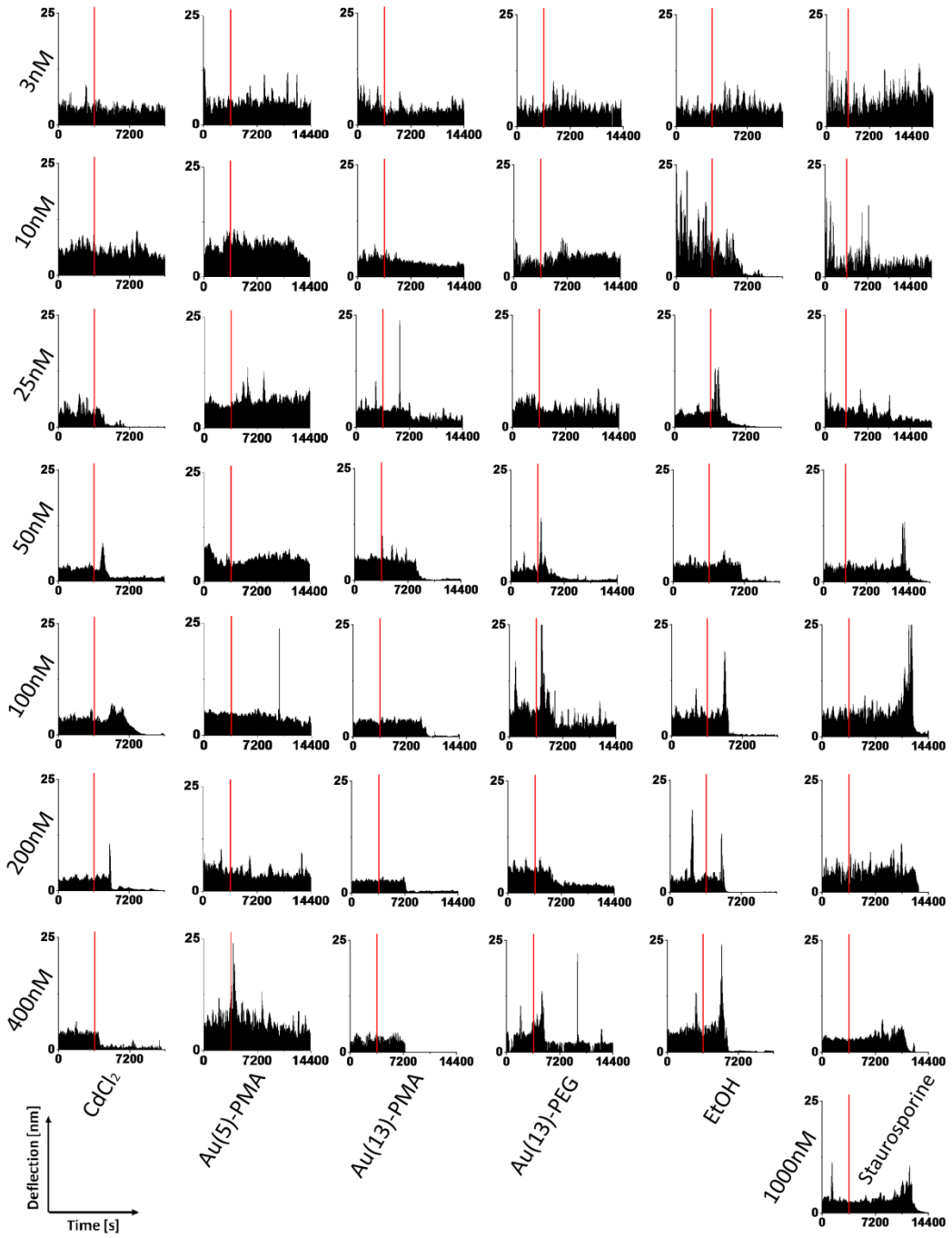

Figure S9-2: Raw data of all deflection curves upon addition of the different agents with different concentration from 3 nM to 400 nM or 1000 nM to MCF7 cells. The red lines indicate the time when the agents were injected to the cells.

Using a homemade software, the B-values of each trace were calculated. For each series of agents, at least double measurements were done, the mean B-values for both cell lines upon incubation with different agents were collected and are shown in Table S2 below.

	HeLa			MCF7	
	Con[nM]	B-value [1/s]	Deviation [1/s]	B-value [1/s]	Deviation [1/s]
$CdCl_2$	3	8,01E-05	1,46E-04	9,27E-05	1,26E-05
	10	1,63E-04	5,22E-05	2,21E-04	7,17E-05
	25	2,70E-04	1,52E-04	9,39E-04	2,06E-04
	50	1,60E-03	7,90E-04	1,28E-03	2,40E-04
	100	1,90E-03	5,97E-04	1,74E-03	7,12E-04
	200	1,90E-03	7,08E-04	2,05E-03	4,70E-04
	400	2,20E-03	4,21E-04	1,96E-03	1,24E-04
EtOH	3	-1,40E-04	3,80E-05	5,41E-05	4,04E-05
	10	9,75E-05	5,30E-05	3,10E-04	4,74E-05
	25	6,94E-05	1,25E-05	3,68E-04	6,79E-05
	50	8,35E-05	4,10E-05	3,20E-05	1,26E-04
	100	2,80E-04	8,10E-05	5,71E-04	1,04E-04
	200	2,48E-04	1,10E-04	4,09E-04	1,51E-04
	400	5,92E-04	2,80E-04	4,54E-04	6,65E-05
Au(5)-PMA	3	1,32E-04	1,05E-04	3,58E-05	1,43E-06
	10	9,23E-05	9,26E-05	8,14E-05	2,50E-05
	25	2,08E-04	3,86E-05	4,04E-04	3,17E-04
	50	6,08E-04	3,23E-04	6,50E-04	8,54E-05
	100	1,87E-03	3,86E-04	7,63E-04	1,93E-04
	200	1,56E-03	2,48E-04	6,88E-04	1,89E-04
	400	1,59E-03	2,74E-06	1,12E-03	1,54E-04
Au(13)-PMA	3	5,10E-05	4,27E-06	-6,97E-06	6,16E-05
	10	2,50E-05	2,24E-05	4,84E-05	5,98E-05
	25	1,99E-04	4,39E-05	3,85E-05	4,95E-05
	50	1,76E-04	1,05E-04	1,98E-04	2,15E-04
	100	1,93E-04	5,62E-06	3,15E-04	2,55E-04
	200	5,79E-04	2,72E-04	6,08E-04	2,71E-04
	400	7,91E-04	2,61E-04	9,21E-04	3,74E-04
Au(13)-PEG	3	7,10E-05	9,77E-05	7,51E-05	3,68E-05
	10	2,27E-04	3,85E-05	5,27E-04	3,78E-04
	25	1,46E-03	4,30E-04	1,17E-03	3,43E-04
	50	1,12E-03	7,07E-05	1,61E-03	6,63E-04
	100	3,37E-03	1,93E-03	1,67E-03	3,28E-04
	200	4,76E-03	2,25E-03	2,09E-03	4,12E-04
	400	4,99E-03	2,41E-03	2,34E-03	1,02E-03
Staurosporine	3	-2,81E-05	4,96E-07	3,20E-05	9,07E-05
	10	9,85E-05	2,33E-05	9,07E-05	1,40E-05
	25	1,68E-04	4,12E-05	3,22E-04	3,13E-04
	50	1,98E-04	4,66E-06	3,46E-04	2,60E-04
	100	2,31E-04	1,05E-05	5,64E-04	2,38E-04
	200	3,76E-04	2,93E-06	7,12E-04	2,65E-04
	400	3,80E-04	9,54E-05	9,50E-04	2,96E-04
	1000	5,42E-04	1,00E-04	1,14E-03	1,22E-04

Table S2: Mean B-values as determined from 2 times measurements for each agent and the respective standard deviations.

X. Reference Assay

Cell culture: HeLa and MCF 7 cells were obtained from the American Type Culture Collection (ATCC, Manassas, VA). Briefly, HeLa cells were cultured in Dulbecco's Modified Eagle's Medium (DMEM) (# D5796) containing 10% Fetal Bovine Serum (FBS) (#S0615), 1% of Penicillin/Streptomycin (P/S) (# 15140-1229) and GlutaMAX™ (#35050-038). MCF7 cells were cultured in Eagle's Minimum Essential Medium (EMEM) (# M5650 supplemented with 10% FBS, 1% of P/S and 0.01 mg/mL human recombinant insulin (# I3536). The cell cultures were kept at 37 °C in a humidified atmosphere of 5% CO_2 in air. At confluence, cells were washed with PBS and detached with 0.05% Trypsin EDTA (# 25300-054) solution. Cells then were reseeded in flasks for cell culture or seeded in 96-well plates for the experiments.

Cell viability assay: Cell viability of HeLa and MCF7 cells exposed to Au NPs and chemical agents was evaluated by the Resazurin assay (AlamarBlue® (# 765506) Thermo Fisher, Germany) as previously reported[10-12]. For that, HeLa and MCF7 cells were seeded in 96 black polystyrene plates at the density of 10.000 cells/well in complete cell culture media and were incubated overnight at 37 °C, 5% CO_2. The next day, cells were exposed to NPs and chemical agents at desired concentration for 4 h in the presence or absence of 5% CO_2 at a final volume of 100 μL per well. After the desired time, cells were washed once with PBS, then 100 μL of 10% resazurin solution (in complete cell media) was added to the cells and incubated for 4 h at 37 °C and 5% CO_2. The fluorescence intensity was measured for the presence of resazurin and resorufin with a 96-microwell plate reader connected to a fluorometer (Fluorolog-3, from Horiba Jobin Yvon, Germany) at an excitation wavelength of 560 nm. The emission was recorded in the range of 570-650 nm, of which an integrated fluorescence intensity was determined. This integrated fluorescence intensity was considered to be proportional to cell viability. Cell viability was normalized to 100% for untreated cells. The results are presented as mean cell viability ± the respective standard deviation (SD), as obtained from three independent experiments (e.g. cell cultures), each one performed in triplicate. Upon incubation with high concentration of toxic agents, cell viability is decreased.

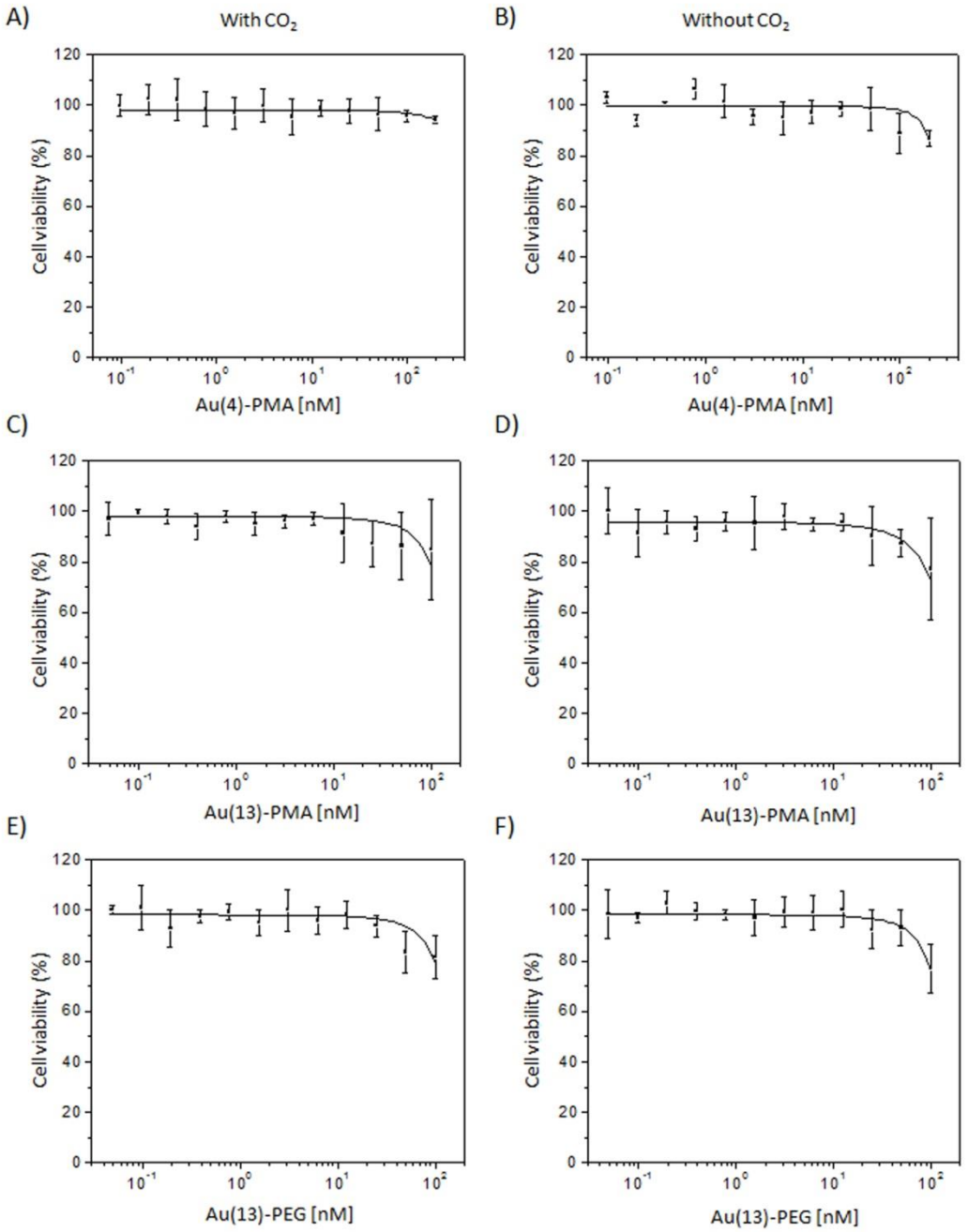

Figure S10-1: Cell viability of HeLa cells exposed to Au NPs. Cell viability was assessed by the resazurin assay upon exposure of HeLa cells to Au(5)-PMA, Au(13)-PMA, and Au(13)-PEG for 4 h, with CO_2 (A, C, E), and without CO_2 (B, D, F). Results are presented as mean cell viability ± SD from three independent experiments.

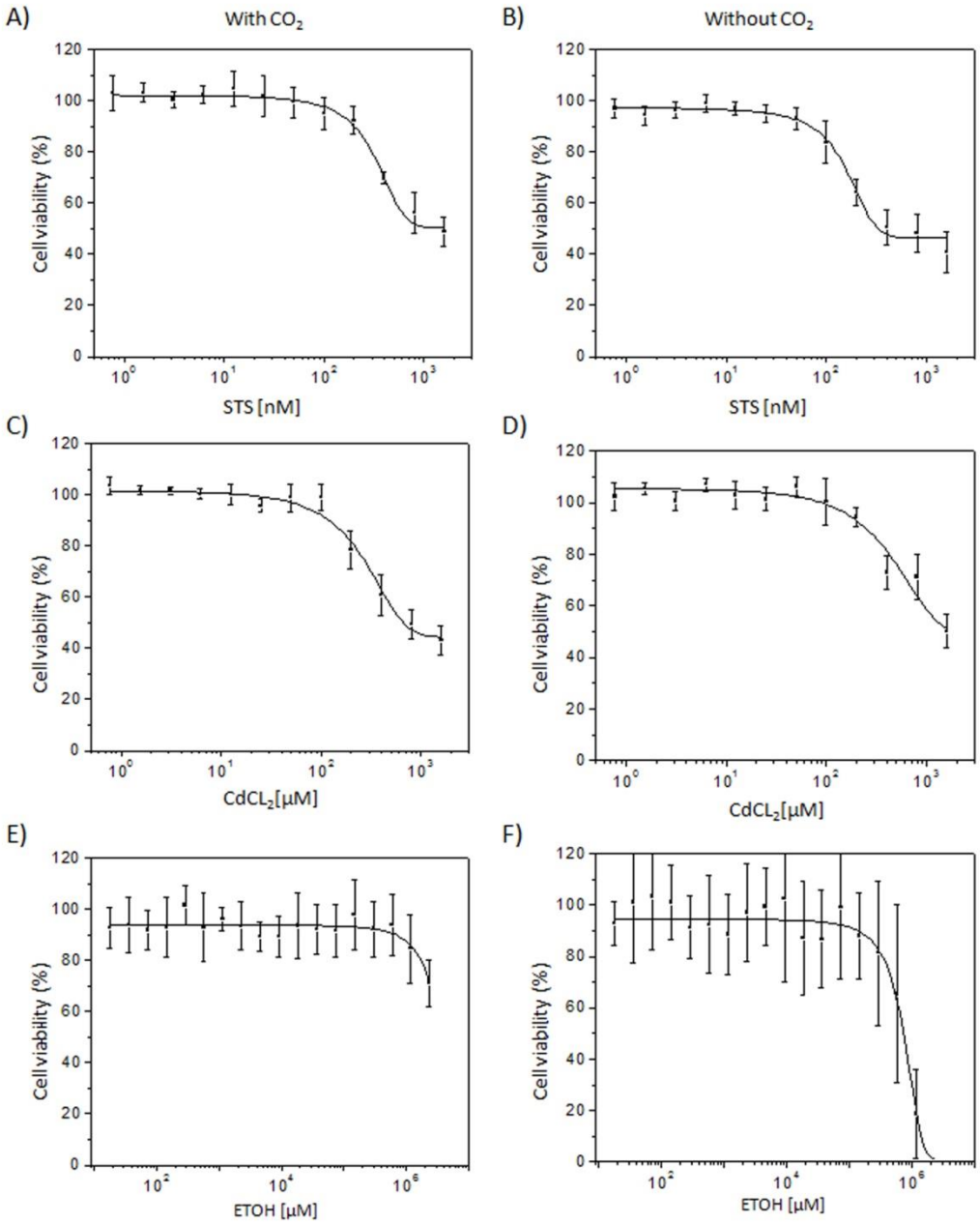

Figure S10-2: Cell viability of HeLa cells exposed to chemical agents. Cell viability was assessed by the resazurin assay upon exposure of HeLa cells to STS, EtOH, and $CdCl_2$ for 4 h with CO_2 (A, C, E), and without CO_2 (B, D, F). Results are presented as mean cell viability ± SD from three independent experiments.

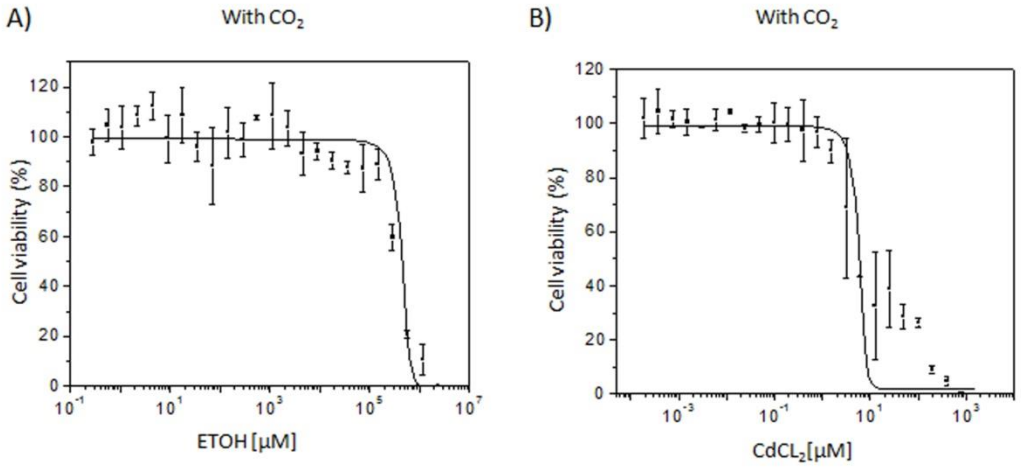

Figure S10-3: Cell viability of HeLa cells exposed to chemical agents. Cell viability was assessed by the resazurin assay upon exposure of HeLa cells to EtOH and $CdCl_2$ for 24 h with CO_2 (A, B). Results are presented as mean cell viability ± SD from three independent experiments.

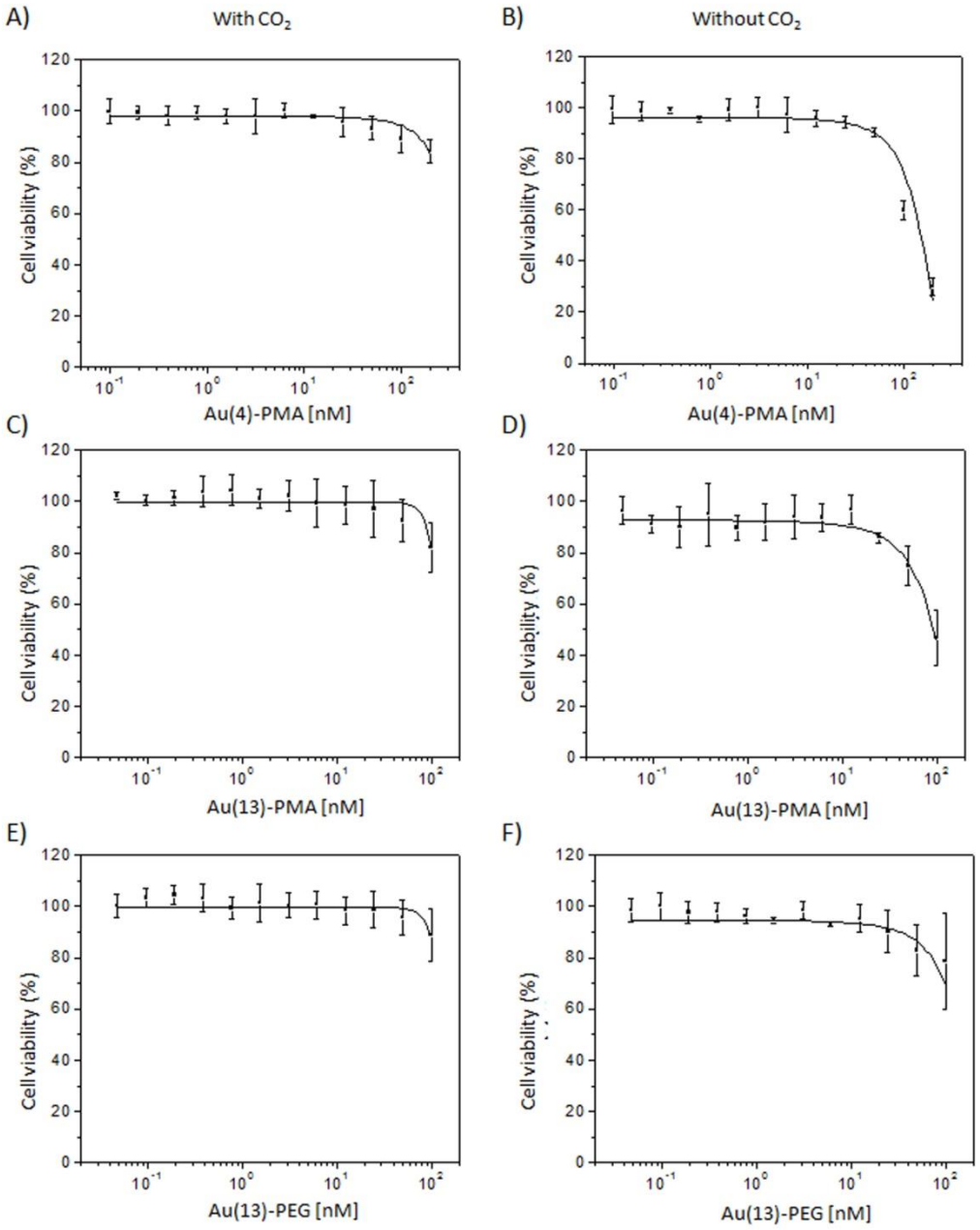

Figure S10-4: Cell viability of MCF7 cells exposed to Au NPs. Cell viability was assessed by the resazurin assay upon exposure of MCF7 cells to Au(5)-PMA, Au(13)-PMA, and Au(13)-PEG for 4 h, with CO_2 (A, C, E), and without CO_2 (B, D, F.) Results are presented as mean cell viability ± SD from three independent experiments.

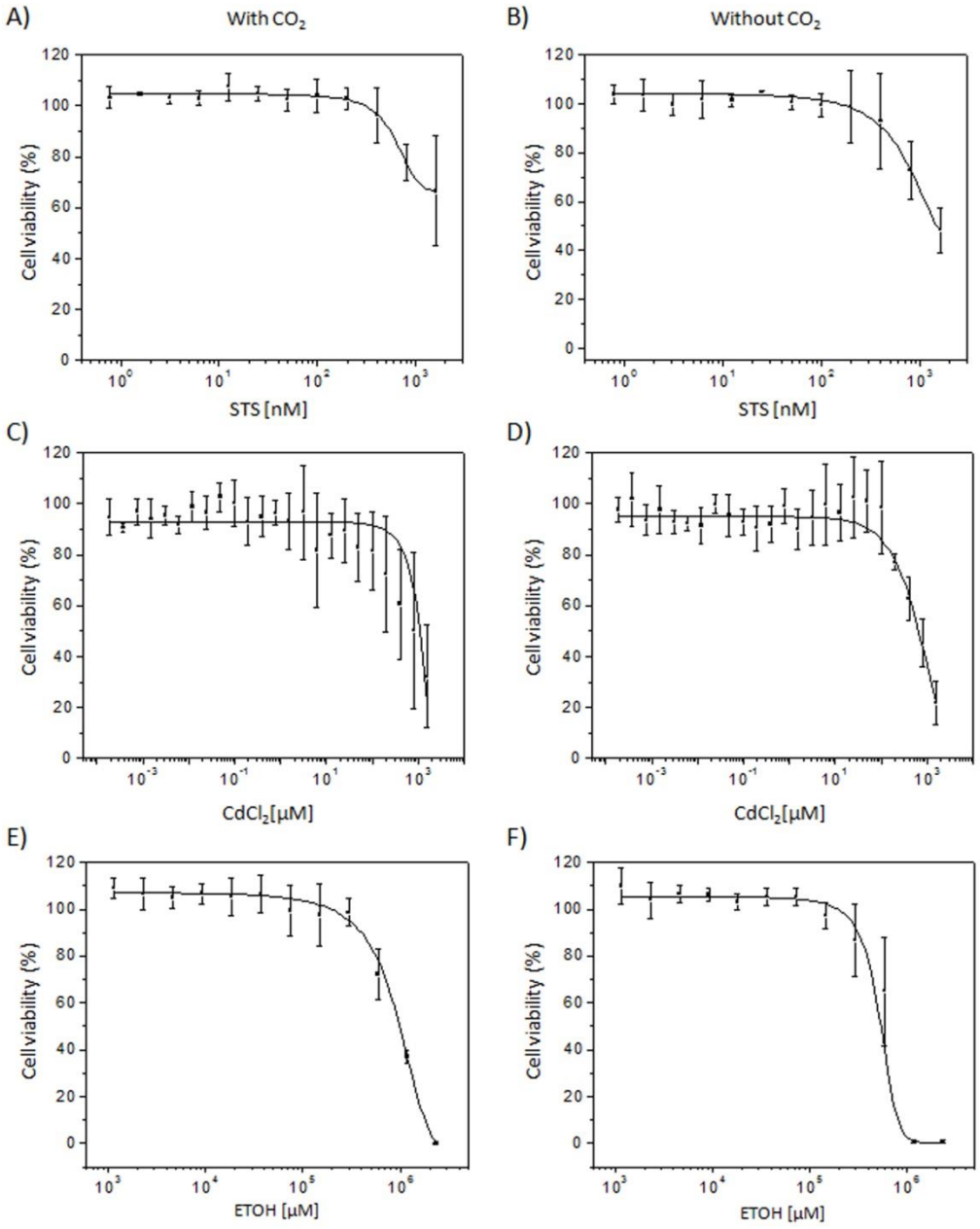

Figure S10-5: Cell viability of MCF7 cells exposed to different chemical agents. Cell viability was assessed by the resazurin assay upon exposure of MCF7 cells to STS, EtOH and CdCl2 for 4 h with CO_2 (A, C, E), and without CO2 (B, D, F). Results are presented as mean cell viability ± SD from three independent experiments.

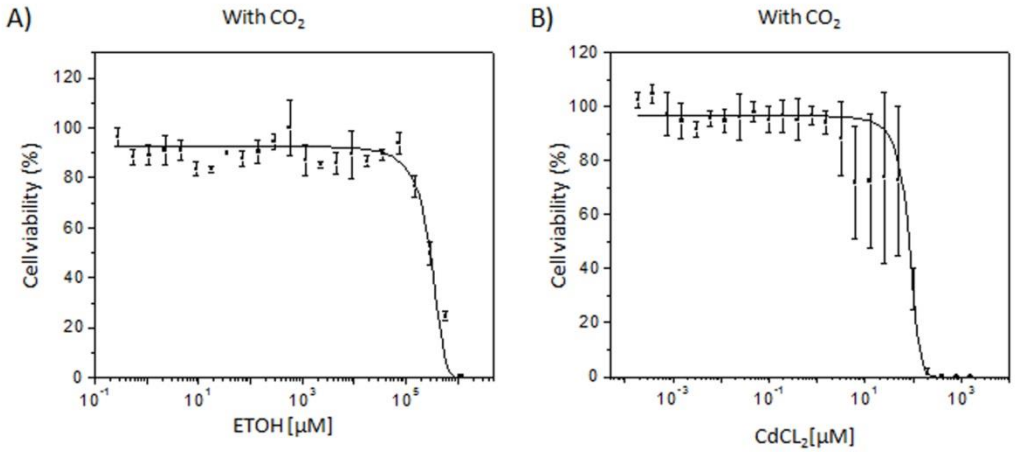

Figure S10-6: Cell viability of MCF7 cells exposed to chemical agents. Cell viability was assessed by the resazurin assay upon exposure of MCF7 cells to EtOH and $CdCl_2$ for 24 h with CO_2 (A, B). Results are presented as mean cell viability ± SD from three independent experiments.

XI. Safety precautions when working with Staurosporine

Staurosporine is protein kinase inhibitor and toxic. CAS number: 62996-74-1, Alfa Aesar.

XI. References

1. Schulz, F.; Homolka, T.; Bastus, N.; Puntes, V.; Weller, H.; Vossmeyer, T. *Langmur* **2014,** 30, (35), 10779-10784.
2. Haiss, W.; Thanh, N. T. K.; Aveyard, J.; Fernig, D. G. *Anal. Chem.* **2007,** 79, (11), 4215-4221.
3. Brust, M.; Walker, M.; Bethell, D.; Schiffrin, D.; Whyman, R. *J. Chem. Soc., Chem. Commun* **1994**, (7), 801-802.
4. Holz, M.; Haselmeier, R.; Mazitov, R.; Weingartner, H. *J. Am. Chem. Soc* **1994,** 116, (2), 801-802.
5. Kreyling, W.; Abdelmonem, A.; Ali, Z.; Alves, F.; Geiser, M.; Haberl, N.; Hartmann, R.; Hirn, S.; de Aberasturi, D.; Kantner, K.; Khadem-Saba, G.; Montenegro, J.; Rejman, J.; Rojo, T.; de Larramendi, I.; Ufartes, R.; Wenk, A.; Parak, W. *Nat Nanotechnol* **2015,** 10, (7), 619-+.
6. Soliman, M.; Pelaz, B.; Parak, W.; del Pino, P. *Chem. Mat* **2015,** 27, (3), 990-997.
7. Lin, C.; Sperling, R.; Li, J.; Yang, T.; Li, P.; Zanella, M.; Chang, W.; Parak, W. *Small* **2008,** 4, (3), 334-341.
8. Longo, G.; Alonso-Sarduy, L.; Rio, L. M.; Bizzini, A.; Trampuz, A.; Notz, J.; Dietler, G.; Kasas, S. *Nat Nanotechnol* **2013,** 8, (7), 522-6.
9. A.Budó, *Theoretische Mechanik*. 11 ed.; VEB Deutscher Verlag der Wissenschaften: Berlin, 1987; 'Vol.' 25, p 604.
10. O'Brien, J.; Wilson, I.; Orton, T.; Pognan, F. *Eur. J. Biochem* **2000,** 267, (17), 5421-6.
11. O'Brien, J.; Wilson, I.; Ortaon, T.; Pognan, F. *Toxicology* **2001,** 164, (1-3), 132-132.
12. Feliu, N.; Kohonen, P.; Ji, J.; Zhang, Y.; Karlsson, H. L.; Palmberg, L.; Nystrom, A.; Fadeel, B. *ACS Nano* **2014,** 9, (1), 146-63.